Wrocław University of Technology
Centre of Advanced Materials and Nanotechnology

Materials Science
Poland

Vol. 25 • No. 4 • 2007

Oficyna Wydawnicza Politechniki Wrocławskiej

Contents

P. K. Biju, M.N. Radhakrishnan Nair, G.V. Thomas, M.R. Gopinathan Nair, Plasticizing effect of epoxidized natural rubber on PVC/ELNR blends prepared by solution blending 919

V. Krylova, Spectroscopic and diffraction studies of chemical deposition of copper sulfide films on polyamide surface using potassium pentathionate 933

D. W. Zhou, J. Zhang, P. Peng, J.S. Liu, Alloying effects on the energy and electronic structures of vanadium hydrides 947

S. Tanriverdi, B. Mavis, G. Gündüz, Ü. Çolak, Electrospinning and characterization of alumina borosilicate ceramic nanofibres 957

Y. -H. Lee, K.-S. Hwang, Preparation of lithium zirconate nanopowder prepared by electrostatic spraying for CO_2 sorbent 969

G. Qinlin, X. Cheng, Nanotribological characteristics of lanthanum-based thin films on phosphorylated 3-aminopropyltriethoxysilane self-assembled monolayers 977

M. Kulczyk, W. Pachla, A. Mazur, M. Suś-Ryszkowska, N. Krasilnikov, K.J. Kurzydłowski, Producing bulk nanocrystalline materials by combined hydrostatic extrusion and equal-channel angular pressing 991

R. Gong, Y. He, X. Li, C. Liu, X. Wang, Study on absorption and mechanical properties of rubber sheet absorbers 1001

G. Ionita, C. Ghica, P. Ionita, Probing cellulose wettability by electron paramagnetic resonance 1011

S. M. Rabiee, F. Moztarzadeh, H.S. Kenari, M. Solati-Hashjin, Preparation and properties of a porous calcium phosphate bone graft substitute 1019

M. Edrissi, R. Norouzbeigi, Synthesis and characterization of alumina nanopowders by combustion of nitrate-amino acid gels 1029

K. Kledzik, M. Jamrógiewicz, M. Gwiazda, E. Wagner-Wysiecka, J. Jezierska, J.F. Biernat, A.M. Kłonkowski, Optical recognition elements. Macrocyclic imidazole chromoionophores entrapped in silica xerogel 1041

W. Skoneczny, M. Bara, Aluminium oxide composite layers obtained by the electrochemical method in the presence of graphite 1053

B. Żurowska, J. Mroziński, J. Ochocki, Coordination properties of the diethyl 2-quinolilmethylphosphonate ligand with chloride and nitrate transition-metal salts 1063

R. V. Mangalaraja, K.V.S. Ramam, J. Ravi, C.P. Camurri, Microwave-flash combustion synthesis of yttria nanopowders 1075

J. Sosnowski, Analysis of the pinning interaction in high-temperature superconductors 1081

K. Baltakys, R. Siauciunas, Formation of gyrolite in the CaO–quartz–Na_2O–H_2O system 1089

C. Wang, S. Hao, F. Shi, J. Qi, Y. Tao, B. Wang, Interactions of high current pulsed electron beam with phosphate laser glass 1101

M. R. Vaezi, A. Esmaielzadeh Kandjani, L. Nikzad, N.A. Arefian, S. Alibeigi, M. Farzalipour Tabriz, S.H. Mir Shah Ghassemi, J. Samei, Synthesis of Zn_2TiO_4 and $ZnTiO_3$ nanocomposites by the CBD method 1109

L. -L. Gao, X.-H. Cheng, Grain refinement and mechanical properties of Cu–Al 10%– Fe 4% alloy produced by ECAE 1119

S. Jana, B. Karmakar, P. Kundu, Unusual visible absorption in high PbO lead borate glass 1127

K. Yildiz, N. Karakus, N. Toplan, H.Ö. Toplan, Densification and grain growth of TiO_2-doped ZnO 1135

B. Zhao, Y. Wang, H. Guo, J. Wang, Y. He, Z. Jiao, M. Wu, Iron oxide(III) nanoparticles fabricated by electron beam irradiation method 1143

S. J. Royaee, M. Sohrabi, C. Falamaki, Methanol dehydration to dimethyl ether using modified clinoptilolite 1149

T. Abbas, M. Ullah, A.M. Rana, R.M. Arif Khalil, Calculation of short range order in Ni–Rh, Ni–Pd and Cu–Rh alloys 1161
G. D. Sharma, V.S. Choudhary, Y. Janu, M.S. Roy, Mechanism of charge generation and photovoltaic effects in lead phthalocyanine based Schottky barrier 1173

II Workshop "Hybrid Nanostructured Materials. Synthesis, Properties, Applications", Dresden, Germany, 8–9 November, 2006

A. Elsner, H. Hermann, Computer simulation and optimization of properties of porous low-*k* dielectrics 1193
K. Zagorodniy, H. Hermann, M. Taut, Molecular design of ultralow-*k* insulator materials 1203
B. Schmidt, K.-H. Heinig, L. Röntzsch, K.-H. Stegemann, Nanocluster memories by ion beam synthesis of Si in SiO_2 1213

Conference of the Scientific Network "New Materials for Magnetoelectronics – MAG-EL-MAT 2007", Będlewo near Poznań, 7–10 May 2007

A. Go, M. Pugaczowa-Michalska, L. Dobrzyński, *Ab initio* study of ordering degree in Fe_3Si doped with Mn 1223
Ł. Wasylkowicz, A. Jezierski, A. Szytuła, B. Penc, Electronic properties of LaNiIn doped with hydrogen 1229
M. Misiorny, J. Barnaś, Current-induced switching of a single-molecule magnet with an arbitrary oriented easy axis 1235
P. Stefański, Two-level quantum dot in the Aharonov–Bohm ring. Towards understanding "phase lapse" 1243
A. Szajek, I. Okońska, M. Jurczyk, Electronic and electrochemical properties of Mg_2Ni alloy doped by Pd atoms 1251
B. Andrzejewski, E. Guilmeau, A. Kowalczyk, A. Szlaferek, New superconducting phases in $Mo_2Re_3B_x$–$Mo_3Re_2B_x$ eutectic 1259
M. Szlawska, A. Pikul, D. Kaczorowski, Ferromagnetic and spin-glass properties of single -crystalline U_2NiSi_3 1267
B. Szymański, M. Urbaniak, F. Stobiecki, Magnetic and magnetoresistive properties of CoFe /Au/Co/Au multilayered structures 1275
J. Dubowik, I. Gościańska, Y.V. Kudryavtsev, V.A. Oksenenko, Structure and magnetism of Co_2CrAl Heusler alloy films 1281
P. Mazalski, I. Sveklo, M. Tekielak, A. Kolendo, A. Maziewski, P. Kuświk, B. Szymański, F. Stobiecki, Magnetic properties of $(Co/Au)_N$ multilayers with various numbers of repetition N 1289

Materials Science-Poland, Vol. 25, No. 4, 2007

Plasticizing effect of epoxidized natural rubber on PVC/ELNR blends prepared by solution blending

P. K. BIJU[1], M. N. RADHAKRISHNAN NAIR[2], G. V. THOMAS[1], M. R. GOPINATHAN NAIR[1*]

[1]School of Chemical Sciences, Mahatma Gandhi University, Priyadarshini Hills, P.O. Kottayan-686560, Kerala, India

[2]Department of Chemistry, D.B.College, Thalayolaparambu, Kottayam-686605, Kerala, India

A series of polymer blends of poly(vinyl chloride) (PVC) and epoxidized liquid natural rubber (ELNR) were prepared and characterized. The aim of the work was to study the plasticizing effect of ELNR on the PVC/ELNR blend systems. Thermal properties of the samples were studied by differential scanning calorimetry (DSC). The glass transition temperature of the samples decreased with both degree of epoxidation and the percentage of composition of the samples. The scanning electron microscope (SEM) studies point to the two phase morphology. Tensile test results for the blend samples have been compared. From tensile tests, it was found that elongation of the materials increased with degree of epoxidation. On the other hand, tensile strength and modulus of the material decreased with the epoxide content. A good plasticization effect was observed for samples of ELNR with wt. 50% of epoxidation.

Key words: *polyvinyl chloride; epoxidized natural rubber; plasticizing effect; blend*

1. Introduction

Polymer blends and alloys have received widespread attention for the last several decades. Polymer blends are defined as physical mixture of two or more polymers. They may be divided into different categories: so-called miscible blends in which the components exist in a simple homogeneous phase and immiscible ones in which the components exist in two distinct separated phases. Generally, the former ones offer various advantages over the latter. The origin of miscibility between the polymer pairs has been understood based on theoretical background and experimental results [1, 2]. Most polymers are thermodynamically immiscible. In immiscible polymer blends,

*Corresponding author, e-mail: mrg.nair@rediffmail.com

morphology is affected by the composition, viscosity ratio, interfacial tension, processing conditions etc. [3–5]. Several studies have been reported in which epoxidised polydienes were used as polymeric plasticizers to PVC. Margaritas et al. [6] reported the plasticization of PVC with epoxidised polybutadiene (EPB) as a function of the degree of PB epoxidation, its microstructure and molecular weight.

As a part of the miscibility studies of chlorinated polymers with epoxidized polyhydrocarbons [7], the compatibility behaviour of PVC with epoxidized natural rubber has been reported. Epoxidized liquid natural rubber (ELNR) forms a new class of modified elastomers with special properties such as increased oil resistance and wet traction, decreased air permeability and the ability to be highly reinforced with a silica filler without coupling agents. Also it is well known that epoxidized oils are used as PVC plasticizers. A common industrial practice is to modify PVC compositions by incorporating a diverse array of additives in order to obtain a polymer with satisfactory processing and end-use performance. The required modifications are more extensive and diversified than those practiced with other polymers of major industrial importance. However, the industrial application of PVC in the form of the resulting materials is more versatile. In flexible and semi-rigid PVC formulations, plasticizers are key ingredients, although other compounding ingredients (e.g. stabilizers) are also extremely important. Plasticizers impart flexibility and play an important role in heat processing by reducing the viscosity of the molten material to ensure good flow properties. The theory of plasticization has been reviewed by many investigators [8–11]. The effects of various concentrations of plasticizers on the mechanical properties of polymers and copolymers in a high concentration range have been reported [9, 11–15]. In addition to the melt flow properties, the flexibility, extensibility, and rigidity of final products at room temperature are influenced by the addition of plasticizers [16–18].

The main objective of the present work was to study the extent of property modification of PVC attainable by blending it with modified liquid natural rubber. For this purpose, a series of blends with various degrees of epoxidation has been prepared. The effect of the degree of epoxidation as well as of the amount of ELNR on the property modification was investigated and the role of epoxidized natural rubber as a plasticizer has been discussed.

2. Experimental

Materials. PVC (*K* value 65, density 1.37 g/cm^3) was supplied by M/s Chemicals and Plastics Ltd., Chennai. NR (ISNR-5, $\bar{M}_v$ = 820 000, intrinsic viscosity in benzene at 30 °C = 4.45 dl/g) was supplied by the Rubber Research Institute of India, Kottayam. Thermal stabilizer, dibutyl tin dilaurate (DBTDL) (Fluka, Switzerland) was used without purification. 2-Butanone used as the solvent for blending was supplied by E. Merck India Ltd. This was dried over anhydrous calcium chloride and distilled before use. Glacial acetic acid, toluene, methanol and hydrogen peroxide (30 v/v) were of

reagent grade. Toluene and methanol were dried and distilled before use. Hydroxyl terminated liquid natural rubber (HTNR) of number average molecular weight 4600 was prepared in the laboratory by the photochemical degradation of natural rubber as per reported procedure [19]. It was reprecipitated thrice from toluene using methanol and dried at 70–80 ºC in vacuum before use.

Preparation of ELNR. Epoxidised LNR of 10 to 50 mol % epoxidation (ELNR-10, ELNR-20, ELNR-30 ELNR-40 and ELNR-50) was prepared in the laboratory by the epoxidation of LNR using glacial acetic acid and hydrogen peroxide as per reported procedure [20]. ELNR-10 was prepared by dissolving LNR (25 g) in 166 dm^3 of toluene to obtain a 15% solution and was stirred at 50 ºC for 3h with 0.55 mol of aqueous hydrogen peroxide and 0.35 mol of glacial acetic acid. Other ELNR samples, with 20, 30, 40 and 50 mol % of epoxidation were also prepared by the same procedure using appropriate amounts of hydrogen peroxide and 5, 6, 8 and 10 hours of stirring, respectively. At the end of the reaction, the product was isolated by precipitation from methanol. It was dried in vacuum and then characterized by titrimetric, IR and NMR techniques [21, 22].

Preparation PVC/ELNR blends. A series of blends of PVC and epoxidised liquid natural rubber with 10, 20, 30, 40 and 50 mol % of epoxidation were prepared from the common solvent 2-butanone as follows. A 3% (w/v) solution of PVC in 2-butanone was prepared with 4 wt. % of DBTDL (based on PVC) as a thermal stabilizer. This solution was then added to the rubber solution in 2-butanone at various compositions. It was thoroughly mixed using a magnetic stirrer for 5 h at 50 ºC and cast on glass plates. The samples were then dried in vacuum at 70 ºC for two days to remove the traces of residual solvent. The cast samples were characterized by various analytical methods such as thermal analysis, tensile measurements and scanning electron microscopy. The blends were designated as, for example PVC/ELNR-50(80/20), the abbreviation meaning a blend of 80 parts PVC and 20 parts ELNR of 50 mol % epoxidation.

Measurements. DSC measurements were done using a Shimadzu DSC60 thermal analyzer (Japan) at a programmed heating rate of 10 °C/min. The experiments were carried out in the temperature range 30–300 °C under dry nitrogen atmosphere (25 mV/min) using aluminium crucibles. The sample weight was 4–5 mg. For measuring subambient transition, the DSC was performed with a Mettler Inc (TA 300) microcalorimeter, (Germany).

Stress-strain behaviour was studied on a Zwick 1474 Universal Testing Machine (Germany) as per ASTM D 412-80 test method at a constant cross head speed of 500 mm/min using dumb bell shaped test specimens. At least five samples were tested in each case and the average value was taken as the result for determining Young's modulus, tensile strength and elongation at break.

Tensile fracture surfaces of thin films were examined using a JEOL 5400 SEM (Tokyo, Japan) at 20 kV using magnifications 500 to 1000 to study the morphology of the samples. The surface was sputter coated with Au/Pd alloy in a sputter coating ma-

chine (Balzers SCD 050, Germany). A minimum of five photographs were taken for each sample for analysis.

3. Results and discussion

Property modification of PVC has been accomplished with the help of modified liquid natural rubber. A few series of blends were prepared and subject to tensile testing, SEM studies, and DSC analysis. The compositions of the blends prepared are given in Table 1.

Table 1. Compositions of PVC/ELNR blends

Blend	PVC [%]	ELNR-50 [%]	Blend	PVC [%]	ELNR-20 [%]
PVC/ELNR-50 (90/10)	90	10	PVC/ELNR-10 (90/10)	90	10
PVC/ELNR-50 (80/20)	80	20	PVC/ELNR-10 (80/20)	80	20
PVC/ELNR-50 (70/30)	70	30	PVC/ELNR-10 (70/30)	70	30
PVC/ELNR-50 (50/50)	50	50	PVC/ELNR-10 (50/50)	50	50
PVC/ELNR-50 (30/70)	30	70	PVC/ELNR-10 (30/70)	30	70
Blend	PVC [%]	ELNR-40 [%]	Blend	PVC [%]	ELNR-20 [%]
PVC/ELNR-40 (70/30)	70	30	PVC/ELNR-30 (70/30)	70	30
PVC/ELNR-40 (50/50)	50	50	PVC/ELNR-30 (50/50)	50	50
PVC/ELNR-40 (30/70)	30	70	PVC/ELNR-30 (30/70)	30	70
Blend	PVC [%]	ELR-20 [%]			
PVC/ELNR-20 (70/30)	70	30			
PVC/ELNR-20 (50/50)	50	50			
PVC/ELNR-20 (30/70)	30	70			

3.1. Differential scanning calorimetry (DSC)

The thermograms of selected samples are given in Figs. 1 and 2. The T_g values obtained from the thermograms are listed in Table 2. T_g of PVC was found to be 80 ºC which is a slightly lower value than that expected of solution cast blends. The corresponding values of ELNR-10, ELNR-20, ELNR-30, ELNR-40 and ELNR-50 were found to be –39, –31, –27, –24 and –20 ºC, respectively. The introduction of polar groups in the form of oxirane rings obviously increased the T_g value of LNR. The values increased from –65 ºC to –39 ºC and to –20 ºC as the degree of epoxidation was increased from zero to 10 and to 50 mol %. This is due to a stronger intermolecular interaction existing in ELNR that was originally absent in NR. The DSC thermograms of the ELNR-10 blends possess two distinct transitions, viz., PVC/ELNR-10 (70/30)

exhibited transitions at 71°C and –36 °C (Fig. 1). The same trend is observed for PVC/ELNR-20 and PVC/ELNR-30 blends. On the other hand, ELNR-40 and ELNR -50 samples show a single transition for all compositions studied (Table 2). For example PVC/ELNR-40 (70/30) and PVC/ELNR-50(70/30) exhibited transitions at 56 and 32 ºC,

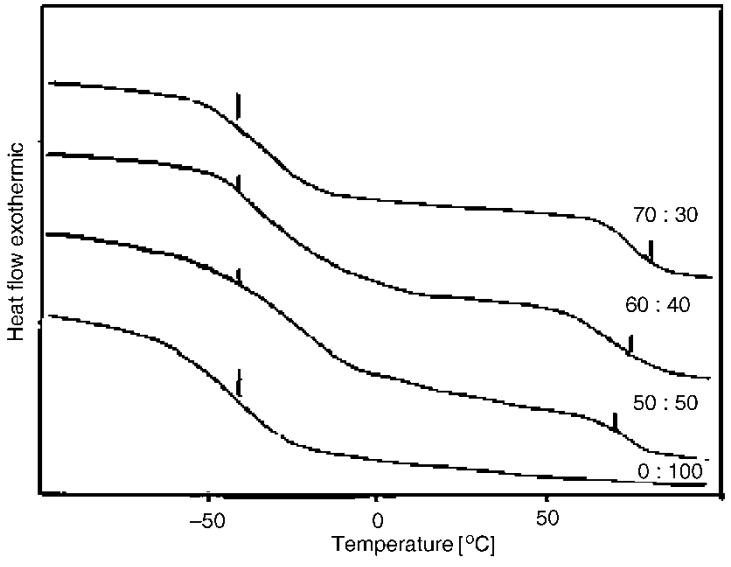

Fig. 1. DSC thermograms of PVC/ELNR-10 blend in various compositions

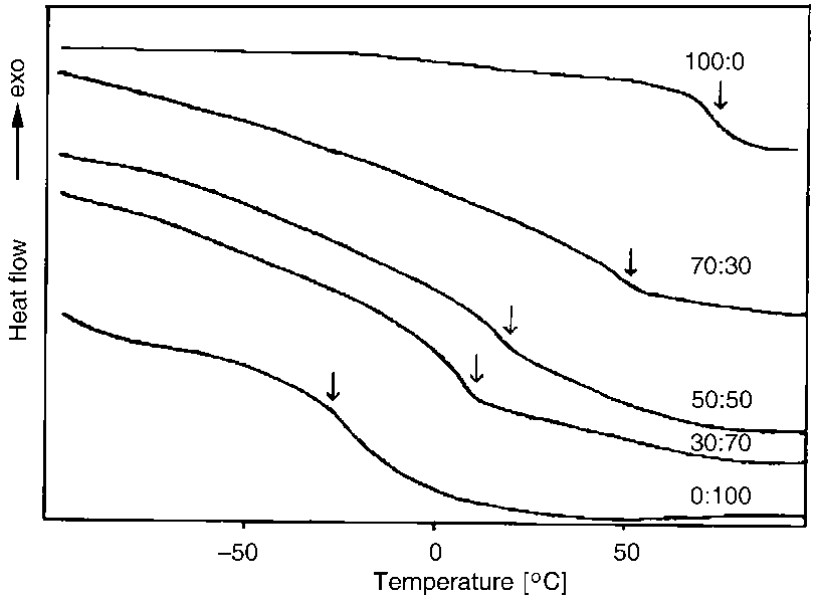

Fig. 2. DSC thermograms of PVC/ELNR-40 blends in various compositions

respectively (Fig. 2). The values are found to be intermediate between those of the component polymers. This corresponds to a miscible system indicating that the ELNR with a sufficiently high epoxy content becomes miscible with polyvinyl chloride.

Table 2. Transition temperatures (T_g) of PVC/ELNR blends and components

Sample	T_g of PVC phase [ºC]	T_g of ELNR phase [ºC]
PVC/ELNR-10 (70/30)	71	–36
PVC/ELNR-10 (50/50)	69	–35
PVC/ELNR-10 (30/70)	67	–33
PVC/ELNR-20 (70/30)	63	–30
PVC/ELNR-30 (70/30)	60	–20
PVC/ELNR-40 (70/30)	56	–
PVC/ELNR-40 (50/50)	42	–
PVC/ELNR-40 (30/70)	48	–
PVC/ELNR-50 (70/30)	32	–
PVC/ELNR-50 (50/50)	20	
PVC/ELNR-50 (30/70)	12	
ELNR-10	–	–39
ELNR-20	–	–31
ELNR-30	–	–27
ELNR-40	–	–24
ELNR-50	–	–20
PVC	80	–

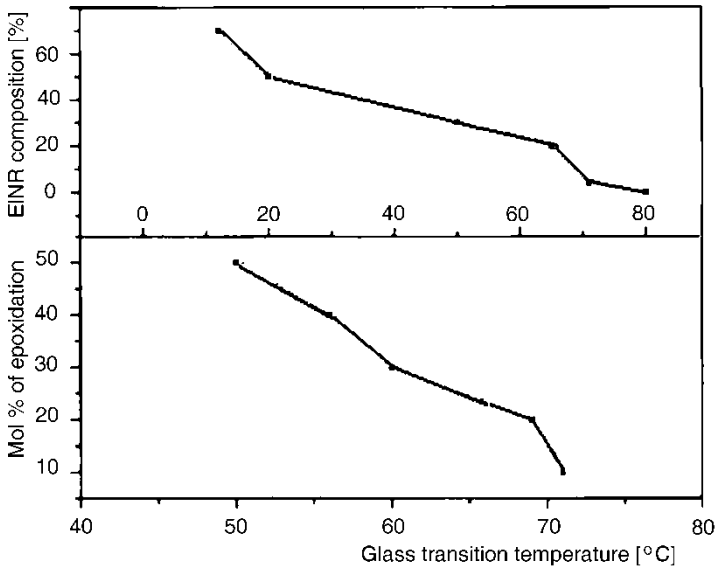

Fig. 3. Variation of glass transition temperatures with composition and degree of epoxidation of ELNR

It provides a stronger interaction with the PVC matrix flexibilising the PVC segments and lowering the T_g value. The variation of glass transition temperature with the degree of epoxidation is shown in Fig. 3. It also indicates the variation of T_g of the representative blends PVC/ELNR-50 with percentage composition of ELNR.

The observed trend in variation of T_g is explained based on a higher degree of miscibility and subsequent plasticization achieved with ELNR of higher epoxidation. The reason for miscibility is attributed to the increase in the solubility parameter of liquid NR to a matching level with polyvinyl chloride due to introduction of sufficient number of epoxy groups into the diene backbone. The molecular origin of miscibility could be attributed to polar–polar interactions. Plasticization of PVC by polymeric or liquid plasticizers enhances the segmental mobility which in turn modifies the material properties and the glass transition temperature of the polymer.

3.2. Tensile properties

The stress-strain measurements were carried out on selected samples from all the series of blends, viz., PVC/ELNR-50, PVC/ELNR-40, PVC/ELNR-30, PVC/ELNR-20 and PVC/ELNR-10 and the tensile curves so obtained are presented in Figs. 4, 5. For the sake of comparison, the tensile curve of unmodified PVC was also presented in Fig. 5. The data obtained from these curves have been given in Table 3.

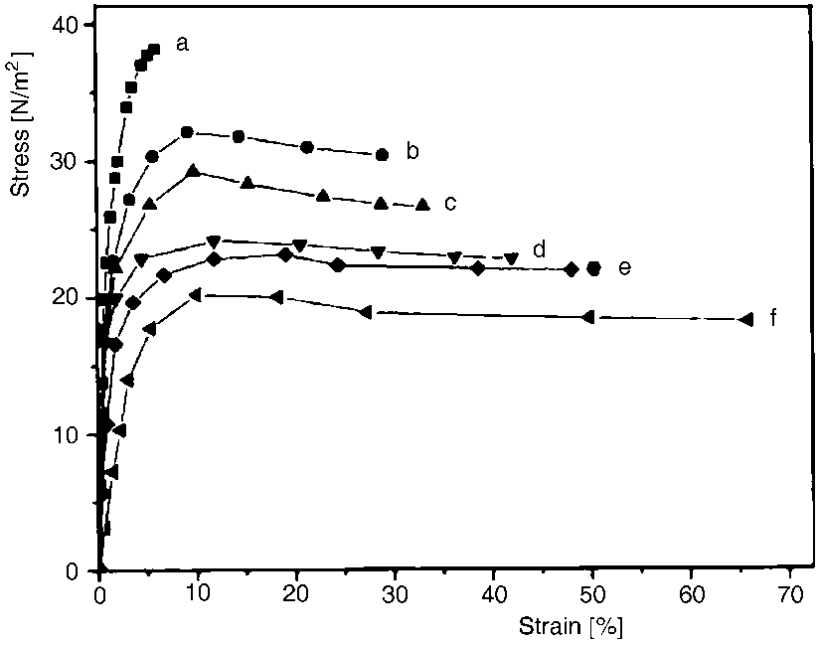

Fig. 4. Tensile curves of PVC/ELNR (50/50) blends: a) PVC/ELNR-10, b) PVC/ELNR-20, c) PVC/ELNR-30, d) PVC/ELNR-40 e) PVC/ELNR-50

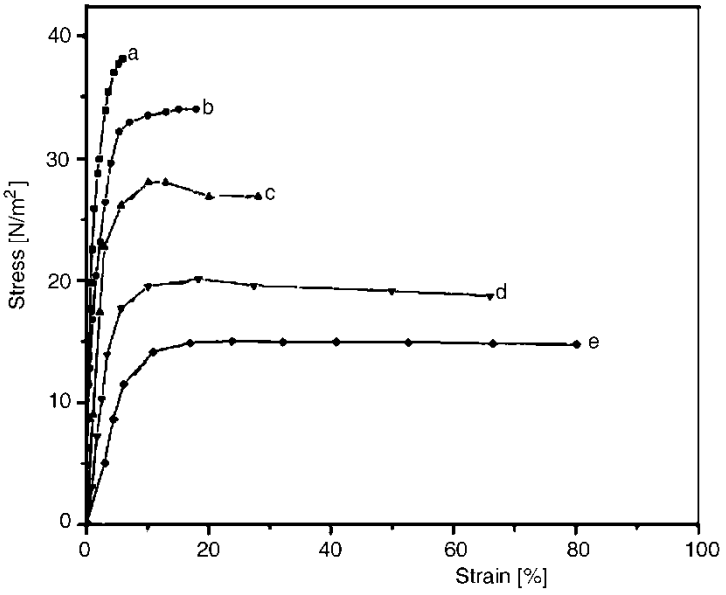

Fig. 5. Tensile curve of PVC/ELNR-50 blends of various compositions: a) PVC, b) PVC/ELNR-50(90/l0), c) PVC/ELNR-50(80/20), d) PVC/ELNR-50(50/50), e) PVC/ELNR-50(30/70)

Table 3. Tensile properties of PVC and PVC/ELNR blends

Blend	Tensile strength [N/mm^2]	Young's modulus [N/mm^2]	Elongation [%]
PVC	38	3200	6
PVC/ELNR-10(90/10)	37	3200	9
PVC/ELNR-10(80/20)	35	2900	12
PVC/ELNR-10(70/30)	34	2800	17
PVC/ELNR-10(50/50)	32	2500	29
PVC/ELNR-10(30/70)	30	2300	35
PVC/ELNR-20(70/30)	33	2570	20
PVC/ELNR-20(50/50)	29	2100	33
PVC/ELNR-20(30/70)	24	1800	42
PVC/ELNR-30(70/30)	30	2530	23
PVC/ELNR-30(50/50)	24	2000	42
PVC/ELNR-30(30/70)	20	1500	60
PVC/ELNR-40(90/10)	35	2980	15
PVC/ELNR-40(80/20)	30	2670	20
PVC/ELNR-40(70/30)	28	2500	29
PVC/ELNR-40(60/40)	26	2360	38
PVC/ELNR-40(50/50)	23	1950	48
PVC/ELNR-40(40/60)	22	1500	60
PVC/ELNR-40(30/70)	16	1000	72
PVC/ELNR-50(70/30)	26	2430	40
PVC/ELNR-50(50/50)	20	1700	66
PVC/ELNR-50(30/70)	9	800	96

The tensile curve of unmodified PVC shows characteristic features of a brittle material (Fig. 5, curve a). It undergoes a very small deformation under stress and failure occurs at 6% elongation without undergoing any yield phenomenon. The tensile strength and modulus of elasticity were found to be very high with values 38 N/mm^2 and 3200 N/mm^2, respectively. It is observed that addition of 10 parts of ELNR-40 and ELNR-50 to PVC formed a blend that shows a yield point which is not observed for unmodified PVC. The yield strength was found to be 34 N/mm^2 for PVC/ELNR-50(90/10). Consistent with this tensile strength, modulus and elongation at break also showed a variation. The first two values are lower than that of PVC whereas elongation at break is higher (Table 3). The tensile curves of samples with composition ranging from 20 to 70 parts of ELNR-40 showed variation with respect to the rubber content. The change in nature of the curves becomes more pronounced with higher ELNR-40 content. The yield point becomes broader and finally it disappears and the tensile curve tends to flatten out. The samples behaved like soft flexible mass when ELNR-40 and ELNR-50 content became too high, viz. 70%. (Table 3).

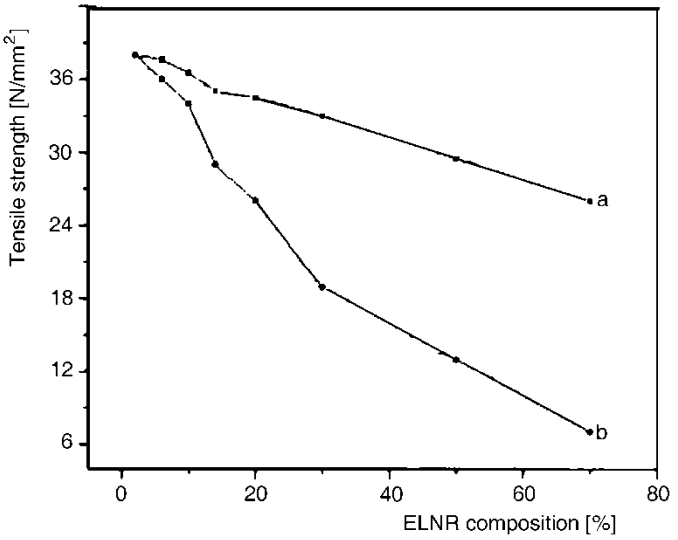

Fig. 6. Variation of tensile strength with composition of: a) PVC/ELNR-20, b) PVC/ELNR-50

Variations in tensile strength, modulus and elongation at break with composition of the blends are given in Figs. 6, 7. It is clearly seen that the strength and modulus values decrease while elongation at break increases with ELNR-50 content. At higher level of rubber content, the tensile strength decreases to a very low value. For example, the tensile strength of PVC/ELNR-40 (90/10) was 35 N/mm^2 whereas that of 30/70 blend was 16 N/mm^2 and for PVC/ELNR-50 blends for the same composition the values are 34 and 9 N/mm^2, respectively. A similar variation was also observed in the modulii. The modulus drops from 2980 N/mm^2 for PVC/ELNR-40 (90/10) to 1000 N/mm^2 for (30/70) composition. The elongation at break shows a large increase with

increasing rubber content. For example, it rose from a low value of 15% for PVC/ELNR-40 (90/10) to a very high value of 72% for PVC/ELNR-40 (30/70).

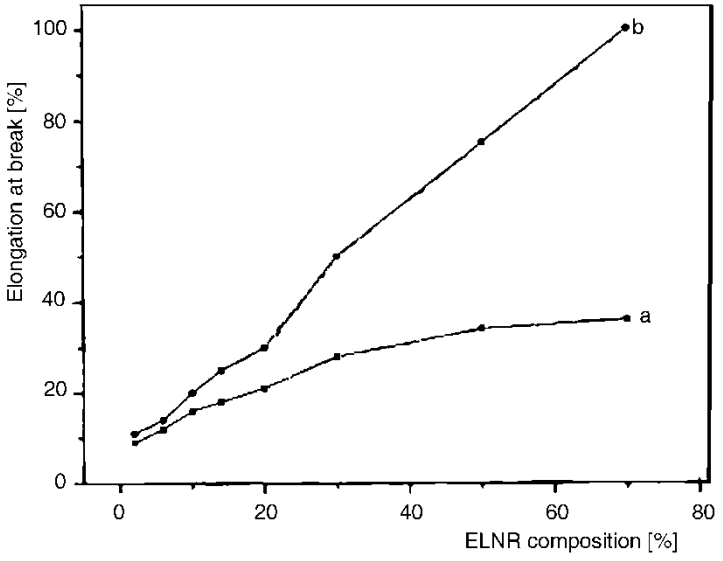

Fig. 7. Variation of elongation at break with composition of: a) PVC/ELNR-20, b) PVC/ELNR-50

The above variation in properties showed that brittle and rigid nature of PVC stands modified with addition of ELNR-50. Hence it can be concluded that ELNR-40 and ELNR-50 exhibit a plasticizing effect on rigid PVC. The above results are in conjunction with the manifestation of single T_g values, which is lower than that of unplasticised PVC, obtained in the DSC analysis of these blend systems.

The tensile strength and modulus decrease and the elongation at break increases. The glass transition temperature tends to decrease with the extent of plasticization of PVC. Plasticization of PVC by ELNR enhances the segmental mobility which in turn modifies the material properties. Although variation in the nature of the tensile curves is observed with rubber content in these blend systems, the trend in the variation suggests that the blends are more heterogeneous in nature. Figure 8 shows the variation of tensile strength and elongation at break versus degree of epoxidation. It can be seen from the figure that the rubber with higher extent of epoxidation provides drastic variation in the yield strength. For example, the yield strength for PVC/ELNR-20 (80/20) is 34 N/mm^2 and the yield strength of PVC/ELNR-50 (80/20) is 28 N/mm^2.

The solubility parameters of PVC ((9.4 (cal/cm^3)$^{1/2}$), ELNR-40 and ELNR-50 ((9.2 (cal/cm^3)$^{1/2}$) in these blend systems are comparable and hence the two components tend to be compatible. As a result of the compatibility, the heterogeneous nature of these blend systems has been lost and plasticization of PVC matrix took place. This is the reason for a drastic decrease in tensile strength and modulus values in PVC/ELNR-40 and PVC/ELNR-50 blends which being miscible, lead to plasticization.

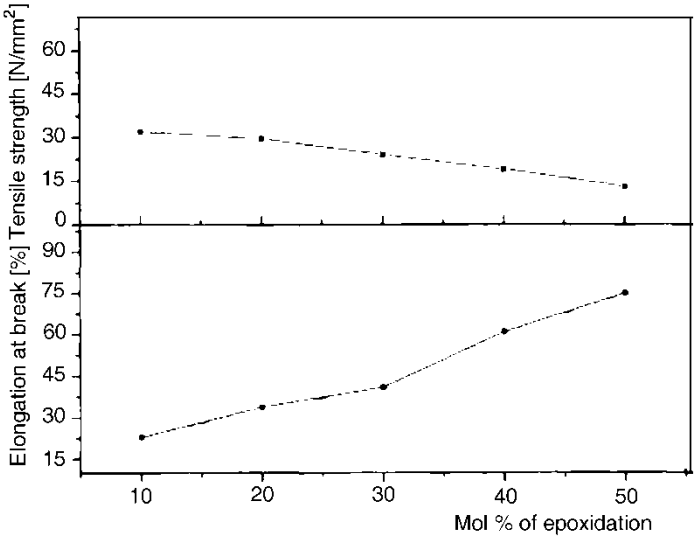

Fig. 8. Variation of elongation at break and tensile strength with the degree of epoxidation in ELNR

These results can be explained based on interaction between the blend components. In the case of rubber with low degree of epoxidation, the interaction between the components is limited but the rubber with higher degree of epoxidation interacts more strongly with PVC affecting all the tensile properties viz., tensile strength, tensile modulus, elongation at break and tensile fracture mechanism.

3.3. Morphological studies using SEM

Fracture surfaces of dumb-bell shaped tensile specimen from selected samples of the blends have been examined using SEM. An attempt has been made to correlate the morphology of fracture surface with the tensile properties of the blend systems.

The fractographs of PVC, PVC/ELNR-10(50/50), and PVC/ELNR-50(50/50) are given in Fig. 9a–c. The tensile fracture surface of rigid PVC (Fig. 9a) showed that the sample undergoes a brittle mode of failure as the fracture surface is characterized by waviness and closely placed line patterns. The stress-strain curve of the material also showed a brittle mode of fracture. The sample undergoes failure without showing a yield point and it has got the highest tensile strength (38 N/mm^2) among all the samples. As the epoxy content of ELNR increases, the brittle fracture changes gradually into a ductile one. On increasing the rubber content to 50%, the fracture front shows increase of plastic deformation. The fracture surface becomes highly deformed and exhibits features of fine fibrils, parabolic and wavy fracture front. Orientation of the matrix along the stress axis is also observed at the fracture surface. All these observations indicate that the ductile nature of the blend increases with rubber content. This finding is supported by the respective tensile curve, being also in conformity with the

fact that the higher amounts of epoxidised rubber in major quantity provide loose and flexible character to the material. This is also reflected in the tensile curve being characteristic of a very flexible and soft material. The results indicate that the epoxidized rubber is miscible with PVC rendering it more flexible. In other words, the ELNR-50 tends to plasticize PVC as a manner generally observed with the commercial PVC plasticizers. This is evident from the tensile curves which show higher extent of elongation and ductile behaviour.

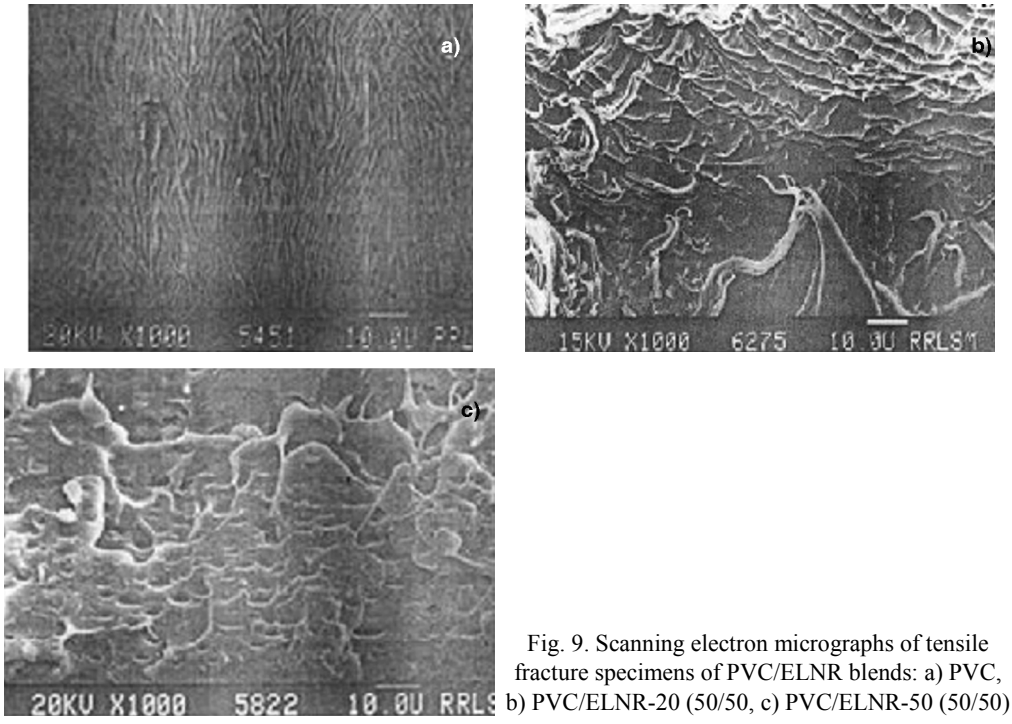

Fig. 9. Scanning electron micrographs of tensile fracture specimens of PVC/ELNR blends: a) PVC, b) PVC/ELNR-20 (50/50, c) PVC/ELNR-50 (50/50)

A comparison of the blend systems shows that the epoxy content influences the failure pattern of the tensile samples. With 30 parts of ELNR-50 added into PVC there seems to be a change in the appearance of the fracture surface to a deformed state. This corresponds to a shift from the brittle fracture to a ductile fracture mechanism which means that the matrix has become more flexible. This is reflected in the tensile test results discussed above. In the case of 70/30 composition, ELNR-50 based blends show ductile fracture mechanism (Fig. 9c). But PVC/ELNR-20 blend deformed in a manner similar to an incompatible blend showing a coarse fracture surface (Fig. 9b). The ductile fracture behaviour of the former is attributed to a higher extent of interaction between the PVC and ELNR with 50 mol % of epoxidation. The lower extent of interaction of the two components is discernible from the brittle mode of fracture in the other systems, viz., PVC/ELNR-20 and PVC/ELNR-10 where the degree of epoxidation is much lower at 10 and 20 mol %. These observations along the tensile

behaviour indicate that the brittle nature of PVC stands modified by the ELNR-50 in these blends. A comparison of the fracture surfaces of PVC/ELNR-50 and PVC/ELNR-20 shows that the PVC/ELNR-50 is found to be a miscible system but PVC/ELNR-20 blend shows heterogeneous nature. It is concluded, therefore, that the epoxidized liquid NR with high extent of epoxidation gives blend showing ductile nature with PVC.

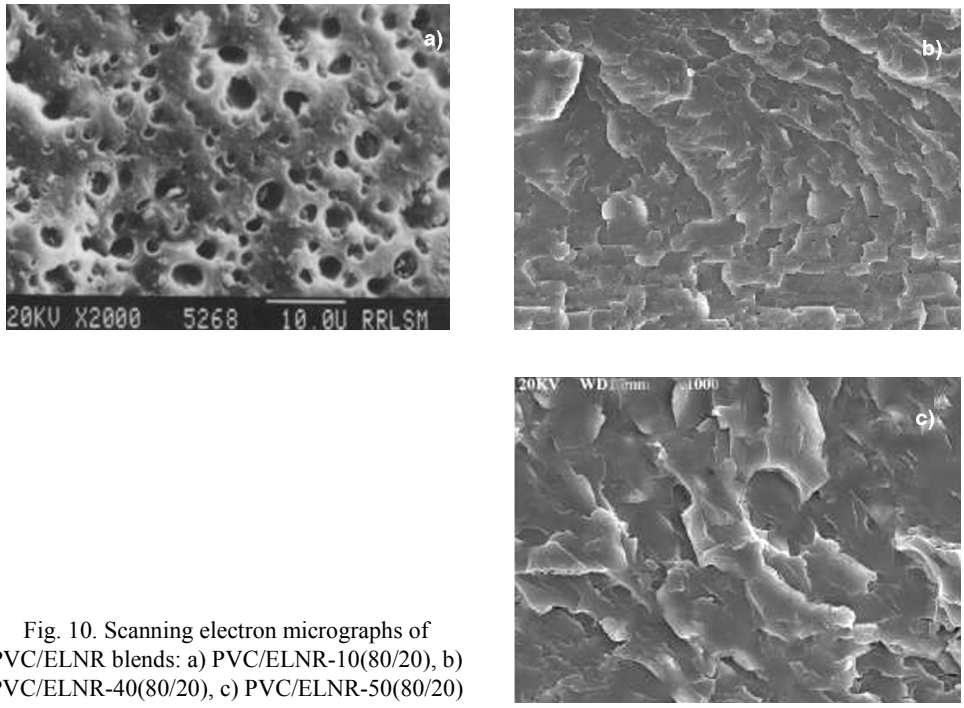

Fig. 10. Scanning electron micrographs of PVC/ELNR blends: a) PVC/ELNR-10(80/20), b) PVC/ELNR-40(80/20), c) PVC/ELNR-50(80/20)

The scanning electron micrographs of PVC/ELNR-10, PVC/ELNR-20, PVC/ELNR-30, PVC/ELNR-40 and PVC/ELNR-50, blends at 80/20 compositions were studied. Micrographs of selected compositions, viz., PVC/ELNR-20(80/20), PVC/ELNR-40(80/20) and PVC/ELNR-50(80/20) are shown in Fig. 10. The micrographs of PVC/ELNR-10 (Fig. 10a) show coarse dispersion of the ELNR phase in the continuous PVC matrix. The same pattern is observed in the case of blends with 20 and 30 mol % of epoxidation with more uniformity in distribution of the dispersed phase and reduction in size. Upon increase of the degree of epoxidation, the dispersed phase gets more uniformly distributed with reduction in the domain size. This trend continues and at 40 and 50 mol % the two phases cannot be distinguished, exhibiting the features of homogeneous blend systems (Figs. 10b, c). The effectiveness in the dispersion is attributed to higher interaction between the two phases promoted by the epoxy groups. Thus it can be inferred that with increase in mol % of epoxidation the interaction increases changing the blend systems from a compatible to miscible level.

4. Conclusions

The role of degree of epoxidation and composition of epoxidized natural rubber on the property improvements of PVC/ELNR blends was investigated in this study. Tensile strengths and modulus values decreased by the addition of ELNR. This seemed to be due to plasticization of PVC. At higher ELNR concentrations, the tensile strength at yield also decreased because of plasticization of the matrix. The elongation at break increased with the ELNR content. SEM micrographs revealed that the addition of ELNR with 50 mol % of epoxidation into PVC matrix changed it into a flexible mass. The study suggests that ELNR-40 and ELNR-50 act as PVC plasticizers.

References

[1] PAUL D.R., NEWMAN S.N., *Polymer Blends*, Academic Press, New York, 1978.
[2] OLABISI O., ROBESON L., SHOW M.T., *Polymer-Polymer Miscibility*, Academic Press, New York, 1979.
[3] HAN C.D., *Multiphase Flow in Polymer Processing,* Academic Press, New York, 1981.
[4] UTRACKI L A., SHI Z.H., Polym. Eng. Sci., 32 (1992), 1824.
[5] BRUKHART R.D., ZUTTY N.L., J. Po1ym. Sci. Part A, 1 (1963), 1137.
[6] MARGARITIS A.G, KALFAGLAU N.K., Eur. Polym. J., 11 (1988), 1043.
[7] MARGARITIS A.G., KALFAGLAU N.K., Polymer, 28 (1987), 497.
[8] TITOW W.V., *PVC Plastics: Properties, Processing, and Applications*, Elsevier, New York, 1990.
[9] TITOW W.V., LANHAM B.I., *Reinforced Thermoplastics*, App. Sci.Publ., London, 1975.
[10] GOMEZ I.L., *Engineering With Rigid PVC: Processabi1ity and Applications*, Marcel Dekker Inc, New York, 1984.
[11] BOYER R.F., Polym. Eng. Sci., 8 (1968), 175.
[12] MATTHEWS G., *Vinyl and Allied Polymers, Vol. 2: Vinyl Chloride and Vinyl Acetate Polymers.* Illiffe Books, London, 1972.
[13] SEARS I.K., DARBY J.R., *The Technology of Plasticizers*, Wiley, Toronto, 1982.
[14] WILSON A.S., *Plasticizers: Principles and Practice,* The Institute of Materials, Cambridge University Press, Cambridge, 1995.
[15] RIDER D.K., SUMNER I.K., Myers R. J., Ind. Eng. Chem., 41 (1949), 709.
[16] DELMONTE I., *Plastics in Engineering*, Penton, Croydon, 1949.
[17] WALTER A.T., J. Polym. Sci., 13 (1954), 207.
[18] GHERS A P., Mod. Plast., 36 (1958), 135.
[19] REVINDRAN T., GOPINATHAN NAYAR M.R., FRANCIS D.J., J. Appl. Polym. Sci., 35 (1988), 1227.
[20] THOMAS G.V., NAIR M.R.G., Kautsch. Gummi Kunst., 50 (1997), 398.
[21] BAC N.V., TERLEMEZYAN L., MIHAILOV M., J. Appl. Polym. Sci., 42 (1991), 2965.
[22] BURFILED D.R., LIM K.L., LAW K.S., SOON N.G., Polymer, 25 (1984), 995.

Received 4 September 2006
Revised 29 March 2007

Materials Science-Poland, Vol. 25, No. 4, 2007

Spectroscopic and diffraction studies of chemical deposition of copper sulfide films on polyamide surface using potassium pentathionate

V. KRYLOVA*

Departament of Inorganic Chemistry, Kaunas University of Technology,
Radvil□nų str. 19, LT-50254 Kaunas, Lithuania

Sulfur sorption–diffusion by polyamide PA 6 film exposed to potassium pentathionate $K_2S_5O_6$ solutions was investigated by the UV, IR absorption spectroscopy and chemical analysis methods. $S_5O_6^{2-}$ anions were found to sorb into the polymer. The study of sulfur sorption–diffusion kinetics showed that the concentration of sorbed pentathionate ions in polyamide film increased with increasing duration of treatment and the temperature of solution. Sulfur concentration in the polymer was found to depend on the conditions of sorption and varied between 0.94 and 7.64 mg/cm^3. The estimated apparent diffusion coefficients of $S_5O_6^{2-}$ ions in polyamide increased with increasing temperature of $K_2S_5O_6$ solution. On treating sulfured polyamide film with copper(I) salt solution, copper sulfide (Cu_xS) layers are formed in the surface matrix of the polymer. The content of Cu_xS depended on the concentration of $S_5O_6^{2-}$ ions in the polyamide matrix. Initially dielectric, polyamide films after formation of Cu_xS layers in their surface matrix become electrical conductors. Samples sulfured in $K_2S_5O_6$ solution at 293 K for 240 min were the most conductive. X-ray diffraction studies of Cu_xS layers revealed the presence of two phases: chalcosine and djurleite.

Key words: *polyamide; potassium pentathionate; sulfuration; copper sulfide layer*

1. Introduction

Polymers modified with various films on their surface represent a new class of materials − composites with a novel combination of properties. Polymers are often modified by thin electrically conductive or semi-conductive films of binary inorganic compounds, particularly copper sulfide [1–4]. Copper sulfide thin films on polymers are relevant in solar radiation absorbers, solar cells. These composites may be used as conductive substances for metal deposition or semiconductor coatings by electrolytic

*E-mail: Valentina.Krylova@ktu.lt

deposition and as a conductive base for optoelectronic device structures [1–4]. Recently, Cu_xS thin films on dielectrics have been used in resistive gas sensors [5].

Various methods, such as vacuum evaporation [7, 8], activated reactive evaporation, spray pyrolysis, electroless deposition, successive ionic layer adsorption and reaction and chemical bath deposition [9] were used for the formation of metal sulfide layers on various dielectrics and polymers. Simple and promising is the sorption –diffusion method [10]. Hydrophilic and semi-hydrophilic polymers, including polyamide (PA 6), are capable of absorbing ions of various sulfuration agents, e.g., sulfur solutions in organic solvents [11], sodium polysulfide (Na_2S_n, n = 4.8) aqueous solutions [12], polythionic acid ($H_2S_nO_6$, n = 9–45) aqueous solutions [13]. To prevent environmental pollution with vapours of toxic solvents and to avoid swelling of some polymers in organic solvents, the use of sulfide solutions is limited because of their high alkalinity. The synthesis of sulfurous polythionic acids appears to be fairly complicated and prolonged (up to 2 days), and it is based on the reaction of interaction of toxic hydrogen sulfide and thiosulfurous acid. Aqueous solutions of polythionic acids are unstable and are rapidly decomposed with isolation of elemental sulfur. Recently, the adsorption–diffusion method of formation of thin copper sulfide layers on PA 6 surface based on the initial treatment of a polymer with solutions containing polythionate anions, $S_nO_6^{2-}$ ($n \le 6$) has been under extensive investigation [14–16].

In the present study, binary compounds of copper sulfide in the surface layer of PA 6 were obtained by the sorption−diffusion method [10, 14]. In the first stage of the process, sulfur-containing particles from 0.15 mol/dm^3 potassium pentathionate ($K_2S_5O_6$) solution were adsorbed on PA 6 samples [15]. In the second stage, sulfurised PA 6 was treated with Cu(II) sulfate solution containing hydroxylamine sulfate as the reducing agent [10].

In the present study, the sulfuration of polyamide film in potassium pentathionate solutions and the generation of Cu_xS layers on the surface of sulfured PA 6 by treatment with copper(I) salt solution have been investigated. The usefulness of composites obtained by modifying polymers with copper sulfide layers was determined by their electrical properties which vary significantly even when the chemical composition is only slightly changed [10, 15]. Electrical resistance itself increases over six times when the value of x in Cu_xS is increased from 1 to 2 [9]. Therefore, electrical measurements provide preliminary information on the composition of the layer. The composition can be more precisely determined by X-ray diffraction studies.

2. Experimental

Copper sulfide layers were deposited on a PA 6 (specification TY 6-05-1775-76, grade PK-4, produced in Russia) film 70 μm thick. The diameters of the pores in the film do not exceed 1.5 nm. The porosity was measured by the BET method [18] using the Quantasorb sorption system (USA). Samples 15×70 mm^2 were used to remove the

remainder of the monomer. Before sulfurisation, the samples were boiled in distilled water for 2 h, they were dried with filter paper and subsequently kept over $CaCl_2$ at least for 24 h [14].

$K_2S_5O_6 \cdot 1.5H_2O$, was prepared and chemically analyzed according to [19, 20]. PA 6 samples were exposed to potassium pentathionate solution. Previous experiments [14] have shown that sorption from 0.1 mol/dm^3 $K_2S_5O_6$ was too slow and insufficient. Therefore, 0.15 mol/dm^3 solutions were chosen for this work. At temperatures higher than 303 K, gradual spontaneous decomposition of polythionate occurs, with liberation of elemental sulfur [19]:

$$S_5O_6^{2-} \longrightarrow 3S + SO_2 + SO_4^{2-} \tag{1}$$

The sorption process was performed at temperatures ranging from 273 to 293 K. The samples were rinsed with distilled water, dried over $CaCl_2$, analyzed, and then used in further experiments. The content of sulfur in PA 6 samples in the form of sulfates was determined turbidimetrically [21]. Samples of sulfurised PA 6 were treated with the solution of 0.4 mol/dm^3 Cu(I) salt prepared from crystalline $CuSO_4 \cdot 5H_2O$ and hydroxylamine sulfate [10]. After treatment, the samples were rinsed with distilled water and dried over $CaCl_2$. The content of copper in PA 6 samples was determined by atomic absorption spectrometry (AAS) [22]. UV spectra (from 200 nm to 400 nm) were recorded on a Spectronic^R Genesys™ 8 UV/Visible spectrophotometer with compensation of PA 6 absorption. IR spectra (from 200 to 1300 cm^{-1}) were recorded on a Perkin-Elmer FT-IR Spectrum GX spectrophotometer by the compensation method. Phase compositions of copper sulfide layers were investigated by X-ray diffraction using a DRON-6 diffractometer (CuK_α radiation). In order to eliminate the maxima of PA 6, X-ray diffractograms were analyzed using the Search Match, ConvX, Xfit, and Microsoft Excel programs. The sheet resistance of Cu_xS layers was measured at a constant current using the E7–8 digital multimeter (Russia) with custom design electrodes. The measurements were carried out per 1 cm^2 square electrodes, therefore the resistance is given in Ω/cm^2.

3. Results and discussion

The nature of sulfur-containing particles sorbed by PA 6 film was studied employing UV and IR spectroscopy. A chain of three divalent sulfur atoms $^-O_3S–S–S–S–SO_3^-$ of a low oxidation state is present in the anion of potassium pentathionate. Optical absorption spectra of thin sulfide films on PA 6 revealed their high absorbance (10^4 cm^{-1}), indicating direct band gap transition. According to data of a study of UV absorption spectra of lower potassium polythionates [23, 24], the most intensive absorption peaks of polythionate ions appear at 256 nm and 295 nm. In addition, the UV absorption spectra of nanofilms formed using a single precursor $K_2S_5O_6$ are identical. UV absorption spectra of PA 6 samples sulfured for various periods of time in a solution of

$K_2S_5O_6$ at various temperatures (273–293 K) are presented in Fig. 1. Two absorption peaks are observed in the spectra: at λ = 250 nm, and as a less intense and shallower band at λ = 295 nm. Thus the UV absorption spectra recorded by us confirm that sulfur is sorbed by PA 6 films in the form of pentathionate ions. The intensity of absorption maxima in the spectra increases upon increasing exposure time and the temperature of polymer treatment with potassium pentathionate solution. With decreasing temperature of the solution, the absorption peak in the spectra is shifted towards λ = 240 nm.

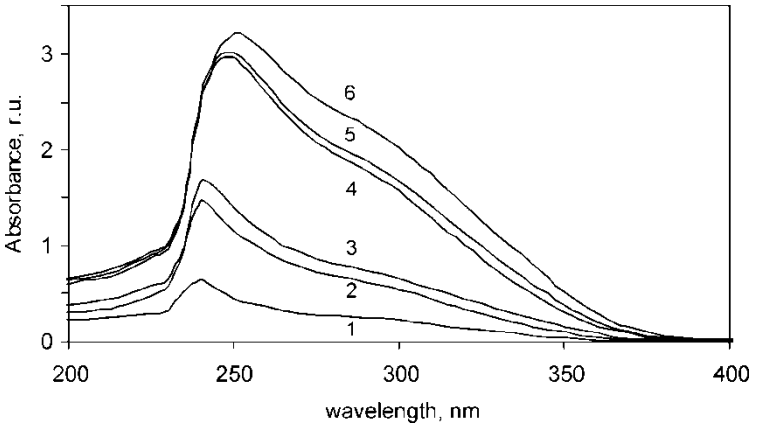

Fig. 1. UV absorption spectra of PA 6 films sulfured in 0.15 mol/dm^3 $K_2S_5O_6$ solution in 0.1 mol/dm^3 HCl, (pH = 1.5) at various times τ_s [min] and temperatures [K]: 1 – 273 (τ_s = 240), 2 – 283 (τ_s = 240), 3 – 293 (τ_s = 60), 4 – 293 (τ_s = 120), 5 – 293 (τ_s = 180), 6 – 293 (τ_s = 240)

The most intensive bands in the IR spectra of PA 6 samples sulfured in $K_2S_5O_6$ solutions, recorded by the compensation method (with PA 6 absorption eliminated), were located at 242–245, 337–385, 421–470, 523–536, 580–611, 1021–1022, 1202–1268 cm^{-1}. For identification of characteristic vibration frequencies, the IR spectra were compared with the spectra of pure $K_2S_5O_6 \cdot 1.5H_2O$ [25] and spectra reported in literature [26–29]. Data on IR spectra are presented in Table 1.

Based on the literature data [25–28], the bands at 1000–1250 cm^{-1} correspond to vibration frequencies of the SO bond (Table 1). The band at 1022 cm^{-1}, corresponding to symmetrical valence vibrations of S–O entity, does not split, and this feature shows that the symmetry of the pentathionate ion is not disrupted. A comparison of the recorded spectra with the spectrum of pure $K_2S_5O_6 \cdot 1.5H_2O$ salt showed the tendency of displacement of their frequencies towards lower values. This might be explained by the formation of hydrogen bonds between SO_3^{2-} ions and the polymer chains. For this reason, the S−O bonds in $S_5O_6^{2-}$ ions become weaker and the absorption peaks shift towards lower frequencies.

Analysis of the IR spectra of sulfured PA 6 samples shows that the intensity of absorption peaks increases on increase $K_2S_5O_6$ solution temperature and exposure time.

These results confirm that the sorption of pentathionate ions by PA 6 occurs during polymer treatment with acidified $K_2S_5O_6$ solution.

Table 1. Characteristic IR absorption bands ν [cm^{-1}] from $K_2S_5O_6 \cdot 1.5H_2O$ and $S_5O_6^{2-}$/PA 6 at 293 K in the frequency range 200–1300 cm^{-1}

$K_2S_5O_6 \cdot 1.5H_2O$	$S_5O_6^{2-}$/PA 6	Assignment	Reference
244	242	δ(SSS)	[29]
342	340 379	$\gamma_r(SO_3)$	[29]
428	426 464	ν(S−S)	[27]
514 542	503 524 536	δ_{as}(O−S−O)	[25, 29]
618 650	611 absent	δ_s(O−S−O)	[25, 29]
1024 1050	1022	ν_s(S−O)	[25–28]
1207 1218 1234 1250 1263*	1203 1222 1263	ν_{as}(S−O)	[25–28]

*Arm of the absorption band.

Chemical analysis of PA 6 samples sulfured in a $K_2S_5O_6$ solution showed that the concentration of sulfur sorbed by the polymer depends on the temperature of the sulfuration solution and exposure time.

Table 2. Dependence of sulfur concentration close to saturation $c_{s\infty}$, in polyamide treated in $K_2S_5O_6$ solution at various temperatures, apparent $S_5O_6^{2-}$ ion diffusion coefficient D and apparent adsorption heat $-\Delta H_{ads}$

Temperature [K]	$c_{s\infty}$ [mg/cm^3]	$D \times 10^{-11}$ [cm^2/s]	$-\Delta H_{ads}$ [kJ/mol]
273	1.52	2.2	–
283	4.25	3.3	66.64
293	7.64	4.7	47.01

It was found that the sulfur concentration (c_s, mg/cm^3) in the samples kept in potassium pentathionate solutions at 273, 283 and 293 K increased with time. The sorption−diffusion process becomes faster on increasing temperature, resulting in a higher sulfur concentration in the film. The sulfur concentrations close to saturation ($c_{s\infty}$) of all films are given in Table 2. The highest values of $c_{s\infty}$ were obtained in samples

treated with potassium pentathionate at 293 K. The sulfur concentrations in samples treated at 293 K were twice or fivefold higher than those in samples treated at 283 K and 273 K. The concentration of sulfur sorbed at 283 and 293 K increased significantly upon increasing temperature of potassium pentathionate solution (Fig. 2).

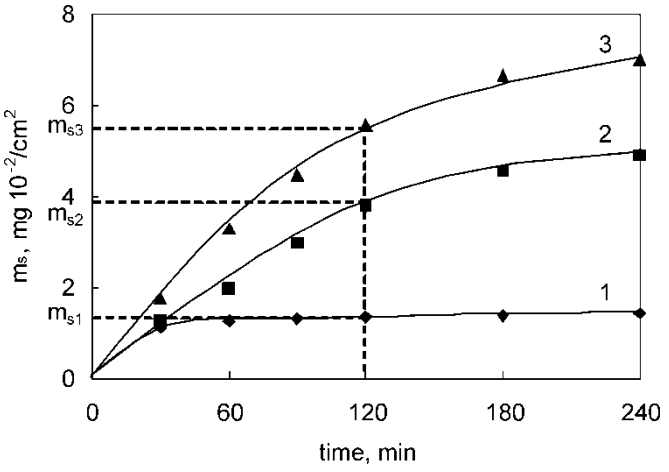

Fig. 2. Dependence of the adsorbed sulfur content in polyamide on the exposure time in solution of $K_2S_5O_6$ (c = 0.15 mol/dm^3). The temperature of PA 6 sulfuration [K]: 1 – 273, 2 – 283, 3 – 293

After lowering the temperature of the sulfuration solution, $c_{s\infty}$ in polyamide film samples clearly decreases: from 293 K to 283 K by a factor of 1.8 and from 283 K to 273 K 2.8 times. These values imply that sulfur sorption–diffusion in polyamide is less affected by the solution temperature. This is confirmed by the lowest value of the apparent adsorption heat $|\Delta H_{ads}|$ obtained (Table 2). We calculated the apparent adsorption heat from the Langmuir equation [30]. Examples representing sulfur adsorption for the determination of $|\Delta H_{ads}|$ are shown in Fig. 2. The apparent adsorption heat was negative, because molecule adsorption on the surface is an exothermic process [30]. We found that $|\Delta H_{ads}|$ increased at lower temperatures: it was almost 1.4 times smaller at the temperature interval from 283 K to 273 K than at the temperature interval from 293 K to 273 K.

To characterize the process kinetically, the apparent diffusion coefficient (D, cm^2/s) of sulfur diffusion into polyamide has been calculated. Since the diffusing substance tends to get uniformly distributed, D becomes a measure of the rate at which the system manages to reduce the concentration gradient. This rate is related to certain system parameters characterizing the thermal mobility of a diffusing particle as a part of the diffusion environment [31, 32].

Calculations of diffusion process parameters are based on Fick's second law [30, 31]. Until the front of the diffusate has not reached the centre of the film, i.e. when $c_{s\tau}/c_{s\infty} > 0.5$, the apparent coefficients of sulfur diffusion in polyamide are calculated

from the slopes [33] of the curves $1-c_{s\tau}/c_{s\infty} = f(\tau^{0.5})$ by means of the Boltzmann resolution for the semi-infinite environment expressed by

$$1-\frac{c_{s\tau}}{c_{s\infty}} = \frac{\pi}{l}\sqrt{\frac{D\tau}{8.2}} \tag{2}$$

where l is the thickness of the film, $c_{s\tau}$ is the concentration of sulfur in the sample at the time τ, and $c_{s\infty}$ is the sulfur concentration close to saturation in a sample. The calculated error in D is within ±10 %. The highest D value was obtained for the sample sulfured at 293 K: $D = 2.2\times10^{-11}$ cm^2/s. The values of D for films increased upon increasing temperature of solution (Table 2).

The dependence $\ln D = f(1/T)$ was found to be linear. Therefore, the apparent activation energy E calculated between 273–293 K by the Arrhenius equation was 25.5 kJ/mol. These values are nine to four times smaller than the energy needed for polythionate decomposition (~100 kJ/mol) [34].

Copper sulfide layers in the surface of polyamide samples were formed by the sorption–diffusion method in a heterogeneous reaction [13]:

$$S_5O_6^{2-} + 2Cu^+ + 2H_2O \longrightarrow Cu_2S + 2S + 2H_2SO_4 \tag{3}$$

Pentathionate anions diffusing into the polymer from $K_2S_5O_6$ solution interact with cuprous ions in the solution of copper(I) salt. Depending on the initial sulfur concentration in the polyamide and the duration of the treatment with the copper salt solution, light brown, brown or even black copper sulfide layers were obtained.

Since the mobility of Cu^+ ions is considerably higher than that of $S_5O_6^{2-}$ ions, the Cu_xS layer is formed by cuprous ions diffusing into sulfured polyamide. A thin sulfide layer formed on the surface of the polymer separates the reacting substances and hinders further diffusion of Cu^+ ions into the polymer. Diffusion of $S_5O_6^{2-}$ ions, as well as copper ions, is possible only in amorphous phase zones of the polyamide, however, due to the presence of structural defects, diffusion of small-molecular compounds continues, despite the presence of Cu_xS layers.

The properties of the obtained copper sulfide layers are not only dependent on the sulfur concentration but also on the content of reacted copper. Therefore, after formation of the sulfide layers, the content of copper per unit area of the layer has been determined. It was found that the content of copper is dependent on the conditions of sulfuration. The content of copper increases with increasing content of sulfur in the polyamide film. Thus, irrespective of sulfuration conditions, the highest values of m_{Cu} were obtained in PA 6 film samples treated at 293 K. Figure 3 shows the dependence of the content of copper in a sulfide layer on the duration of treatment with $K_2S_5O_6$ solutions at 293 K.

It has been found that the content of copper in a layer strongly depends on the concentration of sulfur diffused in polyamide, i.e. the content of copper varies in pro-

portion to the sulfur concentration in PA 6. The data obtained show also that the content of copper in a sulfide layer increases uniformly and depends on the temperature of the sulfuration solution. The highest differences in copper contents were obtained in PA 6 samples sulfured in $K_2S_5O_6$ solutions at 303 K; m_{Cu} was six times higher than in the samples sulfured at 293 K. The highest values of copper content were obtained in samples treated in $K_2S_5O_6$ solution at 303 K. The content of copper in PA 6 samples sulfured at 303 K varies only slightly, i.e. m_{Cu} values in PA 6 samples are only about twice higher.

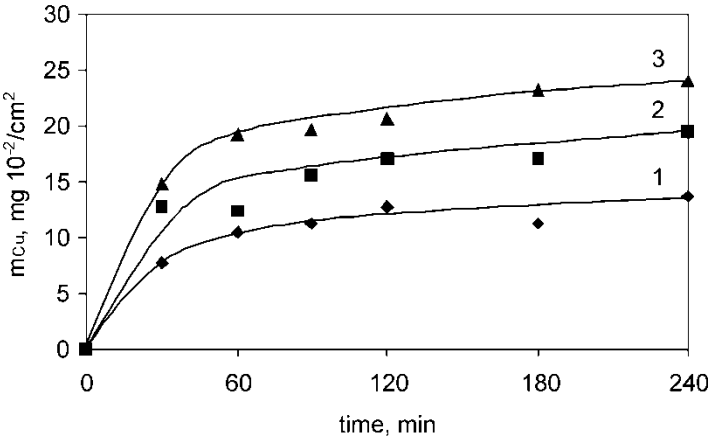

Fig. 3. Dependence of copper content (m_{Cu}) in the Cu_xS layer on polyamide on its exposure time in a 0.15 mol/dm^3 $K_2S_5O_6$ solution in 0.1 mol/dm^3 HCl at various temperatures. Sulfured PA 6 was treated with Cu(I) salt solution at 308 K for 30 min. Temperature [K]: 1 – 273, 2 – 283, 3 – 293

Copper content in PA 6 samples sulfured in $K_2S_5O_6$ solutions at 273 K was approximately 1.5 times smaller than that at 283 K and two times smaller than at 293 K. Since the Cu_xS layer is very thin in comparison with the whole thickness of the PA 6 film, and in the IR spectra not only vibrations corresponding to Cu_xS, but also to the reaction (3) products are observed, the ATR-FTIR spectrum was additionally recorded.

ATR-FTIR spectra of virgin polyamide and polyamide initially treated with $K_2S_5O_6$ solution at 293 K for 240 min and subsequently with a Cu(I) salt solution for 30 min are presented in Fig. 4. In ATR-FTIR spectra of modified polyamide, besides the polymer peaks, a broad absorption band in the range 1000−1100 cm^{-1} and narrow peak at 613 cm^{-1} appear. According to the published data [25−28], the peak at 1062 cm^{-1} is due to symmetrical valence vibrations and another one at 1107 cm^{-1} to asymetrical valence vibrations of S=O group. The peak at 613 cm^{-1} corresponds to δ_s(O−S−O) [25, 29]. Peaks of ν(S−S) and ν(Cu−S) are located in the range 200−500 cm^{-1} and have not been recorded in the presented spectrum. X-ray analysis was carried out for a further characterization of Cu_xS layers.

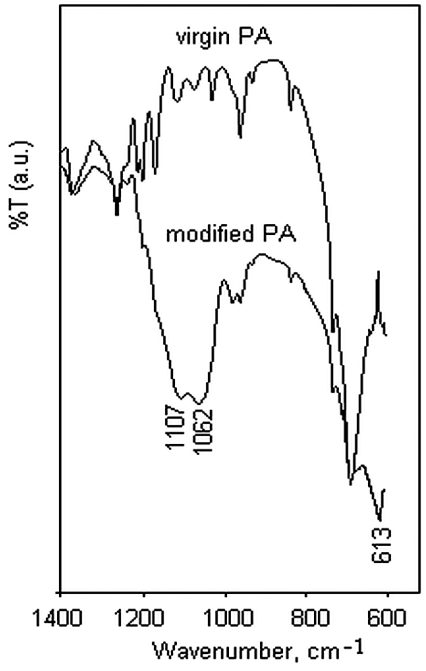

Fig. 4. ATR-FTIR spectra of virgin PA 6 and PA 6 initially treated with solution of $K_2S_5O_6$ at 293 K for 240 min and subsequently with a Cu(I) salt solution for 30 min; *T* – stands for transmittance

Cu/S molar ratios in copper sulfide layers on polyamide sulfured in solutions at various temperatures are presented in Table 3. At 273 K, the ratio is practically independent of the sulfuration time, whereas at higher temperatures it decreases with increasing time. Most probably, due to a high sulfur concentration in the film, the dense Cu_xS layer formed in the surface of PA 6 prevents the penetration of Cu^+ ions into the polymer and the interaction with the diffused pentathionate ions. These results imply that the composition of the copper sulfide layers obtained by the sorption–diffusion method is variable.

Table 3. Cu/S molar ratios in copper sulfide layers on polyamide first treated in $K_2S_5O_6$ solution at various temperatures and then in Cu(I) salt solution at 308 K for 30 min

Exposure time, min	Cu/S (S=1)		
	273 K	283 K	293 K
30	6.3	6.4	6
60	5.8	3.5	4.4
90	5.6	3.5	3.3
120	6.7	3.5	2.5
180	5.8	3.2	2.4
240	6.6	3.2	2.3

Initially, dielectric polyamide films after their modification with copper sulfide layers on their surface matrix become semiconductors (Table 4).

Table 4. Sheet resistance (R) of Cu_xS layers on polyamide first treated in $K_2S_5O_6$ solution at various temperatures and then in Cu(I) salt solution at 308 K for 30 min

Exposure time, min	R, kΩ/cm^2		
	273 K	283 K	293 K
30	7.8×10^3	6.3×10^3	222
60	6.4×10^3	5.3×10^3	224
90	2.7×10^3	3.8×10^3	162
120	0.8×10^3	1.1×10^3	34
180	0.4×10^3	366	28
240	380	498	6.3

Electrical resistance on the surface of a modified PA 6 film decreases upon increasing temperature of the sulfuration solution and its value depends on the sulfuration conditions. Samples sulfured at 273 K and then treated with copper(I) salt solution were not electrically conductive. The lowest resistances were obtained in PA 6 samples sulfured in $K_2S_5O_6$ solution at 283 K. PA 6 samples sulfured at 293 K were found to be most conductive, possibly because of the varying composition of copper sulfide layers formed in the surface of the PA 6 film (Table 3), since it is known [9] that the specific electrical resistance of Cu_xS decreases by six orders of magnitude with a decrease in x from 2 to 1. The lowest resistances were obtained for PA 6 samples when the Cu/S molar ratio in the layer was close to 2.3.

Cu_xS layers are formed both on the surface and in the bulk of the polymer. However, the electrical resistance depends only on the characteristics of the surface layer. Thus, the electrical properties of Cu_xS layers are related not only to the chemical composition but also to the homogeneity of the layer.

Polyamide consists of randomly distributed amorphous and crystalline zones. Copper sulfide isles are formed in amorphous zones, therefore, the coating can be nonuniformly distributed on the surface of the polymer. Due to smaller amorphous zones in polyamide films, thinner, discontinuous and less electrically conductive Cu_xS layers are formed [16].

The phase composition of the deposited film was established by comparing its X-ray images with those of known minerals [2, 4, 35]. The chemical composition and crystal structure of the majority of Cu_xS minerals such as chalcosine (Cu_2S), djurleite ($Cu_{1.95}S$), yarrowite ($Cu_{1.12}S$), and covellite (CuS) were investigated [36]. The crystal structure of Cu_xS depends on the chemical composition and synthesis conditions. The composition of Cu_xS deposited by chemical methods has been scarcely investigated. Structural studies of Cu_xS layers deposited by sorption–diffusion methods are limited by the polycrystallinity of the layers obtained, by the existence of Cu_xS phases of various compositions and structures, and by the crystallinity of the PA 6 film itself. The intensity of its maximum at $\Theta = 130^\circ$ exceeds a few times the intensity of copper sulfide maximum a few times. Therefore, the region of $2\Theta \geq 26.0^\circ$ was investigated in detail. When keeping PA 6 samples with the sorptive pentathionate anions (initially

treated with $K_2S_5O_6$ solution at a temperature of 293 K for different time) in copper salt solution at 308 K, Cu_xS layers of various compositions were obtained. X-ray diffractograms of the layers showed the peaks of two various copper sulfide phases (Fig. 5).

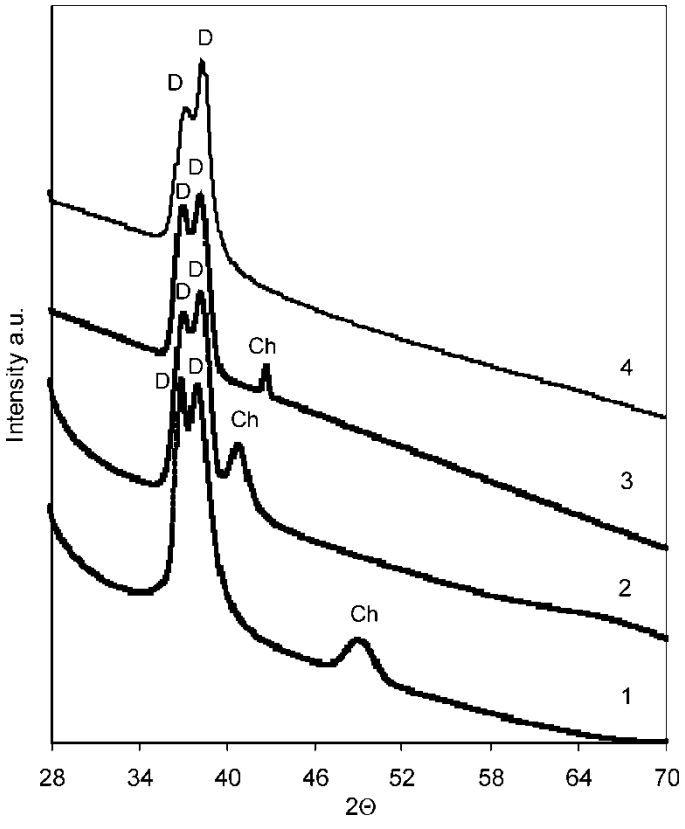

Fig. 5. X-ray diffraction patterns of layers of Cu_xS on PA 6 (D – djurleite, Ch – chalcosine). PA 6 initially treated with solution of $K_2S_5O_6$ at 293 K for various times τ_s and subsequently with a Cu(I) salt solution for 30 min. The concentration of sulfur in the polymer c_s [mol/dm^3]: 1 – 1.85 (τ_s = 30 min), 2 – 4.55 (τ_s = 90 min), 3 – 5.995 (τ_s = 120 min), 4 – 7.64 (τ_s = 240 min)

The monoclinic djurleite ($Cu_{1.9375}S$) prevails (PDF 42–564, maxima 2Θ = 36.96° and 38.2°) in the composition of sulfide films on PA 6 initially sulfurised for 30–240 min (Fig. 5, curves 1–4) in $K_2S_5O_6$ solution at 293 K (the time of the sulfurised PA 6 treatment with Cu(I) salt solution was 35 min, the temperature of the Cu(I) salt solution was 308 K). When the time of treatment in the potassium pentathionate solution is lower than 240 min, changes in the film composition occur: the intensity increases for the peaks of monoclinic djurleite, and a new phase in the composition of the sulfide film on PA 6 – a phase of tetragonal chalkosine (Cu_2S) (PDF 84–209) maxima 2Θ

= 49.28° (Fig. 5, curve 1), maxima 2Θ = 40.96° (Fig. 5, curve 2) and maxima 2Θ = 42.7° (Fig. 5, curve 3) also appears.

The obtained results lead to the conclusion that potassium pentathionate solutions at 293 K are good sulfuring agents for polyamide films. By treating the sulfured PA 6 samples with copper(I) salt solutions, electroconductive or semi-conductive copper sulfide layers of various chemical compositions are obtained.

4. Conclusions

The analysis of UV and IR spectra confirm that sulfur is sorbed by PA 6 films in the form of pentathionate ions. Sulfur concentration in polyamide increases with increasing temperature of the potassium pentathionate solution and the exposure time of the polymer. The apparent diffusion coefficient of sulfur in polycaproamide increases from 2.2×10^{-11} cm^2/s to 4.7×10^{-11} cm^2/s with increasing temperature of the potassium pentathionate solution. The calculated apparent activation energy of pentathionate diffusion in polyamide is four times smaller than that needed for polythionate decomposition. By treating sulfured PA 6 films with Cu(I) salt solution, copper sulfide (Cu_xS) layers are formed on the surface matrix of a polymer. The content of copper in these layers depends on the content of sulfur in the PA 6 matrix. Copper sulfide layers with the Cu/S molar ratio close to 2.3 exhibit low electrical resistance (6.3 kΩ/cm^2). The phase composition of a Cu_xS layer depends on the Cu/S molar ratio. Monoclinic djurleite ($Cu_{1.9375}S$) prevails in the composition of all Cu_xS films obtained on PA 6 surface. When the Cu/S molar ratio is higher than 1 : 2.3, the phase of tetragonal chalkosine (Cu_2S) is also found in film layers.

References

[1] KORZHUEV M. A., Phys. Sol. State, 40 (1998), 217.
[2] CARDOSO J., GOMEZDAZA O., IXTLILCO L., NAIR M. T. S., NAIR P. K., Semicond. Sci. Technol., 16 (2001), 123.
[3] NASCU C., POP I., IONESCU V., INDRA I., BRATU I., Mater. Lett., 32 (1997), 73.
[4] NOMURA R., KONAYO K., MATSUDA H., Ind. Eng. Chem. Res., 28 (1989), 877.
[5] GALDIKAS A., MIRONAS A., STRAZDIEN□ V., ŠETKUS A., ANCUTIEN□ I., JANICKIS V., Sensors Act. B, 67 (2000), 76.
[6] YAMAMOTO T., TANAKA K., KUBOTA E., OSAKADA K., Chem. Mater., 5 (1993), 1352.
[7] HERMANN A.M., FABICK L., J. Cryst. Growth, 61 (1983), 658.
[8] REZIG B., DUCHEMIN S., GUSTAVINO F., Sol Energy Mat., 2 (1979), 53.
[9] ŽEBRAUSKAS A., Chem. Techn., 3 (1996), 39 (in Lithuanian).
[10] ŽEBRAUSKAS A., Chemistry, 2 (1992), 112 (in Russian).
[11] JANICKIS V., ANCUTIEN□ I., ŽUKAUSKAIT□ J., Chem. Techn., 3 (2000), 28 (in Lithuanian).
[12] USSR Patent 895542, 1982.
[13] ANCUTIEN□ I., JANICKIS V., GREVYS S., Chemistry, (1997), No. 2, 3 (in Russian).
[14] KRYLOVA V., IVANAUSKAS R., JANICKIS V., Chem. Techn., 4 (2002), 56 (in Lithuanian).
[15] KRYLOVA V., DUKŠTIEN□ N., Chem. Techn., 2 (2005), 91 (in Lithuanian).

[16] JANICKIS V., MACIULEVIČIUS R., IVANAUSKAS R., ANCUTIEN I., Colloid. Polym. Sci., 281 (2003), 84.
[17] FOSS O., *Structures of Compounds Containing Chains of Sulfur Atoms*, [in:] *Advances in Inorganic Chemistry and Radiochemistry*, H.J. Emeleus, A.G. Sharpe (Eds.), Academic Press, New York, 1960, p. 237.
[18] GREGG S.J., SING K.S.W., *Adsorption Surface Area and Porosity*, Academic Press, New York, 1969.
[19] BRODSKIJ A.I., JERIOMENKO R.K., Rept. USSR Acad. Sci., 101 (1955), 487 (in Russian).
[20] *Handbook of Preparative Inorganic Chemistry 1*, G. Brauer, (Ed.), Ferdinand Enke, Stuttgart, 1975 (in German).
[21] VOGEL A., *Textbook of Quantitative Chemical Analysis I*, Longman, London, 1989.
[22] *Analytical Methods for Atomic Absorption Spectrometry Perkin-Elmer 503*, Perkin-Elmer, 1973.
[23] GOLDING R.M., J. Chem. Phys., 23 (1960), 1666.
[24] ŠUKYT J., IVANAUSKAS R., PETRAŠAUSKIEN N., JANICKIS V., ŽALENKIEN S., Chem. Techn., 2 (2005), 46 (in Lithuanian).
[25] JANICKIS V., JANICKIJ I., Trans. Lithuanian Acad. Sci. B, 6 (1986), 43 (in Russian).
[26] NICKLESS G., *Inorganic Sulphur Chemistry*, Elsevier, Amsterdam, 1968, p. 199.
[27] JULIEN C., BARNIER S., IVANOV I., GUITTARD M., PARDO M.P., CHILOUET A., Mat. Sci. Eng. B, Solid, 57 (1999), 102.
[28] NYQUIST R.A., KAGEL R.O., *Infrared Spectra of Inorganic Compounds*, Academic Press, New York, 1971.
[29] MICKEVIČIUS D., *Methods of Chemical Analysis*, Žiburys, Vilnius, 1998 (in Lithuanian).
[30] ALBERTY R.A., SILBEY R.J., *Physical Chemistry*, Wiley, New York, 1996.
[31] MALKIN A.J., TCHALYCH A.E., *Diffusion and Viscosity of Polymers*, Khimya, Moscow, 1979 (in Russian).
[32] TCHALYCH A.E., *Diffusion in System of Polymers*, Khimiya, Moscow, 1987 (in Russian).
[33] TCHALYCH A.E., *Methods of Measuring Diffusion of Polymers*, Znaniie, Moscow, 1975 (in Russian).
[34] JANICKIS V., *Formation, structure and the physical chemistry properties of derived sulfane and selenane*, Thesis, Polytechnical Institute, Kaunas, 1983, p. 447 (in Russian).
[35] ŽEBRAUSKAS A., MIKALAUSKIEN A., LATVYS V., Chemistry, (1992), No. 2, 131 (in Russian).
[36] GOBLE R., Can. Mineral, 23 (1985), 61.

Received 7 September 2006
Revised 4 May 2007

Materials Science-Poland, Vol. 25, No. 4, 2007

Alloying effects on the energy and electronic structures of vanadium hydrides

D. W. ZHOU[1,2*], J. ZHANG[3], P. PENG[3], J. S. LIU[3]

[1]State Key Laboratory of Advanced Design and Manufacturing for Vehicle Body, Hunan University, Changsha 410082, China

[2]School of Machine and Automobile Engineering, Hunan University, Changsha 410082, China

[3]School of Materials Science and Engineering, Hunan University, Changsha 410082, China

A first-principles plane-wave pseudopotential method based on the density functional theory is used to investigate the energy, electronic structure and stability of VH and VH_2 alloyed by a 3d transition metal. It is found that the stability of VH and VH_2 decreases after alloying, which originates from a small number of bonding electrons at the Fermi level. In the case of VH_2, the ionic interaction is dominant between alloying atoms and H atoms, while the ionic bond interaction between the later 3d alloying atoms and H atoms is important in VH.

Key words: *plane-wave pseudopotential theory; vanadium hydride; electronic structure*

1. Introduction

Magnesium-based hydrogen storage alloys have been extensively studied due to their high hydrogen storage capacity, low density and low cost. However, slow hydriding and dehydrogenating kinetics and high dissociation temperatures caused by their relatively high stability limit their practical application for hydrogen storage. Liang et al [1] have found that mechanical milling of MgH_2 with 5 at. % of V produces a nanocomposite structure of β-MgH_2 + γ-MgH_2 + $VH_{0.81}$, and this nanocomposite solves the problem of slow kinetics of MgH_2 below 473 K in vacuum. They suggest that nucleation of α-Mg at the VH/MgH_2 interface might be easy but there has been little effort to prove the view. Recently, in our group, $VH_{0.81}$ crystal structure is considered as VH phase, and a VH/MgH_2 interfacial model is designed and constituted

* Corresponding author, e_mail: ZDWe_mail@yahoo.com.cn

to investigate the structural stability and hydriding and dehydrogenating kinetics of MgH_2–V system [2]. The results show that the catalytict effect of V on dehydrogenating kinetics of MgH_2 phase can be attributed to the effects of VH/MgH_2 interfaces with a low structural stability [2]. But H atoms in MgH_2 slab are adsorbed by V atoms due to strong interactions between V and H, and a very stable hydride, VH, can be formed. Hence, H atom is not easy to release through the reaction: VH→V+H, which is not benefit for the hydriding and dehydrogenating kinetics of the MgH_2–5 at. % V system. Moreover, as the hydriding proceeds further, another reaction, VH+H→VH_2, takes place and a new hydride, VH_2, is formed [3]. To understand the intrinsic mechanisms of alloying effects on the structural stability of vanadium hydrides, Matumura et al. [4] calculated the electronic structure of V_2H and VH_2 compounds with alloying elements X (X = Ti, V, Cr, Fe, Co, Ni, Zr, Nb, Mo, W) by adopting the DV-X_a cluster method. It was shown that the alloying elements considered destabilized vanadium hydrides and the interaction between alloying atoms and H atoms is important for improving the structural stability and the dehydrogenation properties. However, despite such great efforts, alloying effects of various metals, such as 3d transition metals, have not as yet been elucidated for the structural stability and dehydrogenation properties of VH and VH_2. Based on the previous work [2], in this paper, at first, the stability of VH and VH_2 is analyzed and discussed, and then, the energy, electronic structure and stability of VH and VH_2 alloyed by 3d transition metal are investigated by using first-principles plane-wave pseudopotentials methods based on density functional theory. Some new results will be expected to be of benefit for designing the advanced magnesium-based hydrogen storage materials.

2. Method of computation

Cambridge Serial Total Energy Package (CASTEP) [5], a first-principles plane-wave pseudopotentials method based on the density functional theory, is used in this work. CASTEP uses a plane-wave basis set for the expansion of the single-particle Kohn-Sham wave-functions, and pseudopotentials to describe the computationally expensive electron-iron interaction, in which the exchange-correlation energy by the generalized gradient approximation (GGA) of Perdew is adopted for all elements in our models by adopting the Perdew–Burke–Ernzerhof parameters [6]. Ultrasoft pseudopotentials represented in reciprocal space are used [7]. The atomic orbitals used in the present calculations are: H $1s^1$,Sc $3s^2$, $3p^6$, $3d^1$, $4s^2$, Ti $3s^2$, $3p^6$, $3d^2$, $4s^2$, V $3s^2$, $3p^6$, $3d^3$, $4s^2$, Cr $3s^2$, $3p^6$, $3d^5$, $4s^1$, Mn $3d^5$, $4s^2$, Fe $3d^6$, $4s^2$, Co $3d^7$, $4s^2$, Ni $3d^8$, $4s^2$, Cu $3d^10$, $4s^1$, Zn $3d^10$, $4s^2$. For cluster and crystal models, the cutoff energy of atomic wave functions (PWs), E_{cut}, is set at 220 eV, 310 eV, respectively. Sampling of the irreducible wedge of the Brillouin zone is performed with a regular Monkhorst–Pack grid (12×12×12) of special *k*-points, which is 0.5 nm^{-1}. A finite basis set correction and the Pulay scheme of density mixing [8–10] are applied for the evaluation of en-

ergy and stress. All atomic positions in our model have been relaxed according to the total energy and force using the Broyden–Flecher–Goldfarb–Shanno (BFGS) scheme [12] based on the cell optimization criterion (RMs force of 0.05e V/Å, stress of 0.1 GPa, and displacement of 0.002 Å). The calculation of total energy and electronic structure are followed by the cell optimization with the self-consistent -field (SCF) tolerance of 2.0×10^{-6} eV.

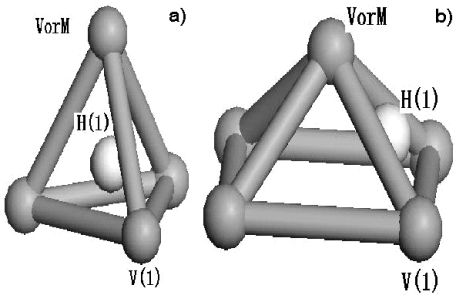

Fig. 1. Cluster model employed in the VH_2 (a) and VH calculations (b), where alloying elements M (M = Sc, Ti, Cr, Mn, Fe, Co, Ni, Cu, Zn) are substituted for one V atom

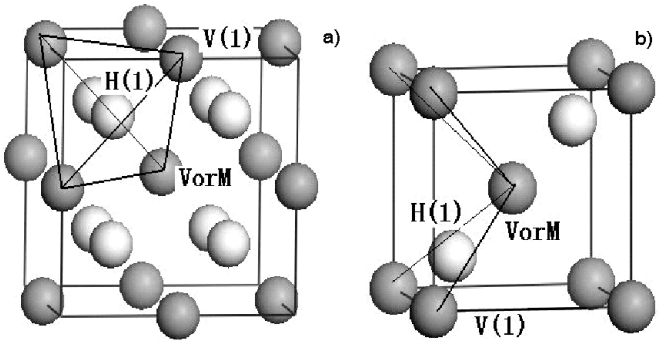

Fig. 2. Crystal models of VH_2 (a) and VH (b)

The cluster model shown in Fig. 1a is constructed based on the CaF_2 type crystal structure of VH_2 (*Fm*3*m*, group No. 225, Fig. 2a) [11]. As far as VH_2 crystal is concerned, the lattice parameters are $a = b = c = 4.271$ Å, and four V atoms occupy (0,0,0) sites and eight H atoms locate in (0.25,0.25,0.25) sites. Another cluster model shown in Fig. 1b is constructed on the basis of a hypothetical structure of VH. For the VH crystal structure (Fig. 2b), we consider that VH crystal cell is similar to the *bcc* V(H) solid solutions and the site occupied by H atoms in this cell is similar to that in MgH_2 crystal [2]. In order to compare the stability of VH and VH_2, the crystal model is used, shown in Figs. 2a, b. In order to examine alloying effects on the energy and electronic structure of vanadium hydrides, one V atom in the cluster shown in Fig. 1a for VH_2, or Fig. 1b for VH are substituted for various alloying elements, M (M = Sc,

Ti, Cr, Mn, Fe, Co, Ni, Cu, Zn). Hence, the corresponding VH_2 and VH cluster models are expressed as V_3MH and V_4MH, respectively.

3. Results and discussion

3.1 Stability of VH and VH_2

In this paper, the stability of VH and VH_2 is discussed by the following [12]

$$\Delta H_1 = E_{\text{tot}}(\text{VH}) - \text{E}_{\text{tot}}(\text{V}) - \frac{1}{2}E_{\text{tot}}(\text{H}_2) \tag{1}$$

$$\Delta H_2 = E_{\text{tot}}(\text{VH}_2) - E_{\text{tot}}(\text{VH}) - \frac{1}{2}E_{\text{tot}}(\text{H}_2) \tag{2}$$

where $E_{\text{tot}}(VH_2)$ and $E_{\text{tot}}(VH)$ are the energies of primitive cells of VH_2 and VH, respectively. $E_{\text{tot}}(V)$ and $E_{\text{tot}}(H_2)$ are the energies of a V atom and a hydrogen molecule, respectively. The value of ΔH_1 calculated from Eq. (1) is 3.5465 eV/atom, which means the heat absorbed during the reaction V + H → VH but the value of ΔH_2 calculated from Eq. (2), is –1.94095 eV/atom, which means that upon further hydriding, another reaction, VH + H→VH_2, proceeds and a new hydride, VH_2 is formed.

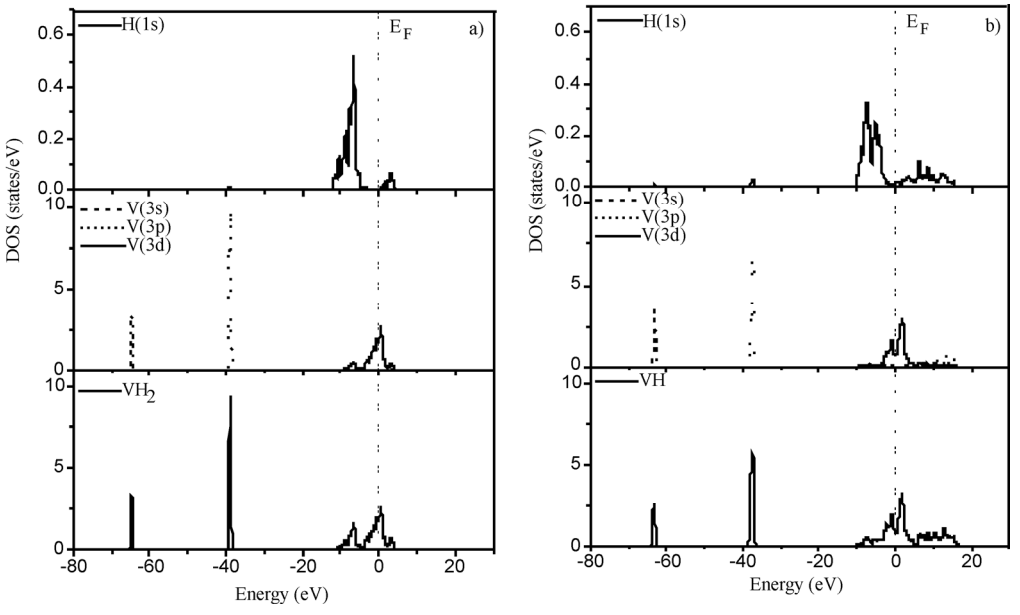

Fig. 3. Total and partial density of states of (a) VH_2 (b) VH crystal structure

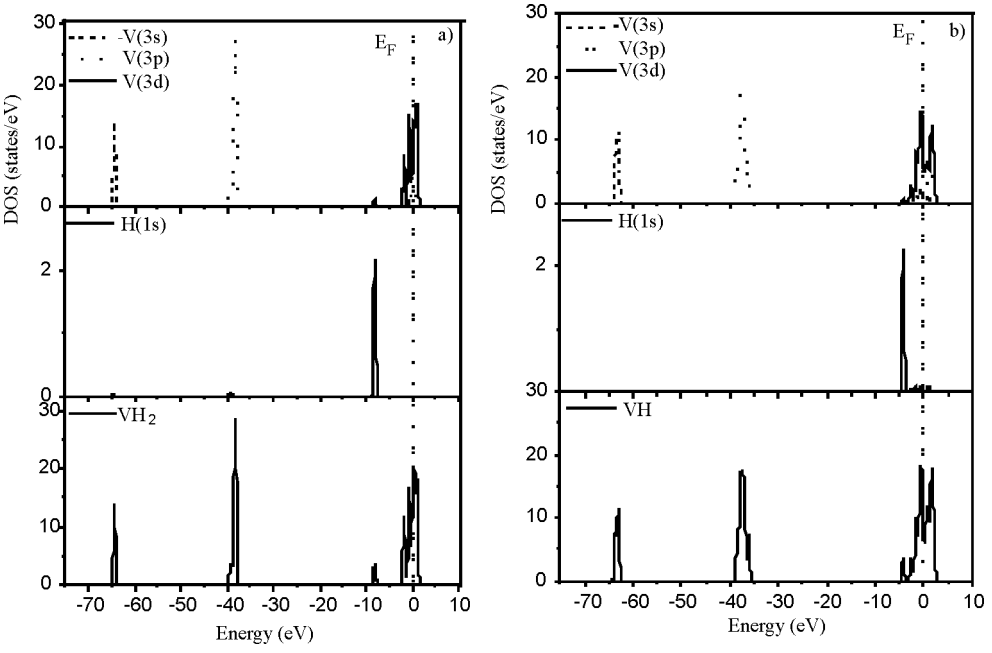

Fig. 4. Total and partial density of states of (a) VH_2 (b) VH cluster structure

Further analysis of total and partial densities of states (DOS, PDOS) of the crystal model for VH_2 and VH has been performed. As shown in Figs. 3a and 3b, for VH_2 and VH, the states located around –65 eV and –40 eV originated from V(3s) and V(3p) electrons, respectively. These electrons are usually considered as inner-core electrons and do not contribute to the bonding between atoms. Here, it must be pointed out that for VH_2, the main bonding peaks at E_F are dominated by the V(3d) electrons, while for VH the bonding peaks at E_F are the result of the bonding between H(1s) and V(3d) electrons. Therefore, this leads to a relatively high formation energy of VH [13–15]. The same analysis get the similar results for VH_2 and VH cluster models, shown in Figs. 4a and 4b, respectively. Since H atom is not easy to release for VH, it is necessary that the stability of VH and VH_2 is reduced by 3d transition metal alloying in order to improve the hydriding and dehydrogenating kinetics of MgH_2-5at%V systems.

3.2. Influence of alloying elements on the stability of VH and VH_2

Heat of formation. In order to study the influence of alloying elements on the stability of VH and VH_2, the heat of formation of the cluster model for VH_1 and VH_2 based on the above analysis of DOS shown in Figs. 3 and is calculated from [16]:

$$H_1 = E_{\text{tot}}\left(\text{V}_3\text{MH}\right) - 3E_{\text{tot}}\left(\text{V}\right) - E_{\text{tot}}\left(\text{M}\right) - \frac{1}{2}E_{\text{tot}}\left(\text{H}_2\right) \tag{3}$$

$$H_2 = E_{\text{tot}}\left(\text{V}_4\text{MH}\right) - 4E_{\text{tot}}\left(\text{V}\right) - E_{\text{tot}}\left(\text{M}\right) - \frac{1}{2}E_{\text{tot}}\left(\text{H}_2\right) \tag{4}$$

where $E_{\text{tot}}(\text{V}_3\text{MH})$ and $E_{\text{tot}}(\text{V}_4\text{MH})$ are total energies of the cluster model for VH_2 and VH, respectively. $E_{\text{tot}}(\text{M})$ is the energy of M atoms. Heats of formation for VH_2 and VH calculated from Eqs. (3) and(4) are shown in Figs. 5a, b, respectively. The results show that heat of formation decreases after alloying. Hence, the stabilities of VH_2 and VH are reduced compared with those without alloying.

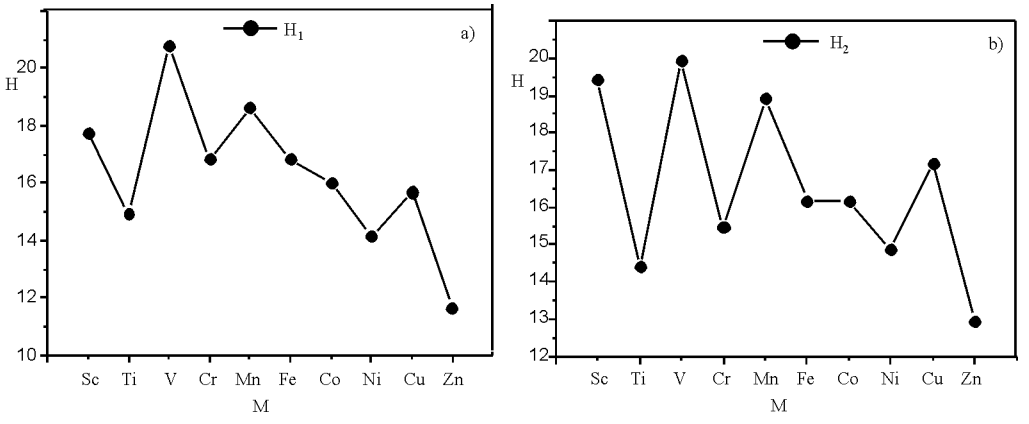

Fig. 5. Heats of formation of VH_2 (a) and VH (b) with alloying elements addition. H_1 and H_2 denote the heat of formation of the cluster model for VH_1, VH_2 (Eqs. (3) and (4), respectively

Density of states. Further analysis of total and partial densities of states (DOS, PDOS) of VH_2 and VH was performed to understand the electronic structure mechanism on the change of the stability. As far as VH_2 is concerned, the main bonding peaks at E_F are dominated by the V(3d) electrons, while for VH the bonding peaks at E_F are the result of the bonding between H(1s) and V(3d) electrons (cf. Sect. 3.1). Calculations of total and partial densities of states (DOS, PDOS) of the cluster model with alloying elements addition have been performed. The results show that the energy range and the contribution of valence electron of VH_2 or VH are almost the same as those without alloying element added. As far as the crystal with the same constituent and various types of structure is concerned, a conclusion about relative stability of phase is often derived from comparison of the values of their densities of states at the Fermi level $N(E_F)$, that is, the lower is $N(E_F)$, the more stable is the corresponding phase [17–19]. To verify if the criterion is valid in the case of VH and VH_2, the calculated values of $N(E_F)$ of VH_2 and VH have been analysed (Figs. 6a, b). As shown in Fig. 6a, $N(E_F)$ value of pure VH_2 is 9.3750 electrons/eV, but for Sc, Ti, Cr, Mn, Fe, Co, Ni, Cu, Zn alloying systems, the $N(E_F)$ value of VH_2 are (in electrons/eV) 10.3676, 10.2206, 10.5147, 9.6547, 13.4449, 12.9596, 9.9265, 11.9485, respectively. As shown in Fig. 6b, the $N(E_F)$ value of pure VH is 6.9118electrons/eV, but for the alloying systems, the $N(E_F)$ value of VH are (in electrons/eV) 7.3529, 8.2353, 6.1765,

7.9044, 8.7500, 12.6471, 10.4412, 8.6765, 7.7206, respectively. Based on the above analysis, as far as VH and VH_2 is concerned, there are less bonding electrons at the Fermi level compared with those without alloying.

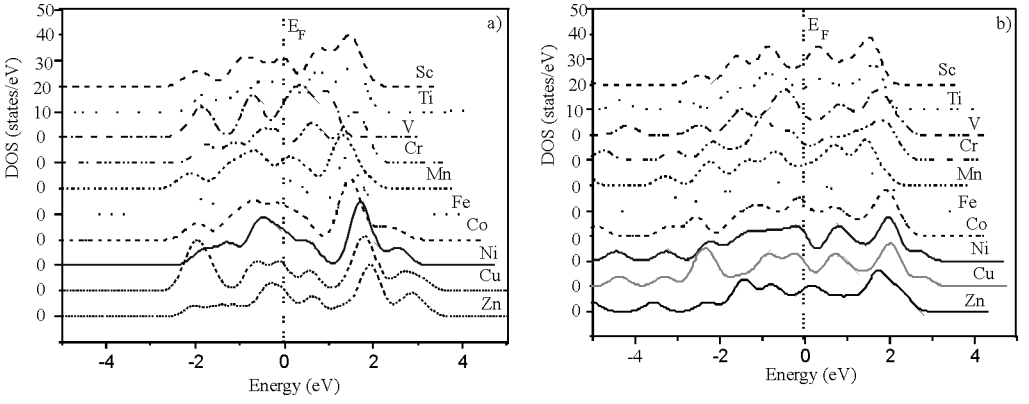

Fig. 6. Density of states of (a) VH_2 (b) VH at Feimi level with alloying elements addition

Bond order between atoms and ionicities. As explained earlier, the bond order is the overlap population of electrons between atoms, and this is a measure of the strength of the covalent bond between atoms. In order to discuss the change in calculated properties (see Fig. 5) when the alloying atom changes from Sc to Zn, the bond order between atoms changing with alloying elements is calculated (Fig. 7). Every bond order shown in this figure is the value per atomic bond in the cluster. M = V means pure VH_2. As shown in Fig. 7, the V(1)–V(2) bond orders are always positive, and there are no obvious changes. The H(1)–V(1) bond orders are also positive, not including Cr and V, indicating that there is a strong interaction between them. On the other hand, the H–M bond orders are negative, not including Cu and Cr. But for the sum of these metal–hydrogen bond orders, a big change can be found. Sc–V, Cu–V and Zn–V bonds cannot be identified, not including Ti, the V–M bond order becomes smaller when the atomic size of alloying elements is larger. This reason is attributable to the atomic size of M being much larger than that of V. The substitution of a large M atom for a small V atom induces the lattice expansion, and the M–V(1) distance becomes longer than the V–V(1) distance. As a result, the strength of the covalent bond between M and V atoms reduces.

Further analysis on the ionicity of each atom in the cluster for VH_2 is also done according to the Mulliken population analysis. The results are shown in Fig. 8. The ionicities of V atoms and M (not including Cr, Cu and Zn) are always positive, whereas the ionicities of hydrogen atoms are always negative. These results indicate that charge transfer takes place mainly from V atoms and alloying elements towards the hydrogen atoms. Such a change transfer induces the ionic interaction between them.

As shown in Fig. 9 (the signs of V atoms are shown as in Figs. 1b and 2b), the V(1)–V(2) bond orders are always positive, and there are not obvious changes. On the

other hand, the H(1)–V(1) bond orders are also positive, indicating that there is a strong interaction between them. The H–M bond orders are also positive. But for the sum of these metal–hydrogen bond orders, a big change can be found. The change of V–M bond order is not distinct when atomic sizes of alloying elements are larger.

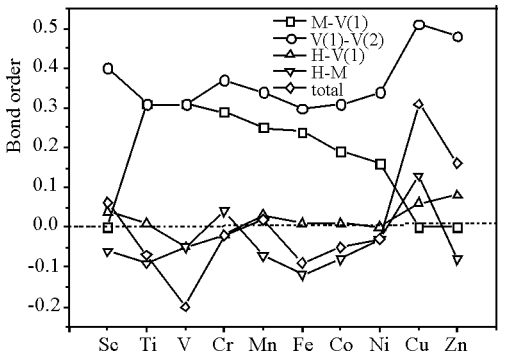

Fig. 7. Bond orders with alloying elements in the VH_2 cluster

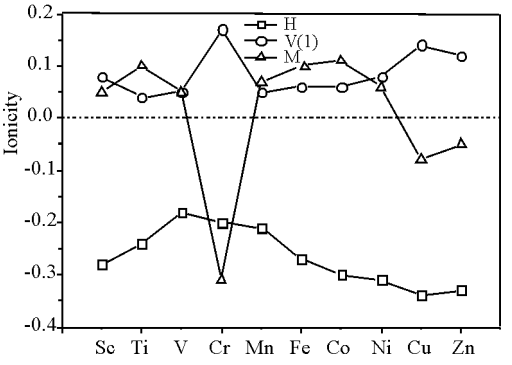

Fig. 8. Ionicities of atoms in the VH_2 cluster with alloying elements

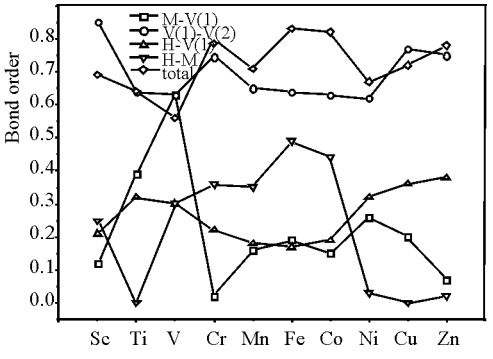

Fig. 9. Bond orders with alloying elements in the VH cluster

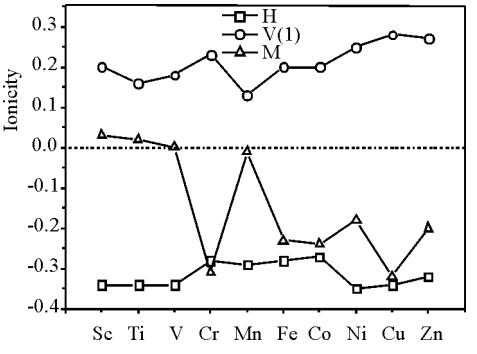

Fig. 10. Ionicities of atoms in the VH cluster with alloying elements

The same analysis is done for the ionicity of each atom in the cluster for VH. The results are shown in Fig. 10. The ionicities of V atoms are always positive, whereas the ionicities of hydrogen atoms are always negative. But the ionicities of M (not including Sc and Cu) are positive. These results indicate that charge transfer takes place mainly from V atoms and alloying elements towards the hydrogen atoms.

The ionicity difference. In the previous section, it was found that there is the ionic bond interaction between alloying atoms and H atoms. Based on this result, in this section, the ionicity difference between H and M atom for VH_2 and VH is calculated and shown in Figs. 11a, b, respectively. As far as VH_2 is concerned, it is apparent that the calculated result from Fig. 11a is similar to heat of formation shown in Fig. 5a,

even though there is a certain discrepancy in Cr and Ni. Thus, the ionic interaction between H and M atoms is important in alloyed VH_2. But this does not necessarily mean that the covalent interaction is not dominant. For VH, it is found that the calcu-

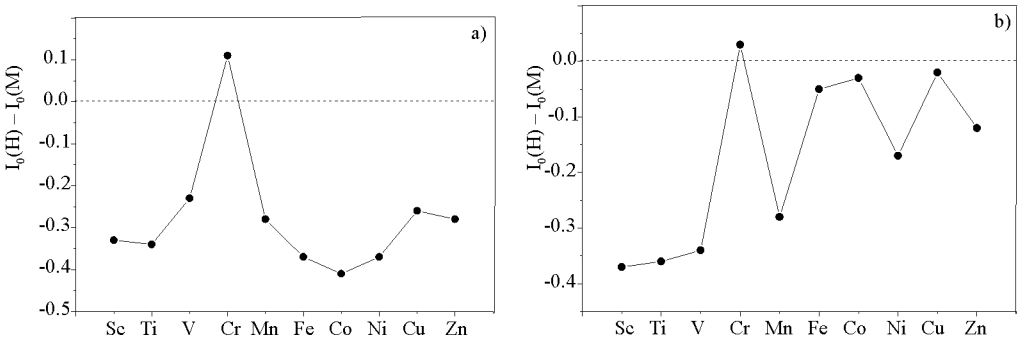

Fig. 11. Comparison between the calculated ionicity differences: a) VH_2, b) VH

lated value from Fig. 11b is not similar to heat of formation shown in Fig. 5b, except for later-3d transition metal alloying elements. Therefore, for the change in calculated properties (See Fig. 5) when the alloying atom changes from Sc to Zn, in the case of VH_2, the ionic interaction is dominant between alloying atoms and H atoms [4], while the ionic bond interaction between the later 3d alloying atoms and H atoms is important in VH. Here, an important view must be pointed out that the work is being done on further studying the reason for the correlation between the ionicity difference and calculated properties.

4. Conclusions

- The stability of VH and VH_2 decreases after alloying, which originates from small numbers of bonding electrons at the Fermi level.
- In the case of VH_2, the ionic interaction is dominant between alloying atoms and H atoms, while the ionic bond interaction between the later 3d alloying atoms and H atoms is important in VH.

Acknowledgement

We wish to thank Dr. Y. Song, Professor of the Department of Materials, Queen Mary, University of London for his helpful discussion. The work was supported by Ph. D Programs Foundation of Ministry of Education of China (20020530012).

References

[1] LIANG G., HUOT J., BOILY S., VAN NESTE A., SCHULZ R., J. Alloys Comp., 292 (1999), 247.
[2] ZHOU D.W., PENG P., LIU J.S., Sci. China Ser. E, 49 (2006), 129.

[3] KLEINER J., SEVILLA E., COTTS R.. Phys. Rev. B, 33 (1986), 6662.
[4] MATUMURA T., YUKAWA H., MORINAGA M., J. Alloys Comp., 284 (1999), 82.
[5] SEGALL M.D., LINDAN P.L.D., PROBERT M.J., PICKARD C.J., HASNIP P.J., CLARK S.J., PAYNE, M.C., J. Phys: Cond. Matter, 14 (2002), 2717.
[6] MARLO M., MILMAN V., Phys. Rev. B, 62 (2000), 2899.
[7] VANDERBILT D., Phys. Rev. B, 41, (1990), 7892.
[8] HAMMER B., HANSEN L.B., NORKOV J.K., Phys Rev B, 59 (1999), 7413.
[9] FRANSCIS G.P., PAYNE M.C., J. Phys: Cond. Matter, 2 (1990), 4395.
[10] MONKHORST H.J., PACK J.D., Phys. Rev. B, 13 (1976), 5188.
[11] MUELLER H., WEYMANN K., J. Less-Common Met., 119 (1986), 115.
[12] ZHOU D.W., PENG P., LIU J.S., CHEN L., HU Y.J., Trans. Nonferrous Met. Soc. China, 16 (2006), 23.
[13] YUKAWA H., MATUMURA T., MORINAGA M., J. Alloys Comp., 293–295 (1999), 227.
[14] MORINAGA M., YUKAWA H., NAKATSUKA K., TAKAGI M., J. Alloys Comp., 330–332 (2002), 20.
[15] NAKATSUKA K., YOSHINO M., YUKAWA H., J. Alloys Comp., 293–295 (1999), 222.
[16] SMITHSON H., MARIANETTI C.A., MORGAN D., VAN DER VEN A., PREDITH A., CEDER G., Phys Rev B, 66 (2002), 144107.
[17] FU C.L., WANG X.D., YE Y.Y., HO K.M., Intermetallics, 7 (1999), 179.
[18] NYLEN J., GARCIA F.J., MOSEL B.D., PÖTTGEN R., HÄUSSERMANN U., Solid State Sci., 6 (2004),147.
[19] VAKHNEY A.G., YARESKO A.N., NEMOSHKALENKO V.V., Int. J. Hydrogen Energy, 26 (2002), 453.

Received 25 September 2006
Revised 15 October 2007

Materials Science-Poland, Vol. 25, No. 4, 2007

Electrospinning and characterization of alumina borosilicate ceramic nanofibres

S. TANRIVERDI[1], B. MAVIS[2*], G. GÜNDÜZ[1], Ü. ÇOLAK[3]

[1]Kimya Mühendisliği Bölümü, Ortadoğu Teknik Üniversitesi, Ankara 06531, Turkey

[2]Makina Mühendisliği Bölümü, Hacettepe Üniversitesi, Beytepe Ankara 06800, Turkey

[3]Nükleer Enerji Mühendisliği Bölümü, Hacettepe Üniversitesi, Beytepe Ankara 06800, Turkey

Alumina borosilicate/polyvinylalcohol (PVA) composite nanofibres were prepared by the sol-gel method and electrospinning technique. Effects of solution viscosity, applied voltage, capillary tip to metal collector distance and calcination temperature were evaluated by scanning electron microscopy, X-ray diffraction, Fourier transform infrared spectroscopy and thermogravimetric/differential thermal analysis. Results indicate that while the initial fibre diameters can be fine-tuned with the right choice of alkoxide–solvent–polymer system and experimental set-up parameters (voltage and capillary tip to collector distance), the final fibre diameter, crystalline phase and morphology of alumina borosilicate fibres are largely influenced by the calcination temperature.

Key words: *electrospinning; sol-gel; nanofibre; alumina; boron; silicate*

1. Introduction

Alumina, silica and boron oxide based fibre present properties important in various applications including thermal protection, composite reinforcement and adsorption in diesel engine filters [1–6]. Alumina fibres, which have poor mechanical properties at high temperatures but good durability and mechanical properties in oxidizing environments, have been successfully prepared using melt cooling and sol-gel methods [1, 2]. On the other hand, aluminum borate fibres have attracted more attention due to their stability at high temperatures. Readey produced $Al_{18}B_4O_{33}$ whisker-like grains and found that aluminum borate phase was stable up to 1700 °C [6].

Recently the use of electrospinning technique for the production of ceramic nanofibres has been on the rise. More than 20 oxide and mixed oxide systems including

*Corresponding author, e-mail: bmavis@hacettepe.edu.tr

silicates and aluminium-borate have been electrospun successfully [7–17]. Silica based nanofibres which have unique properties like high thermal resistance with self-extinguishing character and promise for space-based applications or applications like optoelectronic devices, were synthesized via slight variations in the electrospinning technique [13–16]. Dai et al. have electrospun aluminum-borate oxide system into ultra-fine nanofibres which could potentially be used in ceramic filters and ceramic –metal composites [17].

In this work, applicability of the use of sol-gel and electrospinning techniques in preparation of alumina borosilicate ceramic nanofibres was demonstrated. Electrospinnability of the precursor solutions was ensured by the adjustment of viscosity of the solutions with polymeric additions. Electrospinning of these solutions into nanofibre composites was followed by the calcination of the electrospun fibres to obtain pure ceramic fibres.

2. Experimental

Materials. A target alumina borosilicate composition ($0.8SiO_2 \times 0.1Al_2O_3 \times 0.1B_2O_3$) with low boron content was selected. Alumina borosilicate fibres with this final composition were prepared by a proper heat treatment of the electrospun alumina borosilicate/PVA composite. Sol-gel solutions used in electrospinning were composed of tetraethyl orthosilicate (TEOS, $Si(C_2H_5O)_4$, Sigma-Aldrich, >98%), aluminum isopropoxide ($Al(OC_3H_7)_3$, Sigma-Aldrich, >97%), triethyl borate ($B(OC_2H_5)_3$, Sigma-Aldrich, >99%), polyvinyl alcohol (PVA, Sigma-Aldrich), hydrochloric acid, absolute ethanol (EtOH), isopropyl alcohol (*i*-PrOH) and doubly deionized water.

Preparation of electrospinning solution. Success in electrospinning of mixed alkoxide solutions depends heavily on the control over the hydrolysis rates of individual alkoxides and the polymers used. Therefore the selection of the alkoxide, solvent, polymer and a suitable mixing procedure are a priority. For example, initially selected aluminum alkoxide (aluminum ethoxide) was replaced by aluminum isopropoxide owing to the fact that bigger alkoxide groups decreased hydrolysis rates. Furthermore, the mixing of PVA with the alkoxides independently was found to slow down the hydrolysis rates of alkoxides, providing the means of control on sol-gel kinetics of the final mixture. The PVA and the three alkoxide solutions were prepared as follows:

PVA solution was prepared by stirring respective amounts of PVA powder and deionized water at 80 °C for 1 h. Then, the solution was cooled down to room temperature and stirred for 24 hours. TEOS was first mixed with EtOH in a beaker, and then partially hydrolyzed for 1 h with the addition of appropriate amount of acidic solution (H_2O/HCl) (solution A). Into the PVA solution placed in a beaker, acidic solution, isopropyl alcohol and triethyl borate were added in the respective order (solution B). Solution C was prepared like solution B except that in the final step the aluminum isopropoxide was used instead of triethyl borate.

For the final solution, solutions B and C were simultaneously added drop-wise into solution A and a transparent viscous solution of alumina borosilicate/PVA was obtained. In this work, three different solution mixtures (see Table 1) were used. The flow of the process is summarized in Fig. 1. Upon removal of remnant solvents and PVA from the electrospun fibres, the following final molar ratio was expected: $0.8SiO_2 \times 0.1Al_2O_3 \times 0.1B_2O_3$.

Table 1. Composition of the electrospinning solutions

Solution[a]	Solution A	Solution B		Solution C	
	TEOS:EtOH:H_2O:HCl (molar)	BEH[b] (molar)	BEH : PVA (by weight)	APH[c] (molar)	APH : PVA (by weight)
1	1:10:2:0.01	1:10:8	1:1	1:20:8	1:1
2	1:10:2:0.01	1:10:8	1:3	1:20:8	1:3
3	1:15:2:0.01	1:15:8	1:4	1:20:8	1:4

[a]Solution viscosities: 1– 2.42 P, 2 – 6.50 P, 3 – 4.60 P.
[b]BEH – $B(OC_2H_5)_3$:EtOH:HCl
[c]APH – $Al(OC_3H_7)_3$:*i*-PrOH:HCl

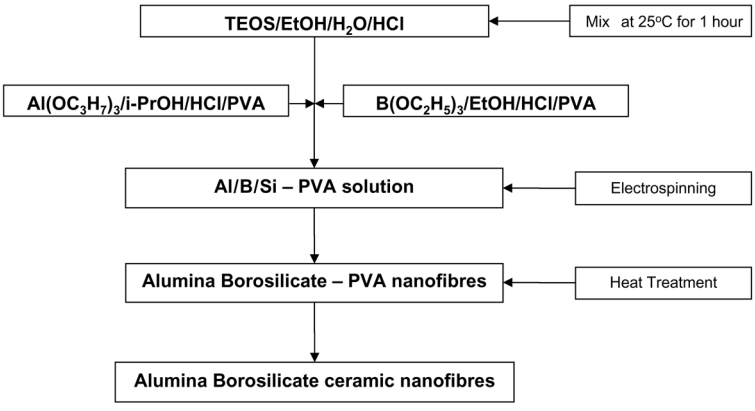

Fig. 1. Flow-chart of the alumina borosilicate ceramic nanofibre production

Preparation of nanofibres. Alumina borosilicate/PVA solutions prepared as given in Table 1 (solutions 1, 2, 3) were placed in a plastic capillary with a copper wire connected to a high voltage generator (Gamma High Voltage Research Inc., Model ES30-20W). A grounded metal drum covered with an aluminum foil, used as a collector, was placed in front of the capillary. The capillary was placed at the angle of 15° to the horizontal position to provide a uniform flow of the solution. The distance between the tip of the capillary and metal collector was varied between 7 and 15 cm. Electrospinning of the solution was performed at four voltages: 8, 10, 12 and 15 kV. Fibres pre-

pared under the applied voltages were dried initially at 70 °C for 6 h under vacuum and then calcined in air at 800, 1000 and 1200 °C for 2 h.

Characterization. For the determination of morphology and size of the nanofibres, gold sputtered samples were examined with scanning electron microscope (SEM, JSM-6400 Electron Microscope (JEOL)) equipped with NORAN System 6 X-ray Microanalysis System & Semafore Digitizer). For the determination of structure; infrared spectra of the fibres were recorded with a Bruker IFS 66/S instrument in the 400–4000 cm^{-1} range and X-ray diffraction patterns (XRD) were collected by using a Philips PW 1140 X-ray powder diffractometer with CuK_{α} radiation and a Ni filter. Combined differential thermal analysis (DTA) and thermogravimetric analysis (TG) were carried out between 25 and 1300 °C (10 °C/min) using a Rigaku (Model No. 2.22E2) system.

3. Results and discussion

3.1. Electrospinnability of sol-gel solutions

In mixing of metal alkoxides for preparation of a suitable sol-gel electrospinning solution, the addition sequence of the components and the duration of stirring have a strong influence on the electrospinnability of the solutions. TEOS is a slowly hydrolyzing alkoxide compared to aluminum isopropoxide and triethyl borate. In order to obtain a starting solution, in which all alkoxides have been evenly hydrolyzed before electrospinning, hydrolysis of TEOS was initiated one hour before the hydrolysis of aluminum isopropoxide and triethyl borate. After the preliminary experiments, it was found that the imperfections in the fibre forms (i.e., extensive bead formation and dendritic growth) could be reduced by dissolving each alkoxide in its parent alcohol. Nevertheless, in the absence of hydrochloric acid, with the 'alkoxide-parent alcohol-PVA' solutions (pH ≈ 4), the beading tendency continued. Upon addition of hydrochloric acid (pH ≈ 1) into the 'alkoxide-parent alcohol-PVA' solutions desired fibre morphologies were achieved (solution 1, viscosity of 2.42 P). In Figure 2, the micrographs of the fibres obtained by the electrospinning of solution 1 are shown.

The slight beading tendency that was still prominent could be overcome with a further adjustment of the viscosity of this 'primary' solution. The imperfect and slightly beaded morphology could be prevented by increasing the viscosity of the solution with further additions of PVA. Micrographs of fibres collected by the electrospinning of solution 2 are given in Fig. 3 (solution 2, 6.50 P).

Although fibre morphologies observed were found satisfactory for investigation of the other experimental parameters, the high viscosity prevented continuous flow of the electrospinning solution 2. Rather than decreasing the viscosity by decreasing the PVA concentration, increasing the ethyl alcohol concentration was found more appropriate for a 'continuous' electrospinning process. Micrographs of fibres collected by the electrospinning of solution 3 are given in Fig. 4 (solution 3, 4.60 P).

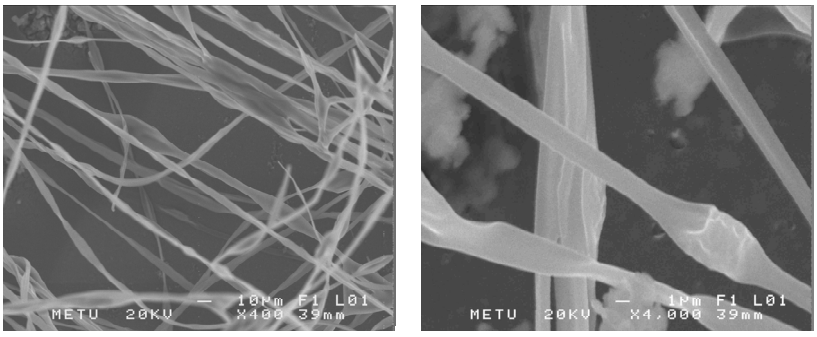

Fig. 2. Alumina borosilicate/PVA nanofibres obtained by electrospinning of solution 1 (2.42 P) (12 kV, 10 cm, pH≈1)

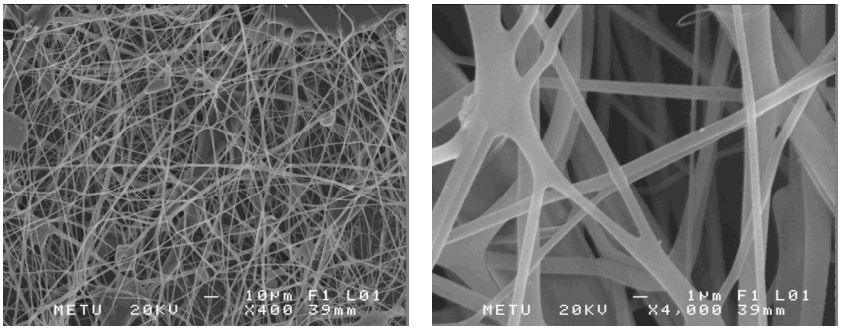

Fig. 3. Alumina borosilicate/PVA nanofibres obtained by electrospinning of solution 2 (6.50 P) (12 kV, 10 cm, pH≈1)

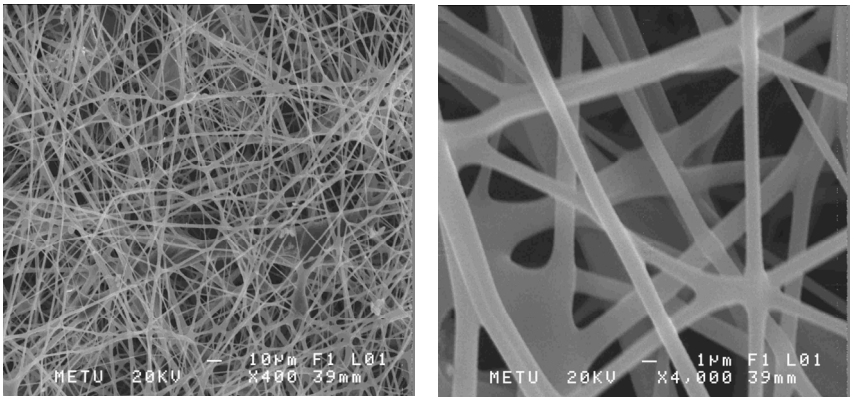

Fig. 4. Alumina borosilicate/PVA nanofibres obtained by electrospinning of solution 3 (4.60 P) (12 kV, 10 cm, pH≈1)

3.2. Parameters affecting the morphology and size of nanofibres

After the critical parameters affecting the electrospinnability of the sol-gel solutions were optimised, the experimental parameters, i.e., applied voltage and capillary

tip to metal collector distance controlling the nanofibre dimensions were studied closely. The applied voltages were 8, 10, 12 and 15 kV at a tip to collector distance of 15 cm, while the effect of distance was evaluated at 7, 10 and 15 cm with the applied voltage of 15 kV. The electrospinning results obtained at various voltages and tip to collector distances are given in Figs. 5 and 6, respectively.

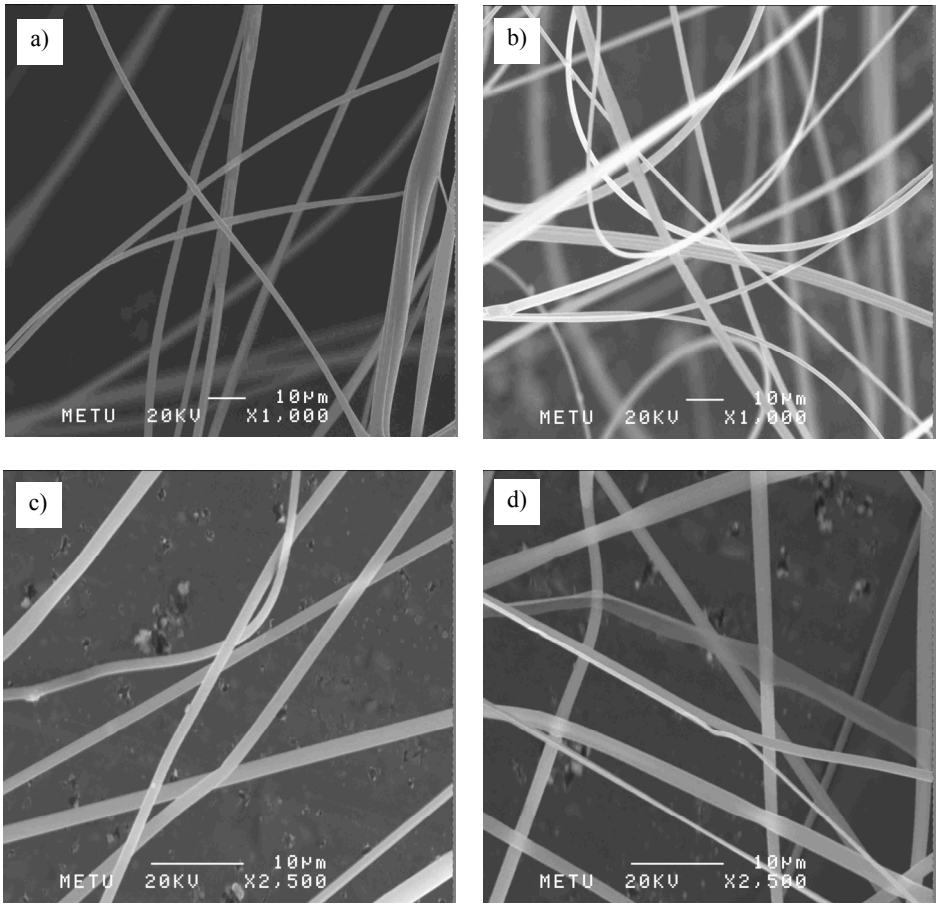

Fig. 5. Alumina borosilicate/PVA nanofibres obtained by electrospinning of solution 3 at a capillary tip to metal collector distance of 15 cm and four voltage values: a) 8, b) 10, c) 12 and d) 15 kV

Tilting the capillary by 15^{o} with respect to the horizontal axis warranted a uniform flow and accumulation of a droplet free loose fibre mat. Micrographs taken from such fibre mats were suitable for image analysis. The changes in average fibre diameters with variations in voltage values and tip to collector distances were obtained by image analysis and are summarized in Tables 2 and 3.

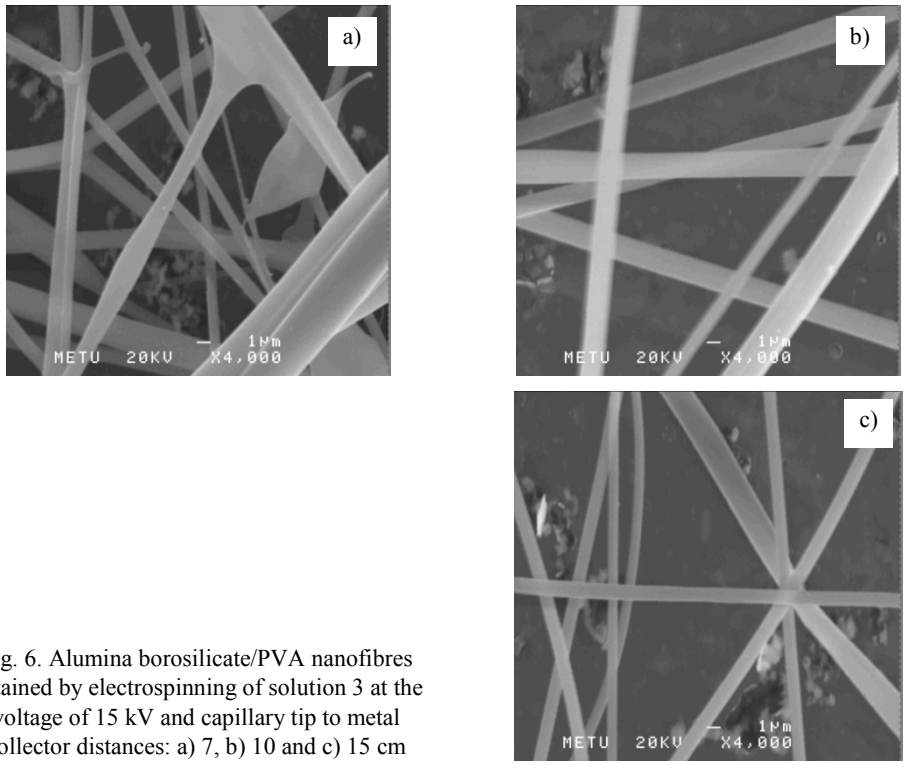

Fig. 6. Alumina borosilicate/PVA nanofibres obtained by electrospinning of solution 3 at the voltage of 15 kV and capillary tip to metal collector distances: a) 7, b) 10 and c) 15 cm

Table 2. Variation of fibre diameters with applied voltage (l = 15 cm)

Voltage [kV]	Average fibre diameter [nm]	Standard deviation [nm]
8	2226	407
10	2012	676
12	1290	368
15	871	183

Table 3. Variation of fibre diameters with capillary tip to metal collector distance (V = 15 kV)

Tip to collector distance [cm]	Average fibre diameter [nm]	Standard deviation [nm]
7	1270	631
10	1233	426
15	871	183

Measured fibre diameters decrease on increasing the applied voltage; the most pronounced effect occurs between 10 kV and 12 kV. In addition, standard deviation of measurements at higher voltage values is smaller. This implies that the fibre diameters show more uniform distribution with increasing voltage. Increasing the capillary tip to metal collector distance over 10 cm had a profound effect on the thinning of fibre di-

ameters. About a 30% decrease in the fibre diameter could be achieved at the tip to collector distance of 15 cm instead of 10 cm.

3.3. Alumina borosilicate ceramic nanofibres

The results of simultaneous TG and DTA analysis of the alumina borosilicate/PVA fibres are given in Fig. 7. In the DTA curve, there are three endothermic peaks around 130, 192 and 205 °C corresponding to the loss of absorbed water, decomposition of alkoxide alkyl groups and the pyrolysis of PVA by the dehydration on the polymer side chain, respectively [18]. The weight loss in this range was observed to be about 70%. The exothermic peaks at about 420, 440, 462 and 550 °C in the DTA curve were ascribed to the continuing decomposition of the main chain of PVA [19]. There was only about 7.3% weight loss from 400 °C up to 700 °C. No further weight loss above 700 °C indicated the formation of pure inorganic oxide in a crystalline form.

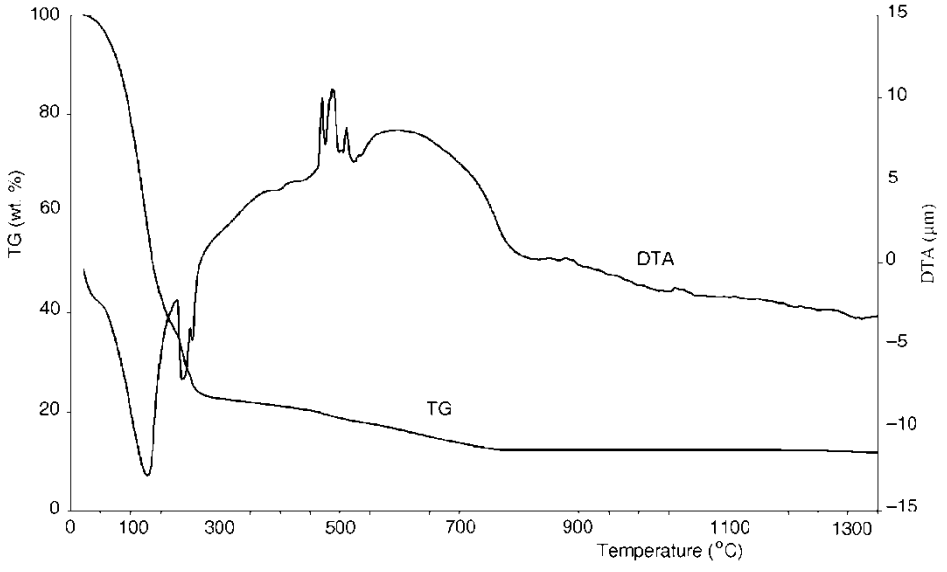

Fig. 7. TG and DTA analysis results of alumina borosilicate/PVA nanofibres obtained by electrospinning of solution 3

The dried electrospun fibre mats were heat treated at 800 °C, 1000 °C and 1200 °C for 2 h. The effect of heat treatment on the morphologies is presented in Fig. 8. At 1000 °C and 1200 °C, calcination caused sintering of the fibres through fibre interconnects and so the loss of the fibre structure due to the uncontrolled association of the fibres. On the other hand, calcination at 800 ºC was promising since its effect on the fibre morphology was minimal. While the decomposition of PVA and other organics slightly deformed the fibres, the fibre diameters had shrunk about another 30% upon removal of organic content.

3.4. Structural characterization

In Figure 9, the FTIR spectra collected from as-prepared and dried alumina borosilicate/PVA nanofibres and alumina borosilicate ceramics obtained by calcination at 600, 800, 1000 and 1200 ºC are given. As it can be seen in Fig. 9A, the alumina borosilicate/PVA fibres show a broad peak around 3400 cm^{-1}. The presence of such an absorption along with the absorptions at 1650 and 578 cm^{-1} implies the presence of water and hydroxyl groups that are excessively hydrogen bonded. Hydrogen bonding that hinders the in-plane OH deformations causes a shift to higher frequencies (530 to 580-700 cm^{-1}), which is another support for the above assignment. The remaining absorption peaks observed at room temperature can be attributed to the remnant solvents, PVA and the alkoxides associated with the PVA molecules [20, 21].

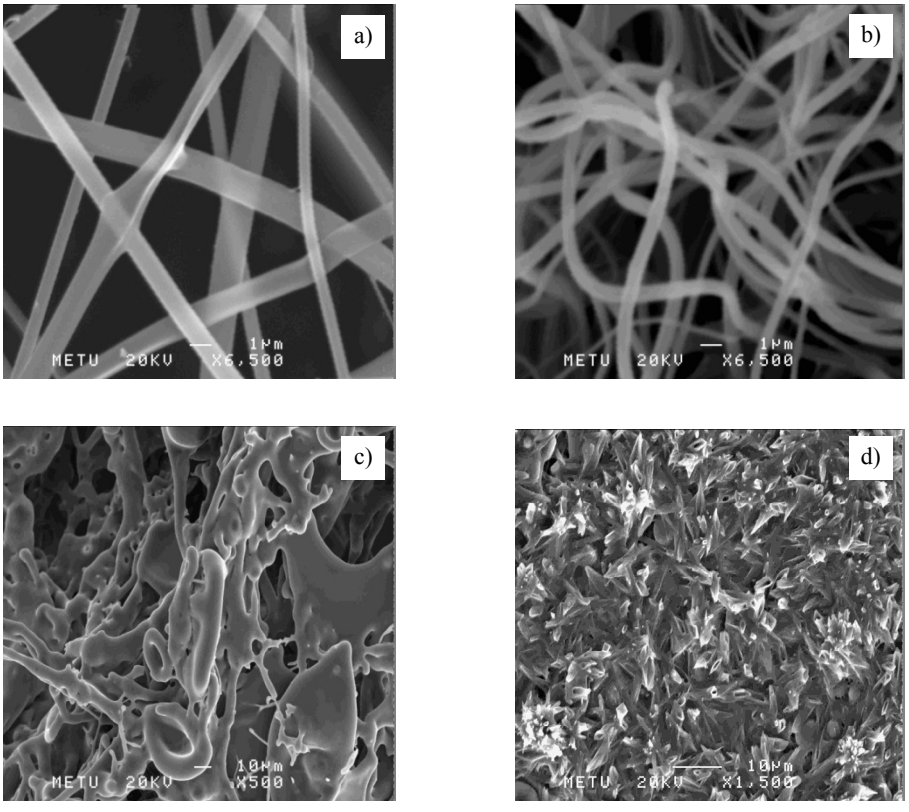

Fig. 8. The as-prepared alumina borosilicate/PVA nanofibres (a) (solution 3, 15 kV, 15 cm) and alumina borosilicate ceramics obtained by calcination of these nanofibres at: b) 800 ºC, c) 1000 ºC, d) 1200 ºC

In accordance with the TG-DTA results, calcination at 600 ºC is insufficient to burn off all the organic content. After calcination above 800°C, the absorption bands due to hydrogen bonded hydroxyls and the organic species disappear, whereas the group of bands at 400–1600 cm^{-1}, some of which already existed in the dried sample,

becomes prominent and can be attributed to the formation of the crystalline inorganic phase. Broad absorption bands at 1400–1450 cm^{-1} and 1000–1200 cm^{-1} and relatively better defined signatures at 910 cm^{-1}, 790 cm^{-1}, 670 cm^{-1} and 455 cm^{-1} can be assigned to; B–O–Si [22], Si–O–Si and/or Al–O–Si [23], B–O–Si [24], Si–O–Si (bending) [22], B–O–Si [22], Si–O–Si and/or Al–O–Si (bending) [25] modes, respectively.

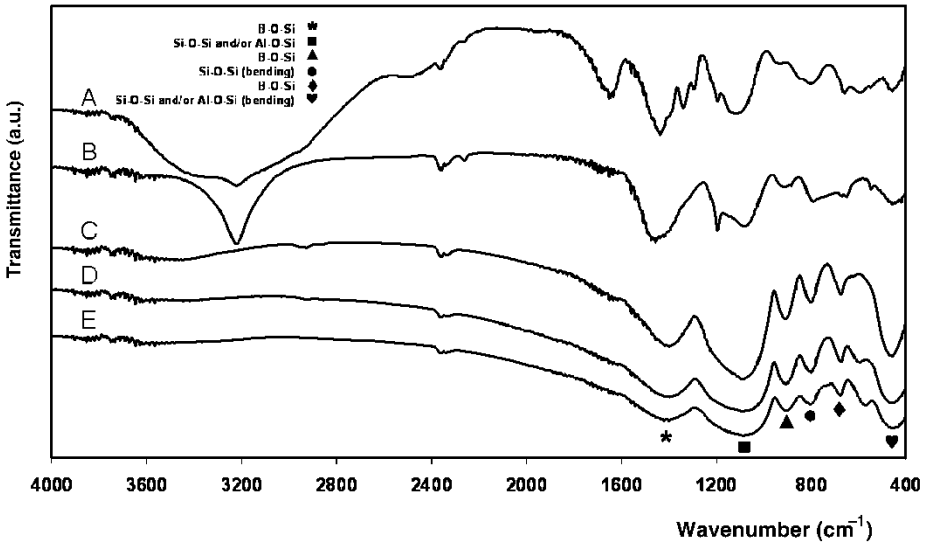

Fig. 9. FTIR spectra of as-prepared alumina borosilicate/PVA nanofibres (solution 3, 15 kV, 15 cm) (A) and alumina borosilicate ceramics obtained by calcination of the nanofibres at: B) 600 ºC, C) 800 ºC, D) 1000 ºC, E) 1200 ºC

Al–O–Si stretching mode normally corresponds to 1050 cm^{-1} [26]. The strong absorption from Si–O–Si mode possibly hinders the clear observation of such a mode due to its broad background. A similar observation is also valid for the other strong absorption at 455 cm^{-1}. Further crystallization at 1000 °C induces a new peak around 600 cm^{-1}, which may be assigned to Al–O stretching mode in AlO_6 (Fig. 9D) [27].

Like TG-DTA results, infrared data also suggests that any thermal treatment would need to be performed at temperatures higher than 600 ºC to burn off all the additives. It can also be inferred from the results that the sol-gel process developed in this work is not only well-optimized for the electrospinning process, but also for bringing the three components (Si/Al/B) in close coordination.

The XRD patterns of the calcined alumina borosilicate/PVA fibres are given in Fig. 10. Crystallization initiates at temperature as low as 600 ºC but, as expected, reaches appreciable levels only above 800 ºC within the time frame studied (2 h of soak at set temperature). Analyses indicate that the XRD peaks emerging above 700 ºC belong mainly to mullite ($Al_6Si_2O_{13}$) and to some extent $Al_4B_2O_9$ structures [28]. Also, there is a broad background around 22° which is the characteristic of vitreous SiO_2

[29]. At 1000°C, vitreous SiO_2 crystallizes. The sharp peak at 22° was assigned to a type of crystalline SiO_2, cristobalite [30]. In addition, new XRD peaks appear indicating the presence of $Al_{18}B_4O_{33}$ crystals [28].

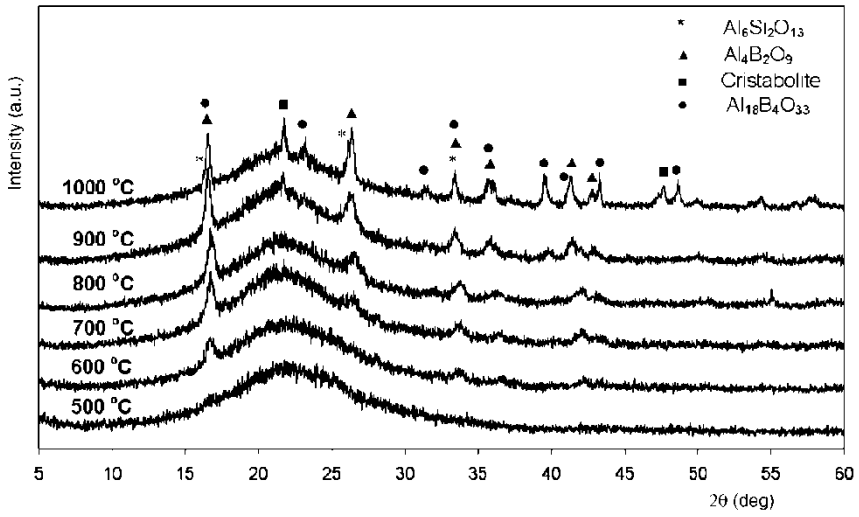

Fig. 10. XRD patterns of alumina borosilicate ceramic nanofibres calcined at various temperatures

XRD results suggest that the structure starting to form above 600 ºC, is not a single phase. Although crystallization is not complete at 800 ºC within 2 h, it can safely be predicted that it would be promoted by increasing the soak period at this temperature. A significantly lower crystallization temperature is typical of many mixed oxide systems synthesized via the sol-gel process, since the atomic level mixing of the components provides smaller diffusions distances that cannot be achieved with solid state reactions of the oxide components [31]. A heat treatment schedule that would be designed for slower burn-out of the organics between 400 and 500 ºC besides the longer soak at 800 ºC, would assure crystallization with minimal deformation on the fibre morphology.

4. Conclusions

Alumina borosilicate/PVA fibres were prepared by the sol-gel method and electrospinning technique. A sol-gel recipe that allows the formation of a homogeneous three component alkoxide solution and provides a control over solution viscosity for electrospinning process was developed. Effects of applied voltage and the capillary tip to metal collector distance on the electrospun fibre diameters were studied. Increasing the applied voltage and capillary tip to metal collector distance were found to decrease the as-spun fibre diameters. Alumina borosilicate ceramic nanofibres, with diameters down to 300 nm, were obtained via high temperature calcination. $Al_6Si_2O_{13}$, $Al_4B_2O_9$ crystals and vitreous silica were formed at 800 ºC. At 1000 ºC the fibre structure disap-

peared due to the uncontrolled association of the fibres. A longer soak at 800 ºC is proposed for achieving the desired crystal structure while preserving the fibre morphology.

Acknowledgements

This work was supported by Turkish Scientific and Technical Research Council (TÜB□TAK) under Grant No. MAG-273.

References

[1] MOUCHON E., COLOMBAN P., Composites, 26 (1995), 175.
[2] ZHU D., JILAVI M., KRIVEN W., Ceram. Eng. Sci. Proc., 18 (1997), 31.
[3] CHEN Y., LI J., J. D., Chem. Phys. Lett., 344 (2001), 450.
[4] LIU Z., ZHOU W., SUN L., TANG D., ZOU X., LI Y., WANG Y., XIE S., Chem. Phys. Lett., 341 (2001), 523.
[5] ZHU Y., HU W., HSU W., Adv. Mater., 11 (1999), 844.
[6] READEY M., J. Am. Cer. Soc., 75 (1992), 3452.
[7] SRINIVASAN D., RAO R., ZRIBI A., J. Electr. Mater., 35 (2006), 504.
[8] SIGMUND W., YUH J., PARK H., MANEERATANA V., PYRGIOTAKIS G., DAGA A., TAYLOR J., NINO J.C., J. Am. Cer. Soc., 89 (2006), 395.
[9] MCCANN J.T., CHEN J.I.L., LI D., YE Z.-G., XIA Y., Chem. Phys. Lett., 424 (2006), 162.
[10] LI D., MCCANN J.T., XIA Y., MARQUEZ M., J. Am. Cer. Soc., 89 (2006), 1861.
[11] KIM H.-W., KIM H.-E., J. Nanosci. Nanotechn., 6 (2006), 505.
[12] AZAD A.-M., Mater. Sci. Eng. A, 435–436 (2006), 468.
[13] ZHANG G., KATAPHINAN W., TEYE-MENSAH R., KATTA P., KHATRI L., EVANS E.A., CHASE G.G., RAMSIER R.D., RENEKER D.H., Mater. Sci. Eng. B: Solid-State Mater. Adv. Techn., 116 (2005), 353.
[14] WANG M., HSIEH A.J., RUTLEDGE G.C., Polymer., 46 (2005), 3407.
[15] KIM G.-M., LACH R., MICHLER G.H., CHANG Y.-W., Macromol. Rapid Comm., 26 (2005), 728.
[16] SHAO C., KIM H., GONG J., LEE D., Nanotech., 13 (2002), 635.
[17] DAI H., GONG J., KIM H., LEE D., Nanotech., 13 (2002), 674.
[18] KOJI N., TOMONORI Y., KENJI I., FUMIO S., J. Appl. Polym. Sci. 74 (1999), 133.
[19] CHIKAKO N., TAKEO S., TOSHIO Y., MASATAKA S., Fuel, 77 (1998), 321.
[20] LIU Y., REN W., ZHANG L., YAO X., Thin Solid Films, 353 (1999), 124.
[21] NAKAMOTO K., *Infrared and Raman Spectra of Inorganic and Coordination Compounds*, Part B: *Applications in Coordination, Organometallic, and Bioinorganic Chemistry*, Wiley, New York, 1997.
[22] NAKAMOTO K., *Infrared and Raman Spectra of Inorganic and Coordination Compounds*, Part A: *Theory and Applications in Inorganic Chemistry*, Wiley, New York, 1997.
[23] NAKANE K., YAMASHITA T., IWAKURA K., SUZUKI F., J. Appl. Polym. Sci., 74 (1999), 133.
[24] KERN W., RCA Review, 32 (1993), 429.
[25] POH N., NUR H., M. M., HAMDAN H., Catal. Today, 114 (2006), 257.
[26] ANDRIANOV K., BRADLEY D., *Metalorganic Polymers*, Polymer Reviews, Interscience, New York, 1965.
[27] SOPICKA-LIZER M., Euroceramic, Elsevier Appl. Sci., 1 (1989), 1609.
[28] HAMZAWY E., ALI A., Ceramics Int., 27 (2001), 607.
[29] RAINHO J., ROCHA J., CARLOS L., ALMEIDA R., J. Mater. Res., 16 (2001), 2369.
[30] XU J., THOMPSON S., O'KEEFE E., PERRY C., Mater. Lett., 58 (2004), 1696.
[31] BRINKER C., SCHERER W., *Sol-Gel Processing*, Pergamon Press, London, 1990.

Received 14 December 2006
Revised 8 February 2007

Materials Science-Poland, Vol. 25, No. 4, 2007

Preparation of lithium zirconate nanopowder prepared by electrostatic spraying for CO_2 sorbent

K.-S. HWANG [1*], Y.-H. LEE [2], S. HWANGBO [3]

[1]Department of Automobile, Chunnam Techno College, 285 Okgwa-ri, Okgwa-Myeon, Gokseong-gun, Jeollanam-do 516-911, Republic of Korea

[2]Department of Biomedical Engineering and Institute of Photoelectronic Technology, Nambu University, 864-1 Wolgye-dong, Gwangsan-gu, Gwangju 506-824, Republic of Korea

Major in Photonic Engineering, Division of Electronic and Photonic Engineering, Honam University, 59-1 Seobong-dong, Gwangsan-gu, Gwangju 506-714, Republic of Korea

Electrostatic spray pyrolysis has been used to prepare Li_2ZrO_3 nanopowder for CO_2 sorbent. Final annealing was done at 900 °C for 30 min in air. The CO_2 sorption/desorption ability of the annealed powder has been investigated by thermogravimetric analysis and Fourier transform infrared spectroscopy. When Li_2ZrO_3 nanopowder was exposed to CO_2 environment at 500 °C, the theoretical absorption weight was gained within 250 min with high sorption rate. Absorbed CO_2 was mostly generated by heating at 800 °C.

Key words: *Li_2ZrO_3; nanopowder; CO_2; sorbent*

1. Introduction

Although coal is the most abundant fossil fuel in the world, the reduction of CO_2 emissions from coal-fired units is an imperative to mitigate global climate change, and consequently, to guarantee the sustainable key role of coal in the 21st century. Environmental concerns have stirred up much interest in CO_2 exhaust from energy power plants. The Kyoto protocol, adopted in 1997, requires a reduction in the release of CO_2. To achieve the goal, practical methods such as saving energy, improvement of conversion efficiency and development of alternative energy sources are required. Moreover, separation of CO_2 from the exhaust gas of power plants and factories and the absorption of CO_2 by forests and oceans are needed. Recently, importance of selecting high temperature CO_2 sorbent gained attention with respect to performing

*Corresponding author, e-mail: khwang@nambu.ac.kr

long-term multi-cycle. Currently, the most widely used high temperature CO_2 sorbent is dolomite, a natural mineral whose most attractive feature is low price. However, in order to use dolomite, energy intensive pre-treatment has to be performed prior to loading. In addition, it has tendency to significantly decrease its capacity through multi-cycle processing [1].

Therefore, a new generation of high temperature CO_2 sorbents such as Li_2ZrO_3, Li_4SiO_4, and Na_2ZrO_3 [2–6] have recently been developed. Among them, Li_2ZrO_3 has been investigated as a candidate of an additive material for molten carbonate fuel cell electrolyte plates. A durability test of this material revealed that Li_2ZrO_3 synthesized by heat-treatment of zirconia and lithium carbonate returned to the starting materials after 1000 h in the presence of CO_2 [7].

Kato el al. has developed a CO_2 separation technology based on a chemical reaction using Li_2ZrO_3 [8]. Since the method is effective in the temperature range from 450 to 700 °C, it has some advantages over the separation of CO_2 from power plants without lowering the temperature, and it can be used with catalysts for the CO shift reaction or methane reforming reaction. However, as far as we know, there is no information on the reaction of Li_2ZrO_3 nanopowder with CO_2, while several works corresponding to micron-sized powder or bulk were performed. Therefore, in this work, we tried to synthesize nanosized $LiZrO_3$ powder using electrostatic spray pyrolysis (ESP) and to evaluate its performance as CO_2 absorbent.

2. Experimental

Lithium nitrate ($LiNO_3$) and zirconyl nitrate (ZrN_2O_7) were used as reactants for synthesis of nanopowders. The sol was diluted with distilled water and methanol to adjust the concentration and viscosity for preparing nanopowders by ESP. Figure 1 shows the flow chart for the preparation of precursor sol and Li_2ZrO_3 nanopowder.

The electrostatic spray pyrolysis (ESP) method has been commonly used to synthesize nanosized particles of oxidic materials [7]. The working principles of the ESP method have been described elsewhere [7, 8]. A stainless steel needle (0.1 mm and 0.23 mm inner and outer diameters, respectively) was connected to a syringe pump (KD200, KD Scientific Inc., PA, U. S. A.) using a silicon rubber tube. The flow rate of the precursor solution was kept at 0.05 cm^3/60 min. In order to obtain a stable cone-jet mode of electrostatic atomization, high voltage, 10–30 kV, was applied between the needle tip and ground electrode by using DC power supply (SHV120-30K-RD, Convertech Co. Ltd., South Korea). A container was introduced on the ground electrode and was heated at 80–120 °C to vaporize organic compound in precursor solution during spraying. A precursor solution was pumped for 5 min through the nozzle placed 15 cm above the powder container. The sprayed powders were placed on the Si substrate and heated up to 900 °C for 30 min in a tube furnace in the presence of air

(flow rate approximately 150–200 cm^3/min). The schematic of the set-up used in the study is shown in Fig. 2.

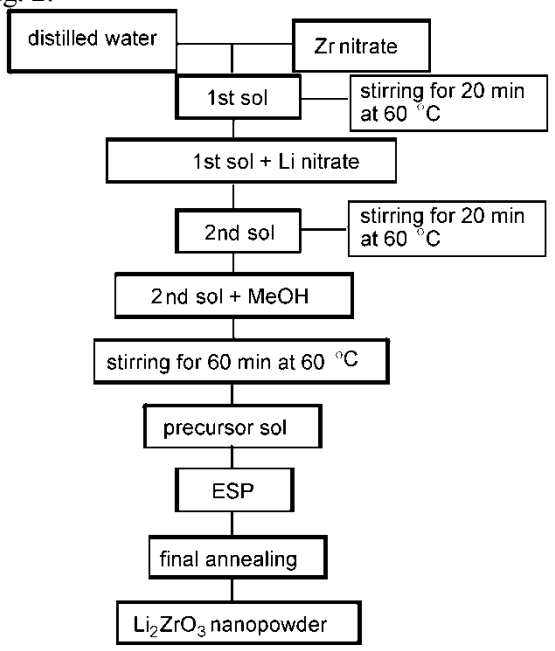

Fig. 1. The flow chart of the process

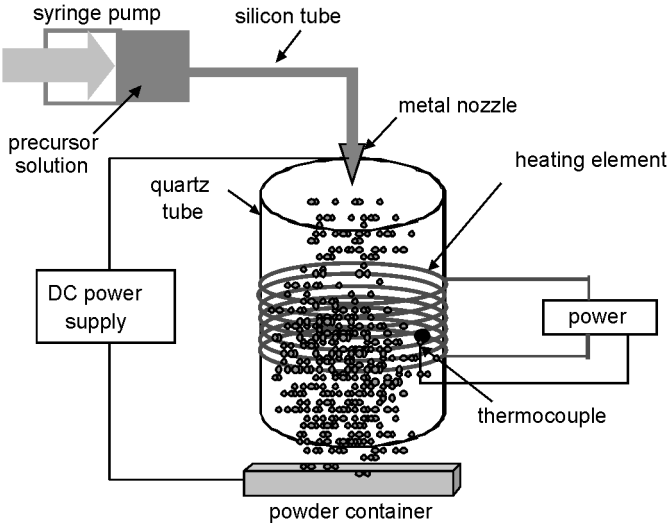

Fig. 2. The scheme of the set-up used in this study

The Fourier transform infrared (FTIR, FTS-60, BIO-RAD Digilab Co., U. S. A.) spectroscopy was performed to analyze chemical structure of the powders before and

after CO_2 absorption. The morphology of the surface of the powders was evaluated by field emission – scanning electron microscope (FE-SEM, S-4700, Hitachi, Japan). CO_2 absorption properties were evaluated using a thermogravimetric analysis (TGA, DTG-60, Shimadzu, Japan). Samples were heated up to 500 °C in pure nitrogen and kept for 20 min. After that, the atmosphere was changed to CO_2 containing gases balanced by air, and kept for 275 min. After keeping at 500 °C for CO_2 absorption, the atmosphere was changed to N_2, heated up to 800 °C and kept for 30 min to release.

3. Results and discussion

FE-SEM images from the powders on Si substrate after annealing at 900 °C for 30 min in air were used to confirm the presence of Li_2ZrO_3 powders (Fig. 3). As can be seen, the average particle size decreases upon raising the heating temperature during spraying. Powders preheated at 120 °C during spraying are composed of nanosized particles, i.e., < 100 nm. A simple estimation of the average particle size gives 50–80 nm. From the FE-SEM results, the heating temperature during spraying was fixed at 120 °C.

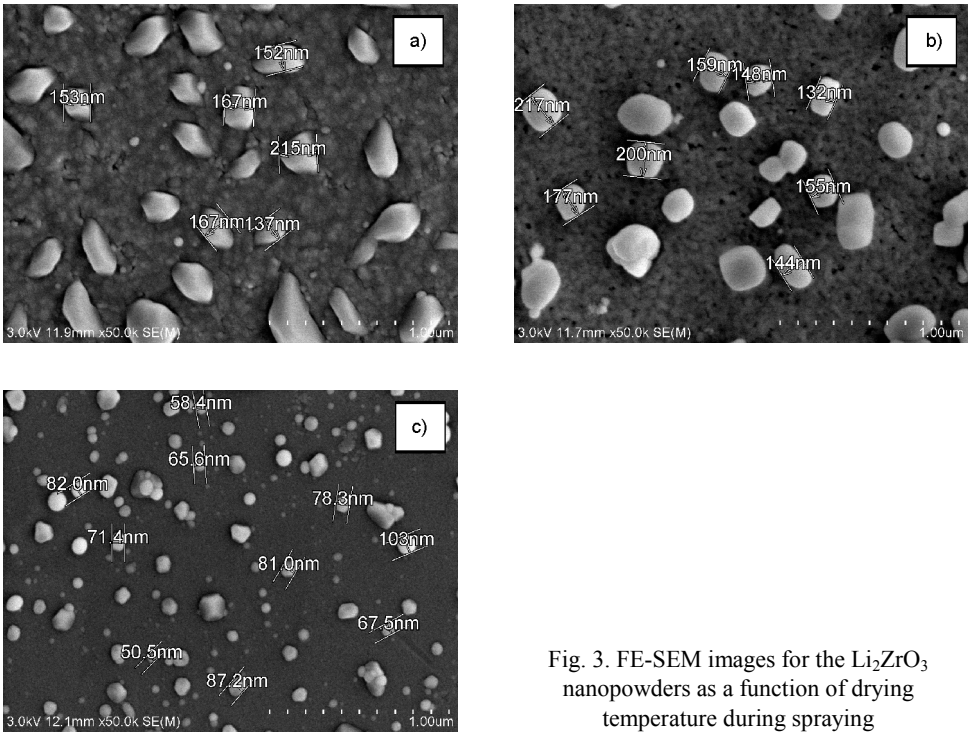

Fig. 3. FE-SEM images for the Li_2ZrO_3 nanopowders as a function of drying temperature during spraying

The following equation represents the reaction between lithium zirconate and CO_2:

$$Li_2ZrO_3 + CO_2 = Li_2CO_3 + ZrO_2 \quad (1)$$

The weight changes are indicators of the absorption and desorption of CO_2, respectively. Figure 4 shows the weight change of the powder during the temperature maintained at 500 °C and at 800 °C. Clear weight increase and decrease are observed during CO_2 sorption/desorption process at 500 °C/at 800 °C. The value of the weight increase was 27–30% at 500 °C in CO_2 after 250 min heating, which agrees with 29% expected of the theoretical maximum. The CO_2 capture rate was higher than for any other Li_2ZrO_3 reported. These values were very well comparable with previous results by Lin et al. [9]. While Li_2ZrO_3 prepared by the solid–solid reaction showed very slow kinetics [9], the nanosized powder prepared using liquid based method showed higher absorption rate probably due to larger surface area.

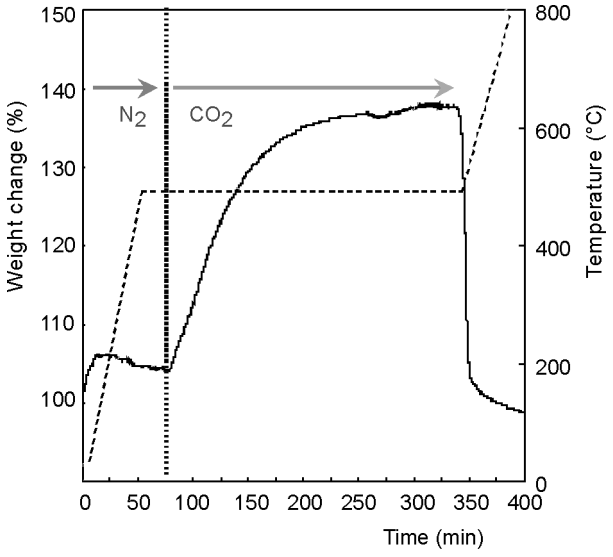

Fig. 4. Weight change of the powder between 500 °C and 800 °C

When Li_2ZrO_3 is exposed to CO_2 at 500 °C, CO_2 molecules move to the surface of Li_2ZrO_3 and react with Li_2ZrO_3 to form ZrO_2 and Li_2CO_3 nuclei (Eq. (1)). As reaction proceeds, ZrO_2 and Li_2CO_3 nuclei touch each other and form a dense Li_2CO_3 shell on the outer surface and a dense ZrO_2 shell in the middle covering the unreacted Li_2ZrO_3 core. Both Li_2CO_3 and ZrO_2 shells are in solid state because their melting points are higher than the operating temperature. After the formation of double shells, CO_2 can diffuse through the solid Li_2CO_3 shell and react with Li^+ and O^{2-} on the outer surface of the ZrO_2 shell [10]. At the same time, another reaction occurs on the surface of unreacted Li_2ZrO_3 to generate Li^+ and O^{2-}. Because ZrO_2 contains a large number of oxygen vacancies in its crystal [11], O^{2-} can diffuse through the ZrO_2 shell. Similarly Li^+ can also diffuse interstitially through the ZrO_2 shell.

In order to analyze chemical structural changes of Li_2ZrO_3 nanopowder during the CO_2 sorption/desorption process, Li_2ZrO_3 samples were rapidly quenched at the room temperature after CO_2 sorption at 500 °C and after CO_2 desorption at 800 °C, respectively. Then, the quenched samples were analyzed by FTIR. To compare, the spectrum of pure Li_2ZrO_3 annealed at 900 °C was determined (curve a in Fig. 5). Results of the FTIR analysis of the obtained samples are shown in Fig. 5.

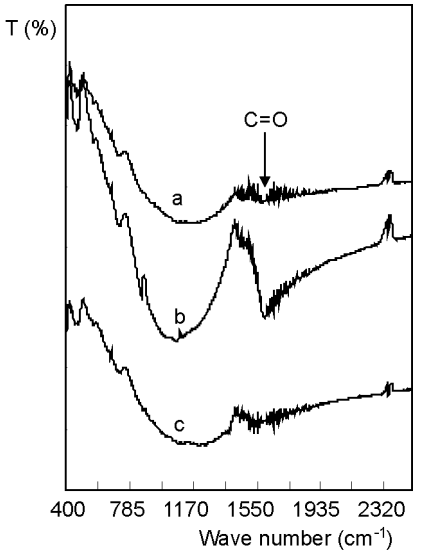

Fig. 5. FTIR patterns of Li_2ZrO_3 nanopowders: a) after annealing at 900 °C, b) after CO_2 absorption at 500 °C, c) after desorption of CO_2 at 800 °C

The FTIR pattern in Li_2ZrO_3 nanopowder after CO_2 sorption clearly includes a peak at 1550–1650cm^{-1} corresponding to C=O bond, as shown in Fig. 5, curve b. This result indicates that after CO_2 sorption, Li_2ZrO_3 reacted with CO_2 to form Li_2CO_3 and ZrO_2. Comparing to curve b in Fig. 5, the FTIR pattern in Fig. 5, curve c after CO_2 desorption shows that the peak corresponds to C=O bond completely disappeared. This means that after CO_2 desorption at 800 °C, Li_2CO_3 and ZrO_2 react to Li_2ZrO_3 again. These results clearly indicate that the reaction represented by Eq. (1) is reversible with reaction rates enabling its use in practice, and is applicable to the CO_2 capture from high-temperature gases.

4. Conclusions

Li_2ZrO_3 nanopowder for CO_2 sorbent was fabricated by the ESP process. Powders preheated at 120 °C during spraying are composed of nanosized particles, 50–80 nm. From the TGA result, clear weight changes are observed during CO_2 sorption/desorption process at 500 °C/at 800 °C. Nanosized powder prepared using liquid based method showed higher absorption rate probably due to larger surface area. FTIR

results clearly indicate that the CO_2 reaction is reversible with practical reaction rates and is applicable to the CO_2 capture from high-temperature gases.

Acknowledgements

This study was supported by a grant of the Korea Sanhak Foundation (2006), Republic of Korea.

References

[1] ORTIZ A., HARRISON D., Ind. Eng. Chem. Res., 40 (2001), 5102.
[2] NAKAGAWA K., OHASHI T., Electrochem., 67 (1999), 618.
[3] NAIR B.N., YAMAGUCHI T., KAWAMURA H., NAKAO S.-I., NAKAGAWA K., J. Am. Ceram. Soc., 87 (2004), 68.
[4] WOO S.K., LEE S., YU J.H., J. Kor. Ceram. Soc., 43 (2006), 309.
[5] MASAHIRO K.K.N., J. Ceram. Soc. Jpn., 109 (2001), 911.
[6] LOPEZ-ORTIZ A., PEREZ RIVERA N.G., REYES ROJAS A., LARDIZABAL GUTIERREZ D., Separ. Sci. Tech., 39 (2004), 3559.
[7] NAKAGAWA K., OHASHI T., J. Electrochem. Soc. 145 (1998), 1344.
[8] KATO M., YOSHIKAWA S., NAKAGAWA K., J. Mater. Sci. Lett., 21 (2002), 485.
[9] IDA J., LIN Y.S., Environ. Sci. Technol. 37 (2003), 1999.
[10] XIONG R., MS Thesis, Univ. of Cincinnati (2003).
[11] LIN Y., DE VRIES K., BRINKMAN H., BURGGRAAF A., J. Membr. Sci., 66, (1992), 211.

Received 26 June 2007
Revised 22 August 2007

Materials Science-Poland, Vol. 25, No. 4, 2007

Nanotribological characteristics of lanthanum-based thin films on phosphorylated 3-aminopropyltriethoxysilane self-assembled monolayers

G. QINLIN[1], X. CHENG[1,2*]

[1]School of Mechanical and Power Engineering, Shanghai Jiao Tong University, 200030, Shanghai, PR. China

[2]National Engineering Research Center for Nanotechnology, 200237, Shanghai, PR. China

Lanthanum-based thin films deposited on phosphonate 3-aminopropyltriethoxysilane (APTES) self-assembled monolayers (SAM) were prepared on a hydroxylated silicon substrate by a self-assembling process from a specially formulated solution. Chemical compositions of the films and chemical states of the elements were detected by X-ray photoelectron spectrometry. The thicknesses of the films was determined with an ellipsometer, while their morphologies and nanotribological properties were analyzed by means of atomic force microscopy. It was found that the lanthanum-based thin films showed the lowest friction and adhesion followed by APTES-SAM and phosphorylated APTES-SAM, while silicon substrate showed high friction and adhesion. Microscale scratch/wear studies clearly showed that lanthanum-based thin films were much more scratch/wear resistant than the other samples. The superior friction reduction and scratch/wear resistance of lanthanum-based thin films may be attributed to low work of adhesion of non-polar terminal groups and the strong bonding strength between the films and the substrate.

Key words: *lanthanum-based thin films; friction; adhesion; scratch; wear*

1. Introduction

Microelectromechanical systems (MEMS) and emerging nanoelectromechanical systems (NEMS) are expected to have a major impact on our lives, much like the way the integrated circuit has affected information technology [1, 2]. However, due to the large surface area to volume ratios in MEMS/NEMS devices as the size scale shrinks, many potential applications for MEMS/NEMS are not really practical at present. For

*Corresponding author, e-mail: xhcheng@sjtu.edu.cn

example, many studies have revealed a profound negative influence of stiction, friction and wear on the efficiency, power output, and steady-state speed of micro/nano-dynamic devices [3–6]. Self-assembled monolayers (SAM) have gained growing interest over the past years because they have advantageous characteristics of well-defined structures, strong head group-substrate binding and dense packing of hydrocarbon chains. Indeed SAM considerably reduces friction and adhesion, and found use in various microelectromechanical systems (MEMS) devices [7–11].

Rare earths have been applied as important materials in high mechanical strength and fracture toughness applications, owing to their superior properties such as good friction-reducing, wear-resistant properties, excellent corrosion resistance and high anti-scuffing ability [12–16]. A number of studies have been done on the nanotribological properties of various SAMs [17, 18] but the study of the rare earth films on the nanotribological behaviour is still much lacking. In this study, lanthanum-based thin films deposited on the phosphorylated 3-aminopropyltriethoxysilane (APTES) SAM were prepared on silicon substrates. Several methods, such as X-ray photoelectron spectroscopy (XPS), atomic force microscopy (AFM), ellipsometer and contact angle measurements were applied to investigate the structure and nanotribological properties of the films.

2. Experimental

Preparation of lanthanum-based thin films on the phosphorylated APTES-SAM. 3-Aminopropyltriethoxysilane was purchased from Aldich Chemical Company, Inc. A single-crystal silicon wafer polished on one side was used as a substrate for the SAM transfer. Other reagents were of analytical grade. Deionized water was used throughout the experiment. For the preparation of the target solution, APTES, toluene, ethanol, acetonitrile, phosphorus oxychloride, and collidine were commercially obtained and used without further purification. The silicon substrates were cleaned with 'piranha' solution (H_2SO_4:H_2O_2=7:3 (v:v)), then exposed to a solution of APTES in toluene (2% V:V, 24h, room temperature), followed by $POCl_3$ in acetonitrile (0.2 M $POCl_3$, 0.2 M collidine, 20 min, room temperature) [19, 20]. This treatment resulted in the surface rich in phosphonate groups (–$PO(OH)_2$) which adsorbed a layer of lanthanum-based thin films when immersed in pre-prepared solution with $LaCl_3$, ethylenediamine tetraacetic acid (EDTA) etc. for 24 h, then cleaned ultrasonically with deionized water to remove other physisorbed ions or molecules and dried for 2 h at 120 °C, then naturally cooled in a desiccator. A schematic of growth of lanthanum-based thin films on phosphorylated APTES-SAM is shown in Fig. 1.

Apparatus and test procedures. Chemical compositions of the films and chemical state of the elements were analyzed with a PHI-5702 XPS system, using MgK_α radiation operating at 250 W and pass energy of 29.35 eV. The binding energy of C 1s (284.6 eV) was used as the reference. The resolution for the measurement of the bind-

ing energy is about ±0.3 eV. The static contact angles were measured in ambient air (relative humidity 40%) using an OCA-20 contact angle measurement device (Data-Physics Instruments Gmbh). Distilled water was used as the spreading reagent. Measurements were performed on at least three samples, and were made at a minimum of three different spots on each sample. The contact angles were typically reproducible to within $\pm 2°$. The thicknesses of the films were measured with an ellipsometer (V-VASE with AutoRetarder from J.A. Woollam Co., polarizer-retarder-sample-rotating analyzer configuration) which was equipped with a He-Ne laser (632.8 nm) set an incident angle of 70°. The index of refraction for the refraction was taken to be 1.45. Thickness data were obtained by averaging five measurements at different spots of each sample surface. The thickness was recorded with the accuracy of ±0.3 nm.

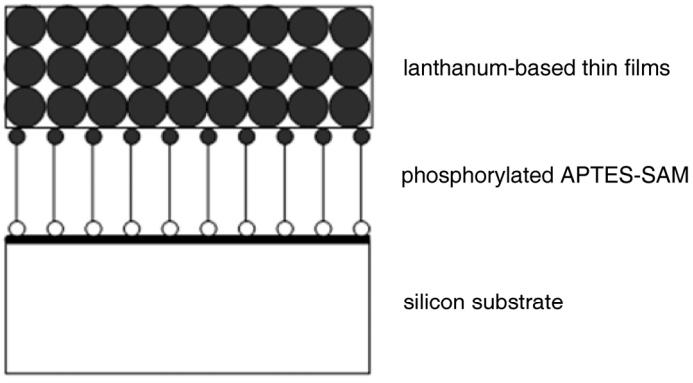

Fig. 1. Schematic of growth of lanthanum-based thin films on phosphorylated APTES-SAM

The surface morphologies and nanotribological properties of the films were investigated using an SPM-9500 atomic force microscope (NanoScope IIIa) produced by Shimadzu Corporation (Kyoto, Japan). Square pyramidal Si_3N_4 tips with the nominal 50 nm radius mounted on gold-coated triangular Si_3N_4 cantilevers with spring constants of 0.6 N/m were used. The adhesion and friction data were measured ten times at each interesting location and average data values were obtained. Adhesive forces were measured using the so called "force calibration plot" [18]. Friction forces were also measured according to Ref. [21]. By following the friction force calibration procedures developed by Bhushan [22], voltages corresponding to friction forces can be converted to force units. The coefficient of friction was obtained from the slope of friction force data measured as a function of normal loads.

For the scratch and wear tests, specially fabricated microtips were used. These microtips consisted of single-crystal natural diamond, ground to the shape of a three-sided pyramid, with an apex angle of 80° and tip radius of about 50 nm, mounted on a platinum-coated stainless steel cantilever beam whose stiffness was 50 N/m. Samples were scanned orthogonal to the long axis of the cantilever with loads ranging from 20 to 100 μN to generate scratch/wear marks. Observations of the sample surface

before and after the wear tests were done by scanning parallel to the long axis of the cantilever with loads ranging from 0.5 to 1 μN. The parallel scans enabled near-zero wear of the sample surface and also eliminated post-data analysis errors in surface feature height scratch/wear tests were performed over a scan area of 2×2 μm^2 at the scan rate of 10 Hz. The reported scratch/wear depths are an average of six runs at separate instances. In this study, all of the measurements were carried out in ambient conditions (22 ºC, RH 40–44%).

3. Results and discussion

3.1. Characterization of the prepared films

Figure 2 shows a series of AFM images taken over regions 1.0×1.0 μm^2 of specimens at various stages of the film deposition process, where a) refers to the bare cleaned silicon substrate, b) to APTES-SAM on the silicon substrates, c) to the phosphorylated APTES-SAM and d) to as-deposited lanthanum-based thin films on the phosphorylated APTES-SAM. It can be seen that the surface of the silicon substrates (Fig. 2a) is clean and smooth with surface root-mean-square (rms) roughness in the range of 0.2–0.3 nm. The surface in Fig. 2b is uniform and homogenous with surface rms roughness about 0.522 nm. The phosphorylated APTES-SAM (Fig. 2c) becomes more and more uniform and homogeneous with rms roughness about 0.393 nm. The possible reason is that the–$PO(OH)_2$ groups are bigger than the terminal groups $–NH_2$ which leads to the $–PO(OH)_2$ terminal molecules providing a more densely packed arrangement than the $–NH_2$ terminal molecules. After the deposition of the lanthanum-based thin films (Fig. 2d) on the phosphorylated APTES-SAM, many differences are visible in the corresponding AFM images. Namely, the surface of the as-deposited lanthanum-based films is rough and quite densely round-looking particles are visible with the rms roughness to be about 0.863 nm which shows wide potential application in lubrication and wear protection.

The XPS spectra applied to detect the chemical states of some typical elements for the prepared films are shown in Figs. 3–6. XPS survey and single scan spectra of APTES-SAM (Fig. 3) show contributions from the substrate and the film: silicon (15.5 at. %), carbon (56.3 at. %), oxygen (20.2 at. %), and nitrogen (8.0 at. %). Nitrogen is detected which indicates successful APTES-SAM deposition, since this element is only contained in this material.

Figure 4 shows single-scan XPS spectra of N 1s peak decomposed into two different nitrogen species occurring in various binding states. The peak at 400.8 eV is assigned to the protonated aliphatic amino groups, while that at 399.5 eV may be ascribed to the aliphatic amino groups. This interpretation is consistent with the data of Ref. [23]. After in situ phosphorylation of the APTES-SAM, the P 2p peak at 134.5 eV is observed (Fig. 5), which is assigned to the P atoms in $–PO(OH)_2$ group; N signal is absent. This indicates that the terminal $–NH_2$ group in the APTES-SAM has been phosphorylated and transformed to $PO(OH)_2$ group successfully and completely.

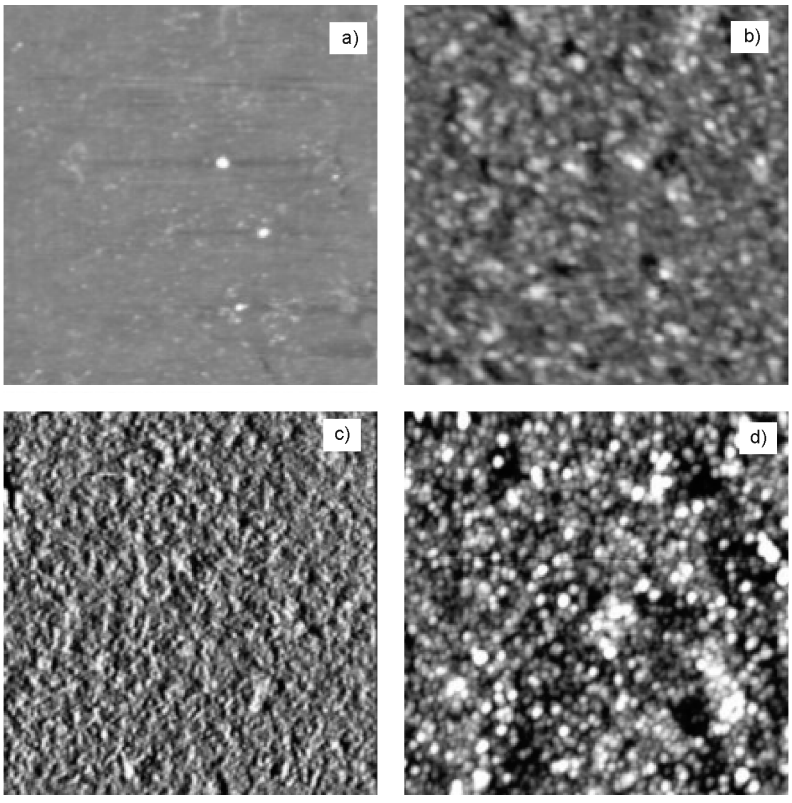

Fig. 2. AFM images of the surface of : a) bare cleaned silicon substrate, b) APTES-SAM on a silicon substrate, c) phosphorylated APTES-SAM, d) as-deposited lanthanum-based thin films on the phosphorylated APTES-SAM

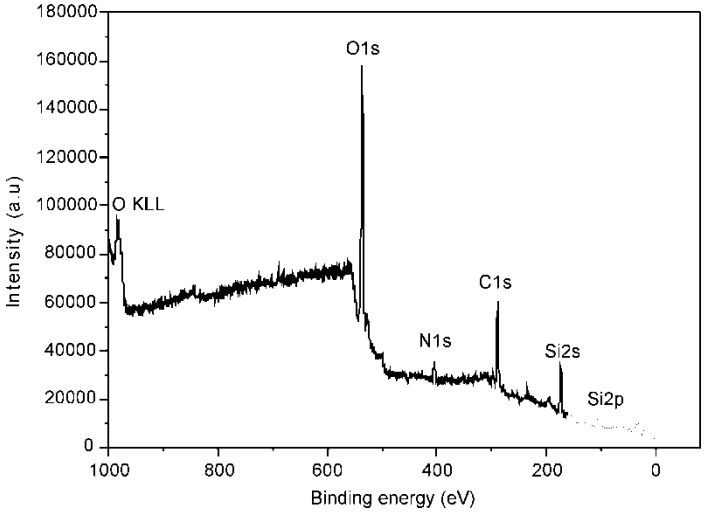

Fig. 3. XPS survey and single scan spectra of an APTES film

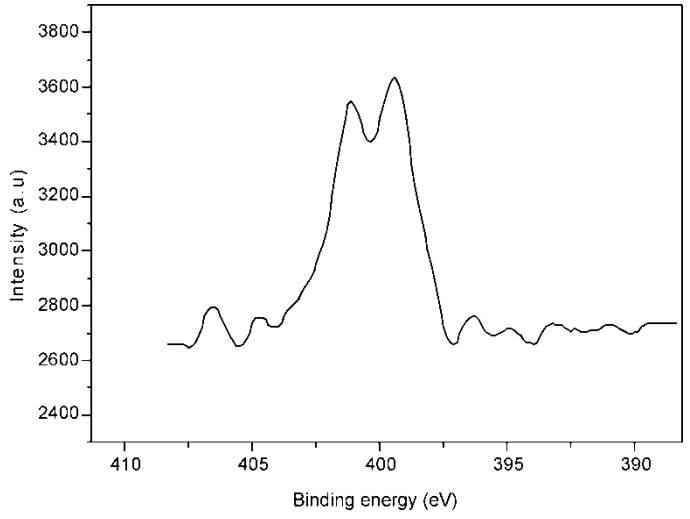

Fig. 4. Single scan XPS spectrum of the N 1s region of an APTMS film

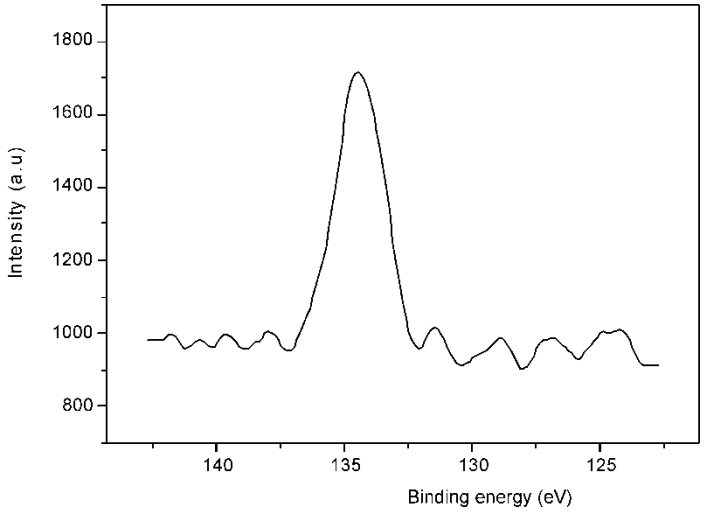

Fig. 5. Single scan XPS spectrum of the P 2p region in an APTMS film

Figure 6 shows a single-scan XPS spectrum of La 3d in the lanthanum-based thin films deposited on the phosphorylated APTES-SAM. The La^{3+} core level band of surface also decomposes into four peaks at binding energies of 835, 838.85, 851.725 and 855.225 eV, while the characteristic peak of La 3d in $LaCl_3$ (seen in Fig. 7) is at binding energies of 853.0 eV and 856.7 eV. As a result, a supposition can be made that lanthanum elements may react with $–PO(OH)_2$ group on the surface of substrate. The absence of Si signal indicates a complete coverage of the underlying silicon substrate by lanthanum elements.

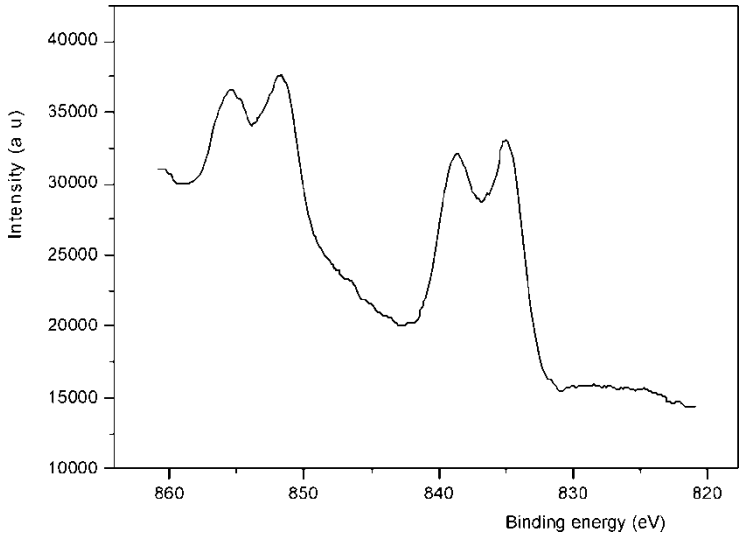

Fig. 6. XPS spectra of La_{3d} in an RE film

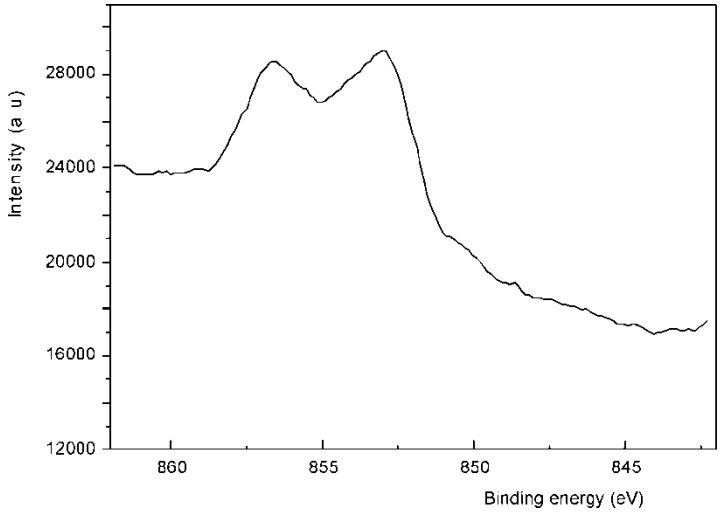

Fig. 7. XPS spectra of La_{3d} in $LaCl_3$

The contact angles of distilled water on the silicon substrate and on the prepared films have been measured. The APTES-SAM has a contact angle of 50º±2º, which is consistent with a moderately polar surface where the amino groups are oriented upward. After phosphorylation in situ for 20 min, a contact angle of 24º±2º is recorded for the phosphorylated surface. The contact angle of lanthanum-based thin films deposited on the phosphorylated APTES- SAM increases to 66º±2º.

In our work, the thicknesses of the prepared films on glass substrates were determined with an ellipsometer. The averaged thickness of the APTES-SAM is about

7.5 nm which matches with the projection of a normally extended molecular chain on the surface. The thickness is hardly changed after the $–NH_2$ is phosphorylated to $–PO(OH)_2$ group which indicates that a monolayer of phosphorylated APTES has been prepared on glass substrates. The thickness increases to ca. 15 nm after the phosphorylated APTES-SAM is immersed in the rare earth solution, which also shows that lanthanum-based thin films have been successfully obtained.

3.2. Nanotribological properties of the prepared films

Adhesion, friction and work of adhesion. Figure 8 shows the average values of the adhesion forces and coefficients of friction of four kinds of flat surfaces measured by contact mode AFM under an applied normal load of 20 nN and the scan rate of 10 Hz.

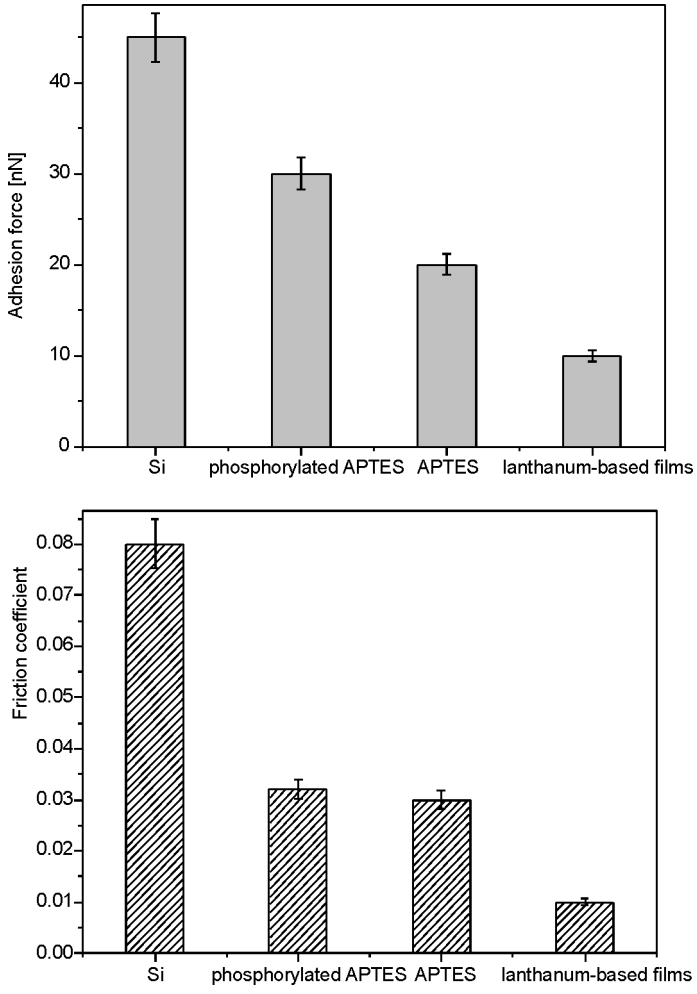

Fig. 8. Adhesive forces and coefficients of friction of silicon and prepared films

This shows that SAMs can reduce the adhesive and frictional forces of silicon substrate. In particular, lanthanum-based thin films exhibit the lowest adhesive force and coefficient of friction. This means that the prepared films can be used as effective molecular lubricants for micro/nanodevices fabricated from silicon. Based on the data, the ranking of adhesive forces F_a is in the following order: $F_{a\text{-Si}} > F_{a\text{-phosphorylated APTES}} > F_{a\text{-APTE}} > F_{a\text{-lanthanum-based films}}$, and the ranking of the coefficients of friction is in the following order: $\mu_{\text{Si}} > \mu_{\text{phosphorylated APTES}} \approx \mu_{\text{APTES}} > \mu_{\text{lanthanum- based films}}$.

Based on the Young–Dupre equation, the work of adhesion W_a

$$W_a = \gamma_{1a}(1 + \cos\theta_1) \tag{1}$$

required to pull apart the unit area of a solid interface [24] has been shown in Fig. 9. In Eq. (1), γ_{1a} is the surface tension of liquid–air interface and θ_1 is the contact angle

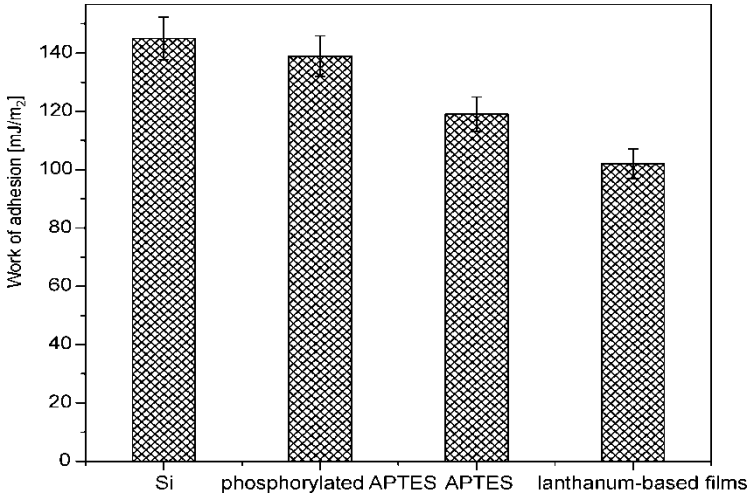

Fig. 9. Work of adhesion of silicon and prepared films

between water and a flat horizontal surface. From Figures 8 and 9 it was found that the adhesive force and friction coefficient decrease as the work of adhesion decreases. This implies that the capillary force acting between the tip and the flat surfaces seriously affects nano-adhesion and nano-friction. From Figure 8, it can also be found that APTES-SAM and phosphorylated APTES-SAM have polar surface groups ($–NH_2$ and $–PO(OH)_2$ groups), thus leading to larger W_a and eventually larger adhesive forces. The lanthanum-based films do not have polar surface groups, thus have a smaller W_a and adhesive force than APTES-SAM and phosphorylated APTES-SAM.

Scratch/wear tests. As explained earlier, the scratch tests of silicon and the prepared films were studied by making scratches (10 cycles per each load) with varying loads. Figure 10 shows the plot of scratch depth vs. normal load for various samples. Scratch depth increases with increasing normal load. APTES-SAM and phosphory-

lated APTES-SAM show similar scratch resistance. From the data, it is clear that the lanthanum-based thin films show the best scratch resistance compared with the silicon substrate, APTES-SAM and phosphorylated APTES-SAM. The increase in scratch depth with normal load is very small and all depths are less than 20 nm, while the silicon substrate and APTES-SAM finally reach depths of about 80 nm and 150 nm, respectively.

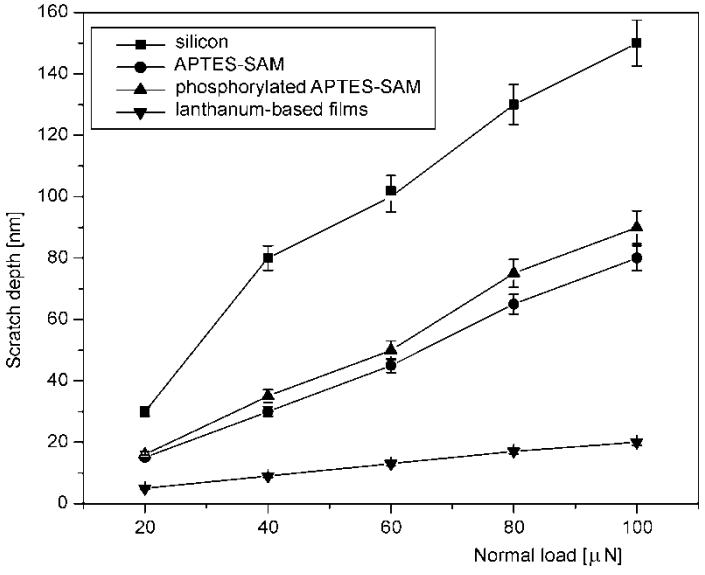

Fig. 10. Scratch depths for 10 cycles as a function of normal load

Wear tests were conducted on the samples by wearing the same region for 30 cycles at a normal load of 20 μN, while observing wear depths at different intervals (1, 5, 15, 20 and 30 cycles). This would give information on the progression of wear of the films. The observed wear depths are plotted against number of cycles in Fig. 11. For all samples, the wear depth increases almost linearly with increasing number of cycles. This suggests that material is removed layer by layer in all materials. Here also, lanthanum-based thin films exhibit a lesser increase in wear depth (lower slope) than the other samples. APTES-SAM wears less than the silicon substrate, which shows similar wear characteristics to the phosphorylated APTES-SAM. Combined with the scratch/wear data and the thickness of the films, it can be found that the scratch/wear depths of APTES-SAM and phosphorylated APTES-SAM are much larger than their thickness (7.5 nm). On the contrary, the scratch/wear depths of lanthanum-based thin films do not exceed their thickness (15 nm) all the time. It shows that APTES-SAM and phosphorylated APTES-SAM are seriously destroyed with the increase of normal load and number of cycles, while lanthanum-based thin films are still not completely worn. The scratch/wear results indicate that lanthanum-based thin films have better

surface mechanical properties than silicon substrate, APTES-SAM and phosphorylated APTES-SAM.

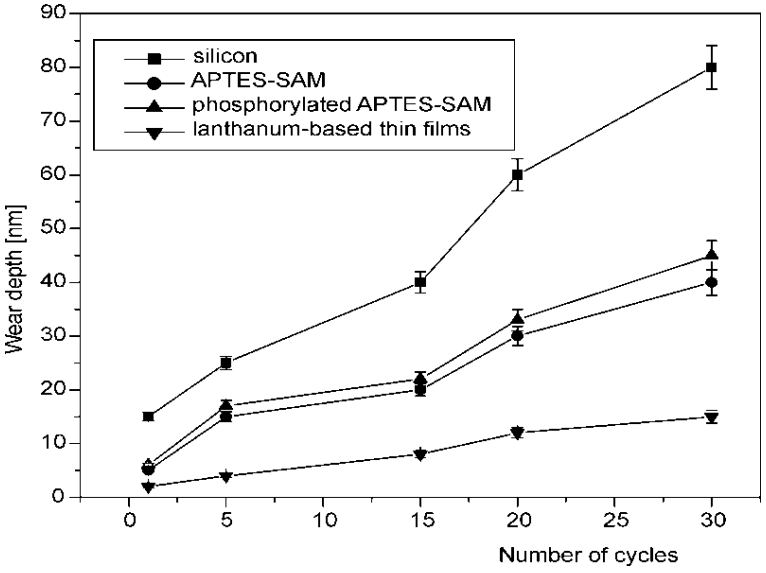

Fig. 11. Wear depths as a function of number of cycles

Rare earth elements have excellent chemical activity which results from their special 4f electron shell structure. Since electrons on the 4f electronic shell do not screen entirely the atomic nucleus, rare earth atom has a high effective nuclear charge [16, 25]. The $–PO(OH)_2$ group on the APTES-SAM provides net negative charge, thus promoting the process of self-assembly. First, La^{3+} ion is adsorbed on the negatively charged surface of phosphorylated APTES-SAM. Then $–PO(OH)_2$ group not only has proton to exchange with lanthanum cation but also can provide a P=O bond as complexing group to react with lanthanum elements after adsorption, thus improving the bonding strength between the films and the silicon substrates [26]. In addition, Hertzian cone cracks can occur when the normal stress exceeds a critical value as the AFM tip slides over the surface [27]. Friction forces during sliding reduce this critical value. In a word, strong bonding strength between the films and the silicon substrates and low coefficient of friction are responsible for the superior scratch/wear resistance of lanthanum-based thin films.

4. Conclusions

In this work, nanotribological properties of silicon substrate, APTES-SAM, phosphorylated APTES-SAM, and the lanthanum-based thin films were characterized by

an AFM. The lanthanum-based thin films showed the lowest friction and adhesion followed by APTES-SAM and phosphorylated APTES-SAM, while silicon substrate showed high friction and adhesion. Microscale scratch/wear studies clearly showed that lanthanum-based thin films were much more scratch/wear resistant than the other samples. The superior friction reduction and scratch/wear resistance of lanthanum-based thin films may be attributed to low work of adhesion of non-polar terminal groups and the strong bonding strength between the films and the substrate.

It is thus concluded the prepared lanthanum-based thin films could be used for protection from scratching as well as reducing friction.

Acknowledgements

Authors would like to thank for the National Natural Science Foundation of China (grant No. 50475023) and Instrumental Analysis Center, Shanghai Jiao Tong University support for the present work.

References

[1] *Microelectromechanical Systems: Advanced Materials and Fabrication Methods*, NMAB-483, National Academy Press, Washington, DC, 1977.
[2] ROUKES M., Phys. World, 14 (2001), 25.
[3] BHUSHAN B., *Tribology Issues and Opportunities in Mems*, Kluwer Academic, Dordrecht, 1998.
[4] BHUSHIAN B., *Handbook of Micro/Nanotribology*, 2nd Ed., CRC, Boca Raton, FL, 1999.
[5] KAYALI S., LAWTON R., SMITH B.H., IRWIN L.W., EEE Links, 5 (1999), 10.
[6] ARNEY S., MRS Bull., 26 (2001), 296.
[7] BHUSHAN B., ISRAELACHVILI J.N., LANDMANN U., Nature, 374 (1995), 607.
[8] DUGGER M.T., SENFT D.C., NELSO G.C., ACS Symp. Ser., 741 (2000), 455.
[9] DEPALMA V., TILLMAN N., Langmuir, 5 (1989), 868.
[10] TSUKRUK V.V., BLIZNYUK V.N., HAZEL J., VISSER D., EVERSON M.P., Langmuir, 12 (1996), 4840.
[11] BOSHUI C., YI Y., JUNXIU D., J. Chin. Rare Earth Soc., 16 (1998), 220.
[12] KONISHI Y., SHIMAOKA J.C., ASAI S., React. Funct. Polym., 36 (1998), 197.
[13] SIDEBOTTOM D.L., HRUSCHKA M.A., POTTER B.G., BROW R.K., J. Non-Cryst. Sol., 222 (1997), 282.
[14] CHENG X.H., BAI T., WU J., LIANG W., Wear, 260 (2006), 745.
[15] YU L.G., LIAN Y.F., XUE Q.J., Wear, 214 (1998), 151.
[16] CHENG X.H., C.Y.XIE, Wear, 254 (2003), 415.
[17] CHA K.H., KIM D.E., Wear, 251 (2001), 1169.
[18] BHUSHAN B., Wear, 259 (2005), 1507.
[19] BUSCHER T.C., MCBRANCH D., DEQUAN L., J. Am. Soc., 118 (1996), 2950.
[20] KATZ H.E., SCHELLER G., PUTVINSKI T.M., SCHILLING M.L., WILSON W.L., CHIDSEY C.E.D., Science, 254 (1991), 1485.
[21] BINNIG G., QUATE C.F., GERBER CH., Phys. Rev. Lett., 56(1986), 930.
[22] GLOSLI J.N., MCLELLAND G.M., Phys. Rev. Lett., 70 (1993), 1960.
[23] BIERBAUM K., KINZLER M., WÖLL CH., GRUZNE M., HÄHNER G., HEID S., EFFENBERGER F., Langmuir, 11 (1995), 512.
[24] ISRAELACHVILI J.N., *Intermolecular and Surface Forces*, Academic Press, New York, 1985.
[25] BELL T., SUN Y., LIN Z., YAN M., Heat Treat. Met., 27 (2000), 12.

[26] KANTIPULY C., KATRAGADDA S., CHOW A., Talanta, 37 (1990), 491.
[27] HUTCHINGS I.M., *Tribology, Friction and Wear of Engineering Materials*, CRC Press, Boca Raton, FL, 1992.

Received 10 July 2007
Revised 7 September 2007

Materials Science-Poland, Vol. 25, No. 4, 2007

Producing bulk nanocrystalline materials by combined hydrostatic extrusion and equal-channel angular pressing

M. KULCZYK[1,2*], W. PACHLA[1], A. MAZUR[1], M. SUŚ-RYSZKOWSKA[2], N. KRASILNIKOV [3,4] K. J. KURZYDŁOWSKI[2]

[1]Institute of High Pressure Physics, Polish Academy of Sciences, ul. Sokolowska 29/37, 01-142 Warsaw, Poland

[2]Warsaw University of Technology, Faculty of Mater. Sci. Eng., Wołoska 141, 02-507 Warsaw, Poland

[3]Institute of Physics of Advanced Materials, Ufa State Aviation Technical University

[4]Ulyanovsk State University (UlGU)

Nickel and copper were subject to severe plastic deformation at room temperature, using hydrostatic extrusion (HE) and equal-channel angular pressing (ECAP). The maximum deformation was 13.5 in nickel and 22.3 in copper. These deformations were obtained by each of the techniques separately and by their combination. It has been found that the combined HE and ECAP deformation greatly increases the homogeneity of the microstructure and improves considerably its mechanical properties comparing with a single technique. After the combined treatment, the grain size of both copper and nickel was of the order of 100 nm. The experiments have shown that the combination of HE and ECAP techniques permits producing homogeneous nanocrystalline materials of large volumes.

Key words: *severe plastic deformation; hydrostatic extrusion; nanocrystalline structure; grain refinement; nickel; copper*

1. Introduction

Severe plastic deformation (SPD) applied to metals and alloys yields solid materials with a nanocrystalline or ultrafine grained structure [1]. Formation of such structures results in a considerable improvement of the mechanical properties of materials. A very high mechanical strength is usually accompanied by a reserve of plasticity on a level unachievable with classical techniques employing conventional hardening me-

*Corresponding author, e-mail: mariusz@unipress.waw.pl

thods [1–3]. Among the most popular SPD techniques there are high-pressure torsion (HPT) and equal channel angular pressing (ECAP) [1, 2, 4–7]. Recently, fabrication of nanocrystalline metals via the SPD techniques has increasingly been concentrated on combinations of these two techniques [2, 8]. By combining the SPD techniques, one can increase the deformation degree and alter plastic deformation paths which results in more fine-grained structures and improved mechanical properties. The authors of Ref. [9–12] have recently reported on successful experiments with the use of hydrostatic extrusion (HE), conducted at room temperature, for fabricating nanocrystalline (NC) and ultra-fine-grained (UFG) structures in titanium, Al-alloys, iron, 316LVM steel and copper.

The aim of the present study is to describe structures produced by a combination of ECAP and HE. This was achieved for nickel and copper widely used in electronics. Because of its plasticity and the microstructural homogeneity, nanocrystalline nickel may replace electro-plated nickel used in MEMS circuits thus far [8–14]. Nanocrystalline copper, on the other hand, may be used instead of gold in electronics, thereby reducing costs and eliminating the purification and doping processes [12].

2. Experimental

Purity of nickel used in the experiments was 99.98%, and that of copper – 99.8%. The SPD parameters employed are given in Table 1. The ECAP process was conducted in a 90° die by route B_C in eight passes for nickel and sixteen passes for copper. The HE process was carried out in a cumulative manner until the final diameter was reduced to 3 mm, with the total length of the product of about 350 mm. Both materials after HE have been water quenched to reduce recovery. Both processes were conducted at room temperature. The deformation rates for HE varied between 9 and $3\times10^{2}\,s^{-1}$, whereas in the ECAP process $8\times10^{-2}\,s^{-1}$. The starting microstructures were analyzed using optical microscopy and, after the SPD by transmission, electron microscopy at the accelerating voltage of 120 kV. A quantitative analyses of the images obtained (grain size distributions) were performed using the "Micrometer" software. The mechanical properties were determined by tensile tests conducted at room temperature at a strain rate of $2\times10^{-3}\,s^{-1}$. HV0.2 (15 s) of the materials subject to combined SPD treatment was also measured.

Table 1. The deformation path layout

Type of SPD	Cu true strain	Ni true strain
ECAP	18.4 (16 passes)	9.2 (8 passes)
HE	5.65	4.6
ECAP + HE	22.3	12.4[a]
HE + ECAP + HE	–	13.5

[a]Presented in [3].

3. Results and discussion

3.1. Investigations of microstructure

The starting average grain size of copper was 250 μm with the standard deviation $SD = 60$ μm, and for nickel 50 μm with $SD = 18$ μm. Both materials were characterized

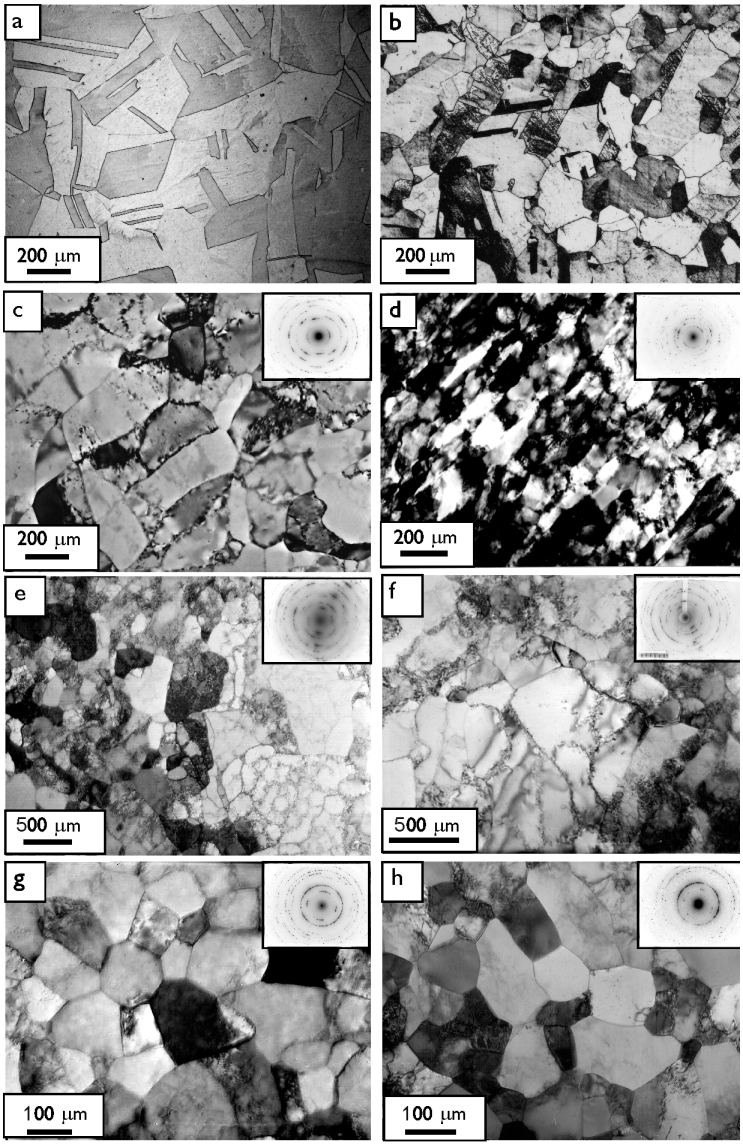

Fig. 1. Microstructures of copper and nickel: a, b) starting state, c, d) after ECAP – 16 passes for copper and 8 passes for nickel, e, f) after HE, g) after combined HE + ECAP (16 passes) for copper, h) after HE + ECAP (8 passes) + HE for nickel

by the presence of deformation twins (Figs. 1a, b). After ECAP, the microstructures of both copper (Fig. 1c) and nickel (Fig. 1d) showed a high degree of heterogeneity. The diffraction images and observations at various angles reveal low-angle grain boundaries, embedded into the initial grain matrix. The diffraction images of the ECAP-processed samples (Figs. 1c, d) suggest preferred crystallographic direction of the grains. In copper, we can see a dislocation structure in the form of sub-grains with the average size of about 250 nm. In nickel, apart from the considerable domination of low angle boundaries, there is a strong localization of deformation in the form of deformation bands (Fig. 1d). The average grain (sub-grain) size in the ECAP nickel was about 400 nm. A similar size was obtained for the HE nickel. In copper, both HE and ECAP, the average grain (subgrain) size was about 250 nm. Figure 1e clearly shows strong heterogeneity of the microstructures. Small grains (crystallites) formed as a result of severe deformation are mixed with regions of a subgrain structure. In both materials, ECAP and HE applied separately resulted in non-homogeneous structures. Similar results have been reported in [15]. Hence the idea was developed to combine the HE and ECAP to increase deformation degree, and after the deformation path to bring about activation of additional slip systems.

Table 2. Grain size copper and nickel after various deformation paths

State	Cu	Ni
Initial	250 μm	50 μm
ECAP	250 nm[a]	400 nm[a]
HE	250 nm[a]	350 nm[a]
ECAP + HE	120 nm	160 nm
HE + ECAP + HE	-	100 nm

[a]Grain/subgrain

With copper, the hydrostatic extrusion was preceded by an ECAP process, with the true strain of 22.3, whereas in nickel, the combined process included the HE + ECAP + HE sequence with a total strain of 13.5. In our earlier study, we experimented with deforming nickel using the ECAP + HE combination [3]. The experiment with double change of the deformation technique aimed at examining how the changes of the deformation path affect the properties of the material.

In copper, the combined ECAP + HE process resulted in an abrupt refinement of the microstructure (Fig. 1g) down to grain size of 120 nm. The refinement was accompanied by microstructure homogenization. The diffraction images suggest that grains are predominately surrounded by high-angle boundaries, which was also confirmed by dark field observations.

The grains shown in the micrographs are equiaxial also in nickel. By changing the deformation path twice and applying a strain of 13.5, nickel was obtained with an average grain size of 100 nm. This material contained a large number of high-angle boundaries. The nickel structure produced by a combined ECAP + HE treatment, re-

ported earlier by the present authors [3], was built of equiaxial grains 160 nm in size. Therefore, the double change of the deformation path, reported in the present paper, resulted in an additional refinement of the structure by about 60%. One can also expect the same with Cu, although the structure obtained in the present experiments already is one of the finest reported in the literature.

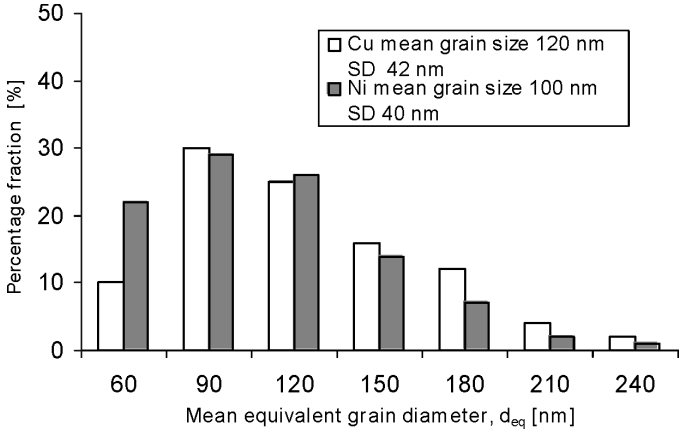

Fig. 2. Grain size distribution in nickel and copper
after combination of ECAP (16×) + HE (Cu) and HE + ECAP (8×) + HE (Ni)

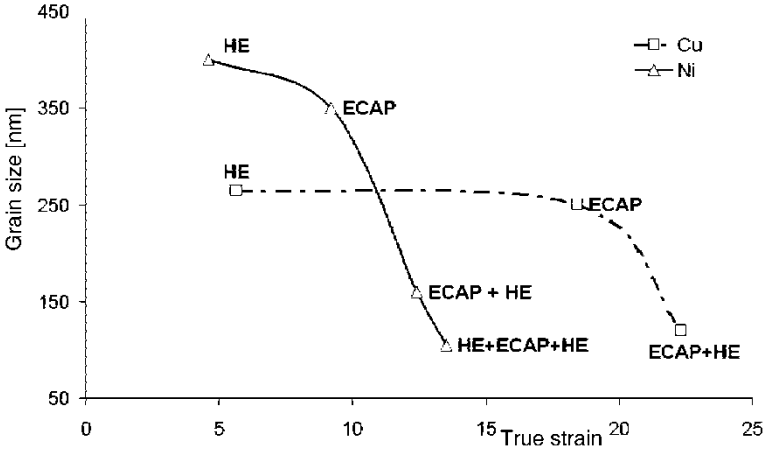

Fig. 3. Structural changes in nickel and copper as a function of true strain

Figure 2 shows the grain size distributions in the materials examined. It should be noted that the grain size distributions in nickel and copper reveal similar characters. In both, there is a certain population of crystallites, of grain sizes below 60 nm, whereas the average grain sizes are similar (100 nm and 120 nm). In spite of a considerable difference in the starting grain sizes, nickel and copper exhibited after treatments similar grain sizes and a similar degrees of homogeneity (the same standard deviation).

Some differences in the behaviour of both materials can be seen when analyzing the structural changes as a function of true strain (Fig. 3). In both materials, a strain of about 5 brings about a clear departure from initial structures. At the first stage of straining, the grains (subgrains) acquire a size which changes only slightly with increasing strain, irrespective of which SPD technique (ECAP or HE) is applied. The materials show 'saturation' and undergo only minimum changes as seen in the diagrams of Fig. 3. It is only the change of SPD process which, by changing the deformation path, gives a structure undergoing further abrupt refinement. For copper, the 'plateau' as function of strain is much longer than in nickel. This is associated with the dynamic recovery which occurs in copper at lover temperatures.

3.2. Mechanical properties

The results of mechanical test for nano-copper and nickel are shown in Tables 3 and 4, respectively. In both materials, the mechanical strength increases with increasing deformation. The strength is higher in the material subject to HE than in the material after ECAP, although HE accumulated strain is almost three times lower. This can be attributed to the different straining rates which in HE are much higher than in ECAP.

Table 3. Mechanical properties of copper at initial state and after various deformation paths[a]

State	True strain	UTS [MPa]	YS [MPa]	ε [%]
Initial	0	290	280	16
HE	5.56	466	460	12
ECAP	16	395	390	10
ECAP + HE	23	550	530	9

[a]UTS – ultimate tensile stress, YS – yield stress, ε – elongation.

Table 4. Mechanical properties of nickel in the initial state and after various deformation paths[a]

State	True strain	UTS [MPa]	YS [MPa]	ε [%]
Initial	0	320	270	38
HE	4.6	946	926	15.0
ECAP	8	780	630	20
ECAP + HE [3]	11.2	1200	1120	9.5
HE + ECAP + HE	12.3	1255	1180	11

[a]UTS – ultimate tensile stress, YS – yield stress, ε – elongation.

These two processes, HE and ECAP, also differ in the strain components. In ECAP we have pure shear, whereas in HE – a three-dimensional compressive strain state. The combined HE and ECAP process gives an abrupt increase of the material

strength. In copper, the yield strength in comparison to the initial one increases by 90%, whereas in nickel, when treated by a HE + ECAP + HE process – by 340%. This is due to the lower propensity of nickel to dynamic recovery. In both materials, in spite of the abrupt increase of strength, a relatively high plasticity of about 10% still remains.

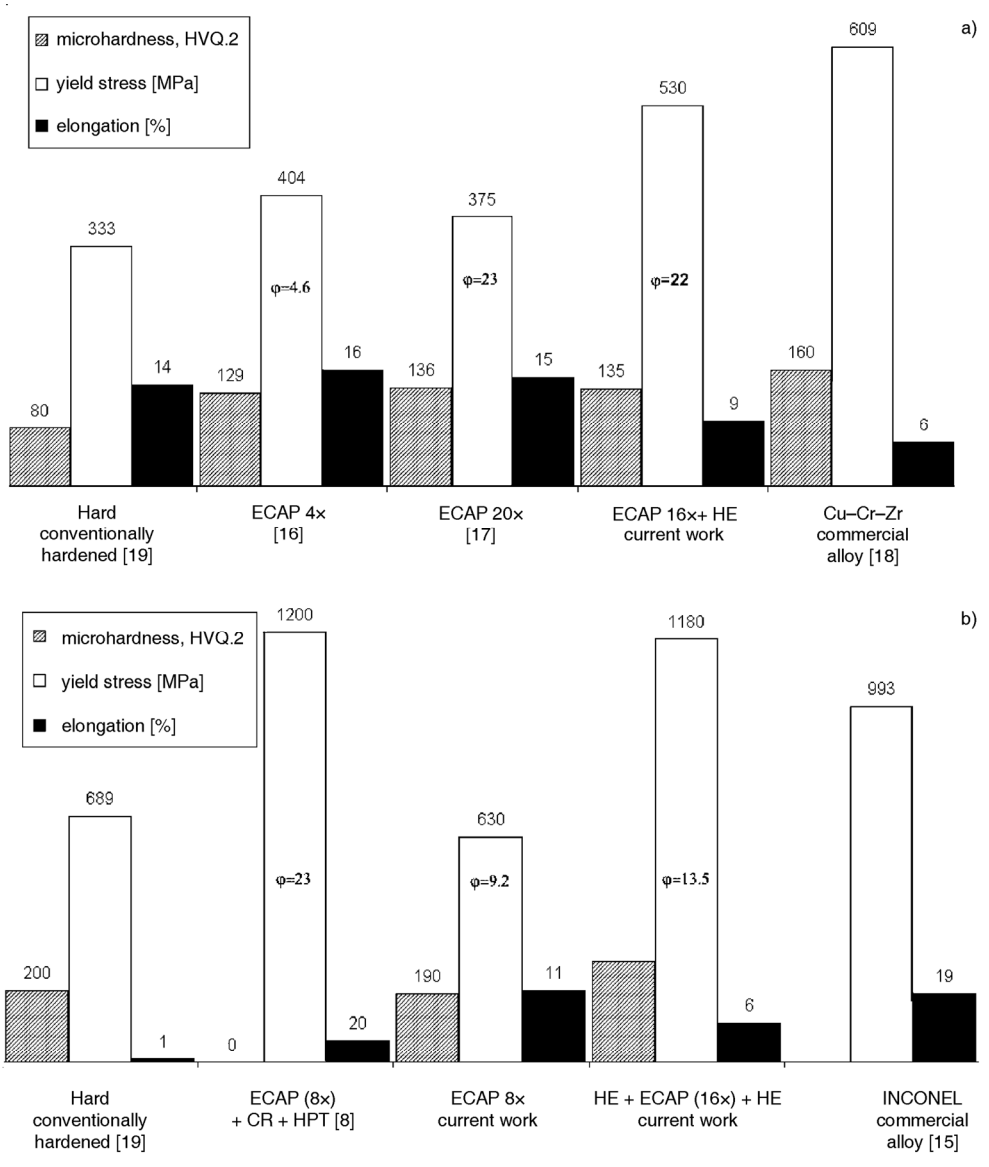

Fig. 4. Comparison between properties of a) copper and b) nickel after application of various deformation methods and commercial base Ni and Cu alloy (HE – hydrostatic extrusion, ECAP – equal channel angular pressing, HPT– high pressure torsion, CR – cold rolling, φ – cumulative true strain

In comparison to a coarse-grained copper strain hardened in a conventional way (Fig. 4a), the ECAP and HE Cu exhibit a similar level of plasticity. For nickel treated by the combination of HE + ECAP + HE, elongation is drastically higher than that observed for coarse-grained material hardened conventionally which shows only the elongation of 1%. The strength obtained here for copper is much higher than those reported in the literature. It is worth noting that at a similar strain applied by ECAP alone [17], the yield point is lower by 40% than that achieved when using the ECAP + HE combination. This confirms that an alteration of the straining technique during the deformation process has a crucial effect on the properties of the material. It should be noted that the strength of pure copper processed here is comparable with the high-strength alloying copper commonly used for the fabrication of welding tips [18]. The results obtained for nickel were compared with those obtained by HPT [8]. The yield stress is on the same level but after the ECAP + HE treatment the elongation is almost twice larger. Moreover, HPT permits treating products of much smaller volumes. The pure nanocrystalline nickel produced by the HE + ECAP + HE combination has the yield point higher than the popular super-strong nickel superalloy known commercially as INCONEL (Fig. 4b).

4. Concluding and remarks

HE and ECAP processes applied separately to nickel and copper brought about an abrupt increase of the strength properties of these materials. However, their structures were non-uniform, with deformations and sub-dislocation structure. Double and triple combinations of two techniques (ECAP, HE) lead to an increase of the deformation degrees and changes of the deformation paths, yielding copper and nickel with homogeneous microstructures with equiaxial grains. In both materials, the 100 nm grain refinement was obtained. This strong refinement resulted in a great improvement of the strength to the level of high-strength commercial alloys. In nickel, the best mechanical properties were obtained by using a combined HE + ECAP + HE treatment under a total true strain of 13.5 (yield stress YS =1180 MPa), whereas in copper subjected to a combined ECAP + HE treatment at a true strain of 22.3, the yield stress was 530 MPa. Both materials preserved a useful plasticity (Ni – 11%, Cu – 9%) unachievable by conventional techniques of strain hardening.

The present experiments enabled developing a technology for production of nanocrystalline Ni and Cu with properties superior to those obtained by traditional SPD techniques, such as ECAP or HPT. The materials fabricated by the proposed technology can be used in micro-electronics (MEMS) for micro-elements intended to carry mechanical loads (Ni), junctions and other electronic components (Cu). This, however, requires further studies of their electrical properties.

This work was supported by the Ministry of Science and Informatics (Grants PBZ- KBN nr 3 T08A 062 29 and 4T08A 04525).

References

[1] VALIEV R., Nature, 3 (2004), 511.
[2] NURISLAMOWA G.V., ISLAMGALIEV R.K., VALIEV R.Z., Mater. Sci. Forum, 503–504 (2006), 579.
[3] KULCZYK M., PACHLA W., SWIDERSKA-SRODA A., KRASILNIKOV N., DIDUSZKO R., MAZUR A., LOJKOWSKI W., KURZYDLOWSKI K.J., Solid State Phen., 114 (2006), 51.
[4] SEGAL V.M., Mater. Sci. Eng. A, 197 (1995), 157.
[5] VALIEV R.Z., ISLAMGALIEV R.K., ALEXANDROV I.V., Prog. Mater. Sci., 45 (2000), 103.
[6] ZHILYAEV A.P., KIM B.-K., SZPUNAR J.A., BARO M.D., LANGDON T.G., Mater. Sci. Eng. A, 391 (2005), 377.
[7] SCHAFLER E., PIPPAN R., Mater. Sci. Eng. A,387-389 (2004), 799.
[8] KRASILNIKOV N., LOJKOWSKI W., PAKIELA Z.AND VALIEV R., Mater. Sci. Eng. A,397 (2005), 330.
[9] LEWANDOWSKA M., GARBACZ H., PACHLA W., MAZUR A., KURZYDLOWSKI K.J., Solid State Phen., 101–102 (2005), 65.
[10] LEWANDOWSKA M., GARBACZ H., PACHLA W., MAZUR A., KURZYDLOWSKI K.J., Mater. Sci.-Poland, 23 (2005), 279.
[11] KULCZYK M., PACHLA W., ŚWIDERSKA-ŚRODA A., SUŚ-RYSZKOWSKA M., MAZUR A., KURZYDŁOWSKI K.J., Proc. 9th Int. ESAFORM Conf. Material Forming, University of Strathclyde, Glasgow, UK, April 26–28 2006, Publishing House "Akapit", Kraków, Poland, p. 531.
[12] PACHLA W., KULCZYK M., ŚWIDERSKA-ŚRODA A., LEWANDOWSKA M., GARBACZ H., MAZUR A., KURZYDŁOWSKI K.J., Proc. 9th Int. ESAFORM Conf. Material Forming, University of Strathclyde, Glasgow, UK, April 26–28 2006, Publishing House "Akapit", Kraków, Poland, p. 535.
[13] DE BOER M.P., MAYER T.M., MRS Bull., 26 (2001), 302.
[14] YOUNG D.J., MRS Bull., 26 (2001), 331.
[15] DALLA TORRE F.H., PERELOMA E.V., DAVIES C.H.J., Acta Mater., 54 (2006), 1135.
[16] RABKIN E., GUTMAN I., KAZAKEVICH M., BUCHMAN E., GORNI D., Mater. Sci. Eng. A, 396 (2005), 11.
[17] VINOGRADOV, SUZUKI T., HASHIMOTO S., KITAGAWA K., KUZNATSOV A., DOBATKIN S., Mater. Sci. Forum, 503–504 (2006), 971.
[18] NAGASAWA H., AOKI S., Papers of RTRI (WCRR '97), Italy (1997), (http://www.rtri.or.jp/), www.matweb.com

Received 14 February 2007
Revised 18 May 2007

Materials Science-Poland, Vol. 25, No. 4, 2007

Study on absorption and mechanical properties of rubber sheet absorbers

R. GONG, Y. HE*, X. LI, C. LIU, X. WANG

Department of Electronic Science and Technology,
Huazhong University of Science and Technology, Wuhan 430074, China

Based on the impedance matching principle and electromagnetic wave propagating law, double-layer absorbers with impedance-matching structure were designed both theoretically and experimentally. Microwave absorbers were prepared by mixing a commercially available rubber with magnetic micropowder (MMP) and/or dielectric materials. The first layer, made up of MMP has large permeability and magnetic loss, while the second layer (matching layer), comprised of MMP and/or dielectric material, has frequency dispersion with the parameters of permittivity and permeability to match the incidence free space over a wide frequency range. Experiments showed that the matching layer plays a key role in the absorption. Electromagnetic parameters and thickness need to be controlled precisely to achieve high absorption. It was reasoned out that with increasing electromagnetic performance of matching layer, matching thickness will decrease. Tests showed that the reflectivity was below –10 dB for samples 1 and 2, and below –8 dB for samples 3–6 in the frequency range of 8–18 GHz. Finally, mechanical characteristics were also investigated with tensile strength above 10 MPa, indicating that the materials may find practical use in the engineering of microwave absorbers.

Key words: *double-layer absorber; impedance matching; reflectivity; tensile strength; MMP*

1. Introduction

The development of microwave absorber continues to attract much attention because of the increasing environmental pollution from wireless telecommunication systems and high-frequency circuit devices and the essential part of a stealth defense system for all military platforms because it can transform undesired electromagnetic waves into heat [1, 2]. An effective electromagnetic wave absorber must fulfil the following requirements [3]:

- maximum absorption of electromagnetic waves with minimum reflection,
- dissipation of incident wave energy changes into heat.

* Corresponding author, e-mail: Husthyf1203@yahoo.com.cn

Distribution of energy density in a sheet absorber with a termination metal is illustrated in Fig. 1 [4]. In the vicinity of the termination metal, electric field energy density (W_e) decreases while magnetic field energy density (W_m) increases. Therefore, an effective double-layer absorber can be designed by arranging strong magnetic loss materials as the first layer and electric loss (larger thickness) or both electric and magnetic loss materials (smaller thickness) as the second layer.

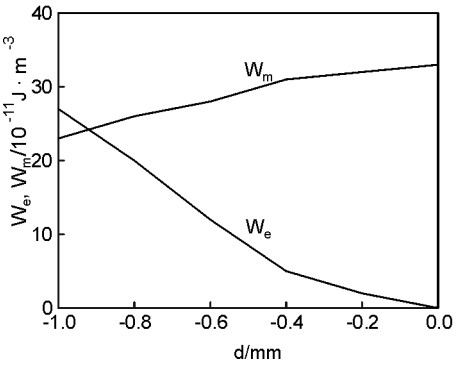

Fig. 1. Distribution of energy density in absorbing materials

Perini and Cohen [5] developed a Powell method to design radar-absorbing materials (RAM) consisting of several dielectric layers. The absorption of RF energy was mostly done in the last layer, and the others were used to match the wave impedance of the RAM to that of the incidence medium. A two-layer absorber composed of the mixture of iron particles and rubber as the inner layer, and of barium hexaferrite powder and rubber as the outer layer, has better attenuation properties compared with the one-layer structure. The reflection of the incident wave can be reduced with increasing matching of the impedance of the outer layer and of free air, while the inner layer can ensure that the microwave power may be mostly exhausted [6]. Meshram et al. reported a two-layer absorber which can provide higher absorption of the order of –9 dB from 8.7 to 10.2 GHz as compared to a single-layer microwave absorber [7].

Since microwave permeabilities of known magnetic materials do not exceed several units above GHz frequency, other approaches to broaden bandwidth of radar absorbers attract great attention. Conventional methods of creating broad-band wave absorbers employ multilayer absorbing structures with impedance-graded composites [8, 9] or the parameters (permittivity and permeability) with frequency dispersion [9, 10]. In this paper, both thicknesses and surface densities of samples (samples 1–6) were gradually reduced, with the reflectivity below –8 dB over the frequency range of 8–18 GHz, to develop light-weight, thin-layer, broad-band, strong-absorption two-layer absorbers.

2. Two-layer structure

The computed reflectivity of a single layer absorber comprising 85 wt. % of magnetic micropowder (MMP) is shown in Fig. 2. The absorption of energy at high frequencies decreases with increasing layer thickness. It is probable that the absorber does not match a free space in the high frequency region because the dielectric parameter $(\varepsilon_r'', \varepsilon_r'')$ has no frequency dispersion, as shown in Fig. 3a.

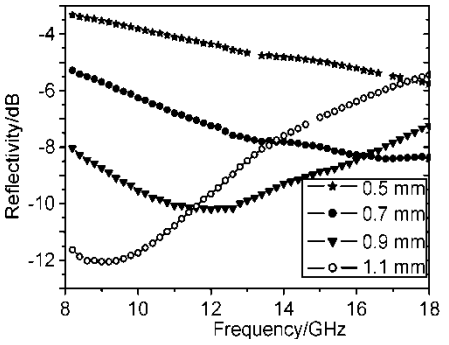

Fig. 2. Reflectivity versus frequency for various thickness rubber composites with 85 wt. % MMP

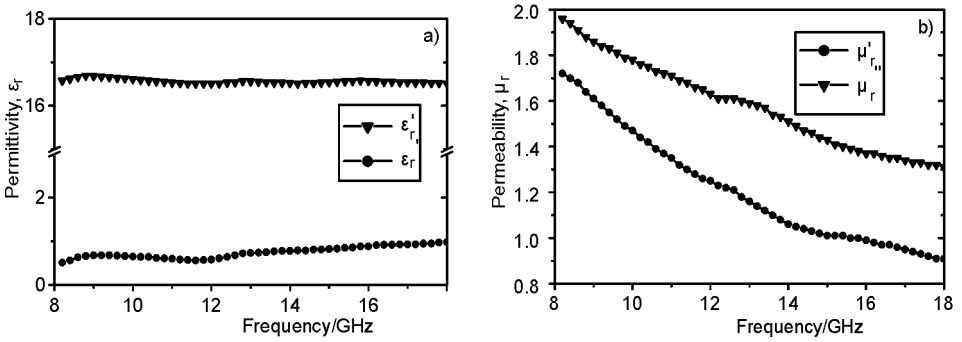

Fig. 3. Relative permittivity (a) and relative permeability (b) as functions of frequency for the rubber composites with 85 wt. % MMP

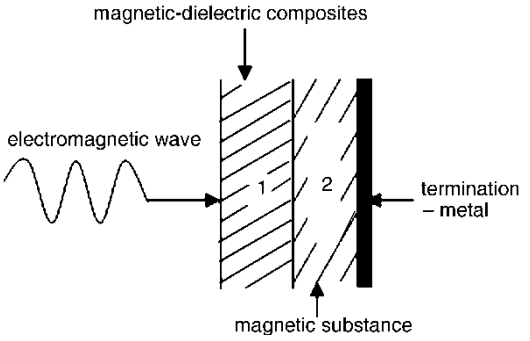

Fig. 4. Structure of a two-layer wave absorber

Table 1. Constitutions and matching thicknesses of the samples[a]

No.	Second layer	Thickness [mm]	First layer	Thickness [mm]
1	10% carbon fibre	1.5	85% MMP	0.8
2	20% TiO_2			
3	10% carbon fibre, 1.6% graphite	1.1		
4	20% TiO_2, 2.3% graphite			
5	10% carbon fibre, 38%MMP, 5% graphite	0.6		0.6
6	20%TiO_2, 30%MMP, 2.9% graphite			

[a]Matching thickness corresponding to the optimum performance ($\leqslant$ –8 dB) in a broad frequency range

The structure of a double-layer absorber with a metal substrate is shown in Fig. 4. The first layer is composed of the rubber composites with 85 wt. % MMP (Table 1) which maintains a higher permeability (particularly imaginary part of the permeability), leading to a larger magnetic loss. The second layer comprises composites of magnetic and/or dielectric materials which induces frequency dispersion and dielectric losses caused by dipole rotation effects (known as Debye relaxation) and others [11].

The return loss coefficient of the two-layer absorber in Fig. 4 is given [12] by

$$R = 20\lg\left|\frac{z_{in} - z_0}{z_{in} + z_0}\right| \tag{1}$$

$$Z_{in} = \frac{z_1 \tanh(\gamma_1 d_1) + z_2 \tanh(\gamma_2 d_2)}{1 + \dfrac{z_1}{z_2}\tanh(\gamma_1 d_1)\tanh(\gamma_2 d_2)} \tag{2}$$

where z_{in} is the input impedance measured from the surface of the absorber to the termination; z_0 is the characteristic impedance of vacuum; z_1, γ_1, d_1 and z_2, γ_2, d_2 are the characteristic impedances, propagation constants and thicknesses of the first (1) and second (2) layers, respectively. They are given by

$$\gamma_i = j2\pi f\sqrt{\mu_i \varepsilon_i}, \qquad i = 1, 2 \tag{3}$$

$$z_i = \sqrt{\frac{\mu_i}{\varepsilon_i}}, \qquad i = 1, 2 \tag{4}$$

where $z_0 = \mu_0/\varepsilon_0$ equals 377 Ω.

3. Preparation of samples and testing methods

MMP was prepared from a compound consisting of fine particles of FeCo and rare earth by ballmill techniques. Carbon fibre, TiO_2, and graphite were purchased in the market. The adhesive matrix is known as hydrogenation acrylonitrile-butadiene rubber (HNBR) and comes from Japan. The materials were blended with HNBR in various proportions in a roll mill, as shown in Table 1. Test specimens were obtained in different sizes: toroidal shape (outer diameter of 7.00 mm, inner diameter of 3.04 mm, and thickness of 3.0–5.0 mm) to test electromagnetic parameters and rectangular shape ($180\times180\times(0.6–2.3)$ mm^3) for reflectivity measurements.

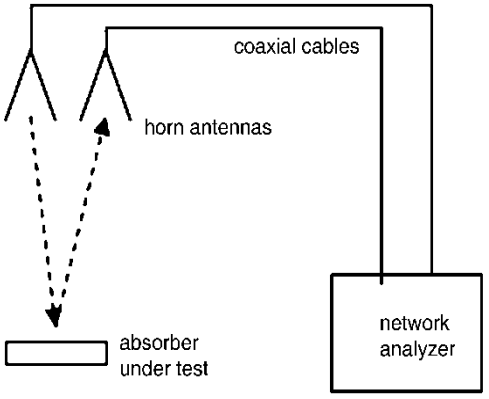

Fig. 5. Schematic diagram of the experiment system

The schematic diagram of the measurement set-up, as a free space measurement system, is shown in Fig. 5, such that two horn antennas and absorber under test are set in an anechoic chamber. The measurements are made with a network analyzer system which consists of a HP8510B network analyzer, an HP83622A synthesized sweeper and an HP8515A S-parameter test set. The antennas are positioned 2 m from samples and set almost normal to their surfaces. The permeability (μ) and permittivity (ε) of the samples are obtained from the transmission/reflection (T/R) method. The reflectivity is attained by comparing the signal reflected by the sample under test to the signal input.

4. Experimental results

4.1. Absorption properties

The dependence of reflectivity on frequency for samples 1–6 is shown in Figs. 6–10. The ε_r and μ_r spectra of the first layer of the double-layer absorber are shown in Fig. 3.

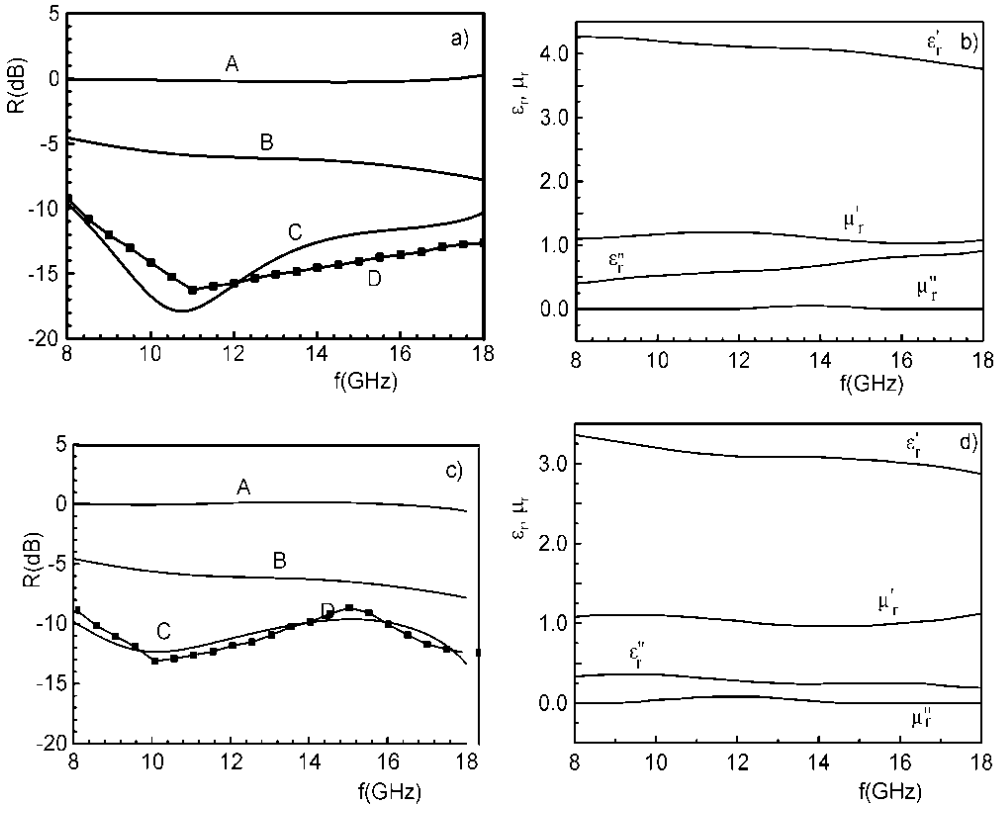

Fig. 6. Reflectivity versus frequency for sample 1 (a), ε_r and μ_r spectra of the second layer of sample 1 (b), reflectivity versus frequency for sample 2 (c), ε_r and μ_r spectra of the second layer of sample 2 (d); A – reflectivity of the second layer, B – reflectivity of the first layer, C – experimental results, D – theoretical curves

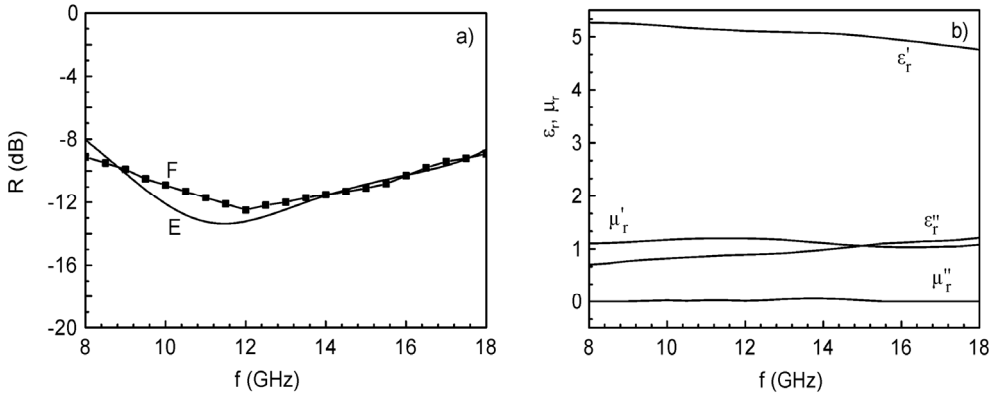

Fig. 7. Reflectivity versus frequency for sample 3 (a): E – experimental results, F – theoretical values, ε_r and μ_r spectra of the second layer of sample 3 (b)

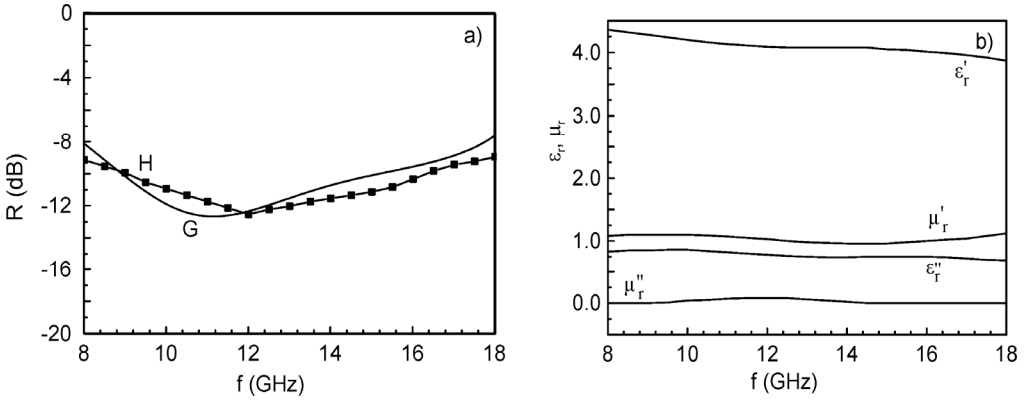

Fig. 8. Reflectivity versus frequency for sample 4 (a): G – experimental results, H – theoretical values, ε_r and μ_r spectra of the second layer of sample 4 (b)

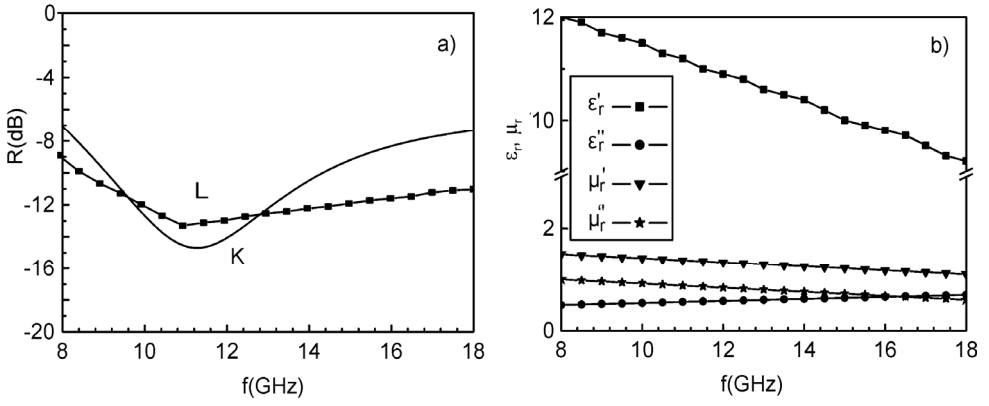

Fig. 9. Reflectivity versus frequency for sample 5 (a): K – experimental results, L – theoretical values, the ε_r and μ_r spectra of the second layer of sample 5 (b)

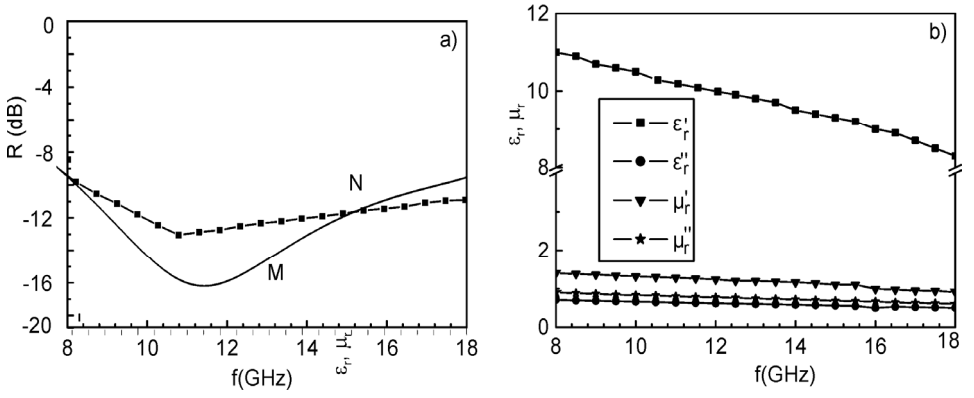

Fig. 10. Reflectivity versus frequency for sample 6 (a): M – experimental results, N – theoretical values, ε_r and μ_r spectra of the second layer of sample 6 (b)

Table 2. Matching thickness (mm), surface density (kg/m^2) and tensile strength (MPa) of the samples

Sample No.	1	2	3	4	5	6
Matching thickness	1.5+0.8 (2.3)	1.5+0.8 (2.3)	1.1+0.8 (1.9)	1.1+0.8 (1.9)	0.6+0.6 (1.2)	0.6+0.6 (1.2)
Surface density	4.0	4.3	3.6	3.8	3.3	3.5
Tensile strength	12.8	10.2	13.8	11.1	11.9	10.3

As shown in Figs. 6–10, the measured reflectivities agree well with theoretical values. Slight differences in measured and predicted results are likely due to the inability to achieve consistent thickness and practical variations in mixing of various materials. The matching thicknesses and surface densities of samples 1–6 are listed in Table 2.

4.2. Mechanical properties

Sample sulfuration was carried out by heating at 165 ºC for 25 min on a QLBD400×400 galvanothermy slab sulfuration machine. Tensile strength was measured in a XL100-pull experiment machine, according to GB/T528-1998 (sample 1, pull velocity – 500 mm/min). The samples were cut into dump-bell (Fig. 11), to test tensile strength after setting for a week. The results are shown in Table 2.

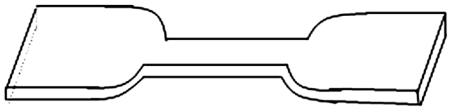

Fig. 11. Structure of the sample to test tensile strength

5. Analysis and discussion

Absorption ratio of absorbers is greatly improved by introducing matching layers (the second layer), as shown in Figs. 6a, c. Though the matching layer hardly dissipates electromagnetic wave, attenuation is improved when it laminates the first layer to form a two-layer structure. Therefore, impedance matching plays a key role in absorbing materials. Since both carbon fibre and TiO_2 have low permittivities and permeabilities (Figs. 6b, d), the thickness of the second layer must increase to form a matching structure. This corresponds to the fact that, ε_1, μ_1 and d_1 being constant, and ε_2 and μ_2 being small, the thickness d_2 should increase to realize the matching of Z_{in} to Z_0 as evident from Eq. (2).

Conductor network is formed in the matching layer by introducing graphite to samples 3 and 4. Current is converted to heat, and absorption is improved (Figs. 7a,

8a). It is also proved by that the electric permittivities (ε', ε'') of the matching layer are increased (Figs. 7b, 8b). Meantime, the matching thickness decreases and the surface density is reduced, too. When too much graphite induces a strong reflection, electromagnetic wave cannot transmit into the absorber to wear down.

Matching layers of samples 1–4 are made of dielectric materials, and they dissipate electromagnetic wave mainly by dielectric polarization. In order to reduce thickness and improve absorption, MMP is added to the matching layer to form electromagnetic media (samples 5, 6). As a result, values of the electromagnetic parameters (μ', μ'', ε', ε'') increase, the matching thickness decreases, absorption is greatly improved due to magnetic and dielectric loss (Figs. 9, 10).

Considering the electromagnetic parameters of samples 1–6, the parameters of the matching layer are lower than those of the first layer, thus also forming electromagnetic parameters – graded structure from the free space, the second layer to the first layer. Meanwhile, frequency band is broadened because of frequency dispersion; parameters decrease as frequency increases.

Dielectric materials are characterized by low density, high strength and good stability, while MMP has large permeability and magnetic loss. When they are combined to form a double-layer absorber, mechanical and absorption properties are improved. These designs offer less weight and higher absorption in the upper frequency region of 10–18 GHz when compared to commercially available flexible magnetic sheet absorbers, e.g. Emerson and Cuming ECCOSORB® FGM. Tensile strength of sample 3 was the best with the value of 13.8 MPa (Table 2). Tensile strengths of samples 1, 3 and 5 were better than those of samples 2, 4 and 6. This is because carbon fibre can build up the sulfuration absorber strength.

6. Conclusion

Impedance matching plays a key role in designing effective electromagnetic wave absorbers. Reflectivity is greatly affected by the electromagnetic parameters and thickness of the matching layer. These parameters need to be controlled precisely to achieve high absorption. In addition, with increasing values of electromagnetic parameters of matching layer, matching thickness will decrease.

In this work, the reflectivities of samples 1, 2 were below –10 dB at the thickness of 2.3 mm and surface density $\leq$ 4.4 kg/m^2; while the reflectivities of samples 3–6 below –8 dB at the thickness $\leq$ 1.9 mm and surface density $\leq$ 3.8 kg/m^2 over 8–18 GHz. Tensile strengths had the values above 10 MPa for all samples, which may meet requirements for the practical use in engineering of microwave absorbers.

Further research could optimize the absorber by having a host material of more complex permeability. In addition, the detailed absorbing wave characteristics in oblique incidence should be the subject of further study.

Acknowledgement

This work was supported by Grant-in-Aid for Scientific Research No.50371029 from the Ministry of Education, Science and Technology of China. The authors would like to thank Professor Xiucheng Zhang for his help with the samples measurement.

References

[1] MAEDA T., SUGIMOTO S., KAGOTANI T., TEZUKA N., INOMATA K., J. Magn. Magn. Mater, 281 (2004), 195.
[2] WU L.Z., DING J., JIANG H.B., CHEN L.F., ONG C.K., J. Magn. Magn. Mater, 285 (2005), 233.
[3] YANFEI HE, RONGZHOU GONG, YAN NIE, HUAHUI HE, ZHENSHENG ZHAO, J. Appl. Phys., 98 (2005), 084903.
[4] MINGZHONG WU, Ph.D Dissertation, Huazhong University of Science and Technology (2000), p. 7.
[5] PERINI J., COHEN L.S., IEEE Trans. Electromag. Compat., 35 (1993), 223.
[6] SHENGPING RUAN, BAOKUN XU, HUI SUO, FENGQING WU, SIQING XIANG, MUYU ZHAO, J. Magn. Magn. Mater., 212 (2000), 176.
[7] MESHRAM M.R., AGRAWAL NAWAL K., BHAROTI SINHA, MISRA P.S., J. Magn. Magn. Mater., 271 (2004), 213.
[8] PARDAVI-HORVATH M., J. Magn. Magn. Mater., 215–216 (2000), 182.
[9] DOSOUDIL R., UŠÁKOVÁ M., FRANEK J., SLÁMA J., OLAH V., J. Magn. Magn. Mater., 304 (2006), e756.
[10] ROZANOV K.N., IEEE Trans. Antennas and Propagation, 48 (2000), 1230.
[11] Mayer F., IEEE Trans. Electromag. Compat., EMC-8(1966), 155.
[12] SHEN G., XU Z., LI Y., J. Magn. Magn. Mater., 301 (2006), 326.

Received 14 February 2007
Revised 27 March 2007

Materials Science-Poland, Vol. 25, No. 4, 2007

Probing cellulose wettability by electron paramagnetic resonance

G. IONITA[1], C. GHICA[2], P. IONITA[1*]

[1]Institute of Physical Chemistry, Spl. Independentei 202, Bucharest 060021, Romania

[2]National Institute for Materials Physics, PO Box MG-7, 077125 Bucharest-Magurele, Romania

Carboxymethyl-cellulose has been labelled with a stable free radical by reaction with 4-aminotempo in the presence of a coupling agent (EEDQ). The spin-labelled cellulose is highly stable, no leaking being noticed after months at room temperature. EPR spectroscopy was used as a main tool to study the wettability of such a material. The EPR spectrum of the dry spin-labelled cellulose shows the expected anisotropy, while addition of several solvents (acetone, ethyl acetate, DCM, methanol, toluene, PEG 200) induces the splitting of the spectrum into a two component system. Thus, the EPR spectrum is composed of a mobile component superimposed onto an immobilized one. Addition of water leads to a monocomponent isotropic spectrum. These data clearly indicate the presence of two types of sites to which the spin-label is attached. Variable temperature EPR spectra showed that an increase of temperature results in an increase in the mobility of the spin-label. Deposition of plain or spin-labelled gold nanoparticles on the cellulose fibres also affects the structure of the polymeric chain, as seen by changes in the EPR spectra.

Key words: *cellulose; EPR; radical; tempo; spin label*

1. Introduction

Cellulose, one of the oldest known and used materials in mankind history [1], is a natural carbohydrate (polysaccharide) consisting of glucose units, linked together through 1–4 glycosidic bond, forming in this way a linear molecular chain [2]. Cellulose forms fibres with porous structure, arranged into amorphous and crystalline regions [3]. However, despite many investigation methods and various approaches to characterize such a natural material, there are unknown or very little understood data regarding cellulose, mainly its interaction with liquids, like organic solvents and water. It is well known that cotton can absorb and retain large amounts of solvents.

A detailed investigation of the structure and of the wettability of cellulose may be performed using electron paramagnetic resonance spectroscopy (EPR or ESR) because

* Corresponding author, e-mail: pionita@icf.ro

EPR can provide information on the micro-environment of the spin-probe (a stable free radical) [4]. The EPR parameters are dramatically affected by the polarity, viscosity and dynamics of the surrounding space next to the spin-probe; major changes are noticed for the recorded EPR parameters [5]. Nitroxide spin probes (stable free radicals, like tempo) can monitor structural and chemical changes occurring during various physicochemical processes. The spin-labelling technique, in which the stable free radical (the spin-probe) is covalently bonded to a material (like cellulose), provides useful information on the flexibility and the mobility of the spacer which links together the solid support (cellulose) and the reagent (spin-probe).

The attachment of a spin-label to cellulose, known since '70s [6], requires certain conditions; several successful strategies have been employed, first derivatizing cellulose (i.e. *via* cyanogens bromide or tosylation), and then reacting it with 4-aminotempo. There is also a recent paper about the effect of humidity on the supramolecular structure of cotton, studied by quantitative spin probing; in this case, the free radicals 4-hydroxytempo were just deposited in cotton at different loadings [7].

2. Materials and method

All materials and solvents were purchased from Aldrich. Carboxymethyl-cellulose (CM-Cel), in the form of fibres, as sodium salt, has been used as a starting material; the labelling was performed as follows: to 1 g of CM-Cel suspended in 50 ml of dry methanol, 1 g of 4-aminotempo and 2 g of EEDQ (2-ethoxy-1-ethoxycarbonyl-1,2-dihydroquinoline) was added, and the mixture was stirred at room temperature for 24 h, then it was centrifuged and the supernatant removed. This step was followed by addition of methanol and re-centrifugation; the process was repeated till no EPR signals were detected in methanol (about 15 times). The solid spin-labelled cellulose (SL-Cel) was then dried *in vacuo* overnight. The average loading was determined by careful double integration of the EPR signal, compared with a tempo standard. For EPR measurements, a very small amount of SL-Cel (around 1 mg) was suspended in various solvents (0.1 ml) and the EPR spectra were recorded at room temperature, or at selected temperatures. Typical settings for the EPR spectra (recorded on a Jeol Jes FA100 spectrometer): centre field 3360 G, sweep field 150 G, frequency 9.50 GHz, power 1 mW, sweep time 60 s, time constant 0.03 s, modulation frequency 100 kHz, gain 50, and modulation width 1 G. Plain and spin-labelled gold-nanoparticles (SL-Au NPs, nanoparticles which contain attached tempo moieties to the Au surface) were synthesized as previously described [8]. The deposition of gold nanoparticles on SL -Cel was performed as follows: 50 mg of SL-Cel were added to 1 mL of gold nanoparticles in toluene (10^{-4} M) and the mixture was stirred for 24 h, after that the solid was filtered off and dried. TEM pictures were taken using a Jeol 200 CX microscope operated at 200 kV.

3. Results and discussion

3.1. Synthesis

Our strategy involved a direct reaction between CM-Cel and 4-aminotempo, in the presence of EEDQ as a coupling agent (Fig. 1).

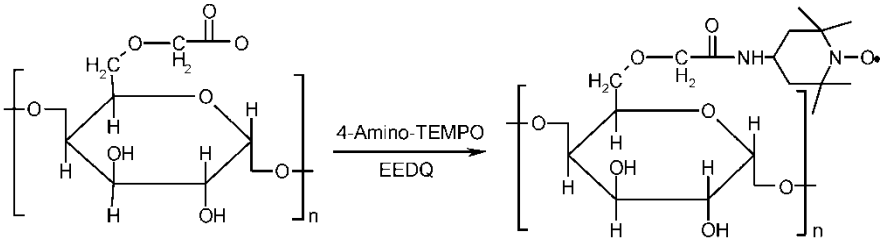

Fig. 1. Spin-labelling of CM-Cel

The obtained material is stable for months at room temperature, and no leaking of the spin-label has been noticed. The loading with tempo moiety was estimated from double integration of the signal arising from a known amount of sample compared with a pure tempo standard: about 10% of the carboxyl groups were labelled.

3.2. EPR spectra at room temperature

The EPR spectrum of the dry SL-Cel showed the well known pattern of an immobilized radical (Fig. 2a). Addition of various solvents (ethyl acetate, acetone, methanol, DCM, water, PEG 200) produces visible changes in EPR spectra (Figs. 2b–g). The spectra (Figs. 2b–f) are characterized by two components, one arising from immobilized tempo moieties (slow motion), while the other one arising from the mobile tempo moieties (fast motion), all of them being linked to the cellulose chains. Such two component spectra are easily characterized by the order parameter *S,* which has values from 0 (isotropic motion) to 1 (non-isotropic motion):

$$S = \frac{A_{\parallel} - A_{\perp}}{A_{ZZ} - \dfrac{A_{xx} + A_{yy}}{2}} \times \frac{A_{xx} + A_{yy} + A_{zz}}{A_{\parallel} + 2A_{\perp}} \tag{1}$$

where A_{zz}, A_{xx}, A_{yy}, $A_{\perp}$, and $A_{\parallel}$ are hyperfine components of the EPR spectra; the factor on the right is a polarity correction to the hyperfine tensor element [9–11].

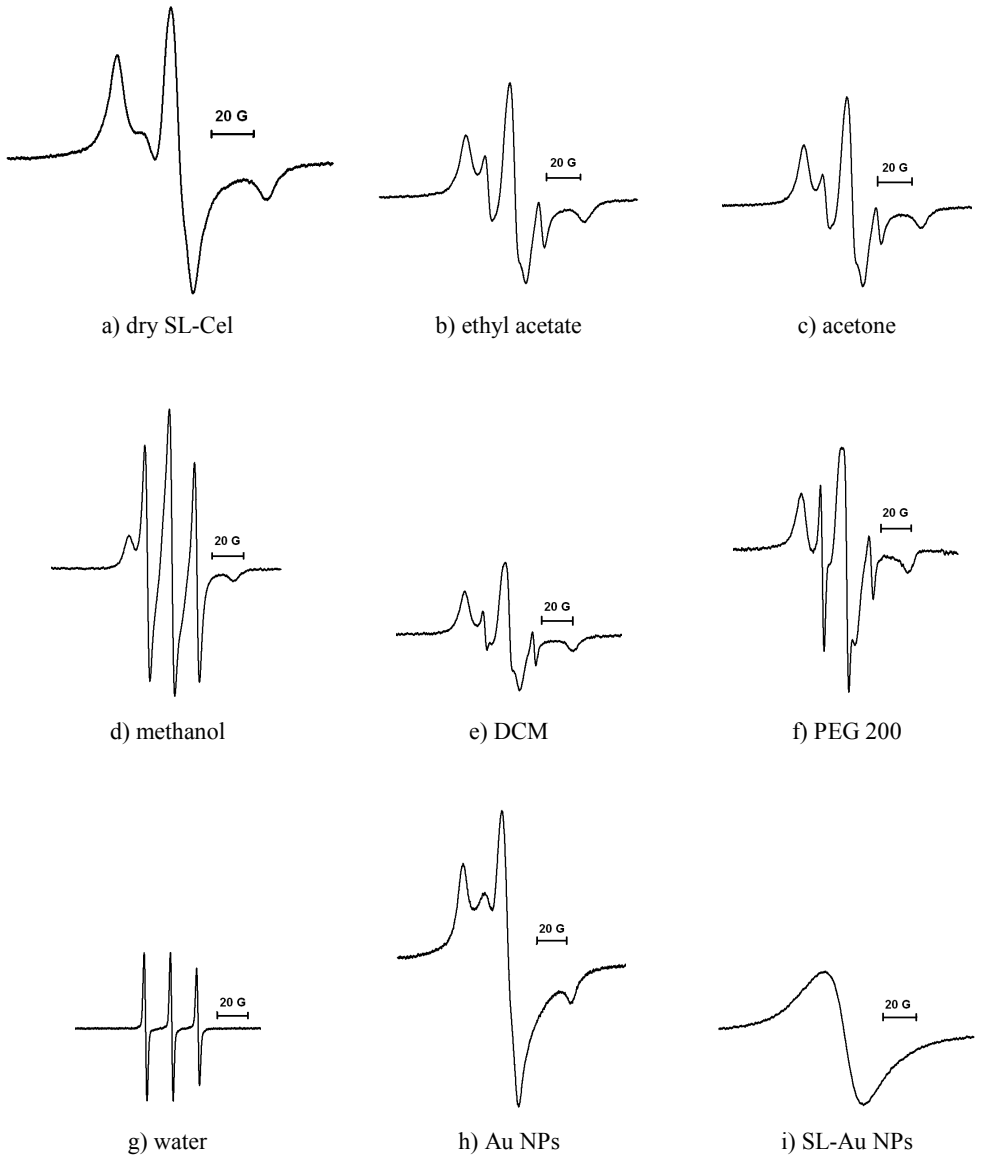

Fig. 2. EPR spectra of SL-Cel, dry (a), in various solvents (b–g), and in the presence of plain (h) and SL-gold nanoparticles (i)

As we mentioned before, the spectra change from the well known type of an immobilized spin-label (Fig. 2a, dry SL-Cel) to the same very well known type of a complete mobile one (Fig. 2g, in the presence of water). These results are not unexpected, as water has the highest E_T value (polarity), and therefore most strongly interacts with cellulose chains. Other solvents (acetone, ethyl acetate, DCM, methanol, toluene, PEG 200) clearly induce the appearance of a mobile component into the re-

corded EPR spectra (Figs. 2b–f), characterized by the hyperfine coupling constants a_N. These data mean that there are two types of sites on the cellulose chains (which are spin-labelled) acting differently; it is well known that cellulose fibres contain crystalline and amorphous domains (the amorphous domains are porous, being easily accessible to external agents like solvents). The order parameter S is high for all samples (besides dry SL-Cel, Table 1), meaning that the spins are likely to be arranged into supramolecular architectures. The cellulose molecules might be as well responsible for the arrangement of the solvent molecules into a certain structural way, which can lead to a highly ordered structure around the spin-labels.

Table 1. EPR and solvent data

Solvent	$2a_{\|\|}$ [G]	$2a_{\perp}$ [G]	S	$2a_N$ [G]	E_T [kcal/mol]	Viscosity at 25 °C [cP]
Dry SL-Cel	69	41	0.481	–	–	–
Ethyl acetate	70	28	0.722	32	38.9	0.441
Acetone	69	28	0.705	31	42.2	0.306
DCM	70	30	0.688	31	41.1	0.404
Water	–	–	–	34	63.1	0.890
Methanol	68	30	0.654	33	55.5	0.547
PEG 200	69	29	0.688	32	–	–
Toluene (300 K)	70	25	0.774	31	33.9	0.552
Toluene (320 K)	69	25	0.757	32	–	–
Toluene (340 K)	68	25	0.740	32	–	–
Toluene (360 K)	68	25	0.740	32	–	–
Toluene (380 K)	68	26	0.722	32	–	–

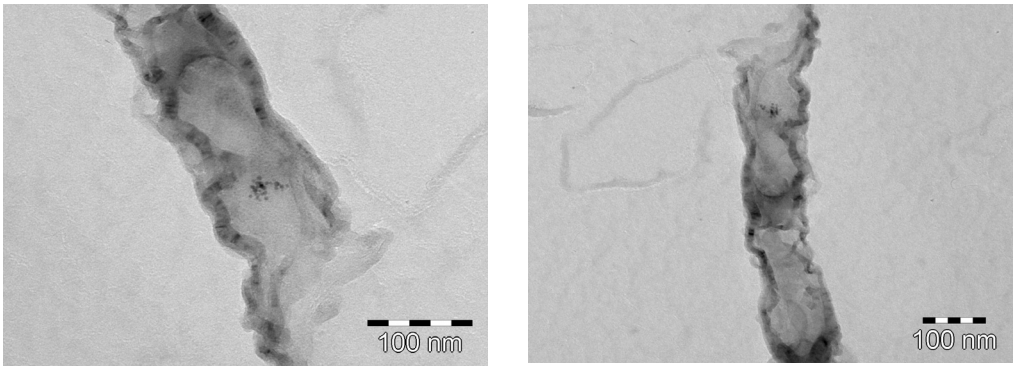

Fig. 3. Typical TEM pictures of SL-Cel with deposited Au NPs

An interesting feature has been noticed when plain gold nanoparticles (Au NPs) were deposited on the cellulose fibres. The EPR spectrum changes, as if the spin-labels became closer (Fig. 2h); this behaviour may be explained by the fact that Au NPs prefer to attach to the amorphous domain rather than the crystalline one, as has

been shown in literature for the direct synthesis of Au NPs on cellulose fibres [12]. In the case of SL-Au NPs, an interaction between the spins from cellulose with the spins from Au NPs is clearly noticed, leading to a single broad line in EPR spectrum (Fig. 2i). Typical TEM pictures of cellulose which contain deposited Au NPs are shown in Fig. 3; Au NPs deposited on the cellulose fibres are easily visible. Table 1 compiles the EPR values of all the recorded spectra, together with the E_T and viscosity values of the solvents used.

3.3. EPR spectra at variable temperatures

Toluene has been chosen as the solvent in which the variable temperature experiments may be performed, due to its high boiling point and also due to the fact that at room temperature a very little amount of the spin-labels are solvated (Fig. 4, 300K). Upon rising the temperature gradually to 380 K, one can easily notice that the mobile component increases with temperature (Fig. 4). This might be explained by the increased mobility of the spin-labels, from the amorphous domains of the cellulose fibres, which can move at higher temperature more freely; moreover, the order parameter S decreases slightly with temperature (Table 1). Due to the complexity of the system, other interaction may be triggered by increasing temperature, leading to a similar effect.

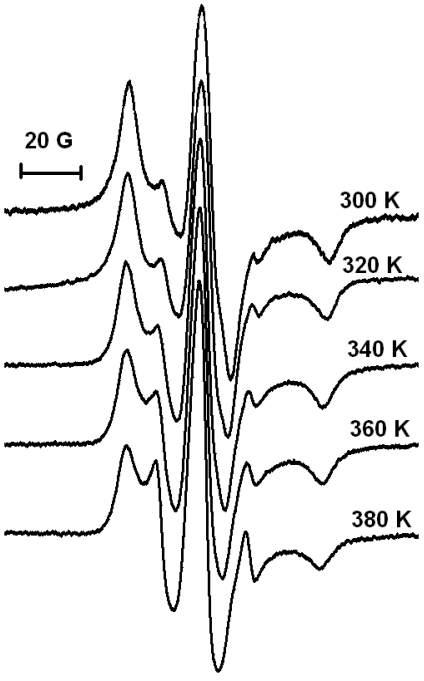

Fig. 4. EPR spectra of SL-Cel in toluene at selected temperatures

4. Conclusions

CM-cellulose has been spin-labelled with a free stable radical, and the wettability (with acetone, ethyl acetate, DCM, methanol, toluene, PEG 200, and water) of the material was studied by EPR spectroscopy. The results show that there are two different labelled sites, which probably belong to amorphous and crystalline domains of cellulose. Only the spin-labels from amorphous domains are easily solvated by different organic solvents, while water solvates the spin-labels from crystalline domain as well. The interaction of the spin-labelled cellulose with gold nanoparticles also leads to changes in the EPR spectra.

Acknowledgements

Partial funding from CNCSIS (PN_II 'Idea' 46_1.10.2007) is gratefully acknowledged.

References

[1] BETTS A., J. Archae. Sci., 21 (1994), 489.
[2] POPE K.O., Science, 292 (2001), 1370.
[3] SCHEUERMANN R., J. Phys. Chem. B, 105 (2001), 11474.
[4] SUNDHOLM F., WESTERMARK B., ROZANTSEV E.G., Acta Chem. Scand., A34 (1980), 177.
[5] IONITA P., TUDOSE M., CONSTANTINESCU T., BALABAN A.T., Appl. Surf. Sci., doi: 10.1016/j.apsusc. 2007.07.184.
[6] HALL L.D., APLIN J.D., J. Am. Chem. Soc., 100 (1978), 1934.
[7] FRANTZ S., HUBNER G.A., WENDLAND O., RODUNER E., MARIANI C., OTTAVIANI M.F., BATCHELOR S.N., J. Phys. Chem. B, 109 (2005), 11572.
[8] CHECHIK V., IONITA P., GILBERT B.C., CARAGHEORGHEOPOL A., CALDARARU H., WELLSTED H., KORTE A., Faraday Discus., 125 (2004), 279.
[9] MARSH D., JOST M., PEGGION C., TONIOLO C., Biophys. J., 92 (2007), 473.
[10] INBARAJ J.J., CARDON T.B., LARYUKHIN M., GROSSER S.M., LORIGAN G.A., J. Am. Chem. Soc., 128 (2006), 9549.
[11] SEELIG J., J. Am. Chem. Soc., 92 (1970), 3881.
[12] HE J., KUNITAKE T., NAKAO A., Chem. Mat., 15 (2003), 4401.

Received 28 March 2007
Revised 8 May 2007

Materials Science-Poland, Vol. 25, No. 4, 2007

Preparation and properties of a porous calcium phosphate bone graft substitute

S. M. RABIEE[1,2*], F. MOZTARZADEH[1], H. S. KENARI[3], M. SOLATI-HASHJIN[1]

[1]Department of Medical Engineering, Amirkabir University, Hafis Ave., Tehran, Iran, P. O. Box: 15875-4413

[2]Department of Engineering and Technology, Mazandaran University, Babolsar, Iran

[3]Department of Polymer-Chemical Engineering, Sahand University of Technology, Tabriz, Iran

The aim of this study was to obtain a biodegradable porous calcium phosphate implants as synthetic bone graft substitutes. Calcium phosphate used in this study consisted of hydroxyapatite and anhydrous dicalcium phosphate. Four different types of porous calcium phosphates were made on addition of polyurethane by sinter processing. The X-ray diffractometry revealed that β-tricalcium phosphate is a dominating phase. Experimental results showed the pore microstructure of the as-sintered bodies to consist of the macropores and micropores. Surface morphology analysis and porosity evaluations were performed. The variation in the compressive strength, elastic modulus and dissolution behaviour of immersed synthetic bone grafts in simulated physiological solutions was investigated.

Key words: *bioceramics; calcium phosphate; porosity; synthetic bone graft substitute*

1. Introduction

Various phases of calcium phosphates were employed to fabricate porous scaffolds to accommodate bone tissue regeneration in vitro or in vivo. The atomic ratio of Ca/P in calcium phosphates can be varied between 1 and 2 to produce compounds ranging from calcium tetraphosphate ($Ca_4P_2O_9$), hydroxyapatite (HA) $Ca_{10}(PO_4)_6(OH)_2$, tricalcium phosphate (TCP) $Ca_3(PO_4)_2$ to anhydrous dicalcium phosphate (DCP) $CaHPO_4$. The degradability of calcium phosphates generally varies with the Ca/P ratio, the highest being of DCP that usually results in the most extensive bone remodelling around the scaffold [1–5].

Porous biodegradable synthetic materials, such as calcium phosphates, poly(lactic acid) (PLA), and poly(glycolic acid) (PGA), are currently tested as implants for the

*Corresponding author, e-mail: r_rabiee@aut.ac.ir

regeneration of damaged and diseased tissues [6–10]. These synthetic biomaterials were chosen based on their biocompability and mechanical properties. Concerning the fabrication of porous ceramic bodies, several techniques such as the use of polymeric sponge [11] and organic additives [12–14], and molding processes [15], have been used. For example, Prado da Silva et al. [12] used three different organic additives, potato starch, almond crust and wax spheres to produce porous structures of a CaO–P_2O_5 glass reinforced hydroxyapatite (HA). With poly(vinyl butyral) powders, Liu [13] fabricated porous HA granules with controlled porosity, pore size, pore size distribution and granule size by using a drip-casting process. Flautre et al. [14] used polymethylmethacrylate microbead as the porous agent to make of HA ceramics of various porosities. The available synthetic biodegradable calcium phosphate ceramics for bone tissue regeneration includes HA, β-tricalcium phosphate (β-TCP) and calcium polyphosphate [10, 11]. The biodegradation behaviour of calcium phosphate materials in both in vitro and animal studies has been reported [16–18]. Shima et al. [16] implanted porous β-TCP between vertebrae of rabbits and found that these porous implants may fracture and were then reduced to granule. Utilizing solid freeform fabrication to build porous parts of calcium polyphosphate, Porter et al. [17] found a decline in mechanical properties in tris-buffered solution. Pilliar et al. [18] studied the effect of particle size of calcium polyphosphates on in vitro degradation. Their findings indicated that there was a significant strength loss for both the fine and coarse powder samples after soaking in buffered solutions at pH 4 and 7.

Previous studies have established that HA in various forms is most widely used but concerns have been raised with regard to the limited degradation properties of this material [19, 20]. Thus, in order to improve their current properties, we have used DCP in combination with HA. In the present study, porous calcium phosphates were prepared by sintering mixtures of HA, DCP and polyurethane (PU). To impart porosity to the ceramic body, PU was burned out during firing, leaving free space in the resulting body.

2. Experimental

Commercially pure hydroxyapatite and anhydrous dicalcium phosphate powders (Merck, Germany) were used. Powder of HA/DCP(HD), with 3:1 weight ratio, was prepared in a planetary ball mil (Retch PMA, Brinkman, USA) for 30 min to ensure homogeneity. The grain was observed by scanning electron microscopy (SEM: Stereoscan 360-Leica Cambridge). The specific surface area was determined by 15-point BET measurement (Micromeritics Gemini 2360). The particles are composed of primary particles with sizes smaller than 10 μm. Specific surface area of the powder was 57 m^2/g. The as-received HD powder was directly mixed with PU in a vacuum mixer (VM-112T, J. Morita, Saitama, Japan) for 15 min to ensure homogeneity. The PU powders have different size fractions, i.e. 100 μm and 400 μm. Four different types of the porous bodies were prepared from mixtures of HD and PU powders with different ratios (4:1, 3:1, 2:1 and 1:1 by weight) (Table 1). The mixture was uniaxially

pressed in a cylindrical stainless mold (6×12 mm^2) at 5 MPa. The green bodies were heated up to 1200 °C in a schedule which minimized disruption during pyrolysis and allowed the bioceramic to achieve high density. This heating schedule consisted of the heating rate of 0.5 °C/min up to 800 °C, 1 h held at this temperature and rapid heating at 5 °C/min from 800 to 1200 °C, 3h held at 1200 °C and then cooling in the furnace. The structure of the sintered material was analyzed by X-ray diffraction method using a Siemens D5000 diffractometer, operating at K_α radiation.

Table 1: Composition of various samples and their properties

Sample code	Composition HD:PU [wt. ratio]	Change in diameter [%]	Porosity		Compressive strength ±S.D. [MPa]	Compressive modulus ±S.D. [MPa]
			By geometry	By Archimedes		
HD4	4:1	2.9±1.1	72±0.1	79.8±4.6	8.0±1.1	131±11
HD3	3:1	–3.1±0.9	70.1±0.1	73.3±4.1	12.1±1.2	180±18
HD2	2:1	8.1±1.5	66.4±0.1	68.6±3.8	7.4±1.4	153±9
HD1	1:1	–6.9±1.0	68.7±0.1	66.0±2.7	4±0.6	136±7

The measurement of the porosity was carried out in two different ways. The first method consisted in calculation the density of the sintered porous body from measured mass and volume, and then the relative density was determined by the ratio of the measured density to the theoretical density of the materials. The difference between the unity and the relative density is the total porosity. The other measurement was conducted by using a conventional Archimedes immersion technique with ethanol [21]. The average value of six determinations was taken as the porosity of sintered bodies. The extracellular solution with the ionic composition similar to that of human blood plasma, Hank's balanced salt solution, was used as supporting solution and for the immersion test. The solution consisted of 8.00 g NaCl, 0.35 g $NaHCO_3$, 0.40 g KCl, 0.06 g KH_2PO_4, 0.10 g $MgCl_2.6H_2O$, 0.14 g $CaCl_2$, 0.06 g $Na_2HPO_4.2H_2O$, 0.06 g $MgSO_4.7H_2O$, 1.00 g glucose in 1000 ml of distilled H_2O. The solution had the initial pH equal to 7.4.

For the immersion test, the specimens were immersed in 10 ml of the solution for the predetermined periods of time at 37 ºC. After immersion, the specimens were removed from the vials and placed in a container with fresh Hanks' solution to evaluate the mechanical properties. Their degradation behaviour was also monitored through the sample weight change. Prior to weighing with a 4-digital balance (AE 240S, Mettler-Toledo AG, Greifensee, Switzerland), the immersed specimens were dried at 100 ºC for 3 h in an oven. At least seven samples were tested for each measurement. All mechanical testing was performed using a Zwick/Roell 2005 with a crosshead speed of 0.01 mm/s. The compressive strength (*Cs*) of the sample was calculated as $Cs = F/A$, where F is the maximum compressive load (N), A the average cross-sectional area (mm^2) of the sample. The diameter and length of each specimen were measured by using a micrometer. The largest compression load at failure was obtained from the recorded load–deflection curves. Young's moduli of the samples were determined from the slope of the initial linear elastic portion of the load–deflection curve. One-way ANOVA statistical analysis was used to evaluate

the statistical significance of the compressive strength data. Tukey HSD multiple comparison testing was used to determine the significance of the deviations in the strength of each sample for different immersion times. In all cases, the results were considered statistically different at $p < 0.05$.

3. Results and discussion

Porous bioceramics of HA/DCP generally seem to biodegrade much more rapidly than do bioceramics made of HA, because dicalcium phosphate resorbed much more rapidly than hydroxyapatite implants of a similar structure [1, 22]. The bioresorbability of calcium phosphate materials appears to be dependent on their chemical/crystal composition, their structure as "materials", and on the environment at the implantation site [4, 5, 22]. Jarcho proposed the existence of two different biologic resorption pathways: one involving solution-mediated processes (implant solubility in physiologic solutions) and the second involving cell-mediated processes (phagocytosis) [4]. Contrary to expectations, the material more closely resembling the body own hard tissue component, the hydroxyapatite, was found to dissolve much more slowly than many of calcium phosphates not naturally occurring in bone if similar ceramic structures and similar degrees of purity were used [4, 5, 23]. It can be stated that implants of crystalline HA have a lesser tendency to bioresorb because of their chemistry and their small surface area. Table 1 lists the porosities measured by simple weighting and by Archimedes principle. The final dimensional changes of the bodies ranged from –8.1 to 2.9%. Due to shrinkage effect [27, 28], the diameters of all sintered specimens were reduced, except for HD4. This change in HD4 body might be explained by the thermal expansion of HD which polymerized into the polyphosphate material. When sintered at 1200 ºC in air, porous bodies of ca. 70% porosity were achieved.

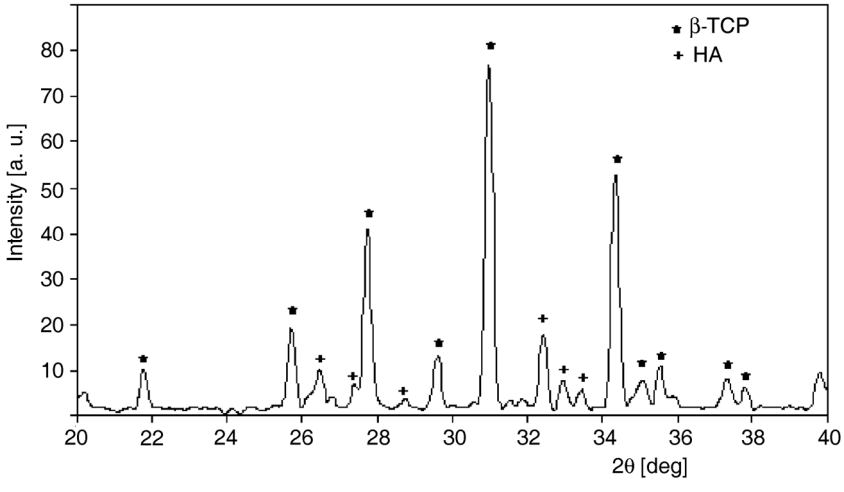

Fig. 1. X-ray diffraction patterns of sintered HD3 over the range of 2θ from 20° to 40°

XRD patterns of sintered samples showed biphasic mixtures of β-TCP and HA (Fig. 1). No obvious difference could be detected in the XRD patterns of mixtures of HD and PU (HD1, HD2, HD3 and HD4). The conversion of $CaHPO_4$ into $Ca_2P_2O_7$ began at 700 ºC and above that temperature, $Ca_2P_2O_7$ and HA transformed into $Ca_3(PO_4)_2$ according to Eqs. (1) and (2) [24, 25, 32]. A little part of HA phase did not change into other phases during the sintering.

$$2CaHPO_4 \rightarrow Ca_2P_2O_7 + H_2O \quad (1)$$

$$Ca_2P_2O_7 + Ca_{10}(PO_4)_6(OH)_2 \rightarrow 4Ca_3(PO_4)_2 + H_2O \quad (2)$$

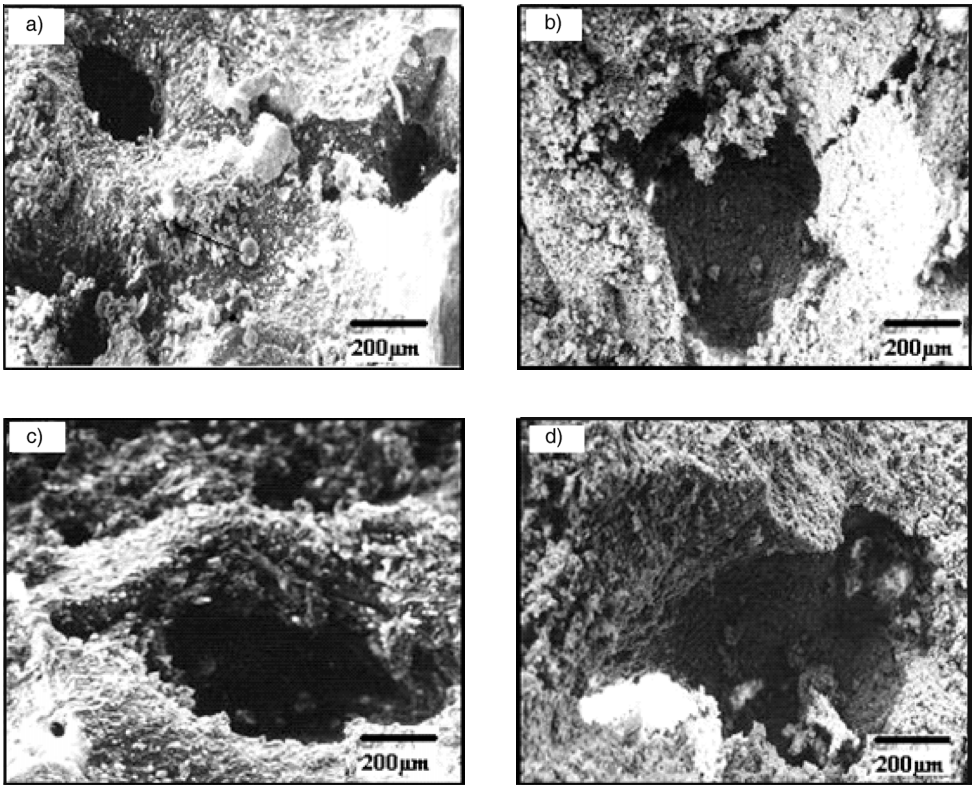

Fig. 2. SEM micrographs of sintered calcium phosphate with various ratios of PU: a) HD4, b) HD3, c) HD2, d) HD1

The morphologies of a series of as-sintered porous bodies are shown in Fig. 2. The SEM micrographs showed the pore structure of calcium phosphate bodies essentially to be as an assembly of macropores and micropores. Macropore sizes as large as hundreds of micrometers were generated and micropores were less than 20 μm. It is obvious that introduction of PU in the HD powder resulted in bodies with macropores and micropores. PU served as a pore-forming agent because of the evolution of water and

carbon dioxide during sinter processing, leading to the development of the highly porous microstructure [26].

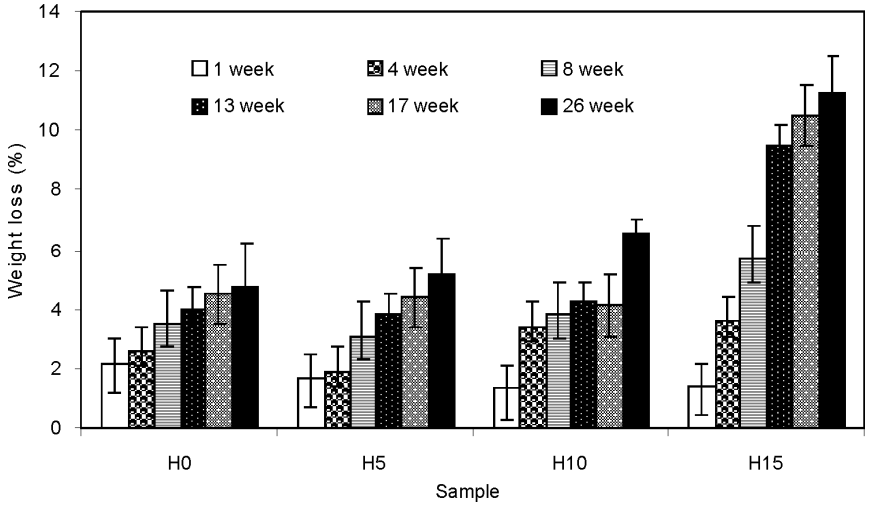

Fig. 3. Weight losses of porous bodies after immersion in Hanks' solution

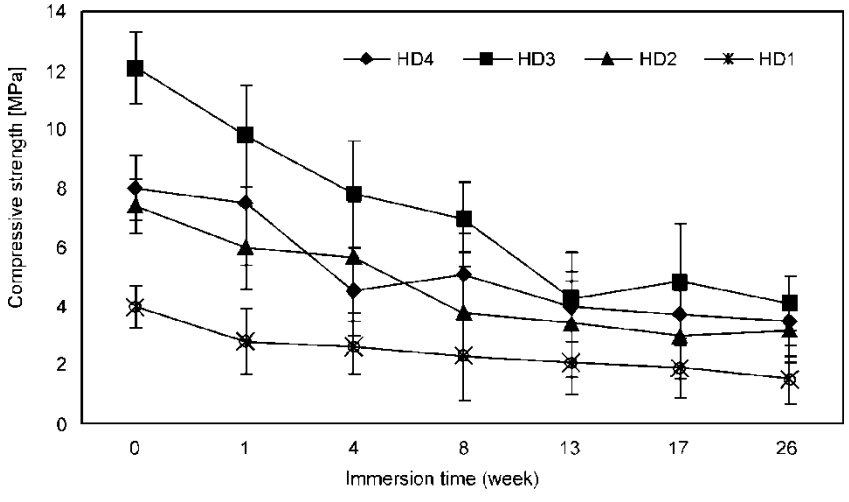

Fig. 4. compressive strength of immersed samples as a function of the immersion time

To further study the immersion-induced dissolution/degradation process, a series of weight change measurements were performed for all immersed samples. Figure 3 shows that all samples continue to dissolve after immersion in Hanks' solution. The dissolution behaviour of immersed calcium phosphate materials in simulated physiological solution has been reported [29, 30]. The resulting weight loss indicated that sample HD4 had the largest weight loss with degradation time, reaching up to 11% after 26 weeks; however, the weight loss still remained about 6% over 26 weeks of

immersion for all other samples. The decrease in sample weight might be explained by degradation of such porous materials.

The variation in the compressive strength with immersion time of the series of porous bodies is presented in Fig. 4. Six immersion regimes of 1, 4, 8, 13, 17 and 26 weeks were selected for testing the porous bodies. The results revealed that, when immersed in Hanks' solution, four different types of porous samples gradually lost the strength with increasing immersion time. The strength of the sample HD3 was significantly reduced from the initial strength of 12.1 MPa down to 9.8 MPa after one-week immersion ($p < 0.05$). When immersed for 26 weeks, its strength decreased to 4.1 MPa. The statistical analysis using Tukey HSD multiple comparison testing showed that the compressive strength of immersed calcium phosphates mixed with 20 wt. % PU in green sample (HD4) significantly declined by about 50% after immersion for 26 weeks ($p < 0.05$). When the green bodies comprised 33 and 50 wt.% PU, the resulting porous bodies lost 48% and 54% of the as-sintered strengths after 26-week immersion, respectively. This deterioration in the strength seems unavoidable for biodegradable porous ceramics immersed in physiological solution and has also been observed in other studies [17, 18, 29]. Porter et al. measured bending strength degradation of 64–100% of the original strength when porous calcium polyphosphates were immersed in a tris-buffered solution. The immersion induced decline in mechanical strength due to less stable zones (particle surfaces or interface regions of grains) of porous ceramic body, where the degradation occurred more rapidly [17]. Besides the porous structures of calcium phosphates, the dissolution of the calcium phosphate in the solution and the penetration of water/ions resulting from the solution possibly accounted for the deterioration in mechanical properties [16, 31].

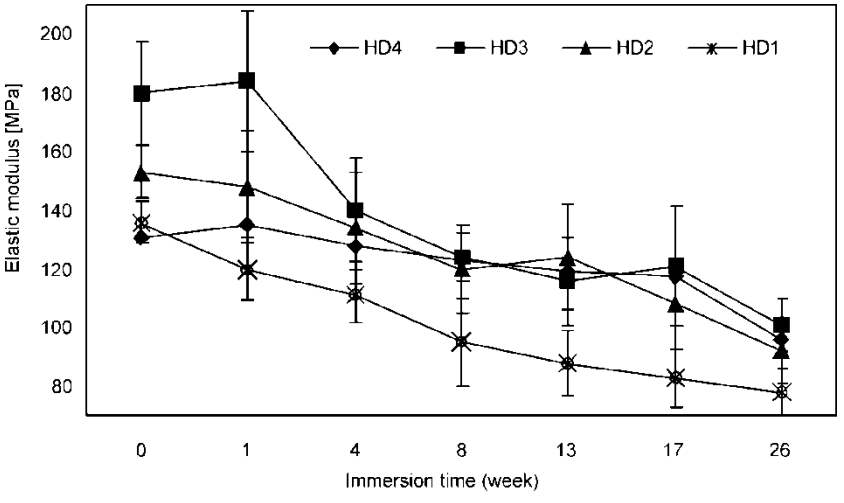

Fig. 5. The variations of the elastic modulus against immersion time for porous samples

The variations of the elastic modulus against immersion time for porous bodies are shown in Fig. 5 as a function of PU content and immersion time. After immersion in solution over 26 weeks, there was also a pronounced decrease in the elastic modulus for all porous bodies, similarly to the compressive strength.

4. Conclusions

The porous HA/DCP bioceramic with various amounts of polyurethane powder as a pore-former can be easily fabricated. The XRD pattern of sintered porous samples showed β-TCP and amount of HA phases. Results showed the compressive strength and elastic modulus of the porous bodies was dependent on the contents of the PU additive. The weight loss data confirmed the degradation behaviour of the porous bodies in Hank's solution. The results revealed that, when immersed in Hanks' solution, the different types of porous samples gradually lost the strength and weight with increasing immersion time.

Acknowledgements

The authors are grateful to the Iran National Science Foundation for their kind financial support on the research.

References

[1] RAYNAUD S., CHAMPION E., BERNACHE-ASSOLLANT D., THOMAS P., Biomater., 23 (2002), 1065.
[2] LU X., LENG Y., Biomater., 26 (2005), 1097.
[3] TAS A.C., KORKUSUZ F., TIMUCIN M., AKKAS N., J. Mater. Sci.: Mater. Med., 8 (1997), 91.
[4] JARCHO M., Clin. Orthop. Rel. Res., 157 (1981), 259.
[5] KLEIN C., DRIESSEN A.A., DE GROOT K., Biomater., 5 (1984), 157.
[6] LU L., CURRIER B.L., YASZEMSK M.J., Curr. Opin. Orthop., 11 (2000), 383.
[7] BAKSH D., DAVIES J.E., KIM S., J. Mater. Sci.Mater. Med. 9 (1998), 743.
[8] KIKUCHI M., KOYAMA Y., TAKAKUDA K., MIYAIRI H., SHIRAHAMA N., J. Biomed. Mater. Res., 62 (2002), 256.
[9] AGRAWAL C.M., RAY R.B., J. Biomed. Mater. Res., 55 (2001), 141.
[10] KLEIN C.P., PATKA P., DEN HOLLANDER W., A *Comparison between Hydroxylapatite and β-Whitlockite Macroporous Ceramics Implanted in Dog Femurs*, [in:] T. Yamamuro, L.L. Hench, J. Wilson (Eds.), *Handbook of Bioactive Ceramics*, Vol. II: *Calcium Phosphate and Hydroxylapatite Ceramics*, CRC Press, Boca Raton, FL, 1990, p. 53.
[11] TAMPIERI A., CELOTTI G., SPRIO S., DELCOGLIANO A., FRANZESE S., Biomater., 22 (2001), 1365.
[12] PRADO DA SILVA M.H., LEMONS A.F., GIBSON I.R., FERREIRA J.M.F., SANTOS J.D., J. Non-Cryst. Solids, 304 (2002), 286.
[13] LIU D.M., Biomater., 17 (1996), 1955.
[14] FLAUTRE B., DESCAMPS M., DELECOURT C., BLARY M.C., HARDOUIM P., J. Mater. Sci. Mater. Med., 12 (2001), 679.
[15] CHU T.M.G., HALLORAN J.W., HOLLISTER S.J., FEINBERG S.E., J. Mater. Sci. Mater. Med., 12 (2001), 471.
[16] SHIMA T., KELLER J.T., ALVIRA M.M., MAYFIELD F.H., DUNSKER S.B., J. Neurosurg., 51 (1979), 533.

[17] PORTER N.L., PILLIAR R.M., GRYNPAS M.D., J. Biomed. Mater. Res., 56 (2001), 504.
[18] PILLIAR R.M., FILIAGI M.J.,. WELLS J.D, GRYNPAS M.D., KANDEL R.A., Biomater., 22 (2001), 963.
[19] HOLINGER J.O., BREKKE J., GRUSKIN E., LEE D., Clin. Orthop., 324 (1996), 55.
[20] YAMAGUCHI K., HIRANO T., YOSHIDA G., IWASAKI K., Biomater. 16 (1995), 983.
[21] ASTM C373-72, Annual Book of ASTM Standard, Vol. 15.02, 1982, p.182.
[22] KLEIN C.P., VAN DER LUBBE H., DRIESSEN A.A., DE GROOT K, VAN DEN HOOF A., *Biodegradation Behaviour of Various Calcium Phosphate Materials in Subcutaneous Tissue*. [In:] P. Vincenzini, (Ed.), *Ceramics in Surgery*, Elsevier, Amsterdam, 1983.
[23] VALLET-REGI M, GONZALEZ-CALBET J.M., Solid State Chem., 32 (2004), 1.
[24] JIAN-JIANG B., DONG-WAN K., KUG-SUN H., Mater. Lett., 58 (2004), 347.
[25] RAYNAUD S., CHAMPION E., BERNACHE-ASSOLLANT D., Biomater. 23 (2002), 1073.
[26] GAUTHIER O., BOULER J.M., AGUADO E., PILET P., DACULSI G., Biomater., 19 (1998), 133.
[27] CHERN LIN J.H., KUO K.H., DING S.J., JU C.P., J. Mater. Sci.: Mater. Med., 12 (2001), 731.
[28] RICHERSON D.W., *Modern Ceramic Engineering*, 2nd Ed., Marcel Dekker, New York, 1992, p. 520.
[29] WANG C.W., YAN M., CANG H.C., DING S.J., J. Med. Biol. Eng., 23 (2003), 159.
[30] DUCHEYNE P., RADIN S., KING L., J. Biomed. Mater. Res., 27 (1993), 25.
[31] OGISO M., YAMASHITA Y., MATSUMOTO T., J. Biomed. Mater. Res., 39 (1998), 23.

Received 13 February 2007
Revised 5 July 2007

Materials Science-Poland, Vol. 25, No. 4, 2007

Synthesis and characterization of alumina nanopowders by combustion of nitrate-amino acid gels

M. EDRISSI[1], R. NOROUZBEIGI[1*]

[1]Chemical Engineering Department, Amirkabir University of Technology, Hafez Ave., P. O. Box 15875-4413, Tehran, Iran

Nanocrystalline alumina powders were synthesized by the combustion method using serine and asparagine as fuels. A screening design was conducted to determine how key process factors influence preparation of nanocrystalline powders. The screening design was utilized to rank effective factors on crystalline size of alumina powders. The product was characterized by XRD, BET, and SEM. Nanocrystalline γ-alumina powders with crystal sizes between 3.95 nm and 6.71 nm and α-alumina powders with crystallite sizes between 22.73 nm and 33.92 nm have been obtained by the combustion synthesis. The specific surface areas of samples ranged between 22 m^2/g and 75 m^2/g. Particle size distributions were determined by LLS and the average particle sizes of γ-alumina powders after sonication were 37.42 nm and 79.32 nm. Results of statistical analysis illustrate that the fuel to oxidizer ratio is the most effective factor to decrease the average crystal size.

Key words: *alumina; combustion synthesis; screening design; serine; asparagine*

1. Introduction

Alumina is one of the most important ceramic materials widely used as electrical insulator, presenting exceptionally high resistance to chemical agents, as well as giving an excellent performance as catalyst or catalytic support for many chemical reactions [1, 2]. It is widely used for structural, microelectronic and membrane applications. Various chemical methods such as spray pyrolysis [3], precipitation [4], sol-gel [5], hydrothermal [6] and combustion synthesis [7] have been employed to synthesize ultrafine Al_2O_3 powders.

Combustion synthesis is a particularly simple, safe and rapid fabrication process wherein the main advantages are energy and time savings. This quick, straightforward process can be used to synthesize homogeneous, high-purity, crystalline oxide ceramic powders including ultrafine alumina powders with a broad range of particle sizes.

*Corresponding author, email: r_noroozbaigi@yahoo.com

The basis for the combustion synthesis comes from the thermochemical concepts used in the field of propellants and explosives [8]. The success of the process is due to an intimate blending among the constituents using a suitable fuel or complexing agent (e.g., citric acid [9], urea [10], glycine [11], etc.) in an aqueous medium and an exothermic redox reaction between the fuel and oxidizer (nitrates). Actually, the mechanism of the combustion reaction is quite complex. The main parameters influencing the reaction include type of the main fuel, fuel to oxidizer ratio, the amount of oxidizer in excess, ratio of fuels, pH of the solution and rate of calcination [12, 13]. In general, a good fuel should not react violently nor produce toxic gases, and must act as a complexing agent for metal cations [14]. In this research, two amino acids, serine ($HOCH_2CH(NH_2)COOH$) and asparagine ($NH_2COCH_2CH(NH_2)COOH$), were used as fuels. The effectiveness of important factors on the crystal size of combustion synthesized γ-alumina powders have been investigated using two-level factors in a screening design. The powders obtained through combustion synthesis were characterized by X-ray diffraction, surface area (BET), scanning electron microscopy (SEM), differential thermal analysis (DTA), thermogravimetric analysis (TG), and laser light scattering (LLS).

2. Experimental procedure

Design of experiments. A two level screening design was utilized for investigating and sorting the effective factors on combustion synthesis of alumina powders. The first step is selection of factors. The seven important factors studied are: the ratio of oxidizer in excess, type of fuel, fuel to oxidizer ratio, type of secondary fuels, secondary fuel to the main fuel ratio, pH of the starting solution and rate of calcination. The second step is determination of high and low levels for each factor. Ammonium nitrate (NH_4NO_3) was used as excess oxidizer (combustion aid) [15]. The molar ratio of ammonium nitrate to aluminum nitrate (main oxidizer) was selected as the first factor and amounts of 0.25 and 0.5 were its low and high levels, respectively. The initial composition of the solution containing aluminum nitrate, $Al(NO_3)_3{\cdot}9H_2O$ and asparagine was derived from the total oxidizing and reducing valences of the oxidizer and fuel using the concepts of propellant chemistry [16]. Carbon, hydrogen and aluminum were considered as reducing elements with the corresponding valences of +4, +1 and +3, respectively. Oxygen was considered as an oxidizing element with the valence of 2, the valence of nitrogen was considered to be 0. The total calculated valence of metal nitrates by arithmetic summation of oxidizing and reducing valences was –15. The calculated valence of asparagine was +18. The stoichiometric composition of the redox mixture demanded that $1(-15) + n(+18) = 0$, or $n = 0.833$ mol. This calculation was done for mixture of aluminum nitrate and serine, so the stoichiometric composition of the redox mixture demands that $1(-15) + n(+13) = 0$, or $n = 1.154$ mol. Selected levels for fuel to oxidizer ratio were stoichiometric amount (*St*) and $1.5\times St$. As mixtures of fuels can influence the final product size [12], we used mixtures of amino acids with

urea and ammonium acetate. In this study, the type of main fuels was a qualitative factor and asparagine and serine were high and low levels respectively; type of added fuel was another qualitative factor with assumption that urea is high level and ammonium acetate is low level, and the molar ratio of added fuel (urea or ammonium acetate) to the main fuel (serine or asparagine) was introduced as one of the quantitative factors. The amounts of 0 and 0.2 were selected as low and high levels, respectively. Other factors investigated were pH of the starting solution and rate of calcinations. The amounts 2 and 4 were chosen as low and high levels for the pH, which was adjusted by adding ammonium hydroxide or nitric acid to the solution. The 10 °C/min and 20 °C/min were selected levels for the calcination rate. The factors studied and the amounts used for high and low levels used in design of experiments are given in Table 1.

Table 1. Factors and levels

Factor	Allocated letter	High level	Low level
Molar ratio of the excess oxidizer to aluminum nitrate	A	0.5	0.25
Fuel to oxidizer ratio	B	1.5×*St*	*St*
Type of main fuel	C	asparagine	serine
Type of added fuel	D	urea	ammonium acetate
Molar ratio of added fuel to the main fuel	E	0.2	0
pH of the starting solution	F	4	2
Calcination rate	G	20 °C/min	10 °C/min

The combination of factors and levels according to screening design is given in Table 2.

Table 2. Screening design table

Sample	A	B	C	D	E	F	G
1	0.5	1.5	asparagine	urea	0.2	4	20 °C/min
2	0.5	1.5	serine	urea	0	2	10 °C/min
3	0.5	1	asparagine	ammonium acetate	0.2	2	10 °C/min
4	0.5	1	serine	ammonium acetate	0	4	20 °C/min
5	0.25	1.5	asparagine	ammonium acetate	0	4	10 °C/min
6	0.25	1.5	serine	ammonium acetate	0.2	2	20 °C/min
7	0.25	1	asparagine	urea	0	2	20 °C/min
8	0.25	1	serine	urea	0.2	4	10 °C/min

Preparation of samples. All materials used, supplied from the Merck Company (Germany), were reagent grade. Eight samples were prepared according to combination of

factors and levels shown in Table 2. In the first step, 0.04 mol of Al $(NO_3)_3 \cdot 9H_2O$ was dissolved in 100 ml of distilled water. The amounts of serine or asparagine with amounts of urea or ammonium acetate and consequent amounts of ammonium nitrate under vigorous stirring (700 r.p.m) were added to the solution. Then pH of the solution was adjusted with addition of ammonium hydroxide solution or nitric acid if required. The solution was then heated on a hot plate and stirred until the solution was boiled at 100 °C. When almost 90% of water evaporated, a yellowish and translucent gel was obtained. Then the obtained gel was transferred to a porcelain crucible, and was heated in a muffle furnace up to 400 °C and ignited at this temperature inside the muffle. At this stage a blackish voluminous fluffy solid product was obtained. It was calcined according to Table 2 up to 900 °C and remained at this temperature for 2 h. White and very fine powders were obtained. The powders were analyzed by X-ray diffraction (XRD) and average crystal sizes were selected as response of the experiments. X-ray diffraction was performed on calcined powders for phase characterization, at the rate of 1°/min, using nickel filtered CuK_α radiation in the 2θ range 25–80°, on a Philips X-ray diffractometer, (model X'Pert, Netherlands). The surface ares of the powders were measured using multipoint BET method (Quantachrome AutosorbI, Micromeritics instrument, USA) assuming a cross sectional area of 0.16 nm^2 for the nitrogen molecule. The porosity and the microstructure of the products were examined by means of scanning electron microscopy (Philips XL30, Netherlands). Thermal analyses were carried out on Shimadzu DTA-50 and Shimadzu TG-50 (Japan) up to 1200 °C with the rate of 10 °C/min. Particle size distribution was determined by laser light scattering (SEMATech model SEM33, USA).

3. Results and discussion

3.1. XRD data

As fuels, we have selected two amino acids with amino groups which may complex with metal cations and decompose at a relative low temperature giving ammonia (NH_3). The redox reaction between ammonia and the nitrogen oxides (NO_x) from the decomposed nitrates gives water and nitrogen:

$$4x\mathrm{NH}_{3(g)} + 10\mathrm{NO}_{x(g)} \rightarrow (5+2x)\mathrm{N}_{2(g)} + 6x\mathrm{H}_2\mathrm{O}_{(g)} + 2x\mathrm{O}_{2(g)} \quad (1)$$

The energy released from the redox reaction accelerates phase formation of γ-alumina [17].

The XRD patterns of powders calcined at 900 °C for 2 h are shown in Fig. 1. Pattern A shows the XRD pattern of sample 1 as-synthesized at 400 °C.

The peak broadening method was used to calculate the average crystallite size. The full width at half maximum (FWHM) of the peak was measured and the average crystallite sizes were estimated using the equation of Scherrer [18]:

$$D = \frac{0.9\lambda}{(\cos\theta)\sqrt{B^2 - b^2}} \tag{2}$$

where D is the average crystallite size, λ the wavelength of the radiation, θ Bragg's angle and B and b are the FWHMs observed for the sample and standard, respectively. Silicon powder was used to measure the instrumental peak broadening.

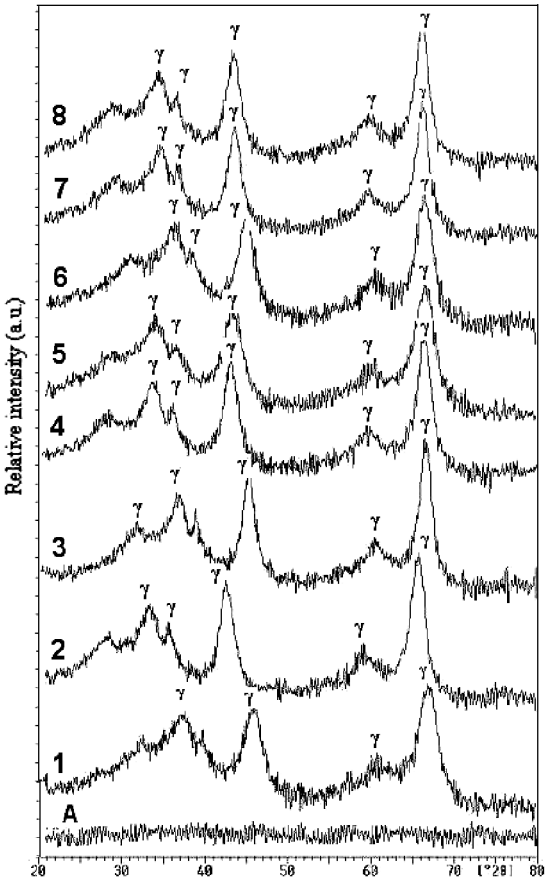

Fig. 1. XRD pattern of sample 1 as-synthesized (A) and samples 1–8 calcined at 900 °C

Terms B and 2θ were obtained from each XRD pattern and PC-APD (X_manager) software that uses information of ICDD (international centre of diffraction data) to recognize alumina phases. The average crystallite size for each sample was calculated from the above formula. Results are shown in Table 3.

The data of Table 3 demonstrate that sample 1 has the smallest average crystallite size (3.95 nm) and sample 7 has the largest one (6.71 nm). It should be mentioned that these results are almost the least average sizes that have been obtained by combustion synthesis.

Table 3. Bragg's angle, 2θ and average crystallite size of samples

Sample	B [deg]	B [rad]	2θ [deg]	Average crystal size D [nm]	Y_i (Response)
1	2.417	0.042184608	67.000	3.95	Y_1
2	1.809	0.030089476	66.872	5.29	Y_2
3	1.724	0.030089476	66.893	5.55	Y_3
4	1.861	0.032480577	66.780	5.14	Y_4
5	2.185	0.038135444	66.921	4.37	Y_5
6	2.241	0.039112828	66.648	4.26	Y_6
7	1.432	0.024993114	66.946	6.71	Y_7
8	1.750	0.030543261	66.830	5.47	Y_8

The pattern A in Fig. 1 confirms the amorphous structure and absence of crystalline phases in the as-synthesized powders. XRD patterns show that samples 1 and 5 have more amorphous particles than the others. Also the crystallinities of samples 2, 3, 6 and 7 are better than those of other samples. Furthermore, samples 2 and 3 are mixtures of δ and γ phases, and samples 6 and 7 are pure γ-alumina. Other samples are mixtures of γ-alumina crystalline powders containing some amorphous particles. The amount of gases released during the exothermic reaction is very high, so it cools the reaction environment. This results in poor crystallinity in some prepared powders. The results show that when an XRD profile has broad peaks, the crystallite sizes are small and the crystallinity is poor but when the peaks are narrow, the corresponding crystals are large. The mentioned software and XRD patterns show that all samples synthesized in this work are γ-alumina.

The effect of changing the level for anyone factor, E_f, is determined by subtracting the average responses (crystal size) when the factor is at its high level (L_+) from the average value when it is at its lower case level (L_-).

$$E_f = \frac{\left(\sum Y_i\right)_{\text{high level}}}{4} - \frac{\left(\sum Y_i\right)_{\text{low level}}}{4} \tag{3}$$

$$E_f = L_+ - L_- \tag{4}$$

$$E_A = \frac{Y_1 + Y_2 + Y_3 + Y_4}{4} - \frac{Y_5 + Y_6 + Y_7 + Y_8}{4} \tag{5}$$

$$E_B = \frac{Y_1 + Y_2 + Y_5 + Y_6}{4} - \frac{Y_3 + Y_4 + Y_7 + Y_8}{4} \tag{6}$$

$$E_c = \frac{Y_1 + Y_3 + Y_5 + Y_7}{4} - \frac{Y_2 + Y_4 + Y_6 + Y_8}{4} \tag{7}$$

$$E_D = \frac{Y_1 + Y_2 + Y_7 + Y_8}{4} - \frac{Y_3 + Y_4 + Y_5 + Y_6}{4} \tag{8}$$

$$E_E = \frac{Y_1 + Y_3 + Y_4 + Y_8}{4} - \frac{Y_2 + Y_4 + Y_5 + Y_7}{4} \tag{9}$$

$$E_F = \frac{Y_1 + Y_4 + Y_5 + Y_8}{4} - \frac{Y_2 + Y_3 + Y_4 + Y_7}{4} \tag{10}$$

$$E_G = \frac{Y_1 + Y_4 + Y_6 + Y_7}{4} - \frac{Y_2 + Y_3 + Y_5 + Y_8}{4} \tag{11}$$

Results of calculations are given in Table 4.

Table 4. Results of average calculations and term E_f for factors and optimum conditions to produce smaller particles

Factor	L_+	L_-	E_f	Comparison (smaller is better)	Optimum condition
A	4.9825	5.2025	–0.22	$L_+ < L_-$	increase of the factor quantity
B	4.4675	5.7175	–1.25	$L_+ < L_-$	increase of the factor quantity
C	5.1450	5.0400	0.105	$L_+ > L_-$	using serine
D	5.3550	4.8300	0.525	$L_+ > L_-$	using ammonium acetate
E	4.8075	5.3775	–0.57	$L_+ < L_-$	increase of the factor quantity
F	4.7325	5.4525	–0.72	$L_+ < L_-$	increase of the factor quantity
G	5.0150	5.1700	–0.155	$L_+ < L_-$	increase of the factor quantity

As we are looking for the production of smaller particles, the least average is considered as the aim of calculations. By utilizing this concept, the optimum condition of factors to produce smaller particles is obtained and it is also given in Table 4.

Sorting of the amounts of E_f without consideration of their signs leads to ranking of factors based on their influence on the combustion synthesis of alumina. Results are given in Table 5.

Factor B (fuel to oxidizer ratio) is the most important factor responsible for reducing the average diameter value of γ-alumina. This result agrees with other reports of nanoalumina combustion synthesis [7]. Other effective factors are F (pH of the solution) and E (molar ratio of added fuel to the main fuel), respectively. Adjustment of pH was done by addition of nitric acid or ammonium hydroxide. Addition of these materials would change the concentration of nitrate ions, and it can change the amount

of fuel to oxidizer ratio. The increase of nitrate ions in the low pHs is expected to decrease the enthalpy of exothermic reaction by decreasing the fuel to oxidizer ratio. Thus the rate of combustion reaction would decrease and in this condition alumina particles come closer to foam structure and agglomeration will increase [9].

Table 5. Ranking of factors (screening) based on sorting the $|E_f|$ values

Ranking of the factors	$\|E_f\|$
1 – fuel to oxidizer ratio	1.25
2 – pH of the starting solution	0.72
3 – molar ratio of added fuel to the main fuel	0.57
4 – type of added fuel	0.525
5 – molar ratio of the excess oxidizer to aluminum nitrate	0.22
6 – calcination rate	0.155
7 – type of main fuel	0.105

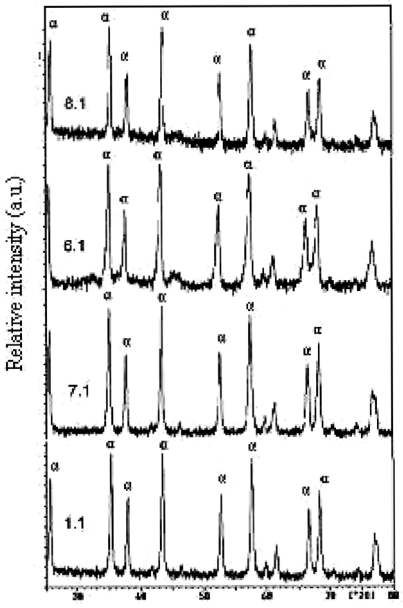

Fig. 2. XRD patterns of powders 1.1, 7.1, 6.1 and 8.1

The effect of D (type of added fuel) is positive, hence in comparison with urea, ammonium acetate fuel is more suitable. Using urea as a fuel leads to a flaming type combustion. When flame persists for a longer time, the particles have enough time and temperature to sinter and thus yield larger particles [14]. The effects of A, G, and C are less important and the least effective factor is C (type of the main fuel). In this research, we selected two similar fuels. These fuels are amino acids, so their influence

on the combustion reaction is almost similar. Differences in organic structure of fuels would make the factor C one the more effective factors of combustion synthesis [11].

In the Table 3, powders 1 and 7 have the lowest and highest responses of alumina production from asparagine, and powders 6 and 8 have the lowest and highest responses of alumina production from serine, respectively; the powders which previously were calcined at 900 °C for 2 h were again calcined from ambient temperature up to 1100 °C and maintained at this temperature for 2 h. Resulting products obtained from powders 1, 6, 7, and 8, were named 1.1, 6.1, 7.1, and 8.1 respectively. Figure 2 shows the XRD patterns of the products. XRD patterns show that all these products are α-alumina. The average crystallite sizes for each powder were calculated by Scherer's formula. The results are given in Table 6.

Table 6. Average crystallite sizes of powders calcined at 1100 °C

Powder number	Average crystallite size [nm]
1.1	33.41
6.1	22.73
7.1	33.92
8.1	25.92

Values of Table 6 show that α-alumina powders with average crystallite sizes between 22.73 and 33.92 nm have been obtained. The crystal sizes increased when calcined at 1100 °C. These results demonstrate that the dimensions obtained by us are smaller than those of α-alumina powders previously produced by other fuels like citric acid, glycine, urea, ammonium acetate, etc. [7]. The results show that serine and asparagine are suitable fuels for combustion synthesis of α-alumina nanostructured powders.

3.2. BET Data

The specific surface areas of samples 1 and 6 were calculated according to the Brunnauer–Emmet–Teller (BET) procedure [19] by using the data of adsorption of nitrogen on the samples at 77 K assuming the cross sectional area of 0.16 nm^2 for the nitrogen molecule. The results show that the specific surface area of sample 1 is 22 m^2/g and the specific surface area of sample 6 is 75 m^2/g. Thus the specific surface area of the sample produced by serine-nitrate combustion is higher than that of the sample being the product of asparagine-nitrate combustion. The surface areas of samples show that these samples are suitable for using as catalyst supports or adsorbents.

3.3. DTA/TG data

The DTA and TG analyses were also performed on sample 6 to investigate the phase transformations. In Fig. 3, the TG curve demonstrates two weight loss steps.

First, it was verified on a significant fall by about 22% at 500 °C. The second drop was slight by about 3% at 1100 °C. Afterwards the curve became horizontal. With DTA analysis it was possible to confirm phase transformation into thermodynamically stable crystallographic alpha alumina at about 1100 °C. This result agrees with that obtained by XRD Analyses. Actually, the temperature of phase transformation is identified on the same manner.

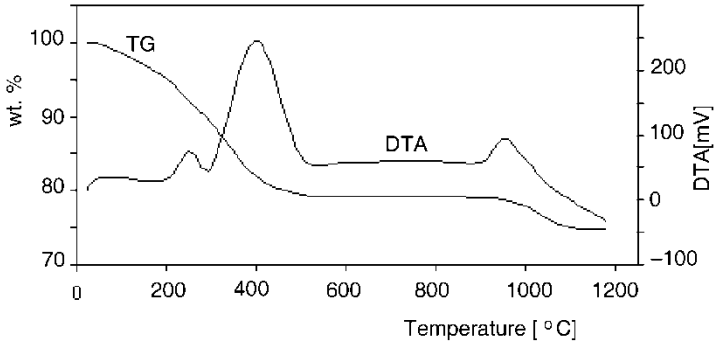

Fig. 3. DTA/TG curves of sample 6

3.4. SEM data

A Phillips XL30 electron microscope was used to take SEM view of the samples 1 and 6 (magnification 50 000×). The SEM photographs of the samples are given in Fig. 4. It was clearly observed from these photographs that sample 6 has a higher porosity and surface area than sample 1. The porosity range of sample 6 is 50–250 nm and could be used as a molecular sieve or a catalyst support [20, 21].

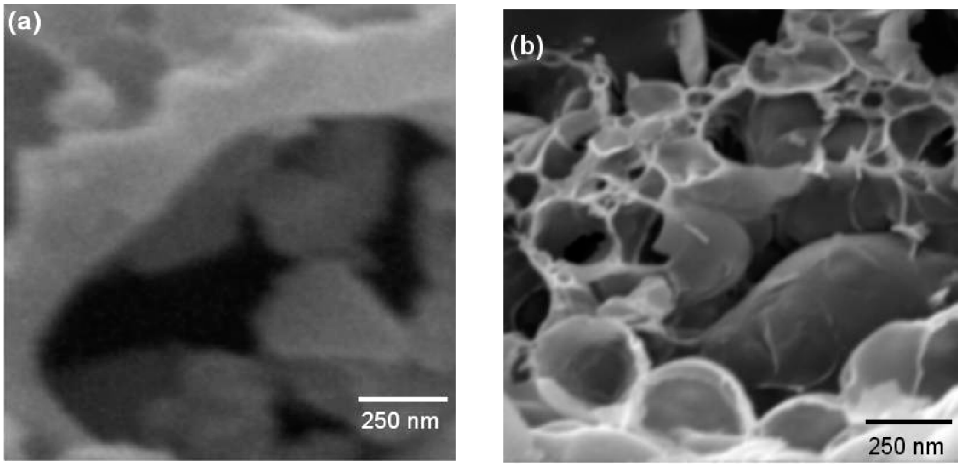

Fig. 4. SEM photographs of the sample 1 (a) and sample 6 (b)

3.5. LLS data

The corresponding particle size distributions of samples 1 and 6 were obtained with laser light scattering in dilute aqueous suspensions after ultrasonic deagglomeration. Results are shown in Figs. 5 and 6. The average particle size of sample 1 was 37.42 nm and the average particle size of sample 6 was 79.32 nm. Particle sizes obtained by combined combustion synthesis and sonication are lower than 100 nm and show success of the method for producing nanopowders. Furthermore, the particle size distribution profiles are narrow and two distributions are homogeneous.

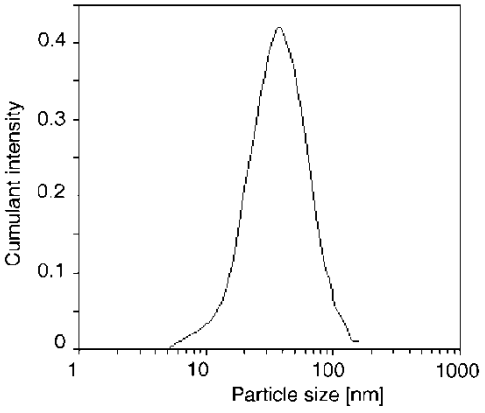

Fig. 5. Particle size distribution of sample 1 after sonication

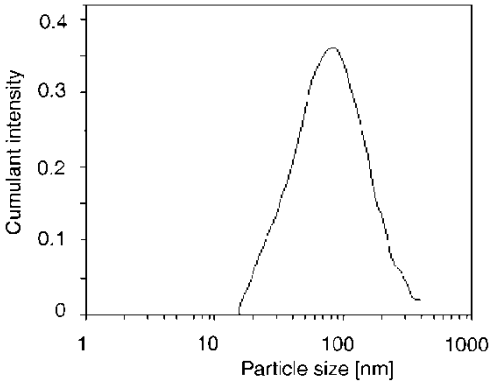

Fig. 6. Particle size distribution of sample 6 after sonication

4. Conclusion

In this research, γ-Al_2O_3 nanopowders with crystallite sizes between 3.95 nm and 6.71 nm and α-alumina with crystal sizes between 22.73 nm and 33.92 nm were successfully synthesized by using serine and asparagine as new fuels. The average particle sizes of γ-alumina powders after sonication were 37.42 nm and 79.32 nm. These results show that serine-nitrate and asparagine-nitrate gel combustion syntheses have outstanding potential for producing nanocrystalline alumina powders in comparison with other conventional fuels.

Using a screening design, the order of effective factors and the optimum combination of their levels required for preparing γ-Al_2O_3 with consideration of smaller crystal sizes was obtained, so the most effective factor was fuel to oxidizer ratio. The specific surface areas of powders were measured and the results show that specific surface areas of samples produced from serine-nitrate combustion are larger than those of samples prepared from asparagine-nitrate combustion.

References

[1] MACEDO M.I.F., OSAWA C.C., BERTRAN C.A., J. Sol-Gel Sci. Techn., 30 (2004), 135.
[2] ADA K., SARIKAYA Y., ALEMDAROGLU T., ONAL M., Ceram. Intern., 29 (2003), 513.
[3] VARATHARAJAN K., DASH S., ARUNKUMAR A., NITHYA R., TYAGI A.K., RAJ B., Mater. Res. Bull., 38 (2003), 577.
[4] SHARMA P.K., VARADAN V.V., VARADAN V.K., J. Europ. Ceram. Soc., 23 (2003), 659.
[5] DUMEIGNIL F., SATO K., IMAMURA M., MATSUBAYASHI N., PAYEN E., SHIMADA H., Appl. Catalysis A: General, 241 (2003), 319.
[6] QU L., HE C., YANG Y., HE Y., LIU Z., Mater. Lett., 59 (2005), 4034.
[7] LI J., PAN Y., XIANG C., GE Q., GUO J., Ceram. Intern., 32 (2006), 587.
[8] FUMO D.A., MORELLI M.R., SEGADAES A.M., Mater. Res. Bull., 31 (1996), 1243.
[9] PATHAK L.C., SINGH T.B., DAS S., VERMA A.K., RAMACHANDRARAO P., Mater. Lett., 57 (2002), 380.
[10] BHADURI S., ZHOU E., BHADURI S.B., Nanostruct. Mater., 7 (1996), 487.
[11] TONIOLO J.C., LIMA M.D., TAKIMI A.S., BERGMANN C.P., Mater. Res. Bull., 40 (2005), 561.
[12] ARUNA S.T., RAJAM K.S., Mater. Res. Bull., 39 (2004), 157.
[13] PENG T., LIU X., DAI K., XIAO J., SONG H., Mater. Res. Bull., 41 (2006), 1638.
[14] KINGSLEY J.J., PEDERSON L.R., J. Mater. Res. Soc. Symp. Proc., 296 (1993), 361.
[15] BURGOS-MONTES O., MORENO R., COLOMER M.T., FARINAS J.C., J. Europ. Ceram. Soc., 26 (2006), 3365.
[16] JAIN S.R., ADIGA K.C., Combust. Flam., 40 (1981), 71.
[17] LI F., HU K., LI J., ZHANG D., CHEN G., J. Nucl. Mater., 300 (2002), 82.
[18] BIAMINO S., FINO P., PAVESE M., BADINI C., Ceram. Intern., 32 (2006), 509.
[19] SARIKAYA Y., ADA K., ALEMDAROGLU T., J. Europ. Ceram. Soc., 22 (2002), 1905.
[20] PARK J.-Y., OH S.-G., PAIK U., MOON S.-K., Mater. Lett., 56 (2002), 429.
[21] ZHU H.Y., RICHES J.D., BARRY J.C., Chem. Mater., 14 (2002), 2086.

Received 24 February 2007
Revised 11 August 2007

Materials Science-Poland, Vol. 25, No. 4, 2007

Optical recognition elements. Macrocyclic imidazole chromoionophores entrapped in silica xerogel

K. KLEDZIK[1], M. JAMRÓGIEWICZ[2], M. GWIAZDA[1], E. WAGNER-WYSIECKA[2], J. JEZIERSKA[3], J. F. BIERNAT[2], A. M. KŁONKOWSKI[1*]

[1]Faculty of Chemistry, University of Gdańsk, Sobieskiego 18, 80-952 Gdańsk, Poland

[2]Department of Chemical Technology, Gdańsk University of Technology, Narutowicza 11, 80-952 Gdańsk, Poland

[3]Faculty of Chemistry, University of Wrocław, ul. F. Joliot-Curie 14, 50-383 Wrocław, Poland

Materials containing new chromoionophores consisting of crown residue and azole moiety as parts of macrocycles were encapsulated by the sol-gel procedure in silica xerogel matrices and proposed as chemical recognition elements especially for such metal ions as Li^+, Cs^+ and Cu^{2+}. Action of these recognition elements is in principle based on changes of reflectance. The recognition elements containing 21-membered chromogenic derivatives of unsubstituted imidazole and 4-methylimidazole are able to distinguish in aqueous solution whether the Li^+ concentration ratio is lower or higher than 1. In the case of Cu^{2+} complexes with 18-membered macrocyclic chromoionophore in which phenol residue was replaced by imidazole and 21-membered chromogenic derivative of 4-methylimidazole, values of the EPR parameters *g* and *A* suggest participation of two oxygen and two nitrogen atoms of the ligand in the equatorial plane of the tetragonally distorted octahedral environment of the central ion.

Key words: *azole azocrown ether; chromoionophore; fluoroionophore; silica xerogel matrix; optical recognition element*

1. Introduction

Polyfunctional molecules combining dyes and polyethers form crown ether analogues belonging to chromoionophores. These compounds show colour changes on complexation with metal ions and may be useful as metallochromic reagents or may serve as sensing compounds for optical chemical sensors. Earlier, majority of such reagents were combinations of chemically bonded azobenzene, phenol residues and polyoxaethylene bridges [1]. Recently, we have described synthesis and properties of

*Corresponding author: e-mail: aklonk@chem.univ.gda.pl

18-membered macrocyclic chromoionophores in which phenol residue was replaced by pyrrole or imidazole [2] (compounds **1** and **2**, Fig. 1). It was found that in acetonitrile solution 18-membered imidazole derivative **2** preferentially complexes sodium among alkali and alkaline earths metal cations. It is known that ligands containing imidazole moiety are of great importance in chemistry and biology; they form very stable complexes with 3d transition metal ions [3]. They are used to mimic binding sites of various metalloenzymes, and they have been used as enzyme inhibitors [4]. A comprehensive review regarding azocrown ethers has been published [1].

In the present work, we describe properties of new chromogenic crown reagents containing imidazole moiety as a part of macrocycle. We have studied the complexation properties of larger, 21-membered chromogenic derivatives of unsubstituted imidazole **3** and 4-methylimidazole **4** in xerogel matrix.

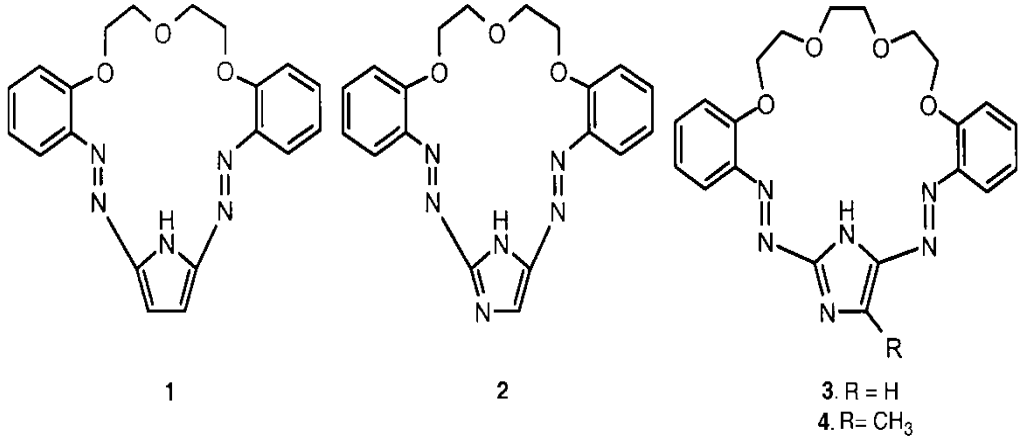

Fig. 1. 18-Membered macrocyclic derivative of pyrrole **1** and imidazole **2** (see Ref. 2) and newly synthesized 21-membered chromogenic derivatives of imidazole **3** and 4-methylimidazole **4**

We have been interested in developing materials which are able to recognize metal ions in aqueous solutions. These materials consist of the above-mentioned chromoionophores entrapped in a porous matrix. Owing to utilizing a low-temperature preparation of oxide materials, such as the sol-gel process [5], it is possible to incorporate organic molecules into an inorganic oxide xerogel. By this technique, a three dimensional network of metal-oxide bonds is formed at room temperature *via* the hydrolysis and condensation reactions of metal alkoxide, followed by low temperature dehydration.

The porous xerogel matrix obtained by this way can trap chromoionophore molecules [6]. Very often silica xerogel plays a role of host matrix for organic molecules with sensor function [7–9]. Several recent observations revealed the feasibility of making one of the most important parts of the chemical sensor, the so-called optical recognition element, which consists, as in our case, of chromoionophore molecules immobilized in a xerogel matrix [10]. In this paper, studies on optical absorption of

chemical recognition elements for potential optical absorption sensors based on chromoionophores (sensing molecules) entrapped in silica xerogel are described. Thus, the aim of our study is to determine the complexation and sensing properties of the optical recognition elements for metal ions in aqueous solutions [11].

2. Experimental

All materials and solvents were of analytical reagent grade. Preparation of compounds **1** and **2** has been described elsewhere [2]. For the synthesis of azacrown ethers with imidazole units **3** and **4** (Fig. 1), their crystallography, cation complexation and behaviour in ion-selective membrane electrodes see [12]. Tetramethoxysilane (TMOS), $Si(OCH_3)_4$, from Aldrich Chemicals Co. and methanol (POCh, Poland) were used without further purification. Metal perchlorates were purchased from Aldrich Chemicals Co.

The sols were prepared by a typical sol-gel procedure [5] from the starting mixture of TMOS (10 g or 0.066 mole), deionized water ([TMOS]/[H_2O] = 1/4), and methanol as diluent ([TMOS]/[CH_3OH] = 1/10). The mixture was stirred to obtain a homogeneous solution and then diluted with NH_3 aqueous solution (NH_3:H_2O = 1:2, v/v) as a catalyst and one of the sensing compounds (in methanol solution, 1×10^{-4} M) as a dopant was added. The ammonia solution was added dropwise to reach pH 8 of the mixture. The sol was then vigorously stirred at room temperature for 2-3 min.

The obtained alcogels were allowed to age and dried for 3 days in air. The xerogel was prepared by heating for 3 h at 120°C under vacuum to remove ammonia and methanol as well as some water from the pores. The concentration of the sensing dopant in the xerogel was equal to 1.0×10^{-4} mol·g^{-1}, estimated on pure and dried SiO_2 xerogel obtained from the alkoxide. Xerogel materials with the immobilized chromo/fluoroionophores, their specific surface area ranging between 312 and 358 (±11) m^2·g^{-1}, were crushed and the grain fraction of 0.25–0.50 mm was used for measurements.

Chemisorption (complexation) of the metal ions by the entrapped sensing dopants in the silica matrix was performed by immersion and agitation in aqueous solutions of a selected metal salt (concentration 1.0×10^{-2} M). After 1 min the recognition material was filtered off, rinsed with deionized water, and then dried at 343 K. By this chemisorption method complexes of the metal ions with the ligands **1**–**4** were formed. Amounts of the recognition material and the aqueous solutions used in the complexation experiment secured 1:1 ligand to metal molar ratio.

Nitrogen sorption at 77 K was used to determine the specific surface area of the prepared silica based recognition materials. Adsorption measurements were made on an AREA meter II (Stroenlein Instruments, Germany) for samples using the Brunauer –Emmett–Teller (BET) theory.

Reflectance spectra of the materials in the UV-Vis region were recorded with a Perkin-Elmer Lambda 35 spectrophotometer equipped with a Labsphere reflection spectra accessory.

EPR spectra were obtained on a Bruker ESP 300E spectrometer operating at X-band (9.1-9.9 GHz) and equipped with the Bruker NMR gaussmeter ER033m as well as the Hewlett-Packard microwave frequency counter. Sealed quartz capillaries (1 mm in diameter) were the sample holders. The magnetic field was modulated at 100 kHz. Standard deviations of the EPR spectral parameters were estimated as follows: $g_{\parallel}$ ±0.003, $g_{\perp}$ = ±0.005, $A_{\parallel}$ = ±4×10^{-4} cm^{-1}, $A_{\perp}$ = ±1×10^{-4} cm^{-1}.

3. Results

3.1. Compounds immobilized in silica

Reflectance. Each of the sensing molecules (Fig. 1) entrapped in silica xerogel exhibits distinctive spectral changes in UV range due to coordination with at least one of the metal ions from the following groups of metals: alkali (Li^+, Na^+, K^+ and Cs^+), alkaline earth (Mg^{2+}, Ca^{2+} and Ba^{2+}), heavy (Cd^{2+}, Sn^{2+} and Pb^{2+}) and transition (Co^{2+}, Ni^{2+}, Cu^{2+} and Zn^{2+}) ions. The most distinctive reflectance spectral changes for some metal ions are shown in Figs. 2A-D. Hence, Cs^+ ion complexed with the ligand **1** shows quite dissimilar reflectance spectrum than the other cations of the alkali group and the free chromoionophore (Fig. 2A). Similarly, spectrum of ligand **1** undergoes specific change after coordination with Mg^{2+} (Fig. 2B). On the other hand, chromoionophore **3** distinguishes Sn^{2+} from Cd^{2+} and Pb^{2+} by spectral change, as illustrated in Fig. 2C. Chromoionophore **4** embedded in silica differentiates spectrally Cu^{2+} ions comparing changes caused by Co^{2+}, Ni^{2+} and Zn^{2+} in aqueous solution (Fig. 2D).

In order to decide which of the reflectance spectra shown in Figs. 2A, C and D are specific for Cs(I), Sn(II) and Cu(II) complexed with ligands **1**, **3** and **4**, the spectra are compared with significant reflectance spectra of the pure silica matrix and the matrix coordinated (absorbed) to the mentioned metal ions (see Fig. 3A-C). It is evident that the specific spectral changes are attributed only to complexes Cs(I) and Cu(II) with ligands **1** and **4**, respectively, while, the spectrum of the Sn(II) complex with **3** is similar to the spectra of Sn(II) adsorbed on SiO_2 and pure SiO_2. In this case specific spectra show Pb(II) or Cd(II) complexed to chromoionophore **3** because their distinct bands at low wavelength are placed at various positions.

Surprisingly, the spectral changes of 21-membered macrocycle **3** and **4** in xerogel matrix upon coordination of Li^+ ions depend on molar ratio x = [Li^+]/[chromoionophore]. The spectra dramatically differ for the ratio lower or higher than 1. The respective spectra for **3** and **4** are collected in Figs. 4A and B, respectively. Three of the bands at ca. 270, 320 and 360 nm are characteristic of free ligands and the ligands complexed with Li^+ if $x < 1$. However, if the molar ratio x exceeds 1, a typical band appears additionally at 237 nm.

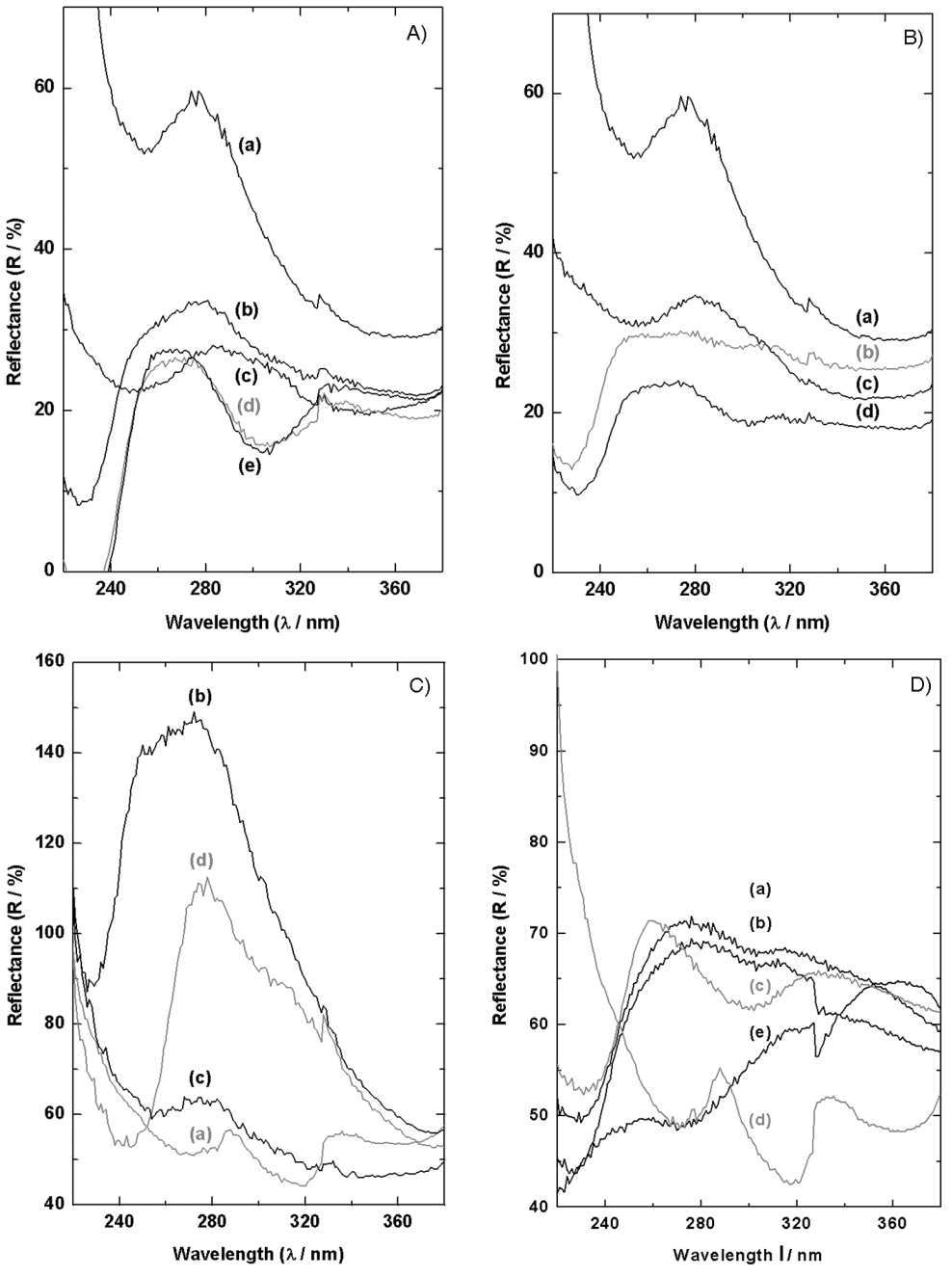

Fig. 2. Reflectance spectra of chromoionophores immobilized in silica xerogel and complexed with metal ions: A) alkali cations with ligand **1**: free ligand (a), K^+ (b), Cs^+ (c), Li^+ (d) , Na^+ (e); B) alkaline earth cations with ligand **1**: free ligand (a), Ba^{2+} (b), Mg^{2+} (c), Ca^{2+} (d); C) heavy cations with ligand **3**: free ligand (a), Cd^{2+} (b), Sn^{2+} (c), Pb^{2+}(d); D) transition cations with ligand **4**: Ni^{2+} (a), Co^{2+} (b), Zn^{2+} (c), free ligand (d), Cu^{2+} (e)

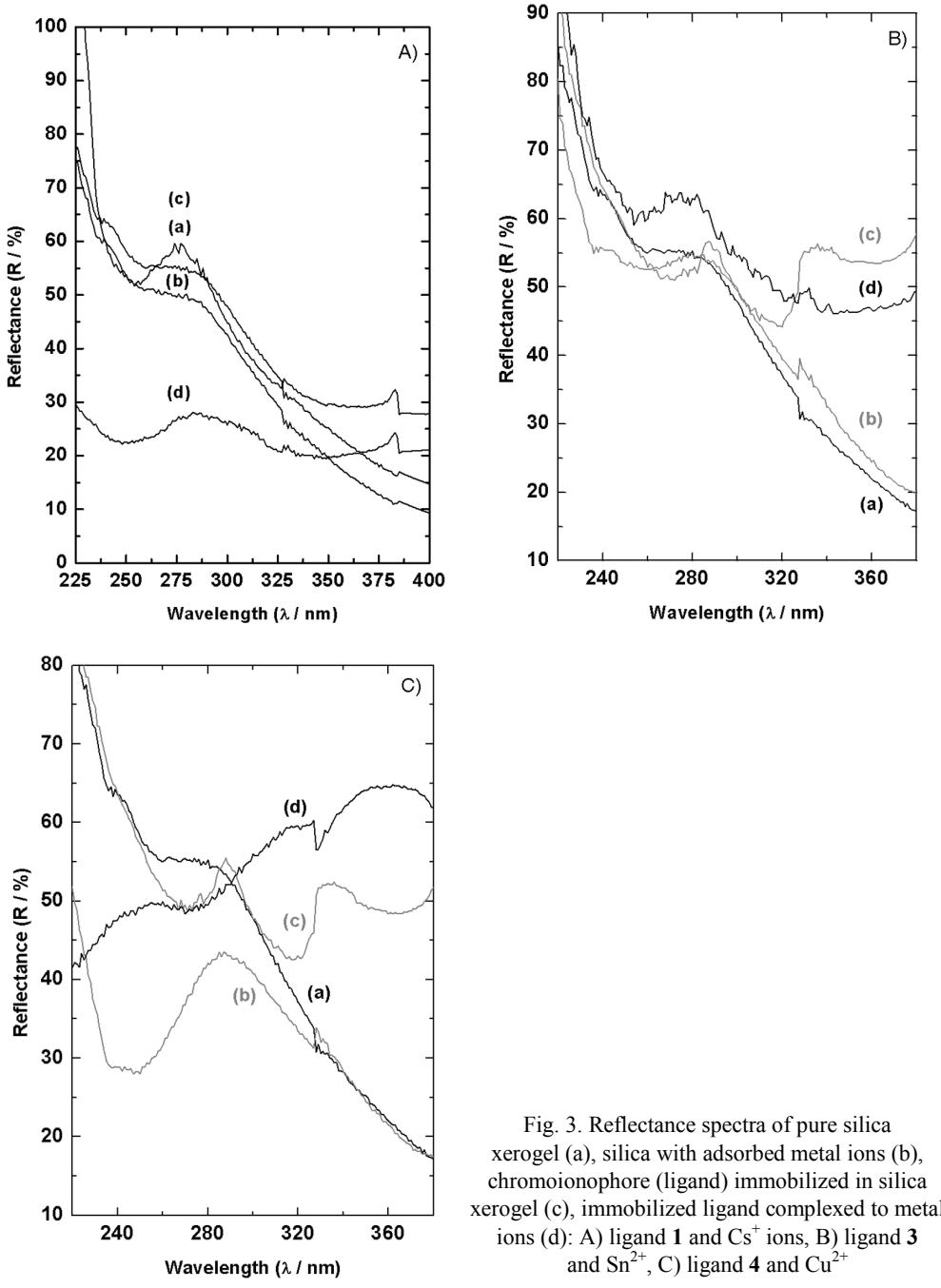

Fig. 3. Reflectance spectra of pure silica xerogel (a), silica with adsorbed metal ions (b), chromoionophore (ligand) immobilized in silica xerogel (c), immobilized ligand complexed to metal ions (d): A) ligand **1** and Cs^{+} ions, B) ligand **3** and Sn^{2+}, C) ligand **4** and Cu^{2+}

In contrast, no drastic spectral changes are observed in the case of 18-membered chromoionophores **1** and **2**, when they coordinate Li^{+} ions at the molar ratio x lower and higher than 1. This is shown, for instance, for **2** in Fig. 4C. For the crown ether of

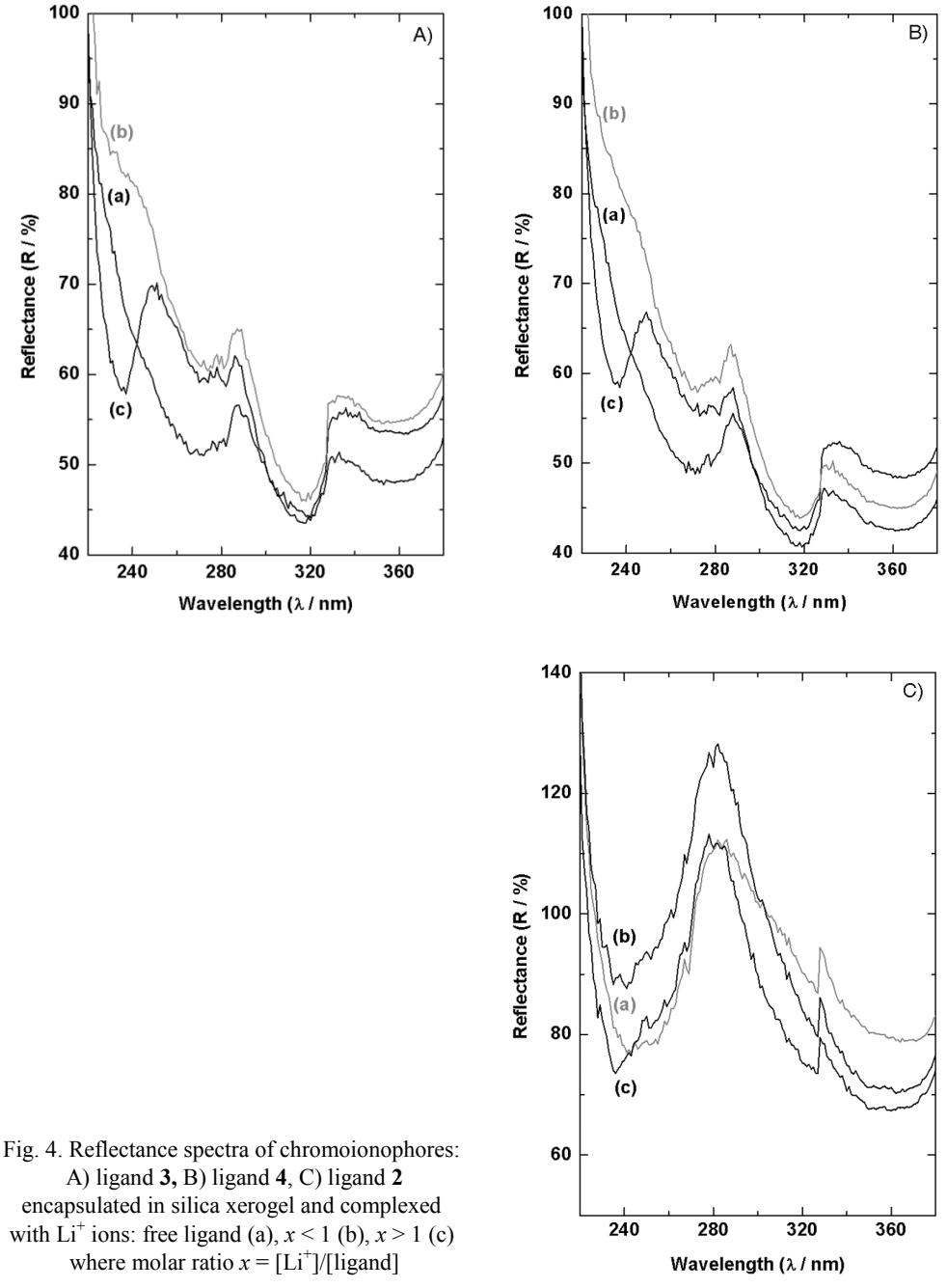

Fig. 4. Reflectance spectra of chromoionophores: A) ligand **3,** B) ligand **4**, C) ligand **2** encapsulated in silica xerogel and complexed with Li^+ ions: free ligand (a), $x < 1$ (b), $x > 1$ (c) where molar ratio $x = [Li^+]/[\text{ligand}]$

a smaller size each spectrum consists of two bands but for the solution with $x > 1$ the band at low wavelength is blue shifted in comparison with the free ligand (**1** or **2**) and for the ligand complexed with Li^+, when $x < 1$.

Electron paramagnetic resonance spectra (EPR). EPR spectra for the complexes formed as a result of Cu^{2+} chemisorption (coordination) by the chromoionophores **2** and **4** entrapped in silica xerogel are shown in Fig. 5, together with appropriate simulated curves. The spectra are compared with that measured for silica xerogel loaded by Cu^{2+} ions. The lines of parallel orientation transitions (resolved due to copper hyperfine coupling) and line of perpendicular orientation transitions are partly overlapped. The anisotropic spectra of Cu^{2+}-ligand **2** and Cu^{2+}-ligand **4** systems are very close to each other and typical of Cu^{2+} complexes of axial symmetry. The spectral parameters of Cu^{2+} coordinated by **2,** $g_{\|} = 2.285$, $g_{\perp} = 2.055$, $A_{\|} = 176\times10^{-4}$ cm^{-1} and $A_{\perp} = 20\times10^{-4}$ cm^{-1} (sim (a/b)), are analogous, within experimental error, to the parameters derived from the spectrum of Cu^{2+} coordinated by **4**. The EPR parameters of Cu^{2+} ions adsorbed in the silica xerogel are distinctly different, $g_{\|} = 2.411$, $g_{\perp} = 2.078$, $A_{\|} = 135\times10^{-4}$ cm^{-1} and $A_{\perp} = 15\times10^{-4}$ cm^{-1} (sim (c)).

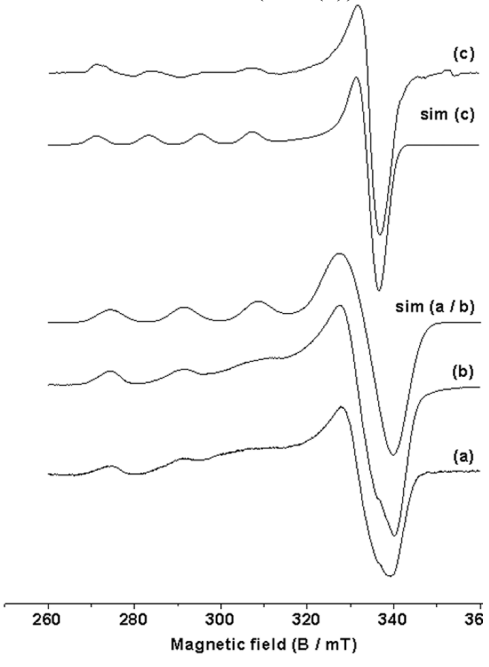

Fig. 5. X-band EPR spectra of the complexes formed by Cu^{2+} with compounds **2** (a) and **4** (b) entrapped in silica xerogel in comparison with the spectrum of silica xerogel loaded by Cu^{2+} (c). The spectra sim (a/b) and sim (c) were simulated using the spin Hamiltonian parameters given in the text. The spectra were recorded at 77 K

4. Discussion

The chromoionophores shown in Fig. 1 are molecules with extended framework consisting of a σ-bonding set and an associated conjugated π-system. The lower energy electronic transitions occur when an electron is promoted from an occupied π-orbital to an unoccupied π^* orbital. It is generally assumed that the low energy π-π^* transitions are principally responsible for UV and visible light absorption [13]. The π-π^* transitions in organic dyes which involve considerable charge transfer in donor-acceptor chromogens, are highly probable, resulting in intense optical absorption in

UV-visible range. The dramatically changed band shape after the metal ions complexation (Fig. 2) reflects a phenomenon attributed to large changes in the arrangement of vibrational energy levels in the ligand molecule that depends on charge density of the complexed metal ion. This effect is distinctly demonstrated for Cs^+ and Cu^{2+} complexes with chromoionophore **1** and **4**, respectively (Figs. 2A and D).

Among the analyzed metal ions, Li^+ possessing the smallest diameter (76 pm) [14] gives a chance to form dinuclear complexes with ligands **3** and **4** of relatively large cavities. Due to the deformation of the macrocycle in such a complex, a dramatic spectral change is expected. The expected effect is confirmed by experimental results shown in Figs. 4A and B. The effect exhibited by larger cavities of **3** and **4** after Li^+ complexation may be attributed to the stepwise formation of 1:1 and 1:2 (ligand to metal) lithium complexes. The large spectral change may be attributed to the distribution of vibrational energy levels in the ligand molecule by two complexed lithium cations creating a double charge density in the dinuclear complex as compared with the mononuclear one. As the material indicates changes of lithium(I) concentration in solution in comparison with the ligand concentration at the level ca. 1×10^{-4} M, this effect was used for Li^+ recognition.

Other cations cause characteristic spectral changes which are due to their specific diameter (compared with the ligand cavity size) and/or preferred symmetry of the coordination sphere. Owing to these reasons, they could be able to change the ligand structure by complexation and consequently the spectrum shape (see Figs. 2A–D).

EPR spectroscopy is a powerful tool enabling one to identify changes in the coordination environment of Cu(II) ions complexed by the receptor groups of the fluoroionophore attached to surface of silica matrix. The signals may be well interpreted in terms of the spin Hamiltonian for d^9 ions in axial symmetry:

$$\mathcal{H} = \beta[g_{\|} H_z S_z + g_{\perp}(H_x S_x + H_y S_y)] + A_{\|} I_z S_z + A_{\perp}(I_x S_x + I_y S_y) \quad (1)$$

where z is the symmetry axis, β the Bohr magneton, S and I are the electron and nuclear spin operators, H_x, H_y, H_z are the static magnetic field components, $g_{\|}$ and $g_{\perp}$ are the parallel and perpendicular components of the **g** tensor, and $A_{\|}$ and $A_{\perp}$ are parallel and perpendicular components of the hyperfine tensor **A**. The nuclear quadrupole contribution is neglected [15]. In this study, the EPR spectra of amorphous samples of the Cu^{2+} complexes immobilized in silica were interpreted according to Kneubühl's method [16].

Computer line shape simulation was performed based on the spin Hamiltonian (Eq. (1)). Cu(II) sites are randomly oriented with respect to the magnetic field in such a way that a spectral envelope encompassing all possible resonance conditions is observed. The spectra were analyzed by a computer simulation program based on resonance fields calculated according to the method of Sakaguchi et al. [17] as well as using WinEPR SimFonia program, version 1.25.

The g-parameter sequence $g_{\|} >> g_{\perp} > 2.0$ and large $|A_{\|}|$ values of the measured EPR spectra (Fig. 5) are typical of d^9 complexes with axial elongated symmetry and a $d_{x^2-y^2}$

ground state. It allows us to identify the Cu^{2+} coordination environment as belonging to tetragonally elongated octahedron (D_{4h}) [18]. The values of EPR parameters derived by simulation of the experimental spectra of the chromoionophores **2** and **4** loaded by Cu^{2+} suggest that coordination sphere in copper(II) plane consists most likely of two nitrogen and two oxygen donors of the ligands [19–21]. The proximity of three nitrogen donors makes also probable their involvement in coordination around Cu(II) plane but increasing width of hyperfine lines (with magnetic field growth) is characteristic for higher participation of oxygen donors. The coordination at axial position is poorly identified by EPR parameters as for $|A_{\|}| >> |A_{\perp}|$ and $g_{\|} >> g_{\perp}$ the most reliable information are provided by the change of $|A_{\|}|$ and $g_{\|}$ values about the donors at the corners of Cu(II) plane [22]. The spectrum of the reference system Cu–silica xerogel is typical of Cu^{2+} surrounded by water and/or Si-OH group oxygen atoms [23] strongly suggesting that quite different Cu^{2+} complexes with ligand **2** and **4** are formed.

5. Conclusions

Materials composed of chromoionophores **1**–**4** entrapped in silica xerogel matrix by the sol-gel procedure, at concentration 1.0×10^{-4} mol·g^{-1} silica, treated as optical recognition elements, selectively recognize some metal ions present in aqueous solutions. The chromoionophores **1** and **4** incorporated into silica xerogel matrices are sensitive especially to Cs^{+} and Cu^{2+} ions in aqueous solutions in this sense that reflectance spectra specifically change in the presence of these cations, compared with free ligands or the other studied metal complexes. This effect is useful for determination of these cations in environmental and physiological fluids by UV-Vis spectrophotometry.

The studied 21-membered chromoionophores (**3** and **4**) in the recognition elements by their dramatical spectral changes are able to signal when the molar ratio $[Li^{+}]$/[ligand] exceeds 1 in aqueous solution. Thus, these recognition materials can serve as indicators of Li^{+} concentration.

The EPR spectral parameters suggest that in chromoionophores **2** and **4** complexed with Cu(II) ion two nitrogen and two ether oxygen atoms take part in the equatorial plane of the tetragonally distorted octahedral sphere. Probably the same atoms of the chromoionophores take part in the complexes with other transition metal ions.

Acknowledgements

Financial support of this work from the Gdańsk University of Technology (DS Grant No. 014668/003), the State Committee for Scientific Research (Grant No. 3 T09A 151 27) and the COST/26/2005 Grant is gratefully acknowledged.

References

[1] LUBOCH E., BILEWICZ R., KOWALCZYK M., WAGNER-WYSIECKA E., BIERNAT J.F., *Azo Macrocyclic Compounds*, Chapt. 3, [in:] G.W. Gokel (Ed.), *Advances in Supramolecular Chemistry*, Vol. 9, Cerberus Press, 2003, p. 71.

[2] WAGNER-WYSIECKA E., LUBOCH E., KOWALCZYK M., BIERNAT J.F., Tetrahedron, 59 (2003), 4415.
[3] VÁRNAGT K., SÓVÁGO I., GOLL W., SÜLI-VARGHA H., MICERA G., SANNA M., Inorg. Chim. Acta, 283 (1998), 233.
[4] BARAN E.J., Biochem. (Moscow) 65 (2000), 789.
[5] BRINKER C.J., SCHERER G.W., *Sol-Gel Science. The Physics and Chemistry of Sol-Gel Processing*, Academic Press, London, 1990.
[6] AVNIR D., KAUFMAN V.R., REISFELD R., J. Non-Cryst. Solids, 74 (1985), 395.
[7] ZUSMAN R., ROTTMAN C., OTTOLENGHI M., AVNIR D., J. Non-Cryst. Solids, 122 (1990), 107.
[8] DUNN B., ZINK J.I., J. Mater. Chem., 1 (1991), 903.
[9] BRAUN S., RAPPOPORT S., ZUSMAN R., AVNIR D., OTTOLENGHI M., Mater. Lett., 10 (1990), 1.
[10] ARNOLD M.A., Anal. Chem., 64 (1992), 1015.
[11] KŁONKOWSKI A.M., KLEDZIK K., WAGNER-WYSIECKA E., BIERNAT J.F., J. Sol-Gel Sci. Techn., 28 (2003), 245.
[12] WAGNER-WYSIECKA E., JAMRÓGIEWICZ M., FONARI M.S., BIERNAT J.F., Tetrahedron, 63 (2007), 4414.
[13] CHRISTIE R.M., *Colour Chemistry*, The Royal Society of Chemistry, Cambridge, 2001.
[14] GREENWOOD N.N., EARNSHAW A., *Chemistry of the Elements*, Pergamon Press, Oxford, 1984, p. 86.
[15] ATHERTON N.M., *Principles of Electron Spin Resonance*, Ellis Horwood, Chichester, 1993.
[16] KNEUBÜHL F.K., J. Chem. Phys., 33 (1960), 1074.
[17] SAKAGUCHI U., ARATA Y., FUJIWARA S., J. Magn. Res., 9 (1973), 118.
[18] KŁONKOWSKI A.M., SCHLAEPFER C.W., J. Non-Cryst. Solids, 129 (1991), 101.
[19] PEISACH J., BLUMBERG W.E., Arch. Biochem. Biophys., 165 (1974), 691.
[20] JEZIERSKA J., TROCHIMCZUK A.W., KĘDZIERSKA J., Polymer, 40 (1999), 3611.
[21] KOLARZ B.N., TROCHIMCZUK A.W., JERMAKOWICZ-BARTKOWIAK D., JEZIERSKA J., Polymer, 43 (2002), 1061.
[22] PILBROW J.R., *Transition Ion Electron Paramagnetic Resonance*, Clarendon Press, Oxford, 1990, p. 165.
[23] DARAB J.G., MACCRONE R.K, Phys. Chem. Glass., 32 (1991), 91.

Received 6 February 2007
Revised 11 October 2007

Materials Science-Poland, Vol. 25, No. 4, 2007

Aluminium oxide composite layers obtained by the electrochemical method in the presence of graphite

W. SKONECZNY*, M. BARA

Chair of Materials Science, University of Silesia, ul. Śnieżna 2, 41-200 Sosnowiec, Poland

The paper presents a new method of obtaining aluminium oxide composite layers formed by means of hard anodizing in an electrolyte composed of water solution of acids and graphite. The produced layers were subject to tests and their results, such as the influence of process parameters on the properties of composite layers, are presented. A possibility of incorporating graphite particles into an anodic oxide layer structure has been demonstrated. The thickness and microhardness of the obtained layers and Al_2O_3 layers fabricated in identical conditions have been compared.

Key words: *composite; aluminium oxide; graphite; scanning microscopy; X-ray diffraction*

1. Introduction

Improvement of mechanical properties of operational materials more and more frequently consists in modifications within the surface layer. Materials characterized by a smooth change of properties from the core to the surface seem to be the best technological solution for upper layers. The inner layer directly adhering to the substrate is supposed to ensure maximum adhesion, while the upper layer is to preserve optimal tribological properties. In the case of modified layers and multilayers produced from materials with intermediate properties superimposed one onto another, this dependence is fulfilled. At present, such layers are produced in multiple technological processes. Layers obtained from composite materials, usually produced by electrochemical methods, are a combination of two or more separate and mutually insoluble phases and collectively they ensure better properties than those of each individual material. If composite layers showed a smooth change of properties from the core to the surface and if they could be obtained in a single, inexpensive process, they would become competitive for intermediate and modified layers, due to a shortened production time and reduced production costs.

*Corresponding author, e-mail: skoneczn@us.edu.pl

Oxide coatings produced electrolytically on aluminium alloys are characterized by very high adhesion to the substrate, making their detachment impossible, and typical porosity of their surface enables sorption of other substances. An advantage of the oxide layer production is the possibility of manipulating its mechanical properties. As a result of changes in the current density and electrolyte temperature, the thickness, porosity and microhardness of the layer change as well [1, 2]. Increased porosity of the oxide layer entails an increased amount of substances absorbed. Both the oxide layer structure and the above-mentioned dependences predispose oxide coatings to serve as matrices for composite layers [3, 4].

By changing the nature of the reinforcing phase in the aluminium oxide matrix, we can use the composite layer in a number of ways. Obtaining a composite material in the form of an abrasion-resisting aluminium oxide matrix enriched with a lubricant, would allow us to obtain an upper layer with good tribological properties. One of the most frequently employed lubricants is graphite whose structure is composed of parallel carbon planes, interlinked by weak van der Waals bonds. A specific crystal structure and low hardness (ca. 1 in Mohs' scale) of the graphite lamellar structure account for its excellent lubricating properties.

The above-mentioned properties have inspired the authors of this paper to research into the possibility of incorporating graphite in the aluminium oxide structure during a hard anodizing process, being the only technological treatment when forming a composite oxide layer.

2. Experimental

All layers were fabricated via hard anodizing method on a substrate made of PA2 alloy (AlMg2). The choice of the alloy was dictated by its easy oxidation and good results of previous studies. The process was preceded by purifying the sample surfaces and degreasing through etching in a 5% KOH and a 10% HNO_3 solutions. The surfaces so prepared were subject to electrolytic oxidation by the direct-current method, using a stabilized GPR-25H30D feeder cable. The electrolysis was conducted in an electrolytic tank of the dimensions: 18×18 cm^2. The foundation of the electrolyzer was in the shape of a square with rounded edges. Electrodes were immersed to the depth of 3 cm from the tank bottom and 3 cm from the electrolyte surface. A 45×17 mm^2 plate made of AlMg2 alloy was used as the anode and a lead plate of the same dimensions was used as the cathode.

The electrolytes constituted water solutions of sulfuric, oxalic and phthalic acids (SFS) for the Al_2O_3 layer formation and water solutions of the same acids with an addition of loose graphite for the production of composite layers. During the anodizing process, the electrolyte was stirred in one direction with a mechanical stirrer at the constant speed of 150 r.p.m. This stirring speed enabled obtaining a homogeneous graphite suspension throughout the electrolyte volume. An addition of the phthalic acid to an electrolyte ensures obtaining layers with the largest possible pores, as well as conducting the process at

room temperature [6, 7]. The purity degree of the graphite used as an addition to the electrolyte-base amounted to 99%, with the average size of grain being smaller than 1 μm. Due to the aluminium oxide nanopore size, graphitization was conducted during the electrolysis, producing a composite layer achieved by incorporating graphite into the oxide structure. The anodizing process was conducted during a constant time period of 1 h, at the current density of 2 or 3 A/dm^2, and electrolyte temperatures of 293 and 303 K. The oxidation conditions for particular samples are summarized in Table 1.

Table 1. Parameters of the anodizing process

Sample	Anodic current density [A/dm^2]	Electrolyte temperature [K]	Electrolyte composition
4A	2	293	SFS + graphite
4B	3	293	SFS + graphite
4C	2	303	SFS + graphite
4D	3	303	SFS + graphite
4A1	2	293	SFS
4B1	3	293	SFS
4C1	2	303	SFS
4D1	3	303	SFS

After completion of the anodizing process, the samples were rinsed for 1 h in distilled water in order to remove remaining electrolyte. The thickness of all layers was measured with a Fischer's Dualscope thickness gauge, by making 10 measurements along the sample length. The Dualscope instrument works based on the current-rotational method, with its maximum error amounting to 1 μm. The structure and surface morphology were examined using a Philips XL30 scanning microscope. No tests were conducted on the composite layer microsections, since their mechanical preparation caused rinsing out of graphite from the oxide layer. Therefore, the analysis of the compositions of the layers was performed using an X-ray diffractometer by the standard method with the use of a Philips PW3710 X-ray diffractometer and the X'PERT computer program. The angular range 2θ of the diffractograms was 5–85º or 5–110º. The substrates of the samples, made of an aluminium alloy with small admixtures of Mg, Mn and Ti, as well as graphite used as an addition to the electrolyte, were subject to the diffractometric analysis. On the layer transverse microsections, within a distance of 15 μm from the substrate, indentations were made with the use of a Hanemann microhardness tester, by applying 0.3 N load. Microhardness was determined based on the photos of microsections taken with a Neophot 21 microscope.

3. Results and discussion

During the oxidation process at a constant current value, measurement of anodizing voltage was made, the value of which was varying with a growing oxide layer. At

the beginning of the process, the voltage increased to a certain maximum value, called critical voltage; next, it decreased slightly and having reached a certain minimum, increased again. The reason for this phenomenon are processes taking place during the oxide coating's formation. The value of voltage was found proportional to the current density, and inversely proportional to the electrolyte temperature.

An examination conducted with a scanning microscope showed a structural architecture typical of oxide layers produced on aluminium alloys. Figure 1 illustrates a columnar-fibrous structure; the fibres are perpendicular to the sample surface. The surface porosity visible in Fig. 2 is the effect of oxide cellular structure, formed as a result of the electrolyte dissolving activity, which occurs in consequence of an increasing solution concentration under the influence of current flow in sites of breakdown.

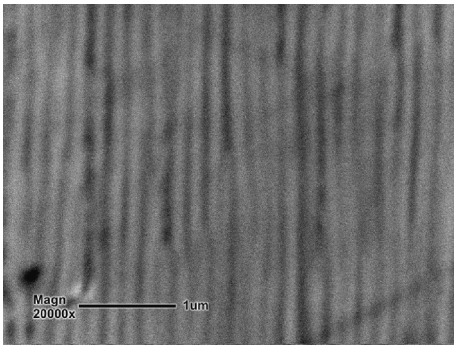

Fig. 1. Structure of the oxide layer obtained at 293 K and current density of 2 A/dm^2

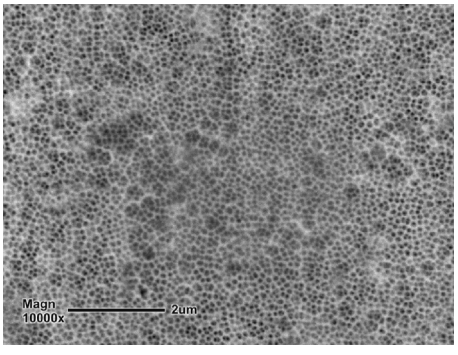

Fig. 2. Morphology of the oxide layer surface obtained at 293 K and current density of 2 A/dm^2

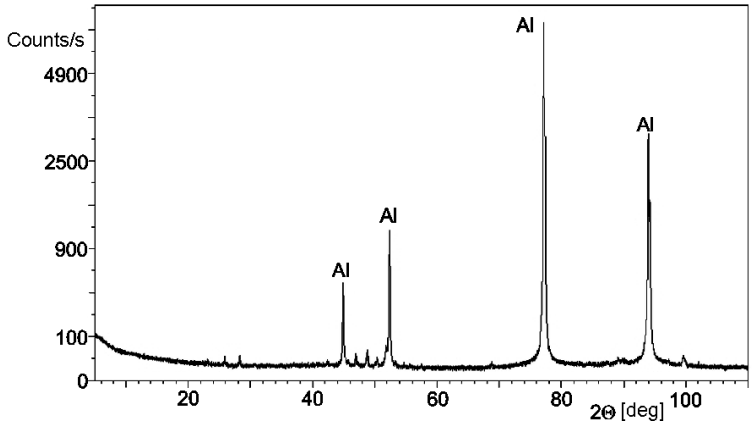

Fig. 3. X-ray diffractogram of the $AlMg_2$ alloy

On the X-ray diffractograms of the substrate and layers of Al_2O_3 + graphite, shown in Figs. 3–5, strong reflexes are visible, in major part belonging to Al, as well

as a number of weak reflexes corresponding to alloying additions and graphite. The depth of X-radiation penetration depends on the type of the matter studied and fluctuates between 0.5 and 2 mm. The thickness of the Al_2O_3 + graphite layers fluctuated within the range of 29–41 μm, which constitutes a fraction of the studied sample percentage volume and therefore, the X-radiation penetrated too deeply, thus giving the image of the material from the sample's entire thickness range. In consequence, the reflexes corresponding to graphite are very weak and have a small number of counts. In all cases, a rise in the diffractogram background can be observed in the 2θ range of 20–45º. A rise in the diffractogram background within the above-mentioned angular range is characteristic of the amorphous Al_2O_3 layer, which does not give any reflexes. The minimum of the amorphous "hump" in the layers examined falls on the *d* value 3.22–3.24 Å.

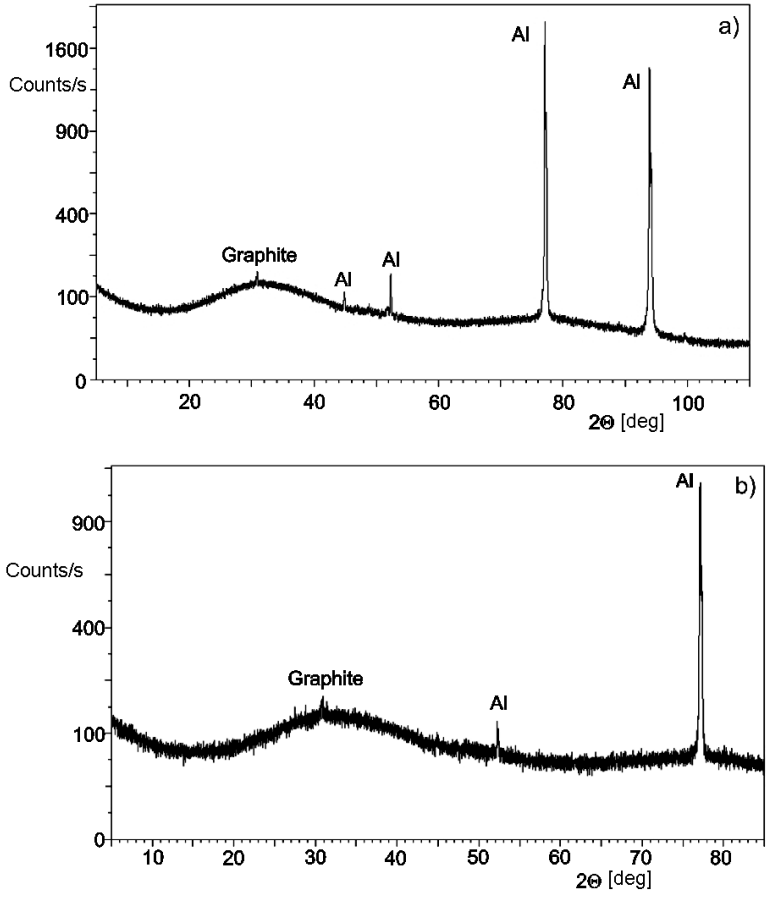

Fig. 4. X-ray diffractograms of the composite layers for samples: a) 4A, b) 4B

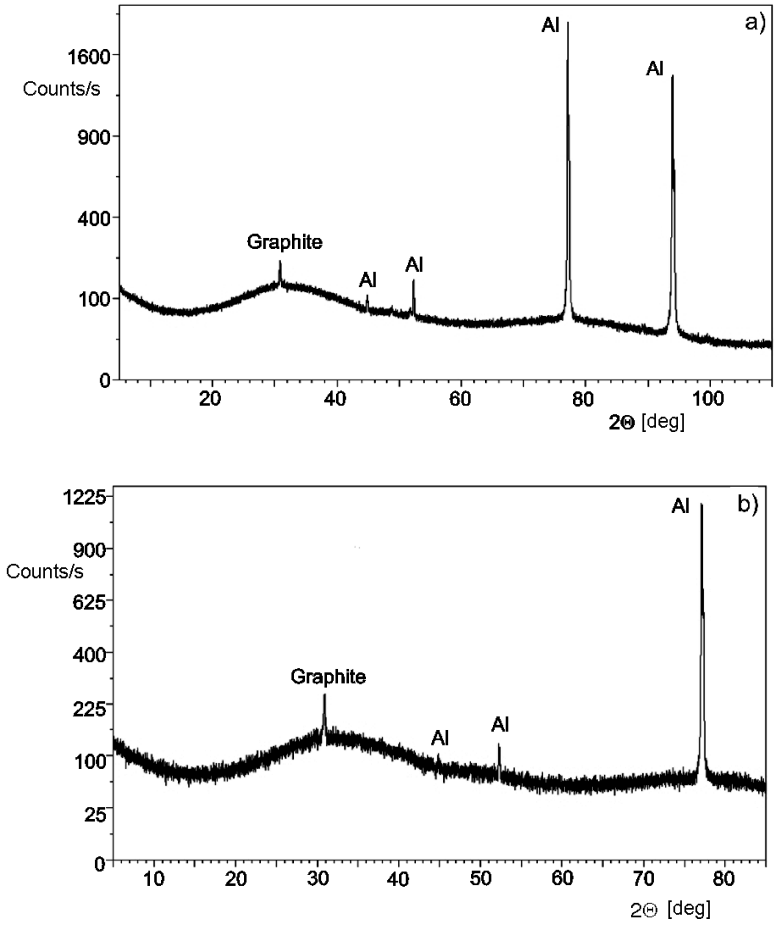

Fig. 5. X-ray diffractograms of the composite layers for samples: a) 4C, b) 4D

The diffractogram in Fig. 4a is dominated by two intense peaks 1.435 Å and 1.223 Å, and a few weak ones, originating from the sample substrate. The only peak belonging to graphite 3.363 Å is characterized by 41 counts/s, which testifies to a small amount of graphite. The diffractogram in Fig. 4b resembles the above-mentioned one. Reflexes 2.342 Å, 2.047 Å, 2.029 Å and 1.435 Å belong to the sample substrate, while the reflex 3.365 Å belongs to the graphite with 41 counts/s. On the diffractogram in Fig. 5a, two strong reflexes, 1.434 Å and 1.223 Å, are visible as well as a few weak reflexes belonging to the sample's substrate. Graphite is marked by one peak 3.362 Å with 82 counts/s, therefore the amount of graphite absorbed into the oxide layer is twice larger than in the two previous samples. The diffractogram in Fig. 5b is similar to those described above. A few weak reflexes and one strong, 1.435 Å, belong to the substrate, whereas the reflex 3.361 Å belongs to graphite, with the number of counts amounting to 116 counts/s, which indicates the largest amount of graphite in the Al_2O_3 layer among the investigated surfaces.

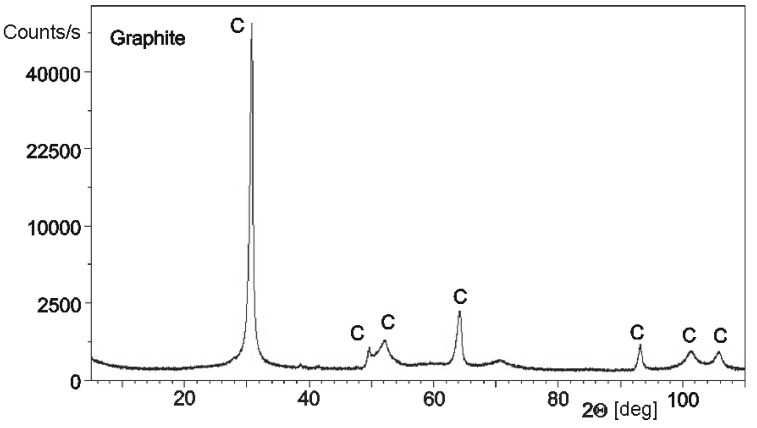

Fig. 6. X-ray diffractogram of graphite

Figure 6 presents a diffractogram of loose graphite. The basic reflex 002, whose value amounts to 3.367 Å and the intensity $I = 100$ achieved a very large number of counts, i.e. 53580 counts/s. This graphite belongs to the polytypic 2H type. The value of reflex 3.367 suggests that we have to do with hexagonal graphite with good lubricating properties.

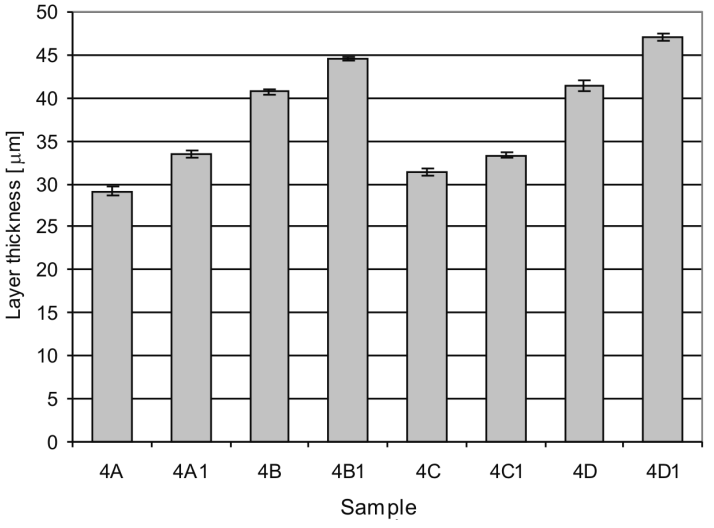

Fig. 7. Influence of current density, electrolyte composition, and temperature on the thickness of the layers produced

As results from the diagram presented in Fig. 7, the values of anodizing voltage, connected with the current density and temperature and composition of electrolyte, have a direct influence on the coatings thickness during the anodizing process. The current density and the electrolyte composition have a decisive influence on the layer

thickness. The influence of electrolyte temperature is scanty, with differences ranging within the error margin of the measuring instrument and a standard deviation. Both, the homogeneity of the oxide layer substrate and the method of the anodizing enabled us to obtain the layers of uniform thickness throughout the sample surface.

Thickness of the Al_2O_3 + graphite layer formed at 293 K amounted to 29.1 μm at 2 A/dm^2 current density and 40. 7 μm at 3 A/dm^2, while at 303 K, it amounted to 31.4 μm at the current density of 2 A/dm^2 and 41.5 μm at 3 A/dm^2 . The thicknesses of Al_2O_3 were was by 6–13% higher than those of composite layers, which results from a better access of the electrolyte ions to the oxidized material.

Microhardness is one of the basic properties connected with the upper layer strength and resistance to wear. Microhardness of oxide layers formed on Al alloys depends on the conditions of the anodizing process, decreasing upon increasing the surface porosity. Based on Fig. 8, it can be concluded that all layers formed in the electrolyte containing graphite have higher microhardness than those formed in the basic electrolyte. The difference in microhardness between the Al_2O_3 layers and the Al_2O_3 + graphite layers varies between 149 and 524 MPa, depending on the current conditions and electrolyte temperature. The nature of changes in microhardness depends mostly on the electrolyte temperature. At of 293 K the layers had higher microhardness during anodizing at current density of 2 A/dm^2, whereas at 303 K the layers had higher microhardness during anodizing at current density of 3 A/dm^2. The above dependences imply that filling of the aluminium oxide fibrous structure results in its enhanced hardness.

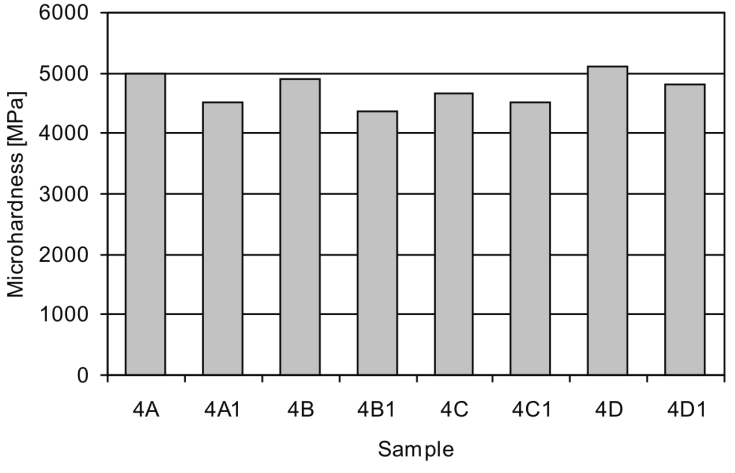

Fig. 8. Effect of anodizing conditions on microhardness of oxide and composite layers

From the difference in size of graphite grains and oxide nanopores it results that the mechanism of obtaining a composite layer consists in simultaneous building-in of graphite grains into the structure of oxide layer during its formation. Figures 9 illus-

trate the relations between the anodizing voltage and the process duration for Al_2O_3 layers and for Al_2O_3 + graphite layers.

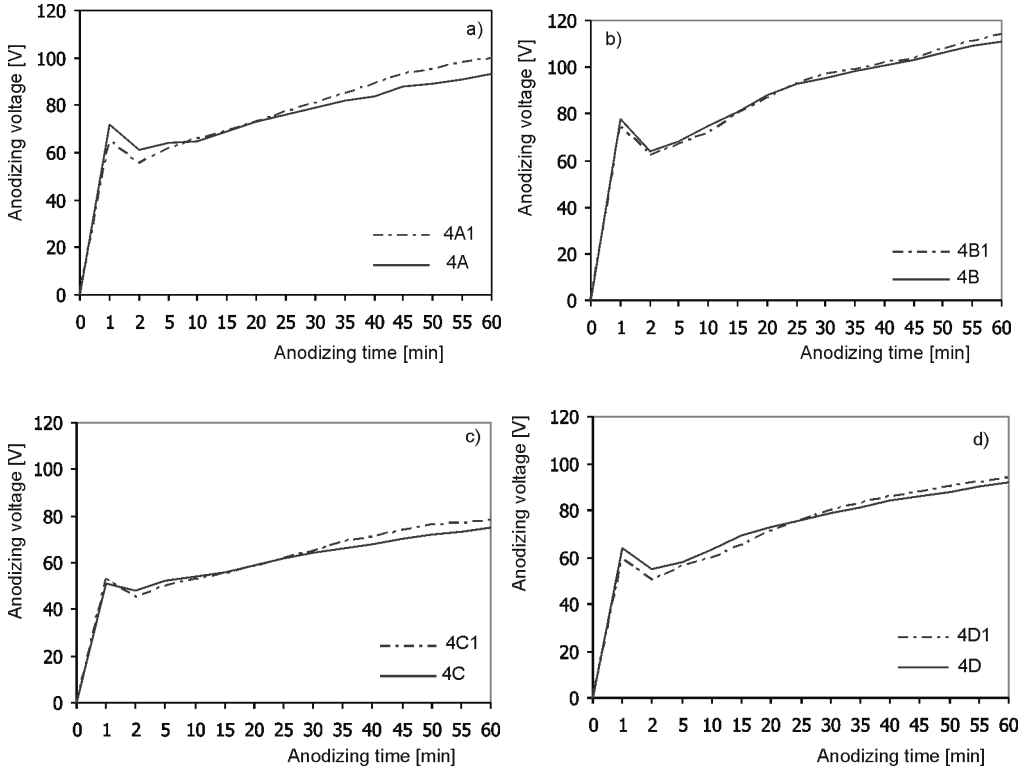

Fig. 9. Relations between anodizing voltage, time of process and composition of electrolyte and temperature for samples: a) 4A1, 4A, b) 4B1, 4B, c) 4C1, 4C, d) 4D1, 4D

During the formation of the Al_2O_3 + graphite layer, the initial anodizing voltage is higher than that of the Al_2O_3 layer. This dependence is connected with partial restriction of access of O^{2-} ions from the electrolyte to the alloy surface, caused by graphite particles. Consequently, growth of the composite layer is slower than that of the Al_2O_3 layer, which in turn results in lower resistance and lower anodizing voltage of the layerin further stages of the process.

4. Conclusions

The developed technology enables obtaining composite layers of aluminium and graphite oxide during one technological process. The largest amount of graphite in the Al_2O_3 layer was obtained at the current density of 3 A/dm^2 and electrolyte temperature of 303 K. Al_2O_3 + graphite composite layers of a smaller thickness, from 6 to 13% have higher microhardness of 3 to 10% when compared to the Al_2O_3 layers fabricated

in the same conditions. At 293 K the layers have higher microhardness after anodizing at the current density of 2 A/dm^2, whereas at 303 K the layers had higher microhardness during anodizing at the current density of 3 A/dm^2.

References

[1] SKONECZNY W., JURUSIK J., BURIAN A., Mater. Sci.-Poland, 3 (2004), 265.
[2] KMITA T., SKONECZNY W., Inż. Chem. Proc., 26 (2005), 735.
[3] MIKULSKAS I., JUODKAZIS S., JAGMINAS A., MEŠKINIS Š., DUMAS J. G., VAITKUS J., TOMAŠIŪNAS R., Opt. Mater., 17 (2001), 343.
[4] LÓPEZ V., OTERO E., BAUTISTA A., GONZÁLEZ J.A., Surf. Coat. Tech., 124 (2000), 76.
[5] HUCZKO A., *Nanorurki węglowe. Czarne diamenty XXI wieku* (*Carbon Nanotubes. Black Diamonds of 21st Century*), Warsaw Univ. Publ., Warsaw, 2004.
[6] DE LAET J., TERRYN H., VEREECKEN J., Thin Solid Films, 320 (1998), 241.
[7] SKONECZNY W., Inż. Pow., 2 (2000), 21.

Received 30 March 2007
Revised 27 July 2007

Materials Science-Poland, Vol. 25, No. 4, 2007

Coordination properties of the diethyl 2-quinolilmethylphosphonate ligand with chloride and nitrate transition-metal salts

B. ŻUROWSKA[1], J. MROZIŃSKI[1*], J. OCHOCKI[2]

[1]Faculty of Chemistry, University of Wroclaw, ul. F. Joliot- Curie 14, 50-383 Wroclaw, Poland

[2]Department of Bioinorganic Chemistry, Faculty of Pharmacy, ul. Muszyńskiego 1, Medical University, 90-151 Łódź, Poland

A new series of the chloride and nitrate transition metal complexes containing the ligand diethyl 2-quinolylmethylphosphonate (2-qmpe) of general formula $M(2\text{-qmpe})(NO_3)_2$ (M = Cu, Co), $[Zn(2\text{-qmpe})(H_2O)_2NO_3]NO_3 \cdot H_2O$, $[Ni(2\text{-qmpe})(H_2O)_2NO_3]NO_3$, $M(2\text{-qmpe})_2Cl_2$ (M = Cu, Ni, Co, Pd) and $M(2\text{-qmpe})Cl_2$ (M = Co, Zn) were prepared. The complexes were identified and characterized by elemental analysis, spectroscopic and magnetic studies. Ligand containing two donor atoms, heterocyclic nitrogen and phosphoryl oxygen atoms exhibits different coordination properties. It was shown that the ligand binds in a bidentate chelate manner via the quinoline nitrogen and the phosphoryl oxygen atoms (complexes with 1:1 metal to ligand molar ratio) and it can also acts as a monodentate ligand coordinated through the nitrogen in the Pd(II) or oxygen atom in the Cu(II) and Co(II) complexes (complexes with 1:2 metal to ligand molar ratio). The magnetic behaviour of the Cu(II), Ni(II) and Co(II) and spectroscopic investigation of Zn(II) complexes suggests mononuclear structure of all the complexes and the existence of a weak intermolecular exchange coupling between magnetic centres inside crystal lattice.

Key words: *N,O ligand; transition-metal complexes; spectroscopy; magnetism*

1. Introduction

Many of chelating ligands containing nitrogen and oxygen donor atoms show biological activity and are of special interest due to a variety of ways in which they are bonded to metal ions [1, 2]. The ligand species include some organophosphorus compounds containing phosphonic acids and their esters, derivatives of pyridine or quinoline. These ligands and their metal complexes exhibit significant biological and pharmacological activity [3–7]. These compounds might be considered as analogues of

*Corresponding author, e-mail: jmroz@wchuwr.chem.uni.wroc.pl

naturally occurring phosphates. Aminophosphate complexes of platinum group metals have attracted attention as a result of their potential antitumor agents [3–8]. Biological activity of coordination compounds depends on the presence of metal ions [10]. Hence the investigation of interaction between the phosphonate ligands containing mononitrogen aromatic bases such as pyridine and quinoline with various metal ions may contribute to a better understanding of their biological activity and facilitate meaningful biochemical and pharmacological studies.

It is worth noting that quinoline derivatives, contrary to pyridine derivatives are barely studied groups of ligands in coordination chemistry. A structural study of these ligands seen also as pyridine derivatives seems interesting and useful in view of numerous applications [11].

The present paper is a continuation of our earlier investigation of the coordination compounds of the diethyl 2-pyridyl-, 4-pyridyl and 2-quinolylmethylphosphonate (Fig. 1) ligands (2-pmpe, 4-pmpe, 2-qmpe, respectively), containing two potential donor atoms, the heterocyclic nitrogen and phosphoryl oxygen atoms, with the several transition-metal ions and various anions [9, 13–17]. These were investigated with regard to their spectral and magnetic properties, which provide a chemical bases for their biological activity.

The crystal structures of the representative compounds, i.e. $Co(2\text{-pmpe})_2Cl_2$ [14], $[Co(2\text{-pmpe})_2(H_2O)_2](ClO_4)_2$ [15] (with N,O-bonded chelate ligand) and $[Co(4\text{-pmpe})_2(H_2O)_2](ClO_4)_2\cdot 2H_2O$ (with N,O-bridging ligand) [9] as well as $[M(2\text{-qmpe})_4(H_2O)_2](ClO_4)_2$ (with O-bonded ligand), where M = Ni, Mn [16] were determined. It is worth noting that the interaction of 2-pmpe and 2-qmpe with some copper(II) salts leads to a novel oxidative P-dealkylation/dephosphorylation reaction of the ligand [17] in which pyridyl-2-carboxylate and quinolil-2-carboxylate, respectively ligands are produced. The results of structural and physicochemical studies of such complexes, as has been shown by us earlier [9, 14–17], are interesting from the point of view of inorganic and bioinorganic chemistry as well as their activity in biological systems.

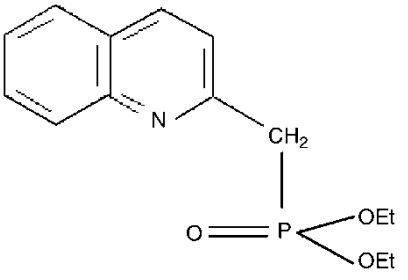

Fig. 1. Formula of the 2-quinolylmethylphosphonate (2-qmpe) ligand

Recently, we have reported the coordination properties of the 2-qmpe ligand towards perchlorate transition-metal salts [16]. In this case, the ligand is able to coordinate only by phosphoryl oxygen atom. The quinolil nitrogen atom is not included in the coordination. Here we extend our studies to the synthesis and characterization of new nitrate and chloride compounds for the purpose of study the coordination behav-

iour of diethyl 2-quinolilmethylphosphonate (2-qmpe), stoichiometries and geometric preferences of the resulting species. Additionally, our interest is the study of stability in solution metal(II) compounds. Unfortunately, we have not succeeded in preparing crystals suitable for the X-ray studies of the complexes. Physicochemical properties of the compounds and their possible structures are discussed based on the spectral (infrared, electronic and EPR spectra) and magnetic studies. Our findings on these complexes will be compared with results of our previous studies of the perchlorate metal-transition compounds with 2-qmpe.

2. Experimental

Reagents and physical measurements. The starting materials and solvents for synthesis were obtained commercially and used as received. Metal content was determined using a Carl Zeiss Jena atomic absorption spectrophotometer and an ARL Model 3410 ICP spectrometer. Elemental analyses were carried out using a Perkin -Elmer elemental analyzer 2400CHN. Solid-state electronic spectra (28 000–4000 cm^{-1}) were determined with a Cary 500 spectrophotometer. Solid-state EPR spectra were recorded at room temperature and at 77K on a Bruker ESP 300E spectrometer operating at X-band, equipped with a Bruker NMR gaussmeter ER 0.35 M and a Hewlett Packard microwave frequency counter HP 5350B.

Magnetic measurements were carried out on solid polycrystalline samples by the Faraday method in the temperature range 77–300 K by using a sensitive Sartorius M-25D electrobalance. The susceptometer was equipped with an Oxford Instruments CF-1200 continuous-flow cryostat and an electromagnet operating at 5.25 kG. The calibrant employed was $HgCo(NCS)_4$ for which the susceptibility was assumed to be $16.44\times10^{-6} cm^3\cdot g^{-1}$ [18]. The corrections for diamagnetism of the constituent atoms were made by use of Pascal constants [19] and the effective magnetic moments were calculated from $\mu_{eff} = 2.83(\chi_M T)^{1/2}$ using temperature-independent paramagnetism (TIP) [20–22] of [$cm^3\cdot mol^{-1}$] 60×10^{-6} for Cu (**1**), 235×10^{-6} for Ni (**2**), 150×10^{-6} for Co (**3**), 522×10^{-6} for Co (**7**) and 568 for Co (**8**) compounds.

Synthesis of ligand and complexes. 2-qmpe was prepared by phosphorylation of 2-chloromethylquinoline with diethyl phosphine according to the procedure described in detail elsewhere [16] and checked for purity by spectroscopic and analytical methods. The nitrate complexes were prepared by dissolving the appropriate hydrated metal nitrate (1 mmol) in ethanol (10 cm^3) and adding to a solution of the ligand (1 or 2 mmol) in ethanol (15 cm^3). After filtration of the hot reaction mixture to remove any impurities, the complexes crystallized on cooling. In some cases, however, evaporation of a part of the solvent was necessary before the crystallization would occur.

The chloride complexes 1:1 and 1:2 were prepared as described above using metal chloride hexahydrate and 2-qmpe ligand (1 mmol) and (2 mmol), respectively. Their calculated and determined compositions are as follows:

Anal. calc. for $[C_{14}H_{18}N_3PO_9Cu]$ (**1**):	C, 36.01; H, 3.89; N, 9.00; Cu, 13.61 %
Found	C, 36.65; H, 3.40; N, 8.59; Cu, 13.76 %
Anal. calc. for $[C_{14}H_{22}N_3PO_{11}Ni]$ (**2**):	C, 33.76; H, 4.46; N, 8.44; Ni, 11.78 %
Found:	C, 33.65; H, 4.30; N, 8.59; Ni, 11.12%
Anal. calc. for $[C_{14}H_{18}N_3PO_9Co]$ (**3**):	C, 36.37; H, 3.93; N, 9.09; Co,12.75%
Found:	C, 36.42; H, 3.58; N, 9.29; Co, 12.65%
Anal. calc. for $[C_{14}H_{24}N_3PO_{12}Zn]$ (**4**):	C, 32.17; H, 4.64; N, 8.04; Zn, 12.51 %
Found:	C, 32.65; H, 4.30; N, 8.59; Zn, 12.65%
Anal. calc. for $[C_{28}H_{36}N_2P_2O_6Cl_2Cu]$ (**5**):	C, 48.52; H, 5.25; N, 4.04; Cu, 9.17 %
Found:	C, 49.14; H, 5.50; N, 4.29; Cu, 9.33%
Anal. calc. for $[C_{28}H_{36}N_2P_2O_6Cl_2Ni]$ (**6**):	C, 48.86; H, 5.28; N, 4.07; Ni, 8.53%
Found:	C, 48.65; H, 5.30; N, 4.32; Ni, 8.66%
Anal. calc. for $[C_{14}H_{18}NPO_3Cl_2Co]$ (**7**):	C, 41.10; H, 4.44; N, 3.42; Co, 14.40, %
Found:	C, 41.61; H, 4.56; N, 3.66; Co, 14.62%
Anal. calc. for $[C_{28}H_{36}N_2P_2O_6Cl_2Co]$ (**8**):	C, 48.85; H, 5.28; N, 4.07; Co, 8.56%
Found:	C, 49.01; H, 5.30; N, 4.59; Co, 8.65%
Anal. calc. for $[C_{14}H_{28}NPO_3Cl_2Zn]$ (**9**):	C, 40.46; H, 4.37; N, 3.37; Zn, 15.73 %
Found:	C, 40.65; H, 4.30; N, 3.59; Zn, 15.65%
Anal. calc. for $[C_{28}H_{36}N_2P_2O_6Cl_2Pd]$ (**10**):	C, 45.69; H, 4.94; N, 3.81; Pd, 14.46 %
Found:	C, 45.65; H, 4.30; N, 3.59; Pd, 14.65%

3. Results and discussion

The stoichiometry of the investigated complexes was established from the elemental analysis and metal determination. The analytical results demonstrated that the 2-qmpe is a ligand able to form coordination compounds with M(II) nitrate and chloride salts with the M(II) to 2-qmpe ligand molar ratio 1:1 and 1:2 with the following stoichiometries: M(2-qmpe) $(NO_3)_2$, [M = Cu (**1**), Co (**3**)], $[Ni(2\text{-qmpe})(H_2O)_2NO_3]NO_3$ (**2**), $[Zn(2\text{-qmpe})(H_2O)_2NO_3]NO_3 \cdot H_2O$ (**4**), M(2-qmpe)Cl_2 (M = Co (**7**), Zn (**9**)) and M(2-qmpe)$_2Cl_2$ [M = Cu (**5**), Ni(**6**), Co (**8**), Pd (**10**)]. The interaction of 2-qmpe with $CuCl_2$ salt produces an unstable compound of the formula Cu(2-qmpe)$_2Cl_2$ (**5**), [17] undergoing an oxidative decomposition when exposed to air. In this reaction, the compound of the formula $Cu(2\text{-qca})_2 \cdot H_2O$ (2-qca – quinoline-2-carboxylate ion) is formed as has been presented elsewhere [17].

3.1. Spectroscopic properties

In general, the IR spectra of the all complexes are very complex and complete assignment of the bands is difficult. Only these bands which are diagnostic for the nature of the metal(II) to ligand bonding have been analysed (Table 1).

Table 1. Selected infrared frequencies [cm^{-1}] of metal complexes with 2-qmpe

Compound	ν(P=O)	δ(C=N)[a]	δ(C=N)[b]	ν(M–N(L)	ν(M–O) ν(M–Cl)	Other bands of NO_3
2-qmpe	1254 vs	620w	396 w			
$Cu(2\text{-qmpe})(NO_3)_2$ (**1**)	1172 s	640w	408 w	279 m	309 m, 327 m	1013 vs[c], 1274 vs, 1516 vs
$[Ni(2\text{-qmpe})(H_2O)_2NO_3]NO_3$ (**2**)	1190 m	640w	415 w	276 v,br	300 v, br	1020 vs[c], 1292 s, 1384 vs, 1496 s
$Co(2\text{-qmpe})(NO_3)_2$ (**3**)	1160 s	640w	410 w	268 m	300 m	1005 vs[c], 1245 vs, 1470 vs
$[Zn(2\text{-qmpe})(H_2O)_2NO_3]NO_3{\cdot}H_2O$ (**4**)	1190 s	636w	408 w	283 w	310 m	1005 vs[c], 1270 s, 1384 vs, 1510 s
$Cu(2\text{-qmpe})_2Cl_2$ (**5**)	1225 s	635w	415 w		310 m	
$Ni(2\text{-qmpe})_2Cl_2$ (**6**)	1187 m	635w	412 w	275 m	212 m	
$Co(2\text{-qmpe})Cl_2$ (**7**)	1189 vs	636w	404 w	262 w	308 m, 338 m	
$Co(2\text{-qmpe})_2Cl_2$ (**8**)	1224 s	627w	399 w		303 m, 334 m	
$Zn(2\text{-qmpe})Cl_2$ (**9**)	1180	638	416	270 m	306 vs, 337 vs	
$Pd(2\text{-qmpe})_2Cl_2$ (**10**)	1260 vs	640w	418 w	272 w	352 m	

[a]In-plane-ring quinoline deformation.
[b]Out-of-plane ring deformation.
[c]Overlapped with ν(P–OC).

In the IR spectra of the complexes studied (except $Cu(2\text{-qmpe})_2Cl_2$ (**5**) and $Co(2\text{-qmpe})_2Cl_2$ (**8**)), the bands due to stretching modes of the quinoline C=C and C=N bands in the region 1600–1500 cm^{-1} are not shifted appreciably, whereas the characteristic out-of-plane and in-plane ring deformation bands of the 2-substituted quinoline ring (observed at 396 and 620 cm^{-1}, respectively, in free ligand) are shifted to higher frequencies by ca. 8–22 cm^{-1} and 16–20 cm^{-1}, respectively, suggesting coordination of the quinolyl nitrogen donor atom [23, 24]. In the spectrum of $Cu(2\text{-qmpe})_2Cl_2$ (**5**) and $Co(2\text{-qmpe})_2Cl_2$ (**8**) compounds, characteristic deformation bands of the quinoline ring remain at the same position as for free ligand, indicating that the quinolyl nitrogen atom is not involved in the coordination sphere.

The strong absorption band at 1254 cm^{-1} corresponding to the P=O stretching frequencies of a free ligand, in the spectra of all complexes (except $Pd(2\text{-qmpe})_2Cl_2$ (**10**)) is shifted by ca. 30–70 cm^{-1} towards lower frequencies, indicating coordination of the phosphoryl oxygen to the metal ions. A larger shift of this band is observed when 2-qmpe acts as N,O-bonded chelate ligand. Thus the spectrum of **5** indicates that 2-qmpe acts as O-bonded monodentate ligand. In the spectrum of **10** containing the N-

bonded quinoline group, the characteristic ligand band assigned to the P=O group remains almost at the same position as in the free ligand, indicating monodentate coordination of 2-qmpe. In fact, X-ray structural determination [25] of *trans*-[Pd(2-qmpe)$_2$Cl$_2$] confirmed that the metal ion is bound in a N-monodentate way to the pyridine. Other ligand bands characteristic of the phosphonate moiety, δ(PO-C) at 1130–1170 cm^{-1} and ν(P–OC) at 1050–1030 cm^{-1} do not show any significant shifts upon M(II) complex formation. These assignments are consistent with our earlier observation of the IR spectral features of this ligand [16].

For Cu(2-qmpe)(NO$_3$)$_2$ (**1**) and Co(2-qmpe)(NO$_3$)$_2$ (**3**) it appears that the nitrate group is chelating bidentate in nature. For these compounds, nitrate ions form strong splitting bands at 1499–1470 cm^{-1} and 1274–1245 cm^{-1} with large separation (204–225 cm^{-1}). The $\nu_1 + \nu_4$ region of the spectrum contains two weak broad bands at about 1720–1770 cm^{-1} supportive for this assignment. The band of the ionic nitrate is not observed.

The Ni(2-qmpe)(H$_2$O)$_2$NO$_3$]NO$_3$ (**2**) and Zn(2-qmpe)(H$_2$O)$_2$NO$_3$]NO$_3$·H$_2$O (**4**) complexes contain both ionic and bidentate coordinated NO$_3$ groups [26,27]. Very strong band at 1384 cm^{-1} assigned as ν_3 of ionic nitrate and the splitting of the band ν_3 at 1510–1496 cm^{-1} as the ν_1 and ν_4 modes of coordinated NO$_3$ is observed. The position of ν_1 and ν_4 and their separation of 204–240 cm^{-1} clearly indicate bidentate coordination of the nitrate groups. The presence of both ionic and coordinated nitrate is also demonstrated by the occurrence of three distinct absorption bands at 1700–1800 cm^{-1} ($\nu_1 + \nu_4$) due to combination of vibrational modes of ionic and coordinated nitrate. The ν_2 modes about 810 and 830 cm^{-1} were also observed. The band observed at far IR region at 300–327 cm^{-1} in the spectrum of the nitrate compounds has been assigned to a ν(M-O) mode for coordinated nitrate ligand [28].

The analysis of nitrate compounds by IR spectroscopy was carried out both as dispersion in KBr and, where appropriate, as mulls in fluorinated mineral oil (Kel-F). It was because of the compounds Ni and Zn (recorded in KBr) complexes displaying a strong band at 1390 cm^{-1} characteristic of the asymmetric stretch of free nitrate anion in addition to coordinated nitrate bands. Grinding of the complexes with KBr can give rise to displacement of a part of the nitrate ions by bromide under moderate pressure and uncertain assignment to be made of a free nitrate ion. This phenomenon has been observed in nitrate complexes [29, 30]. In this study, substantial differences between samples prepared in KBr and Kel-F have not been observed.

The presence of water molecules in the compounds is deduced from the elemental analysis and IR spectrum [26]. The IR spectrum of Zn(2-qmpe)(H$_2$O)$_2$NO$_3$]NO$_3$·H$_2$O (**4**) have a sharp δ(OH$_2$) bending mode at 1656 cm^{-1} and broad, jagged ν(OH) absorption bands with maxima at 3240 and 3430 cm^{-1}, confirming the presence of lattice water molecules linked by the hydrogen bond and coordinated water, respectively. The Ni(2-qmpe)(H$_2$O)$_2$NO$_3$]NO$_3$ (**2**) compound shows in the O–H stretching and bending region only the presence of coordinated water molecules (3410 and 1655 cm^{-1}, respectively). IR spectra of the Cu(II) (**1**, **5**), Co(II) (**7**, **8**), Zn (**9**),) and Pd(II) (**10**) compounds show the absence of all vibrations which might be assigned to water molecules.

The far IR region of $Pd(2\text{-qmpe})_2Cl_2$ (**10**) shows one band at 352 cm^{-1} attributed to the Pd–Cl stretching vibration, suggesting that the compound is the *trans* square-planar in the D_{2h} symmetry according to X-ray crystal structure determination [25]. For chloride copper (**1**) and nickel (**2**) compounds the bands at 310 and 210 cm^{-1} are observed, respectively. The ν(M-Cl) symmetric and asymmetric frequencies in other chloride compounds are consistent with a pseudotetrahedral environment [26, 31–34]. Namely, for $Zn(2\text{-qmpe})Cl_2$ (**9**) strong bands at 306 and 337 cm^{-1} are observed. It is interesting that the interaction of the $CoCl_2$ with 2-qmpe leads to the formation of compounds displaying different stoichiometries, i. e. $Co(2\text{-qmpe})Cl_2$ (dark blue) (**7**) and $Co(2\text{-qmpe})_2Cl_2$ (dark green-blue) (**8**). In the far IR region, very strong bands at 303 and 334 cm^{-1} as well as at 308 and 339 cm^{-1}, respectively, are observed, characteristic of tetrahedral environment of the cobalt(II) ion.

Table 2. Electronic and EPR spectral data of the metal complexes with 2-qmpe

Compound	Wavenumber [cm^{-1}]	D_q [cm^{-1}]	B [cm^{-1}]	Splitting factor g	
				298 K	77 K
$Cu(2\text{-qmpe})(NO_3)_2$ (**1**)	14 280			$g_{\parallel} \cong 2.3$ $g_{\perp} = 2.10_2$	$g_{\parallel} = 2.31_1$ $g_{\perp} = 2.07_7$
$[Ni(2\text{-qmpe})(H_2O)_2NO_3]NO_3$ (**2**)	24 690, 21 050 sh, 14 710, 13 070 sh, 8560	860	910	no line	
$Co(2\text{-qmpe})(NO_3)_2$ (**3**)	21050, 19050, 8170	890	865		
$Cu(2\text{-qmpe})Cl_2$ (**5**)	12 100	780	800	$g_{\parallel} = 2.37_7$ $g_{\perp} = 2.10_4$	$g_{\parallel} = 2.32_3$ $g_{\perp} = 2.09_4$
$Ni(2\text{-qmpe})_2Cl_2$ (**6**)	23 250, 28 840, 13 160, 7810	400	750	no line	
$Co(2\text{-qmpe})Cl_2$ (**7**)	16 345, 6930	368	778	no line	$g = 2.11$
$Co(2\text{-qmpe})_2Cl_2$ (**8**)	16 310, 6400			no line	$g = 2.16$

Basic features of the absorption spectra of the studied compounds are presented in Table 2. The electronic spectrum of $Cu(2\text{-qmpe})(NO_3)_2$ (**1**) shows one broad asymmetric band with the maximum at 14280 cm^{-1} characteristic of the transition in O_h symmetry. The position as well as the shape of this band suggests $CuNO_5$ chromophore in a tetragonally elongated octahedral geometry [35]. The electronic spectrum of the nitrate (**2**) and chloride nickel(II) (**6**) complexes exhibit spin-allowed bands and also spin-forbidden absorption observed as a shoulder typical of high-spin octahedral structure [36]. The d-d spectrum of $Co(2\text{-qmpe})(NO_3)_2$ (**3**) also show bands typical of high-spin an octahedral environment [37, 38].

The spectrochemical parameters (D_q and B) for octahedral compounds calculated with well-known methods [36, 37] are D_q = 860, 890 and 780 cm^{-1} for (**2**), (**3**) and (**6**) compounds, respectively. The values of D_q for (**2**) and (**3**) are in good agreement with

those expected for isomorphous nickel and cobalt compounds [36, 37]. The D_q value of (**6**) ($N_2O_2Cl_2$) is lower than this obtained for (**2**) (N_2O_4), reflecting weak ligand field produced by the chloride ligand. A rather high value of *B* calculated for **2** and **3** (910, 865 cm^{-1}, respectively) may suggests a distorted octahedral geometry [36, 37].

The electronic spectrum of Cu(2-qmpe)$_2$Cl$_2$ (**5**) shows one broad asymmetric band with the maximum centred at 12 100 cm^{-1} and shoulder at about 9100 cm^{-1}. Bands lower in energy than ca. 25 000 cm^{-1} in the spectra of the chloride complexes may be assigned to chlorine-to-copper(II) charge transfer bands and confirm their coordination to the Cu(II) centre [38]. Therefore, yellow colour of **5** for which the tetrahedral coordination is proposed is due to the charge-transfer band observed at 24 700 cm^{-1} [39].

The electronic spectra of **7** and **8** are typical of pseudotetrahedral ligand arrangements around Co(II) [35, 38, 39]. In the spectra, two sets of the bands can be distinguished; one in the visible region and the other in the near infrared one. The presence of three bands in the near-infrared region is typical of ligands which differ significantly in strength. The centres of the multiple visible bands appears at 16 340 and 16 310 cm^{-1} for **7** and **8**, respectively. Splitting of the band is probably due to the interaction with a doublet through spin-orbit coupling [40]. The near-IR multiple bands are perceptibly broadened and show a long tail towards lower wavenumbers. The complexity is caused by the components of $^4T_1(F)$ level which becomes allowed transition in the C_{2v} symmetry [41]. A large splitting of ν_2 bands (4000 cm^{-1}) can be attributed to a large distortion from the ideal tetrahedral symmetry [40–42]. The calculated parameters D_q and *B* using the secular equation for tetrahedral cobalt(II) transition energies [43, 44] are based on the centres of gravity of the respective multiplets. These values (400, 750 cm^{-1} and 370, 780 cm^{-1}, respectively for **7** and **8** are consistent with those reported for tetrahedral Co(II) complexes [39, 41] and are in agreement with mixed nitrogen-oxygen donation [45]. The higher value of D_q and lower value of *B* calculated for Co(2-qmpe)Cl$_2$ (**7**) are consistent with contribution of the nitrogen atom of the quinoline ring to the ligand field in this complex.

3.2. Magnetic properties

The X-band EPR spectrum (Table 2) of a polycrystalline sample of **1** shows at room temperature a resonance line with broad perpendicular and parallel components ($g_{\|} \cong 2.30$, $g_{\perp} = 2.08_2$). At liquid nitrogen temperature, the spectrum indicates the same line with $g_{\|} = 2.31_1$, $g_{\perp} = 2.07_7$). The spectrum is characteristic of elongated tetragonal stereochemistry [46]. The high value of $g_{\|}$ suggests planar geometry of $CuNO_3$with relatively strong axial bonding. The spectrum of **5** at room temperature is of axial type with $g_{\|} = 2.37_7$, $g_{\perp} = 2.10_4$ normal for copper in a tetrahedral environment [46, 47]. The spectrum is independent of temperature. It is interesting to note that we observed lack of a transition in the $\Delta M = 2$ region of the spectra (i.e. 1600 G). This seems to indicate that these complexes are monomeric in their nature, as is confirmed by magnetic measurements. Nickel **2** and **6** compounds do not exhibit X-band spectra, and **3,**

7 and **8** show no lines at room temperature but a single broad line was observed at 77 K for the cobalt(II) compounds (g = 2.14, 2.11 and 2.16, respectively).

Table 3. Magnetic data of metal complexes with 2-qmpe ligand

Compound	C [$cm^3 \cdot mol^{-1} \cdot K$]	Θ [K]	$10^6\chi_M$ [$cm^3 \cdot mol^{-1}$]	μ_{eff} [B.M.]	
				298 K	77K
(**1**) $Cu(2–qmpe)(NO_3)_2$	0.47	–2.2	1560	1.92	1.93
(**2**) $[Ni(2–qmpe)(H_2O)_2NO_3]NO_3$	1.35	–1.9	4760	3.31	3.28
(**3**) $Co(2–qmpe)(NO_3)_2$	19.9	–6.4	9260	4.60	4.29
(**5**) $Cu(2–qmpe)_2Cl_2$	0.42	–1.6	1410	1.83	1.84
(**6**) $Ni(2–qmpe)_2Cl_2$	1.10	–3.0	4160	3.12	3.10
(**7**) $Co(2–qmpe)Cl_2$	2.38	–1.4	8010	4.37	4.36
(**8**) $Co(2–qmpe)_2Cl_2$	2.84	–0.8	9630	4.76	4.77

Variable-temperature (77–300 K) magnetic susceptibility data were collected for all studied paramagnetic complexes (Table 3). The effective magnetic moments for **1**, **2**, **3** and **6** compounds are within usually observed range of experimental values for high-spin complexes in octahedral environment [48]. The magnetic moments of $Co(2\text{-qmpe})Cl_2$ (**7**) and $Co(2\text{-qmpe})_2Cl_2$ (**8**) are in accordance with tetrahedral stereochemistries [48]. The negative values of the Weiss constants (θ) obtained from the equation $\chi_M = C/(T - \theta)$ within the measured temperature range may suggest the possibility of weak magnetic interaction between magnetic centres inside the crystal lattice at lower temperatures. Based on the spectral and magnetic data, a mononuclear structure is proposed for all studied compounds.

4. Summary

The results described in the present paper have shown that the complexes of 2-qmpe ligand with nitrate salts of Cu(II) and Co(II) are six-coordinate formed by one N,O-bonded chelate 2-qmpe ligand and two bidentate nitrate ions (MNO_5 chromophore), while six-coordination of Ni(II) and Zn(II) nitrate complexes are formed via one N,O-bonded 2-qmpe ligand, one bidentate nitrate ion and two water molecules (MNO_5 chromophore). Unexpectedly, 2-qmpe in its compounds with cobalt chloride adopts monodentate and bidentate mode giving rise to tetrahedral arrangement of cobalt ions in both compounds. In $Co(2\text{-qmpe})_2Cl_2$, cobalt ions are coordinated by two chloride ions and two phosphoryl oxygen atoms (CoO_2Cl_2 chromophore). However, in $Co(2\text{-qmpe})Cl_2$, 2-qmpe acts in bidentate manner through pyridyl nitrogen and phosphoryl oxygen atoms ($CoNOCl_2$ chromophore). In the Pd(II) compound, 2-qmpe acts as an N-bonded ligand (PdN_2Cl_2 chromophore). This compound has a *trans* square-planar structure as was demonstrated by the crystal structure [8].

The previous report [16] described the unusual O-monodentate properties of the 2-qmpe ligand towards divalent transition metal perchlorate salts. In this case, the metal(II) ions react with the ligand in 1:4 metal to ligand molar ratio. As has been presented in this paper, 2-qmpe reacts with other metal salts in 1:1 or 1:2 metal to ligand molar ratios and indicates different coordination properties. Namely, 2-qmpe is able to coordinate in a didentate chelate manner via the quinoline nitrogen and the phosphoryl oxygen donor atoms (complexes with 1:1 metal to ligand ratio) and it can also act as a monodentate ligand coordinated through the nitrogen or oxygen atom. Thereby, the 2-qmpe ligand engagement into monodentate coordination prefers coordination by O donor atoms (perchlorate metal compounds, chloride cobalt and copper compounds) in contrast to compound with $PdCl_2$. In this case Pd, as a soft metal, coordinates by N-donor atoms. The non-coordinating behaviour of the pyridine nitrogen atom is probably due to poor donor properties in combination with possible steric constraints and/or crystal packing effects.

It is interesting that the interactions of 2-pmpe and 2-qmpe ligands with some Cu(II) salts studied earlier [17] lead to formation of solid complexes, unstable in solution in air. The results of this studies clearly demonstrate that copper(II) ions promote/enhance decomposition of the ligands and catalyze oxidation by atmospheric oxygen according to the scheme: $R–CH_2P(O)–(OEt)_2 \rightarrow R–COOH + OH–P(O)(OEt)_2$. Other divalent transition metal ions do not exhibit this activity under similar experimental conditions [9, 16, 17].

The results obtained earlier indicate that copper(II) coordination compounds with N,O-bonded (chelate or bridging) ligands 2-pmpe and 4-pmpe with nitrate and perchlorate metal salts [8, 16] are stable in solution. However, those with monodentate coordinating 2-pmpe and 2-qmpe ligands after exposition to air undergo decomposition [17]. The study presented in this paper supports our earlier supposition. Namely, $Cu(2\text{-qmpe})(NO_3)_2$ compound in which 2-qmpe acts as N,O-bonded chelate ligand is stable in solution, is probably stabilized by didentate coordination. However, as mentioned earlier [6], the interaction of 2-qmpe with $CuCl_2$ salt produces an unstable compound in which 2-qmpe acts as O-bonded monodentate ligands. In this case, Cu(II) ion promotes and catalyzes oxidative conversion of 2-qmpe to $R–COO^-$ ligand. However, nitrate and chloride complexes with other divalent metal salts with N,O bonded chelate ligand (Cu, Ni, Zn) and O-bonded ligand (Co) and also N-bonded ligand (Pd) are stable in solution

Finally, it is worth to stress that the chemical degradation of phosphonates, due to their role played in the environment as pesticides and herbicides, is of fundamental importance and will be the subject of further studies.

Acknowledgments

The work was supported by the Polish Ministry of Science and Higher Education **(**Grant No. 1T09A 12430 **(**J.M.**)**, and Grant No. 502-13-339 and 503-3016-2 of the Medical University of Łódź **(**J.O.**)**.

References

[1] SYAMAL A., MAURYA M.R., Coord. Chem. Rev., 95 (1985), 95.
[2] KUHAR V.P., HUDSON H.R., [in:] *Aminophosphonic and Aminophosphinic Acids. Chemistry and Biological Activity*, V. P. Kukhar, H.R. Hudson (Eds.), Wiley, London, 1999.
[3] ARANOWSKA K., GRACZYK J., CHĘCIŃSKA L., PAKULSKA W., OCHOCKI J., Pharm., 61 (2006), 457.
[4] ZIĘBA R., MALINOWSKA K., WIEWIÓROWSKI M., GRACZYK J., Acta Pol. Pharm., 57 (2000), 136.
[5] CHĘCIŃSKA L., WAŁECKA M., OCHOCKI J., ARANOWSKA K., Acta Cryst., E 59,(2003), 350.
[6] BRZEZIŃSKA-BŁASZCZYK E., MIŃCIKIEWICZ M., OCHOCKI J., Eur. J. Pharmacol., 298, (1996), 155.
[7] KOSTKA B., OCHOCKI J., Pharm., 51 (1996), 990.
[8] OCHOCKI J., KOSTKA K., ŻUROWSKA B., MROZIŃSKI J., GAŁDECKA E., GAŁDECKI Z., REEDIJK J., J. Chem. Soc. Dalton Trans., (1992), 2955.
[9] TUŠEK-BOŽIĆ L., FURLANI A., STARCIA V., DE CLERCQ E., BALZARINI J., J. Inorg. Biochem., 72 (1998), 201.
[10] BLOEMINK M.J., DORENBOS J.P., HEETEBRIJ R.J., KEPLER B.K., REEDIJK J., ZAHN H., Inorg. Chem., 33 (1994), 1127.
[11] LIPPERT B., *An Inorganic Perspective of Life*, NATO ASI Series, Kluwer, Dordrecht, 1995, p. 179.
[12] The IUPAC-recommended names for diethyl 2-pyridylmethylphosphonate and diethyl 2-quinolylmethylphosphonate are diethyl pyridyl-2-ylmethylphosphonate and diethyl quinolyl-2-ylmethylphosphonate, respectively.
[13] ŻUROWSKA B., MROZIŃSKI J., OCHOCKI J., Mater. Sci., 18, 1992.
[14] OCHOCKI.J., ŻUROWSKA.B., MROZIŃSKI.J., REEDIJK.J., Proc. III Symphosium on Inorganic Biochemistry and Molecular Biophysics, VI International Scientific School on Biological Macromolecules, 1991, p.212.
[15] ŻUROWSKA B., MROZIŃSKI J., CIUNIK Z., OCHOCKI J., J. Mol. Struct. 791 (2006), 98
[16] OCHOCKI J., ŻUROWSKA B., MROZIŃSKI J., KOOIJMAN H., SPEK A.L., REEDIJK J., Eur. J. Inorg. Chem. 169 (1998).
[17] ŻUROWSKA B., OCHOCKI J., MROZIŃSKI J., CIUNIK Z., REEDIJK J., Inorg. Chim. Acta 357 (2003), 755.
[18] FIGGIS B.N., NYHOLM R.S., J. Chem. Soc., (1958), 4190.
[19] KÖNIG E., *Magnetic Properties of Coordination and Organometallic Transition Metal Compounds*, Springer, Berlin, 1966.
[20] CARLIN R.L., *Magnetochemistry*, Springer, Berlin, 1986.
[21] Tip for Ni(II), an Co(II), calculated as $N\alpha = 8N\beta^2/10Dq$.
[22] EARNSHAW A., *Introduction to Magnetochemistry*, Academic Press, London, 1968.
[23] WITTEVEEN H.T., REEDIJK J., J. Solid State Chem., 10, (1974), 151.
[24] CLARK R.J.H., WILIAMS C.S.W., Inorg. Chem., 4 (1965), 350.
[25] TUŠEK-BOŽIĆ L., MATIJASIĆ I., BOCELLI G., CALESTANI G., FURLANI A., STARCIA V., PAPAIOANNOU A., J. Chem. Soc. Dalton Trans., 195 (1991).
[26] NAKAMOTO K., *Infrared and Raman Spectra of Inorganic and Coordination Compounds*, Wiley, 1986.
[27] CURTIS N.F., CURTIS Y.M., Inorg. Chem., 4 (1965), 804.
[28] NUTTALL R.H., TAYLOR D.W., J. Chem. Soc. Chem. Commun., (1968), 1417.
[29] KLEIJWEGT G.J., WIESMEIJER W.G.R., VAN DRIEL G.J., DRIESSEN W.L., REEDIJK J., NOORDIK J.H., J. Chem. Soc. Dalton Trans., (1985), 2177.
[30] NEENAN T.X., DRIESSEN W.L., HASNOOT J.G., J.REEDIJK, Inorg. Chim. Acta, 247 (1996), 43.
[31] ADAMS D.M..*Metal–Ligand and Related Vibration*, Edward Arnold, London, 1967.
[32] FERRARO J.R., *Low Frequency Vibrations of Inorganic and Coordination Compounds*, Plenum, New York, 1971.
[33] CLARK R.J.H., *Halogen Chemistry*, Vol. 3, V. Guttman (Ed.), Academic Press, New York , 1967.

[34] REEDIJK J., SIEDLE A.R, VELAPOLDI R.A, HEST J.A.M, Inorg. Chim. Acta, 74 (1983), 109 and references therein.
[35] LEVER A.B.P., *Inorganic Electronic Spectroscopy*, Elsevier, Amsterdam, 1986.
[36] REEDIJK J., VAN LEEUWEN P.W.N.M., GROENEVELD W.L., Recl. Trav. Chim. Pays Bas., 87 (1968), 129.
[37] REEDIJK J., DRIESSEN W.L., GROENEVELD W.L., Recl. Trav. Chim. Pays Bas., 88 (1969), 1095.
[38] MASLEJOVA A., UHRINOVA S., MROZIŃSKI J., ŻUROWSKA B., MUNOZ M.C., JULVE M., Inorg. Chim. Acta, 255, 343 (1997),.
[39] WEST D.X., HARTLEY R., J. Inorg. Nucl. Chem., 43 (1969), 957.
[40] COTTON F.A., GOODGAME M., J. Am. Chem. Soc., 83 (1961),1777.
[41] LEVER A.B.P., NELSON S.M., J. Chem Soc. A, (1966), 859.
[42] COTTON .F.A., GOODGAME D.M ., GOODGAME M., J. Am. Chem. Soc., 83 (1961), 4690.
[43] LEVER A.B., J. Chem. Ed., 45 (1968), 711.
[44] KOKOSZKA G.F., GORDON G., Trans. Met. Chem., 5 (1969), 181.
[45] DISSOUKY A.EL., REFAAT L.S., Inorg. Chim. Acta, 87 (1984), 213.
[46] HATHAWAY B.J., BILLING D.E., Coord. Chem. Rev., 5 (1970), 143.
[47] REEDIJK J., Trans. Met. Chem., 6 (1981), 195.
[48] FIGGIS F.N., LEVIS J., Progress Inorg. Chem., 6 (1964), 37.

Received 27 December 2006
Revised 23 April 2007

Materials Science-Poland, Vol. 25, No. 4, 2007

Microwave-flash combustion synthesis of yttria nanopowders

R.V. MANGALARAJA[1*], K.V.S. RAMAM[1], J. RAVI[2], C. P. CAMURRI[1]

[1]Department of Materials Engineering, University of Concepción, Casilla 160-C, Concepción, Chile

[2]Department of Physics, University of Concepción, Casilla 160-C, Concepción, Chile

Single phase yttria nanopowders for transparent ceramics were successfully prepared by using a novel approach called microwave-flash combustion technique. This technique involves the reaction of yttrium nitrate and urea in microwave oven for few minutes. The as-prepared precursor powder was later calcined at 1100 °C for 4h to form cubic crystalline yttria nanopowders. The as-prepared and calcined powders were analysed by such methods as thermogravimetry, Brunauer–Emmett–Teller surface area measurement, X-ray diffraction, scanning electron microscopy and transmission electron microscopy. The results confirmed that the yttria powder synthesized by microwave-flash combustion was homogeneous and the particles size was in the range of 50–120 nm for calcined powders.

Key words: *synthesis; microwave-flash combustion; yttria nanopowders; transparent ceramics*

1. Introduction

Transparent yttria ceramics find applications in IR windows in heat seeking rockets, luminous pipes for high-intensity discharge lamps and as laser host materials [1–3]. Their properties include high thermal conductivity, high thermal stability, low thermal expansion, high melting point, chemical stability and good transparency to infrared radiation [1–5]. In order to fabricate a transparent polycrystalline yttria ceramic by sintering, there are several requirements like fine particle size and its distribution, purity, homogeneity and low agglomeration that the starting powder must meet. The method of processing yttria powder is an important factor to provide uniform and high density ceramics. Several methods have been used to produce ultrafine yttria powders such as precipitation [3], hydrothermal method [6], electro spray pyrolysis [7], sol-gel [5] and combustion [2, 8, 9] methods. However, flash combustion technique is an unconventional technique reported earlier [10] in which heat is gener-

*Corresponding author, e-mail: mangal@udec.cl

ated by heating elements. Microwave-assisted process is a novel technique, used for rapid and controlled processing of advanced ceramic materials. Many researchers used microwave-assisted method for different types of ceramic materials [11–17]. In the microwave heating process, heat is generated internally within the material instead of originating from external heating sources and hence is fundamentally different from other heating processes. Microwave-flash combustion technique is the modified combustion technique and is reported for the synthesis of Ni–Zn ferrite nanopowders [18] in which the combustion process takes place by heating the reactant mixture using the absorption of microwaves. This microwave assisted flash-combustion process is simple and inexpensive due to energy savings and shorter processing times. Furthermore, the synthesized powder is generally more homogeneous, and the uniformity and yield are high. The present work reports the synthesis and characterization of yttria nanopowders under microwave-assisted flash combustion technique for transparent ceramics.

2. Experimental

The microwave assisted flash-combustion technique for synthesizing yttria nanopowders involves dissolving yttrium nitrate (oxidizer) and urea (fuel) in water by mixing thoroughly and then heating the solution in a microwave oven. It was calculated that 5 mol of urea was needed to prepare 1 mol of yttria by complete combustion. The oxidizer to fuel ratio (O/F) plays a crucial role in determining the exothermicity of the combustion product. The equivalence ratio, i.e. the ratio of the oxidizing valency to reducing valency (O/F) was maintained at unity. The valency of nitrogen was not considered because of its conversion to molecular nitrogen (N_2) during combustion. The solution mixture of yttrium nitrate, urea and water were transferred to an alumina crucible and later introduced into a microwave oven followed by the application of microwave field at 2.45 GHz to undergo decomposition. When the solution reaches the point of spontaneous combustion, it starts to burn in solid form at high temperature. After few minutes, the combustion was completed and a foamy porous precursor powder was left out as a residue. The foamy porous precursor was then collected and crushed for further processing. During combustion, the only gaseous products released were N_2, CO_2 and H_2O. The theoretical reaction of the assumed complete combustion can be written as:

$$2Y(NO_3)_3 + 5NH_2CONH_2 \rightarrow Y_2O_3 + 5CO_2 + 10H_2O + 8N_2$$

The as-prepared precursor powder was calcined at 1100 °C for 4 h [4, 5, 10, 19, 20] soaking in oxygen atmosphere to get pure crystalline powder. The as-prepared precursor powder was characterized by thermogravimetry (TG) and differential scanning colorimetry (DSC) techniques using a Netzsch-STA 449C equipped with a mass spectrometer (Netzech-QMS 403C) for the identification of evolving gases. The as-prepared precursor powder and calcined powder were studied by X-ray diffractometry (XRD) to establish the formation of crystalline phases and to determine the crystalline

size of fine powders. The diffraction patterns were recorded by a Philips X'Pert X-ray diffractometer using CuK_α radiation. The crystallite sizes were calculated from the X-ray broadening technique as per the Scherrer formula [21]:

$$D = \frac{0.9\lambda}{\left(\beta^2_{\text{sample}} - \beta^2_{\text{ref}}\right)^{1/2} \cos\theta}$$

Where D is the crystallite diameter (nm), $\lambda = 1.54$ Å, θ is the diffraction angle, β_{sample} is the full width at half maximum (FWHM) of the diffraction peak and β_{ref} corresponds to the instrumental FWHM. The powder morphology and the particle size of the crystalline powder were studied by using a scanning electron microscope (SEM -JEOL 6460 LV) and a transmission electron microscope (TEM-JEOL JEM 2000 EX), respectively.

3. Results and discussion

The phase formation of as-prepared yttria powder was studied using TG/DSC measurement analysis. Figure 1 shows the results of thermal analysis of the as-prepared precursor yttria powder. The weight loss of about 35% was obtained, which corresponds to the evolution of absorbed moisture (water molecules), burn out of carbon dioxide and excess nitrate gases present in the as-prepared precursor yttria powder.

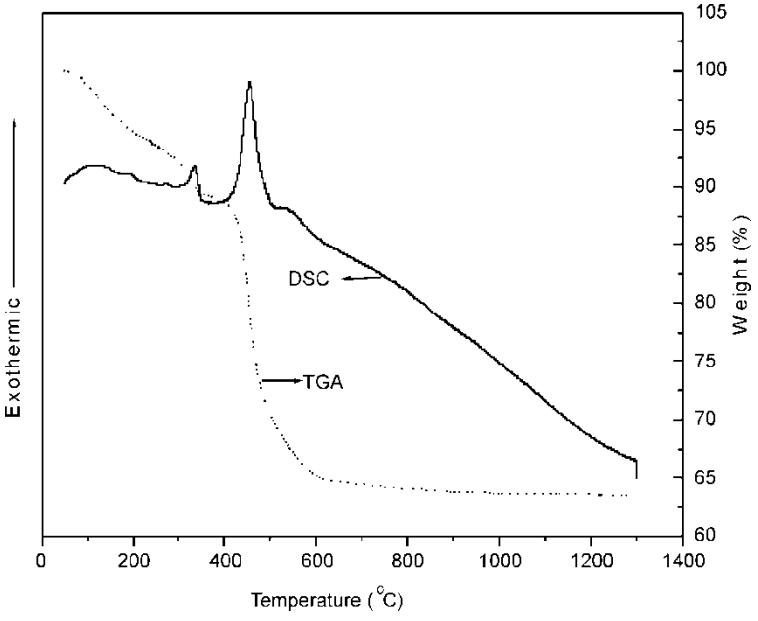

Fig. 1. TGA and DSC curves of yttria precursor powders as-prepared by microwave-flash combustion technique

The DSC curve shows three steps decomposition behaviour of exothermic peaks between 100 and 530 °C. First small broad peak between 100 and 120 °C corresponds to desorption of moisture from precursor powder and the second peak corresponds to removal of water molecules from the hydroxyl group. Third peak corresponds to the evolution of nitrate gases due to the presence of excess nitrate in the precursor powder. There is also a small amount of carbon dioxide gas evolution at this stage.

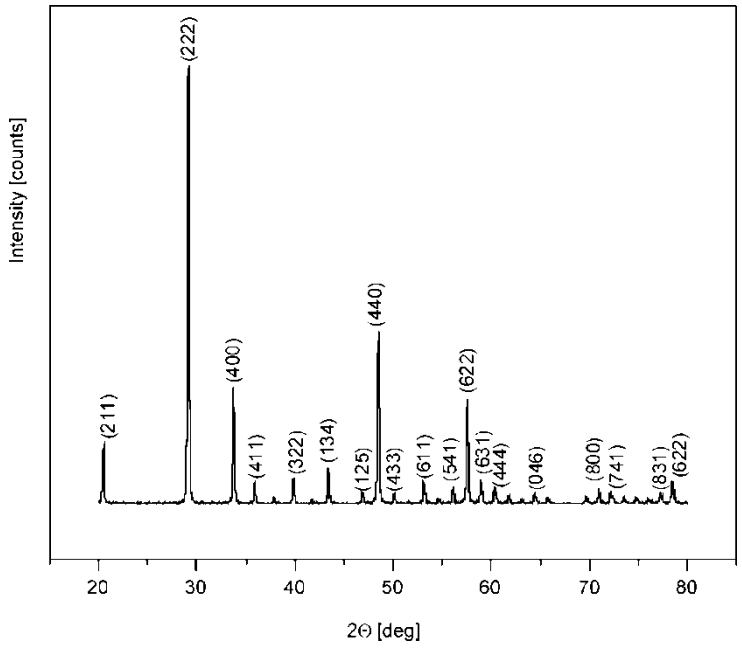

Fig. 2. XRD pattern of yttria powders calcined at 1100 °C

Figure 2 shows the X-ray diffraction pattern of calcined at 1100°C yttria nanopowders prepared by microwave assisted flash combustion technique. The XRD pattern confirms the formation of single-phase cubic crystalline yttria nanopowders. The formation of a single phase is attributed to high in-situ temperature generated during microwave absorbed combustion and rapid cooling. The peaks observed in the XRD pattern for the powder calcined at 1100 °C were found to match well with those reported earlier [8, 9, 22]. The average diameter of the crystallite size was 7 and 90 nm for as-prepared precursor and calcined yttria powders, respectively. The Brunauer –Emmett–Teller (BET) surface area of the as-prepared and calcined powders was 15.42 and 4.56 m^2/g, respectively.

Figure 3 shows the morphologies of the as-prepared precursor foam and powder, respectively. The as-prepared foam (Fig. 3a) is a fluffy foam with porous structure. The crispy foam with pores and voids is due to the evolution of gases during combustion. This porous structure is highly friable and fine particles are easy to obtain by

grinding [23]. The crushed precursor powder (Fig. 3b) shows the flaky and thin platelet type of loosely agglomerated particles.

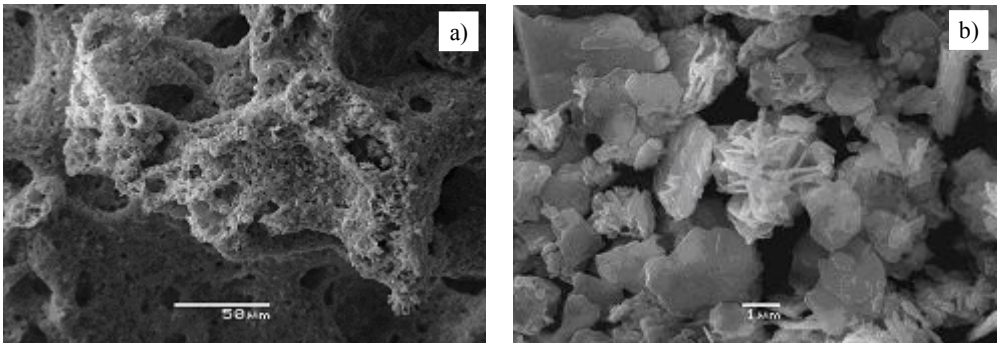

Fig. 3. SEM photographs of as-prepared yttria precursor: a) foam, b) powder

The morphologies of the as-prepared precursor foam and powder depend on the nature and the concentration of organic fuel. During combustion, yttrium nitrate impregnates into the polymeric product and gets ignited. Heat dissipates by the evolution of gaseous products in minimization and thus it leads to a localization of heat due to the polymeric nature of the fuel [24]. After calcination at 1100 °C, flaky agglomerated particles break into smaller pieces of nanometric, non-agglomerated and regular shape particles.

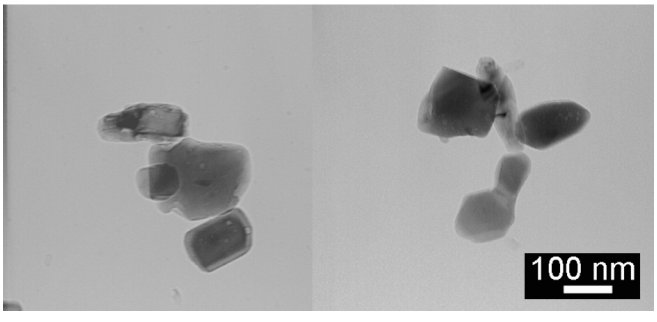

Fig. 4. TEM photograph of yttria powder calcined at 1100°C

The TEM photograph of the yttria powder calcined at 1100 °C for 4h is shown in Fig. 4. The particle sizes were observed to be in the range 50–120 nm. The shape of the particles in the calcined powder was the mixture of rectangular and spherical. This is in fair agreement with the crystallite size measured by XRD broadened peak. The use of these nanosized and more homogeneous calcined powder leads to low sintering temperature, fast densification, and maximum density with improved microstructure which are essential for the fabrication of transparent yttria ceramics.

4. Conclusions

Yttria nanopowders were synthesized by microwave assisted flash combustion technique using yttrium nitrate and urea. The synthesized powders reveal the formation of single-phase cubic nanocrystalline yttria. For powders calcined at 1100 °C for 4 h, the particle sizes were in the range 50–120 nm. Homogeneous yttria powders with nanodimensions are suitable for the fabrication of transparent ceramics, which finds applications in the fields of optics and opto-electronics.

Acknowledgement

One of the authors (R.V. M.) would like to thank Direction of Investigation, University of Concepción and FONDECYT, Govt. of Chile, Santiago for financial assistance.

References

[1] IKEGAMI T., LI J.-G., MORI T., J. Am. Ceram. Soc., 85 (2002), 1725.
[2] DASGUPTA N., KRISHNAMOORTHY R., JACOB K.T., Int. J. Inorg. Mater., 3 (2001), 143.
[3] SAITO N., MATSUDA SH.-I., IKEGAMI T., J. Am. Ceram. Soc., 81 (1998), 2023.
[4] MICHELI A.L., DUNGAN D.F., MANTESE J.V., J. Am. Ceram. Soc., 75 (1992), 709.
[5] DUPONT A., PARENT C., LE GARREC B., HEINTZ J.M., J. Sol. State Chem., 171 (2003), 152.
[6] SHARMA P.K., JILAVI M.H., NAB R., SCHMIDT H., J. Mater. Sci. Lett., 17 (1998), 823.
[7] RULISON A.J., FLAGAN R.C., J. Am. Ceram. Soc., 77 (1994), 3244.
[8] EKAMBARAM S., PATIL K.C., J. Mater. Chem., 5 (1995), 905.
[9] MANGALARAJA R.V., MOUZON J., HEDSTRÖM P., KERO I., ODÉN M., unpublished results.
[10] MANGALARAJA R.V., ANANTHAKUMAR S., MANOHAR P., GNANAM F.D., J. Magn. Magn. Mater., 253 (2002), 56.
[11] KATSUKI H., KOMARNENI S., J. Am. Ceram. Soc., 84 (2001), 2313.
[12] FU Y.-P., LIN C.-H., J. Magn. Magn. Mater., 251 (2002), 74.
[13] BONDIOLI F., FERRARI A.M., LEONELLI C., SILIGARDI C., PELLACANI G.C., J. Am. Ceram. Soc., 84 (2001), 2728.
[14] COMBEMALE L., CABOCHE G., STUERGA D., CHAUMOUNT D., Mater. Res. Bull., 40 (2005), 529.
[15] CHUNG D.Y., LEE E.H., J. Alloys Compds., 374 (2004), 69.
[16] FU Y.-P., LIN CH.-H., J. Alloys Compds., 354 (2003), 232.
[17] FU Y.-P., LIN CH.-H., PAN K.-Y., J. Alloys Compds., 349 (2003), 228.
[18] MANGALARAJA R.V., ANANTHAKUMAR S., MANOHAR P., GNANAM F.D., AWANO M., Mater. Lett., 58 (2004), 1593.
[19] DUPONT A., LARGETEAU A., PARENT C., LE GARREC B., HEINTZ J.M., J. Eur. Ceram. Soc., 25 (2005), 2097.
[20] WEN L., SUN X., XIU Z., CHEN S., TSAI C.-T., J. Eur. Ceram. Soc., 24 (2004), 2681.
[21] CULLITY B.D., *Elements of X-ray Diffraction*, 2nd Ed., Addison-Wesley, New York, MA, 1978.
[22] HUANG Z., SUN X., Z.XIU, CHEN S., TSAI C.-T., Mater. Lett., 58 (2004), 2137.
[23] ZHANG Y., STANGLE G.C., J. Mater. Res., 9 (1994), 1997.
[24] KOTTAISAMY M., JEYAKUMAR D., JAGANNATHAN R., MOHAN RAO M., Mater. Res. Bull., 31 (1996), 1013.

Received 20 April 2007
Revised 25 June 2007

Materials Science-Poland, Vol. 25, No. 4, 2007

Analysis of the pinning interaction in high-temperature superconductors

J. SOSNOWSKI*

Electrotechnical Institute, Pożaryskiego 28, 04-703 Warsaw, Poland

Analysis of the pinning interaction in high-temperature (HTc) superconductors is presented. The model based on analysis of the enhancement of the energy of a superconductor under the vortex motion against its equilibrium position is described. The influence of the dimensions of pinning centres and of the elasticity forces of the vortex lattice on the critical current is considered. The magnetic induction profiles in HTc superconductors are obtained, taking into account the granular structure of ceramic materials, while the flux trapped is determined. The magnetic hysteresis losses, modified by the existence of the magnetic nickel substrates in HTc tapes of second generation are considered too.

Key words: *HTc superconductors; nanotechnology; pinning; critical current*

1. Introduction

The effect of the capturing vortices in high-temperature superconductors (HTS) has essential meaning from the point of view of electric current transport. It is also a very intriguing statistical problem of the occupation on a fixed concentration of the pinning centres, varying number of vortices, interacting with each other through the elasticity forces (cf. [1–4]). The present paper is a continuation of the author's works [5–7]. From the point of view of applications, the pinning subject deals especially with the case of the HTc superconducting tapes, an example of the second generation one being shown in Fig. 1.

Ni-W substrate enables epitaxial growth of the HTS layer but on the other hand is the reason of additional magnetic losses, due to magnetic properties of nickel. The magnetization characteristic of nickel leads to enhancement of the magnetic field in the superconducting filaments and therefore to an increase in the magnetic hysteresis losses, connected with alternating current flow.

*E-mail: sosnow@iel.waw.pl

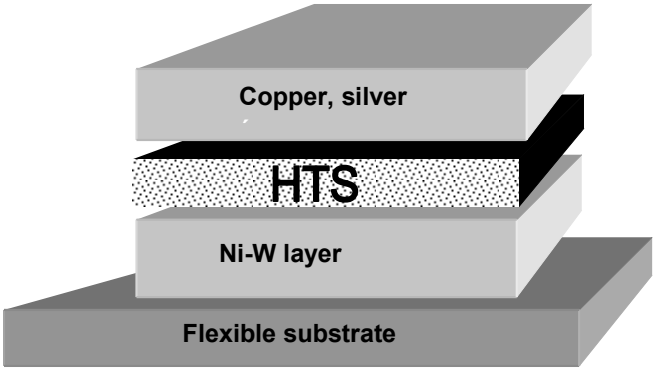

Fig. 1. The structure of the second generation HTc tape

The temperature and quality of nickel substrate may lead to modifications of magnetic characteristic, roughly described by the hyperbolic tangent function $B \propto \tanh(\mu_0 H)$, which will strongly influence the generated losses, as follows from the calculated results shown in Fig. 2 for three slightly modified characteristics of substrates.

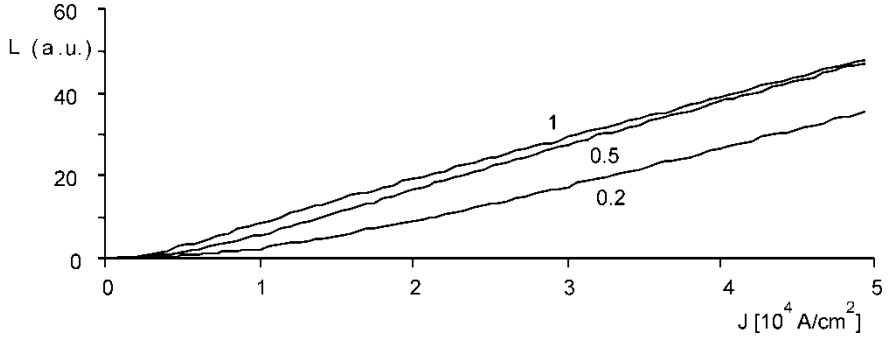

Fig. 2. Dependence of the value of losses on the transport current density for three nickel substrate magnetic characteristics described by Eq. (1); $B \propto 0.65\tanh(\beta\mu_0 H)$ for $\beta = 0{,}2,\ 0.5,\ 1$

The calculations were performed for the rectangular wire of the dimensions 5×1.5 mm^2 with 30 filaments distributed in three layers. The losses were calculated for the filament near to the middle of the wire.

2. Analysis of a new model of the pinning interaction

An important feature of the HTc superconducting materials is the sensitivity of their properties to the existence of structural defects, which if created in the superconducting windings working in nuclear reactors are of the nanometric size and are referred to as the columnar defects. These defects interact with the pancake vortices arising in HTc superconductors, thus stabilizing the vortex structure and permit in this

way the resistiveless current flow. A new model of the pinning interaction has been developed in the paper, based on an analysis of the increase in the normal state energy during the pancake vortex deflection from nanosized pinning centre, against its equilibrium position, which is shown in Fig. 3.

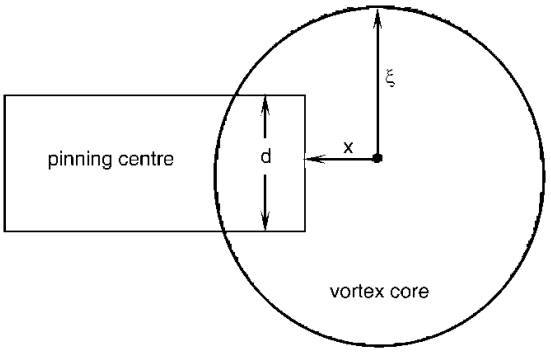

Fig. 3. View of the vortex core of the radius equal to the coherence length (ξ_0) captured on the pinning centre of the width d

The approach corresponds roughly to the consideration of the first two terms in the Ginzburg–Landau theory. As compared with previous pinning models based mainly on the force balance equation in the regime of flux flow, being the continuation of the critical state Bean's approach [8], in the present theory we consider the condition of the energy equilibrium and flux creep approximation. Two effects have been investigated of the increase in the normal state energy during the vortex movement, as well as opposite one of the increase in the elasticity energy of the vortex lattice during the capturing process, deflecting vortex from its equilibrium site in the vortex matrix.

In the initial state of the captured vortex on the flat pinning centre of nanosized dimensions d, smaller than the coherence length ξ, the normal state energy of the vortex core is:

$$U_1(0) = \frac{\mu_0 H_c^2 l}{2}\left[\pi\xi^2 - \xi^2 \arcsin\frac{d}{2\xi} - \frac{d\xi}{2}\sqrt{1-\left(\frac{d}{2\xi}\right)^2}\right] \tag{1}$$

while for a vortex deflected by the distance x against this equilibrium position it is given, as follows from Fig. 3:

$$U_2(x) = \frac{\mu_0 H_c^2 l}{2}\left[\pi\xi^2 + dx - \xi^2 \arcsin\frac{d}{2\xi} - \frac{d\xi}{2}\sqrt{1-\left(\frac{d}{2\xi}\right)^2}\right] \tag{2}$$

for $x < x_c$, where x_c is defined as:

$$x_c = \xi\sqrt{1-\left(\frac{d}{2\xi}\right)^2} \tag{3}$$

The deflection of vortex is caused by the flow of current which leads to the Lorentz force appearance. Additionally, the elasticity forces are taken into account also related to the magnitude of the vortex deflection in the vortex lattice. Thus a barrier of potential ΔU arises, being a function of the ratio of the current density j and the critical current density for the flux creep process j_C, defined as the current density for which barrier of potential disappears, for pinning centre dimension equal to the vortex core diameter:

$$\Delta U(i) = \frac{\mu_0 H_c^2 l \xi^2}{2} z + \alpha\xi^2\sqrt{1-i^2}\left(\sqrt{1-i^2}-2\right) \tag{4}$$

The parameter z in Eq. (4) is determined here according to the relation:

$$z = \arcsin\frac{d}{2\xi} + \frac{d}{2\xi}\sqrt{1-\left(\frac{d}{2\xi}\right)^2} - i\sqrt{1-i^2} - \arcsin i \tag{5}$$

where $i = j/j_c$ is the reduced current density, H_c magnetic thermodynamic critical field, l the pinning centre thickness. Parameter α describes the elasticity energy of the vortex lattice. Inserting Eqs. (4), (5) into the constitutive relation:

$$E = -B\omega a\left[\exp\left[-\frac{\Delta U_0}{k_B T}\left(1+\frac{j}{j_C}\right)\right] - \exp\left(-\frac{\Delta U}{k_B T}\right)\right] \tag{6}$$

describing the generated electric field in the flux creep process, just as a function of the potential barrier height, we obtain the dependence of the real critical current density, i.e. that satisfying the electric field criterium, on the material parameters. ΔU_0 is the potential barrier height without current, ω – a characteristic frequency, which in the present paper has been assumed constant, T – temperature and k_B – Boltzmann's constant, the parameter a describes the defect concentration. Selected results of calculations are presented in Figs. 4, 5, pointing to the importance of the pinning centre dimensions as well as the elasticity constant α for the critical current density.

For too low pinning centre dimensions as well as too high elasticity constant of the vortex lattice, the critical current density vanishes; this result should be interesting from the technological point of view. The new model of the pinning mechanism allows us therefore to predict the critical current of the HTc materials in function of material parameters. The peculiar property of these ceramic superconductors is the existence of Josephson's junctions on the grain boundaries which modify the total critical current density. We will investigate this subject focusing on the trapped flux analysis.

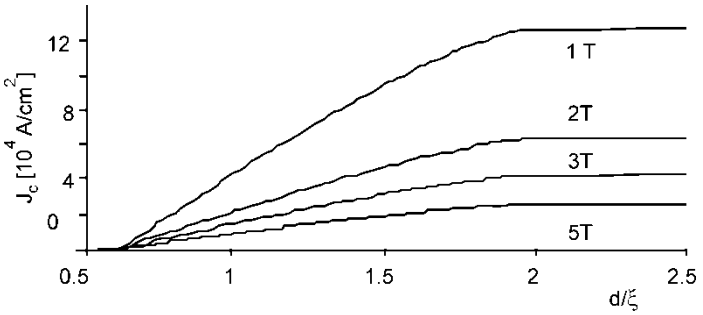

Fig. 4. Dependence of the critical current density satisfying the electric field criterion on the pinning centre dimensions for various magnetic fields; pinning centre concentration equal to 2×10^{14} cm^{-3}

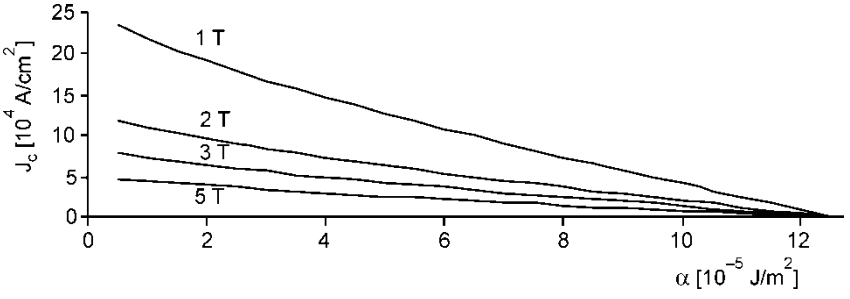

Fig. 5. Dependence of the critical current density on the elasticity force of the vortex lattice (described by the parameter *J*) versus magnetic induction for pinning centre concentration equal to 2×10^{14} cm^{-3}

3. Influence of Josephson's currents on trapped flux in HTc ceramics

The trapped flux shown in Fig. 6 is defined as the remnant moment of the magnetization curve in the magnetic field cycle 0–B_m–0.

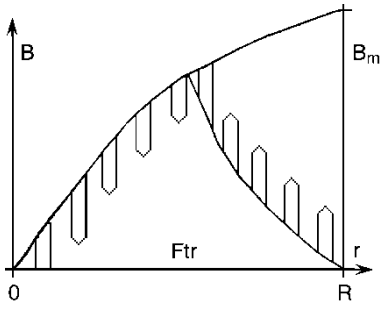

Fig. 6. Magnetic induction profile in the trapped flux state of the ceramic HTc superconductor for the magnetic field cycle 0–B_m–0

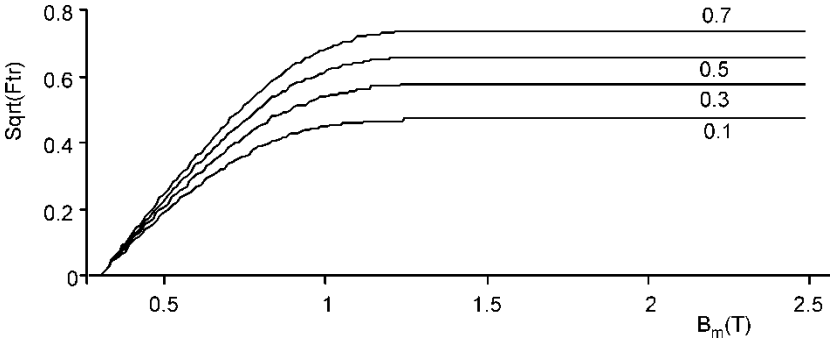

Fig. 7. Influence of filling the ceramic superconductor with grains on the square root of the flux trapped [Sqrt(Ftr)] versus maximum magnetic field in a cycle

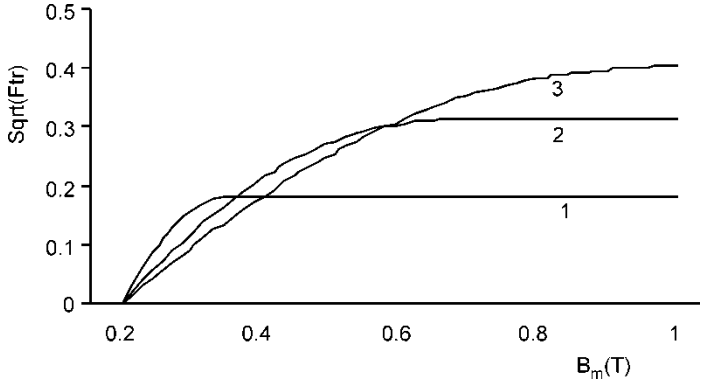

Fig. 8. The influence of the intergranular critical current density of the ceramic superconductor on a square root of the flux trapped [Sqrt(Ftr)] versus maximum magnetic field in the cycle. Indexes 1–3 indicate the case of the increasing critical current density

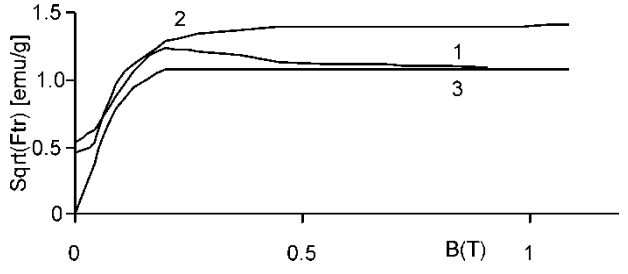

Fig. 9. Experimental shape of the measured flux trapped versus maximum magnetic field for three YBaCuO–Fe (4%) doped samples [9]. Numbers 1–3 refer to: original bulk ceramics (1) bulk ceramics measured after one week (2), and powdered sample (3)

The existence of weak intergranular Josephson's currents, mentioned previously, and the current inside grains lead to the tooth-like shape of the magnetic induction profile given schematically in this diagram. The performed analysis of this effect allowed us to determine the influence on the trapped flux (Ftr) of the superconductor

filling with the grains as well as of the intergranular critical current. The results of calculations presented in Figs. 7, 8, correspond well with the experimental data shown in Fig. 9, measured on YBaCuO-Fe doped samples.

4. Conclusions

In the paper, analysis is presented of the pinning interaction in HTc superconducting materials taking into account the specific structure of these granular materials. Performed calculations indicated the importance of the dimensions of the nanosized pinning centres and the elasticity constants of the vortex lattice for determining the critical current density. Analysis of the influence of the critical current density in granular HTc superconductors on the flux trapped has also been performed. The comparison of the theoretical results with previous experimental data is enclosed.

References

[1] YAMADA H., YAMASAKI H., DEVELOS-BAGARINAO K., NAKAGAWA Y., MAWATARI Y., NIE J. C., OBARA H., KOSAKA S., Supercond. Sci. Techn., 17 (2004), 58.
[2] OKAMURA K., KIUCHI M., OTABE E. S., YASUDA T., MATSUSHITA T., OKAYASU S., Supercond. Sci. Techn., 17 (2004), S20.
[3] ZHAO Y., CHENG C. H., FENG Y., SHIBATA S., KOSHIZUKA N., MURAKAMI M., Supercond. Sci. Techn., 17 (2004), S83.
[4] MISKO V. R., SAVELEV S., RAKHMANOV A. L., NORI F., Phys. Rev., B 75 (2007), 24509.
[5] SOSNOWSKI J., Mater. Sci.-Poland, 23 (2005), 613.
[6] SOSNOWSKI J., Acta Phys. Polon., 106 (2004), 767.
[7] SOSNOWSKI J., *Critical current problems in HTc superconductors with nanoscale pinning centres*, Proc. EUCAS 2005, J. Phys., Conf. Ser. 43 (2006), 659.
[8] BEAN C.P., Phys. Rev. Lett., 8, 250, 1962
[9] SOSNOWSKI J., *Superconductivity and Applications*, Electrotechnical Institute Publ., Warsaw, 2003, pp. 1–200, (in Polish).

Received 9 May 2007
Revised 28 September 2007

Materials Science-Poland, Vol. 25, No. 4, 2007

Formation of gyrolite in the CaO–quartz–Na_2O–H_2O system

K. BALTAKYS*, R. SIAUCIUNAS

Department of Silicate Technology, Kaunas University of Technology,
Radvilenu 19, LT – 50270 Kaunas, Lithuania

Optimizing the duration and/or the temperature of hydrothermal synthesis of gyrolite has been investigated by adding NaOH solution into an initial mixture of CaO–quartz–H_2O. The molar ratio of the primary mixture was C/S = 0.66 (C – CaO; S – SiO_2). An amount of NaOH, corresponding to 5 % Na_2O from the mass of dry materials, added in the form of solution and additional water was used so that the water/solid ratio of the suspension was equal to 10.0. Hydrothermal synthesis of the unstirred suspension was carried out in saturated steam at 150, 175, 200 ºC. The duration of isothermal curing was 4, 8, 16, 24, 32, 48, 72 and 168 h. The temperature of 150 ºC is too low for the synthesis of gyrolite; the stoichiometric ratio C/S = 0.66 is not reached even after 168 h of synthesis neither in pure mixtures nor in mixtures with addition of Na_2O. Na^+ ions significantly influence the formation of gyrolite from the CaO–quartz mixtures in the temperature range from 175 ºC to 200 ºC. Gyrolite is formed at 175 ºC after 168 h and at 200 ºC after 16 h of isothermal curing. On the contrary, in pure mixtures it does not form even after 72 h at 200 ºC. Na^+ ions also change the compositions of intermediate and final products of the synthesis. In mixtures with 5% Na_2O, intermediate compounds are C–S–H(I) and Z-phase, and the final products are gyrolite and pectolite. Meanwhile, in mixtures without this additive, the main intermediate compounds are α-C_2S hydrate and C–S–H(II), and the main products are 1.13 nm tobermorite and xonotlite.

Key words: *gyrolite; Z-phase; calcium silicate hydrate; X-ray diffraction*

1. Introduction

Gyrolite ($Ca_2Si_3O_7(OH)_2{\cdot}xH_2O$), calcium silicate hydrate (C–S–H), rarely occurs as a natural mineral in association with zeolites and often forms nodular aggregates. These aggregates can appear glassy, dull or even fibrous [1]. Hydrothermal synthesis of gyrolite is a long and complex process. Flint et al. [2], who first synthesized gyrolite, reported that the product is formed from a mixture of CaO and SiO_2 after 6–42 days of hydrothermal synthesis at 150–350 ºC when the molar ratio CaO/SiO_2

*Corresponding author, e-mail: kestutis.baltakys@ktu.lt

(C/S) of the starting materials changes from 0.5 to 0.66. This data was later confirmed by the results of thermodynamical calculations [3].

It is known that various ions (Na^+, K^+, Cs^+, Cu^{2+}, Fe^{2+}, Zn^{2+}, Cd^{2+}, Pb^{2+}, Mg^{2+}) in the crystal lattice of calcium silicate hydrates (mainly 1.13 nm tobermorite, 1.13 nm-substituted tobermorites and xonotlite) can substitute some of Ca^{2+} or Si^{4+} ions in the structure under hydrothermal reaction, altering their physicochemical behaviour. The effectiveness of each additive may change depending on the properties of the raw materials, parameters of the hydrothermal reactions and other factors. Numerous authors describe the influence of alkali metals [4–6], aluminum [7–10] and other elements with additives [11, 12] on the synthesis and properties of calcium silicate hydrates, however little is known about the cavities into which these ions substitute.

Basicity of synthesized calcium silicate hydrates described in terms of the C/S molar ratio is influenced more by alkaline additives than by changes in temperature. Depending on the concentration of Na^+ ions, the ratio of water/solid materials and the initial composition of the mixture, duration of the hydrothermal synthesis may be significantly reduced [9]. Blakeman et al. [6] found that at a constant C/S molar ratio of 0.83 and a varying quantity of NaOH in the primary mixtures, various compounds are formed (C–S–H(I), 1.13 nm tobermorite, pectolite, xonotlite).

Nocun-Wczelik [9, 10] investigated the influence of additives containing sodium and aluminum oxides on the composition and properties of calcium silicate hydrates. The author found that during hydrothermal treatment of CaO- and SiO_2-bearing components, Na^+ ions accelerate the formation of poorly crystallized calcium silicate hydrates but further transformation of this intermediate product into more-ordered, well-developed crystalline forms can be disturbed at some admixture content. Xonotlite is the final product of the synthesis when the C/S molar ratio of the primary mixture is equal to 1.0. However, if over 20% of Na_2O is added into the mixture, all of the intermediate products, which are ordered phases of calcium silicate hydrates transform into tobermorite. Meanwhile, the formation of gyrolite or Z-phase in mixtures with a lower C/S ratios (0.67 or less) is faster in pure suspensions and, in addition, a C–S–H(I) residue is present when there is a Na_2O admixture of 5–10%.

It is often stated that the crystal lattice of natural gyrolite always contains both sodium and aluminium ions [13]. This presumption has been confirmed by many tests of Merlino who reported that the most likely composition of natural gyrolite is $NaCa_{16}Si_{23}Al_{60}(OH)_8 \cdot 14H_2O$. However, Sukheswala et al. [14] reported that natural gyrolite from both the Deccan Traps near Bombay, India, and the Dean quarry apparently contain no Al. According to Seager [15], gyrolite was formed later than calcite in which it is embedded, or perhaps simultaneously with late stages of calcite formation. Hydrothermal solutions responsible for the formation of gyrolite may have become depleted of Al by earlier deposition of prehnite, providing a possible explanation for the unusually low Al content in gyrolite both in the Deccan Traps and at a Dean quarry [16].

Many authors investigated crystal structure of gyrolite [13, 17, 18]. They noticed that the interlayer sheets with a thickness of about 0.3 nm in gyrolite are available for

the intercalation of a new guest by controlling the charge in the host. For example, Na^+ ions can be incorporated into the interlayer sheets by replacing Si^{4+} with Al^{3+} ions in the complex layers in order to maintain charge neutrality. Intercalated Na^+ ions were expected to be exchangeable for univalent cations in aqueous solution [8].

Shaw [19] reported that the rate for gyrolite formation in a sodium-bearing system is significantly higher than reactions in a pure calcic system at the same temperature. The presence of sodium in this system in the form of a 1 M NaOH solution changes the mechanism of gyrolite formation. There is no intermediate formation of Z-phase and a mixture of gyrolite and pectolite forms directly from C–S–H gel [19].

Miyake, Iwaya and Suzuki [8] successfully synthesized Al-substituted gyrolite ($Ca_8Si_{11.32}Al_{0.68}Na_{0.44}O_{30}(OH)_4{\cdot}6.6H_2O$) and used it for the exchange reactions of ions (K^+ and Cs^+) in aqueous solutions. Since the specimen has a smaller amount of Na^+ ions than of substituted Al^{3+} ions, it was supposed that Ca^{2+} ions make up for the deficiency in order to keep charge neutrality. Al-substituted gyrolites retained their crystal structure and showed the same behaviour on heating and the same lamellar morphologies as the original one. In addition, basal spacing of gyrolite, d-spacing 2.2 nm, was not altered after the uptake of K^+ and Cs^+ ions. Moreover, it is easier to intercalate K^+ ions than Cs^+ ions into the crystal lattice of this compound. However, the authors noticed that Cs^+ ions are better absorbed by Al-substituted tobermorite [20, 21]. Al-substituted gyrolite may be used to eliminate heavy metal ions and remove them from wastewaters [22, 23] and it is known for its selectivity to DNA [24].

However, all of these tests were performed with SiO_2 component using its active forms such as amorphous SiO_2, finely dispersed aerosol and silicic acid. There is little data about the effect of a less active form of SiO_2 on the synthesis of gyrolite and the sequence of the formed new compounds and the influence of additives on these processes. Our results show that in the CaO–quartz–H_2O mixtures neither Z-phase, nor gyrolite forms, even during 72 h of hydrothermal curing due to low quartz solubility rate at temperature range from 150 °C to 200 °C [25, 26]. The results published elsewhere [9, 10, 19] demonstrate that Na^+ ions in many cases stimulate the formation of calcium silicate hydrates, especially when the starting materials are not very active. It is likely that they will have a positive influence the gyrolite formation processes as well. The purpose of this paper was to examine the possibility of reducing the duration and/or temperature of hydrothermal synthesis of gyrolite by adding NaOH solution into the initial CaO–quartz–H_2O mixture.

2. Experimental

The following reagents were used as starting materials: fine-grained quartz (specific surface area 1100 m²/kg by Blaine), after grinding washed away from iron impurities by hydrochloric acid; NaOH solution (1.04 %); calcium oxide (specific surface area 548 m²/kg by Blaine) which had been produced by burning calcium carbonate at 1000 ºC for 6 h.

The synthesis of calcium silicate hydrates has been carried out in unstirred suspensions in vessels of stainless steel. The molar ratio C/S of the primary mixture was 0.66. The amount of NaOH corresponding to 5% of Na_2O from the mass of dry materials was added in the form of solution. The suspension was diluted with water so that the water/solid ratio was equal to 10.0. Hydrothermal synthesis has been carried out under the saturated steam pressure at 150, 175, 200 ºC; the duration of isothermal curing was 4, 8, 16, 24, 32, 48, 72 or 168 h. The products of the synthesis were filtered, rinsed with ethyl alcohol to prevent carbonization of the material, dried at 100 ± 5 ºC and sieved through the sieve No. 005.

The X-ray powder diffraction data were collected with a DRON-6 powder X-ray diffractometer with the Bragg–Brentano geometry using Ni-filtered CuK_α radiation and graphite monochromator, operating at a voltage of 30 kV and emission current of 20 mA. The step-scan covered the angular range 2–60° (2θ) in steps of $2\theta = 0.02°$. For diffraction profile refinement under the pseudoVoid function and for a description of the diffractional background under the 3rd degree Tchebyshev polynomial, we used the X-fit computer program [27].

Thermal analyzer DuPont 990 (USA) with computerized control and data recording was applied for differential thermal analysis (DTA) and for differential scanning calorimetry (DSC) studies. For DTA, the heating was carried out in air, the rate of temperature increase was 10 ºC/min, the temperature range from 100 up to 1000 ºC. The ceramic sample handlers and Al_2O_3, as an inert material, were used. The DSC parameters were: the rate of temperature increase was 10 ºC/min, temperature interval was 20–550 ºC, and empty aluminum capsule as an inert material was used.

The specific surface area of the raw materials was determined by the Blaine's method. FTIR spectra have been obtained with a Perkin Elmer FT–IR system Spectrum X spectrometer. The specimens were prepared by mixing 1 mg of the sample in 200 mg of KBr. The spectral analysis was performed in the range 4000–400 cm^{-1} with the spectral resolution of 1 cm^{-1}.

3. Results and discussion

Na_2O additive positively affects the hydrothermal reactions in the CaO–quartz $–H_2O$ system. After first 4 h of synthesis at 150 ºC, traces of α-C_2S hydrate are already formed in the products and a large quantity of $Ca(OH)_2$ and quartz remain unreacted (Fig. 1, curve 1). Due to the fact that quartz dissolves slower than $Ca(OH)_2$ and the solution contains a significant excess of Ca^{2+} ions, the compounds of a higher basicity – dicalcium silicate hydrates – are formed. These results were confirmed by DTA and DSC analysis data. The endothermic effect, which is characteristic of the α-C_2S hydrate, was possible to identify only by the DSC method (Fig. 2, curve 1, endothermic peak at t = 505 ºC). This peak is covered by a wide and more intensive $Ca(OH)_2$ dehydration peak in the DTA curve (Fig. 1b, curve 1, endothermic peak at t = 503 ºC).

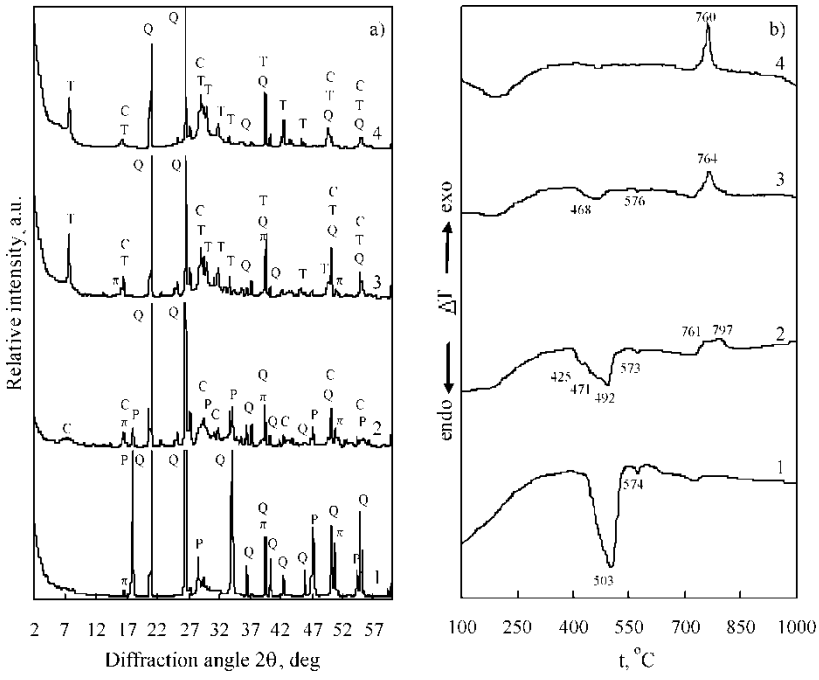

Fig. 1. X-ray diffraction patterns (a) and DTA curves (b) of synthesis products; duration of hydrothermal synthesis at 150 ºC: 1 – 4 h, 2 – 16 h, 3 – 24 h, 4 – 72 h; P – portlandite, Q – quartz, T – 1.13 nm tobermorite, α – α-C_2S hydrate, C – C–S–H(I)

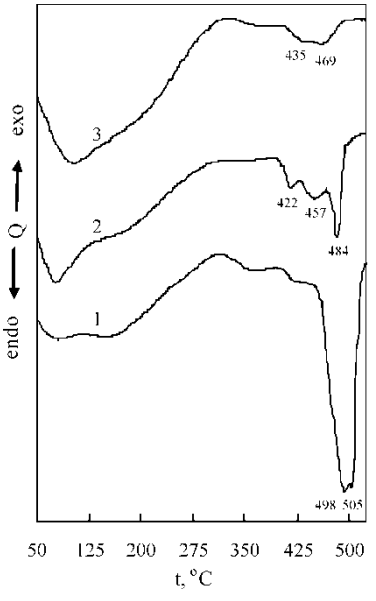

Fig. 2. DSC curves of the synthesis products; duration of hydrothermal synthesis at 150 ºC: 1 – 4 h, 2 – 16 h, 3 – 24 h

When hydrothermal synthesis is extended to 16 h, almost all $Ca(OH)_2$ reacts, and larger quantities of α-C_2S hydrate (Fig. 2, curve 2, endothermic effect at t = 484 ºC)

and C–S–H(II) (Fig. 1b, curve 2, exothermic peak at t = 797 ºC) are formed. It should be emphasized that the amount of unreacted quartz decreases. Due to this fact, not only dicalcium silicate hydrates form but also a compound of lower basicity, of C–S–H(I) type calcium silicate hydrate (Fig. 1, curve 2, exothermic peak at t = 761 ºC). Compared with the pure mixtures, we notice that the shape of the peak corresponding to wollastonite formation (t = 797 ºC) changes in the DTA curve and shifts towards lower temperatures. Thus, it may be concluded that Na^+ ions accelerate the recrystallization of C–S–H(I) into wollastonite.

When the time of isothermal curing is longer (24 h), α-C_2S hydrate and C–S–H(II) are destroyed because more and more quartz dissolves. Instead, 1.13 nm tobermorite and C–S–H(I) are identified in the products (Fig. 1, curve 3, the intensity of exothermic peak increases at 764 ºC). However, in mixtures without Na^+ ions, α-C_2S hydrate and C–S–H(II), which have not yet decomposed, prevail in the products. It should be noted that quartz does not react completely even after 72 h of synthesis, neither in pure mixtures nor in mixtures with Na_2O (Fig. 1a, curve 4). Thus, at low temperature addition of Na_2O accelerates the transfer of dicalcium silicate hydrates into the compounds of lower basicity, i.e. it stimulates formation of C–S–H(I) and 1.13 nm tobermorite. However, due to a low quartz dissolution rate, the stoichiometric C/S ratio (0.66) of the primary mixture is not reached. It is one of the main reasons why the temperature of 150 ºC is too low for the synthesis of low base calcium silicate hydrates (Z-phase, gyrolite) both in pure mixtures and in mixtures with Na_2O additive.

After increasing the temperature to 175 ºC, $Ca(OH)_2$ reacts completely and only semi-crystalline C–S–H(I) is formed in the first 4 h of synthesis (Fig. 3b, curve 1, exothermic peak at 802 ºC). Dibasic calcium silicate hydrates are not formed at this temperature. This is partly due to the presence of Na^+ ions in the solution, which accelerate dissolution of quartz by eroding the surface of the particles. After 8 h of synthesis, no essential changes are noticed in the X-ray diffraction pattern and in the DTA curve – an unchanged amount of C–S–H(I) remains, although its molar ratio C/S probably decreases because more quartz reacts (Fig. 3, curve 2). It should be noted that after 72 h of isothermal curing only traces of quartz remain (Fig. 3, curve 3). It was observed that in pure mixtures it is very difficult to dissolve all of the quartz. Approximately, 11% of this compound remained after 168 h at 150 ºC, 72 h at 175 ºC and 32–72 h at 200 ºC [26].

At 175 ºC, the formation of 1.13 nm tobermorite is delayed in mixtures containing Na_2O. Traces of this compound are identified only after 72 h of synthesis, while at 150 ºC a larger quantity of tobermorite formed after only 24 h. We suppose that it depends on the stability of the compounds that are formed during the first stage of the hydrothermal reactions. This stability is influenced by both temperature and the amount of unreacted quartz. Due to a larger amount of dissolved quartz at 175 ºC, the molar ratio C/S in the mixture becomes lower than 0.83 (which corresponds to the stoichiometric composition of 1.13 nm tobermorite) and decreases to the stoichiometric composition (C/S = 0.66) of low base calcium silicate hydrates. Also, it is found

that Na^+ ions stimulate formation of a new compound (pectolite – $Ca_2NaH(SiO_3)_3$). After 72 h at 175 ºC, pectolite together with traces of tobermorite have been identified in the products (Fig. 3, curve 3). Basic reflections of pectolite (*d*-spacing – 0.2905, 0.2917, 0.3081, 0.3066, 0.3306 nm) are not intense (Fig. 3, curve 3). However, when the synthesis is continued until one week, not only gyrolite and Z-phase but also 1.13 nm tobermorite and pectolite are formed (Fig. 3, curve 4).

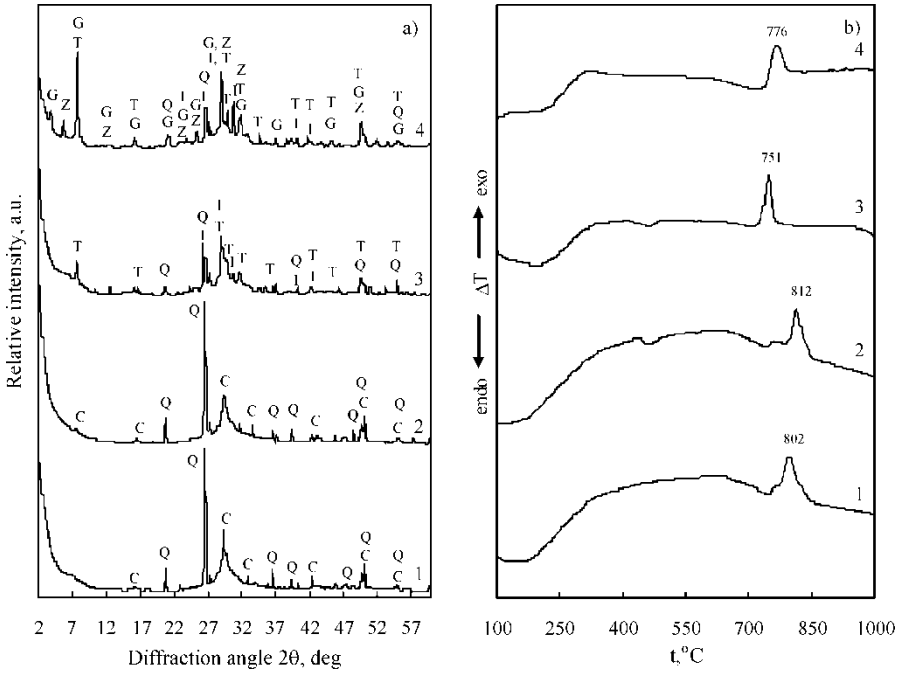

Fig. 3. X-ray diffraction patterns (a) and DTA curves (b) of synthesis products; duration of hydrothermal synthesis at 175 ºC: 1 – 4 h, 2 – 8 h, 3 – 72 h, 4 – 168 h; Q – quartz, C – C–S–H(I), Z – Z-phase, G – gyrolite, T – 1.13 nm tobermorite, I – pectolite

On the contrary, when pure mixtures are hydrothermally treated under the same conditions (72 h at 175 ºC), quartz, xonotlite, and 1.13 nm tobermorite prevail in the products. As far as we know this is the first evidence that gyrolite can be synthesized when a less active SiO_2 modification – quartz and sodium additive are used. However, a larger quantity of this compound forms only after 168 h of isothermal curing at 175 ºC. DTA measurements show a wide exothermic effect at 776 ºC, characterizing the transformation of gyrolite into wollastonite (Fig. 3b, curve 4). Moreover, other calcium silicate hydrates are formed together with gyrolite: Z-phase, pectolite, and 1.13 nm tobermorite.

When C–S–H(I) and gyrolite recrystallize into wollastonite, Na_2O reacts as flux (alloying additive), because the exothermic peak, characterizing the formation of wollastonite, significantly shifts towards lower temperatures from 840–860 ºC (in pure

mixtures) to 800–750 ºC (in mixtures with Na_2O). In order to get the only product of the synthesis – gyrolite – and shorten the time of hydrothermal processing, we increased the temperature of isothermal curing to 200 ºC. As expected, just after 4 h a large quantity of semi-crystallized C–S–H(I) was formed (Fig. 4b, curve 1, exothermic peak at 772 ºC) and a larger amount of quartz reacted. This is because an endothermic effect at 573 ºC was not identified in the DTA curve, and only small intensity peaks, which can be attributed to the quartz, appeared on the X-ray diffraction pattern (Fig. 4a, curve 1).

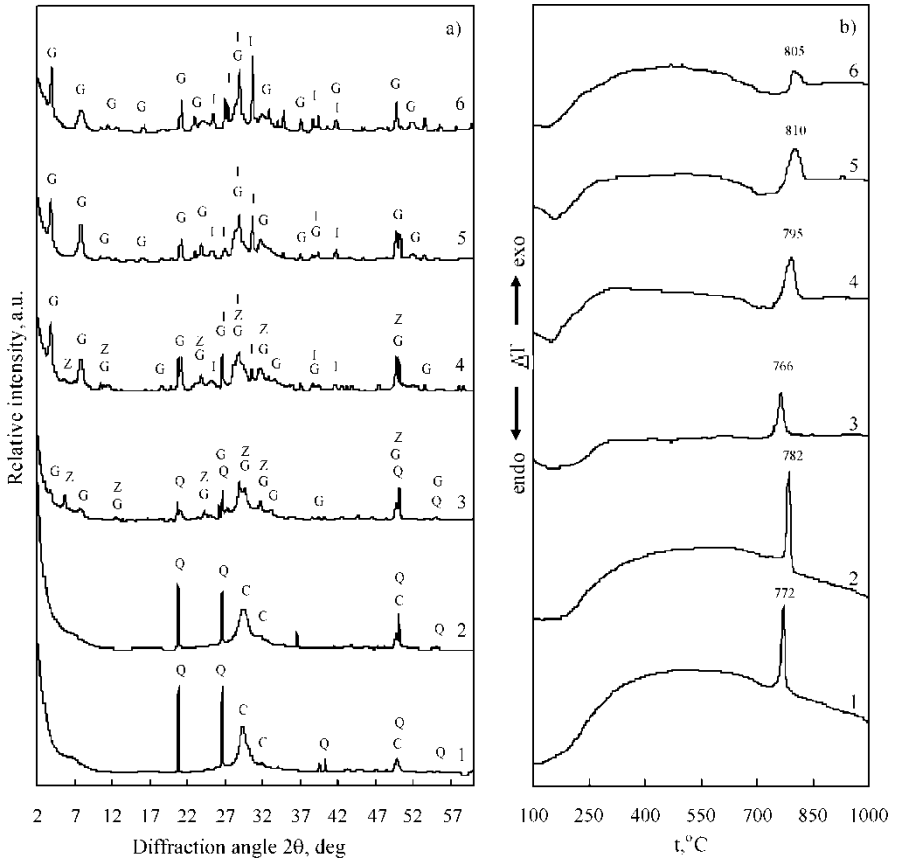

Fig. 4. X-ray diffraction patterns (a) and DTA curves (b) of synthesis products; duration of hydrothermal synthesis at 200 ºC: 1 – 4 h, 2 – 8 h, 3 – 16 h, 4 – 24 h, 5 – 32 h, 6 – 168 h; Q – Q – quartz, C – C–S–H(I), Z – Z-phase, G – gyrolite, T – 1.13 nm tobermorite, I – pectolite

When the synthesis is continued, after 8 h the intensity of the basic reflections of quartz slightly decreases. This means that more Si^{4+} ions are transferred to the solution and the molar ratio C/S of the mixture becomes closer to the estimated 0.66, creating favourable conditions for the formation of low base calcium silicate hydrates (Fig. 4, curve 2). After a longer time (16 h) almost all quartz reacts. Therefore, it is not a coincidence that basic reflections characteristic of gyrolite (*d*-spacing – 2.2 nm) and Z-

phase (*d*-spacing – 1.5 nm) start to dominate in the X-ray diffraction pattern of the reaction products (Fig. 4a, curve 3). This is confirmed by DTA data as well: the exothermic peak at ~ 782 ºC shifts towards lower temperatures (~ 766 ºC) and becomes wider (Fig. 4b, curve 3).

As has already been mentioned, in mixtures without Na_2O approximately 11% of quartz does not react even after 72 h of synthesis. The C/S ratio approaches 0.8 and stable calcium silicate hydrates – 1.13 nm tobermorite and xonotlite form. As a result, gyrolite is not formed in those mixtures [26]. Z-phase is not stable in mixtures with a Na_2O. After 24 h of hydrothermal synthesis at 200 ºC only traces of this compound remain (Fig. 4, curve 4). Z-phase finishes transferring into new compounds – gyrolite and pectolite – after 32 h of isothermal curing (Fig. 4, curve 5).

In order to examine the stability of both gyrolite and pectolite, we prolonged the time of hydrothermal synthesis up to 48 h. The intensity of the main peak (*d*-spacing 0,291 nm) of pectolite slightly increased, and the intensity of gyrolite (*d*-spacing 2.2 nm) remained unchanged. When the duration of isothermal curing was increased even more (72 h), the quantities of calcium silicate hydrates do not change any more. It is interesting that at 200 ºC 1.13 nm tobermorite does not form. One of the main reasons for this is fast dissolution of quartz, which influences the decrease of the C/S ratio and the formation of calcium silicate hydrates, which are stable under these conditions. Thus, at 200 ºC, in the system CaO–quartz–Na_2O–H_2O, reactions of formation of gyrolite are quite intensive – it is formed much faster (after 16 h) than at 175 ºC (after 168 h). It should be noted that Z-phase and/or pectolite remained and coexisted with gyrolite. If the former compound under given conditions is metastable, then the latter one does not decompose even after 168 h of isothermal curing at 200 ºC (Fig. 4, curve 6). It is likely that such reaction mechanism is influenced by Na^+ ions.

All the data has been confirmed by the IR spectroscopy measurements which may be used to distinguish gyrolite from Z-phase as well as from other calcium silicate hydrates [28, 29]. After comparing the IR spectra of Z-phase and gyrolite it was stated that a weaker band near 595 cm^{-1} is characteristic of Z-phase when a doublet near 595 and 614 cm^{-1} is noticed in the IR spectra of gyrolite (Fig. 5, curve 2). The band near approximately 976 cm^{-1} is more intensive in the IR spectrum of Z-phase (Fig. 5, curve 1) than in gyrolite spectrum (Fig. 5, curve 2). IR spectrum of Z-phase displays a shoulder near 1130 cm^{-1} corresponding to a strong peak in the spectrum of gyrolite.

A sharp peak near 3635 cm^{-1} is visible only in the gyrolite spectra (Fig. 5, curves 2–4). This proves that clearly distinguished OH positions exist in the structure of gyrolite which are connected only with Ca atoms being not influenced by hydrogen bridge links. The OH groups are not so well positioned in the Z-phase structure. A wide band near 3446 cm^{-1} indicates that molecular water forms hydrogen bridges in the interlayers. The bands in the range of 1634 cm^{-1} are assigned to $\delta(H_2O)$ vibrations and confirm this presumption. This peak in the gyrolite spectra is a bit wider (compared with Z-phase or tobermorite), which corresponds to a greater quantity of molecular H_2O in gyrolite structure (Fig. 5, curves 2–4). It is likely that absorption bands in the range of

904 and 926 cm^{-1} are characteristic of pectolite because these peaks were not present in the IR spectra of pure gyrolite. They may be attributed to some modification in the crystal lattice of gyrolite due to intercalation of Na^+ ions into the structure (Fig. 5, curves 3–4).

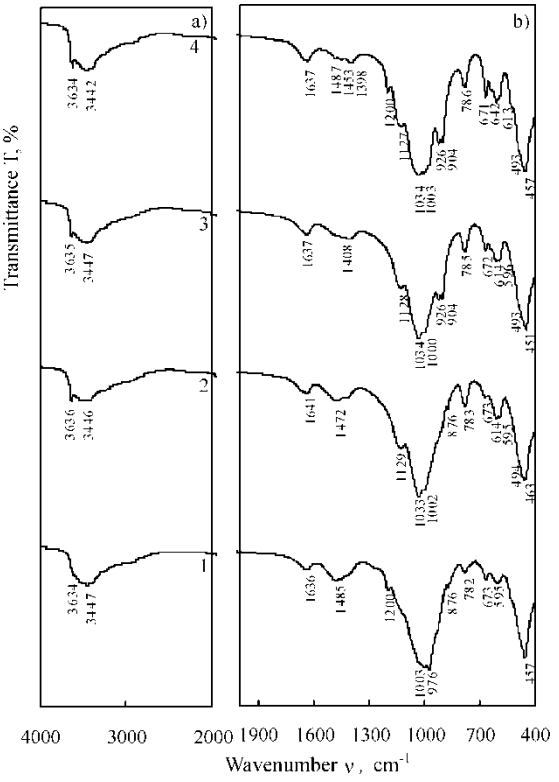

Fig. 5. IR spectra of the synthesis products; duration of hydrothermal synthesis at 200 ºC: 1 – 16 h, 2 – 24 h, 3 – 32 h, 4 – 72 h

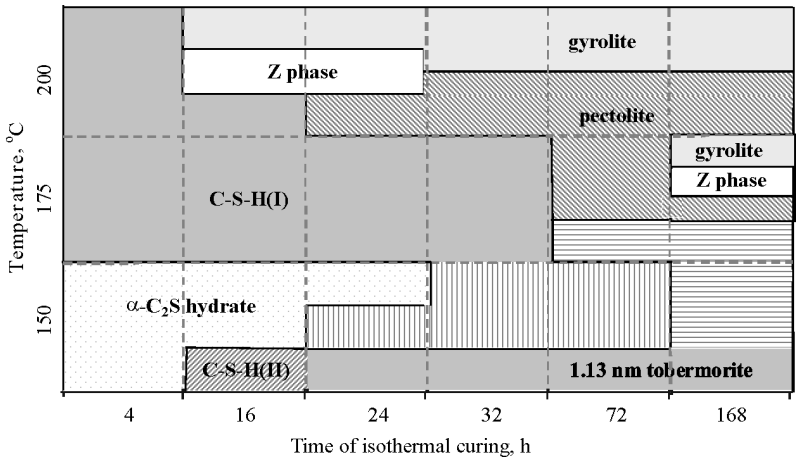

Fig. 6. Dependence of the phase compositions of the products on the temperature and duration of synthesis. Molar ratio of the primary mixture C/S = 0.66, Na_2O content – 5%

The sequence of compounds formed in the synthesis, depending on the temperature and duration of hydrothermal treatment, is demonstrated in Fig. 6. At the beginning of the synthesis α-C_2–S hydrate and C–S–H(II) are formed. They are transferred into compounds of lower basicity – C–S–H(I) and 1.13 nm tobermorite – when the duration and temperature of isothermal curing are increased. Later on, when more and more quartz dissolves, compounds with the stoichiometric composition corresponding to the molar ratio of the primary mixture – Z-phase, gyrolite and pectolite – are formed. The first one exists for a short time, while gyrolite and pectolite remain stable even after 168 h of synthesis at 200 ºC.

Acknowledgement

We gratefully thank A. Baltusnikas, the Head of X-ray Diffraction Analysis Laboratory of KTU for carrying out X-ray analysis experiments and for his constructive comments on the paper.

4. Conclusions

The temperature of 150 ºC is too low for the synthesis of gyrolite. Due to low quartz dissolution rate, the stoichiometric ratio C/S = 0.66 is not reached even after 168 h of synthesis, neither in pure mixtures nor in mixtures with addition of Na_2O. Na^+ ions in the CaO–quartz–H_2O mixtures significantly influence the formation of gyrolite in the temperature range from 175 ºC to 200 ºC. Gyrolite is formed at 175 ºC after 168 h and at 200 ºC after 16 h of isothermal curing. On the contrary, in pure mixtures gyrolite did not form even after 72 h at 200 ºC. Na^+ ions change the composition of intermediate and final products of the synthesis. In the mixtures with 5% Na_2O, intermediate compounds are C–S–H(I) and Z-phase, and the final products are gyrolite and pectolite. In the mixtures without Na_2O, the main intermediate compounds are α-C_2–S hydrate and C–S–H(II), and the main products are 1.13 nm tobermorite and xonotlite. Na^+ ions influence the temperature of recrystallization of C–S–H(I) and gyrolite into wollastonite, by reducing it about 50 ºC.

References

[1] http://mineral.galleries.com/minerals/silicate/gyrolite/gyrolite.htm, as on 17 March 2007.
[2] FLINT E.P., MCMURDIE H.F., WELLS L.S., J. Res. Natl. Bur. Stand., 21 (1938), 617.
[3] BABUSHKIN V.I., MATVEEV G.M., MCHEDLOW-PETROSSYAN O.P., *Thermodynamics of Silicates*, Stroyizdat, Moscow, 1962 (in Russian).
[4] EL-HEMALY S.A.S., ABO-EL-ENEIN S.A., DESSOUKI A.M., ISMAIL M.R., II Cemento, 3 (1986), 227.
[5] SUZUKI K., NISHIKAWA T., IKENAGA H., ITO S., Cem. Concr. Res., 16, (1986), 333.
[6] BLAKEMAN E.A., GARD J.A., RAMSAY C.G., TAYLOR H.F.W., J. Appl. Chem. Biotechn. 24 (1974), 239.
[7] AL-WAKEEL E.I., EL-KORASHY S.A., EL-HEMALY S.A., RIZK M.A., J. Mater. Sci., 36 (2001), 2405.
[8] MIYAKE M., IWAYA M., SUZUKI T., J. Amer. Ceram. Soc., 73 (1990), 3524.
[9] NOCUN-WCZELIK W., Cem. Concr. Res., 29 (1999), 1759.
[10] NOCUN-WCZELIK W., Cem. Concr. Res., 27, (1997), 83.

[11] FAUCON P., CLAUDE-PETIT J., J. Amer. Ceram. Soc., 82, (1999), 1307.
[12] SHRIVASTAVA O.P., KOMARNENI S., Cem. Concr. Res., 21, (1991), 83.
[13] MERLINO S., Mineral. Mag., 52 (1988), 377.
[14] SUKHESWALA N., AVASIA R.K., GANGOPADHYAY M., Mineral. Mag., 39 (1974), 658.
[15] SEAGER A., Mineral. Mag., 37 (1969), 147.
[16] ELTON N.J., HOOPER J.J., HOLYER V.A.D., Mineral. Mag., 62, (1998), 271.
[17] MACKAY A.L., TAYLOR H.F.W., Mineral. Mag., 30 (1953), 80.
[18] SHAW S., HENDERSON C.M.B., CLARK S.M., Amer. Min., 87 (2002), 533.
[19] SHAW S., Ph.D. Thesis, University of Manchester, 1999.
[20] MIYAKE M., KOMARNENI S., ROY R., Mater. Res. Bull., 24 (1989), 311.
[21] KOMARNENI S., BREVAL E., MIYAKE M., ROY R., Clays Clay Miner., 35 (1987), 385.
[22] EL-KORASHY S.A., J. Ion Exch., 15, (2004), 2.
[23] EL-KORASHY S.A., AL-WAKEEL E.I., EL-HEMALY S.A., RIZK M.A., Egypt J. Chem., 45, (2002), 723.
[24] WINTERS M.A., RICHTER J.D., SAGAR S.L., LEE A.L., LANDER R.J., Biotechnol. Prog., 19 (2003), 440.
[25] SIAUCIUNAS R., BALTAKYS K., Cem. Concr. Res., 34 (2004), 2029.
[26] BALTAKYS K., ŠIAUČIŪNAS R., BALTUŠNIKAS A., Chem. Techn., 1 (2004), 45.
[27] CHEARY R.W., COELHO A.A., Programs XFIT and FOURYA, deposited in CCP14 Powder Diffraction Library, Engineering and Physical Sciences Research Council, Daresbury Laboratory, Warrington, England, (1996), (http://www.ccp14.ac.uk/tutorial/xfit-95/xfit.htm).
[28] YU P., KIRKPATRICK R.J., POE B., MCMILLAN P.F., CONG X., J. Am. Ceram. Soc., 82, (1999), 724.
[29] GARBEV K., Ph.D. Thesis, Faculty of Geology and Geography, St. Kliment Ohridski University, Sofia, 2004.

Received 28 June 2007

Materials Science-Poland, Vol. 25, No. 4, 2007

Interactions of high current pulsed electron beam with phosphate laser glass

C. WANG [1*], S. HAO [2], F. SHI [1], J. QI [3, 4], Y. TAO [1], B. WANG [5]

[1]Institute of Glass and New Inorganic Material, Dalian Institute of Light Industry, Dalian, China

[2]State Key Laboratory for Materials Modification by Ion, Electron and Laser Beams, Dalian University of Technology, Dalian, China

[3]Department of Chemical Engineering, Life Science College, Dalian Nationalities University, Dalian, China

[4]State Key Laboratory of Fine Chemicals, Dalian University of Technology, Dalian, China

[5]World Minerals Inc., Lompoc, California, USA

Impact of electron beam bombardment on the surface of Nd^{3+} doped P_2O_5–B_2O_3–Al_2O_3–BaO laser glass was investigated. Physical properties of the bombarded glass were measured by 3D laser roughometer, microhardness tester, UV/VIS spectrometer, EDS and contact goniometer. Low beam energy had no significant impact on glass surface morphology and other properties. High beam energy increased glass surface roughness and decreased micro-hardness, UV/VIS transmittance and wetting angle. Thermal stress generated by high energy electron beam bombardment expanded the Griffith flaws and increased glass surface roughness.

Key words: *pulsed electron beam; phosphate glass; laser; micro-cracks; surface morphology*

1. Introduction

High energy electron beam was first used for simulation of nuclear explosion and X-ray radiograph by Bernesein and Champney in 1973 [1, 2]. Since then high energy electron beam has been widely used for modifying properties of materials to improve hardness, strength and anticorrosion and wear resistance [3–6]. Phosphorite bioglass was irradiated with electron beam to improve wetting properties to increase glass compatibility with biologic cells and to prevent dew formation on the glass surface [7]. The energy intensity of pulse electron beam applied to modify metallic materials

*Corresponding author, e-mail: cwangtao@yahoo.com

is normally up to 10^8–10^9 W/cm^2 [8] while the corresponding energy intensity applied to glass surface modification is relatively low [7]. When soda lime silicate glass was bombarded with electron beam with energy intensity of 10^{12} W/cm^2, micro-flaws were formed on the glass surface due to a high thermal stress [9]. In this paper, we report on the impact of electron beam bombardment on properties of the surface of commercial Nd^{3+} doped P_2O_5–B_2O_3–Al_2O_3–BaO laser glass.

2. Experimental

Nadezhda-2 type pulsed high current electron beam developed by Proskurovsky et al. [10, 11], was used in this study. The beam energy and peak current were between 10–40 keV and 10^2–10^3 A/cm^2, respectively. Pulse duration was between 0.8 and 2 μs, beam area was 30 cm^2 and energy intensity was between 1 and 6 J/cm^2. The Nd_2O_3 doped phosphate glass for this study contained 67.29 wt. % of P_2O_5, 4.50 wt. % of B_2O_3, 3.40 wt. % of Al_2O_3 and 24.81 wt. % of BaO. Glass batch was melted in a platinum crucible and then cast to flat sheet, annealed, polished, and cut into the plate samples (10×10×1 mm^3). The glass plates were washed with tap water, ethanol and de-ionized water, dried in a vacuum chamber and then irradiated with electron beam at 19.869, 23.807, 26.85 and 28.64 keV, respectively.

Glass surface morphology was examined by a Zygo 5022 3D Laser roughometer. Surface hardness was measured with a Matsuzawa DMH-2LS microhardness tester. A Perkin Elmer LAMBDA 35 UV/VIS spectrometer was used to record UV/VIS spectra. An Oxford Instruments INCA energy disperse spectrometer was used to analyze glass surface composition. Wetting angle was measured by a JY-B type contact goniometer.

3. Results

As shown in Fig. 1, glass surface morphology is about the same after irradiation with electron beam at 19.869 keV (Fig. 1b). When beam energy is 23.807 keV (Fig. 1c), some arborization flaws consisting of stem flaws and offshoot flaws are formed on the glass surface. These flaws propagate when beam energy is increased to 26.85 keV (Fig. 1d). Concave and protruding annular concentric flaws are formed when beam energy is 28.64 keV (Fig. 1e). The dependence between the surface roughness and electron beam accelerating voltage is shown in Fig. 2. Compared to the starting glass sample, there is no change in the mean square roughness (Rms) and the average roughness of (Ra) after bombardment with electron beam at 19.869 keV. The roughness increases sharply when the beam energy is increased to 23.807 keV. At 28.64 keV, Rms increases to 410 nm. Microhardness as a function of beam energy is

shown in Fig. 3. It can be seen that microhardness decreases with increasing beam energy with pronounced decreasing rate between beam energy of 23.807 keV and 26.85 keV. As shown in Fig. 4, the wetting angle decreases with increasing beam energy.

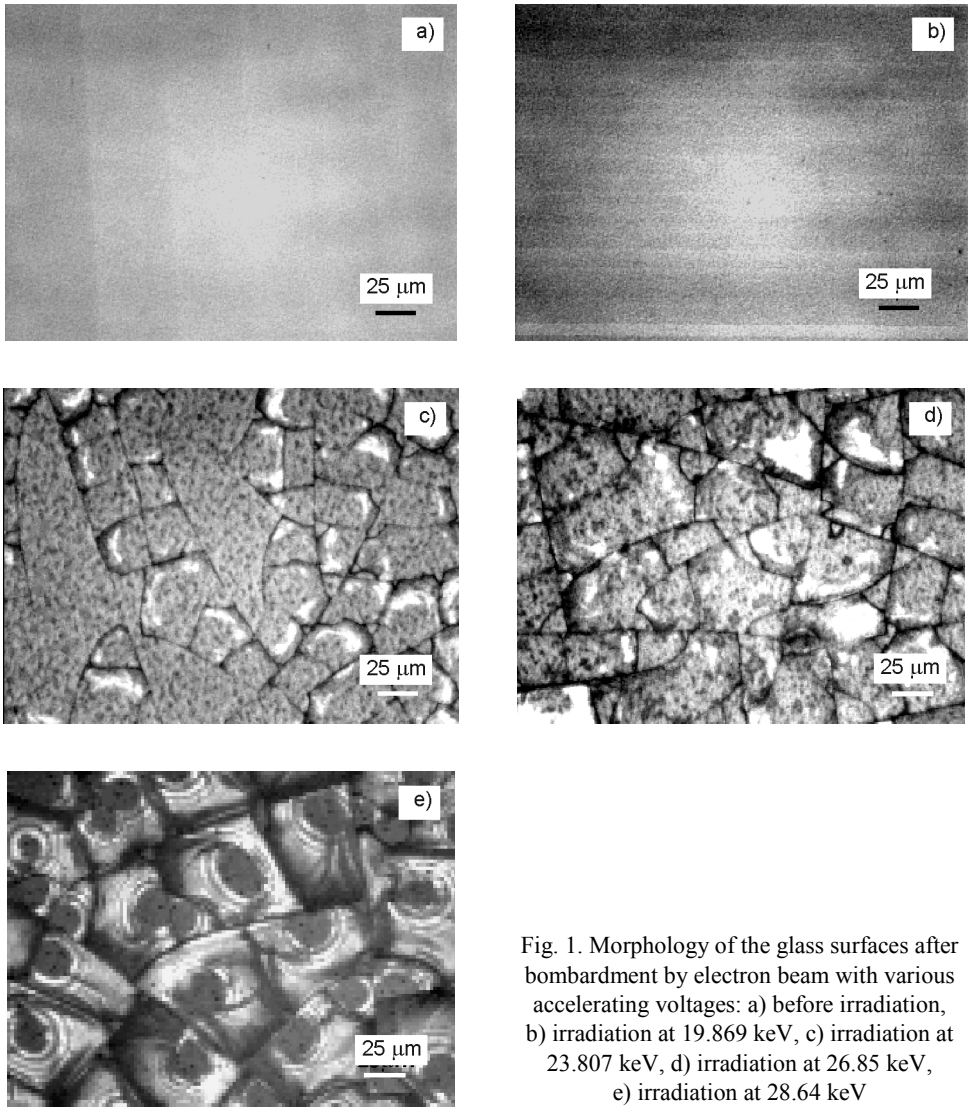

Fig. 1. Morphology of the glass surfaces after bombardment by electron beam with various accelerating voltages: a) before irradiation, b) irradiation at 19.869 keV, c) irradiation at 23.807 keV, d) irradiation at 26.85 keV, e) irradiation at 28.64 keV

Figure 5 shows UV/VIS spectra of the electron beam bombarded sample. The absorption peaks can be attributed to Nd^{3+} electron transitions between various energy levels. Peaks at 350, 356, 430, 476, 511, 524, 582, 682, 746, 802, 874 nm correspond to ^4D, $^4D_{5/2}$, $^2P_{1/2}$, $^{3/2}G_{9/2}$, $^4G_{9/2}$, $^2K_{13/2}$, $^2G_{5/2}$, $^4F_{9/2}$, $^4F_{7/2}$, $^4F_{5/2}$, $^4F_{3/2}$ energy level transitions, respectively. These results are slightly different from the results reported in ref-

erence [12] due to different substrate glass compositions. The transmittance decreases with increasing beam energy with no shift in peak positions.

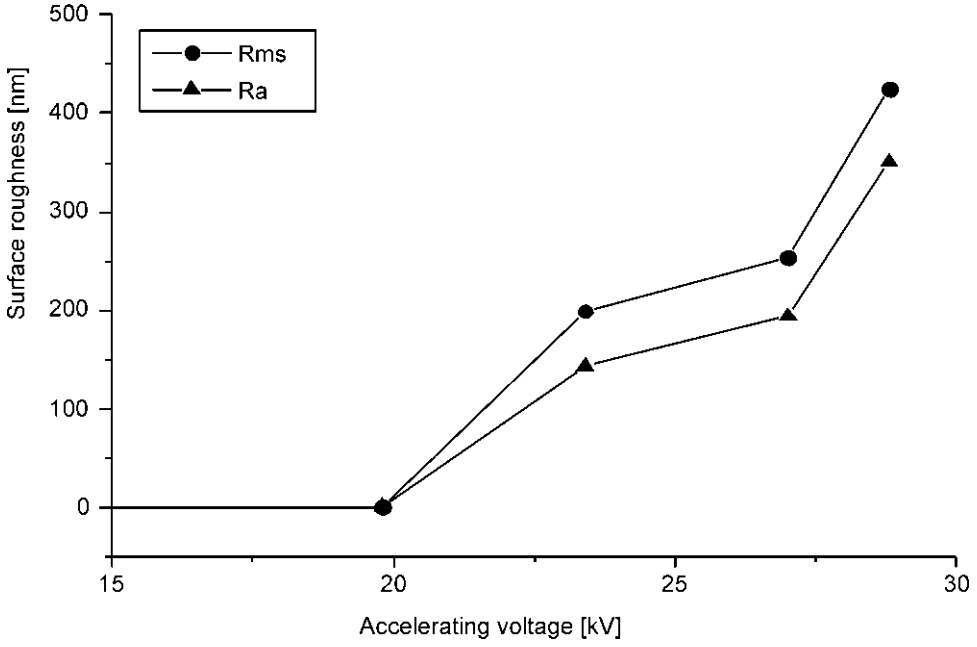

Fig. 2. Roughness of glass surface as a function of the accelerating voltage of electron beam

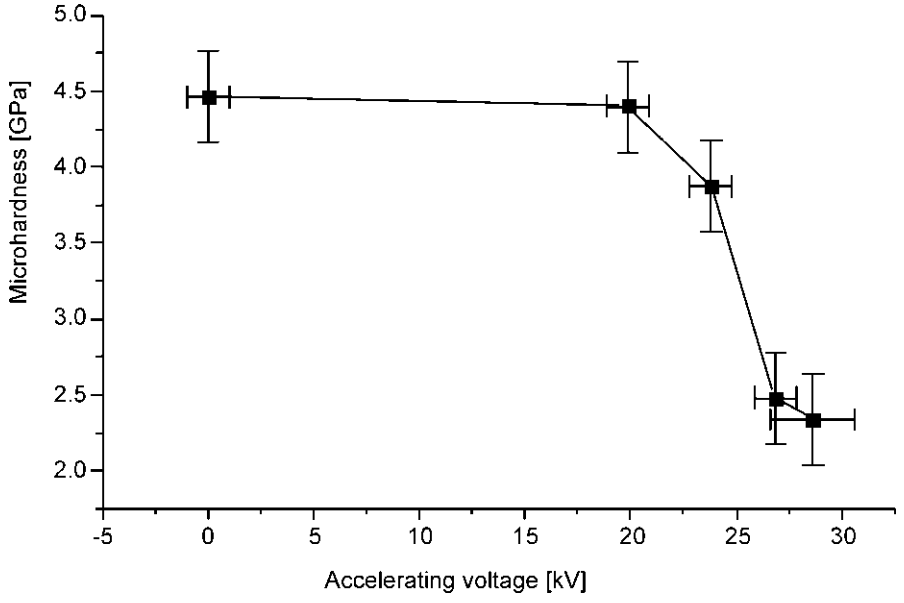

Fig. 3. Dependence of glass microhardness on the accelerating voltage of electron beam

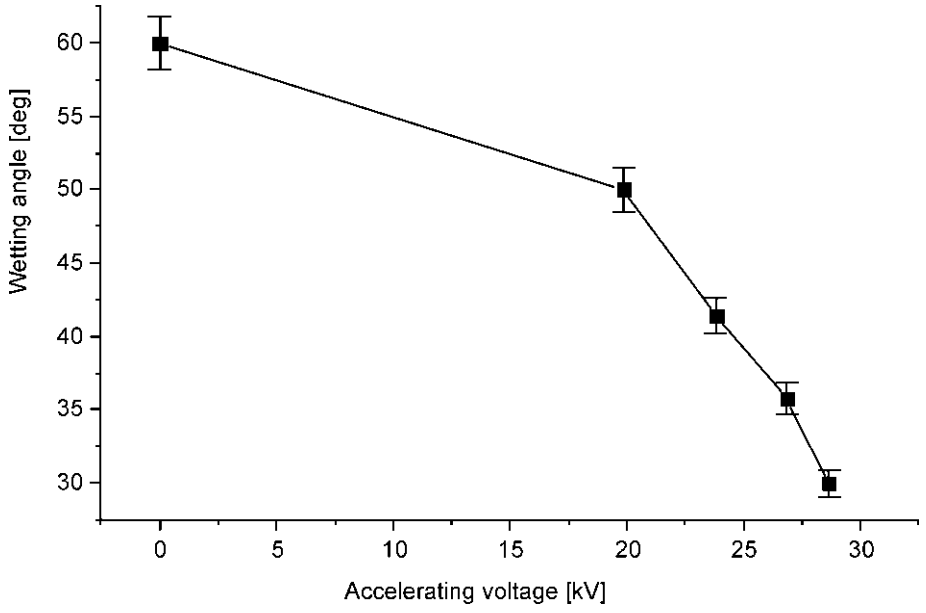

Fig. 4. Dependence of glass surface wetting angle on the accelerating voltage of electron beam

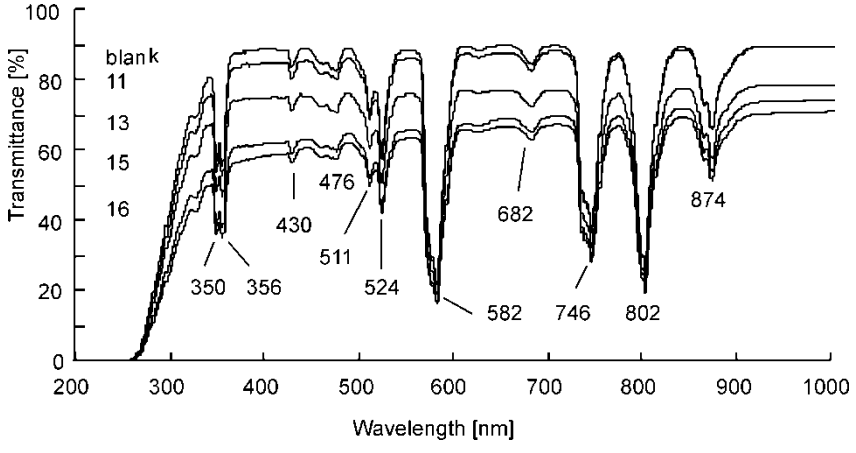

Fig. 5. UV/VIS transmittance spectra of glass after bombardment by electron beam with various accelerating voltages

Glass surface compositions (at. %) of O, P, Ba and Al as a function of accelerating voltages are shown in Figs. 6–9, respectively. When electron beams irradiate the glass surface, oxygen atoms are sputtered from the surface. Therefore, the oxygen concentration decreases with increasing beam energy. Other atoms with higher atom weight such as P and Ba are difficult to be sputtered so the concentrations of these atoms increase with the beam energy. The aluminium concentration appears to increase with

increasing beam energy probably due to the abnormal fluctuation in EDS measurement.

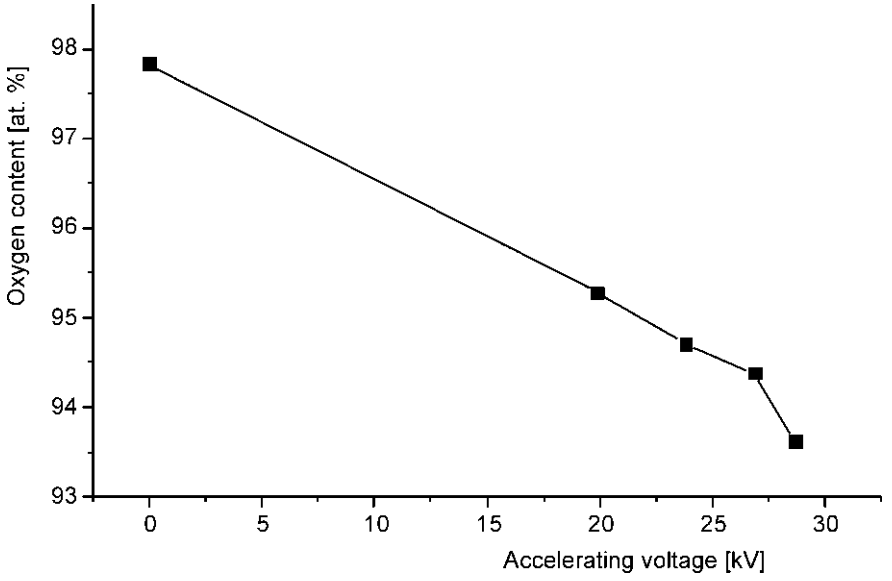

Fig. 6. Oxygen contents (at. %) on the glass surface after bombardment by electron beam with different accelerating voltages

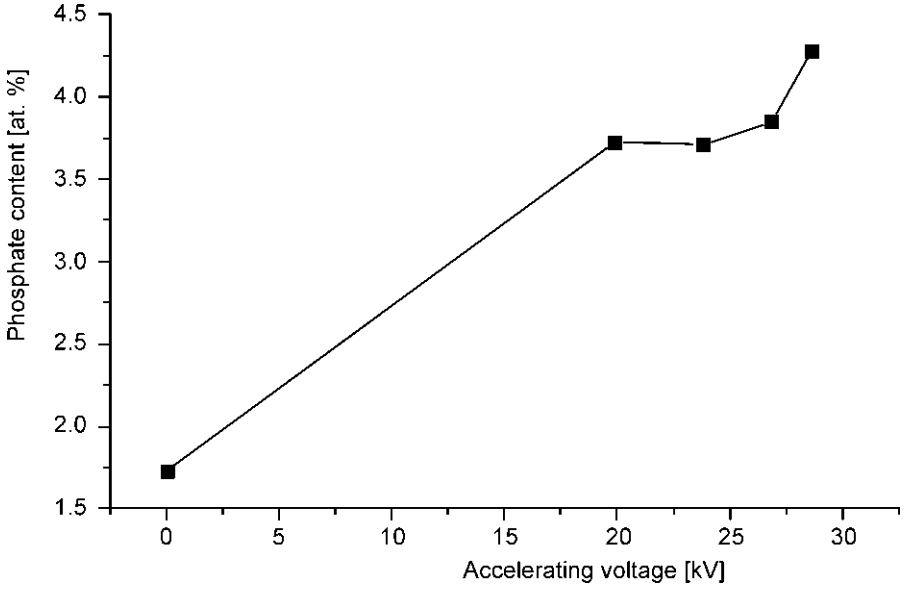

Fig. 7. Phosphate contents [at. %] on the glass surface after bombardment by electron beam with various accelerating voltages

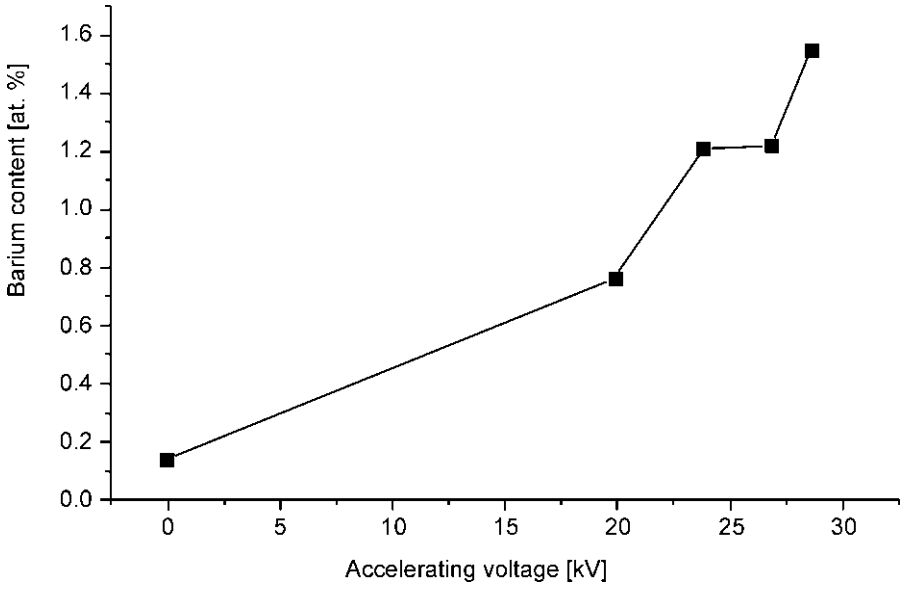

Fig. 8. Barium contents [at. %] on the glass surface after bombardment by electron beam with various accelerating voltages

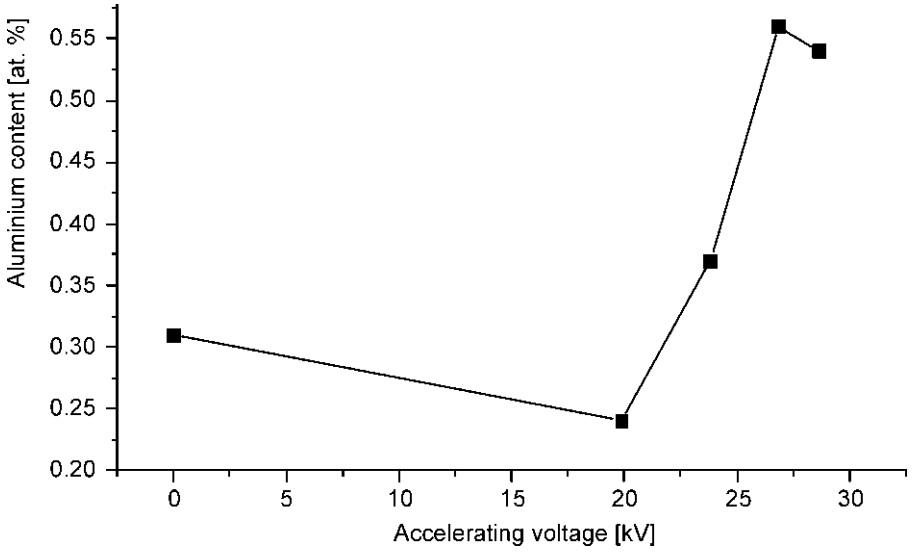

Fig. 9. Aluminium contents [at. %] on the glass surface after bombardment by electron beam with various accelerating voltages

4. Discussion

When high energy electron beams bombard glass surface, excitation and ionization of the surface atoms occurs. A large amount of energy concentrates on a small

area of the glass surface (the maximum energy intensity is up to 10^{12} W/cm^2) and the local temperature rapidly increases. Since the temperature of other areas on the glass surface is relatively low, a temperature gradient is formed to cause strong thermal expansion. The thermal stress expands the Griffith flaws to form more microflaws. These microflaws propagate with increasing beam energy.

When glass surface is bombarded with high current pulsed electron beams, the first pulsed electron beam bombardment forms stem flaws and then offshoot flaws. The second pulsed electron beam bombardment forms pulse stress. The transmitting rate of pulse stress is higher than the diffusion of offshoot flaws. Interaction between pulse stress and offshoot flaws changes the diffusion direction of the flaws to form annular ripples as shown in Fig. 1e).

After bombardment with electron beams, microflaws formed on the glass increase surface roughness and decrease microhardness. The contact area between water and glass increases due to rougher surface. This will decrease the wetting angle and improve wetting property. The dispersion of visible light on the glass surface increases with increasing surface roughness and this leads to low transmittance.

5. Conclusions

High pressure and temperature gradients generated by high current pulsed electron beam bombardment on the phosphate glass surface produce high stress. This stress expands the Griffith flaws to form arborization flaws and cross flaws. The micro flaws propagate with increasing electron beam energy and annular ripples are formed at a high beam energy. The roughness of glass surface increases, and micro hardness, visible light, ultra violet transmittance and wetting angle decrease with increasing beam energy.

References

[1] BERNSEIN B., IEEE. Trans. Nucl. Sci., NS-20 (1973), 294.
[2] CHAMPNEY P., IEEE. Trans. Nucl. Sci., NS-22 (1973), 970.
[3] ZENKER R. MULLER M., Heat Treat. Metal, 15 (1988), 79.
[4] MLADENOV G. VUTOVA K., WOJCICKI S., Vacuum, 51(1998), 231.
[5] DONG C. WU A., HAO S., Surf. Coat. Techn., 163 (2003), 620.
[6] HAO S. GAO B., ZHOU J., Trans. Mater. Heat Treat., 21(2004), 1934.
[7] MA J., Bull. Chin. Ceram. Soc., 20 (2001), 63 (in Chinese).
[8] STARK R., CHRISTIANSEN J., IEEE Trans. Plasma Sci., 23 (1995), 258.
[9] WANG C., TAO Y., LIU G., J. Chin. Ceram. Soc., 31(2003), 99 (in Chinese).
[10] PROSKUROVSKY D.I., ROTSHTEIN V.P., OZUR G.E., Vacuum. Soc. Technol., A 16 (1998), 248.
[11] PROSKUROVSKY D.I. ROTSHTEIN V.P., OZUR G.E., Surf. Coat. Technol.,125 (2000), 49.
[12] GAN F., *Optical and Spectroscopic Properties of Glass*, Science and Technology Press, Shanghai, 1992 (in Chinese).

Received 20 August 2007

Materials Science-Poland, Vol. 25, No. 4, 2007

Synthesis of Zn_2TiO_4 and $ZnTiO_3$ nanocomposites by the CBD method

M.R. VAEZI[1*], A. ESMAIELZADEH KANDJANI[2], L. NIKZAD[1], N.A. AREFIAN[2], S. ALIBEIGI[2], M. FARZALIPOUR TABRIZ[3], S.H. MIR SHAH GHASSEMI[2], J. SAMEI[2]

[1]Research Center of Advanced Materials, Materials and Energy Research Center, Karaj, Iran

[2]Department of Material Science and Engineering, Faculty of Mechanical Engineering, K. N. Toosi University of Technology, Tehran, Iran

[3]Department of Material Science and Engineering, Faculty of Mechanical Engineering, University of Tabriz, Tabriz 51666-16471, Iran

$Zn_2TiO_4/ZnTiO_3$ nanopowders were synthesized via CBD method. $TiCl_4$, $ZnCl_2$ and NaOH were used as precursors. The effect of temperature was investigated on morphologies and compositions of final product. The calcinations of the samples were carried out at 630 ºC. The structures and morphologies of the products were studied by X-ray diffraction and scanning electron microscopy. The results show that the best temperature for fabrication of the compounds without ZnO is 25 ºC.

Key words: *Zn_2TiO_4; $ZnTiO_3$; nanopowder; composite; chemical bath deposition*

1. Introduction

Because of interesting optical and electrical properties of ZnO, this material has extensively been studied. Low cost of precursors, simplicity and high efficiency of its chemical synthesis encourage scientists to investigate on nano-ZnO. ZnO obtained under various conditions has different nanomorphologies, in turn affecting properties of this metal oxide. Also, TiO_2 is one of the most extensively studied oxides because of its remarkable optical and electrical properties.

Zinc titanates are promising candidates as dielectric materials [1–3]. It has been reported that three compounds exist in $ZnO–TiO_2$ system, including Zn_2TiO_4 (cubic), $ZnTiO_3$ (hexagonal), and $Zn_2Ti_3O_8$ (cubic) [4–6]. Among these compounds, ilmenite

[*]Corresponding author, e-mail: vaezi9016@yahoo.com

type hexagonal $ZnTiO_3$ has been reported to have superior electrical properties: the dielectric constant of 19, high quality factor Q = 3000 (at 10 GHz), and the temperature coefficient of resonance frequency τ_f = –55 ppm/ºC, very similar to those of other ilmenite type titanates [3, 7, 8]. Li et al. [9] reported the formation of a new $ZnTiO_3$ (cubic) phase as a precipitate inside the Zn_2TiO_4 matrix having the same structure and lattice parameter with Zn_2TiO_4 phase. Zinc orthotitanate, Zn_2TiO_4, can be easily prepared via the conventional solid-state reaction of $2ZnO{\cdot}TiO_2$.

According to XRD patterns of CBD synthesis of ZnO, upon increasing temperature, the particle size and morphology of ZnO can be changed. As noticed in related papers, in dropwise CBD synthesis, if aqueous solutions of $ZnCl_2$ and NaOH were used as precursors, nano-ZnO flakes are observed at ambient temperature. On the other hand, in reaction between $TiCl_4$ and NaOH, amorphous TiO_2 particles are formed, which convert to rutile at about 600 ºC, according to DTA diagram. One of the main procedures for producing mixed oxides is to arrange conditions for diffusion of oxides into each other [10, 11]. Due to dependence of the diffusion coefficient of oxides on their structure, surface area, etc., the crystallography and physical properties of the obtained particles can be changed by changing their morphology and particle sizes.

Although rich literature exist on the synthesis of oxide nanocomposite powder, very little attention has been paid to the effect of synthesis conditions such as synthesis temperature on the morphology and particle size distribution of these nanocomposites. Furthermore, no previous studies have been conducted on the influence of synthesis temperature on the diffusion processing of oxide particles (ZnO and TiO_2) into each other. It is interesting to know how the morphology and size distribution of the obtained particles change with the variation of temperature. Therefore, the purpose of this paper is to present results of such studies for chemical bath deposited Zn_2TiO_4 and $ZnTiO_3$ nanocomposites.

We obtained nanocomposites of crystalline ZnO with amorphous TiO_2 before calcination processing. After calcination, nanocrystalline Zn_2TiO_4 and $ZnTiO_3$ from $ZnO–TiO_2$ (1:1 mol %) were prepared.

2. Experimental

The starting materials, $TiCl_4$, and NaOH purchased from Merck and $ZnCl_2$ purchased from Fluka were used without further purification.

Scanning electron microscopy studies were preformed using an OXFORD Leo 440i microscope. The size measurements were carried out with an Able Image Analyzer v3.6. Powder X-ray diffraction studies were carried out using a Philips (PW3710) diffractometer with CuKα radiation source (λ = 0.154178 nm). Quantitative analyses were performed by X-ray fluorescence (XRF) using an XRF- 8410 RH operated at 60 kV. Simultaneous differential thermal analysis (DTA) and thermogravimetric analysis (TGA) were performed in the powder samples with a thermal analyzer system model STA 1640.

Two separate aqueous solutions of $ZnCl_2$ (1 M, 100 ml) and NaOH (6 M, 100 ml) were prepared. Due to high chemical reactivity of $TiCl_4$ with water, it was used without being dissolved in water. After preparation of the solutions, a separate $ZnCl_2$ solution and $TiCl_4$ were added dropwise to the NaOH solution simultaneously. This procedure lasted 30 min at various temperatures, as shown in Table 1. Then the samples were kept for 2 h at the same operating conditions. The obtained precipitates were centrifuged and then washed with distilled water and absolute methanol for several times. Finally, the precipitates were dried at about 50–60 ºC for 24 h.

Table 1. Conditions of syntheses

Sample	Temperature [ºC]	Stirring time [h]
I	25	2.5
II	55	2.5
III	75	2.5

All synthesized powders were calcined at about 630 ºC for 4 h and then naturally cooled to room temperature. The structures and morphologies of the powders were investigated by XRD and SEM, respectively.

3. Results and discussion

3.1. Synthesis of crystalline ZnO/amorphous TiO_2 nanocomposite powder

XRD patterns of ZnO–TiO_2 nanocomposite powder without calcination treatment are shown in Fig. 1. ZnO peaks were identified while amorphous TiO_2 particles were detected by XRF. Percentages of components are given in Table 2.

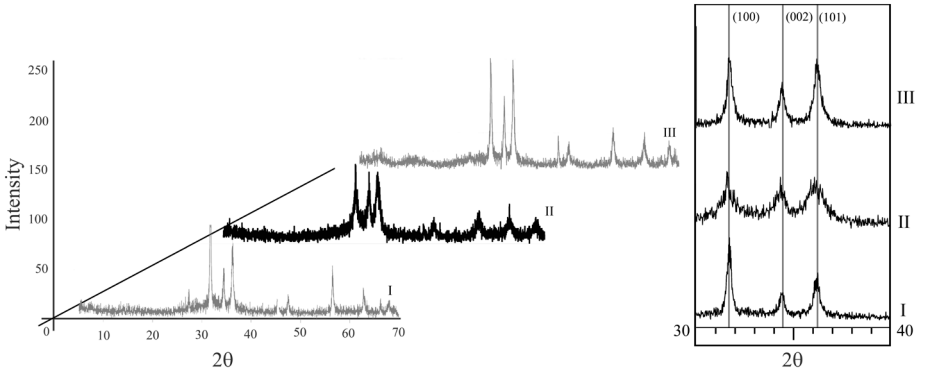

Fig. 1. XRD patterns of samples I (25 ºC), II (45–50 ºC) and III (70–75 ºC) without calcination

With the increasing reaction temperature, the intensity of ZnO XRD peaks increased. Also with increasing temperature, the sizes of obtained nanoparticles decreased and their morphologies tended to form semi-spherical particles which affected the XRD peaks of obtained nano-ZnO. This well agrees with reported observations of pure ZnO synthesis.

Table 2. XRF results of samples I, II and II

Sample	Percentage of oxides [wt. %]			Percentage of elements [wt. %]			
	TiO_2	ZnO	Na	Cl	Ti	Zn	Other
I	39.7	42.2	18.1	14.1	30.2	48.6	5.3
II	39.9	42.4	17.7	12.6	31.7	48.3	6.9
III	34.8	44.8	20.4	10.2	31.3	51.2	6.2

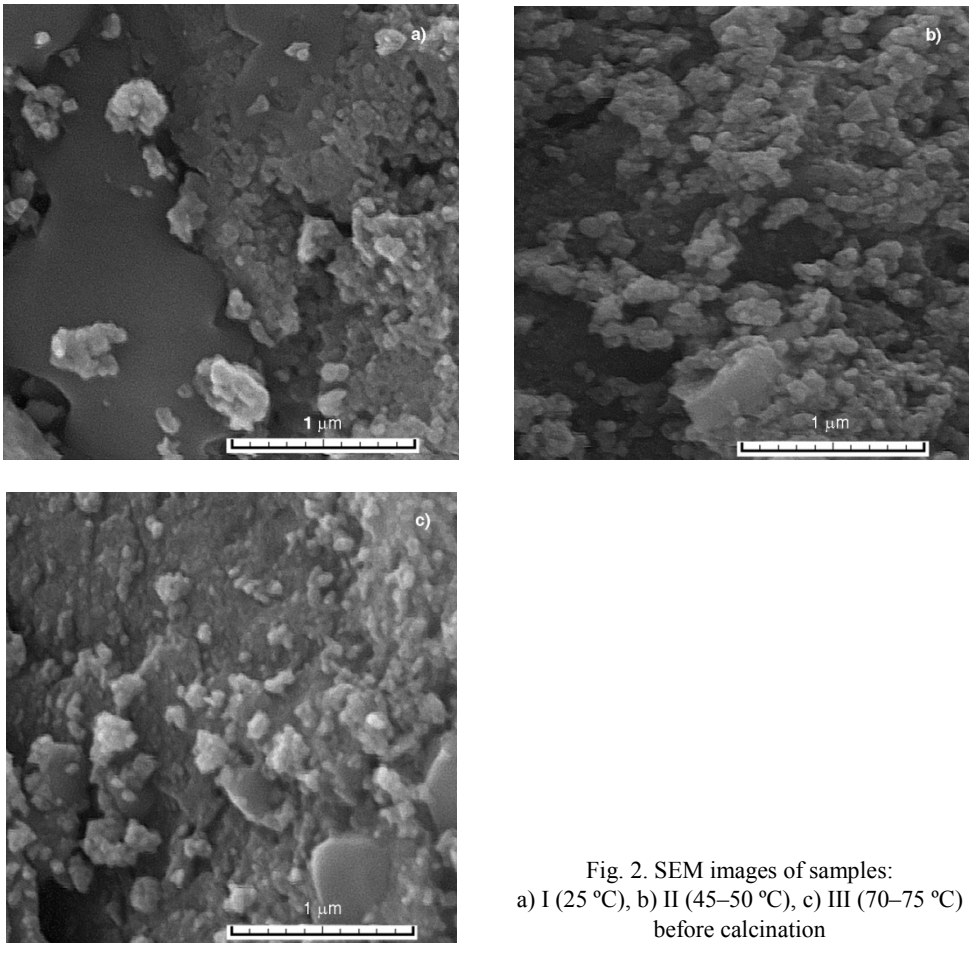

Fig. 2. SEM images of samples:
a) I (25 ºC), b) II (45–50 ºC), c) III (70–75 ºC)
before calcination

Figure 2 shows SEM images of the samples before calcination. EDAX analysis of sample I (Fig. 3) indicates that the uniform areas are TiO_2 flakes. These flakes become finer upon increasing temperature.

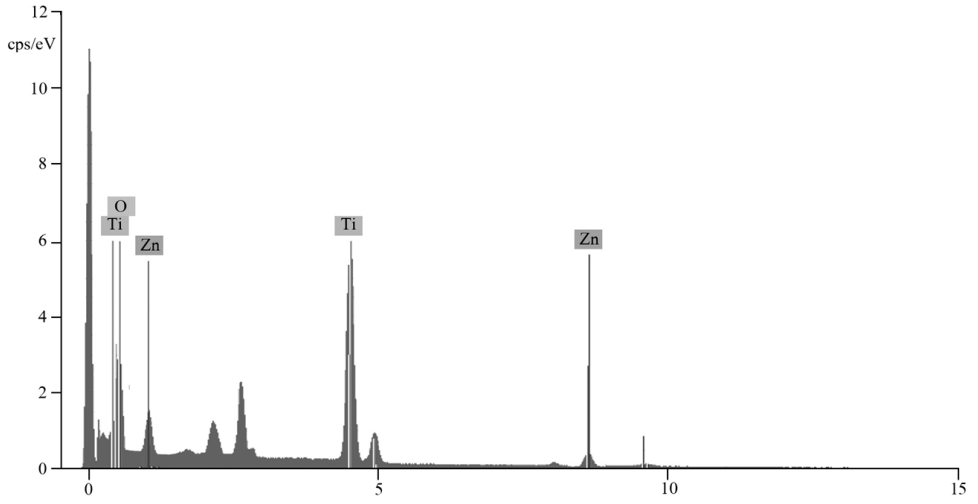

Fig. 3. EDAX result of flakes in sample I

Based on the DTA results of pure TiO_2 reported in literature [12, 13], the transformation from amorphous TiO_2 to crystalline TiO_2 is exothermic. Consequently, the temperature of 630 ºC is selected for crystallization of amorphous TiO_2. All three samples were calcined for 4 h at this temperature.

3.2. Formation of ZnO–$ZnTiO_3$–Zn_2TiO_4 nanocomposite powders

Figure 4 shows TGA/ DTA curves of the nanocomposite powders produced by the CBD method. As can be seen, there is an undulating shape in the TGA curves (Figs. 4a–c). The undulating shape of the TGA curves occurs at $T > 350$ ºC. Also, a broad exothermic peak is clearly visible in the DTA curves close to temperature initializing the undulating behaviour of TGA curves. The undulating shape of the TGA curves is due to the diffusion of ZnO and TiO_2. Because of the diffusion of ZnO and TiO_2 phases, the compounds such as $ZnTiO_3$ and Zn_2TiO_4 may be formed. A broad exothermic peak observed at 350 ºC $< T <$ 600 ºC in the DTA curves corresponds to atomic diffusion and therefore no considerable mass loss was detected in this region. No sharp exothermic peak was also observed at ~ 630 ºC in Figs. 4b, c. This peak corresponds to a phase transformation process of TiO_2 from amorphous to a crystalline state.

After calcination for 4 h at 630 ºC, XRD patterns indicate that ZnO coexists with $ZnTiO_3$, Zn_2TiO_4 and Ti_3O_5 (Fig. 5a). In the XRD pattern of sample I synthesized at 25 ºC, $ZnTiO_3$ and Zn_2TiO_4 phases can be detected, and the intensity of ZnO and Ti_3O_5 phases is negligible (Fig. 5a). It can be observed from these patterns that in-

creasing the synthesis temperature decreases the amount of $ZnTiO_3$ and Zn_2TiO_4 phases and increases that of ZnO and Ti_3O_5 phases.

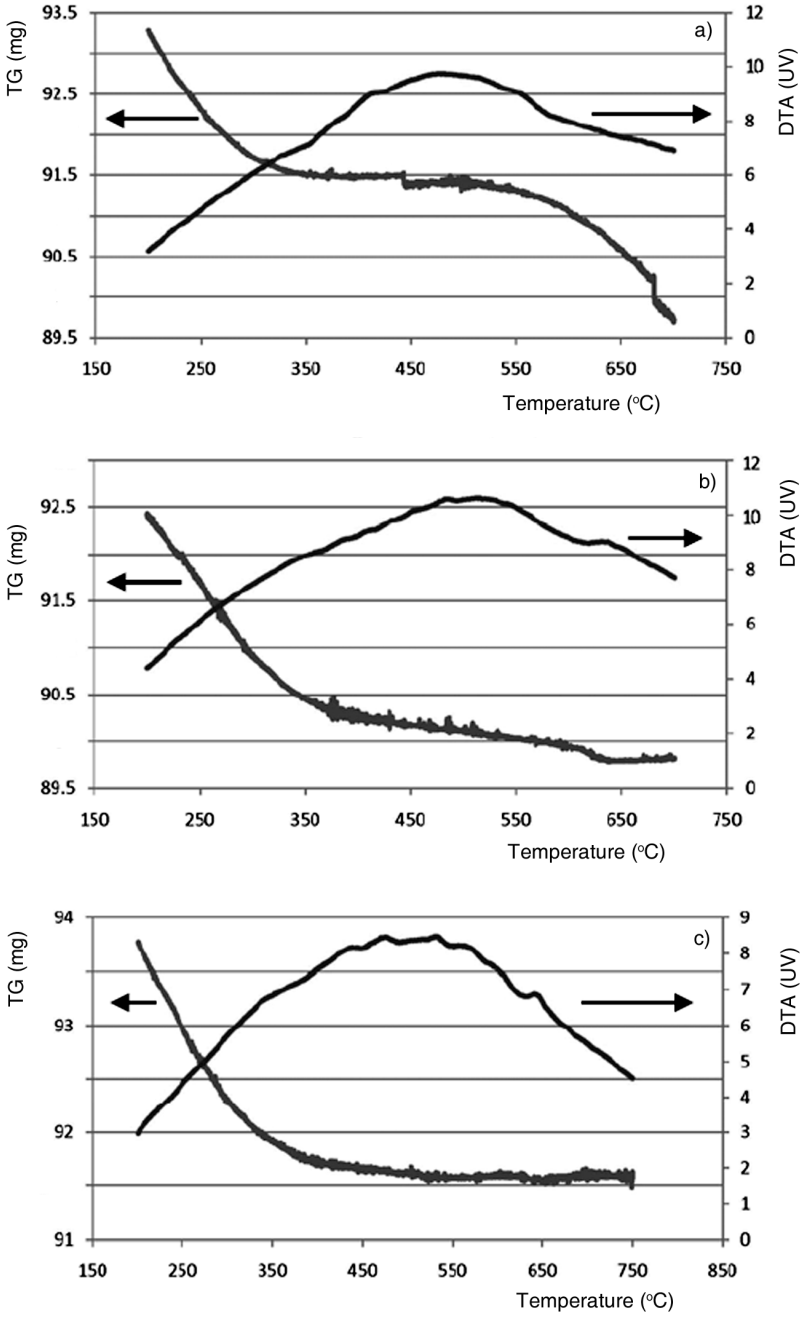

Fig. 4. TGA/DTA curves of the samples: a) I, b) II, c) III

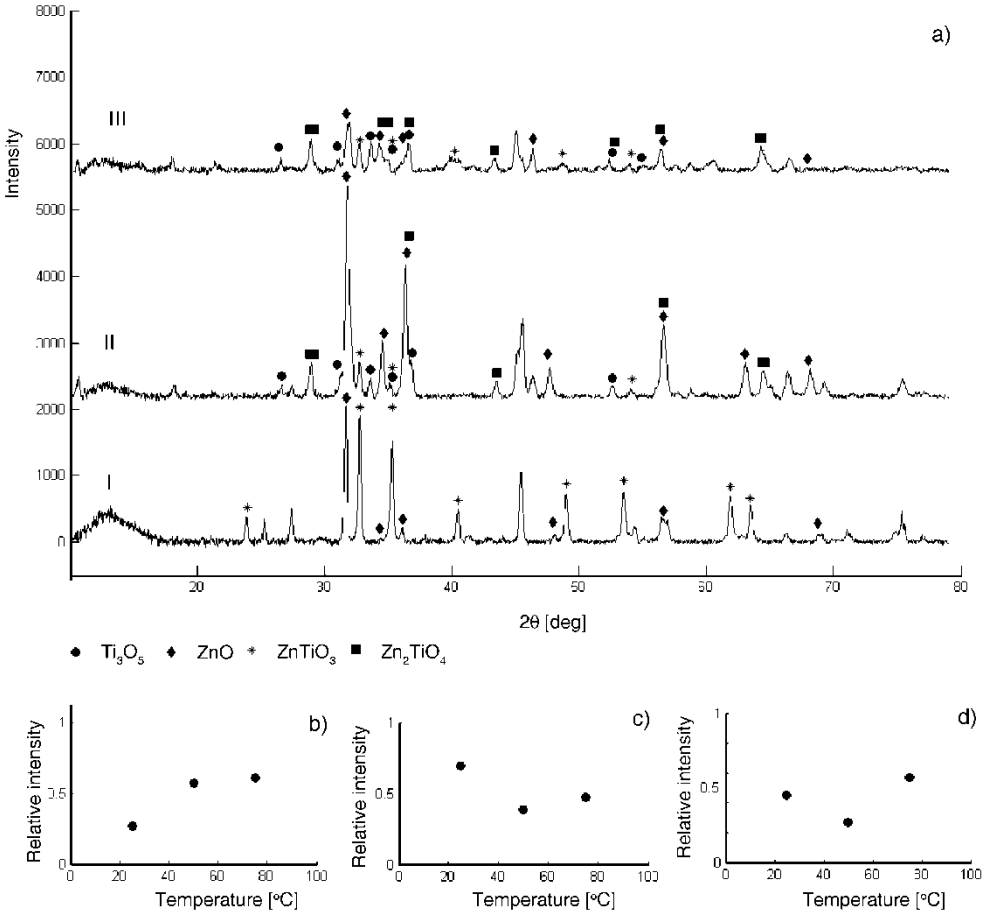

Fig. 5. XRD patterns of samples calcined at 630 ºC (a) and the relative intensity of (101) peak for ZnO (b), (104) peak for $ZnTiO_3$ (c), and (211) peak for Zn_2TiO_4 (d) vs. the synthesis temperature

Relative intensities of the peaks corresponding to (104) plane of $ZnTiO_3$ and (211) plane of Zn_2TiO_4 decreased with increasing synthesis temperature and that of the peak belonging to (101) plane of ZnO increased with increasing the synthesis temperature. Figures 5b–d show the dependence of relative intensities of ZnO ($I_{(101)}/(I_{(100)} + I_{(002)} + I_{(101)} + I_{(110)} + I_{(103)} + I_{(102)})$), $ZnTiO_3$ ($I_{(104)}/(I_{(110)} + I_{(104)} + I_{(012)} + I_{(024)} + I_{(116)})$), and Zn_2TiO_4 ($I_{(211)}/(I_{(103)} + I_{(211)} + I_{(112)} + I_{(200)} + I_{(220)} + I_{(321)} + I_{(224)})$) with the synthesis temperature. As is shown in Fig. 5b, the relative intensity of ZnO decreased after synthesizing at 55 ºC (Fig. 5b), whereas those of $ZnTiO_3$ and Zn_2TiO_4 phases decrease with increasing the synthesis temperature up to 55 ºC and then gradually increase (Figs. 5c, d). It can be concluded that the optimum temperatures of synthesis in which ZnO and $ZnTiO_3/Zn_2TiO_4$ can be considerably formed are 55 ºC and 25 ºC, respectively. Also, it can be observed from Fig. 5 that the appropriate temperature of synthesis for producing the $ZnO/ZnTiO_3/Zn_2TiO_4$ nanocomposite powder is in the range

between 25 ºC and 55 ºC. It is believed that the most intensive peaks are caused by the minimization of internal stress and surface energy.

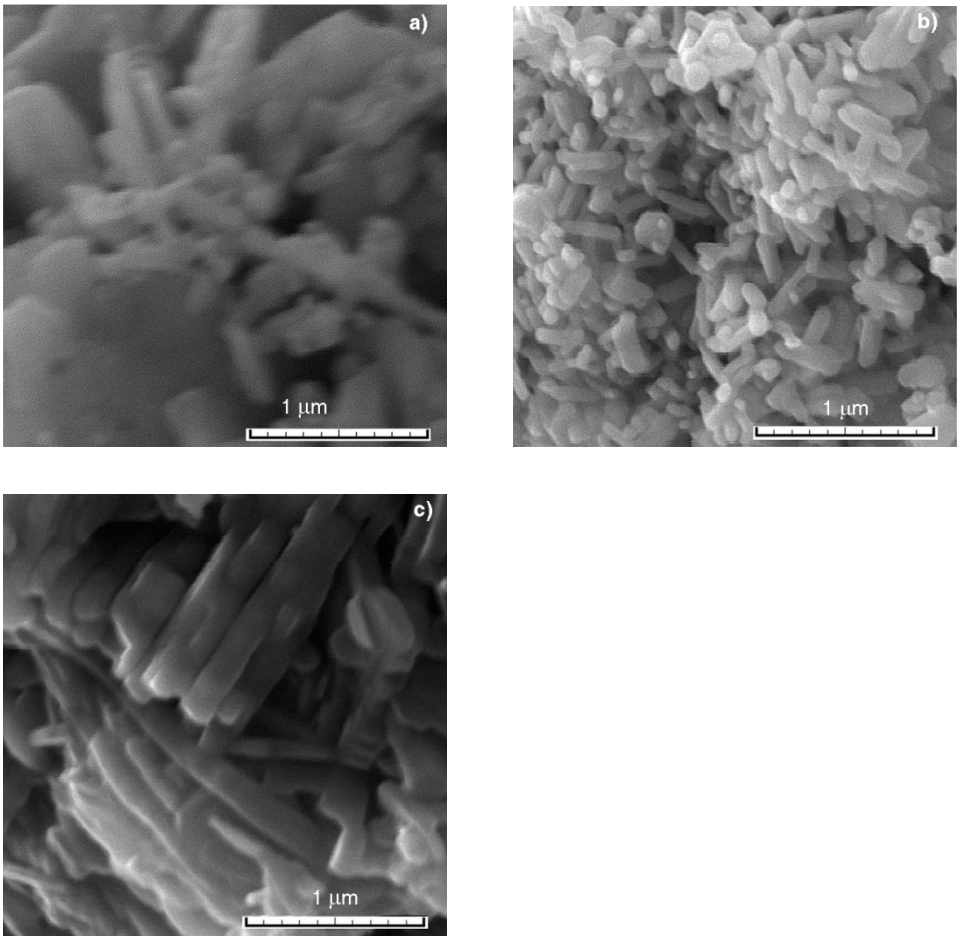

Fig. 6. SEM micrographs of samples: a) I, b) II, c) III

In Figure 6, the SEM images of samples I, II and III calcined at 630 ºC are shown. They have the same morphology and particle sizes.

4. Conclusion

Nanosized $ZnTiO_3/Zn_2TiO_4$ in CBD processing have been synthesized. The best temperature for fabrication of these compounds without ZnO is 25 ºC. Also, the appropriate temperature of synthesis $ZnO/ZnTiO_3/Zn_2TiO_4$ nanocomposite powders is in the range between 25 ºC and 55 ºC. From the thermal analysis, it can be concluded

that the diffusion process is the main factor playing a key role in synthesizing $ZnTiO_3$ / Zn_2TiO_4 nanocomposite powders.

References

[1] HAGA K., ISHII T., MASHIYAMA J., IKEDA T., Japan. J. Appl. Phys., 31 (1992), 3156.
[2] KIM H.T., BYUN J.D., KIM Y., Materi. Res. Bull., 33 (1998), 963.
[3] KIM H.T., KIM S.H., NAHM S., BYUN J.D., J. Am. Cer. Soc., 82 (1999), 3043.
[4] DULIN F.H., RASE D.E., J. Am. Cer. Soc., 43 (1960), 125.
[5] CHANG Y.S., CHANG Y.H., CHEN I.G., CHEN G.J., CHAI Y.L., WU S., FANG T. H., J. Alloys Comp., 354 (2003), 303.
[6] KIM H.T., NAHM S., BYUN J.D., KIM Y., J. Am. Cer. Soc., 82 (1999), 3476.
[7] GOLOVCHANSKI A., KIM H.T., KIM Y.H., J. Korean Phys. Soc., 32 (1998), S1167.
[8] SOHN J.H., INAGUMA Y., YOON S.O., ITOH M., NAKAMURA T., YOON S. J., KIM H. J., Japan. J. Appl. Phys., 33 (1994), 5466.
[9] LI C.F., BANDO Y., NAKAMURA M., KIMIZUKA N., KITO H., Mater. Res. Bull., 35 (2000), 351.
[10] ZAKRZEWSKA K., Thin Solid Films, 391 (2001), 229.
[11] ESMAIELZADEH KANDJANI A., FARZALIPOUR TABRIZ M., POURABBAS B., Mater. Res. Bull., doi:10.1016/j.materresbull. 2007.04.005.
[12] HARO-PONIATOWSKI E., OSTUSKI H., SADA E., J. Mater. Res., 9 (1994), 2102.
[13] TANG Z., ZHANG J., CHENG Z., ZHANG Z., J. Mater. Chem. Phys., 77 (2002), 314.

Received 16 June 2007
Revised 2 September 2007

Materials Science-Poland, Vol. 25, No. 4, 2007

Grain refinement and mechanical properties of Cu–Al 10%– Fe 4% alloy produced by equal channel angular extrusion

L.-L. GAO[1*], X.-H. CHENG[1,2]

[1]School of Mechanical and Power Engineering, Shanghai Jiao Tong University, Shanghai 200030, P.R. China

[2]National Power Traction Laboratory of Southwest Jiaotong University, Chengdu 610031, PR China

Equal channel angular extrusion (ECAE) process was carried out for a commercial aliminium bronze alloy (Cu–Al 10%–Fe 4%) produced by hot-rolling at high temperatures. A suitable processing temperature of ECAE for the alloy was determined. The effect of ECAE on microstructural evolution and mechanical properties of the alloy was investigated. Experimental results showed that the extrusion temperature must be higher than the eutectoid reaction temperature of the alloy. Optical electron microscopy and X-ray diffraction (XRD) were used to study the microstructural evolution of the alloy. The results showed that the grains of the alloy were refined after ECAE and gradually reduced with the increase of the pass number; accordingly, the mechanical properties of the alloy were significantly improved after ECAE.

Key words: *fine-grained aliminium bronze alloy; ECAE; microstructural evolution; mechanical properties*

1. Introduction

Equal channel angular extrusion (ECAE) technique is a severe plastic deformation process invented by Segal et al. [1]. An important advantage of ECAE is that it imposes much higher plastic strain during pressing without reducing the cross-sectional area of working billets, resulting in unique combinations of mechanical properties and grain size. Recently, active research efforts have been made and successful applications have been reported for various materials such as pure copper [2–4], Al alloys [5–8], magnesium alloys [9, 10] and Ti alloys [11, 12], etc.

The effect of ECAE on microstructure and mechanical properties of pure copper has been investigated in detail. However, previous ECAE studies have mostly been

*Corresponding author, e-mail: gaoleilei@sjtu.edu.cn

concerned with producing an ultrafine-grained microstructure from single-phase alloys. For single-phase alloys with high ductility, ECAE is usually carried out at room temperature. For two-phase alloys, an increase of the extrusion temperature is generally required to increase their ductility because the two-phase microstructure with a high volume fraction of the second phase is too brittle to be deformed during ECAE at low temperature [13]. Not many attempts have been made so far to process two-phase alloys by ECAE. Therefore it is essential to establish optimum processing conditions of such difficult-to-fabricate materials to study the effects of ECAE on microstructural changes and mechanical properties of two-phase alloys.

In this study, a commercial aliminium bronze alloy (Cu–Al 10%–Fe 4%) was chosen to determine its suitable processing temperature for ECAE, and the effect of ECAE on the microstructure and mechanical properties was also investigated.

2. Experimental

A Cu–Al 10%–Fe 4% alloy rod obtained in the as-rolling conditions was used as experimental material for ECAE. The billets with 9.6×9.6 mm^2 in cross-sections and 100 mm long were cut from the alloy rod. The die used for ECAE consisted of two rectangular channels with the cross-section area of 10×10 mm^2 intersecting at the angle of 90°. The billets were coated with a graphite lubricant to reduce the friction between the die and the billets during ECAE. The ECAE processes were carried out at 550 °C, 600 °C and 650 °C , respectively.

Optical electron microscopy and XRD were used to study the microstructural evolution of the alloys. The specimens for microstructure observation were cut along the extrusion direction. They were ground mechanically using abrasive papers and alumina powders, and their surfaces were etched by immersing in a solution of 8% HF, 22% HNO_3 and 70% H_2O for about 15 s.

Vickers microhardness measurements were taken with loads of 50 g applied for 13 s. The specimens for tensile test were machined from the as-received and the extruded billets with the gauge length of 25 mm and cross-section of 2×2 mm^2. The specimen axis was aligned with the extrusion direction. The tensile test was conducted at room temperature with the strain rate of 10^{-3} s^{-1}.

3. Results and discussion

Figure 1 shows the external appearances of the billets with ECAE after one pass at three different temperatures. It can be seen from Fig. 1 that, at the temperature of 550 °C and 600 °C, the ECAE process has not been carried out successfully. At the extrusion temperature of 550 °C, the billet exhibits failure characterized by the formation of a series of segments, as shown in Fig. 1a. At the extrusion temperature of 600 °C, there are some extensive cracks on the surface of the billet but the billet does not break, as shown in Fig. 1b. When using a higher extrusion temperature (650 °C), the

billet is extruded successfully without breaking and any surface cracks, as shown in Fig. 1c. In addition, the extruded material with ECAE after one pass is pressed easily at 650 °C through four passes without surface cracks.

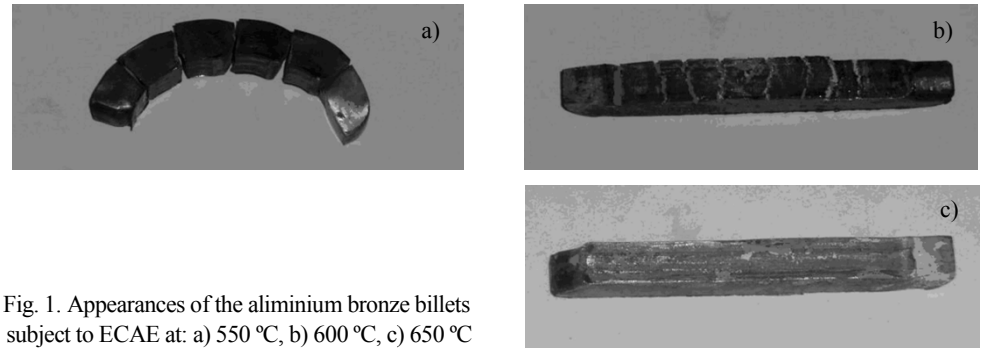

Fig. 1. Appearances of the aliminium bronze billets subject to ECAE at: a) 550 ºC, b) 600 ºC, c) 650 ºC

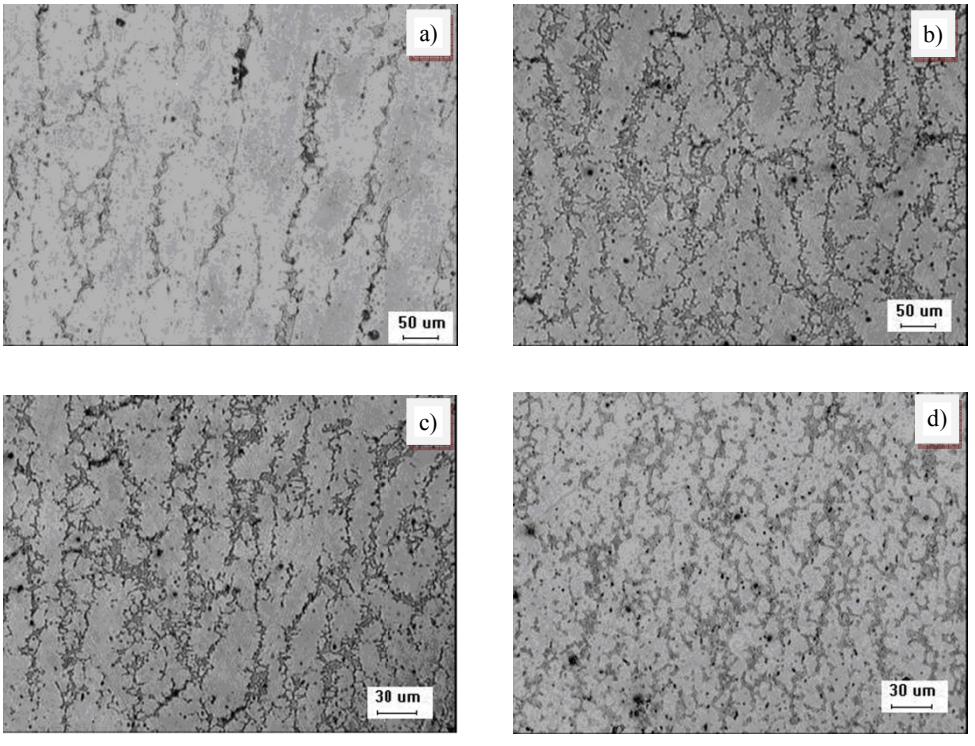

Fig. 2. Microstructures of aliminium bronze specimens: a) without ECAE, b) after ECAE with one pass, c) after ECAE with two passes, d) after ECAE with four passes

Microstructure of the as-received aluminium bronze alloy consists of two phases, α phase and ($\alpha + \gamma_2$) eutectoid structure, as shown in Fig. 2. The γ_2 phase is brittle and difficult to deform during ECAE. At the extrusion temperature of 550 °C, ECAE is carried out below the eutectoid reaction temperature and γ_2 phase still exists in the microstructure of

the alloy. Thus, ECAE process failed because of the brittle nature of γ_2 phase. At 600 °C, although the extrusion temperature is higher than the actual eutectoid reaction temperature, extensive cracks are still present on the surfaces of the specimens. The main reason is due to heat losses when the billet and the die are taken out from furnace during ECAE. When the extrusion temperature increases, for example to 650 °C, ECAE process can be performed successfully. It is reasonably explained that γ_2 phase disappears when the extrusion temperature is higher than the eutectoid reaction temperature of the alloy.

Figure 2 shows the optical images of the specimens without ECAE, after one pass, after two passes and after four passes of ECAE. It can be seen form Fig. 2a that the microstructure of the specimens without ECAE exhibits strong wire texture and the measured average width of the texture is about 70 μm. The α phase parallels the second phase and both of them are elongated along the rolling direction. After one pass of ECAE, the grain structure is refined and the microstructure of the specimen evolves into a structure with a considerable fraction of low-angle boundaries, as seen in Fig. 2b. Most of the low-angle grain boundaries still align along the extrusion direction, but some low-angle boundaries deviate from the extrusion direction. Therefore, it can be seen that in some areas, α phase intersects the second phase and the grain boundaries are no longer straight, but more curved than the boundaries without ECAE. After two passes of ECAE, the spacing of the boundaries is about 30 μm and some equiaxed grains occur in some areas, although the proportion of low angle grains is large, as shown in Fig. 2c. After four passes of ECAE, the grain size is further refined and the spacing of the boundaries is about 21 μm, as shown in Fig. 2d.

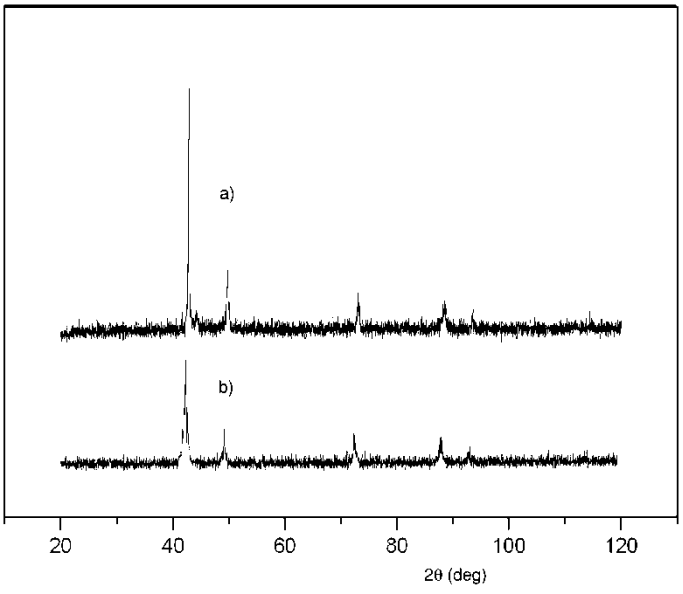

Fig. 3. XRD patterns of aliminium bronze alloy specimens without ECAE (a) and after ECAE (b) with two passes

The occurrence of some equiaxed grain structure in a few areas of the specimen indicates localized deformation and new slip systems operate during ECAE [14]. Prior low-angle boundaries are truncated by different shear planes, forming a microstructure with large angle boundaries. As a result, the grain size reduces progressively with the increase of pass number of ECAE.

Figure 3 shows the XRD patterns of specimens without ECAE and after ECAE with two passes. It can be seen that the XRD pattern of a specimen with ECAE after two passes exhibits significant broadening of all peaks, which is associated with the grain refinement, defect density increase and higher lattice distortion [15]. It also can be seen that the volume fraction of eutectoid structure of the specimens after ECAE is higher than that of the specimen without ECAE. This is attributed to the use of a high extrusion temperature which leads to an increase of the second phase. ECAE is carried out at a temperature of 650 °C, which is higher than the eutectoid reaction temperature of the alloy. After ECAE process, the temperature of the billet drops quickly because of larger difference in temperature between the billet and the atmosphere. The phase transformation ($\beta \rightarrow \alpha$) cannot be carried out completely and the β phase is still partially preserved. As a result, more β phase is available to the subsequent eutectoid reaction ($\beta \rightarrow \alpha + \gamma_2$) and the volume fraction of the second phase increases after ECAE.

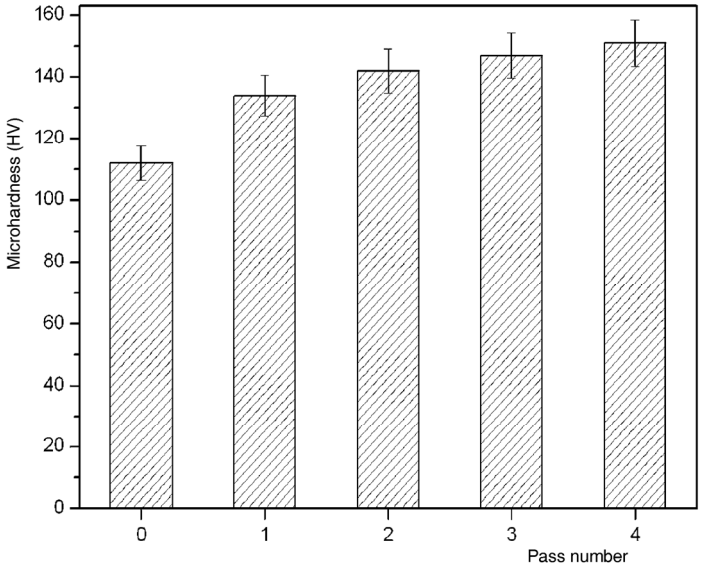

Fig. 4. Vickers microhardness of the aliminium bronze specimens with various pass numbers

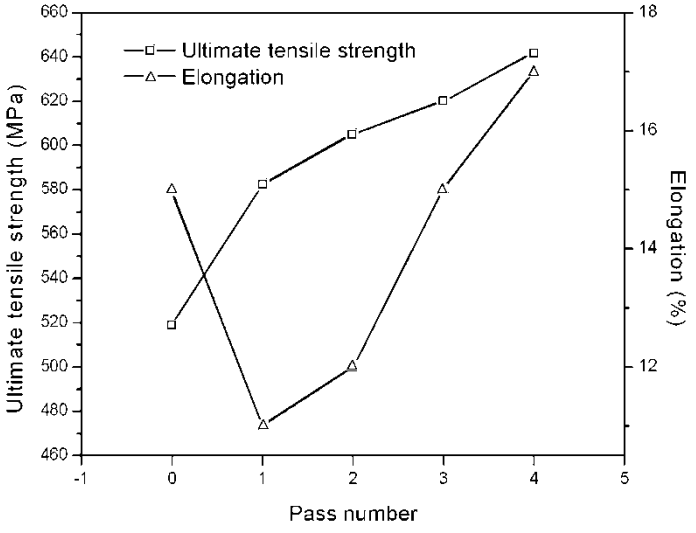

Fig. 5. Ultimate tensile strengths and tensile elongations of the aliminium bronze specimens with various pass numbers

Vickers hardness, ultimate tensile strength and tensile elongation of specimens with various pass numbers are shown in Figs. 4 and 5, respectively. It is seen that the hardness and the ultimate tensile strength of the specimens after ECAE are higher than that of the specimen without ECAE. The hardness and the ultimate tensile strength increases remarkably with a significant decrease in elongation after one pass of ECAE. However, the hardness, ultimate tensile strength and elongation increase with the increase of the pass number after two passes of ECAE.

The improvement of the mechanical properties is attributed to the difference in microstructures between as-received and extruded aliminium bronze specimens. Grain size decreased and grain was refined during the progress of ECAE. Grain refinement can affect mechanical properties of polycrystalline materials [16]. The classical effect of grain size on hardness can be explained by the Hall–Petch model [17]:

$$H = H_0 + kd^{-0.5} \tag{1}$$

where H_0 is the hardness constant, k the constant and d is the diameter of the grain. The Hall–Petch effect in grain refinement materials is attributed to the grain boundaries acting as efficient obstacles to dislocations. Consequently, a dislocation pile-up can be formed against a grain boundary inside a grain. In addition, it can be seen from Figs. 2a, b that the volume fraction of the second phase increases remarkably after one pass of ECAE. However, the volume fraction of the second phase does not increase after two passes of ECAE, as shown in Figs. 2b, c. It is well known that hardness and ultimate tensile strength are directly proportional to the volume fraction of the second phase [18]. Thus, the increase in hardness and ultimate tensile strength after the first

pass is larger than that of the specimen with ECAE after two passes. And the decrease in elongation after one pass is also mainly due to a high volume of the second phase produced at high temperature. After two passes of ECAE, the distribution of the second phase is rearranged and some equiaxed grains occur in the microstructure of the alloy, which leads to a stronger material with more dispersed distribution of the second phase. In addition, the grain size of the alloy is further refined after the second pass, and this grain refinement can result in an increase in strength and elongation of the alloy [19]. Therefore, the improvement in mechanical properties of the billet after two passes of ECAE is due to rearrangement of the second phase and grain refinement.

4. Conclusions

It is demonstrated that the extrusion temperature of ECAE for aliminium bronze alloy must be higher than the eutectoid reaction temperature of the alloy. After ECAE, the alloy has more homogeneous fine-grained structure than the as-received one and some equiaxed grains occur in some areas. The fraction volume of the second phase increases after one pass while it does not increase during the subsequent pass. With the increase of the pass number of ECAE, the grain size of the alloy progressively decreases, and the hardness and strength gradually increase. After one pass of ECAE, the increase of hardness and strength of the specimen is due to grain refinement and the increase of the second phase, while the improvement in mechanical properties of the alloy after two passes of ECAE is a consequence of grain refinement and rearrangement of the second phase.

Acknowledgements

This research was financially supported by the National Natural Science Foundation of China (Grant No. 50275093), the open fund of State Key Laboratory of Tribology, Tsinghua University and Instrumental Analysis Center of Shanghai Jiao Tong University.

References

[1] SEGAL V.M., REZNIKOV V.I., DROBYSHEVSKIY A.E., KOPYLOV V.I., Russian Metall., 1 (1981), 99.
[2] HAOUAOUI M., HARTWIG K.T., PAYZANT E.A., Acta Mater., 53 (2005), 801.
[3] WU S.D., WANG Z.G., JIANG C.B., LI G.Y., ALEXANDROV I.V., VALIEV R.Z., Mater. Sci. Eng. A, 387–389 (2004), 560.
[4] HUANG W.H., CHANG L., KAO P.W., CHANG C.P., Mater. Sci. Eng. A, 307 (2001), 113.
[5] CHAKKINGAL U., THOMSON P.F., J. Mater. Process. Tech., 117 (2001), 169.
[6] BOWEN J.R., MISHIN O.V., PRANGNELL P.B., JENSEN D.J., Scripta Mater., 47 (2002), 289.
[7] CHEN Y.C., HUANG Y.Y., CHANG C.P., KAO P.W., Acta Mater., 51 (2003), 2005.
[8] CAO W.Q., GODFREY A., LIU Q., Mater. Sci. Eng. A, 361 (2003), 9.
[9] AGNEW S.R., HORTON J.A., LILLO T.M., BROWN D.W., Scripta Mater, 50 (2004), 377.
[10] LIU T., ZHANG W., WU S.D., JIANG C.B., LI S.X., XU Y.B., Mater. Sci. Eng. A, 360 (2003), 345.

[11] LI Z.H., XIANG G.Q., CHENG X.H., Mater. Des., 27 (2006), 324.
[12] Li Z.H., CHENG X.H., SHANGGUAN Q.Q., Mater. Lett., 59 (2005), 705.
[13] DUPUY L., BLANDIN J.-J., Acta Mater., 50 (2002), 3251.
[14] DALLA TORRE F., LAPOVOK R., SANDLIN J., THOMSON P.F., DAVIES C.H.J., PERELOMA E.V., Acta Mater. 52 (2004), 4819.
[15] STOLYAROV V.V., ZHU Y.T., ALEXANDROV I.V., LOWE T.C., VALIEV R.Z., Mater. Sci. Eng. A, 343 (2003), 43.
[16] ARZT E., Acta Mater., 46 (1998), 5611.
[17] BOWEN J.R., PRANGNELL P.B., JENSEN D. J., HANSEN N., Mater. Sci. Eng. A, 387–389 (2004), 235.
[18] STOLYAROV V.V., LAPOVOK R., BRODOVA I.G., THOMSON P.F., Mater. Sci. Eng. A, 357 (2003), 159.
[19] MATSUBARA K., MIYAHARA Y., HORITA Z., LANGDON T.G., Acta Mater., 51 (2003), 3073.

Received 31 October 2006
Revised 17 May 2007

Materials Science-Poland, Vol. 25, No. 4, 2007

Unusual visible absorption in high PbO lead borate glass

S. JANA*, B. KARMAKAR, P. KUNDU

Glass Technology Laboratory, Central Glass and Ceramic Research Institute,
196 Raja S. C. Mullick Road, Kolkata 700 032, India

A series of glasses in the system xPbO·(100 – x)B_2O_3 (x = 45, 55, 65 mol %) were prepared using analytical grade PbO consisting of a mixture of orthorhombic and tetragonal phases (ca. 1:1, w/w) and H_3BO_3 melted in silica beaker in the temperature range of 575–900 ºC for 30 min under normal atmosphere. Only the 55PbO·45B_2O_3 glass prepared at 575 (L2), 650 (L3) and 700 ºC (L4) showed several optical absorption bands in the visible region. However, all the bands disappeared either when a 1.7 mol % equivalent PbO from Pb_3O_4 was added in the batch or the melting temperature was increased to more than 800 ºC. L2 glass showed a broad absorption band at ca. 485 nm which was thought to be due to combined effect of nanometallic lead (Pb^0) and Pb^+. The formation of hexagonal nano-Pb^0 particles of 7–13 nm size in 55PbO·45B_2O_3 glass melted at 575–700 ºC was confirmed by TEM and Pb^+ was identified by a broad EPR signal with g-value at ca. 2.00. Optical absorption at ca. 485 nm and 565 nm (broad shoulder) was observed in L3 glass whereas a new peak at ca. 525 nm appeared in L4 which was identified due to Pb^{3+} by EPR signal with g-value ca. 2.176 and **A**-tensor, ca. 6340×10^{-4} cm^{-1}. A mechanism for the formation of Pb^0, Pb^+ and Pb^{3+} has been proposed.

Key words: *lead borate glass; nanometallic lead; microstructure; EPR; visible absorption*

1. Introduction

Lead borate glasses possess an enhanced optical non-linearity due to high polarizability [1, 2] of Pb^{2+} ions in glass matrices. They are attractive materials [2] for applications in waveguides, all optical switches, stimulated Raman amplifiers etc. Metallic lead particles [3] of nanometer dimensions have been found in silica glasses implanted with Pb^+. Such glasses have non-linear optical properties which make them possible candidates for optical switching devices [3]. Reduced lead silicate glasses [4] having three different valence states of lead, i.e Pb^0, Pb^+ and Pb^{2+} are used as continuous strip dynode materials in electron multipliers. Although lead borate glasses par-

*Corresponding author, e-mail: sjana@cgcri.res.in, presently at Sol-Gel Division

ticularly with high lead content have low glass transformation temperature and characteristic light yellow colour due to a tail of Pb^{2+} ion absorption [5] in the UV-region, they are highly transparent [2] in the visible and NIR regions. On exposure to high-energy particles, lead containing glasses exhibit optical absorption [6, 7] in the ultraviolet, visible and NIR regions due to trapping of holes and electrons in the vicinity of Pb^{2+} ions.

In preparation of lead borate glasses, Pb_3O_4 is the main source of PbO but sometimes lead monooxide (PbO) is also used. Extensive studies [1, 2, 5, 6, 8–12] have been carried out on the optical properties of the glasses which have been prepared at and above 800 ºC but no data have been found on the glasses melted at low temperature (below 800 ºC). On the other hand, optical properties of the low-melting lead borate glasses prepared from PbO of orthorhombic (*o*-PbO) and tetragonal (*t*-PbO) mixtures are also not available in the literature. Therefore, in the present work high PbO containing lead borate glasses were prepared in the range of 575–900 ºC using analytical grade lead(II) oxide (PbO) (consisting of *o*-PbO and *t*-PbO mixture, ca. 1:1, w/w) and boric acid and characterized by UV-VIS spectra, electron paramagnetic resonance spectrometry and transmission electron microscopy to find out visible absorption behaviours.

2. Experimental

A series of glasses (Table 1) in 50 g quantity were prepared in the system, $x\text{PbO}\cdot(100 - x)\text{B}_2\text{O}_3$ (x = 45, 55, 65 mol %) using analytical grade lead(II) oxide

Table 1. Compositions and characteristics of lead–borate glasses

Glass No.	Batch composition [mol %]		Melting temperature [ºC]	Annealing temperature [ºC]	Colour	Density [g·cm^{-3}]	UV cut off wavelength, λ_{50} [nm]
	PbO	B_2O_3					
L1	45	55	770	400	light yellow	5·55	347.4
L2	55	45	575	340	pink	6.25	385.5
L3	55	45	650	340	pink	6.22	385.0
L4	55	45	700	340	pink	6.21	382.8
L5	55	45	800	340	light yellow	6.09	374.9
L6	55	45	900	340	light yellow	5.87	366.2
L7	55[a]	45	650	340	light yellow	6.20	382.5
L8	65	35	620	320	light yellow	6.46	390.1

[a]1.7 mol % equivalent PbO from Pb_3O_4 and the rest from lead(II) oxide yellow.

yellow (PbO, puriss., ≥ 99.0%, Fluka, Switzerland), red lead (Pb_3O_4, 99.0%, Aldrich, Wisconsin) and boric acid (H_3BO_3, puriss., ≥ 99.5%, Fluka, Switzerland) and melted in the temperature range 575–900 ºC for 30 min under normal atmosphere in silica beaker (150 ml capacity, Infusil, India) with stirring by silica glass rod. The melt was poured onto preheated mild steel mould and annealed at 320–400 ºC for 1 h depending upon composition. The glasses were cut with diamond cutting tool, ground and polished into rectangular plates. Density of polished glass samples (25×15×10 mm^3) were measured following Archimedes principle using xylene as an immersion fluid. UV-VIS absorption and transmission spectra of the polished glass samples (25×15×1 mm^3) were measured using Perkin Elmer spectrophotometer (Lambda 20, wavelength accuracy: ±0.3 nm; photometric accuracy: abs. ±0.003, < 0.02 % T) and X-band electron paramagnetic resonance (EPR) spectra of powder glass samples were recorded by using Varian Spectrometer (model, E109) with 100 kHz field modulation and 9.500–9.515 GHz microwave frequency region at room temperature. Microstructure of the powdered glass samples was evaluated by transmission electron microscopy (TEM, JEOL, JEM-200CX).

3. Results and discussion

The absorption spectra of the glasses (L1–L8) are shown in Fig. 1. The spectral behaviour of the glasses with the same composition ($55PbO{\cdot}45B_2O_3$) and annealing time (1 h) differs with changing of the melting temperature. A broad absorption band, peaking at ca. 485 nm appeared (curve L2) for the glass sample melted at 575 ºC. The

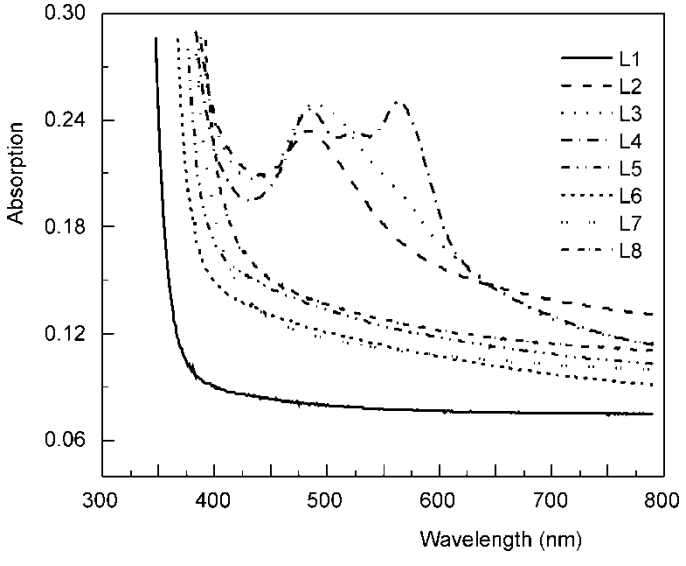

Fig. 1. UV-VIS absorption spectra of glasses (1.0 mm thick).
L1–L8 symbols indicate the glass numbers as given in Table 1

intensity of this band increased with a broad shoulder at ca. 565 nm (curve L3) when melted at 650 ºC. It is very interesting to note that when melted at 700 ºC, the spectral behaviour dramatically changed and three distinct peaks (curve L4) appeared at ca. 485 nm, ca. 525 nm and ca. 565 nm. All the glasses having the same composition ($55PbO{\cdot}45B_2O_3$) and melted in the temperature range 575–700 ºC were light pink in colour, and the colour disappeared when the melting temperature was increased over 800 ºC showing no absorption peaks in the visible region (curves L5 and L6). Further, it was also observed that the light pink colour as well as absorption peaks of the glass samples also disappeared (curve L7) when 1.7 mol % equivalent PbO was introduced in the same glass composition (L7) from Pb_3O_4 and melted at 650 ºC for 30 min. No absorption peaks (curves L1 and L8) appeared for the glasses having the compositions, $45PbO{\cdot}55\ B_2O_3$ and $65PbO{\cdot}35\ B_2O_3$.

To show the effect of melting temperature on the UV cut off wavelength ($\lambda_{50,}$ arbitrarily defined as the wavelength at which the transmission rises to 50.00%) which is associated [13] with the excitation of electrons of oxygen anions in the glass, the λ_{50} was determined from transmission spectra (Fig. 2) and has been shown in Table 1. The

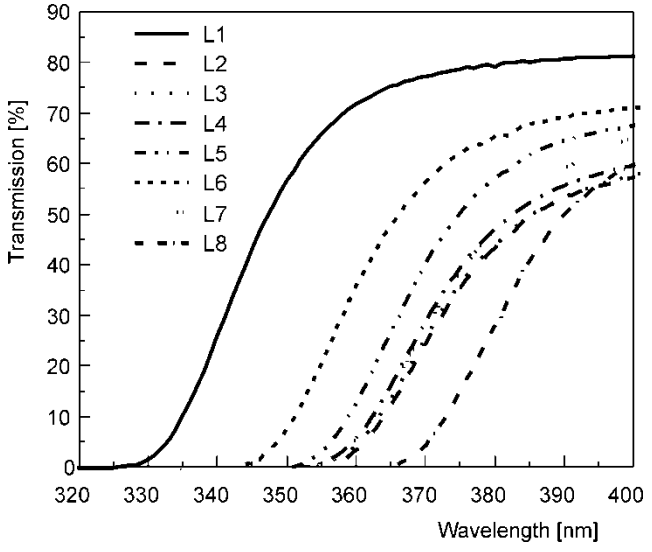

Fig. 2. Transmission spectra of glasses (1.0 mm thick) showing UV cut off wavelengths. L1–L8 symbols indicate the glass numbers as given in Table 1

shifting of λ_{50} towards higher wavelength region [13] indicates the increase in concentration of non-bridging oxygen (NBOs) in the glass. It is also known [13] that with increasing concentration of PbO, λ_{50} shifts towards longer wavelengths. In L1 ($45PbO{\cdot}55B_2O_3$) glass λ_{50} appeared at 347.4 nm (curve L1) which shifted to 390.1 nm (curve L8) in L8 ($65PbO{\cdot}35B_2O_3$) in line with the above principle. In the case of $55PbO{\cdot}45B_2O_3$ glasses prepared in the temperature range of 575–900 ºC, it is seen (Table 1) that with increasing melting temperature from 575^o to 700 ºC, there is a little

shifting of λ_{50} (2.7 nm) and change of density (0.04 g·cm^{-3}) indicating the minor composition change during this melting temperature range due to little loss of PbO by evaporation [14]. However, unless there had been evaporation of B_2O_3 from the melt it would have shown an increase in density [13]. But at or above 800 ºC melting temperature, λ_{50} shifted little more (> 8 nm) towards shorter wavelengths indicating more loss of PbO from the glass melt.

Sometimes in high lead glasses the formation of metallic lead particles has been observed [15] during glass melting due to reduction caused by the unavailability of oxygen. If the same phenomenon is presumed in the present study, then the introduction of an additional source of oxygen could prevent the reduction problem. Therefore, addition of 1.7 mol % equivalent PbO from analytical grade Pb_3O_4, an additional source of oxygen, resulted in a light yellow coloured glass when melted at 650 ºC temperature. This indicates that addition of Pb_3O_4 supplies the available oxygen to the glass network by the following decomposition reaction [16] (Eq. (1)) and prevents the reduction reaction:

$$2Pb_3O_4 = 6PbO + O_2 \tag{1}$$

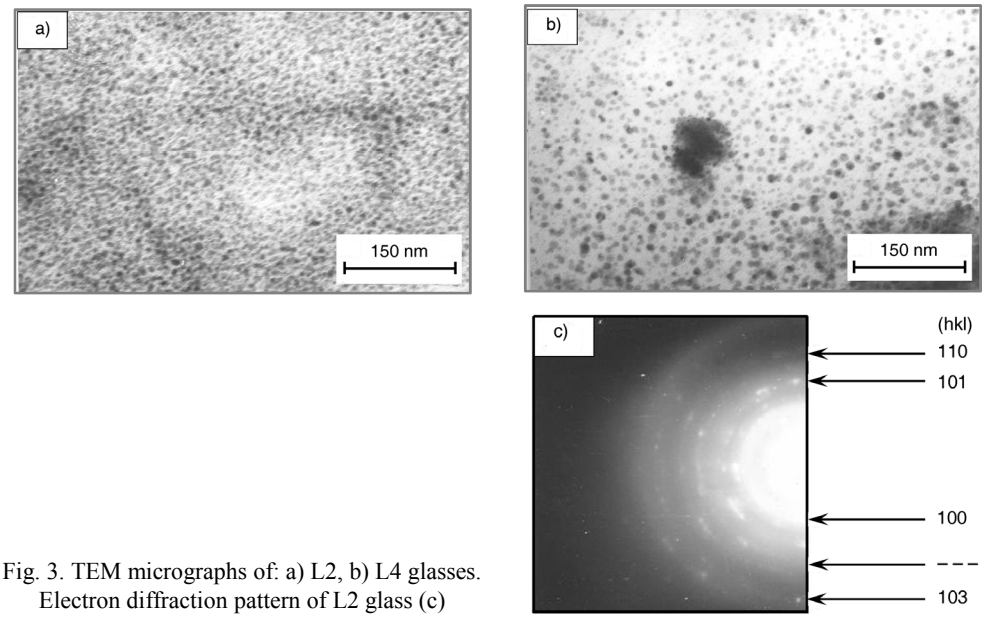

Fig. 3. TEM micrographs of: a) L2, b) L4 glasses. Electron diffraction pattern of L2 glass (c)

To confirm the above assumption and the presence of metallic lead particles formed in the $55PbO{\cdot}45B_2O_3$ glasses during melting in the temperature range from 575 ºC to 700 ºC, a transmission electron microscopic (TEM) study was done. It was observed that only the pink coloured glass samples showed the presence of nanometallic lead particles. The microstructure (Fig. 3a) of L2 glass shows nanoparticles (black dot) in the range of 7–11 nm. With increasing melting temperature to 700 ºC

(L4 glass), the particle size (Fig. 3b) slightly increases (8–13 nm). It was seen that electron diffraction patterns of these samples are identical (Fig. 3c) and support the presence of metallic lead particles with hexagonal crystal structure [17]. No evidences of the presence of nano-lead particles were observed in L5 and L7 glasses.

The reduction of Pb^{2+} to Pb^0 in lead glasses can be explained if we consider the asymmetric electron density distribution due to strong polarizability of Pb^{2+} ions [18]. In lead glasses, Pb^{2+} ions may be similar to Pb^{4+} ions in one direction and metallic lead atom in the other which can be considered as an internal redox reaction [18] as given in Eq. (2).

$$Pb^{2+} \rightleftharpoons \frac{1}{2}Pb^{4+} + \frac{1}{2}Pb^0 \tag{2}$$

It might be possible in Eq. (2) that the effect of increasing oxygen concentration favours backward reaction and vice versa. In this way, it is believed that when oxygen availability is lower, the system favours the forward reaction as shown in Eq. 2.

The optical absorptions at ca. 485 nm of lead–borate glass prepared at 575 ºC may be thought of due to presence of nanometallic lead particles which is commonly referred to as surface plasmon resonance (SPR). However, the optical absorption [19] which is dependent on the size and electronic structure of lead particles appeared in the UV region. Hence, the absorption at ca. 485 nm may not be solely due to nanometallic lead particles. It can be presumed that formation of metallic lead particles reduces its adjacent higher valent lead ions i.e. Pb^{2+} and Pb^{4+} present in the glass and forms lower valent ions as proposed in the following equations:

$$Pb^{2+} + Pb^0 = 2Pb^+ \tag{3}$$

$$Pb^{4+} + Pb^0 = Pb^{3+} + Pb^+ \tag{4}$$

From the above two equations, the formation of both Pb^+ and Pb^{3+} ions is probable in the lead borate glass in presence of metallic lead particles. Barker et al. [7] showed that two bands appear at ca. 375 nm and ca. 525 nm in γ-rays irradiated high lead-silicate glasses, and it seems reasonable to associate them with Pb^{3+} in network-modifying PbO_4 units. In irradiated lead-doped fluoride glasses, absorption band observed [7] at ca. 404 nm in the visible region has been identified as Pb^+ ion formation. Therefore, the optical absorption at ca. 485 nm for the glasses melted within the range of 575–650 ºC is not purely either due to nano-Pb^0 particle or Pb^+ alone, formed according to the Eqs. (3) and (4) but might be responsible due to combined effect of both. Again, with increasing melting temperature to 700 ºC one distinct peak appeared at ca. 525 nm which could be responsible [7] for Pb^{3+} ions.

Since all the species, Pb^0, Pb^+ and Pb^{3+} are paramagnetic [3] due to presence of conduction electrons, p-electrons ($6s^26p^1$) and s-electrons ($6s^1$), respectively, it is imperative that electron paramagnetic resonance (EPR) study could be able to explain their existence in the glasses. EPR of all the glass samples were done and it was observed that only the pink coloured samples (L2, L3 and L4) were found paramagnetic

(Fig. 4). L2 and L3 glass samples showed a very broad resonance signal (curves L2 and L3) with $g \approx 2.0$ indicating the presence of Pb^{+} ion [3] which supported the above reactions (Eqs. (3), (4)). The sample L4 showed a prominent broad EPR signal (curve L4) with $g \approx 2.176$ and gave a large **A**-tensor, ca. 6340×10^{-4} cm^{-1} indicating that the resonance was due to unpaired 6s electrons [20] of Pb^{3+} ions with non-magnetic nuclei (maximum abundance) [21] showing absorption at ca. 525 nm [7] in the visible region (curve L4, Fig. 1). The large positive *g*-value shift of Pb^{3+} ions might have been caused by the covalency [20] of Pb–O bond. The presence of Pb^{+} ions could be a reason for the anisotropic nature of EPR signal observed in L4 glass sample. There is no characteristic EPR signal of Pb^{0} ions observed in L2 to L4 glasses, which might have overlapped due to the spectral broadening of EPR signal of Pb^{+}. The absorption peak at 565 nm (curves L3 and L4, Fig. 1) could not be identified as any extra EPR signal was found for its appearance.

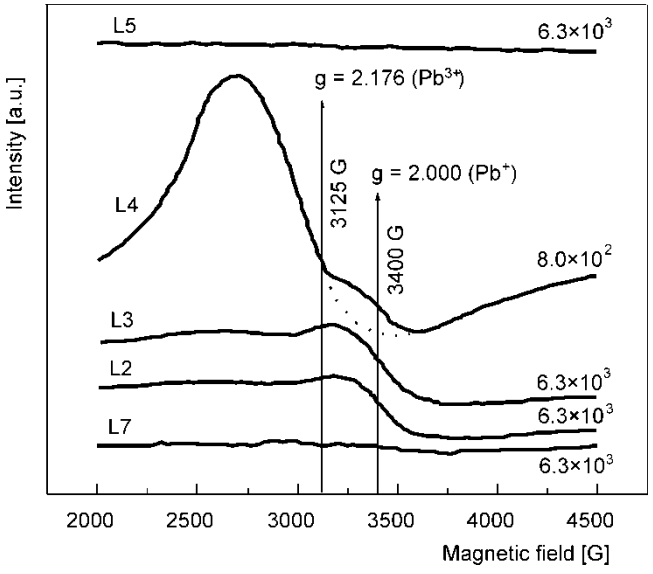

Fig. 4. Room temperature EPR spectra of L2–L5 and L7 glasses (receiver gain is given inside the figure at the right hand side)

Oxygen diffusion [22] from the ambient atmosphere into the glass melt is possible and the rate of oxygen diffusion depends upon the viscosity of the glass melt which in turn depends on the melting temperature. Thus, with increasing melting temperature, viscosity of the glass melts decreases, which enhances the rate of oxygen diffusion at the higher melting temperatures. Therefore, disappearance of absorption peaks at ≥800 ºC might be due to dissolution [19] of elemental lead cluster and subsequent oxidation of Pb^{0} and Pb^{+} to Pb^{2+} (the normal oxidation state of lead) and Pb^{3+} to Pb^{4+}. The reason for the peculiar visible absorptions restricted only to $55PbO{\cdot}45B_2O_3$ glass composition is yet to be explored and further research work is required for its explanation.

4. Conclusion

Lead borate glass, $55PbO{\cdot}45B_2O_3$ (mol %) melted at 575–700 ºC in air using PbO consisting of tetragonal and orthorhombic mixture, exhibits several unusual visible absorption bands originating from hexagonal nanometallic lead particles together with aliovalent lead ions.

Acknowledgements

The authors express their sincere thanks to Dr. H. S. Maiti, Director, CGCRI for his kind permission to publish this paper. They also thank Prof. (Dr.) A. K. Pal, IACS, Kolkata for providing EPR measurement facility at his laboratory.

References

[1] DIMITROV V.V., KIM S.-H., YOKO T., SAKKA S., J. Ceram. Soc. Jpn., 101 (1993), 59.
[2] PAN Z., MORGAN S.H., LONG B.H., J. Non-Cryst. Solids, 185 (1995), 127.
[3] BOGOMOLOVA L.D., JACHKIN V.A., PRUSHINSKY S.A., DMITRIEV S.A., STEFANOVSKY S.V., TEPLYAKOV Y.G., CACCAVALE F., J. Non-Cryst. Solids, 241 (1998), 174.
[4] BATES Jr. C.W., LENIART D., STRAKA E., Solid State Commun., 13 (1973), 1057.
[5] ZHOU Z., NAVROTSKY A., MCCLURE D.S., Phys. Chem. Glass., 34 (1993), 251.
[6] BISHAY A.M., MAKLAD M., Phys. Chem. Glass., 7 (1966), 149.
[7] FRIEBELE E.J., *Radiation Effects*, [in:] D.R. Uhlmann, N.J. Kreidl (Eds.), *Optical Properties of Glass*, The American Ceramic Society Inc., Westerville, OH, 1991, p. 256.
[8] WITKE K., HARDER U., WILLFAHRT M., HÜBERT T., REICH P., Glastech. Ber. Glass Sci. Tech., 69 (1996), 143.
[9] TERASHIMA K., SHIMOTA T.H., YOKO T., Phys. Chem. Glass., 38 (1997), 211.
[10] EAGAN R.J., BERGERON C.G., J. Am. Ceram. Soc., 55 (1972), 53.
[11] BISHAY A. M., J. Am. Ceram. Soc., 43 (1960), 417.
[12] TARTE P., POTTIER M.J., *Far Infrared Spectrum of Lead Borate Glasses: Evidence for the Simultaneous Occurrence of Ionic and Covalent Pb-O Bonds*, [in:] P.H. Gaskell (Ed.), *The Structure of Non-Crystalline Materials*, Taylor and Francies Ltd., London, 1977, p. 227.
[13] KHANNA A., Phys. Chem. Glass., 41 (2000), 330.
[14] CABLE V.M., APAK C., CHAUDHRY M.A., Glastech. Ber., 48 (1975), 1.
[15] HOSONO H., KAWAZOE H., KANAZAWA T., J. Ceram. Soc. Jpn., 90 (1982), 544.
[16] LIPTROT G.F., *Modern Inorganic Chemistry*, 2nd Ed., ELBS and Mills & Boon Ltd., London, 1974, p. 241.
[17] AKHTAR D., VANKAR V.D., GOEL T.C., CHOPRA K.L., J. Mater. Sci., 14 (1979), 983.
[18] RABINOVICH E.M., J. Mater. Sci., 11 (1976), 925.
[19] MAGRUDER III R.H., HENDERSON D.O., MORGAN S.H., ZUHR R.A., J. Non-Cryst. Solids, 152 (1993), 258.
[20] SUTO K., AOKI M., J. Phys. Soc. Jpn., 22 (1967), 1307.
[21] SCHOEMAKER D., KOLOPUS J.L., Solid State Commun., 8 (1970), 435.
[22] DOREMUS R.H., *Glass Science*, Chap. 8, Wiley, New York, 1973.

Received 12 March 2007
Revised 7 July 2007

Materials Science-Poland, Vol. 25, No. 4, 2007

Densification and grain growth of TiO_2-doped ZnO

K. YILDIZ*, N. KARAKU□, N. TOPLAN, H. Ö. TOPLAN

Sakarya University, Metallurgy and Materials Engineering, 54187, Sakarya, Turkey

The kinetics of grain growth in 1–4 wt. % TiO_2-doped ZnO was studied using the simplified phenomenological grain growth kinetics equation together with examination of microstructure and densification of the sintered samples. The grain growth exponent values n were found to be 3 for 1 and 2 wt. % TiO_2-doped ZnO, 5 for 3 and 4 wt. % TiO_2-doped ZnO. The apparent activation energy of 435 kJ/mol was found for 1 and 2 wt. % of TiO_2 in ZnO. It was found to be 608 kJ/mol and 615 kJ/mol for 3 and 4 wt. % TiO_2, respectively. The apparent activation energy increased with TiO_2 content due to formation of spinel Zn_2TiO_4 phase at the grain boundaries which inhibited the grain growth of ZnO. Also densification decreased with increasing TiO_2 content.

Key words: *ZnO; TiO_2 doping; grain growth kinetics; densification*

1. Introduction

ZnO-based materials have been developed for various technological applications, such as varistors, gas sensors, and optoelectronic devices due to their electrical and optical properties [1]. A typical ZnO-based varistor is a very complex chemical system containing several dopants, such as Bi, Sb, Mn, Cr, Co, Ti and Al [2].

The electrical properties of ZnO varistors directly depend on the composition and microstructural characteristics such as grain size, density, morphology and the distribution of second phases. Many studies have been conducted on the sintering of several ZnO systems doped with Bi_2O_3 [3, 4], Sb_2O_3 [5], Al_2O_3 [1], PbO [6] and CuO [7]. Among numerous papers published on the subject, Senda and Bradt [3] presented the most detailed study covering the grain growth kinetics in ZnO ceramics containing up to 4 wt. % Bi_2O_3. They used a simplified grain growth kinetics equation

$$G^n = K_0 t \exp\left(-\frac{Q}{RT}\right) \tag{1}$$

*Corresponding author, e-mail: kenyil@sakarya.edu.tr

where G is the average grain size at time t, n is the kinetic grain growth exponent, K_0 is a constant, Q is the apparent activation energy, R is the gas constant and T is the absolute temperature. Using this equation, Senda and Bradt have calculated the grain growth exponent $n = 3$ and apparent activation energy $Q = 224\pm16$ kJ/mol in the sintering of the pure ZnO system.

The additions of MnO [8] and CoO [9] to the ZnO–Bi_2O_3 6 wt. % system, the addition of MnO [10] to the ZnO–Sb_2O_3 system and the addition of PbO [6], CuO [7] and SiO_2 [11] to ZnO have been studied by our group. The aim of the present work is to study the effect of TiO_2 addition on microstructure and the sintering behaviour of ZnO.

2. Experimental

High purity ZnO (99.7 % Metal Bile□ikleri A.□, Gebze, Turkey) and TiO_2 powders (pure grade) were used in preparation of four basic compositions – ZnO containing 1, 2, 3 and 4 wt. % TiO_2. ZnO powders contained a needle like fine crystals 0.5 μm wide and 0.5–2 μm long. The calculated amounts of oxides for the indicated compositions were ball milled in ashless rubber lined ceramic jars for 6 h using zirconia balls and distilled water as the milling media. The mixtures were dried to 10–15% moisture content and then granulated. Samples of 10 mm in diameter and 8 mm thick were prepared by semi-dry pressing of the granules of (150±75) μm in size range at the pressure of 100 MPa. The specimens were sintered at 1000, 1100, 1200 and 1300 ºC for 1, 2, 3 and 5 h with the heating rate of 5 ºC/min, then were naturally cooled in the furnace.

The bulk densities of the samples were calculated from their weights and dimensions. Characterizations of the phases in the sintered specimens were carried out by X-ray diffraction using CuK_α radiation. For the microstructural observations, both scanning electron microscopy (SEM) of the fracture surfaces and optical microscopy of polished and etched surfaces were used. Grain size measurements were carried out on the micrographs of the etched samples using the following equation,

$$G = 1.56\overline{L} \tag{2}$$

where G is the average grain size, $\overline{L}$ is the average grain boundary intercept length of four random lines on two different micrographs of each sample [12].

3. Results and discussion

3.1. Physical properties of the sintered samples

The presence of ZnO (ASTM Card No. 5-0664) and Zn_2TiO_4 (ASTM Card No. 18-1487) phases was determined using of the X-ray powder diffraction of the TiO_2 -doped samples sintered at various temperatures and various periods of time. TiO_2 formed a spinel phase (Zn_2TiO_4) with ZnO as expected from the phase diagram of the

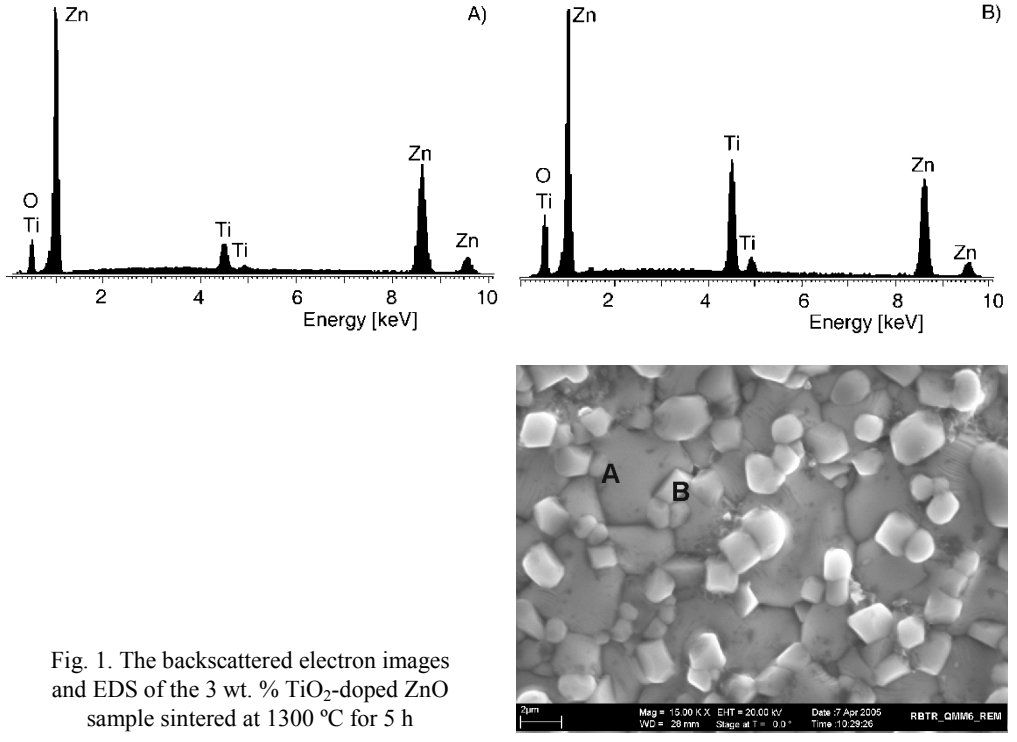

Fig. 1. The backscattered electron images and EDS of the 3 wt. % TiO_2-doped ZnO sample sintered at 1300 ºC for 5 h

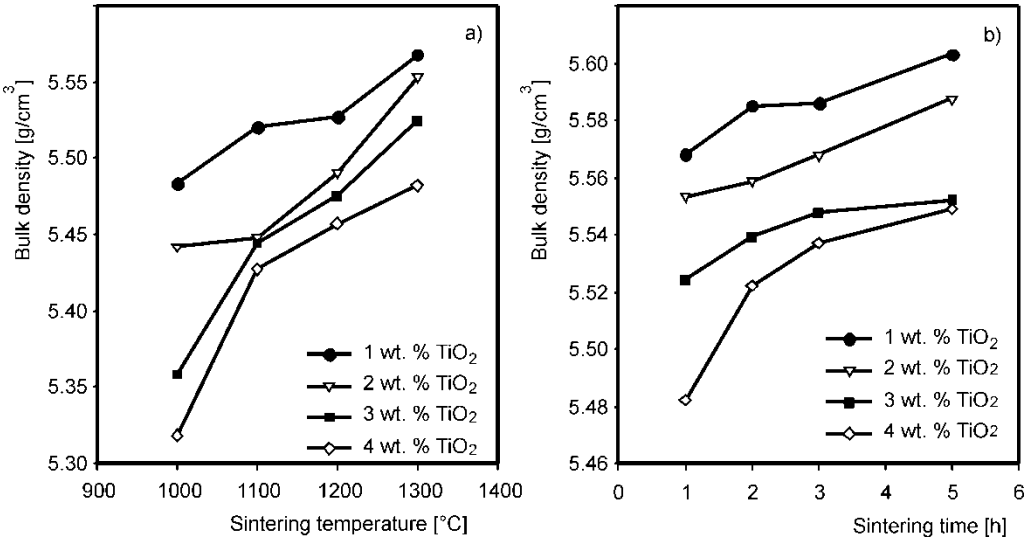

Fig. 2. The bulk density vs. sintering temperature (a) and the bulk density vs. sintering time (b) for TiO_2 doped ZnO

ZnO–TiO_2 binary system [13]. The backscattered electron and energy dispersive X-Ray spectrometer (EDS) images of 3 wt. % TiO_2-added ZnO samples sintered at

1300 ºC for 5 h are shown in Fig. 1. The micrograph clearly shows spinel phases (Zn_2TiO_4) as bright regions between ZnO grains.

The effects of sintering temperatures and sintering time on the bulk densities of the specimens with different TiO_2 contents are shown in Fig. 2. The highest densifications are obtained at high sintering temperatures and high sintering times. The calculated density of Zn_2TiO_4 spinel phase is about 5.28 g/cm^3. The amount of Zn_2TiO_4 spinel phase increased with increasing TiO_2 content. This resulted in decreasing of the bulk density.

3.2. Kinetics of grain growth

The SEM micrographs of the fracture surfaces of the samples with 1, 2, 3 and 4 wt. % of TiO_2 sintered at 1000 and 1300 ºC for 1 h are shown in Fig. 3. The samples sintered at 1000 °C for 1 h resulted in a porous and fine (<1 μm) crystalline microstructure. The sintering at 1300 °C caused a sudden grain growth, which in turn entrapped porosity within and among grains. Also the average grain size of each sample increased with increasing sintering temperature from 1000 °C to 1300 °C. As seen in Fig. 3, the grain growth of ZnO is inhibited with increasing TiO_2 doping. This is because of the formation of Zn_2TiO_4 phase in the grain boundaries, as seen in Fig.1. The relationship between the average grain size and the level of TiO_2-doping for the samples sintered at 1200 ºC and 1300 ºC for 1 h is shown in Fig. 4. As seen from this figure, the average grain size of undoped ZnO is about 17.5 μm at 1200 ºC for 1 h sintering and about 20 μm at 1300 ºC for 1 h [3]. The average grain size of ZnO decreases with TiO_2 content. A sharp decrease in the grain size of the samples sintered at 1200 °C for 1 h is observed. The grain growth of ZnO occurred with the solid-state diffusion of Zn^{2+} cations. The solid-state diffusion of Zn^{2+} cations [3] is strongly inhibited by the formation of Zn_2TiO_4 phase in the grain boundaries at the sintering of 1200 ºC (the grain size of ZnO is 6.3 μm in the 1 wt. % TiO_2-doped sample). But the same situation is not observed at the sintering of 1300 °C. The grain size of ZnO is 11.8 μm in the 1 wt. % TiO_2-doped sample.

The grain growth kinetics can be determined using a simplified phenomenological kinetics (Eq. (1)). The value of the grain growth exponent n in the equation can be found at isothermal conditions where the kinetic equation is expressed in the form of

$$n \log G = \log t + \log K_0 - 0.434\left(\frac{Q}{RT}\right) \tag{3}$$

The n value can be calculated from the slope of the log(grain size) versus log(time) plot which is equal to $(1/n)$. Such plots were made for isothermal conditions employed at the sintering temperatures and the n values were calculated by the method of linear regression. Figs. 5a, b show the plots of log$G$ vs. log$t$ for various TiO_2 contents at 1200 ºC and 1300 ºC and the calculated n values are listed in Table 1. Similar plots

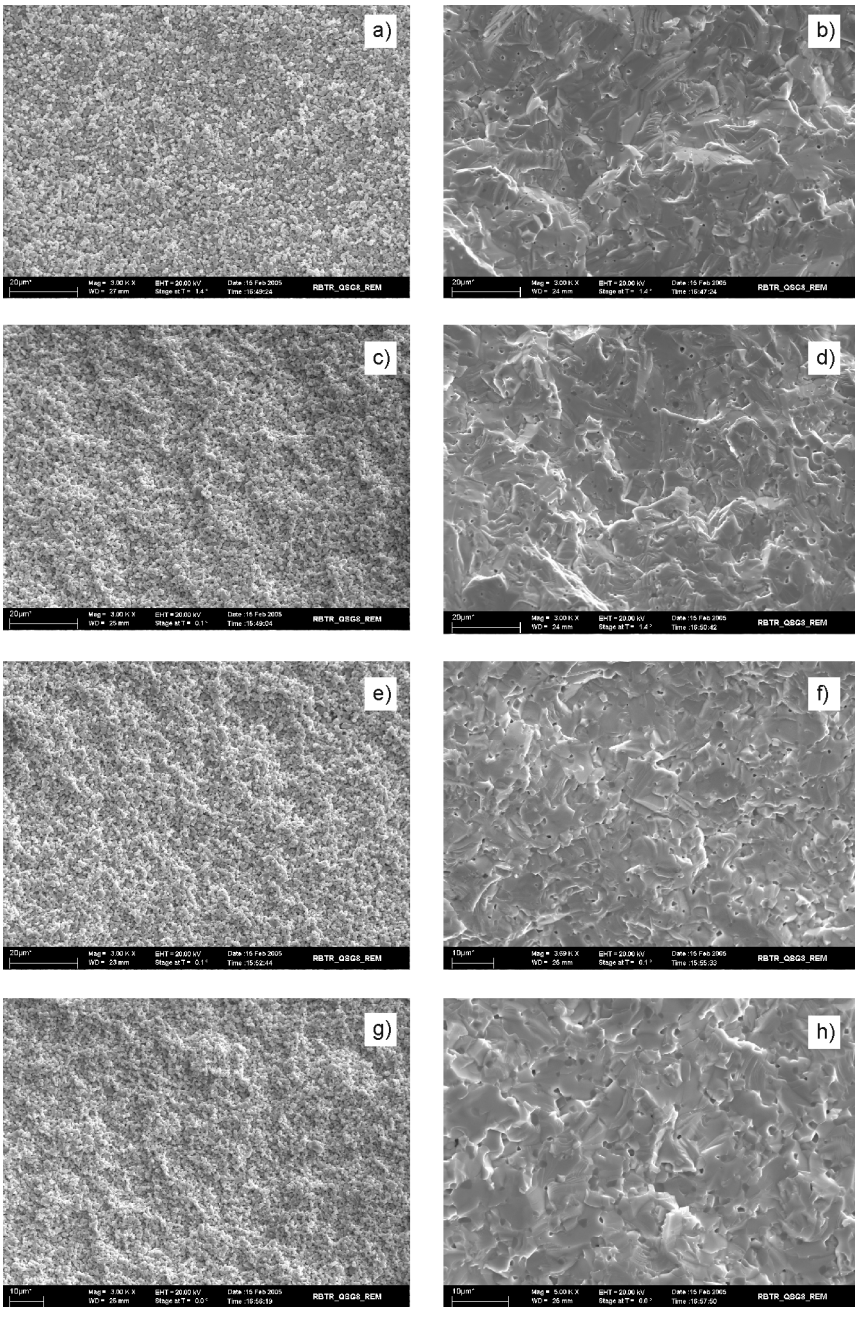

Fig. 3. SEM micrographs of the fracture surfaces of samples with 1, 2, 3 and 4 wt. %TiO_2 doping sintered at 1000 °C /1 h (a, c, e, g) and 1300 ºC/1 h (b, d, f, h)

could not be constructed for isothermal sintering at 1000 and 1100 ºC, since the samples had a fine crystalline size (<1 μm) and very porous microstructure which gave

rise to a large amount of grain pull-outs in the sample polishing process for optical microscopy. Therefore the grain sizes used as starting points for plots in the evaluation of the activation energies were deduced from the SEM micrographs in the samples sintered at 1000 ºC.

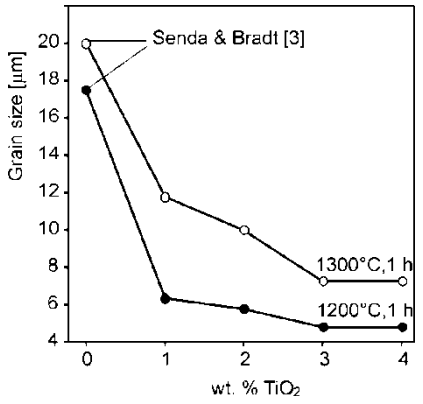

Fig. 4. The relationship between the average grain size and the level of TiO_2 doping for samples sintered at 1200 ºC and 1300 ºC for 1 h

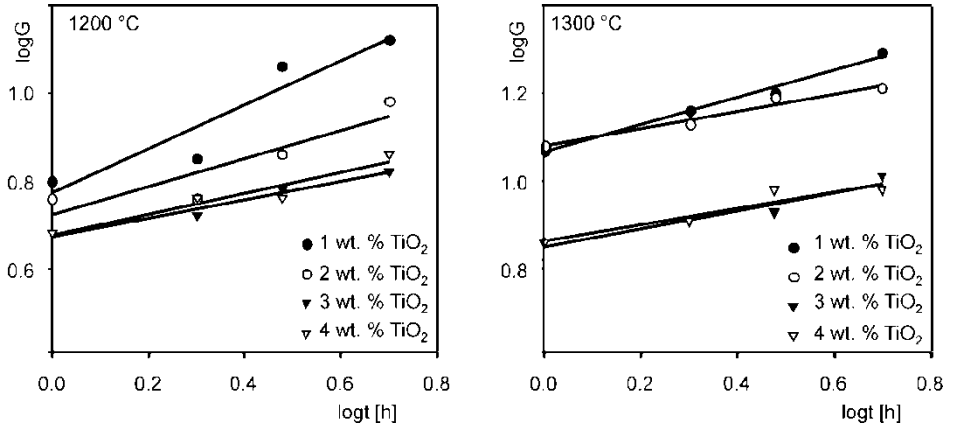

Fig. 5. Isothermal grain growth of ZnO with doping 1–4 wt. % TiO_2 sintered at: 1200 °C and 1300 °C

Senda and Bradt [3–5] reported the n values for ZnO and ZnO–2.38 wt. % Sb_2O_3 as 3 and 6, respectively. They also pointed out that the n value in the system indicated the mechanism of inhibition of grain growth. The n values for grain growth of the ZnO–TiO_2 1–4 wt. % studied in this work were found to be 3, 3, 5 and 5, respectively. They were affected by the high level of TiO_2 addition. If Eq. (2) is expressed as

$$\log\left(\frac{G^n}{t}\right) = \log K_0 - 0.434\left(\frac{Q}{RT}\right) \tag{4}$$

the apparent activation energy Q of the grain growth process can be calculated from the gradient of the Arrhenius plot of $\log(G^n/t)$ vs. $1/T$ (K^{-1}). Such plots for the studied

system are given in Fig. 6. In Table 1, the *n* values accepted in the construction of these plots are given together with the calculated values of the logarithm of rate constants and the apparent activation energies.

Table 1. Values of grain size, calculated grain growth exponent *n*, apparent activation energy *Q* and preexponential constant K_0

TiO_2 content [wt. %]	Grain size [μm]		*n*	logK_0	*Q* [kJ/mol]
	1200 ºC, 1 h	1300 ºC, 1 h			
0 [3]	17.5	20	3	11.49	225
1	6.3	11.8	3	17.47	435
2	5.7	10	3	17.85	435
3	4.8	7.3	5	24.65	608
4	4.8	7.3	5	24.95	615

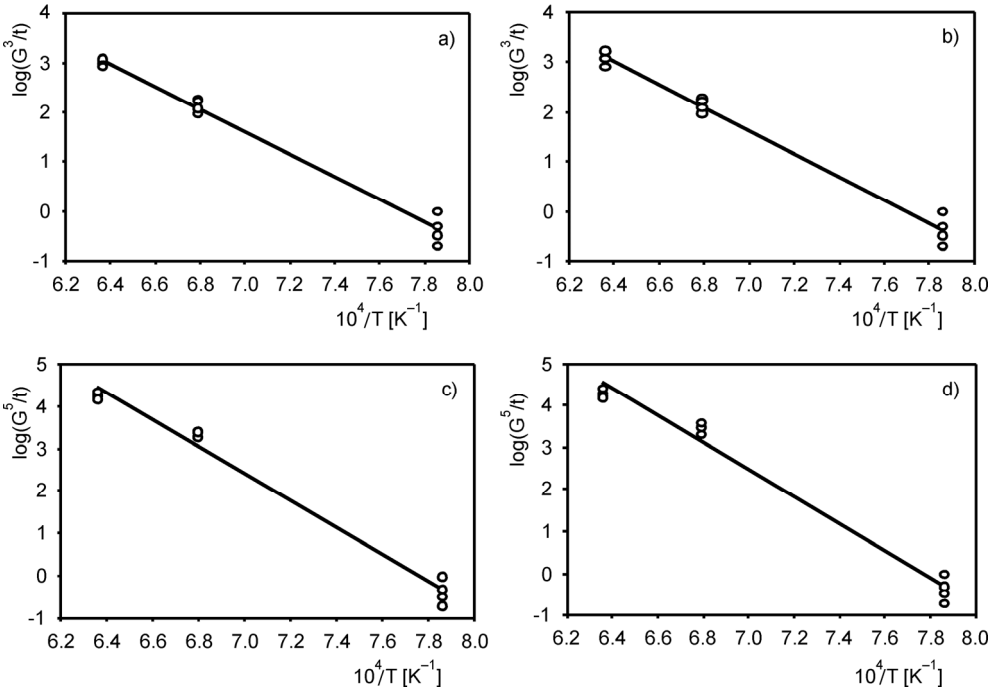

Fig. 6. Arrhenius plots for the grain growth of ZnO with TiO_2: a) 1 wt. % of TiO_2, $Q = 435$ kJ/mol, b) 2 wt. % of TiO_2, $Q = 435$ kJ/mol, c) 3 wt. % of TiO_2, $Q = 608$ kJ/mol, d) 4 wt. % of TiO_2, $Q = 615$ kJ/mol

Numerous studies on the kinetics of grain growth of ZnO have revealed that the rate controlling mechanism is the solid-state diffusion of Zn^{2+} cations. The apparent activation energy for this process is about 225 kJ/mol. As indicated in Table 1, the apparent activation energy of 435 kJ/mol was found for 1 and 2 wt. % TiO_2 content in the system. A sharp increase in the apparent activation energy to the value of 608 and 615 kJ/mol was found for 3 and 4 wt. % of TiO_2, respectively.

Since the microstructural and phase analysis of ZnO ceramics containing TiO_2 indicates the presence of Zn_2TiO_4 spinels as distinct crystals at the grain boundaries, inhibition of the ZnO grain growth must be considered related to presence of those spinel grains. The type of grain growth inhibition has been previously reported for other ZnO systems such as ZnO–Sb_2O_3 ($Zn_7Sb_2O_{12}$) [5] and ZnO–Al_2O_3 ($ZnAl_2O_4$) [1].

4. Conclusions

The effects of TiO_2 additions on the grain growth of ZnO were studied. Samples containing TiO_2 additions from 1 to 4 wt. % were sintered in air at 1000–1300 °C for 1–5 h. The resulting microstructures were observed by optical and electron microscopy methods and the phases were identified by the X-ray diffraction.

The apparent activation energy of 435 kJ/mol was found for samples containing 1 and 2 wt. % of TiO_2. A sharp increase in the apparent activation energy to the value of 608 and 615 kJ/mol was found for 3 and 4 wt. % of TiO_2, respectively. The apparent activation energy increased upon increasing content of TiO_2. The addition of TiO_2 to ZnO inhibits strongly the grain growth of ZnO. The inhibition is dependent on TiO_2 content, so higher contents of TiO_2 yield finer average ZnO grain sizes. When TiO_2 is added to ZnO, Zn_2TiO_4 spinel particles form at the grain boundaries. The process appears to be dominated by a grain boundary particle drag mechanism that is related to the formation of second-phase Zn_2TiO_4 spinel particles. The TiO_2 additions reduce the densification in the initial stages of sintering.

References

[1] HAN J., MANTAS P.Q., SENOS A.M.R., J. Mater. Res., 16 (2001), 459.
[2] HAN J., MANTAS P.Q., SENOS A.M.R., J. Europ. Ceram. Soc., 20 (2000), 2753.
[3] SENDA T., BRADT R.C., J. Am. Ceram. Soc., 73 (1990), 106.
[4] DEY D., BRADT R.C., J. Am. Ceram. Soc., 75 (1992), 2529.
[5] SENDA T., BRADT R.C., J. Am. Ceram. Soc., 74 (1991), 1296.
[6] TOPLAN H.Ö., ERKALFA H., ÖZKAN O.T., Ceramics-Silikaty, 47 (2003), 116.
[7] APAYDIN F., TOPLAN H.Ö., YILDIZ K., J. Mater. Sci., 40 (2005), 677.
[8] ÖZKAN O.T., AVCI M., OKTAY E., ERKALFA H., Ceram. Int., 24 (1988), 151.
[9] GÜNAY V., GELECEK-SULAN O., ÖZKAN O.T., Ceram. Int., 30 (2004), 105.
[10] TOPLAN Ö., GÜNAY V., ÖZKAN O.T., Ceram. Int., 23 (1997), 251.
[11] CANIKOĞLU N., TOPLAN N., YILDIZ K., TOPLAN H.Ö., Ceram. Int., 32 (2006), 127.
[12] *Metals Handbooks*, Vol. 8, 8th Ed., The American Society for Metals, PA, USA, 1973.
[13] LEVIN E.M., ROBBINS C., MC MURDIE F., *Phase Diagrams for Ceramics*, The American Ceramic Society Inc., Columbus, OH, 1965.

Received 16 June 2006
Revised 21 November 2006

Materials Science-Poland, Vol. 25, No. 4, 2007

Iron oxide(III) nanoparticles fabricated by electron beam irradiation method

B. ZHAO[1], Y. WANG[1], H. GUO[1], J. WANG[2], Y. HE[2], Z. JIAO[1*], M. WU[2]

[1]Institute of Nanochemistry and Nanobiology, Shanghai University, Shanghai 201800, China

[2]School of Environmental and Chemical Engineering, Shanghai University, Shanghai 201800, P.R. China

Iron oxide(III) nanoparticles were fabricated by the electron beam irradiation method. The structure and morphology of the iron oxide nanoparticles were analyzed by XRD, TEM, AFM and FTIR. Phase transformation temperatures were determined by DSC–TGA. Results showed that the phase transition point and melting point decreased greatly. The size effects were discussed to explain the reason.

Key words: iron oxide(III); electron beam; irradiation; nanoparticles

1. Introduction

Iron oxide(III) is an extensively investigated material because of its magnetic, optical and catalytic properties. It has been used as electrodes in non-aqueous and alkaline batteries [1], as cathodes in brine electrolysis [2], shows photocatalytic properties for N_2 fixation [3], etc. It is possible to change its semiconducting character from n- to p-type by applying an appropriate dopant. Also iron oxide is used to fabricate pigments, sorbents and gas sensors [4].

Iron oxide(III) has been prepared by various methods such as chemical vapour deposition [5], sol-gel processes [6], pulsed laser evaporation [7], reactive sputtering [8], hydrothermal technique [9] and spray pyrolysis [10, 11]. In this paper, electron beam irradiation, a novel method to fabricate nanocrystalline iron oxide(III) has been described. The microstructure, morphology and thermodynamic properties of iron oxide were studied.

*Corresponding author, e-mail: zjiao@shu.edu.cn

2. Experimental

$FeCl_3 \cdot 6H_2O$, NaOH, isopropyl alcohol and polyvinyl alcohol, all of analytical grade, were used to fabricate iron oxide(III) nanoparticles. $FeCl_3 \cdot 6H_2O$ was dissolved in deionized water and the the following solutions were added: 1 M NaOH to adjust pH between 4 and 8, poly(vinyl) alcohol (PVA) to control the nanoparticle sizes and to prevent aggregation as well as isopropyl alcohol (IPA) as scavenger of oxidative radicals ($OH^{\cdot}$).

A GJ-2-II electronic accelerator was used to generate electron beams, working at 2 MeV 10 mA. The solutions were irradiated under electron beam at various doses. After irradiation, the suspensions were left for several hours to allow precipitation. The sediments were collected by centrifuging, and washed several times with deionized water to remove by-products. After vacuum drying at 60 ºC for 12 h, the powders were heat treated at 600 ºC for half an hour to obtain iron oxide nanoparticles.

The particle structure was characterized by a D-MAX-rC X-ray diffraction. The crystallite sizes were calculated based on the X-ray diffraction spectrum using the Scherrer equation. The morphology and microstructure of particles were examined by Hitachi H-800 TEM. In order to study the fine structure of the films, the surface morphology of the film was also examined by a Nanofirst-3000 AFM. Characteristic absorption bands of the powder were investigated by Avatar-370 FTIR. Thermal stability of samples was analyzed by TA SDT Q600 DSC-under dry nitrogen (containing less than 1% of oxygen) at a heating rate of 10 ºC/min from 20 ºC to 1400 ºC.

3. Results and discussion

The XRD pattern of fabricated iron oxide nanoparticles is shown in Fig. 1. The XRD peaks are at $2\theta = 24.16^{o}$, 33.20^{o}, 35.66^{o}, 40.90^{o}, 49.52^{o}, 54.12^{o}, 57.64^{o}, 69.62^{o} and 72.00^{o}. According to JCPDS card (76-1821), the powder is hexagonal α-Fe_2O_3. Calculated from the Scherrer equation, the sizes of crystals ranged from 34.2 nm to 53.9 nm (mean value – 42.5 nm).

The TEM images are shown in Fig. 2. The iron oxide(III) particles have spherical shape morphology, fine dispersion and mean particle sizes between 20 and 60 nm. The nanoparticle sizes observed by TEM are in agreement with those calculated by XRD.

AFM was also used to investigate the morphology and roughness of a nanometer-order of magnitude in an area up to 1 μm^2. Figure 3a shows a representative AFM image of α-Fe_2O_3 nanoparticles by electron beam irradiation. It can be seen that the powders have spherical particles, and the mean size of particles is about 39 nm. Figure 3b is a three-dimensional AFM image of the same sample, all island-like grains are strongly elongated in one direction. The size distribution of nanoparticles is shown in Fig. 3c, α-Fe_2O_3 nanoparticles obtained by electron beam irradiation have mean particle sizes of 39 nm.

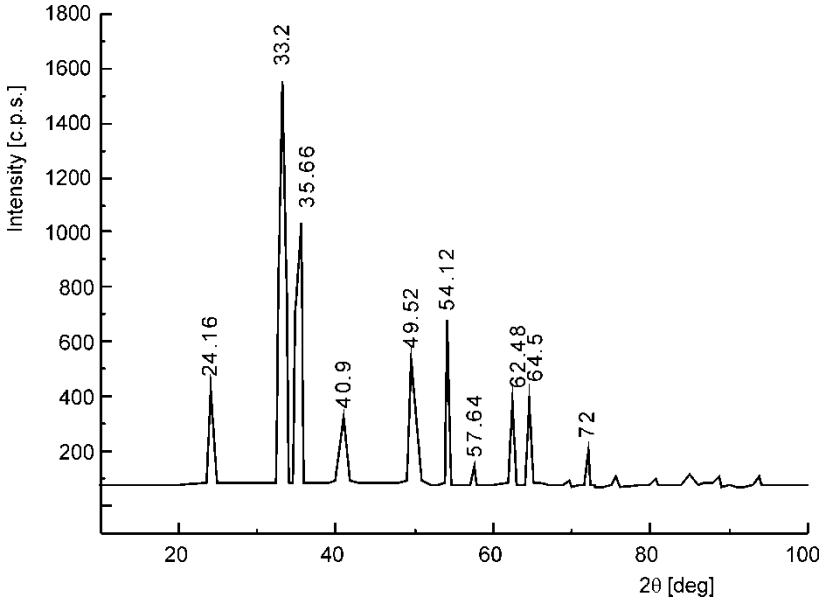

Fig. 1. The XRD pattern of α-Fe_2O_3 powder prepared by electron beam irradiation

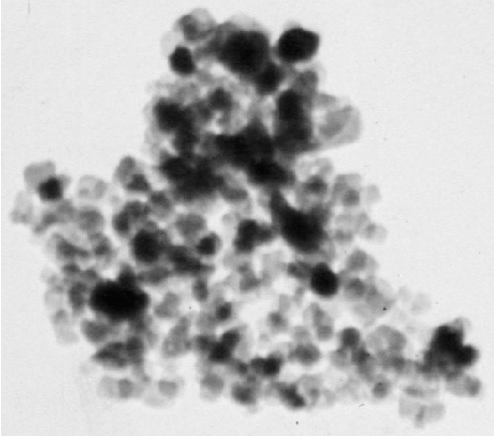

Fig. 2. The TEM morphology of α-Fe_2O_3 powder

The FTIR spectrum of α-Fe_2O_3 powder is shown in Fig. 4. Characteristic absorption bands at 536.57 cm^{-1} and 460.09 cm^{-1} for powder are assigned to α-Fe_2O_3. From the IR data, there is no evidence that α-Fe_2O_3 nanoparticles are contaminated by foreign materials in the system.

DSC/TGA results were shown in Fig. 5. From the TGA curve, the sample dried at 60 ºC undergoes a total weight loss of 25% with four decomposition steps from 20 ºC to 1400 ºC. The weight loss below 200 ºC is due to the removal of loosely bound water of the sample. The decomposition step between 220 and 400 ºC is due to the decomposition of nitrate ions and dehydroxylation of the sample. The third step between

400 and 900 ºC is attributed to the phase transformation from γ-Fe_2O_3 to α-Fe_2O_3. The weight loss over 900 ºC is extremely small.

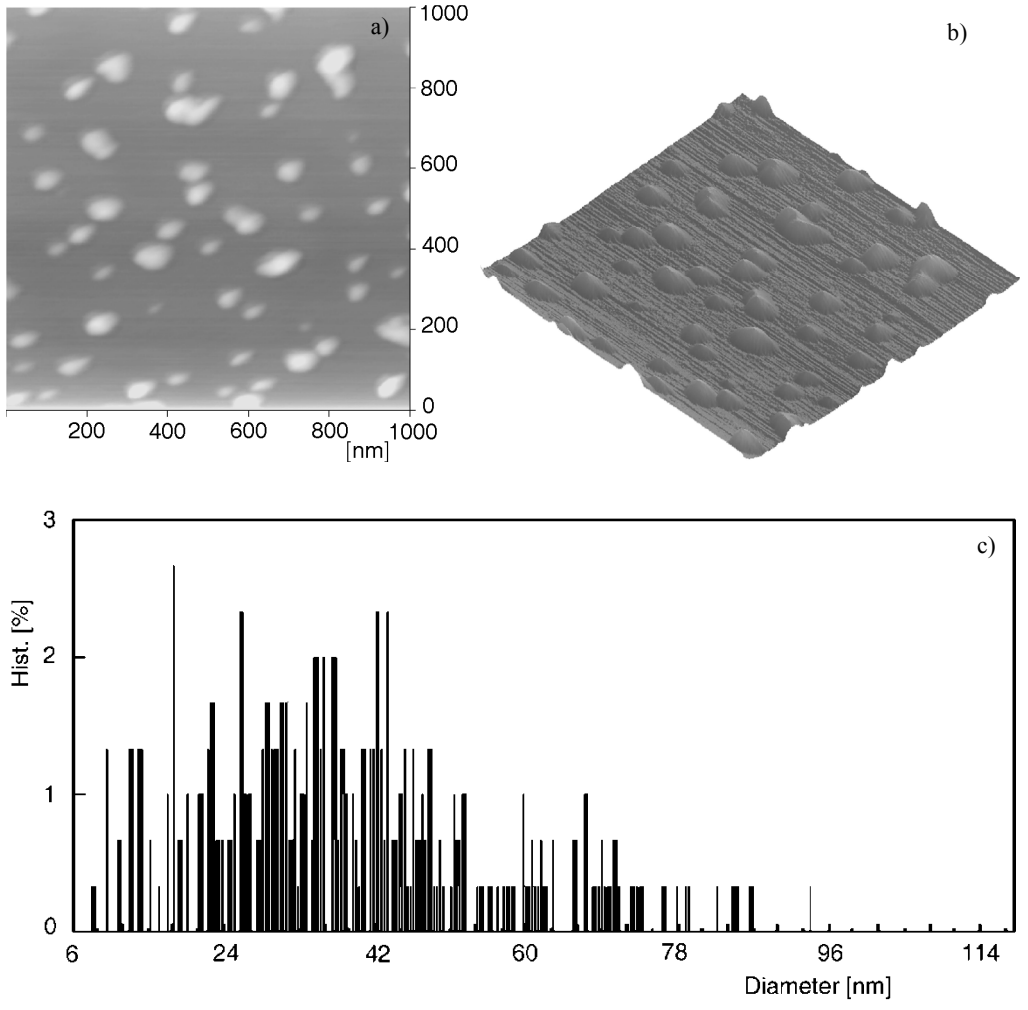

Fig. 3. AFM images of α-Fe_2O_3 powder prepared by electron beam irradiation: a) topography, b) 3D image, c) size distribution

From the DSC curve, two main peaks can be observed at 770 ºC and 1355 ºC during heating up to 1400 ºC indicating that two phase transformations occur. The peak temperature was employed to identify different phase transformation. The exothermic peak at 770 ºC should be ascribed to the phase transformation process of crystal type from γ-Fe_2O_3 (low temperature type) to α-Fe_2O_3 (high temperature type). In previous paper, Trautmann determined the enthalpy difference between γ-Fe_2O_3 and α-Fe_2O_3 as 19.5 kJ /mol [12], In our works, the enthalpy change for the peak at 770 ºC (corresponding to phase transition) is 99.90 J/g, equal to 15.98 kJ/mol. This is because the

nanoparticles have small particle sizes and high surface area, which bring high activity and decrease phase transition energy. The exothermic peak at 1355 ºC is attributed to the phase transformation process of α-Fe_2O_3 from solid to liquid state, lower than the normal melting point of Fe_2O_3, 1530 ºC.

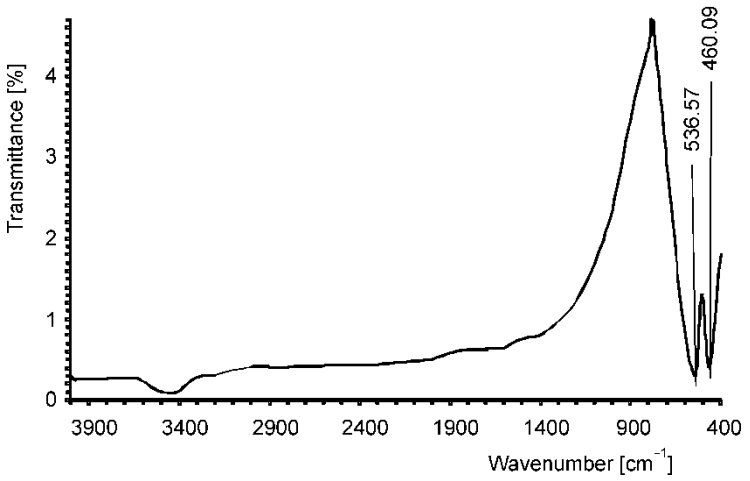

Fig. 4. FTIR spectrum of α-Fe_2O_3 powder

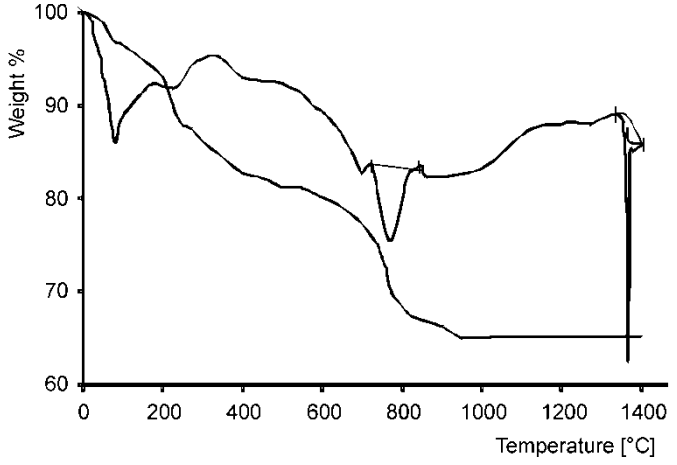

Fig. 5. DSC-TGA curves for α- Fe_2O_3 powder

According to Kelvin equation, $RT\ln(p_r/p) = 2\gamma V_m/r$, the saturated vapour pressure of small particles is higher than that over a flat surface. For nanoparticles, the saturated vapour pressure will be several times higher than that in normal state, which we think will cause the decrease of the melting point.

4. Conclusion

In this paper nanocrystalline iron oxide(III) has been prepared by electron beam irradiation. The optimal experiment condition was obtained at pH 6.0 and 300 kGy irradiation dose. XRD, TEM, AFM and FTIR results shown that the obtained particles by electron beam irradiation method are hexagonal α-Fe_2O_3, nanoparticles have average diameters around 30–60 nm, and have spherical shape morphology, well-degree of dispersion. The phase transition energy and melting point decreased from normal value, which are due to small size effects.

Acknowledgements

The authors gratefully acknowledge support from Shanghai Committee of Science & Technology Qimingxin project (05QMX1423, 06QH14005), Shanghai Committee of Education (07ZZ11, 50578090) and Shanghai Leading Academic Disciplines (T0105).

References

[1] KENICHI S., AKINIDE J., KIYOHIDE T., Japan Patents, 61 (1986), 147.
[2] KEIJI K., ITSUAKI M., Japan Patents, 79 (1979), 78.
[3] KHADAR M.M., LICHTIN N.N., VURNES G.H., SALMENON M., SOMORAJ G.A., Langmuir, 3 (1987), 303.
[4] KULKARNI S.S., LOKHANDE C.D., Mater. Chem. Phys., 82 (2003), 151.
[5] CHAI C.C., PENG J., YAN B.P., Sensors Actuators B, 34 (1996), 412.
[6] ZHU Y., QIAN Y., Mater. Res. Bull., 29(1994), 377.
[7] JOSHI S., NAWATHEY R., KOINKAR V.N., J. Appl. Phys., 64 (1988), 5647.
[8] WILHELM S.M., YUN K.S., BALLANGER L.W., HACKERMAN N., J. Electrochem. Soc., 126 (1979), 419.
[9] CHEN Q.W., QIAN Y.T., Mater. Res. Bull., 30 (1995), 443.
[10] QIAN Y.T., NIU C-M., HANNIGAN C., Yang S., J. Solid State Chem., 92 (1991), 208.
[11] XIE Y., WANG W., QIAN Y.T., J. Cryst. Growth, 167 (1996), 656.
[12] MAJZLAN J., NAVROTSKY A., SCHWERTMANN U., Geochim. Cosmochim. Acta. 68(2004),s1049.

Received 23 July 2007

Materials Science-Poland, Vol. 25, No. 4, 2007

Methanol dehydration to dimethyl ether using modified clinoptilolite

S. J. ROYAEE[*1], M. SOHRABI[1*], C. FALAMAKI[2]

[1]Chemical Engineering Department, Amirkabir University of Technology, Hafez Ave., P.O. Box 15875-4413, Tehran, Iran

[2]Ceramics Department, Materials and Energy Research Center, P. O. Box 14155-4777, Tehran, Iran

Clinoptilolite, a natural zeolite from the Semnan region in the West of Iran, has been converted to a catalyst for the methanol dehydration to dimethyl ether process. To produce such a catalyst and to create acidic sites on the latter, the ion-exchange process has been used. In addition, to investigate and optimize the effective factors of the catalyst synthesis process, a L9 Taguchi experimental design method has been implemented. The effects of four factors have been considered: the type of ion-exchange solution (2 levels); ion-exchange solution concentration; calcination temperature and calcination time (the last three factors have been studied in 3 levels). The yield of catalyst (conversion×selectivity) has been chosen as the response of the system. The catalytic behaviour of the produced samples was investigated using a fixed bed reactor (T = 350 ºC, P = 1 atm and WHSV = 4.78 h^{-1}). The results of the statistical design showed that the optimum conditions were: calcination time – 3 h, calcination temperature – 500 ºC, ion-exchange solution concentration – 2M, and ion-exchange solution – ammonium chloride. The optimum catalyst was tested using a fixed bed reactor at 330 ºC, 1 atm and WHSV= 3.8 h^{-1} resulting in 98.1% conversion and 96.5% selectivity. In order to investigate the catalyst behaviour under industrial operating conditions, the catalyst was tested in a fixed bed reactor at 300 ºC, 16 atm pressure, and WHSV = 52.5 h^{-1}. The results were 67.02% conversion and 99.74% selectivity.

Key words: *clinoptilolite; dimethyl ether; catalyst; zeolite; Taguchi experimental design*

1. Introduction

Dimethyl ether (DME), as a multi-source, multi-purpose product, has received growing attention due to the present global environmental pollution and energy supply problems. DME can be produced from syngas, which in turn is formed from natural gas, coal or biomass. DME has a wide range of applications such as LPG substitute,

[*]Corresponding author, e-mail: sjroyaee@yahoo.com; sohrabi@aut.ac.ir

propellant, chemical feedstock and transportation fuel, and in fuel cells [1, 2]. Catalytic dehydration of methanol over an acidic catalyst offers a potential method for the production of DME, a new spray propellant. Being identified as a potential diesel and cooking fuel, DME has many excellent characteristics. It has the oxygen content of 34.78% and can be burned without soot emission, whereas for traditional diesel fuels, simultaneous NO_x and soot emission control target cannot be expected. It has a boiling point of –25 ºC, which is 20 ºC higher than LPG and can be liquefied at 0.54 MPa (20 ºC). Therefore, based on the matured technology of LPG application, as far as storage, transportation, and usage, no remarkable problem for the use of DME exists [2, 3]. The reaction occurs in zeolite and pure γ-alumina and on γ-alumina slightly modified with phosphates or titanates, in a temperature range of 250–400 ºC and pressures up to 16 bar [4–7].

The aim of this research was to investigate the potential of the clinoptilolite-rich tuff of the Semnan region of Iran to achieve catalytic properties, especially for the MTD (methanol to dimethyl ether) reaction. Adsorptive characteristics of this material in various forms have been recently reported by Falamaki et al. [8]. The size of the channels (0.72×0.44, 0.47×0.41, 0.55×0.4 and 0.72×0.44 nm^2) as reported by Ackley and Yang [9] are of the same order of the pentasil family (0.53×0.56 and 0.51×0.55 nm^2) [10], thus making it eligible to catalyze important petrochemical reactions like methanol to dimethyl ether (MTD), methanol to olefins (MTO) and syngas to dimethyl ether (STD).

2. Experimental

Catalyst synthesis. An Iranian commercial natural clinoptilolite zeolite (Afrand Tuska Company) with less than 10 wt. % crystalline SiO_2 (quartz and cristobalite), the Si/Al ratio of 5.78, and the approximate formula $(Ca_{1.41}Mg_{0.96}Na_{1.66}K_{1.01})(Al_{7.4}Si_{42.78}O_{72.00})\cdot 23H_2O$ [8] has been used. In order to perform the ion-exchange process, the zeolite was first crushed into 100 μ granules and then thoroughly washed with distilled water. In the next step, 2 dm^3 of the solution of ammonium chloride or sulphuric acid with specific concentration was used per 30 g of raw zeolite for the ion-exchange process. The mixture was mixed for 24 h at room temperature using a propellant mixer with a mixing velocity of 1000 rpm. Then the solid product was filtered out and washed with hot deionized water until pH of the water leaving the filter was about 7. Then wet solid product was again subject to the process described above. Finally, the washed and filtered solid product was dried for 12 h at 100 °C. The ion-exchanged samples were calcined for a certain period of time.

Fabrication of acidic sites on the raw zeolite was achieved through the following methods:

1. Ion-exchange with H_2SO_4:

$$Na^+ [^-O\text{-}Z] + H^+ \rightarrow [^+H^-O\text{-}Z] + Na^+$$

2. Ion-exchange with ammonium chloride and further transformation of NH_4^+ cations into protons via thermal treatment:

$$Na^+ [^-O\text{-}Z] + NH_4^+ \rightarrow NH_4^+ [^-O\text{-}Z] + Na^+$$

$$NH_4^+ [^-O\text{-}Z] \rightarrow [^+H^-O\text{-}Z] + NH_3$$

2.1. Fixed bed reactor tests

Fixed bed reactor system. A catatest system (Fig. 1), equipped with a fixed bed reactor with the inner diameter of 1.5 cm was used to examine the catalyst activity and selectivity.

Fig. 1. The catatest system

The pressure of the system was adjusted by imparting back pressure. The reactor and the pre-heater temperatures were set by an electric jacket equipped with a PID controller to the predetermined temperature with the accuracy of ±0.5 °C. Nitrogen was used as a carrier gas to provide the required pressure and for creating the desired methanol partial pressure. The flow rate of nitrogen gas was controlled by a mass flow controller (l5850E, Brooks). Liquid methanol, which consequently evaporated in the pre-heater and was mixed in gaseous state with nitrogen, was injected into the system by a dozing pump (H94X, Milton Roy). The reactor output stream, after passing through a shell and tube heat exchanger, entered a two-phase separator. The output gas from the reactor was analyzed every 10 min by an on-line gas chromatograph (Agilent model 6890N) using a TCD detector, a 0.53 mm×30 m HP-Plot Q capillary column and helium as the carrier gas.

Reactor operating conditions. In order to better investigate the catalyst selectivity, median conditions of methanol conversion to DME and to light linear olefins were

chosen as the operating conditions of the reactor. For this reason, 3 g of synthesized catalyst samples were loaded into the reactor. At first, the catalyst was activated in the presence of nitrogen with a 50 $cm^3 \cdot min^{-1}$ flow rate, at the temperature of 350 °C. Then, the nitrogen flow was increased to 180 $cm^3 \cdot min^{-1}$. After stabilization of temperature, liquid methanol at a flow rate of 0.3 $cm^3 \cdot min^{-1}$ was injected into the reactor. The methanol partial pressure and WHSV in the reactor were 0.5 atm and 4.78 h^{-1}, espectively. Reaction temperature was fixed at 350 °C under atmospheric pressure.

3. Results and discussion

3.1. Taguchi experimental design catalyst

Among the most influential synthesis parameters affecting the catalytic behaviour of the modified zeolites, the following were considered based on our previous experience:

- ion-exchange solution type,
- ion-exchange solution concentration,
- calcination temperature,
- calcination time.

The method of L9 Taguchi experimental design was used to optimize the above factors in order to obtain a high active and selective catalyst for the production of DME. Two levels were selected for the first factor (ammonium chloride solution and sulphuric acid). For the remaining factors, three levels were considered.

In this study, the yield of the catalyst (conversion×selectivity) was chosen as the main target function (response). In addition, the effects of the parameters on the crystallinity (area under XRD curve in the range of 2θ from 5° to 35°) of the catalyst samples were also examined as target functions. The conditions for catalyst preparation according to the proposed Taguchi experimental design are summarized in Table 1.

Table 1. Design for optimization of catalysts preparation

No.	Sample	Calcination temperature [°C]	Ion-exchange solution concentration [M]	Calcination time [h]	Ion-exchange solution type
1	8	500	2	1	NH_4Cl
2	4	425	1	3	NH_4Cl
3	9	500	3	3	NH_4Cl
4	7	500	0.5	5	H_2SO_4
5	2	350	1	3	H_2SO_4
6	1	350	1	1	NH_4Cl
7	3	350	1.5	5	H_2SO_4
8	6	425	1.5	1	H_2SO_4
9	5	425	2	5	NH_4Cl

The catalyst samples were analyzed and tested in a fixed bed differential reactor. Moreover, the samples were also chemically analyzed.

3.2. ICP and XRD analysis

ICP and XRD analyses were performed on the catalyst samples produced according to the conditions given in Table 1. Table 2 shows the ICP analysis of the samples.

Table 2. ICP analysis results

Ions	Sulphuric acid solution concentration [M]			Ammonium chloride solution concentration [M]			Raw zeolite
	0.5	1	1.5	1	2	3	
Mg^{2+}	0.409	0.392	0.393	0.446	0.449	0.431	0.670
Ca^{2+}	0.867	0.848	0.799	0.551	0.511	0.296	1.620
Na^{+}	0.299	0.283	0.257	0.319	0.293	0.278	1.100
K^{+}	0.365	0.386	0.419	0.374	0.365	0.266	1.140
Sample No.	7	2	6	4	5	9	

For both ion-exchange solutions, the extent of Ca^{2+} and Na^{+} exchange increased with the increase of the concentration of the ion-exchange solution. The extent of Mg^{2+} exchange is higher for the samples treated with sulphuric acid (compared with the samples treated with ammonium chloride). The opposite holds in the case of Ca^{2+}. The extent of K^{+} exchange with ammonium ion increased with the increase of the solution concentration, while treating it with sulphuric acid cause the K^{+} exchange to decrease.

The degree of substitution of alkaline and alkaline earth metals with proton (DS) is defined as:

$$D.S = \frac{\sum m_{\text{eq (cations, raw zeolite)}} - \sum m_{\text{eq (cations, ion-exchange zeolite)}}}{\sum m_{\text{eq (cations, raw zeolite)}}}$$

The degree of proton substitution for samples is summarized in Table 3. The results presented in Table 3 show that proton substitution increases with the increase of the concentration of the ion-exchange solution.

XRD analysis of the samples (Table 4) showed that the area under the curves for samples which were ion-exchanged with sulphuric acid was considerably smaller than for those ion-exchanged with ammonium chloride. In other words, the samples that were ion-exchanged with sulphuric acid were subject to significant de-alumination and amorphization. The increase in acid concentration was accompanied with the loss of crystallinity and destruction of zeolite structure.

Table 3. Degree of proton substitution

Ions	Sulphuric acid solution concentration [M]			Ammonium chloride solution concentration [M]		
	0.5	1	1.5	1	2	3
Mg^{2+}	33.91	33.34	34.37	41.88	43.71	51.30
Ca^{2+}	43.59	43.73	42.37	31.38	30.17	21.37
Na^{+}	13.10	12.72	11.87	15.83	15.07	17.48
K^{+}	9.40	10.20	11.39	10.92	11.04	9.84
Sum of equivalent	0.0993	0.0967	0.0941	0.0876	0.0845	0.0961
D.S.	53.60	54.77	56.01	59.03	60.48	67.68
Sample No.	7	2	6	4	5	9

XRD of ion-exchanged samples with ammonium chloride showed that the peaks at 9.71° and 22.27° were significantly higher than those in the samples treated with sulphuric acid. This may be attributed to a higher degree of K^{+} and Ca^{2+} substitution for the samples treated with ammonium chloride*.

Table 4. The area under XRD curve

No.	Sample No.	Area under XRD curve 2θ (5º–35º)
1	8	481.44
2	4	558.94
3	9	589.5
4	7	529.14
5	2	537.2
6	1	427.61
7	3	431.65
8	6	422.39
9	5	529.55

3.3. Evaluation of the target functions

Steady state conditions (constant reactor output stream concentration) were established after about 2.5 h from the start of the experiments while the catalyst bed temperature was constant (350 ºC). Table 5 shows the selectivity, conversion percent, and yield of the samples. These results reveal major differences in the behaviour of various catalyst samples:

*XRD diffraction patterns of the samples have been published in the electronic version of the present issue (Attachments, pp. I–IV).

• The average conversion for the catalysts ion-exchanged with sulphuric acid was higher than for those ion-exchanged with ammonium chloride.

• DME selectivity in the case of catalysts ion-exchanged with ammonium chloride was relatively higher than that for catalysts ion-exchanged with sulphuric acid.

• It is observed that methanol conversion on catalysts prepared from ion-exchange with sulphuric acid of low concentration was higher than that on the catalysts prepared with ammonium chloride. It should be mentioned that generally low amounts of side products like light hydrocarbons resulted in selectivity deviation from 1.

Table 5. Reaction selectivity and conversion for each catalyst sample

No.	Sample	Conversion	Selectivity	Yield
1	8	0.0698	0.9668	0.0675
2	4	0.0649	0.9528	0.0618
3	9	0.0723	0.9803	0.0709
4	7	0.0653	0.9035	0.0590
5	2	0.0792	0.8930	0.0708
6	1	0.0478	0.9826	0.0470
7	3	0.0584	0.8829	0.0516
8	6	0.0636	0.8968	0.0570
9	5	0.0664	0.9650	0.0641

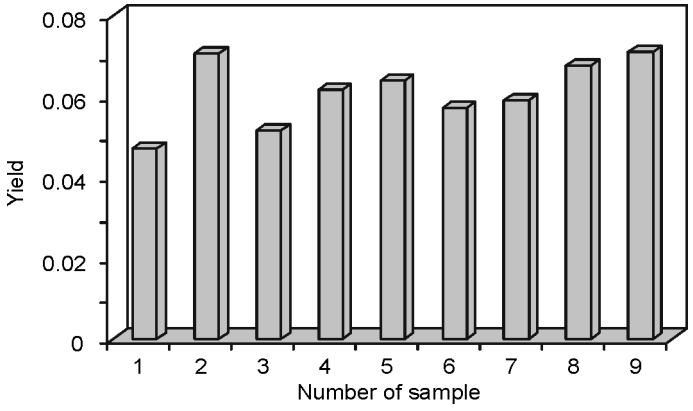

Fig. 2. The yield due to the various samples

Since, in addition to the conversion percent, the selectivity for DME is also an important factor in catalyst application, its yield, i.e. the product of conversion percent and selectivity, was considered the main response in the analysis of the variance (ANOVA) in order to evaluate the results. Figure 2 shows the changes of response for 9 samples of the Taguchi table.

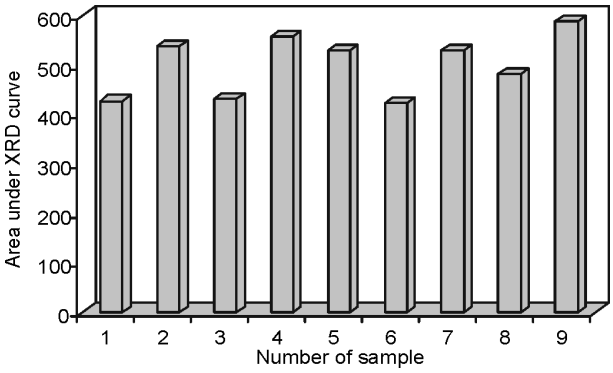

Fig. 3. The changes of crystallinity of the samples

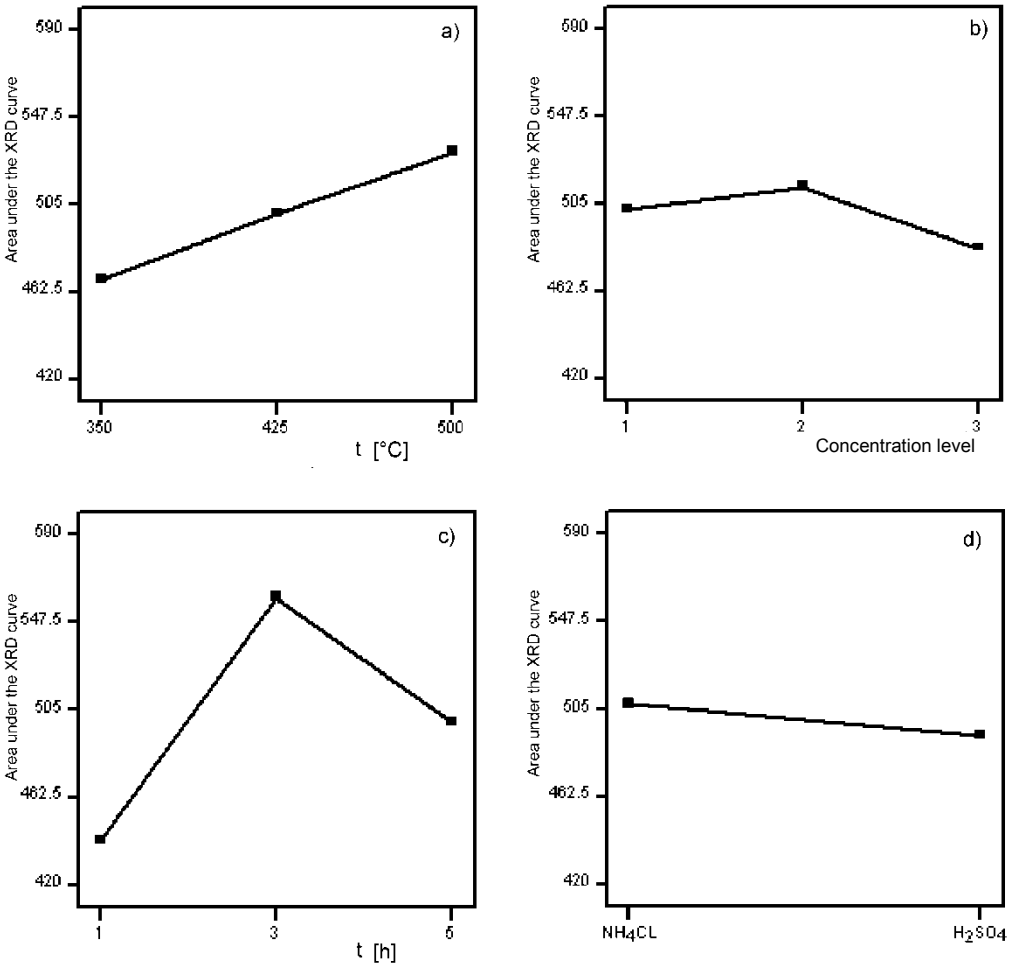

Fig. 4. The effect of the respective factors on crystallinity

Figure 3 shows the second target in this study (crystallinity, the area of the XRD curve in the range of $2\theta = 5°–35°$) for 9 samples. The effect of factor levels on crystallinity degree is shown in Fig. 4. A comparison between Figs. 2 and 3 shows that the trend of response changes versus experiment number is the same except for experiment No. 8. Generally, high concentration of acid solution results in loss of crystallinity. Calcination temperature has a positive effect on crystallinity while a long calcination causes destruction of the crystal structure.

Based on ANOVA, the following relation between crystallinity and the factor levels has been obtained:

$$\begin{aligned}&\text{Area under XRD Curve} \equiv \text{crystallinity}\\&= 499.97\\&+ 31.38A[1] - 0.55A[2]\\&-9.47\,B[1] - 6.77B[2]\\&+ 29.04C[1] - 29.67C[2]\\&-7.68D\end{aligned} \tag{1}$$

Applying Eq. (1), the first three parameter configurations resulting in high crystallinity have been determined and summarized in Table 6. The order of factor influence on this target function is as follows:

1) calcination time,
2) calcination temperature,
3) ion-exchange solution type,
4) ion-exchange solution concentration.

Table 6. Synthesis conditions for obtaining high crystallinity

Arrangement	Predicted response	Calcination temperature [°C]	Ion-exchange solution concentration [M]	Calcination time [h]	Ion-exchange solution type
1	611.361	500	2	3	NH_4Cl
2	600.528	500	1	3	NH_4Cl
3	596.002	500	2	1	H_2SO_4

Based on ANOVA, the following relation between reaction yield and factor levels has been obtained:

$$\begin{aligned}&\text{Yield}\\&= 0.061\\&+ 4.985\times10^{-3}A[1] - 5.866\times10^{-5}A[2]\\&+ 1.631\times10^{-3}B[1] - 3.290\times10^{-3}B[2]\\&+ 2.260\times10^{-4}C[1] - 3.477\times10^{-3}C[2]\\&+ 9.114\times10^{-4}D\end{aligned} \tag{2}$$

The effect of each factor at different parameter levels is shown in Fig. 5.

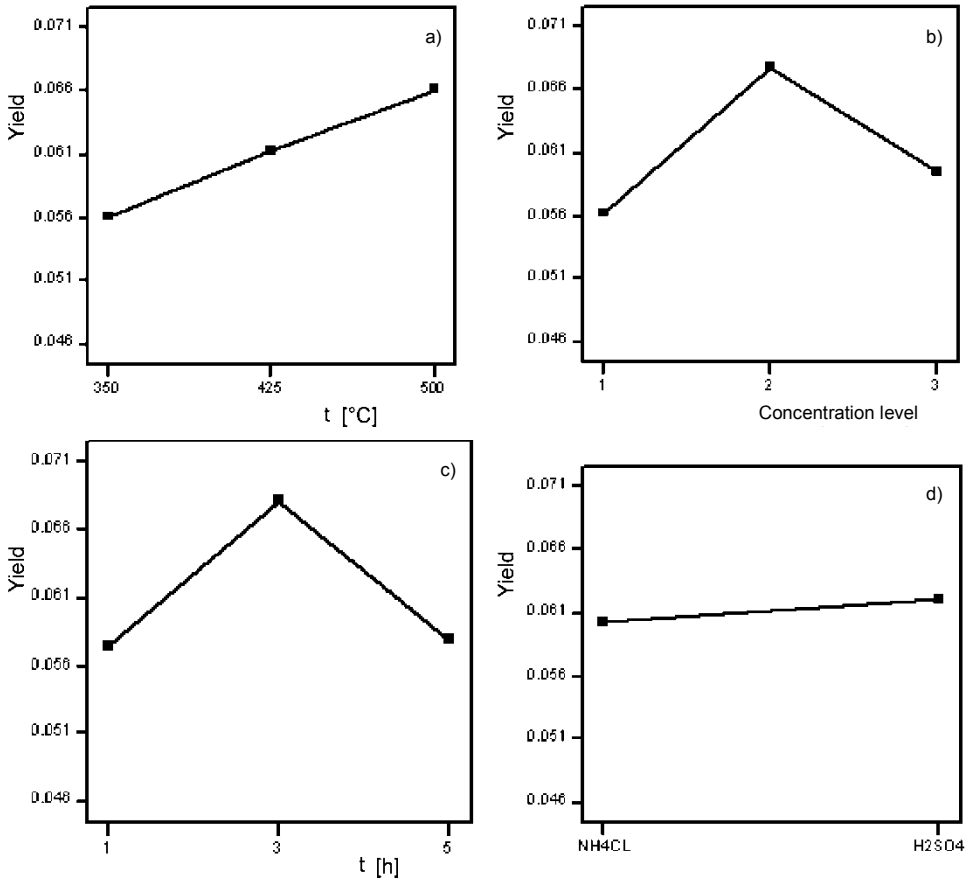

Fig. 5. The effect of factor levels on yield

The order of factor influence on the yield (main target function) is as follows:

1) ion-exchange solution concentration,
2) calcination time,
3) calcination temperature,
4) ion-exchange solution type.

Considering catalyst yield as the target function, the ion-exchange solution concentration is the most influential factor. Figure 5b indicates the 2nd concentration level as the suitable level for this factor, and increasing the solution concentration to 3rd concentration level results in the loss of catalyst yield. Based on the XRD analysis, the latter conclusion may be considered an artefact. In fact, the results of the Taguchi table for the 3M concentrations outshine the cases in which sulphuric acid was used. As previously explained, high acid concentration results in severe loss of crystallinity.

The second parameter with a positive effect on catalyst yield is the catalyst calcination time. Long calcination periods, especially at high temperatures, may cause the destruction of the zeolite structure and, consequently, the loss of catalyst yield.

Referring to Fig. 5d, the ion-exchanged sample with sulphuric acid shows more catalytic yield compared with the one ion-exchanged with ammonium chloride. However, it should be noted that although the conversion of the synthesized samples with sulphuric acid was somewhat higher than of those ion-exchanged with ammonium chloride, the selectivity of the samples treated with ammonium chloride was higher. Also, the only side products formed were trace amounts of methane and carbon dioxide. On the other hand, the application to sulphuric acid results in catalyst amorphization and faster deactivation. In conclusion, the ion-exchanged samples with ammonium chloride are practically more suitable than those treated with acid, due to the higher stability and reaction selectivity.

Based on Eq. (2), the factor configurations leading to the two highest target responses (yield) have been calculated and are summarized in Table 7. The first configuration shown in Table 7 is unacceptable as the concentration of acid equal to 1 M may indeed cause severe amorphization. Therefore, the optimum factor level configuration proposed is calcination temperature 500 ºC, ion-exchange solution concentration 2 M, calcination time 3 h, and ion-exchange solution – ammonium chloride.

Table 7. Factor configurations resulting in the two highest target functions (yield)

No.	Predicted response	Calcination temperature [°C]	Ion-exchange solution concentration [M]	Calcination time [h]	Ion-exchange solution type
1	0.081	500	1	3	H_2SO_4
2	0.079	500	2	3	NH_4Cl

To check the validity of the Taguchi experimental design in obtaining the optimum catalyst preparation procedure, a catalyst was prepared accordingly. The catalytic behaviour of the latter was investigated using a fixed bed reactor, charged with 5 g of the catalyst. The reaction conditions without nitrogen flow were: pressure – 1atm, reaction temperature – 330 °C, liquid methanol flow rate – 0.4 $cm^3 \cdot min^{-1}$ (WHSV = 3.8 h^{-1}). In this test, the catalyst was activated for 1 h in the presence of nitrogen prior to methanol injection.

The steady state conditions were established within 2.5 h. Analysis of the output gas stream showed the conversion level of 98.1% and the selectivity of 96.5%. In order to investigate the catalyst deactivation, the reaction was continued for 14 h. No deactivation was observed. Methane and carbon dioxide were the only side products.

In addition, to investigate the optimum catalyst behaviour under industrial operational conditions, a fixed bed reactor test was performed using 1 g of the catalyst at the pressure of 16 atm and temperature of 300 °C, with a liquid methanol flow rate of 1.1 $cm^3 \cdot min^{-1}$ and nitrogen flow rate of 50 $cm^3 \cdot min^{-1}$ (WHSV = 52.5 h^{-1}) for 40 h.

The Arak petrochemical complex (Arak, Iran) facilities were applied in the latter experimental run. The corresponding results are summarized in Table 8.

Table 8. Results of the test of industrial operational conditions

At steady state		After 40 hours on stream	
Conversion [%]	Selectivity [%]	Conversion [%]	Selectivity [%]
67.02	99.74	58.42	99.8

4. Conclusions

The optimally modified clinoptilolite zeolite that is the subject of this study is a potential candidate for being used as a methanol dehydration catalyst for DME production. The Taguchi experimental design was successfully applied for obtaining the optimum ion-exchange and calcination conditions for modifying the raw zeolitic material. The optimized catalyst of this work has a high selectivity for the MTD reaction, the only analyzable side products being methane and carbon dioxide. At the same time, catalysts like H-ZSM5 and H-Mordenite result in side products like ethane, propane, ethylene, which induce deactivation.

Acknowledgement

Appreciation and thanks are due to Engs. Mahdi Chavoshi and Fereidoon Yaripoor for their kind collaboration.

References

[1] NG K.L., CHADWICK D., TOSELAND B.A., Chem. Eng. Sci., 54 (1999), 3587.
[2] WEN ZHI LU LI HUA TENGWEN DE XIAO, Chem. Eng. Sci., 59 (2004), 5455.
[3] FLEISCH T., MCCARTHY C., BASU A., UDOVICH C., International Congress & Exposition, Detroit, Michigan, February 27 March 2, 1995.
[4] BRAKE L.D., U.S. Patent 4.595.785, 1986.
[5] WOODHOUSE J.C., U.S. Patent 2.014.408, 1935.
[6] BANDIERA J.,NACCACHE C., Appl. Catal., 69 (1991), 139.
[7] BERCIC G., LEVEC J., Ind. Eng. Chem. Res., 31 (1992), 1035.
[8] FALAMAKI C., MOHAMMADI A., SOHRABI M., Coll. Surf. A, Physicochem. Eng. Asp., 246 (2004), 31.
[9] ACKLEY M.W., YANG R.T., AIChE J., 37 (1991), 1645.
[10] MEIER M.W., OLSON D.H., *Atlas of Zeolite Structure Types*, 3rd Ed., Butterworth-Heinemann, 1992, p. 138.

Received 24 February 2007
Revised 24 March 2007

Attachments. XRD diffraction patterns of the samples

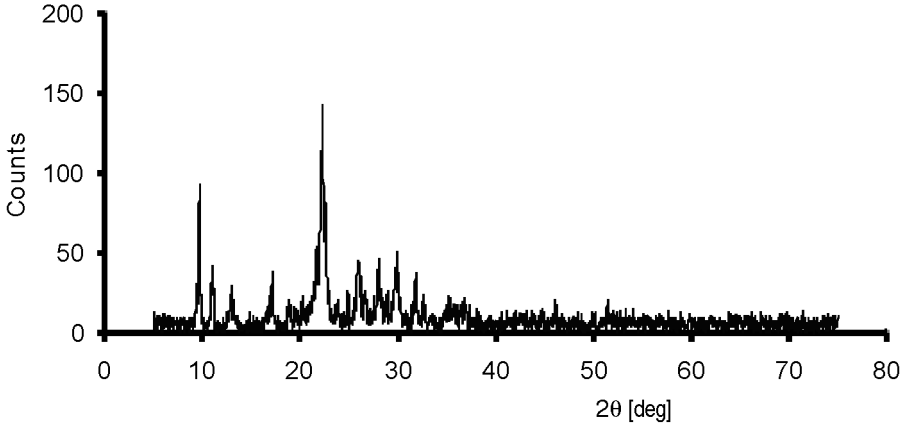

Sample 1 from table 4

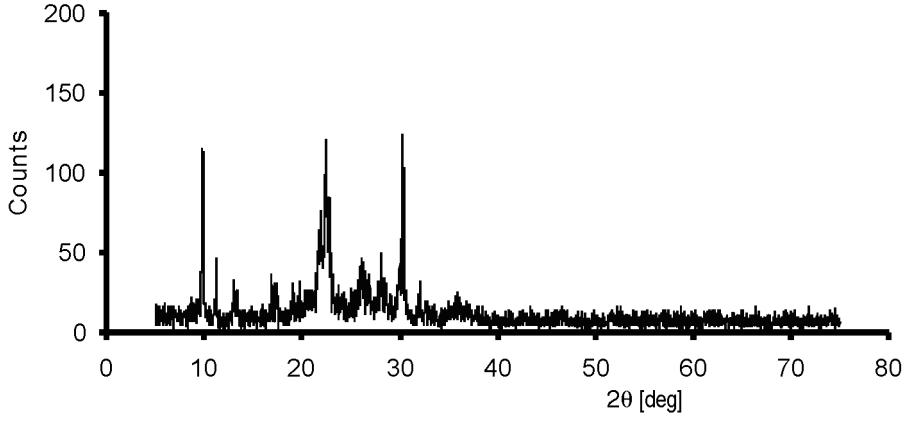

Sample 2 from table 4

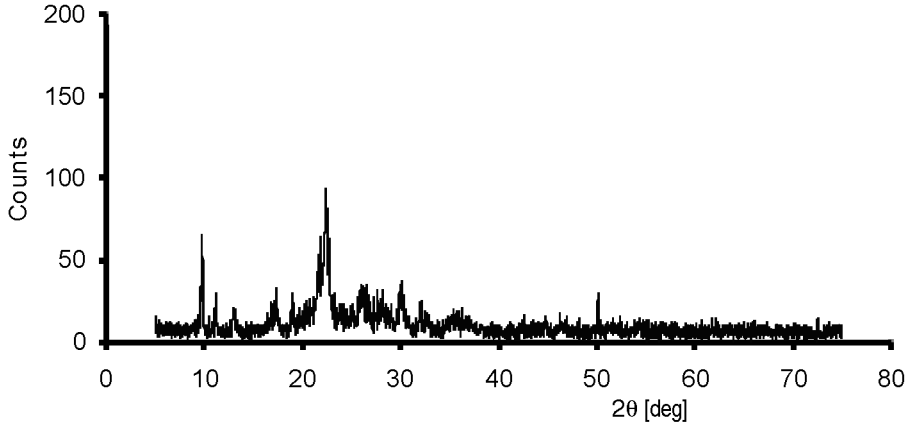

Sample 3 from table 4

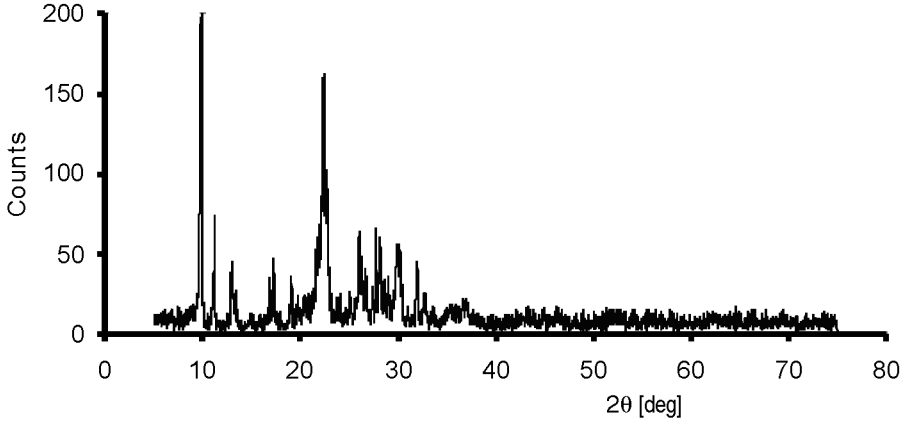

Sample 4 from table 4

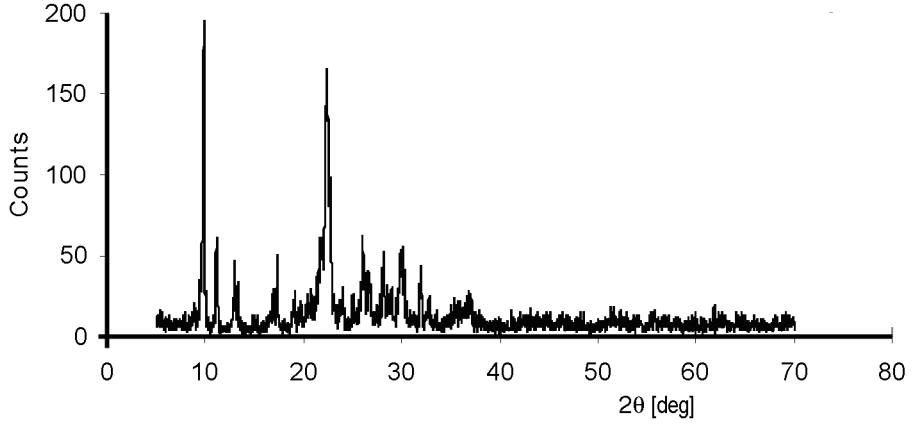

Sample 5 from table 4

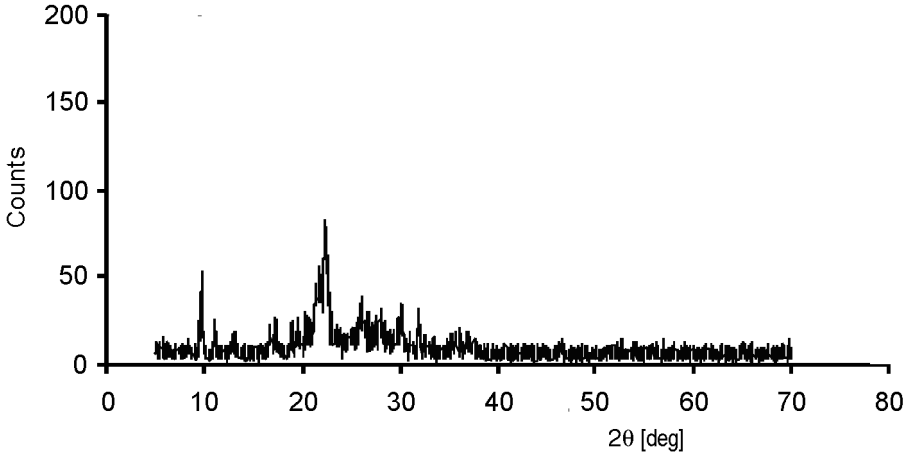

Sample 6 from table 4

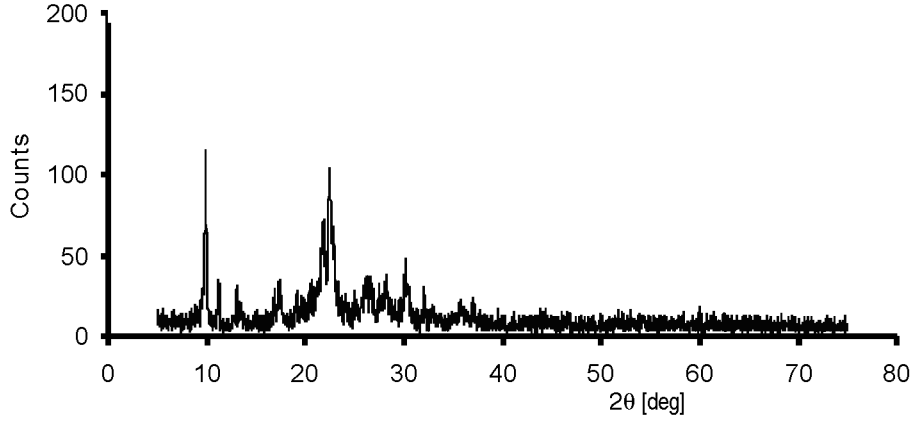

Sample 7 from table 4

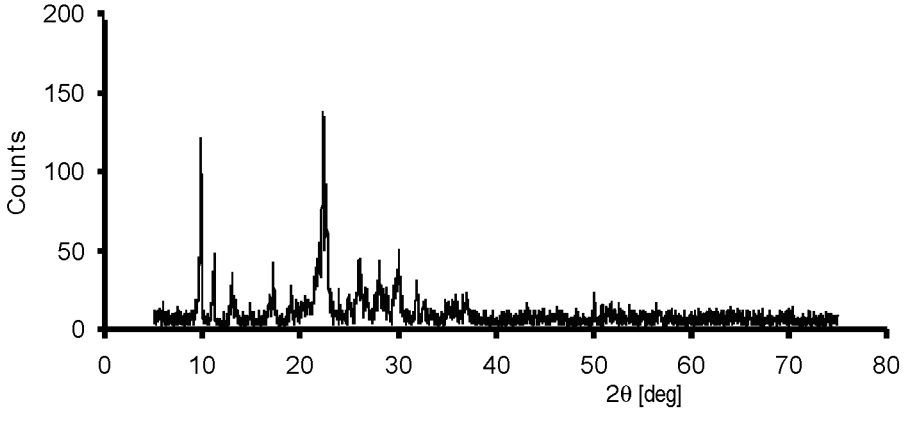

Sample 8 from table 4

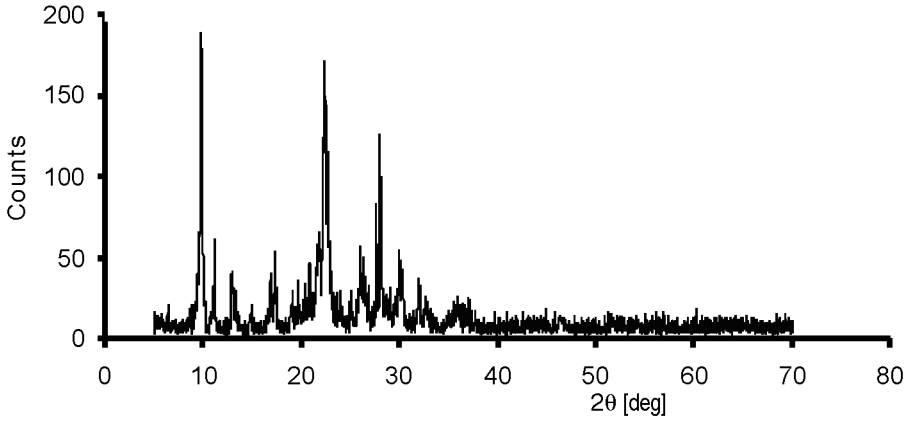

Sample 9 from table 4

Materials Science-Poland, Vol. 25, No. 4, 2007

Calculation of short range order in Ni–Rh, Ni–Pd and Cu–Rh alloys

T. ABBAS, M. ULLAH, A. M. RANA*, R. M. ARIF KHALIL

Department of Physics, Bahauddin Zakariya University, Multan-60800, Pakistan

Transition metal model pseudopotential (TMMP) technique has been applied to study the short range order (SRO) in nickel alloys Ni_{100-x}–Rh_x and Ni_{100-x}–Pd_x and a copper alloy Cu_{100-x}–Rh_x (x = 2, 5, 8, 11 at. %). All these transition metal alloys form *fcc* solid solutions for the chosen compositions. The static electrical permittivity $\varepsilon(q)$ was taken from the Hubbard–Sham model and/or Geldart–Vosko model to account for the exchange energies and correlation correction factors. Ordering energies and the Warren–Cowley SRO parameters have been calculated for all these alloys. Both models gave almost the same values for both the ordering energies and the Warren–Cowley SRO parameters. The TMMP model is found to predict the correct sign of SRO parameters for all these alloys.

Key words: *clustering; lattice constant; pseudopotential theory; transition metal model pseudopotential*

1. Introduction

Short range order (SRO) is an arrangement of atoms in the immediate neighbourhood of a particular atom in the lattice. It can decrease with increasing distance and can be restricted to the microcrystals which are joined to one another in a disjointed fashion. SRO is thus related to those arrangements where unlike atoms tend to become near neighbours [1]. Tendency for like atoms to be near neighbours is named as clustering. SRO, its degree, type and sign depend on concentration, nature, temperature of solid solution and history of the specimen [2]. The degree of SRO could be related to the diffraction effects produced. In terms of a suitable parameter termed as the Warren–Cowley parameter α_i (WCP) SRO can be defined as [1]:

$$\alpha_i = 1 - \frac{P_A^i}{C_A} = 1 - \frac{P_B^i}{C_B}$$

where P_A^i, P_B^i denote the conditional probabilities of having B and A atoms as neighbours in the i-th coordination sphere, respectively, and C_A and C_B are concentra-

*Corresponding author, e-mail: anwar_manzoor_rana@yahoo.com

tions of atoms A and B. Being composed of like and unlike atoms with particular forces of attraction or repulsion operating between them, all real solid solutions probably exhibit either short range order or clusters to a greater and lesser degree [3]. The presence of SRO may be decided based on the value of the Warren–Cowley parameter α_i:

- $\alpha_i < 0$ for SRO,
- $\alpha_i > 0$ for clustering or local order,
- $\alpha_i = 0$ for complete randomness.

Differences in the interatomic pair interaction energies E_{AB} of the AA, BB and AB pairs in an i-th coordination sphere, defined by $E_{AB} = V_{AB} - 1/2(V_{AA} + V_{BB})$, may cause SRO formation [1]. Ordering energy determines the tendency of atoms to order in the system, e.g. an increase in the number of AB pairs ($E_{AB} > 0$), i.e. SRO formation or decrease in the number of AB pairs ($E_{AB} < 0$), i.e. disordering. The absolute value of the ordering energy near the critical temperature T_C is $E_{AB} = k_B T_C$ below which lies the long range order (LRO) and above which lies SRO, which becomes weaker with the increase of temperature leading to a random statistical distribution of atoms at high temperatures.

In solid solution alloys, SRO is usually described by two basic models: homogeneous and heterogeneous ones. The homogeneous model assumes that ordering proceeds uniformly throughout the specimen, i.e. for any site i occupied by A atom, there will be some probability (independent of the choice of i) that adjacent sites will be occupied by atoms of different kind (B). As there is no correlation between distinct sites, widely separated regions may or may not contain the same ordering sequence. On the other hand, the heterogeneous model involves the development of SRO by the emergence of small domains (which may differ in composition from that of the nominal alloy) having some equilibrium degree of order (micro-domain model). These domains have dimensions lower than the coherence length (i.e., electron mean free path). The anti-phase domain model assumes that early stages of ordering are characterized by a very fine random network of anti-phase domains, each domain having some equilibrium degree of order. In both micro-domain and anti-phase domain models, if the domain size is lower than the coherence length, such ordering will result in diffuse scattering and be properly classified as SRO.

High resolution electron microscopy (HREM) can be used to gain information about the type of SRO prevailing in a system or SRO can be indirectly studied by a detailed analysis of the diffuse scattered intensity with the assistance of some of the modeling techniques. Valuable additional information can also be obtained by using probes of different coherence lengths (e.g., Mössbauer effect, neutron scattering and resistivity). X-ray and neutron diffraction techniques have been used to study SRO mainly due to the reason that they provide a direct measurement of the degree of SRO. The SRO parameters have been determined experimentally for a large number of metallic solid solutions by diffuse X-ray/neutron scattering intensity measurements (DSIM) [4–12]. Vrijen and Radelaar [13] observed in Cu–Ni alloys that cluster parameters had a strong asymmetry in their composition dependence. Electrical resistivity measurements were used to study SRO in various metallic systems [10, 12, 14].

The differential scanning calorimetry (DSC) was applied for SRO studies in mechanically alloyed $Hf_{75}Al_{7.5}Cu_{7.5}Ni_{10}$ and amorphous $Zr_{75}Al_{7.5}Cu_{7.5}Ni_{10}$ alloys [15]. Blizmuk et al. [16] studied the effect of nitrogen on SRO in duplex steel by Mössbauer spectroscopy, internal friction and the Cowley parameters measurements. Theoretical investigations of SRO have been made by various simulation techniques using statistical and electronic theories of SRO as well as pseudopotential theory. Gruner et al. [9] and Kramer and Sordelet [17] applied reverse Monte Carlo simulation technique to study SRO and atomic clusters in Cu–Sn and Zr–Pd alloys, respectively. Electronic theory of ordering has been applied to calculate SRO parameters in Ni–Rh and Ni–Ir alloys by Abbas et al. [5]. The SRO investigations have also been performed using the pseudopotential theory for the calculations of many atomic properties and was found useful for studying ordering characteristics of alloy formation, if not for all, then at least for a series of groups [4, 18]. Khawaja et al. [19] and Abbas et al. [20, 21] used pseudopotential technique in the second order perturbation theory to calculate local ordering energy and showed good agreement with the experimental results.

In the present investigations, the transition metal model pseudopotential (TMMP) technique has been successfully applied to study the SRO in Ni–Rh, Ni–Pd and Cu –Rh alloys in the second order perturbation theory. The Warren–Cowley SRO parameters, as modified by Katsnelson et al. [22], and local ordering energies have been calculated using the dielectric screening function $\varepsilon(q)$ in the Hartree approximation [23], and the energy exchange and correlation correction parameters $f(q)$ by applying two different approaches as proposed by Hubbard and Sham [24, 25], and Geldart and Vosko [26]. This research is the continuation of our earlier work on SRO [20, 21].

2. Theory of ordering energy and the Warren–Cowley SRO parameters

According to the second order perturbation theory, the band structure contribution to the structure and configuration dependent part of the total energy [19] may be defined as:

$$E_{bs} = \frac{\Omega_0}{8\pi} \sum_q q^2 F'(q) \tag{1}$$

where $\Omega_0 = \Omega/N$ is the volume per atom and N is the number of atoms in a crystal of volume Ω. $F'(q)$ denotes the energy wave number characteristics. In the local pseudopotential approximation [27], $F'(q)$ may be expressed as:

$$F'(q) = \left|W^0(q)\right|^2 \frac{\varepsilon(q)-1}{\varepsilon^*(q)} \tag{2}$$

here $W^0(q)$ is the local approximation of total unscreened pseudopotential form factor and is related to the wave number q:

$$W^0(q) = -\frac{4\pi z e^2}{\Omega_o}\cos\left(\frac{qR_m}{q^2}\right) \tag{2a}$$

whereas $\varepsilon(q)$ is the static electrical permittivity. In the Hartree approximation [22], it is given by:

$$\varepsilon(q) - 1 = \left(\frac{4\pi z e^2}{\Omega_o q^2}\right)\chi\left(\frac{q}{2K_F}\right) \tag{2b}$$

and $\varepsilon^*(q)$ is the modified dielectric screening function which accounts for the exchange and correlation effect and is defined as:

$$\varepsilon^*(q) = 1 + \left[1 - f(q)\right]\left[\varepsilon(q) - 1\right] \tag{3}$$

The term $\chi(q)$ represents the perturbation characteristic expressed by:

$$\chi(q) = \frac{3E_F^{-1}}{2}\left[\frac{1}{2} + \frac{4K_F^2 - q^2}{8K_F q}\ln\left|\frac{2K_F + q}{2K_F - q}\right|\right] \tag{4}$$

here $E_F = \dfrac{\hbar^2 K_F^2}{2m}$ is the Fermi energy,

$$K_F = \left(\frac{3\pi^2 Z}{\Omega}\right)^{1/3}$$

the Fermi vector and $f(q)$ is the exchange and correlation correction factor. According to Hubbard-Sham [24, 25] and Geldart-Vosko [26], $f(q)$ can be expressed as follows:

- Hubbard–Sham:

$$f(q) = \frac{q^2}{2}\left[q^2 + K_F^2 + K_S^2\right]^{-1} \tag{5}$$

where K_s is a screening parameter and can be written in terms of K_F as:

$$K_S^2 = \frac{2K_F}{\pi} \tag{5a}$$

- Geldart–Vosko:

$$f(q) = \frac{q^2}{2}\left[q^2 + \xi K_F^2\right]^{-1} \tag{6}$$

where $\xi = 2(1 + 0.026(m^*/m)\gamma_s$ and $\gamma_s < 2$, γ_s is taken as unity, m is the mass of electron and m^* is its effective mass.

The SRO-dependent part of the band structure energy [19] may be written as:

$$E_{bs}^{\mathrm{SRO}} = \frac{\Omega_0}{8\pi}\frac{c(1-c)}{N}\sum_R\sum_q q^2\alpha(R)\mathrm{e}^{iqR}\left|\Delta W^0(q)\right|^2\frac{\varepsilon(q)-1}{\varepsilon^*(q)} \tag{7}$$

Similarly, the SRO-dependent part of the electrostatic energy contribution to the total energy of the crystal may be given in the form:

$$E_{es}^{\mathrm{SRO}} = \frac{c(1-c)}{N}\sum_q\sum_R\frac{(Z_A-Z_B)^2}{2}\frac{4\pi}{\Omega_O q^2}e^{(-q^2/4\eta)}\alpha(R)\ e^{iqR} \tag{8}$$

where Z_A, Z_B are valences of the component atoms A and B of the A–B alloy, and η is the Ewald parameter defined as $\eta = \alpha_{\mathrm{eff}}/\Omega^{1/3}$. By adding Eqs. (7) and (8), the expression for the total energy of the crystal [19] may be written as:

$$E^{\mathrm{SRO}} = E_{bs}^{\mathrm{SRO}} + E_{es}^{\mathrm{SRO}} = \frac{c(1-c)}{N}\sum_q\sum_{\{R\}}\alpha(R)\ e^{iqR}F(q) \tag{9}$$

where $F(q)$ is an additive energy wave number characteristics depending upon the band structure and electrostatic energy contributions:

$$F(q) = \frac{\Omega_0}{8\pi}q^2\left|\Delta W^0(q)\right|^2\frac{\varepsilon(q)-1}{\varepsilon^*(q)} + 2\pi\frac{(Z_A-Z_B)^2}{\Omega_0 q^2}\mathrm{e}^{(-q^2/4\eta)} \tag{10}$$

Changing the summation in Eq. (9) to integration and averaging it over all lattice sites q and R, the total energy of the crystal can be rewritten as:

$$E^{\mathrm{SRO}} = c(1-c)\sum_{\{R_i\}}\alpha(R_i)\mathrm{e}^{iqR}V(R_i) \tag{11}$$

where

$$V(R_i) = \frac{\Omega_0}{\pi^2}\int dq q^2F(q)\frac{\sin(qR_i)}{qR_i} \tag{12}$$

$V(R_i)$ being the local ordering energy of the i-th coordination sphere of the radius R_i [28].

Using the expression for the entropy [21], the Warren–Cowley SRO parameter α_1 for the first coordination sphere can be written as:

$$\frac{\alpha_1}{(1-\alpha_1)^2} = c(1-c)\left[\mathrm{e}^{-V(R_i)/(k_BT)} - 1\right] \tag{13}$$

where k_B is the Boltzmann constant.

3. Results and discussion

Transition metal model pseudopotential (TMMP) technique has been applied to study the short range order (SRO) in two nickel alloys: Ni–Rh and Ni–Pd, and in a copper alloy Cu–Rh. All these transition metal alloys form *fcc* solid solutions for the chosen compositions. The static electrical permittivity $\varepsilon(q)$ in this study is either from Hubbard–Sham [24, 25] or from Geldart–Vosko [26].

3.1. Ni–Rh system

The phase diagram of Ni–Rh system has not been completely established [29] but it appears that the solid Ni lattice can accommodate large amount of Rh before the solubility limit is exceeded. The lattice constants for the *fcc* Ni–Rh alloys have been calculated based on an average lattice and are given in Table 1. It is clear from this table that the lattice parameter a increases with increasing Rh content. This rise of a could be associated with the size of two elements. The radii of coordination spheres are related to the lattice constants. The calculated radii of the first three coordination spheres are also presented in the same table, which also show a slight rise with increasing Rh concentration in the Ni–Rh alloys.

Table 1. Lattice constants and radii of coordination spheres in Ni–Rh alloys

Rh content [at. %]	$R_1 = \frac{a}{\sqrt{2}}$ [Å]	$R_2 = a$ [Å]	$R_3 = \sqrt{2}a$ [Å]
2	2.4929	3.5256	4.9859
5	2.4998	3.5340	4.9978
8	2.5048	3.5424	5.0097
11	2.5048	3.5424	5.0097

a_{Ni} = 3.52 Å, a_{Rh} = 3.84 Å

Ordering energies $V(R_i)$ of three coordination spheres and the short range order parameters α_i were calculated by applying Eqs. (12) and (13) using a computer program written in MATLAB 7. The input parameters for TMMP calculations for Ni–Rh alloys, taken from Animalu [30], are given in Table 2.

Table 2. Input parameters for the transition metal model pseudopotential used in the calculation of ordering energy $V(R_i)$

Metal	R_m	Ω	Z	$\lvert R_c \rvert$	α_{eff}	E_C	η
Ni	2.2	73.6	2	1.304	0.063	0.093	0.0150
Pd	2.6	99.3	2	1.512	0.073	0.091	0.0157
Rh	2.0	92.6	3	1.258	0.048	0.960	0.0106
Cu	2.2	79.4	1	1.814	0.157	0.960	0.0365

The ordering energies thus calculated for three coordination spheres are given in Table 3.

Table 3. Ordering energies for Ni–Rh alloys calculated by taking into account the exchange and correlation correction parameters $f(q)$

Rh content [at. %]	$V(R_1)$ [a.u.]	$V(R_2)$ [a.u.]	$V(R_3)$ [a.u.]
Habbard–Sham [24, 25]			
2	0.0005	–0.0008	–0.0005
5	0.0015	–0.0020	–0.0013
8	0.0023	–0.0031	–0.0020
11	0.0032	–0.0041	–0.0027
Geldart–Vosko [26]			
2	0.0005	–0.0008	–0.0005
5	0.0015	–0.0020	–0.0013
8	0.0023	–0.0031	–0.0020
11	0.0032	–0.0041	–0.0027

The table shows that ordering energies for the first coordination sphere are positive for all concentrations of Ni–Rh alloys but have negative values for the second and third coordination spheres. The values of ordering energies increase upon increasing Rh concentration. These results show that there is a tendency of unlike atoms (i.e., Ni–Rh) to be the nearest neighbours which indicates the short range order for the first coordination sphere but for the second and third ones, the probability of like atoms (i.e., Ni–Ni and Rh–Rh) is more likely indicating clustering.

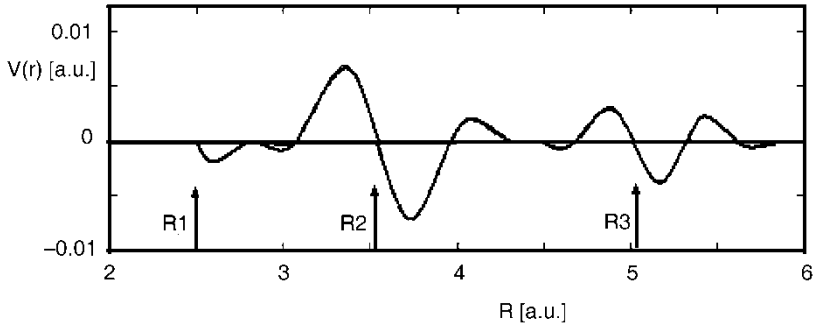

Fig. 1. Ordering energies $V(R)$ as a function of radii R of the coordination spheres in $Ni_{89}Rh_{11}$ alloys

This behaviour shows semi-oscillatory characteristics of ordering energies (Fig. 1). This result is also obvious from the Warren–Cowley SRO parameters as presented in Table 4, where negative values of α_1 refer to short-range order but positive

values of α_2 and α_3 refer to clustering [20]. The present results are found to be in good agreement with those of Abbas [5].

Table 4. Warren–Cowley SRO α_i parameters for Ni–Rh alloys

Rh content [at. %]	α_1	α_2	α_3
Habbard–Sham [24, 25]			
2	–0.0004	0.0006	0.0004
5	–0.0011	0.0014	0.0009
8	–0.0017	0.0021	0.0014
11	–0.0024	0.0028	0.0019
Geldart–Vosko [26]			
2	–0.0004	0.0006	0.0004
5	–0.0011	0.0014	0.0009
8	–0.0017	0.0021	0.0014
11	–0.0024	0.0028	0.0019

3.2. Ni–Pd system

The phase diagram of Ni–Pd alloy shows that it crystallizes in a complete series of solid solution alloys [29]. The lattice constants for the *fcc* Ni–Pd alloys have been calculated based on an average lattice (Table 5). It is clear that the lattice parameter a increases with increasing Pd content. This rise of a could be associated with the size of two elements. The calculated radii of the first three coordination spheres are also presented in Table 5, which also show a slight increase with increasing Pd concentration in the Ni–Pd alloys.

Table 5. Lattice constants and radii of coordination spheres in Ni–Pd alloys

Pd content [at. %]	$R_1 = \frac{a}{\sqrt{2}}$ [Å]	$R_2 = a$ [Å]	$R_3 = \sqrt{2}a$ [Å]
2	2.4942	3.5274	4.9884
5	2.5020	3.5385	5.0041
8	2.5099	3.5496	5.0198
11	2.5177	3.5607	5.0355

a_{Ni} = 3.52 Å, a_{Pd} = 3.89 Å

Using MATLAB 7, the ordering energies $V(R_i)$ of three coordination spheres and the short range order parameters α_i have been calculated (Tables 6 and 7).

Table 6. Ordering energies for Ni–Pd alloys calculated by taking into account exchange and correlation correction parameters $f(q)$

Pd content [at. %]	$V(R_1)$ [a.u.]	$V(R_2)$ [a.u.]	$V(R_3)$ [a.u.]
Habbard–Sham [24, 25]			
2	0.0002	–0.0008	–0.0001
5	0.0005	–0.0090	–0.0004
8	0.0009	–0.0012	–0.0007
11	0.0013	–0.0016	–0.0011
Geldart–Vosko [26]			
2	0.0002	–0.0008	–0.0001
5	0.0005	–0.0090	–0.0004
8	0.0009	–0.0012	–0.0007
11	0.0013	–0.0016	–0.0011

Table 7. Warren–Cowley SRO α_i parameters for Ni–Pd alloys

Pd content [at. %]	α_1	α_2	α_3
Habbard–Sham [24, 25]			
2	–0.0002	0.0008	0.0001
5	–0.0004	0.0010	0.0004
8	–0.0007	0.0012	0.0007
11	–0.0009	0.0016	0.0011
Geldart–Vosko [26]			
2	–0.0002	0.0008	0.0001
5	–0.0004	0.0010	0.0004
8	–0.0007	0.0012	0.0007
11	–0.0009	0.0016	0.0011

Table 6 shows that ordering energies for the first coordination sphere are positive for all concentrations of Ni–Pd alloys but have negative values for the second and third coordination spheres, with a decreasing trend on increasing Pd concentration. These results show that there is a tendency of unlike atoms, i.e. Ni–Pd to be the nearest neighbours which indicate the short range order for the first coordination sphere but for the second and third coordination spheres the probability of like atoms, i.e. Ni–Ni and Pd–Pd is more likely indicating clustering. This behaviour points to a semi-oscillatory characteristic of ordering energies as is clear from Fig. 2. This result is also obvious from the Warren–Cowley SRO parameters as given in Table 7 where negative values of α_1 refer to short-range order but positive values of α_2 and α_3 refer to clustering [20, 21].

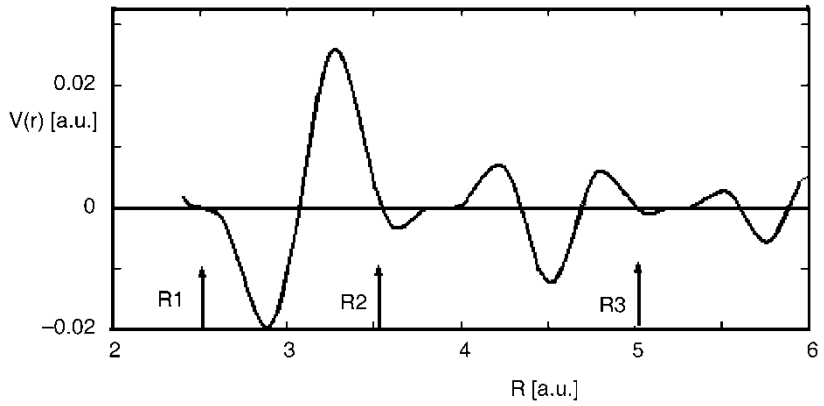

Fig. 2. Ordering energies $V(R)$ as a function of radii R of the coordination spheres in $Ni_{89}Pd_{11}$ alloy

3.3. Cu–Rh system

The Cu–Rh phase diagram [29] indicates a peritectic reaction at 1100 ºC which suggests that a single phase exists in Cu–Rh alloys at 25 ºC as primary solid solution of α-CuRh between 0 and 20 at. % Rh, and α-RhCu between 90 and 100 at. % Rh. The alloys of intermediate compositions are two-phase mixtures of α-CuRh and α-RhCu. Therefore, the chosen compositions of Cu–Rh alloys lie within that composition range (between 0 and 20 at. % Rh), which form α solid solutions. The lattice constants for the *fcc* Cu–Rh alloys calculated based on an average lattice using Vegard's rule are given in Table 8, which shows a rise in the lattice parameter a with increasing Rh content associated with its larger size as compared to Cu. The calculated radii of the first three coordination spheres are also presented in Table 8, which also show a slight rise with increasing Rh concentration in the Cu–Rh alloys.

Table 8. Lattice constants and radii of coordination spheres in Cu–Rh alloys

Rh content [at. %]	$R_1 = \frac{a}{\sqrt{2}}$ [Å]	$R_2 = a$ [Å]	$R_3 = \sqrt{2}a$ [Å]
2	2.5553	3.6238	5.1106
5	2.5593	3.6295	5.1187
8	2.5634	3.6252	5.1268
11	2.5674	3.6309	5.1348

a_{Cu} = 3.61 Å, a_{Rh} = 3.84 Å

The calculated ordering energies for the three coordination spheres are presented in Table 9 and found positive for first coordination spheres for all concentration of Cu–Rh alloys but show negative values for second and third coordination spheres.

Table 9. Ordering energies for alloys Cu–Rh calculated by taking into account the exchange and correlation correction parameters $f(q)$

Rh content [at. %]	$V(R_1)$ [a.u.]	$V(R_2)$ [a.u.]	$V(R_3)$ [a.u.]
Habbard–Sham [24, 25]			
2	0.0001	–0.0001	–0.0001
5	0.0003	–0.0003	–0.0002
8	0.0007	–0.0005	–0.0004
11	0.0008	–0.0007	–0.0005
Geldart–Vosko [26]			
2	0.0001	–0.0001	–0.0001
5	0.0003	–0.0003	–0.0002
8	0.0007	–0.0005	–0.0004
11	0.0008	–0.0007	–0.0005

Table 10. Warren–Cowley SRO α_i parameters for Cu–Rh alloys

Rh content [at. %]	α_1	α_2	α_3
Habbard–Sham [24, 25]			
2	–0.0001	0.0001	0.0001
5	–0.0003	0.0002	0.0002
8	–0.0005	0.0004	0.0003
11	–0.0006	0.0005	0.0004
Geldart–Vosko [26]			
2	–0.0001	0.0001	0.0001
5	–0.0003	0.0002	0.0002
8	–0.0005	0.0004	0.0003
11	–0.0006	0.0005	0.0004

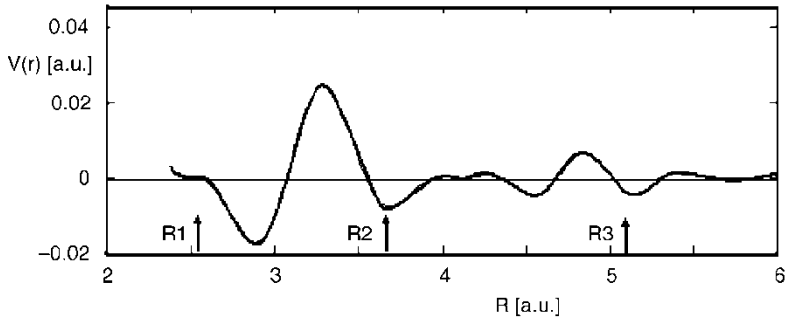

Fig. 3. Ordering energies $V(R)$ as a function of radii R of the coordination spheres in $Cu_{89}Rh_{11}$ alloy

The values of ordering energies increase with increase of Rh concentration. Therefore, the tendency of unlike atoms, i.e. Cu–Rh to be the nearest neighbours is high indicating SRO for the first coordination sphere and clustering seems to be more likely

due to the maximum probability of like atoms i.e. Cu-Cu and Rh–Rh to be nearest neighbours within the second and third coordination spheres. This result again represents a semi-oscillatory characteristic of ordering energies (Fig. 3). The SRO parameters (Table 10) also indicate a similar trend where negative values of α_1 refer to short-range order but positive values of α_2 and α_3 denote clustering [20, 21].

References

[1] WARREN B.E., *X-ray Diffraction*, New York, Dover Publications, 1999, p. 227.
[2] CULLITY B.D., *Elements of X-ray diffraction*, Addison-Wesley, Philippines, 1978.
[3] IVERONOVA V.I., KATSNELSON A.A., *Modern Problems of Short-Range Order*, Report, 1973, pp. 307–331.
[4] KATSNELSON A.A., SILONOV V.M., KHAWAJA FARID A. Phys. Stat. Sol. B, 91 (1979), 11.
[5] ABBAS T., *ICTP International Report*, Trieste, Italy, International Centre for Theoretical Physics, 1982.
[6] SAHA D.K., SHISHIDO T., OSHIMA K.-I., J. Phys. Soc. Jpn., 71 (2002), 2456.
[7] SAHA D.K., SHISHIDO T., OSHIMA K.-I., J. Phys. Soc. Jpn., 72 (2003), 1670.
[8] SEMBIRING T., SAHA D.K., TAKAHASHI M., SHISHIDO T., OSHIMA K-I., J. Phys. Soc. Jpn., 72 (2003), 107.
[9] GRUNER S., KOBANA L., KLEINHEMPEL R., HOYER W., JOVARY P., DELAPLANE R.G., J. Non-Cryst. Sol., 351 (2005), 3490.
[10] SHIN J.S., BAE J.S., KIM H.J., LEE H.M., LEE T.-D., LAVANIA E.J., LEE Z.H., Mater. Sci. Eng. A, 407 (2005), 282.
[11] BRAUDE I.S., PECHERSKA V.I., BOLSHUTKIN D.N., CHERNIK M.M., Cryst. Res. Techn., 21 (1996), 253.
[12] ZIYA A.B., OSHIMA K., Phys. B, Cond. Matt., 365 (2005), 225.
[13] VRIJEN J., RADELAAR S., Phys. Rev. B, 17 (1978), 409.
[14] IKRAM N., ALI S., J. Phys. Chem. Sol., 54 (1993), 747.
[15] DAMONTE L., MENDOZA C., ECKERT L., Mater. Sci. Eng. A, 278 (2000), 16.
[16] BLIZMUK T., MOLA M., POLISHIN E., POHL M., GAVRILJUK V., Effect of nitrogen on short-range atomic order in the ferritic δ-phase of duplex steel, Mater. Sci. Eng. A, 405 (2005), 11.
[17] KRAMER M.J., SORDELET D.J., J. Non-Cryst .Sol., 351 (2005), 1586.
[18] ABBAS T., Lecture delivered in the first regional school on short-range order, Islamabad, 1986, unpublished.
[19] KHAWAJA F.A., KATSNELSON A.A., SILONOV V.M., KHRUSHCHOV M.M., Phys. Stat. Sol. B, 82 (1977), 701.
[20] ABBAS T., ARIF KHALIL R.M., RANA A.M., ULLAH M., J. Res. Sci., 16 (2005), 87.
[21] ABBAS T., ARIF KHALIL R.M., RANA A.M., ULLAH M., Int. J. Modern Phys. B, 20 (2006), 2425.
[22] KATSNELSON A.A., SILONOV V.M., KHWAJA F.A., KHRUSHOV V.M., *Three bodies interaction in the electronic theory of the atomic local order in binary alloys*, Int. Symp. Electronic Structure of Metals and Alloys, P. Zschech (Ed), Dresden, (1978), p. 221.
[23] HARTREE W., HARTREE D.R., MANNING M.F., Phys. Rev., 60 (1941), 857.
[24] HUBBARD J., Proc. Roy. Soc. A, 240 (1957), 359.
[25] SHAM L.J., Proc. Roy. Soc. A, 283 (1965), 39.
[26] GELDART D., VOSKO S.H., J. Phys. Soc. Japan, 70 (1965), 20.
[27] HARRISSON W.A., *Pseudopotential in the Theory of Metals*, Benjamin, New York, 1966.
[28] HAIL G.L., PHIHOURS J., Phys. Rev., 139 (1965), 160.
[29] *Handbook of Electrical Resistivities of Binary Metallic Alloys*, K. Schröder (Ed.), CRC Press, Boca Raton, FL, 1983, pp. 230, 323, 325.
[30] ANIMALU A.O.E., Phys. Rev. B, 8 (1973), 3542.

Received 21 September 2007

Materials Science-Poland, Vol. 25, No. 4, 2007

Mechanism of charge generation and photovoltaic effects in lead phthalocyanine based Schottky barrier

G. D. SHARMA* , V. S. CHOUDHARY, Y. JANU, M. S. ROY

Molecular Electronics and Optoelectronics Devices Laboratory,
Department of Physics, J.N.V. University, Defence Laboratory, Jodhpur, India

Photovoltaic properties of lead phtalocyanine (PbPc) thin films sandwiched between indium tin oxide (ITO) and aluminum electrodes (ITO/PbPc/Al) have been investigated. The *J–V* characteristics of the device reveals that current flow across the device is limited by hole injection at Al/PbPc below 300 K, wherein Al is kept at higher bias. Junction parameters such as built-in potential (V_{bi}), carrier concentration (N_a), the width of depletion layer (W) were evaluated from the *C–V* measurements. The mechanism of transport of carriers in Al/PbPc/ITO has been investigated based on the detailed analysis of current–voltage characteristics at various temperatures in the dark. The PbPc form hole injection barriers with both Al and ITO electrodes which are 0.88 eV and 0.11 eV, respectively, indicating the formation of nearly Ohmic contact with ITO and the Schottky barrier with Al. The photovoltaic parameters of the device have been estimated from the analysis of the current–voltage characteristics under illumination and discussed in detail. Electrically active defects were investigated by the space charge capacitance spectroscopy methods at various temperatures (from 250 K to 350 K) and frequencies (from 5 Hz to 1 MHz), respectively. The activation energy calculated from the capacitance spectroscopy at various temperatures is about 0.32 eV suggesting that the defects originate from the trapping centres at Al/PbPc interface.

Key words: *charge generation; photovoltaic effect; lead phthalocyanine; Schottky barrier*

1. Introduction

During the last couple of decades, much effort has been put into the development of solar cells based on organic electronic materials because of their low cost and easy fabrication [1–8]. In molecular materials, the relevant molecules can be easily prepared and their properties modified to meet the optical and electronics requirements. Among a variety of molecular materials, phthalocyanines (Pcs) are well known stable materials with versatile functions [9–11]. Phthalocyanine molecule contains four iso-

*Corresponding author, e-mail: sharmagd_in@yahoo.com; on sabbatical leave from JNV University, Jodhpur (Raj), present address : MIT, Mandsaur (MP), India.

indole units (pyrrole ring conjugated with benzene ring). A large family of Pcs can be chemically modified by attaching various peripheral groups to outer ring of isoindoles. The difference in the molecular structure leads to the difference in their photophysical properties. Pcs absorb light in various spectral regions between 500 nm and 720 nm. Photovoltaic devices made from organic pigments reach power conversion efficiency of a few percent [10, 11] that is much lower than those of their inorganic counterparts, demanding further research for more efficient organic materials and their combinations. One of possible improvements for this type of photovoltaic devices is implementation of new materials, absorbing red or near infrared part of the solar spectrum, where maximum photon flux of the Sun light is located. Up till now CuPcs are among the promising donor materials for organic solar cells [12]. Lead phthalocyanine (PbPc) can also be used as a donor absorbing light in the range of 550–700 nm with absorption maximum about 680 nm and absorption edge around 740 nm. PbPc has received much attention as a promising material for gas sensor but it has not been explored in photovoltaic devices.

In the present work, we have characterized lead phthalocyanine (PbPc) in the form of a Schottky barrier device and investigated the mechanism of charge generation and photovoltaic response. PbPc is a p type organic semiconductor possessing high thermal stability and narrow optical band gap. We have studied the temperature dependence of current–voltage (*J–V*) characteristics of PbPc thin films sandwiched between indium tin oxide (ITO) and Al electrodes (Al/PbPc/ITO), with the aim to understand the charge generation mechanism and photovoltaic response in this device. The variation of concentration of injected charge carriers and their mobility with temperature, bias voltage carrier trap density arising due to the defects and impurities are very important information required for improving the device performance. The measurements of *J–V* characteristics at various temperatures and electric fields have been used as powerful tools for the above mentioned studies. We have shown that the measured current in ITO/PbPc/Al device is limited by hole injection at Al–PbPc contact when the device is reverse biased. The current becomes space charge limited at high voltages when tunnelling contributes significantly to charge injection.

2. Experimental

Thin films of PbPc were deposited on cleaned ITO coated glass substrates by spin coating technique employing ethanol containing DMSO as a solvent for PbPc. The thickness of the PbPc layer was controlled by the concentration of PbPc in solvent and rotation speed (about 2500 r.p.m.). The top electrode contact was made by evaporation of aluminum through an appropriate mask at a vacuum of 10^{-5} Torr. The resulting area of the device was about 1 cm^2. The optical absorption spectrum was recorded on 100 nm thin film of PbPc layer on a glass slide employing a Perkin Elmer double beam spectrophotometer. The cyclic voltammetry experiment was performed with

AutoLab potentiostat at room temperature in a conventional three electrode cell with ITO as the working electrode. For the current–voltage measurements, a Keithley electrometer with built in power supply was used. The capacitance spectroscopy and capacitance–voltage (*C–V*) measurements were recorded using an HP 4294 A impedance analyzer in parallel RC equivalent circuit mode, in the frequency range between 5 Hz and 10 MHz. The temperature of device was measured with a digital temperature controller and monitored by an indicator. The incident light was provided with a 100 W halogen lamp and the intensity of the light was measured by a lux meter. The photoaction spectra of the device were measured employing a monochromator with a halogen lamp as a source. The electrodes were illuminated through both sides of the electrodes and the resulting photocurrent was monitored with a Keithley electrometer.

3. Results and discussion

3.1. Current–voltage characteristics in dark

Current–voltage characteristics of the ITO/PbPc/Al device recorded at various temperatures ranging from 250 K to 350 K is shown in Fig. 1 in semi-log scale. The forward bias was obtained with positive and negative bias to ITO and Al electrodes, respectively. The asymmetrical nature of curves is attributed to the difference in work function of the electrodes, implying different barriers at each electrode/PbPc interface. As PbPc is a p type organic semiconductor, we assume that Al and ITO form Schottky barrier and nearly ohmic contact with PbPc, respectively, giving rise to asymmetrical nature of *J–V* characteristics, i.e. to the rectification effect.

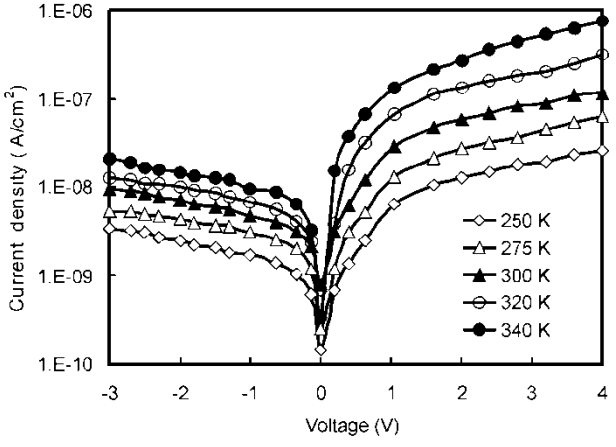

Fig. 1. Current–voltage characteristics of Al/PbPc/ITO device in dark at various temperatures when positive bias is applied to ITO

Figure 2a shows typical *J–V* characteristics of an ITO/PbPc/Al device in log–log scale at various temperatures when Al is negatively biased with respect to ITO. This situation corresponds to hole injection in the HOMO of PbPc through ITO and electron injection through Al into LUMO of PbPc. In each case, two distinct regions were observed in *J–V* characteristics of the device at temperatures below 300 K. At low voltages, the slopes of log$J$ vs. log$V$ plots are approximately equal to unity, while at higher voltages above a well defined transit voltage, the slopes are approximately between 2.0 and 2.5. These plots are typical of ohmic conduction at low voltages. It is well known that metal phthalocyanines (MPcs) are p type organic semiconductors, the conduction is via holes only, and the current may be simply expressed in the form [13]

$$J = p_0 q \mu \left(\frac{V}{d} \right)$$

where p_0 is the concentration of thermally generated holes, q is the electronic charge, μ is the hole mobility, V is the applied voltage and d is the thickness of the PbPc layer. At high voltage range, the power law dependence of $J(V)$ is indicative of space charge limited conductivity (SCLC) controlled by single dominant trapping.

The *J–V* characteristics of metal–organic semiconductor devices are controlled by two basic processes: injection of the charge carriers from electrodes into organic semiconductor and vice versa and transport of the charge carriers in the bulk of film. Steady state current is determined by the applied electric field, height of the injection barrier, i.e. difference between electrode work function and corresponding transport levels of the organic semiconductor and temperature. The current is either injection limited or bulk transport limited. For the injection of charge carriers into the organic semiconductor, the charge carriers must overcome a potential barrier at the electrode –organic semiconductor interface. In the case of small barrier or at high temperatures, a large number of charge carriers will have energies large enough to cross the interface barrier, hence thermionic emission takes place. But when temperature decreases or when the barrier height is large, a reduced number of charge carriers have energies larger than the potential barrier and therefore thermionic emission becomes insignificant. In this case injection occurs via quantum mechanical tunneling through the potential barrier.

The Al contact with organic semiconductor form a relatively high barrier at low temperatures and therefore thermally generated carriers are few and the injected charge density is small so that the overall behaviour becomes ohmic. As the voltage is increased, the number of injected carriers increases so that space charge accumulates limiting the current. The number of thermally generated carriers increases with temperature, therefore the current increases with temperature. The superlinear behaviour seen in the Fig. 2 suggests that the injected charge carrier overcomes the transport capabilities of PbPc, hence giving rise to the accumulation of positive charge near the Al hole injecting electrode and the bulk properties of the organic layer control the *J–V* characteristics.

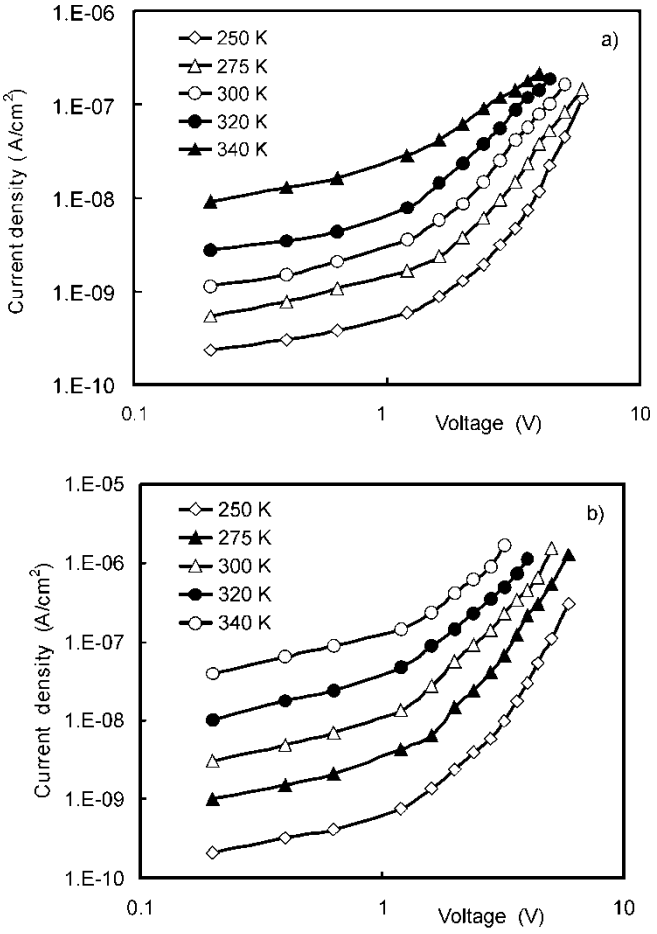

Fig. 2. Current–voltage characteristics in log–log scale for Al/PbPc/ITO device when Al (a) or ITO (b) are positively biased

The current–voltage characteristics shown in Fig. 2b have been measured with ITO as positively biased with respect to Al. This corresponds to the electron injection into the LUMO and hole injection into the HOMO of PbPc through Al and ITO, respectively. In this case the slope of *J–V* characteristics below 1.5 V is approximately two, which is an indication of SCLC behaviour. The injection of holes from ITO into HOMO of PbPc is more due to the low barrier for holes (as the ITO form nearly ohmic contact with PbPc) and injected carrier density becomes so large that the field due to the carriers themselves dominates over the applied field and becomes space charge limited. SCLC occurs when the transit time of any excess injected carrier is shorter than the bulk relaxation time. Under these conditions, the space charge limited current (TFSCLC) flows, as described by [14]:

$$J_{\mathrm{SCLC}} = \frac{9\varepsilon\mu V^2}{8d^3} \tag{2}$$

where μ is the effective mobility of charge carrier, ε – electric permittivity of PbPc, V is applied voltage and d is the thickness of the PbPc layer. This behaviour is characterized by a quadratic dependence of the current on voltage, i.e. the slope of J–V curve in the log–log scale is two. At higher temperatures, the slope of J–V curves is between 1 and 2. This indicates that the thermally generated carrier density exceeds that of the injected charges. The change in slope with applied voltages as seen in Fig. 2a, b are different due to the different hole injection barriers.

In the case when Al is positively biased, the slope of log$J$ vs. log$V$ curve is about unity, the region is considered as ohmic. Above the ohmic region, the J–V characteristics may be fitted to the Richardson–Schottky (RS) emission model. At higher fields, the metal work function for thermionic emission is reduced, thus lowering the Schottky barrier (image force lowering). The Schottky equation, taking into account image force lowering may be written as [15,16]

$$J = A^* T^2 \exp\left(-\frac{\varphi_b}{kT}\right)\exp\left[\frac{\left(\frac{q^3 V}{4\pi\varepsilon d}\right)^{1/2}}{kT}\right] \tag{3}$$

where V is applied voltage, positive for forward bias and negative for reverse bias. The equation can be rewritten as

$$\ln\frac{J}{T^2} = \ln A^* + \frac{-\varphi_b + \left(\frac{q^3 V}{4\pi\varepsilon d}\right)^{1/2}}{kT} \tag{4}$$

According to above equation, the plots of ln(J/T^2) vs. 1000/T are straight lines at a given bias voltage V. The effective barrier between the electrode and organic film may be calculated from the slope of the straight line as

$$\varphi_b = kS + \left(\frac{q^3 V}{4\pi\varepsilon d}\right)^{1/2} \tag{5}$$

where S is slope of the straight line. As seen from the Fig. 3, the plots of ln(J/T^2) vs. 1000/T at various voltages tend to be straight lines at higher temperatures. This is particularly clear in the case when ITO is positively biased, the straight line observed beyond room temperature (300 K) (Fig. 3a). When Al is positively biased (Fig. 3b), the linearity occurs at above 320 K. However, the domination of the thermionic emission observed at higher temperatures indicates that a higher hole injection barrier exists at Al/PbPc interface, since more thermal energy is required to overcome the potential barrier. Employing Eq. (5) and straight line fitting in Fig. 3 yield a hole injection

barrier equal to 0.11 eV and 0.88 eV for ITO/PbPc and Al/PbPc interfaces, respectively.

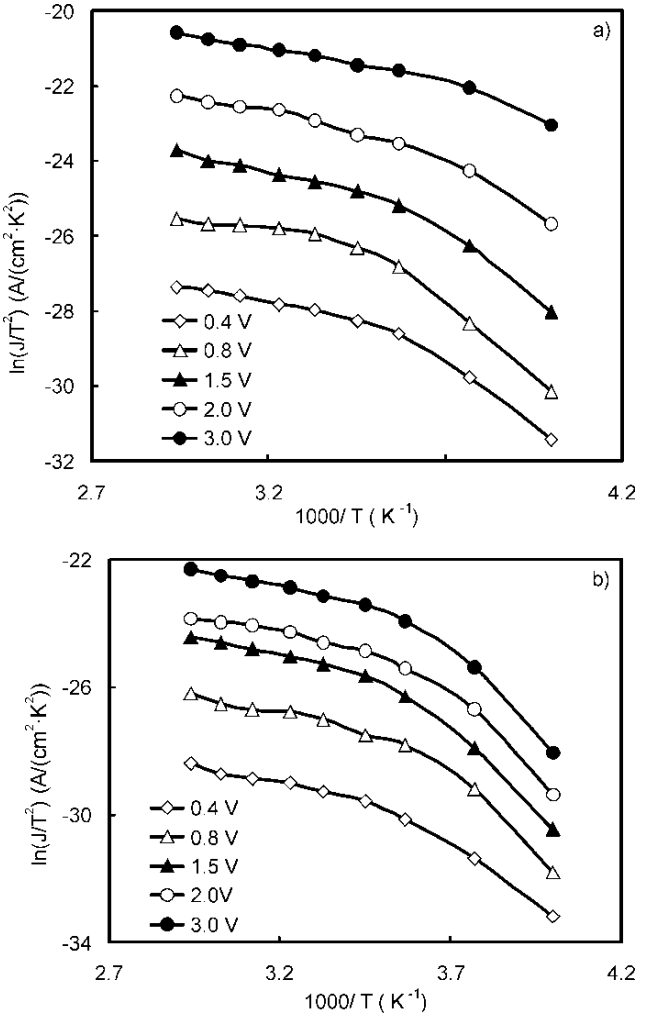

Fig. 3. $\ln(J/T^2)$ vs. $1000/T$ for Al/PbPc/ITO device when ITO (a) or Al (b) are biased positively

The electric field at which the transition from ohmic to SCLC takes place increases with temperature. In forward bias, the ITO/PbPc interface supplies a high amount of charges in PbPc bulk and the current is space charge limited in the whole voltage and temperature range, suggesting the formation of ohmic contact for hole injection at the ITO/PbPc interface.

The forward current density as a function of applied voltage at various temperatures shows non ideal junction characteristics (Fig. 1) and can be given by

$$J = J_{s1}[\exp(qV/nkT - 1] + J_{s2}[\exp(qV/2nkT) - 1] + \frac{J - JR_s}{R_{sh}} \tag{6}$$

where J_s is the reverse saturation current density, q is the electronic charge, V is the applied voltage, k is the Boltzmann constant, T is the temperature and n is the ideality factor of the diode. The subscripts 1 and 2 indicate that two possible contributions to the current could be present.

In a low forward voltage region ($0 < V < 0.6$ V) (as shown in Fig. 2b), the current density was suggested to be limited by the thermionic emission of holes from ITO over the ITO–PbPc barrier. According to the theory of thermionic emission mechanism, the forward bias current can be given by [17, 18]:

$$J = J_s[\exp(qN/nkT - 1] \tag{7}$$

The saturation current density J_s is given by

$$J_s = AT^2 \exp(-q\varphi_b/kT) \tag{8}$$

where A^* is the Richardson constant and ϕ_b is the barrier height. The values of n and J_s at room temperature were estimated to be 2.6 and 4.5×10^{-11} A/cm^2, respectively. The barrier height between ITO and PbPc layer being about 0.12 eV has been estimated in from Eq. (8), using Fig. 2b. This value is in good agreement with the value calculated from Eq. (5).

On the other hand, the current density as a function of applied voltage in the range 0.6 V$< V <$ 1.6 V, shows a power law dependence of the form $J \propto V^m$, where $m = 2$, indicating that the current density in the PbPc layer is an indication of SCLC. The current density in this region is given by Eq. (2). Note that the slope equal to two does not necessarily implies the absence of traps in the materials. Since the mobility of the charge carrier in organic semiconductor is so low that the extra injected charges cannot be swept to the collecting electrode at same time at which they are being injected.

As the voltage increases above 1.6 V, the current density in the PbPc layer is a space charge limited current (SCLC) dominated by a single trapping level. The current density in this region is given by [19, 20]:

$$J = \frac{9\varepsilon\mu_0\theta V^2}{8d^3} \tag{9}$$

where ε is the permittivity of PbPc, μ_0 is the mobility of a charge carrier taken as 7.8×10^{-4} cm^2/(V·s) at room temperature (calculated from the analysis of J–V characteristics at various temperatures), d is the thickness of the PbPc layer and θ is the trapping factor given by:

$$\theta = \frac{N_V}{N_t}\exp(-E_t/kT) \tag{10}$$

where N_V and N_t are the effective densities of states in the valence band and total trap concentration situated at energy level E_t above the valence band edge.

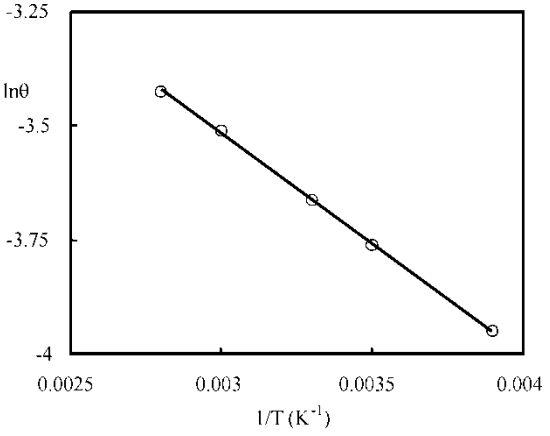

Fig. 4. Dependence of $\ln\theta$ on $1/T$ for Al/PbPc/ITO device

The values of θ corresponding to various temperatures can be estimated from the intercept of the straight line of $\log J$ vs. $\log V$ on current axis in the space charge region ($V > 1.6$ V). According to Eq. (10), the plot of $\ln\theta$ vs. $1//T$ is shown in Fig. 4. Assuming $N_v = 10^{27}$ m^{-3} [18], the analysis of Fig. 4 yields $N_t = 1.26\times10^{21}$ m^{-3} situated at 0.35 eV above the valance band edge. Similar values of the total trap concentration and trap energy levels for different metal phthalocyanines have been reported earlier [18–20].

3.2. Mobility calculations from *J–V* characteristics

It is observed that the *J–V* characteristics of the device, when positive voltage is applied to the ITO electrode, in the voltage range 0.6 V< V < 1.6 V, the current density in the entire temperature range varies in accordance with the relation for SCLC for trap filled organic materials described by Eq. (2). We have fitted our experimental results taking into account temperatures where *J–V* curves exhibited slope = 2 to Eq. (2), considering permittivity $\varepsilon = 3.4\times10^{-11}$ F/m and calculated the mobility under space charge limitation of current.

For low field region, the mobility is calculated at various temperatures using Eq. (2). The variation of the low field mobility with the temperature is shown in Fig. 5. It is found that the mobility is thermally activated in accordance with the relation

$$\mu = \mu_0 \exp[-\nabla/kT] \tag{11}$$

where μ_0 is the pre-exponential factor, ∇ is the thermal activation energy. The values of ∇ and μ_0 are found to be 0.31 eV and 5.78×10^{-4} cm^2/Vs, respectively. The plot of $\log\mu$ vs. 1000/T yields a straight line (Fig. 5), which indicates that the PbPc material is

inhomogeneous, i.e. the ordered regions are separated by amorphous regions. The activated behaviour of mobility is indication of inhomogeneity of the PbPc layer. A low value of the mobility activation energy represents the variation in the average energy of the adjacent hopping sites for polarons [21]. The charge transport occurs by hopping between adjacent sites through the disordered regions, which creates a potential barrier for the mobility of the carriers [22]. The mobility is therefore thermally activated and the value of thermal activation energy in PbPc film is lower than the in crystalline regions due to small sizes of amorphous regions.

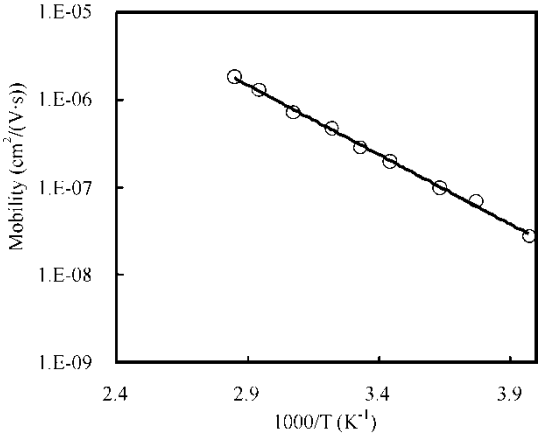

Fig. 5. Dependence of low field mobility on 1000/*T*

For bias voltages higher than 1.6 V, the current density does not follow Eq. (2). As the voltage increases, the barrier for the flow of holes from organic material into Al decreases and at sufficient high voltages, flat band condition is approached, i.e. the barrier at Al contact tends to zero. The current is now dominated by bulk of organic layer. The current in the bulk of the device is determined by the space charge created by injected carriers. Thus, as the voltage increases, the contact limited mechanism of current flow changes to the bulk limited mechanism.

At any temperature, the high bias field mobility can be fitted by [23]:

$$\mu(E) = \mu_0 \exp\left(\gamma\sqrt{E}\right) \tag{12}$$

where μ_0 is the low field mobility and the coefficient γ corresponds to the Poole Frenkel effect for disordered materials. This depends on the interaction between the charge carriers and randomly distributed dipoles in organic semiconductors [24]. The variation of $\mu(E)$ with E ($\log\mu$ vs. $E^{1/2}$) at room temperature is shown in Fig. 6. Similar variation of $\mu(E)$ is observed for other temperatures. The value of the slope of field dependence of mobility γ calculated from the slope of Fig. 6 is about 3.5×10^{-3} cm/V$^{1/2}$

and is found to decrease with the increase in temperature whereas the zero field mobility (the mobility extrapolated to zero field) is increasing with increasing temperature.

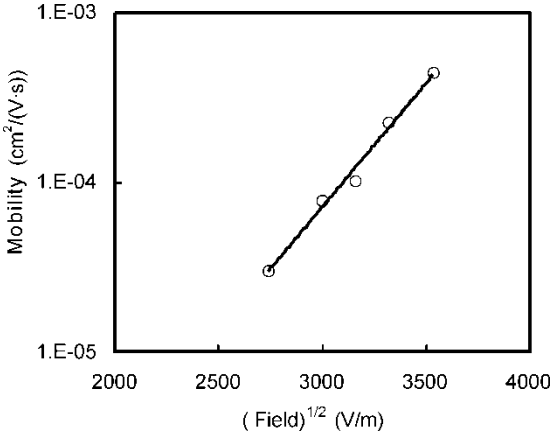

Fig. 6. Dependence of high field mobility on the square of electric field at room temperature

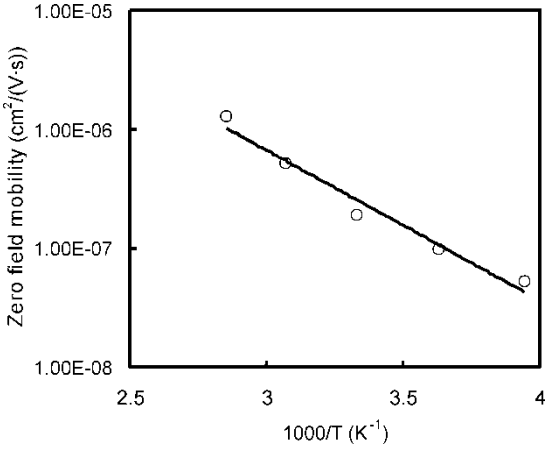

Fig. 7. Dependence of zero field mobility on 1000/T

Comparing Eqs. (11) and (12), the mobility variation with the field and temperature is given by

$$\mu(E,T) = [\mu_0 \exp(-\nabla/kT)]\exp(\beta\sqrt{E}/kT) \tag{13}$$

The expression in the bracket is field independent and μ_0 is the zero field mobility at any temperature T. The electric field helps the hopping carriers to overcome the potential barrier resulting in an increase of mobility with the increase in electric field E. The extrapolation of field dependences of the hole mobilities to zero field (Fig. 6) yields zero field mobilities at various temperatures and it is observed that it also shows

Arrhenius type temperature dependences (Fig. 7). From the slope and intercept of straight line ∇ and μ_0 are estimated to be 0.30 eV and 4.0×10^{-3}cm^2/(V·s), respectively. It is interesting to note that the value of ∇ is the same as calculated earlier. This relies upon the assumption that the charge transport is controlled by traps which are charged when empty, giving the Poole–Frenkel type mobility field dependences. It has been observed that the temperature dependence of the hole mobility in the PbPc shows an Arrhenius type behaviour and the energy of activation calculated has been found to show a negative field dependence.

3.3. Capacitance–voltage characteristics

In Figure 8, the capacitance spectrum at zero bias of the ITO/PbPc/Al device is shown at temperatures ranging between 250 K and 350 K and frequencies between 5 Hz and 1 MHz. One can notice the presence of steps due to the release of trapped charges from the trapping states. There is a shift of these steps to higher frequencies with increasing temperature, which indicates that the detrapping time constant of charge carriers is temperature dependent. Characteristic features of these states can be derived from the $C(f)$ spectra at certain critical frequencies ω_0, where an instantaneous decrease of the capacitance is observed.

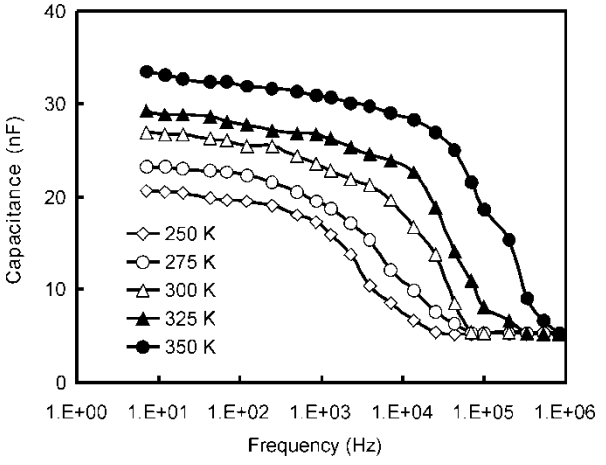

Fig. 8. Dependence of capacitance on frequency at various temperatures for Al/PbPc/ITO device

If a trapping state with the emission rate $\tau = 1/\omega_0$ is considered, the dependence of the capacitance on the frequency ω is given by [25]

$$C \propto \frac{\omega_0^2}{\omega + \omega_0^2} \tag{14}$$

The equation is a stepwise function, whereas the critical frequency ω_0 is the temperature-dependent parameter and can be described by the following expression

$$\omega_0 = \tau^{-1} = N_v \nu_{th} \sigma_h \exp(-E_a/kT) \tag{15}$$

where E_a is the activation energy, N_v is the effective density of states in valence band, ν_{th} is the thermal velocity of the charge carriers and σ_h is the capture cross section for holes. Assuming that $\nu_{\text{th}} \propto T^{1/2}$ and $N_v \propto T^{3/2}$, one may express Eq. (15) as

$$\omega_0 = \tau^{-1} = \xi_0 T^2 \sigma_h \exp(-E_a/kT) \tag{16}$$

where ξ_0 is the pre-exponential factor.

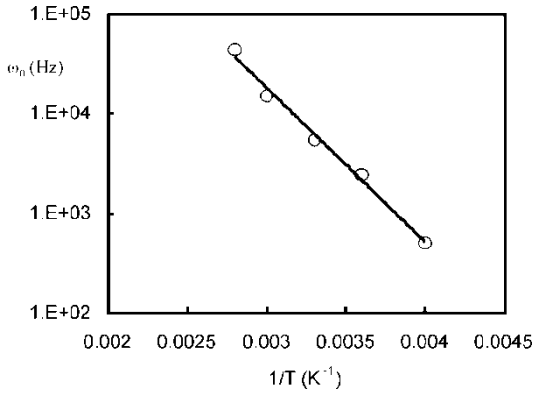

Fig. 9. Arrhenius plot of ω_0 for Al/PbPc/ITO device

Based on the model of Walter et. al. [26], from the minimum value of the capacitance derivative with respect to frequency at various temperatures, we have plotted ω_0 as a function of the reciprocal temperature T^{-1} (Fig. 9). We have calculated the activation energy form the slope of the Arrhenius plot and the temperature dependent pre-exponential factor $\nu_p = \xi_0 T^2 \sigma_h$ have been estimated from intercept on T^{-1} axis. The values of activation energy E_a and ν_p for PbPc are 0.32 eV and 8.0×10^8 s^{-1}, respectively, being in good agreement with the values reported for other metal phthalocyanines. The value of activation energy suggests that the defects originate from the trapping centres at the metal–PbPc interface. For the occurrence of these trapping centres, one would expect a weak bias sensitivity due to the hopping nature of the charge transport. At high electric field, the Coulomb barriers which separate adjacent hopping centres should be lowered or increased when the DC voltage is applied (Poole–Frenkel mechanism).

In the higher voltage region, we have also observed a change in the dominant conduction mechanism as shown in *J–V* characteristics in dark. The variation of log*J* with $V^{1/2}$ shows a linear relationship and is attributed to either the Poole–Frenkel (PF) or the Schottky effect [27]. Both mechanisms present a voltage variation described by:

$$J = J_0 \exp(AV^{1/2}) \tag{17}$$

where $A = \beta/kTd^{1/2}$, d is the film thickness and β is the field lowering coefficient which is twice higher in the PF effect as compared to the Schottky effect. β_{PF} is defined as

$$\beta_{PF} = \left(\frac{q^3}{\pi\varepsilon}\right)^{1/2} \tag{18}$$

where q is the electronic charge, and ε is the permittivity of the organic layer. From the J–$V^{1/2}$ plot we obtained the parameter A defined in Eq. (17) and consequently, the value of β. This value is approximately equal to β_{PF} calculated from Eq. (18) and is consistent with the values reported for other metal phthalocyanines for the Poole –Frenkel conduction is the Schottky junction [28, 29].

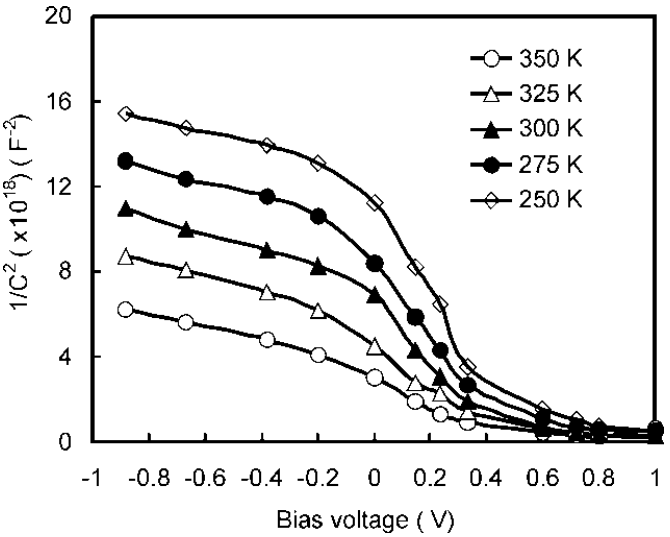

Fig. 10. Dependence of $1/C^2$ on bias voltage for Al/PbPc/ITO device at various temperatures

Figure 10 shows the $1/C^2$–V characteristics of the ITO/PbPc/Al device measured in dark at various temperatures at low frequency (40 Hz). The capacitance of the device can be expressed by two series: the junction capacitance C_j and the geometrical capacitance C_b referring to the bulk region of the PbPc; it can be expressed by

$$\frac{1}{C} = \frac{1}{C_j} + \frac{1}{C_b} \tag{19}$$

The dependence between C_j and the reverse bias for an abrupt junction can be described by [20, 30]:

$$\frac{1}{C_j} = \frac{2\left(V_{bi} - V_j - \dfrac{kT}{q}\right)}{q\varepsilon N_a A^2} \tag{20}$$

where V_{bi} is the built-in potential, N_a is the free carrier concentration, A is the effective surface area of the device and ε is the dielectric constant.

The carrier concentration can be experimentally estimated from [31]:

$$\frac{d\left(\dfrac{1}{C_j}\right)}{dV} = -\frac{2}{q\varepsilon N_a A^2} \tag{21}$$

where $d(1/C_j)/dV$ is the slope of the straight line and the intercept with the horizontal asymptote gives the built-in potential V_{bi} [32].

The asymptote represents the geometrical capacitance of the bulk region. The carrier concentration and built-in potential have been estimated (Table 1). The width of the depletion region W is related to the junction capacitance at $V = 0$:

$$W = \left(\frac{2\varepsilon V_{bi}}{qN_a}\right)^{1/2} \tag{22}$$

where ε is the permittivity of PbPc.

Table 1. Electrical parameters of Al/PbPc/ITO derived from capacitance–voltage characteristics at various temperatures

Parmeter	Temperature, T				
	250 K	275 K	300 K	325 K	350 K
V_{bi} (V)	0.65	0.63	0.61	0.59	0.58
ϕ_b (eV)	0.92	0.87	0.85	0.78	0.71
W (nm)	68	62	56	45	41
N_a (m^{-3})	2.3×10^{21}	6.7×10^{21}	2.3×10^{22}	5.6×10^{22}	8.9×10^{22}

The potential barrier ϕ_b between Al and PbPc has been calculated from the following expression:

$$\phi_b = V_{bi} + kT \ln\left(\frac{N_v}{N_a}\right) \tag{23}$$

where N_v is the density of states in valence band. The values of N_a, W and ϕ_b are presented in Table 1. The potential barrier at Al–PbPc in the device estimated from the C–V characteristics is almost equal to that calculated from the J–V characteristics.

3.4. Optical and photovoltaic properties

The energy gap was measured from the optical absorption curves, fitting data taken in the visible energy range. The energy gap $E_{g(\mathrm{opt})}$ is related to the absorbance α by Eq. (24), where $h\nu$ is the photon energy and A is a proportionality constant

$$\alpha h\nu = A\left(h\nu - E_{\mathrm{g(opt)}}\right)^{1/2} \tag{24}$$

The value of $E_{g(\mathrm{opt})}$ was determined by the extrapolation of the linear region to zero absorption [33], which is about 1.8 eV.

The energy levels for HOMO and LUMO of the PbPc were obtained by cyclic voltammetry with the method described by Bredas et al. [34]. The value of HOMO and LUMO levels for PbPc are 5.2 eV and 3.5 eV, respectively. These values lead us to electrochemical energy band gap for PbPc being about 1.7 eV, which is in a good agreement with those reported for other metal phthalocyanines [29, 35] from photo-emission spectroscopy and cyclic voltammetry measurements.

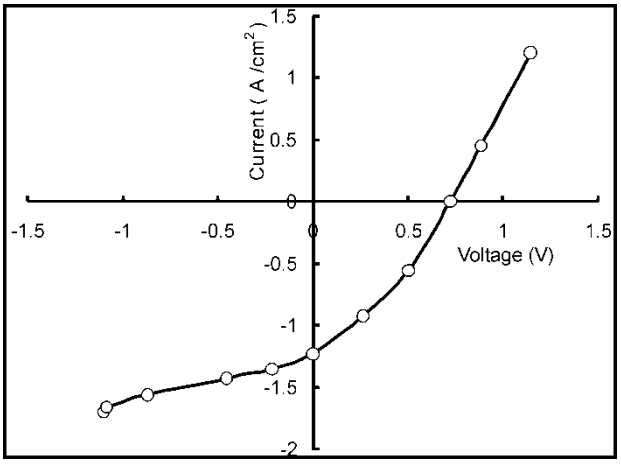

Fig. 11. *J–V* characteristics under illumination for Al/PbPc/ITO device at room temperature

The current–voltage characteristics of the Al/PbPc/ITO device under illumination of 5 mW/cm^2 is shown in Fig. 11. The values of photovoltaic parameters, i.e. short circuit current J_{sc}, open circuit voltage V_{oc}, fill factor FF and power conversion efficiency η) have been calculated from the following expression [36]:

$$FF = \frac{V_m J_m}{V_{oc} J_{sc}} \tag{25}$$

and

$$\eta = \frac{J_{sc} V_{oc} FF}{P_{in}} \tag{26}$$

J_m and V_m are the current and voltage maximum values, respectively and P_{in} is the intensity of incident light. The variation of V_{oc} with incident intensity P_{in} (corrected for absorption by ITO) are shown in Fig. 12. We have found the following results: The short circuit photocurrent J_{sc} increases as $(P_{in})^{0.6}$ between 0.01 and 5 mW/cm^2 and tends to saturate beyond this value. The fill factor decreases slightly up to 0.1 mW/cm^2 and then saturates.

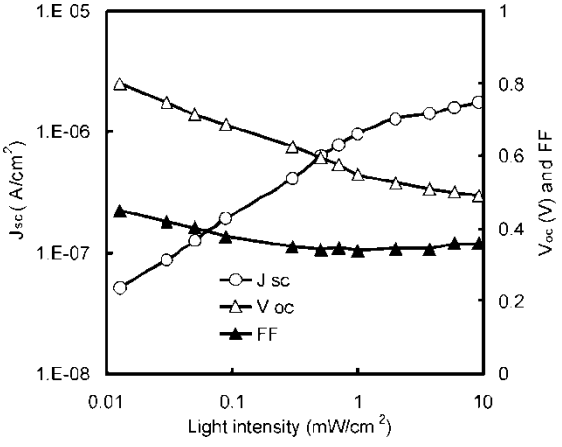

Fig. 12. Dependences of J_{sc}, V_{oc} and FF on the light intensity at room temperature

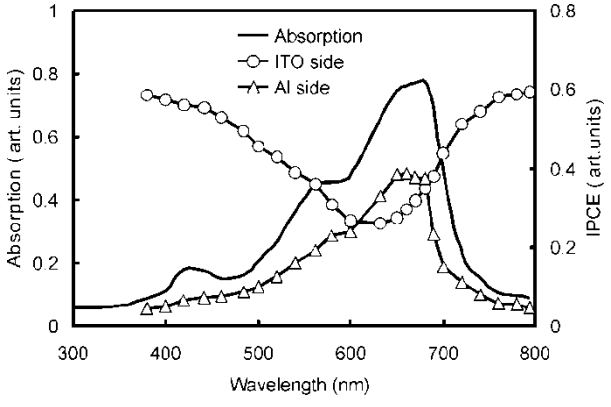

Fig. 13. Photoaction spectra for illumination of Al/PbPc/ITO device through ITO and Al electrodes along with absorption spectra of PbPc thin films

The consequence is a decrease in power conversion efficiency with P_{in}. The variation of short circuit photocurrent with light intensities below 1 mW/cm^2 indicates that photocur-

rent is limited by electron–hole bimolecular recombination leading to a decrease in over all power conversion efficiency. The values of short circuit photocurrent J_{sc}, open circuit voltage V_{oc}, fill factor FF and power conversion efficiency η are 1.23 μA/cm^2, 0.72 V, 0.43 and 0.077 %, respectively at the light intensity of 5 mW/cm^2.

Figure 13 shows the photoaction spectra of short circuit current for ITO/PbPc/Al Schottky barrier device illuminated through Al and ITO electrodes along with the spectrum of the PbPc layer. The absorption spectra of PbPc layer and photoaction spectra match fairly well when the device is illuminated through Al electrode. However, when the device is illuminated through ITO electrode, the photoaction spectra exhibit a minimum at the maximum of the absorption of PbPc layer. This behaviour is consistent with the Schottky junction located at the Al–PbPc interface which is responsible for the rectification behaviour observed in current–voltage characteristics in dark.

4. Conclusions

We have studied electrical and optical properties of the device based on PbPc sandwiched between Al and ITO. Based on the optical absorption spectra and cyclic voltammetry techniques, we have estimated optical and electrochemical band gaps of PbPc, being 1.8 eV and 1.7 eV, respectively. The current in this device is limited by hole injection at the Al/PbPc interface when the device is reverse biased and becomes space charge limited at high voltages, wherein tunneling contributes significantly to the charge injection. In the forward bias, the ITO/PbPc interface supplies high amount of charges in the PbPc bulk, and the current is space charge limited in the whole voltage range beyond 0.6 V, indicating the formation of an ohmic contact for hole injection at ITO/PbPc interface. From the detailed analysis of J–V characteristics, we have evaluated the potential barrier at Al/PbPc and ITO/PbPc, i.e. about 0.88 eV and 0.12 eV, respectively, which is in good agreement with the values calculated from the capacitance –voltage characteristics. The hole current is found to be space charge limited providing a direct measurement of mobility as a function of temperature and electric field. The hole mobility exhibits field dependence in accordance with the Poole–Frenkel effect.

Electroactive defects were also investigated by the space charge capacitance spectroscopy methods as a function of temperature and frequency in the range 250–350 K and 5 Hz–1 MHz, respectively. From the Arrhenius plots of critical frequency, we have concluded that the defects are thermally activated with the activation energy about 0.32 eV. The values of potential barrier and thickness of the depletion layer have also been estimated from the capacitance–voltage characteristics and found to be about 0.86 eV and 72 nm, respectively, and decreases with increasing temperature. The photoaction spectra of the device and optical absorption spectra of PbPc also lead to a conclusion regarding the formation of ohmic and Schottky barriers at ITO and Al contacts, respectively. The photovoltaic parameters of the device are: J_{sc} = 1.23 μA/cm^2, V_{oc} = 0.7 V, FF = 0.43 and η = 0.077 %.

Acknowledgement

We are grateful to the Department of Science and Technology, Govt of India, New Delhi for financial support through the project.

References

[1] WÖHRLE D., MEISSNER D., Adv. Mater., 3 (1991), 129.
[2] WHITLOCK J.B., PANAYOTATOS P., SHARMA G.D., COX M.D., SAUERS R.R., BIRD G.R., Opt. Eng., 32 (1993), 1921.
[3] ROSTALSKI J., MEISSNER M., Sol. Energ. Mater. Sol. Cells, 61 (2000), 78.
[4] SCHON J.H., KLOC CH., BUCHER E., BATTLOG B., Nature, 403 (2000), 408.
[5] WROBEL D., BOGUTA A., ION R.M., Int. J. Photoen., 2 (2000), 87.
[6] TANG C.W., Appl. Phys. Lett .,48 (1986), 183.
[7] PEUMANS P., YAKIMOV A., FORREST S.R., J. Appl. Phys., 93 (2003), 3693.
[8] *Organic photovoltaics*. *Concepts and Realisation*, Vol. 60, C.J. Brabec, V. Dyakonov, J. Parisi, N.S. Sariciftci (Eds.), Springer, Berlin, 2003.
[9] GREGG B.A., J. Phys. Chem B, 107 (2003), 4688.
[10] PEUMANS P., FORREST S.R., Appl. Phys. Lett., 79 (2001), 1261667.
[11] YAKIMOV A., FORREST S.R., Appl. Phys. Lett., 80 (2002), 1667.
[12] PEUMANS P., BULOVIC V., FORREST S.R., Appl. Phys. Lett., 76 (2000), 2650.
[13] LAMPERT M.A., MARK P., *Current Injection in Solids*, Academic Press, New York, 1970.
[14] ABKOWITZ M., FACCI J.S., REHM J., J. Appl. Phys., 83 (1998), 2670.
[15] BRAUN D., J. Polym. Sci. B, 41 (2003), 2622.
[16] KAO K.C., HWANG W., *Electrical Transport in Solids*, Pergamon Press, Oxford, 1981.
[17] ANTOHE S., TOMOZEIU N., GOGONEA S., Phys. Stat. Sol. (a), 125 (1991), 397.
[18] ANTHOPOULOS T.D., SHAFAI T.S., Phys. Stat. Sol. (a), 186 (2001), 89.
[19] SHARMA G.D., SANGODKAR S.G., ROY M.S., Mater. Sci. Eng. B, 41 (1996), 222.
[20] RIAD A.S., Physica B, 270 (1999), 148.
[21] RAKHMANOVA S.V., CONWELL E.M., Synth. Met., 116 (2001), 389.
[22] VISSENBERG M.C.J.M., BLOM P.W.M., Synth. Met., 102 (1999), 1053.
[23] CRONE B.K., DAVIDS P.S., CAMPBELL J.H., SMITH D.L., J. Appl. Phys.,84 (1998), 8333.
[24] DUNLAP D.H., PARRIS P.E., KENKRE V.M., Phys. Rev. Lett., 77 (1996), 542.
[25] HERBERHOLZ R., IGALSON M., SCHOCK H.W., J. Appl. Phys., 83 (1998), 318.
[26] WALTER T., HERBERHOLZ R., MULLER C., SCHOCK H.W., J. Appl. Phys., 80 (1996), 441.
[27] GOULD R.D., Coord. Chem. Rev., 156 (1996), 237.
[28] RASSAN A.K., GOULD R.D., Int. J. Electron., 69 (1990), 11.
[29] REIS F.T., MENCARAGLIA D., SAAD S.O., SEGUY I., OUKACHMIH M., JOLINAT P., DESTRUEL P., Synth. Met., 138 (2003), 33.
[30] ANTHOPOULOS T.D., SHAFAI T.S., Thin Solid Films, 441 (2003), 207.
[31] RIAD A.S., Thin Solid Films, 370 (2000), 253.
[32] ANTHOPOULOS T.D., SHAFAI T.S., J. Phys. Chem. Solids, 65 (2004), 1345.
[33] FUJITA S., NAKUZAWA T., ASANO M., FUJITA S., Jpn. J. Appl. Phys., 34 (2000), 5301.
[34] BRADES J.L., SILBEY R., BROUDREUX D.S., CHANCE R.R., J. Am. Chem. Soc., 105 (1983), 6555.
[35] ZHU L., TANG H., HARIMA Y., KUNUGI Y., YAMASHITA K., OHSHITA J., KUNAI A., Thin Solid Films, 396 (2001), 213.
[36] ASHOK S., PANDF K.P., Solar Cells, 14 (1985), 8.

Received 10 June 2007
Revised 25 July 2007

Materials Science-Poland, Vol. 25, No. 4, 2007

Computer simulation and optimization of properties of porous low-*k* dielectrics*

A. ELSNER**, H. HERMANN

Institute for Solid State and Materials Research, IFW Dresden,
P.O. Box 270116, D-01171 Dresden, Germany

Due to progressive miniaturization one of the current challenges in microelectronics is to find materials with very low electric permittivity. The model of dense random packed spheres is applied to generate model systems of porous dielectric materials. Pores are represented by dense packed spheres. By optimizing the parameters, the porosity and therefore the theoretical electric permittivity was reduced significantly. Another task is optimization of mechanical properties. Mechanical stability is an important criterion for the processability in industrial fabrication of microlectronics components. The mechanical stability is mostly negatively correlated to porosity. Simulated open pore and closed pore systems with high porosity were analyzed in terms of mechanical properties. Other methods like an adapted random walk algorithm were used to characterize further important properties like particle permeability. In porous materials, the so-called "random voiding" may appear. This happens when pores are larger than the layer thickness. Simulation of porous structures can show limitations in pore size and spatial distribution where the requirements of industrial processability are no longer satisfied. Advantageous parameters for porosity in dielectric materials are advised.

Key words: *porous structure; low-k dielectrics; computer simulation; dense random sphere packings*

1. Introduction

Introducing porosity in dielectric materials is one of the most promising methods to decrease the static electric permittivity [1, 2]. Production of porous dielectric materials is a non-trivial task, because mechanical and processing properties often heavily change with degree of porosity. Computer simulation of porous materials may help to optimize porous structures relative to their mechanical and dielectric properties.

One of the most dreaded defects is the so-called voiding. There, pores appearing in the material are so large that they form a hole where gas or fluids can diffuse

---

*Presented at the 2nd Workshop "Hybrid Nanostructured Materials. Synthesis, Properties, Applications", Dresden, Germany, 8–9 November, 2006.

**Corresponding author, e-mail: A.Elsner@ifw-dresden.de

through [3]. To avoid this, the pore size distribution has to keep limiting conditions. Likewise, the penetrability by small particles plays a role. It is not desired that particles infiltrate the material because the dielectric properties may change or even short-circuits may appear.

Another simulation shall demonstrate the behaviour of porous dielectrics when investigated by positron annihilation lifetime spectroscopy (PALS) [4]. A non-lattice random walk method is applied to porous models as a first approach to simulate the way of positronium particles in the structure. Statistical analyzis of free ways and lifetimes of particles are compared with experimental results.

2. Generation of model systems

In a previous work [5], we studied random dense sphere packings generated by the force biased algorithm wherein the spheres constitute the pores and the space around these spheres is the base dielectric material, for example silicon dioxide. From experimental studies on porous silica gel, a power-law pore size distribution was estimated. The power-law size distribution with adjustable parameters was then used to analyze corresponding closed-pore systems (Eq. (1)). The computer simulation models were optimized with respect to the highest porosity. A local maximum of porosity could be obtained at an exponent of $a = -3.3$, $r_1 = 1.0$ and $r_2 = 5.0$.

$$f(r) = c\left(\frac{r}{r_0}\right)^a, \qquad r_1 \le r \le r_2 \tag{1}$$

Our model systems contain usually between 1000 and 10 000 spheres but larger systems of more than 10^6 pores can be easily calculated as well. The simulation volume is defined in 3D Cartesian coordinates. One corner of the simulation volume is placed at the origin, hence the whole volume is defined in positive coordinates. The boundary conditions are periodical in all three space dimensions. The sides of the simulation box are of arbitrary length; here we used a cubic box of 20 unit lengths in every direction.

Based on the fact that pore diameter distribution depends on the production process, various pore size distributions were analyzed. Here we study power-law and log–normal pore size distributions. These pore size distributions were applied in a wide parameter range and recommendations are given for optimum parameterization.

3. Structure optimization

As described in [1], we optimized power-law distributed pore systems in terms of maximum porosity. The packing fraction or porosity for this closed pore model was $P \approx 0.71$. Now we present another optimized system with log–normal diameter distri-

bution. We used heuristic methods and numerical methods like the Nelder–Mead simplex method [6] to optimize the packed sphere systems. Every simulation series included 1000 randomly distributed spheres. The pore diameters are log–normal distributed according to the probability density function:

$$f(x;\mu,\sigma) = \frac{1}{x\sigma\sqrt{2\pi}} \exp\left[-(\ln x - \mu)^2 / \left(2\sigma^2\right)\right] \tag{2}$$

Mean pore size was fixed at $\mu = 1.0$, the standard deviation was varied in steps of 0.1 in the range of 0.1 to 1.2. The task was to find the optimum value of standard deviation for this constellation. We found that for a standard deviation of $\sigma = 0.9$, the highest packing fractions around $P \approx 0.73$ were generated (Fig. 1), independently of diameter scaling.

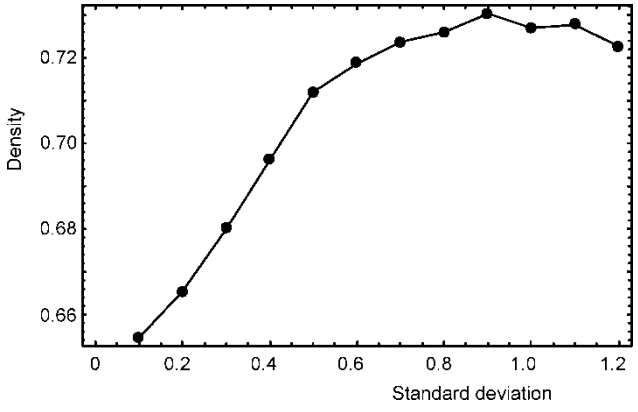

Fig. 1. Packing fraction vs. standard deviation for a log–normal distributed system

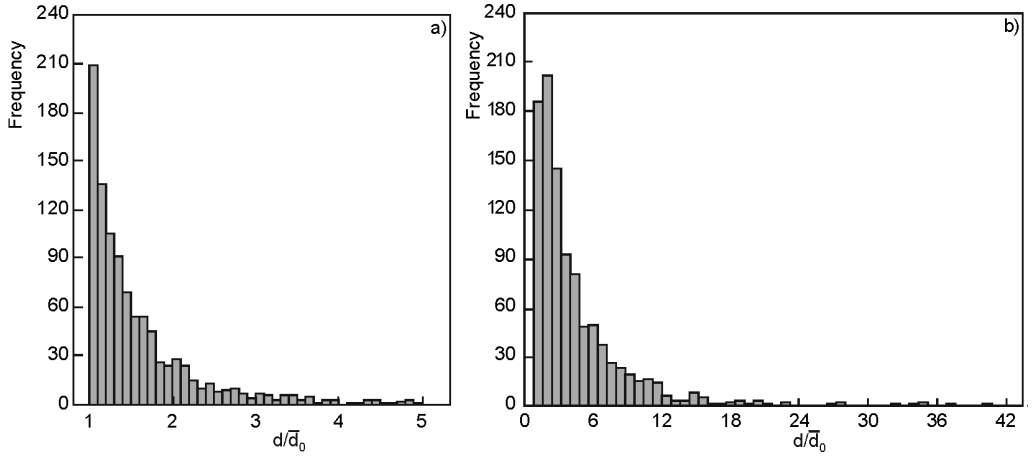

Fig. 2. Diameter distributions of the analyzed systems: a) power-law distribution with $a = -3.3$, b) log–normal distribution with parameters $\mu = 1.0$ and $\sigma = 0.9$

This optimization series was refined with a reduced range of standard deviation from 0.85 to 1.15 and smaller steps (step width 0.05). The above conjectured optimum value of $\sigma = 0.90$ could be verified here. The systems analyzed in the following were generated using this optimized log–normal pore size distribution and the optimized power-law pore size distribution given in [5].

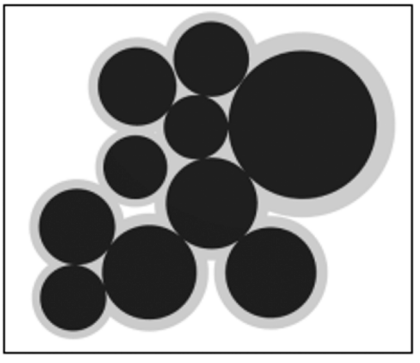

Fig. 3. Cherry-pit extension of a 2D disc system. The shells are increased proportional to their diameters. Dark discs are hard discs, the shell around is shown in gray. Shell diameters are calculated by $D_{shell} = (1+ m)D_{sphere}$ with $m = 0.25$

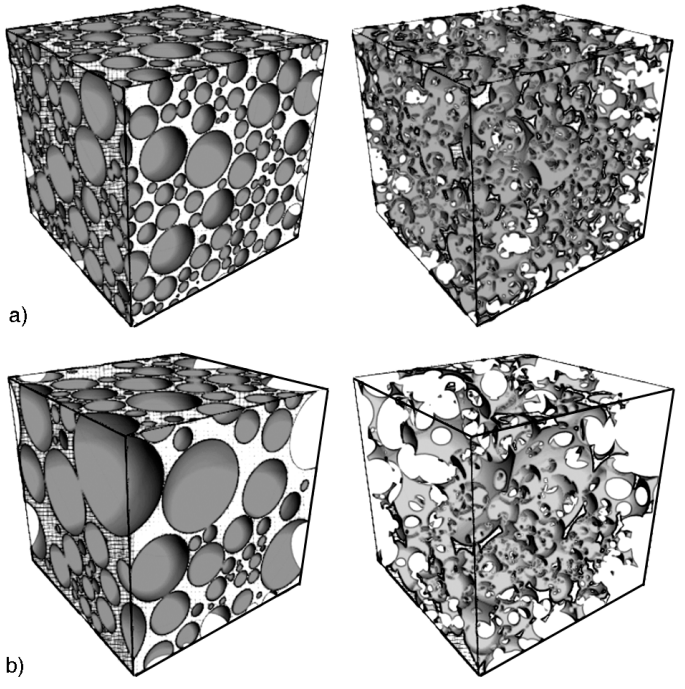

Fig. 4. Sectional view of model pore systems: a) power-law distributed diameters with $m = 0$ (closed pores, left) and $m = 0.15$ (open pores, right), b) log–normal distributed diameters, with $m = 0.0$ (closed pores, left) and $m = 0.15$ (open pores, right)

The generated porous systems are systems with closed pores due to the hard sphere properties of the sphere packing algorithm described in [7, 8]. To generate open

pore systems, we extended our packings to the cherry-pit model as described in [9]. This model is characterized by the fact that hard spheres feature a defined shell wherein they may overlap so they are partially penetrable. In Figure 3, a 2D representation of a sample model is shown to illustrate this principle.

There exist alternatives to create cherry-pit extensions of hard sphere systems. One approach is to increase all spheres with the same additive value, another one is to increase the diameters proportional to the hard sphere diameter. Because of the desired conservation of size distribution, we used here the latter one, the shell diameters are calculated according to equation $D_{\text{shell}} = (1+ m)D_{\text{sphere}}$.

The optimized log-normal and power-law distribution structure referred to in [5] were transformed to open pore structures according to the above mentioned cherry-pit model. The value of the scaling factor m was increased in 0.05 steps from 0 (closed pores) to 0.50. In Figure 4, one can see sectional views of sample systems. Figure 4a shows the power-law distributed porous model with closed pores (left) and increased pores (right, for m = 0.15), likewise Fig. 4b shows the log–normal distributed model with closed and open pores with the same parameter m.

4. Process simulation and properties

One of our intentions is to show that experimental results and simulated processes evidence a comparable behaviour. Positron annihilation lifetime spectroscopy is one of the experimental methods to characterize the porosity of materials [4]. The main principle is that the lifetime of a positronium – an atom-like couple of electron and positron – strongly depends on the free way of a particle. The larger the pores are, the longer the positronium lives – up to the maximum lifetime of 142 ns. When positroniums collide with a pore wall or when their lifetime is over, their components are annihilated to gamma radiation. This radiation and the time difference between formation and annihilation can be measured. The procedure is very appropriate for nanosized pores which cannot be normally investigated by traditional procedures like mercury porosimetry. In open pore systems, the average pore diameter can be estimated, in closed pore systems even the pore size distribution can be measured. In our simulations, the process of positronium implantation and lifetime measurement is calculated in a first approximation by random dimensionless particles which perform a non lattice-confined random walk through the simulated pore systems. In the following, this calculation process is described and some first results are given.

$$R(N) = \left| P_{\text{start}} - P_N \right| \tag{3}$$

$$t(N) = \frac{1}{V} \sum_{1}^{N} \left| P_{i+1} - P_i \right| \tag{4}$$

Particles without geometrical dimension are sequentially generated in the pores. A particle gets a random start vector and then it moves through the system. Reflections at the pore walls change the way of the particle according to the reflection laws. Positions P_{start}, P_i and P_N denote the starting point, intermediate points of reflection and the final position of the particle after N reflection events. After these reflections, the random walk of a particle ends at the position P_N. The effective covered distance $R(N)$ is calculated as the Euclidian distance between start position P_{start} and the particles final position after N reflections. The lifetime $t(N)$ is calculated as a quotient of the whole covered distance between all N reflections and assumed constant velocity V (Eqs. (3) and (4)). The porous model is assumed to be capped.

Another important property is the penetrability of open and closed pore systems. The penetrability for gases or fluids is one of the most important characteristics [3]. Interlayer dielectrics should not only avoid leakage current, they also protect the conducting layers. This protection is endangered when fluids or gases interfuse the dielectrics. Like in the simulations described above, a number of dimensionless particles are generated and sent through the system. All particles are generated at coordinates $p_i < 0, y_i, z_i>$ of the simulation volume with randomly generated y and z coordinates. Every particle gets a random directional vector which points into the simulation volume. The porous material is represented by our sphere packings described above with optimized log–normal and power-law distributions. The degree of open porosity varies from $m = 0$ (completely closed pores) to $m = 0.30$ (this means that all pores are scaled to 130% of their original diameters). All porous models are assumed as capped. The analyzed parameter is the maximum depth all particles reached. Mean depth and the maximum depth can show critical characteristics of variably parameterized porous systems.

5. Results

Analyzing the time after N reflections and the effective covered distance of particles in several pore size distributions with variable open porosity, one can see that for closed pores the estimated lifetime corresponds directly to the pore size distribution. There is a qualitative important leap in the behaviour from closed pores to pores with 5% overlap. Figure 5 shows that the more open the pore structure is, the better the estimated distribution of lifetimes approximate Gaussian behaviour. Mean lifetime increases because of the longer collision-free path of the particles. The distance covered and the lifetime of particles trivially increase heavily with increasing overlap of pores.

The flow rate $F(N)$ is defined as the ratio of the number of flown-through particles after N reflections $n_{flow}(N)$ and the number of all particles n_{all} (Eq. (5)). The flow rate was analyzed for 10 000 particles which are generated at coordinates $p_i < 0, y_i, z_i>$. A particle is declared as flown through when it reaches the opposite side of the simula-

tion box. This rate is zero in closed pore systems except for systems where the layer thickness is smaller than the maximum pore diameter. Simulations showed a critical point where the flow rate is rapidly increasing. At this point, the system becomes "transparent" for moving particles. These points differ for diverse pore size distributions and overlaps of pores

$$F(N) = \frac{n_{flow}(N)}{n_{all}} \tag{5}$$

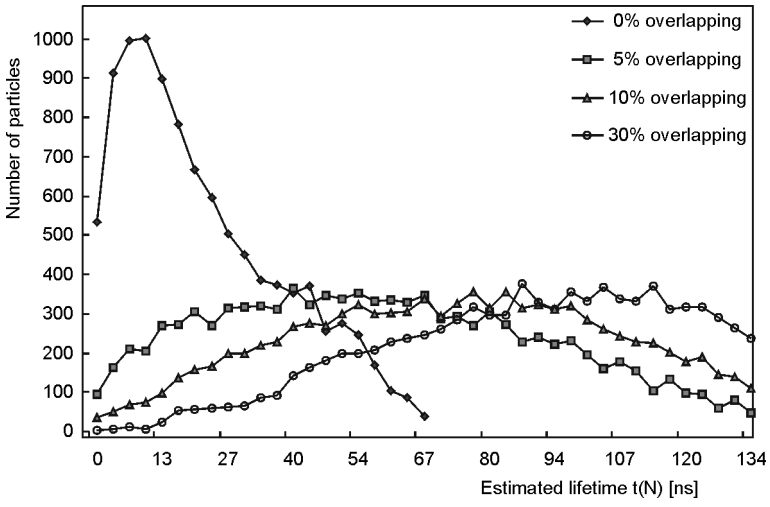

Fig. 5. Distribution of the estimated lifetime $t(N)$ for 10 000 particles and number of reflections $N = 50$ in a log–normal distributed pore system with various degrees of open porosity

The flow rate of particles passing through the system increases with increasing diameters (Fig. 6a). The diffusion resistance of the power-law structure is higher than the resistance of the log-normal system in case of equal porosity. The point where particles begin to flow through the system is increasing with $m = 0.15$ for the power-law system whereas this point is just reached below $m = 0.05$ for the log-normal system. For the power-law system one can say that this critical point is more definitely marked as for the log-normal system.

Mean interpenetration depth of particles in closed pore systems show stability against exogenous influences like vapor. Like in the simulations before, randomly generated particles are sent on one side to the surface of the pore system. They survive a predefined number of reflections with the pore walls. The deepest point reached by one particle is saved. In Fig. 6b one can see that this increases with increasing overlap of pores and differs for various pore size distributions. The distribution of the particle penetration depth is according to the depth profile of the surface in case of closed pores. With increasing open porosity the mean and maximum penetration depths increased.

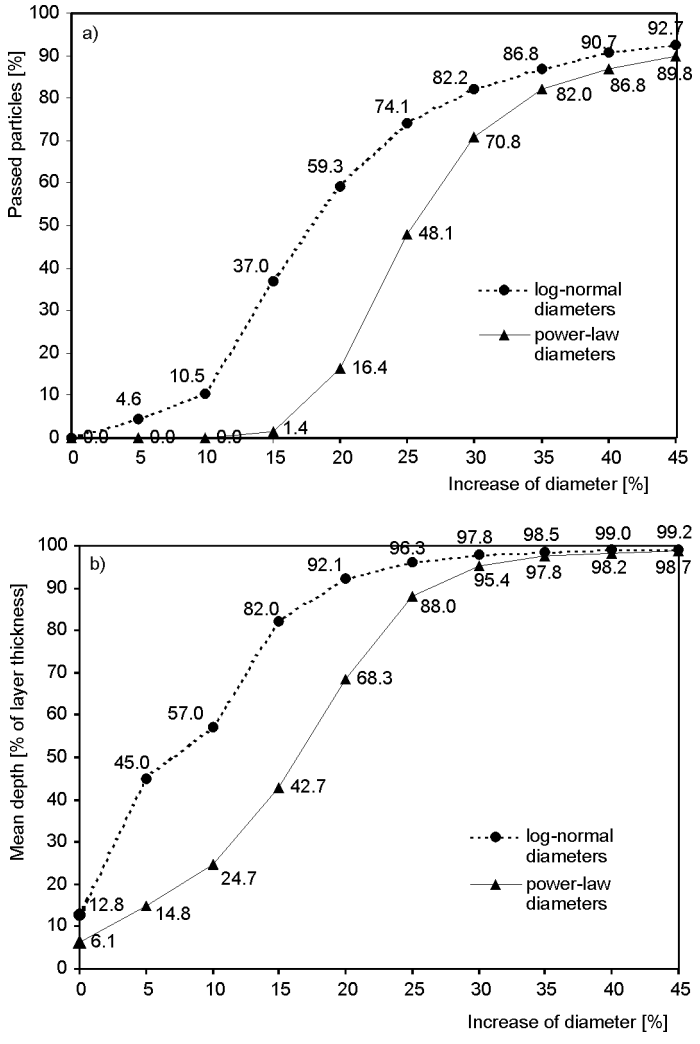

Fig. 6. Flow rates and mean penetration depths for capped porous layers with the thickness of 20 a.u. and $N = 50$ reflections: a) flow rate for 10 000 particles in a log-normal and a power-law porous system with different degree of open porosity, b) mean penetration depth of 10.000 particles for the same systems like above

A number of random walk particles is generated in the center of the simulation box under non-periodic boundary conditions. The system boundary is capped so that no particle can escape from the system. The mean squared distance R^2 is calculated and compared against passed time for assumed constant velocity (see Fig. 7).

The theoretical diffusion coefficient for dimensionless particles was estimated from these data for systems with both power-law and log-normal size distribution.

$$D = \frac{\overline{R^2}(N)}{6\,t(N)} \tag{6}$$

It was calculated according to the above given Eq. (6).

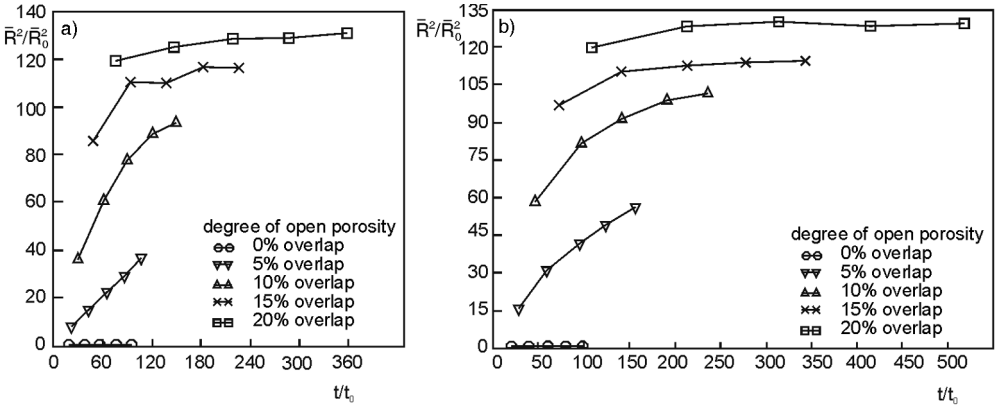

Fig. 7. The mean squared distance of particles to their start point against elapsed time calculated for constant velocity and different degrees of diameter increasing: a) for power-law distributed pores with $N = 50$ reflections, b) for log-normal distributed pores with $N = 50$ reflections

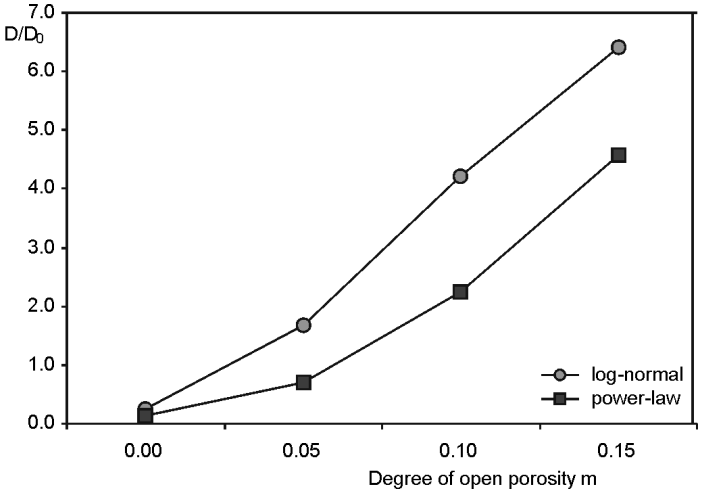

Fig. 8. Estimated diffusion coefficient for closed pores and open pores from $m = 0.05$ to $m = 0.15$

The power-law system shows a lower increase of the diffusion constant with increasing scaling factor m as the log-normal system. The general behaviour of the diffusion coefficients is similar in both pore size distributions and agrees with results given in [3].

6. Conclusion

Computer simulations of porous systems based on dense packed spheres are an appropriate model for the estimation and calculation of properties of real porous media. Low-*k* dielectrics of the porous type require a detailed control of their properties, because some desired properties are negatively correlated. Simulations as described are a useful method to optimize these properties and investigate the influence of one parameter on the others. The model of dense packed hard spheres was extended to the cherry-pit model to simulate open porous systems. Properties resulting from open porosity are estimated. The preferred pore size distribution is the power-law distribution with an exponent of $a = -3.3$ whereas the log–normal distribution showed an unfavourable behaviour.

Simulated flow rates of particles in finite porous systems show that diffusion behaviour for log–normal porous models seems to be less favourable than for the power -law models. The flow rate trivially increases with the increasing diameter scaling factor *m*. All analyzed model systems suggest that not only the value of porosity but also the pore diameter distribution and the degree of pore overlapping influence the properties of porous dielectric media. Additional simulations with described model systems should show further important properties of porous dielectrics like mechanical strength and thermal conductivity.

Acknowledgements

This work was supported by the Deutsche Forschungsgemeinschaft.

References

[1] GLADKOV S. O., *Dielectric Properties of Porous Materials*, Springer, Berlin, 2003.
[2] PLAWSKY J.L., GILL W.N., JAIN A., ROGOJEVIC S., *Nanoporous dielectric films: fundamental property relations and microelectronics applications*, [in:] *Interlayer Dielectrics*, S.P. Murarka, M. Eizenberg, A.K. Sinha (Eds.), Elsevier, Amsterdam, 2003, pp. 261–325.
[3] SHAMIRYAN D., BAKLANOV M.R., LYONS P., BECKX S., BOULLART W., MAEX K., Coll. Surf. A: Physicochem. Eng. Aspects, 300 (2007), 111.
[4] PENG H.-G., VALLERY R.S., LIU M., SKALSEY M., GIDLEY D.W., Col. Surf. A: Physicochem. Eng. Aspects, 300 (2007), 154.
[5] HERMANN H., ELSNER A., HECKER M. AND STOYAN D., Microel. Eng., 81 (2005), 535.
[6] NELDER J.A., MEAD R., Comput. J., 7 (1965), 308.
[7] JODREY W.S., TORY E.M., Phys. Rev. A, 34 (1986), 675.
[8] BEZRUKOV A., BARGIEL M., STOYAN D., Part. Part. Syst. Charact., 19 (2002), 111.
[9] A. R. KANSAL, S. TORQUATO, F. H. STILLINGER, J. Chem. Phys., 117 (2002), 8212.

Received 15 June 2007
Revised 19 November 2007

Materials Science-Poland, Vol. 25, No. 4, 2007

Molecular design of ultralow-*k* insulator materials*

K. ZAGORODNIY**, H. HERMANN, M. TAUT

Institute for Solid State and Materials Research, IFW Dresden, PF 270116, D-01171 Dresden, Germany

Dielectric materials with low permittivity (low *k*) are required for insulation to reduce the interconnect *RC*-delay in deep submicron integrated circuits. Combinations of classical and quantum-theoretical approaches for the assessment of the dielectric properties of fullerene-based materials with the goal to find ultralow-*k* dielectrics with suitable mechanical properties were used. We study the covalent linking of C_{60} molecules and vary the length and chemical composition of the linker molecule as well as the linkage geometry. The (static) electric permittivities, *k*, and elastic bulk moduli, *B*, of the proposed materials are in the range of 1.7–2.2 and 5–23 GPa, respectively.

Key words: *ultralow-k dielectrics; interlayer dielectrics; molecular design; dielectric properties; mechanical properties; fullerene-based dielectrics; microelectronics*

1. Introduction

The continuous shrinking of device dimensions of ultra-large-scale integrated (ULSI) chips imposes strong demands on the backend of the line (BEoL) interconnect structures [1]. The higher wire resistance of smaller metal lines and the crosstalk between closely spaced metal increase the interconnect *RC* delay, crosstalk noise, and power dissipation of the interconnect structure. It has fuelled a frantic search for new insulator materials [2, 3]. In order to decrease the first term of the *RC* product, the traditionally used in interconnects Al, with a resistivity of 2.7 μΩ·cm, was replaced by Cu, whose resistivity is 1.8 μΩ·cm [4]. The electric permittivity of SiO_2 also cannot sufficiently prevent cross talk between closely spaced copper wires in the semiconductor devices [5]. Using dielectric materials with smaller permittivity values, referred to as low-*k* dielectrics, in turn, can reduce the value of *C*. A great deal of intensive research has been conducted in this area. The candidate materials include non-fluorinated polymers [6], inorganic-organic hybrids [7, 8], porous polymers [9], and silica [10, 3].

---

*Presented at the 2nd Workshop "Hybrid Nanostructured Materials. Synthesis, Properties, Applications", Dresden, Germany, 8–9 November, 2006.

**Corresponding author, e-mail: K.Zagorodniy@ifw-dresden.de

The first generation of low-k dielectrics had a k value lower than that of SiO_2 ($k = 4.2$). Such materials included fluorinated SiO_2 (referred to as fluorosilicated glass, FSG), and hydrogen silsesquioxanes (HSQ). The first generation of low-k dielectrics has been successfully implemented in the manufacturing of integrated circuits (IC) with dimensions down to 0.25 μm. The second generation of low-k dielectrics mostly includes organic polymers [4].

In order to achieve low electric permittivity, it is necessary to reduce, for example, the material density. This means these dielectric materials will need to be produced in a porous form [11]. However, depending on the structural details, porosity can also adversely affect other properties crucial to chip performance, such as mechanical strength [12], electrical properties, and Cu diffusion into the insulator [5].

The primary consideration in selecting an interlayer dielectric material (ILD) for IC applications is the electric permittivity, k. But the k values need to be further reduced to 2.0 for the 45 nm technology node or bellow in the next few years [5, 13]. Although many materials have been studied, nowadays there is no material available with ultralow electric permittivity and sufficient mechanical properties.

Here we study a structure model for new ultralow-k materials proposed recently [14]. This model is generated as an ordered three-dimensional (3D) network consisting of two components: Fullerenes as nodes and bridge molecules as edges connecting the nodes. In the present study, simple cubic (sc) and diamond-like arrangements of fullerenes are considered where the fullerenes are connected by hydrocarbons and Teflon-like bridge molecules. The calculation of electronic and mechanical properties is rather complex, and, therefore, the theoretical tools used range from classical approaches to *ab-initio* quantum-mechanical methods.

2. Computational methods and model

2.1. Computational methods

We use molecular mechanics and density-functional based quantum chemical methods [15, 16] for structure optimization of the structural units and for calculation mechanical and dielectric properties. Considered structures were constructed by molecular mechanics as periodic arrangements of fullerenes and bridge molecules. For the construction the HyperChem 7.51 [16] program packet was used. The structures within the unit cell and the lattice parameters were optimized using either the conjugated gradient or the steepest descent method at the density functional tight binding (DFTB) level [17, 18]. Periodic boundary conditions were imposed on the polymers. The DFTB method is the density-functional based tight-binding method as described in [17]. This method is suitable for theoretical analyses of carbon-based clusters [19] and has been successfully applied to several problems of surfaces and interfaces of carbon structures [20].

2.2. Molecular design

We have developed the next model for investigations of the properties of dielectric materials. We consider spherical molecules and connect them by bridge molecules forming an ordered 3D network. Our model is based on the well-known C_{60} fullerene molecules which are used as spherical molecules. Pure fullerene molecule can also be modified, for example, by decorating with different number of fluorine atoms to change its electronic properties [21]. The detailed researches of influence of the fluorine atoms on the electronic properties of C_{60} molecules are presented in [21]. The bridge molecules are realized by hydrocarbon chains C_nH_{2n} and Teflon-like structures (C_nF_{2n}). The distance between C_{60} molecules can be modified by using bridge molecules with various lengths covalently bound to the fullerenes. Fullerenes connected by bridge molecules are used as structural units for the construction of the 3D network.

Introduction of bridge molecules with various lengths between neighbouring C_{60} molecules reduces the density of the material. It can be also considered as incorporation of pores with mono-disperse pore size distribution on the scale of 1 nm.

Pure C_{60} fullerenes deposited on a substrate arrange in a face centred cubic (fcc) lattice. The lattice can be theoretically expanded. Bridging next-nearest fullerene neighbours by chain molecules one obtains a possible realization of 3D networks of connected fullerenes. In the fcc lattice, each fullerene molecule has 12 next-nearest neighbours. Other networks may be generated, for example, according to the sc lattice, where each fullerene molecule has 6 next-nearest neighbours, or the diamond lattice, where each C_{60} molecule has 4 next-nearest neighbours. An example of the 3D network of the fullerene with the diamond like symmetry is shown in Fig. 1.

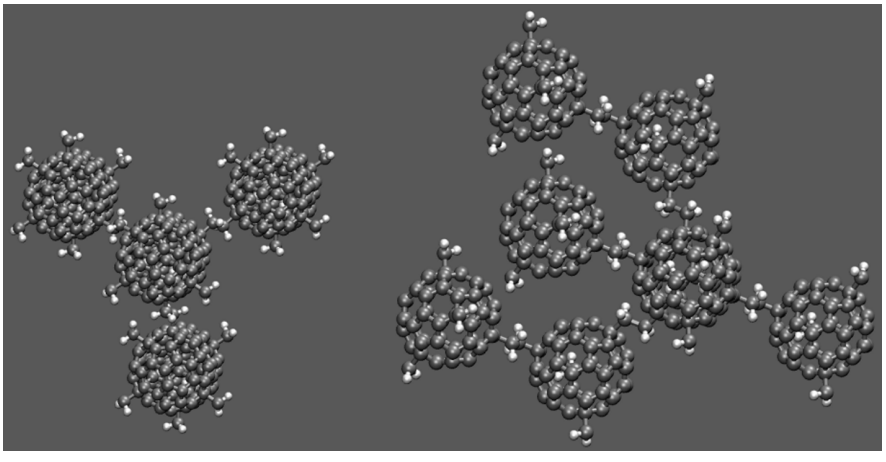

Fig. 1. Arrangement of C_{60} fullerenes into an ordered 3D network with a diamond like symmetry interconnected by hydrocarbon molecules C_2H_4

Fullerene chemistry has shown that it is possible to attach fullerene to existing polymers by covalent bonds [22, 23]. One of the possible reactions results in C_{60}

fullerene decorated with four CH_3 groups. By combining fourfold decorated fullerenes it should be possible to generate a diamond like lattice, where the lattice sites occupied by fullerenes and the bonds between them are arranged tetrahedrally by C_nH_{2n} or by other chemical groups. This is the experimental background of the present model which consists of fullerenes situated at the sites of a lattice and of bridge molecules connecting next-nearest fullerene neighbours.

Expansion of the fullerene lattice as described would lead to reduction of the density and to the formation of a nanoporous material. The pore size would be of the order of the length of the bridge molecules. Varying the length of the bridge molecules, its chemical realization and the topology of the 3D network (sc, fcc, and diamond like symmetry), the properties of the material can be modified and various process requirements adopted. Such materials can be classified as hybrid materials tailoring the properties of C_{60} together with the properties of polymeric linker molecules.

3. Results and discussion

3.1. Dielectric properties

The static electric permittivity of materials is an important issue for microelectronics. The calculation of this parameter for a solid material is a non-trivial task. The electric permittivity, k, depends on the polarizability of materials under the influence of an external electric field. The electronic, ionic, and dipolar components of the polarizability contribute to the electric permittivity of dielectric materials. Reduction of the polarizability lowers the electric permittivity. One of the ways to reduce the polarizability is to introduce hydrogen, carbon and fluorine atoms in dielectric materials [24].

Defining a structural unit, the polarizability of this unit and its response to the electric field at the position of this unit must be considered. Unfortunately, the strength of the local field acting on the polarizable unit can differ considerably from that of the applied external field. This is one of the main problems: a given structural unit in the material is not polarized by the mean of an internal electric field but by the macroscopic one present at the structural unit (local field corrections). Therefore, it is important not only to count the local polarizabilities but also to consider the influence of the environment of a local dipole. A recent review of methods for the calculation of the polarizability of atoms, molecules and clusters is given in [25]. The treatment of extended systems has been re-formulated in the past decade with the result that the information about the polarization is not in the electronic density but in the phases of the wave functions [26–28]. A simple approach to describe the complex interplay of external field, local field and polarizability of a local unit is the Clausius–Mossotti model (see [29]). The Clausius–Mosotti model is a continuum theoretical approach to the interaction of a molecule and a polarizable environment [30].

In a recent theoretical paper [31], this approach was applied to calculate the electric permittivity of low-*k* materials consisting of chemical groups such as Si–H, Si–CH_3, Si–O, where the polarizability of the groups was calculated using the density functional theory (DFT). Chemical bonds of this type appear as structural components in hydrogen silsesquioxane (HSQ) and methyl silsesquioxane (MSQ) low-*k* materials.

Replacing the neighbouring molecular units by a polarizable continuum with a spherical cavity where the unit under consideration is situated, the Clausius –Mossotti model applies [29, 30, 32–37]:

$$k = \frac{1 + 2c\alpha}{1 - c\alpha}, \qquad c = \frac{4\pi}{3}\frac{N}{V},$$

where N/V is the number density of molecular units and α is the molecular polarizability.

The quantity N/V is a geometrical parameter determined from the structures. The molecular polarizability can be calculated by means of several methods [38].

According to the model presented here, the electric permittivity of the fullerene solid is supposed to be reduced by creating cross-linkage between the fullerene monomers, increasing the C_{60}–C_{60} distance and, consequently, by decreasing the number of dipoles per the unit volume. Choosing the sc lattice as a skeleton for the fullerene network, the density for $n = 4$ takes the value $\rho = 0.621$ g/cm^3. It leads to the value of electric permittivity $k = 1.7$. The diamond lattice is even more efficient with respect to the reduction of the *k* value. In this case, *k* values below 1.5 are possible for $n > 4$. The results of calculation of *k* for the structures with diamond like symmetry with different *n* are shown in the Table 1.

Table 1. Lattice constant *a*, mass density ρ, and electric permittivity *k* for fullerene networks with C_nH_{2n} bridge molecules

n	Sc like			Diamond like		
	a [nm]	ρ [g/cm^3]	*k*	*a* [nm]	ρ [g/cm^3]	*k*
2	1.14	0.905	2.18	2.60	0.586	1.68
4	1.33	0.620	1.72	3.08	0.378	1.41

3.2. Mechanical properties

The bulk modulus *B* was calculated for fullerene 3D networks described above with sc and diamond symmetry. To calculate the mechanical properties, three-dimensional periodic boundary conditions were applied to the 3D network of interconnected C_{60}. The lattice parameters are the results of the DFTB structure optimization procedure. The bulk modulus *B* was determined from the relation $B = V_0(\partial^2 E/\partial V^2)$, where *E* is the DFTB energy per unit cell at hydrostatic strain of the elementary cell. Volume V_0 applies for the strain-free state. All atoms have been fully relaxed for given

cell parameters and the moduli were obtained for the equilibrium structures by a polynomial fitting method.

Firstly we consider the sc symmetry. The lattice constants of the sc model structures with C_nH_{2n} as bridge molecules increase monotonously with increasing length n of the hydrocarbon molecules (Table 1). For $n = 2$ and 4, the lattice constant takes the value of 1.136 nm and 1.335 nm, respectively. The corresponding electric permittivities are $k = 2.2$ ($n = 2$) and 1.8 ($n = 4$). The structures with $n = 2$ show robust and stable behaviour ($B = 5.0$ GPa), while for $n = 4$ fluctuations of energy appear, pointing to possible instabilities ($B = 0.4$ GPa). This means that increasing length of hydrocarbon bridge molecules decreases k-values but also deteriorates mechanical properties. Nevertheless, the sc model with C_2H_4 bridge molecules shows already a very good combination of dielectric and mechanical properties.

Fluorination of materials is one of possible ways to reduce the electric permittivity k. In order to obtain low-k materials many new fluorine containing polymers such as fluorinated silicate glass [39, 40], fluoromethylene cyanate ester, fluoroaromatic triallyl ether copolymer [41], etc., were developed and researched in the last few years. The C–F bond is the bond with one of the lowest polarizabilities. That is why the fluorination is one of the promising methods to improve the dielectric properties of the materials. We replaced in the previous model with $n = 2$ the hydrogen atoms of the bridge molecules by fluorine. The results for the series $C_{60}(CH_2)_6$, $C_{60}(CF_2)_2(CH_2)_4$ and $C_{60}(CF_2)_6$ are collected in Table 2. The k-value is slightly reduced (5%) and the bulk modulus is enhanced by about 20% compared to the data for the C_2H_4 sc model. Therefore, we conclude that the transition from hydrocarbon to Teflon-like bridge molecules in the sc basic structure improves gradually the properties of the hypothetical low-k dielectric material.

Table 2. Properties of sc structures with C_2X_4 bridge molecules, X = H, (H, F), F

Molecule	$C_{60}(CH_2)_6$	$C_{60}(CF_2)_2(CH_2)_4$	$C_{60}(CF_2)_6$
Lattice constant, a [nm]	1.14	1.15	1.16
Mass density, ρ [g/cm^3]	0.906	0.967	1.087
Electric permittivity, k	2.18	2.16	2.11
Bulk modulus B (GPa)	5.0	5.1	6.1

The results of the structure optimization of the models with fullerenes situated at the lattice sites of a diamond like elementary cell and hydrocarbon bridge molecules C_nH_{2n} are given in Table 1. As expected, the lattice constant increases with growing length n, of the hydrocarbon molecule which results in a reduced mass density. Accordingly, the electric permittivity scales down and reaches extremely low values of $k < 1.5$ for $n \geq 4$.

Regarding the mechanical properties of the diamond-like network, we expect improved results as compared to the sc model with equal bridge molecules because of the

different topology. Indeed, the simulated hydrostatic deformation of the $C_{60}(CH_2)_4$ model (equilibrium lattice constant 2.602 nm) and the fitting of the energy values by a parabola gives the value of 23 GPa. The statistical error due to deviations of the data from the ideal parabolic shape is of the order of 30%. The electric permittivity k is 1.7. These results suggest that diamond like C_{60}-based networks are excellent candidates for future ultralow-k dielectric materials.

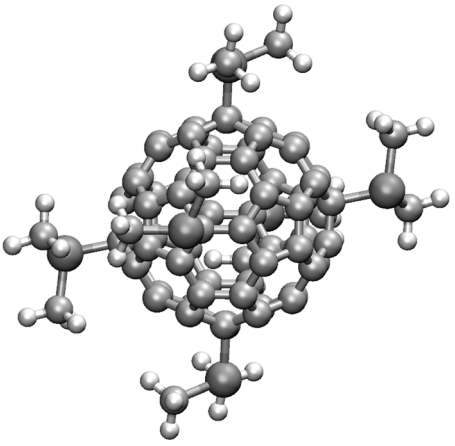

Fig. 2. Atomic structure of a $C_{60}(SiC_2H_6)_6$ unit optimized for periodic boundary conditions. Large spheres represent Si atoms, middle size – carbon atoms, and small ones are hydrogen atoms

Further improvements could include the use of Teflon-like or even other bridge molecules. Figure 2 shows an example of the fullerene network with methylsilane like bridge molecules, as an example of the further theoretical investigation. Another structures with Si-containing bridge molecules was presented in [42].

4. Conclusion

Molecular design was applied to generate models for new insulating materials with extremely low electric permittivities and good mechanical properties. The models are mosaic structures with fullerenes at the nodes and bridge molecules along the edges of the mosaic cells. The interior of a mosaic cell represents a pore on the 1 nm scale. Promising candidates based on sc and diamond-like lattices and hydrocarbon or Teflon-like bridge molecules were generated. The search for model structures with low electric permittivity k and sufficient elastic bulk modulus B started with the sc structure and C_2H_4 bridge molecules. The strategy of improving the properties by structural modification included three options: (i) change of the bridge molecules from C_2H_4 to C_nH_{2n}, $n > 2$, for sc fullerene arrangement with variable lattice constant; (ii) replacement of hydrogen by fluorine in the bridge molecules C_2X_4, X = H, F for the sc structure; (iii) transition from sc to diamond-like arrangement of fullerenes with C_nH_{2n} bridge molecules.

At the moment, property combinations with electric permittivity of k = 1.7 and elastic bulk modulus of about 20 GPa are achieved. Strategies for further improvement of the materials are discussed.

References

[1] GRILL A., PATEL V., J. Appl. Phys., 85 (1999), 3314.
[2] WANG M.R., RUSLI E., YU M.B., BABU N., LI C.Y., RAKESH K., Thin Solid Films, 462–463 (2004), 219.
[3] YU S., WONG T.K.S., PITA K., HU X., LIGATCHEV V., J. Appl. Phys. 92 (2002), 3338.
[4] VASILOPOULOU M., DOUVAS A.M., KOUVATSOS D., ARGITIS P., DAVAZOGLOU D., Microel. Rel., 45 (2005), 990.
[5] LEE H.-J., SOLES C.L., I LIU D.-W., BAUER B.J., LIN E.K., WU W.-L., GRILL A., J. Appl. Phys., 95 (2004), 2355.
[6] HENDRICS N.H., Mater. Res. Soc. Symp. Proc., 443 (1997), 3.
[7] GUO L., LEE J.H., BEAUCAGE G., J. Non-Cryst. Sol., 243 (1999), 61.
[8] HONG J.K., YANG H.S., JO M.H., PARK H.H., CHOI S.Y., Thin Solid Films, 308–309 (1997), 495.
[9] XU Y., TSAI Y., TU K.N., ZHAO B., LIU Q., BRONGO M., SHENG G.T.T., TUNG C.H., Appl. Phys. Lett. 75 (1999), 853.
[10] MORGEN M., RYAN E.T., ZHAO J., HU A., CHO T., HO P.S., Ann.. Rev. Mater. Sci.. 30 (2000), 645.
[11] DAMAYANTI M., GAN Z.H., SRITHARAN T., MHAISALKAR S.G., NAMAN A., WIDODO J., TAN H.S., Thin Solid Films, 504 (2006), 213.
[12] HERMANN H., ELSNER A., HECKER M., STOYAN D., Microel. Eng., 81 (2005), 535.
[13] Semiconductor Industry Association, *The International Technology Roadmap for Semiconductors* (1999), 2000 Update (2000), 2004 Update (2004), 2005 Edition (2005),. (http://www.itrs.net).
[14] HERMANN H., ZAGORODNIY K., TOUZIK A., TAUT M., SEIFERT G., Microel. Eng., 82 (2005), 387.
[15] KÖSTER A.M., FLORES R., GEUDTNER G., GOURSOT A., HEINE T., PATCHKOVSKII S., REVELES J.U., VELA A., SALAHUB D.R., deMon2003exp (C), NRC Ottawa, Canada, 2003.
[16] HyperChem7.52: http://www.hyper.com/products/Professional/index.htm.
[17] POREZAG D., FRAUENHEIM T., KÖHLER T., SEIFERT G., KASCHNER R., Phys. Rev. B, 51 (1995), 12947.
[18] DUARTE H.A., HEINE T., SEIFERT G., Theor. Chem. Acc. 114 (2005), 68.
[19] SEIFERT G., POREZAG D., FRAUENHEIM T., Int. J. Quantum Chem., 58 (1996), 185.
[20] JUNGNICKEL G., POREZAG D., FRAUENHEIM T., HEGGIE M.I., LAMBRECHT W.R.L., SEGALL B., ANGUS J.C., Phys. Stat. Sol. A, 154 (1996), 109.
[21] ZAGORODNIY K., TAUT M., HERMANN H., Phys. Rev. A, 73 (2006), 054501.
[22] MEIER M.S., *Solution-State Syntheses of Fullerene-Based Pendant, Pearl Chain, and Dendritic Polymers*, [in:] *Fullerene Polymers and Eullerene Polymer Composites*, P. C. Eklund, A. M. Rao, (Eds.), Springer, Berlin, 2000, p. 369.
[23] PENG H., LAM J.W.Y., LEUNG F.S.M., POON T.Y W.H., WU A.X., YU N.-T., TANG B.Z., J. Sol-Gel Sci. Techn., 22 (2001), 205.
[24] HOMMA T., Mater. Sci. Eng., R, 23 (1998), 243.
[25] BONIN K.D., KRESIN V.V., *Electric Dipole Polarizabilities of Atoms, Molecules and Clusters*, World Scientific, Singapore, 1997.
[26] RESTA R., Ferroelectrics, 136 (1992), 51.
[27] KING R.D., VANDERBILT D., Phys. Rev. B, 47 (1993), 1651.
[28] RESTA R., arXiv: cond-mat/9903216.
[29] JACKSON H.D., *Classical Electrodynamics*, Wiley, Chichester, 1962.
[30] BÖTTCHER C.J.F., *Theory of Polarization*, Elsevier, Amsterdam, 1973.
[31] COURTOT-DESCHARLES A., PIRES F., PAILLET P., LERAY J.L., Microel. Rel., 39 (1999), 279.

[32] VAN DUIJNEN P.T., DE VRIES A.H., Int. J. Quantum Chem., Quantum Chem. Symp. 29 (1995), 523.
[33] DE VRIES A.H., VAN DUIJNEN P.T., JUFFER A.H., RULLMANN J.A.C., DIJKMAN J.P., MERENGA H., THOLE B.T., J. Comput. Chem., 16 (1995), 37.
[34] THOLE B.T., VAN DUIJNEN P.T., Chem. Phys., 71 (1982), 211.
[35] THOLE B.T., VAN DUIJNEN P.T., Theor. Chim. Acta, 55 (1980), 307.
[36] VAN DUIJNEN P.T., DE VRIES A.H., SWART M., GROZEMA F., J. Chem. Phys., 117 (2002), 8442.
[37] CHIPMAN D.M., J. Chem. Phys., 110, (1999), 8012.
[38] ZAGORODNIY K., TAUT M., HERMANN H., Phys. Rev. A, 73 (2006), 054501.
[39] HASEGAWA S., TSUKAOKA T., INOKUMA T., KURATA Y., J. Non-Cryst. Sol., 240 (1998), 154.
[40] DENISON D.R., BARBOUR J.C., BURKHART J.H., J. Vac. Sci. Techn. A, 14 (1996), 1124.
[41] MURARKA S.P., *Low-k Polymers*, [in:] *Interlayer Dielectrics for Semiconductor Technologies*, S.P. Murarka, M. Einzenberg, A.H. Sinha (Eds.), Elsevier, Amsterdam, 2003, p. 168.
[42] WANG Y., SEIFERT G., HERMANN H., Phys. Stat. Sol. A, 203 (2006), 3868.

Received 15 June 2007
Revised 19 November 2007

Materials Science-Poland, Vol. 25, No. 4, 2007

Nanocluster memories by ion beam synthesis of Si in SiO_2*

B. SCHMIDT[1**], K.-H. HEINIG[1], L. RÖNTZSCH[1], K.-H. STEGEMANN[2]

[1]Research Center Dresden Rossendorf, Institute of Ion Beam Physics and Materials Research, Dresden, Germany

[2]ZMD AG, Dresden, Germany[***]

Ion implantation and ion irradiation induced interface mixing were used to synthesise silicon nanoclusters in the gate oxide of metal–oxide–semiconductor (MOS) structures aiming at electronic memory applications. In the present study silicon nanocrystals for multi-dot floating-gate memories produced by ion irradiation through SiO_2/Si nterfaces have been investigated to demonstrate possible advantages of this approach compared to conventional application of ion beam synthesis to the fabrication of silicon nanocrystal memories. The memory properties of the fabricated structures as a function of Si^+-irradiation dose and post-irradiation annealing temperature and time have been examined through electrical measurements on n-channel MOS field-effect transistors. Low-voltage operating devices that can endure more than 10^6 programming/erasing cycles have been successfully achieved. More research is still required to improve charge retention and ensure the standard 10-year retention time needed for true non-volatile memory applications.

Key words: ion beam synthesis; silicon nanocrystal; nonvolatile memories

1. Introduction

At conventional low- and medium-fluence ($<10^{16}$ ions/cm^2) ion implantation in microelectronics the concentration of introduced dopants is usually below their solubility limit in silicon. At certain annealing temperatures, the impurity atoms are dissolved in Si and located on crystal lattice sites or, as a small part, remain as soluted interstitial atoms.

At high-fluence ($\geq 10^{16}$ ions/cm^2) ion implantation, or at so-called ion beam synthesis (IBS), a far-from-equilibrium state (supersaturated solid) is achieved which relaxes towards thermodynamic equilibrium during subsequent annealing by phase

---

*Presented at the 2ndWorkshop "Hybrid Nanostructured Materials. Synthesis, Properties, Applications", Dresden, Germany, 8–9 November, 2006.

**Corresponding author, e-mail: Bernd.Schmidt@fzd.de

***Now at Signet Solar GmbH Dresden, Germany

separation through precipitation and ripening (Ostwald ripening) of nanoclusters (NC) [1] (Fig. 1). Phase separation of ion implanted, immiscible impurity atoms from the surrounding matrix, i.e. the formation of NCs, can also occur during the implantation process if the impurity atoms are sufficiently mobile due to collisional ion mixing; otherwise a subsequent annealing is always necessary.

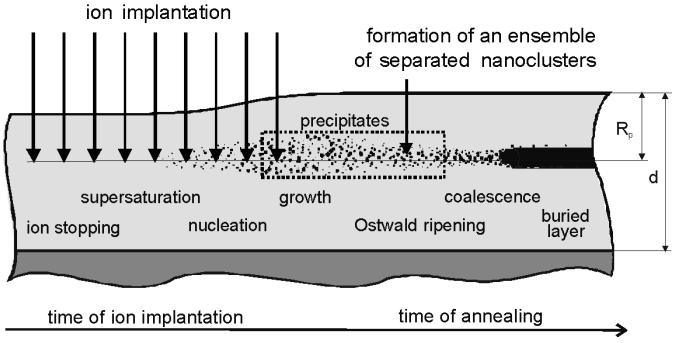

Fig. 1. Scheme of ion beam synthesis of nanostructures. High dose ion implantation into a solid leads to supersaturation of impurity atoms. NCs nucleate and grow during ion implantation or, for impurity atoms immobile during implantation, during subsequent thermal treatment. The mean NC size as well as their spatial and size distributions changes during the Ostwald ripening. At very high fluences, buried layers can form by coalescence of NCs

Although there are possibilities to tailor the mean NC size (mainly by variation of ion fluence and annealing temperature and time) at conventional IBS the possibilities for tailoring the NC size distribution by the variation of ion implantation parameters are rather limited.

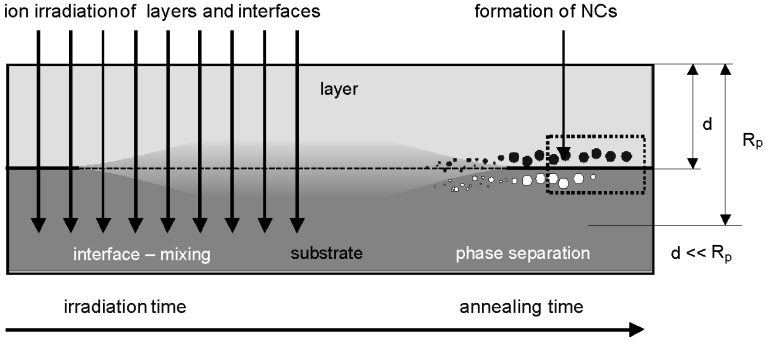

Fig. 2. Scheme of ion beam induced self-alignment of a NC δ layer near the layer/substrate interface by ion irradiation through the interface and subsequent thermal treatment leading to the phase separation in the ion mixed non-stoichiometric near-interface layer through precipitation and Ostwald ripening of NCs

Ion irradiation not only causes supersaturation and damage to the substrate but also affects the interface between the thin layer and the substrate or interfaces between

thin stacked layers. As schematically shown in Fig. 2, primary energetic ions produce collisional cascades which cause substantial interface mixing leading to non-stoichiometric and non-stable phases near the interface. Subsequent annealing restores the interface region rapidly via spinodal decomposition. However, the tails of the mixing profiles do not reach the recovered interfaces by diffusion, thus, phase separation proceeds via nucleation and growth of NCs near the interface. The competition between interface restoration and nucleation self-aligns nearly monodispersive δ layers of NCs in proximity to the interface. Recently, self-organization of a δ layer of Ge NCs in SiO_2 has been found [2, 3] close to the Si/SiO_2 interface after appropriate Ge^+ implantation into a SiO_2 layer on a Si substrate. The NC δ layers were found when the following conditions were fulfilled : a negligibly small amount of ions is implanted in the Si/SiO_2 interface region (i), and the cascade of energetic O and Si recoils produced by primary collisions produces a few displacements per atom (dpa) in the Si $/SiO_2$ region (ii). Different contributions to the self-organization and self-alignment of NC δ layers have been described and investigated and predicted by kinetic MC simulations and reaction-diffusion equations [4]. Very recently, this prediction has been verified experimentally by transmission electron microscopy [5, 6].

The IBS of semiconducting NCs has attracted much interest due to their compatibility with CMOS technology and due to unique physical properties of NCs as zero-dimensional objects. A great effort is currently devoted to their applications in new microelectronic devices, e.g. charge storing Si and Ge NCs in non-volatile memory circuits [7–10]. An example is the non-volatile multi-nanocrystal floating-gate memory proposed by Tiwari et al. [11]. The idea of this novel NC memory concept is simple: in comparison to conventional MOSFETs the only evolutionary step is the replacement of the poly-Si floating gate by a layer of electrically isolated Si NCs. However, the fabrication of monodispersive and small Si NCs (≤ 3 nm) separated from the transistor channel by a thin (2–3 nm) oxide represents a strong challenge. At the common IBS of Si NCs, low energy ion implantation into SiO_2 with ion energies lower than 5 keV and relatively high ion fluences in the order of $(1–2)\times10^{16}$ cm^{-2} is applied [8, 9]. Alternatively, the approach for ion irradiation induced self-alignment of Si NCs near SiO_2/Si interfaces can also be applied to the fabrication of non-volatile multi-dot floating gate memory devices [12]. The present contribution will be addressed to self-organization processes of silicon nanoparticles during ion irradiation of flat Si/SiO_2 interfaces during Si^+ ion irradiation and to the fabrication of Si NC memory devices using this approach.

2. Experimental

A MOS-like $Si/SiO_2/Si$ structure was selected and submitted to Si^+ ion irradiation to mix the interfaces of this layer stack. The ion irradiation experiments were carried out on 6” (100)Si wafers covered with a 15 nm thermally grown SiO_2 layer and a 50 nm

poly-Si layer deposited by LPCVD on top of the SiO_2 layer. The upper poly-Si layer was used as a capping layer to prevent any influence of contaminants from ambient and annealing atmosphere (mainly humidity) on the NC formation process in the gate oxide [13]. The poly-Si/SiO_2/Si stack was irradiated with 50 keV Si^+ ions at fluences in the range of 3×10^{15}–1×10^{16} cm^{-2}. After ion irradiation a highly n^+-doped and 250 nm thick poly-Si gate was deposited onto the irradiated stack. Subsequently, the samples were annealed (RTA) at various temperatures (950–1100 °C) and times (5–180 s) and further processed for the fabrication of nMOSFETs in the standard 0.6 μm CMOS process line of the ZMD company [14]. Transistors with long-channel (20 μm) and short-channel (0.6 μm) gate length and 20 μm gate width have been fabricated and tested.

3. Results

During ion irradiation, through a MOS-like Si/SiO_2/Si structure unstable non-stoichiometric SiO_x ($x < 2$) phases are formed, sandwiched between stable phases of SiO_2 and Si. Annealing restores the upper and lower SiO_2/Si interfaces by spinodal decomposition. However, the tails of the Si atom mixing profiles do not reach the recovered interfaces by diffusion thus, the phase separation proceeds via nucleation and growth of Si NCs in SiO_2. The competition between interface restoration and nucleation self-aligns δ layers of Si NCs in SiO_2 along the two interfaces. This self-alignment of δ layers of Si NCs with the SiO_2/Si interfaces has been predicted by atomistic computer simulations [15]. As shown in Fig. 3, Si precipitates in SiO_2 have developed to Si NC δ layers which are aligned with the SiO_2/Si interfaces. The mean Si NC diameter is 2 nm and the mean distance from the interfaces is 2 nm, too. In each δ layer, the Si NC areal density is in the order of 10^{12} cm^{-2}. This prediction has been verified experimentally by energy filtered transmission electron microscopy (EFTEM) [6]. As can be seen in Fig. 4, bright and dark areas are visible in dark and white regions of the SiO_2 layer, respectively. These spherical regions refer to Si NCs in the oxide. Accordingly, the Si NCs are separated from the SiO_2/Si interfaces by a mean distance of 3 nm, i.e. they are aligned in a δ layer at each interface. The mean diameter of the NCs was estimated to be 3 nm. These morphological features are in accordance with the KLMC simulation from [15].

Electrical measurements of memory properties show that devices exhibit significant memory windows at low gate voltages. Devices with a memory window of about 0.5 V for write/erase voltages of ±7 V and the programming time t_{pp} of 10 μs have been achieved. In terms of memory window and transistor characteristics, an implanted fluence of $(5–7)\times10^{15}$ Si^+ cm^{-2} and annealing at T_A =1050 °C for t_A = 30 s appear as promising conditions for device fabrication (Fig. 5a). The memory window can be increased by annealing at higher temperatures (1100 °C) and/or for longer time (over 120 s) resulting in a further phase separation and Si NC formation. As shown in Fig. 5b, in this case a large stable memory window of $\Delta V_{th} \sim 3$ V can be achieved.

No degradation in memory windows was observed for devices after 10^7 write/erase cycles with V_{pp} = +7V/–7V, t_{pp} = 1 ms programming conditions (Fig. 6), which means that the fabricated memory devices exhibit a superior endurance (very limited degradation up to 10^7 cycles). It was found that data retention time tested at 85 °C is

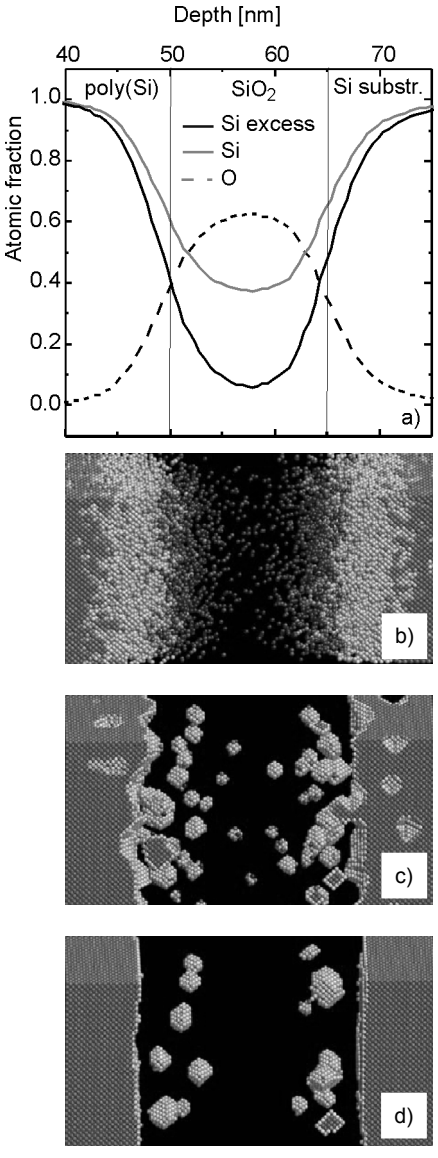

Fig. 3. Self-aligned Si NC formation by ion irradiation of SiO_2/Si interfaces: a) TRIDYN results of Si ion irradiation (E = 50 keV, $D = 1\times10^{16}$ cm^{-2}) through a layer stack of 50 nm poly-Si, 15 nm SiO_2, into the Si substrate. KLMC simulation snapshots referring to: b) the as-irradiated state, c) the early state of phase separation, d) to a later stage

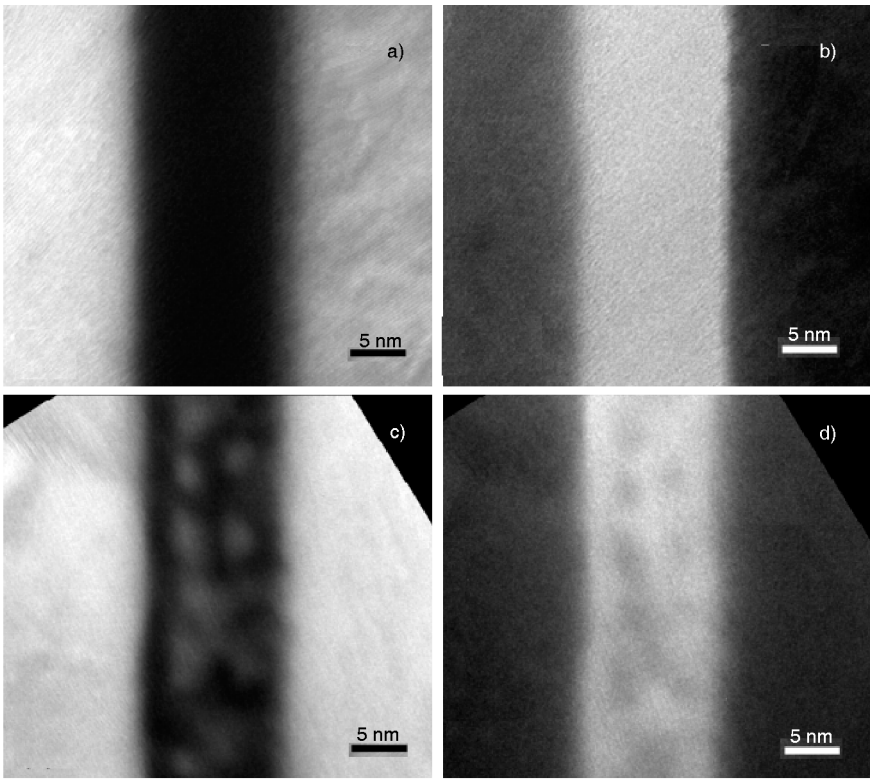

Fig. 4. Energy-filtered XTEM images of the poly-Si/SiO_2/Si structure: a, b) referring to the as-deposited state, c, d) after Si^+ ion irradiation (E = 50 keV, $D = 7\times10^{15}$ cm^{-2}) and post-irradiation annealing (T = 1050 °C, t = 120 s)

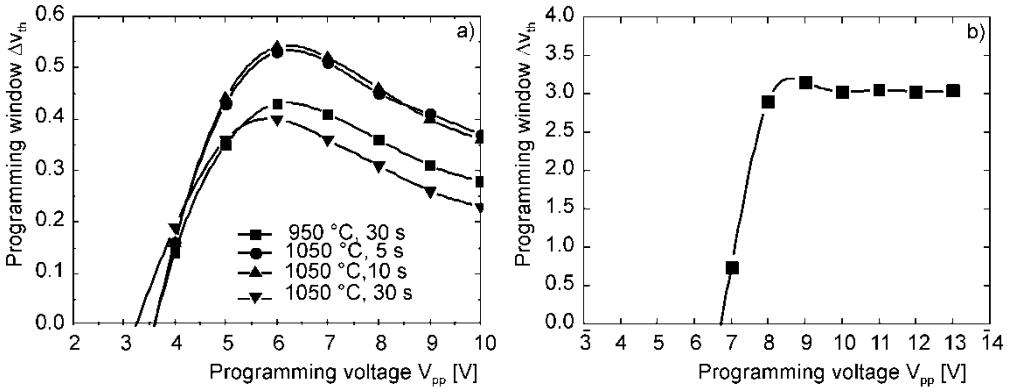

Fig. 5. Memory window ΔV_{th} vs. programming voltage V_{pp} (pulse length t_{pp} = 10 ms) of n-channel MOSFETs with self-aligned Si NCs in the gate oxide. Si^+ irradiation was performed at the ion energy of 50 keV and the fluence of 7×10^{15} cm^{-2}: a) for low thermal budget at various RTA annealing parameters, b) for high thermal budget and annealing at 1050 °C for 120 s

too low for EEPROM application (100 days at room temperature and 8 h at 85 °C). The fabricated nMOS devices exhibit maximum memory windows at low gate voltages indicating that the charge storage nodes are located near to the Si/SiO_2 interface. This implies the possibility of direct charge carrier tunneling into Si NCs during low programming voltages. The lowering of the programming window at programming voltages $V_{pp} > 6$ V (Fig. 5a) can be explained by trap-assisted tunneling through the gate insulator.

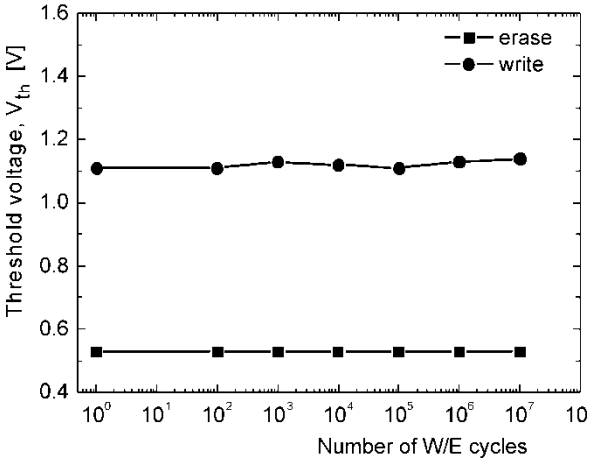

Fig. 6. Endurance characteristics of *n*MOSFETs obtained with write/erase voltages V_{pp} of ±7 V and pulses t_{pp} = 1 ms. The sample was irradiated with 50 keV Si^+ ions at the fluence of 7×10^{15} cm^{-2} and annealed at 1050 °C for 30 s

Besides retention, all electric parameters of the devices fulfil current requirements for non-volatile memory devices. The low data retention might be explained by direct re-tunneling of charge carriers to the channel which could be a common problem of multi-dot floating-gate memories.

4. Discussion

From structural examination of Si^+ ion irradiation induced self-organization of Si NCs in SiO_2, carried out using energy filtered transmission electron microscopy (EF-TEM) we conclude that the diameter of the NCs is smaller than 3 nm. Independent experiments using special techniques for decoration of the tiny Si precipitates by Ge or Si also demonstrated their existence [4, 5]. Additionally, for samples annealed after ion irradiation, ToF-SIMS [16] verifies two δ layers of Si excess within SiO_2. One δ layer is close to the upper Si/SiO_2 interface, the other is close to the lower one. Each δ

layer is separated from its interface by a narrow zone of ~ 3 nm denuded of Si excess, which is in agreement with our MC simulations.

The fabricated nMOS devices exhibit large memory windows at very low gate voltages, e.g. 1.9 V for 10 ms ±6 V and 3 V for 10 ms ±9 V) similar to the ones measured also on MOS capacitors indicating that the charge storage nodes are located near the Si/SiO_2 interface. This implies the possibility of direct charge carrier tunneling into Si NCs during low programming voltages. The lowering of the programming window at programming voltages $V_{pp} > 6$ V (Fig. 5a) can be explained by partial charge loss of the lower NC δ layer towards the gate and/or charging of the upper NC δ layer.

Besides retention, all electric parameters of our device fulfil current requirements. The low data retention might be explained by direct re-tunneling of charge carriers to the channel which could be a common problem to improve charge retention and ensure the standard 10-year retention time needed for true non-volatile memory applications. A fast charge loss could be avoided by an asymmetric tunneling behavior, e.g. by tunneling oxide engineering [17]. To solve this problem, additional studies are necessary.

Table 1. Ion beam synthesis of Si NCs in SiO_2; low energy Si^+ ion implantation into SiO_2 in comparison with ion irradiation through Si/SiO_2 interfaces

Si^+ ion implantation into SiO_2	Si^+ ion irradiation through interfaces
Unprotected gate oxide: serious impact of the ambient during processing	Gate oxide protected by poly-Si: no contamination by impurities and/or humidity during processing
Low energy, high dose implantation: strong sputtering and swelling of SiO_2	Irradiation with low fluences: no sputtering and no swelling of SiO_2
NC location due to implantation: difficulty to place NCs close to channel (ion energy critical)	NCs due to ion beam mixing: self-alignment of NC layer close to the channel (ion energy is not critical)
Ions and recoils come to rest in the interface region: degradation of the channel	Ions come to rest deep within Si: defects do not deteriorate the channel

Compared to conventional IBS of Si NC in SiO_2 by direct Si^+ ion implantation into thin SiO_2 layers ion irradiation through Si/SiO_2 interfaces results in some processing advantages which are summarized in Table 1. The protection of thin gate oxide by a poly-Si during processing (ion beam and thermal treatment) suppresses contamination by impurities and/or humidity [13] which can influence significantly the NC formation process. Compared to low energy and high dose ion implantation

into SiO_2 [10, 18, 19], the irradiation with relatively low fluences does not cause sputtering and/or swelling of the thin SiO_2 layer which is an important result from the technological point of view. Due to ion beam mixing, where the ion energy is not a critical parameter, a thin layer of nearly mono-dispersive Si NCs self-aligns close to the transistor channel. Furthermore, the ion energy can be selected in such a way that the ions come to rest deep within the Si substrate and remaining defects after annealing (end-of-range defects) do not deteriorate the transistor channel. Therefore, at ion beam synthesis of Si NCs in the transistor gate oxide, the ion beam mixing delivers a more stable process compared to direct ion implantation into thin SiO_2 layers.

5. Conclusion

Ion irradiation assisted formation of Si NC is appropriate for discrete charge trapping memories where no direct Si implantation into SiO_2 is required. No particular processing issues have been encountered during integration of this technique in standard sub-micron CMOS technology. The predictions of theoretical studies of ion irradiation assisted formation of Si NC δ layer are confirmed by experimental investigations. 0.6 μm n-channel MOSFETs with Si NCs in a 14.5 nm gate oxide were fabricated which exhibit charging at very low voltages and programming times in the ms range. The high endurance of 10^7 at low current consumption and short retention time are determined by the charging/decharging of the Si NCs by (direct) tunneling due to the location of the NCs close to the MOSFET channel.

Acknowledgement

This work was a part of the NEON project supported by the EC as GROWTH GRD1-2000-25619. The authors especially thank M. Perego and T. Gemming for carrying out ToF-SIMS measurements and EF-TEM investigations, respectively. The authors also would like to thank P. Dimitrakis and E. Votintseva for characterization of nMOSFETs by electrical measurements.

References

[1] REISS S., HEINIG K.H., Nucl. Instr. Meth. Phys. Res. B, 102 (1995), 256.
[2] HEINIG K.H., SCHMIDT, MARKWITZ A., GRÖTZSCHEL R., STROBEL M., OSWALD S., Nucl. Instr. Meth. Phys. Res. B, 148 (1999), 969.
[3] VON BORANY J., GRÖTZSCHEL G., HEINIG K.H., MARKWITZ A., SCHMIDT B., SKORUPA W., Sol.-State Electron., 43 (1999), 1159.
[4] HEINIG K.H., MÜLLER T., SCHMIDT B., STROBEL M, MÖLLER W., Appl. Phys. A, 77 (2003), 17.
[5] RÖNTZSCH L., HEINIG K.H., SCHMIDT B., MÜCKLICH A., Nucl. Instr. Meth. B, 242 (2006), 149.
[6] RÖNTZSCH L., HEINIG K.H., SCHMIDT B., MÜCKLICH A., MÖLLER W., THOMAS J., GEMMING T., Phys. Stat. Sol. (a), 202 (2006), R170.
[7] BEYER V., VON BORANY J., [in:] *Materials for Information Technologies*, E. Zschech, H. Mikolajick, (Eds.), Springer, Berlin, 2005, 139.

[8] NORMAND P., KAPETANAKIS E., DIMITRAKIS P., TSOUKALAS D., BELTSIOS K., CHERKASHIN N., BONAFOS C., BENASSAYAG G., COFFIN H., CLAVERIE A., SONCINI V., AGARWAL A., AMEEN M., Appl. Phys. Lett., 83 (2003), 168.
[9] NORMAND P., KAPETANAKIS E., DIMITRAKIS P., SKARLATOS D., BELTSIOS K., TSOUKALAS D., BONAFOS C., BENASSAYAG G., CHERKASHIN N., CLAVERIE A, VAN DEN BERG J.A., SONCINI V., AGARWAL A., AMEEN M., PEREGO M., FRANCIULLI M., Nucl. Instr. Meth. Phys. Res. B, 216 (2004), 228.
[10] MÜLLER T., HEINIG K.H., MÖLLER W., BONAFOS C., COFFIN H., CHERKASHIN N., BENASSAYAG G., SCHAMM S., ZANCHI G., CLAVERIE A., TENCÉ M, COLLIEX C., Appl. Phys. Lett., 85, (2004), 2373.
[11] TIWARI S., RANA F., HANAFI H., HARSTEIN A., CRABBE E., Appl. Phys. Lett., 68 (1996), 1377.
[12] SCHMIDT B., HEINIG K.H., RÖNTZSCH L., MÜLLER T., STEGEMANN K.H., VOTINTSEVA E., Nucl. Instr. Meth. Phys. Res. B, 242 (2006), 146.
[13] SCHMIDT B., GRAMBOLE D., HERRMANN F., Nucl. Instr. Meth. B, 191 (2002), 482.
[14] http://www.zmd.de
[15] RÖNTZSCH L., HEINIG K.H., SCHMIDT B., Mater. Sci. Semicond. Proc., 7 (2004), 357.
[16] PEREGO M., private communication.
[17] CASPERSON J.D., BELL L.D., ATWATER H.A., J. Appl. Phys., 92 (2002), 261.
[18] BONAFOS C., CARRADA M., CHERKASHIN N., COFFIN H., CHASSAING D., BENASSAYAG G., CLAVERIE A., J. Appl. Phys., 95 (2004), 5696.
[19] CARRADA M., CHERKASHIN N., BONAFOS C., BENASSAYA,G G., CHASSAING D., NORMAND P., TSOUKALAS D., SONCINI V., CLAVERIE A., Mater. Sci. Eng. B, 101 (2003), 204.

Received 2 July 2007

Materials Science–Poland, Vol. 25, No. 4, 2007

Ab initio study of ordering degree in Fe_3Si doped with Mn*

A. GO[1**], M. PUGACZOWA-MICHALSKA[2], L. DOBRZYŃSKI[1,3]

[1]Institute of Experimental Physics, University of Białystok, 15-424 Białystok, Poland

[2]Institute of Molecular Physics, Polish Academy of Sciences, 60-179 Poznań, Poland

[3]The Soltan Institute for Nuclear Studies, 05-400 Otwock-Świerk, Poland

Energetic stability of atomic exchange of sites between different sublattices in Fe_3Si, pure and doped with Mn, crystallizing in the DO_3-type structure is studied by *ab initio* calculations. A small chemical disorder between B and D sites preferred in Fe_3Si and $Fe_{2.875}Mn_{0.125}Si$ is in good agreement with the Mössbauer studies.

Key words: *iron alloy; electronic structure; disordered alloy; local magnetic moment*

1. Introduction

Fe_3Si alloy doped with 3d transition metals (Mn and Cr) has been investigated by *ab initio* calculations [1–3]. The object of the present study is Fe_3Si which has the DO_3-type structure. In this structure, there are two nonequivalent sublattices (A, C) and B, which are occupied by Fe atoms, whereas all D sites are taken by Si. However, some Mössbauer measurements indicate that a small disorder exists between B and D sites [4, 5]. This means that some Si atoms occupy B sites and small fraction of Fe is also located at D sites.

In $Fe_{3-x}Mn_xSi$ alloy, Mössbauer measurements indicated an additional partial disorder between (A, C) and D sites [6]. Because of some discrepancies between theoretical and experimental results, it is attractive to go a little further and perform calculations in which experimentally found disorder would be taken into account.

---

*Presented at the Conference of the Scientific Network "New Materials for Magnetoelectronics – MAG-EL-MAT 2007", Będlewo near Poznań, 7–10 May 2007.

**Corresponding author, e-mail: annago@alpha.uwb.edu.pl

2. Details of calculations

Electronic structures of Fe_3Si and $Fe_{2.875}Mn_{0.125}Si$ have been studied within the framework of the local spin-density approximation, using the self-consistent spin -polarized tight-binding linear muffin–tin orbital method in the atomic sphere approximation [7]. The exchange correlation potential was taken like in [1] with the non -local exchange correlation correction [8]. Similar to [1] the supercell with 32 atoms was used here. The calculations were carried out for ordered structure (all Si occupied only D sites) as well as for disordered ones in which one of Si atom occupied either B or (A, C) sites and thereby one of Fe atoms was located at D site. Mn impurity atom was allowed to occupy only B or (A, C) sites. Experimental values of lattice constants were used [9].

3. Results and discussion

3.1. Properties of Fe_3Si

We studied electronic structure of Fe_3Si assuming three different arrangements of atoms in the supercell: Fe atoms are located at (A, C) and B sites only (1); "disorder B–D": one of the Si atom occupies B site and one of the Fe atoms locates at D site (2); "disorder (A, C)–D": B sites are occupied by Fe only, one of D sites is occupied by Fe atom, other D sites are occupied by Si, and one of (A, C) position is occupied by Si atom (3). Table 1 shows the results of total energy calculations. Our calculations confirmed experimental findings that small disorder between B and D sublattices may occur in Fe_3Si.

Table 1. Difference between total energy of the considered configuration and minimum total energy (ΔE [mRy/atom]); total [μ_B /f.u.]) and local magnetic moments [μ_B/atom] in Fe_3Si

Fe_3Si	ΔE	μ_{total}	$\mu_{Fe(A, C)}$	$\mu_{Fe(B)}$	$\mu_{Fe(D)}$	$\mu_{Si(D)}$	$\mu_{Si(B)}$	$\mu_{Si(A, C)}$
Ordered	5	5.34	1.42	2.62	–	–0.12	–	–
Disorder B–D	0	5.27	1.39	2.61	2.66	–0.13	–0.11	–
Disorder (A, C)–D	78	5.81	1.66	2.47	2.57	–0.11	–	–0.09

Minimum of the total energy was obtained for the supercell arrangement, where one Si atom is located in B site and thereby one Fe atom occupies D site. Such a disorder causes a decrease of total energy by 5 mRy/atom in comparison with the ordered structure. (A, C)–D disorder is energetically unprofitable and causes an increase of total energy by at least 78 mRy/atom. In B–D disordered state the total magnetic moment diminishes to $5.27\mu_B$ which is closer to the experimental value [10] than the total

moment calculated for perfectly ordered phase. Furthermore, values of moments are generally slightly lower than in the ordered state. A small negative magnetic moment is induced on Si atom as postulated earlier in [5, 11]. Magnetic moment of Si(A, C) is lower than that of Si(B). This is connected with a smaller average magnetic moment of local environment of (A, C) site than the one of B site.

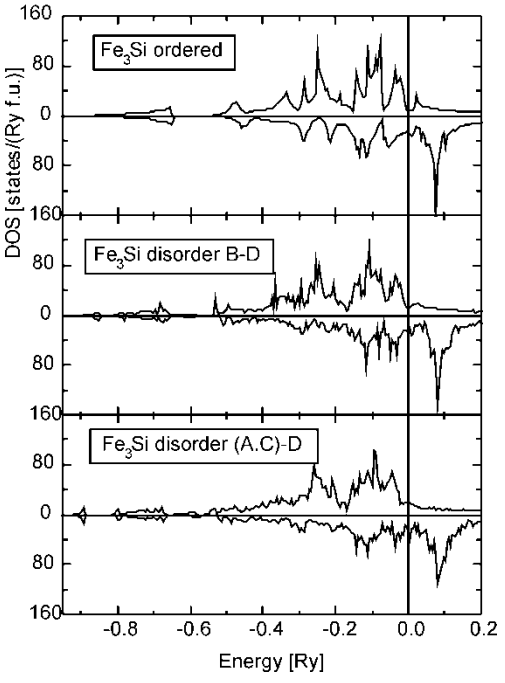

Fig. 1. The spin-projected total densities of states for Fe_3Si in ordered, B–D and (A, C)–D disordered configurations

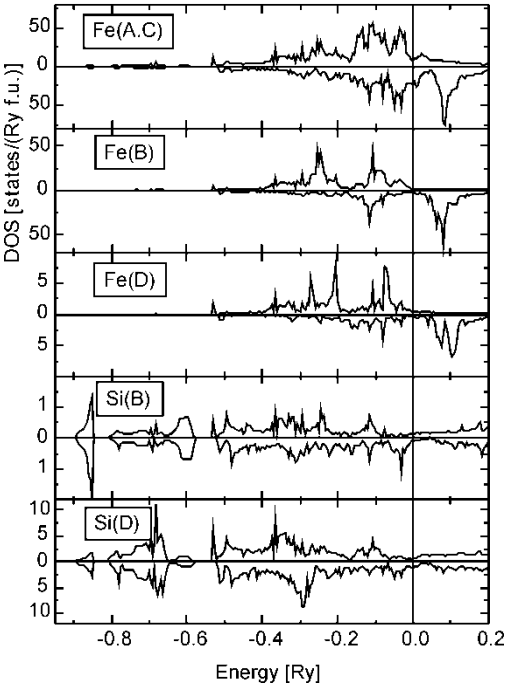

Fig. 2. The spin-projected local densities of states for Fe_3Si in B–D disordered configuration

Total densities of states (DOS) in Fe_3Si for three different arrangements of the supercell are presented in Fig. 1. The Fermi level (FL) is taken as the origin of the energy axis. In the perfectly ordered phase, the DOS is divided into two parts. The lower part (below –0.64 Ry) is mainly built by 3s states of Si with a small admixture of s, p states of Fe. In the upper part (above –0.53 Ry) 3d states of Fe overlap with 3p Si states. In region between –0.81 Ry and –0.57 Ry s and p states overlap. Above –0.54 Ry the total DOS is predominantly built of 3d states of Fe. The two gaps in the DOS of Fe_3Si, also visible at the (A, C)–D type of disorder (Fig. 1), are shifted towards lower energy region ([–0.88 Ry; –0.82 Ry], [–0.65 Ry; –0.64 Ry]). The disorder causes a decrease of the maximum peak in minority subband above FL thereby reducing a number of hole states in this energy range.

Figure 2 presents the DOS of Fe and Si atoms occupying different crystallographic positions in Fe_3Si with B–D type disordered case. The shape of the DOS of Fe(B) is similar to DOS of *bcc* iron [12] because of the same nearest neighbour shell. Although Fe(D) has the same first nearest neighbours as Fe(B), its DOS differs because their second and third shells are different. However, the magnetic moment of Fe(D) is only slightly higher than the Fe(B) moment. Below the FL two main peaks in majority subband of Fe(D) exhibit pronounced splitting caused by crystal field. In the case of Fe(D) its d orbitals are more strongly affected than d orbitals of Fe(B). The additional crystal field splitting occurs in the DOS of Fe(D) when the orbitals are located in a region of high electron density. The nearest neighbourhood of Fe(A, C) in Fe_3Si is formed by Fe and Si atoms. This is reflected in a much more complex DOS. For higher energies (above –0.54 Ry), the densities of states of Si(B) and Si(D) show similar shape formed mainly by p states but for s states (below –0.57 Ry) strong differences are visible. It is observed that s states of Si(B) are shifted towards lower energies.

3.2. Properties of $Fe_{2.875}Mn_{0.125}Si$

The results of calculations for $Fe_{2.875}Mn_{0.125}Si$ are summarized in Table 2. The lowest energy is obtained for the atomic configuration where Mn occupies B site and a small disorder between B and D sublattices exists. All other investigated configurations have total energies higher by at least 8 mRy/atom. Position exchange of Fe and Si causes a decrease of total magnetic moment with respect to the ordered phase. This may explain the experimentally observed situation [13]. B–D disorder causes simultaneously a slight increase of Fe(B) moment and a decrease of Fe(A, C) moment. The calculations show that the spin of Mn(A, C) surrounded by 5 Fe and 3 Si atoms would reverse in (A, C)–D disordered case. Migration of Si to the B site causes an increase of the absolute value of its local moment to $-0.16\mu_B$ whereas Si(A, C) has 25% smaller spin polarisation than Si(D). For all considered atomic arrangements of the supercell, Si(D) has a small moment ($-0.12\mu_B$).

Table 2. The difference between total energy of the considered configuration and minimum total energy (ΔE [mRy/atom]); the total [μ_B /f.u.]) and local magnetic moments [μ_B/atom] in $Fe_{2.875}Mn_{0.125}Si$

$Fe_{2.875}Mn_{0.125}Si$		ΔE	μ_{total}	$\mu_{Fe(A, C)}$	$\mu_{Fe(B)}$	$\mu_{Fe(D)}$	μ_{Mn}	$\mu_{Si(D)}$	$\mu_{Si(B)}$	$\mu_{Si(A, C)}$
Mn (B)	ordered	8 mRy	5.25	1.38	2.61	–	2.53	–0.12	–	–
	disorder B–D	0	5.17	1.35	2.63	2.65	2.44	–0.12	–0.16	–
	disorder (A, C)–D	74 mRy	5.67	1.59	2.50	2.56	2.31	–0.12	–	–0.09
Mn (A, C)	ordered	29 mRy	5.39	1.45	2.60	–	1.50	–0.12	–	–
	disorder B–D	17 mRy	5.29	1.40	2.60	2.59	1.60	–0.12	–0.16	–
	disorder (A, C)–D	23 mRy	5.32	1.61	2.45	2.51	–1.35	–0.10	–	–0.09

4. Conclusions

Ab initio studies of total energy indicate possibility of a B–D disorder in Fe_3Si. This explains why in the Mössbauer studies of Fe_3Si [4], a hyperfine field on Fe(D) is observed. The magnetic moments of Fe(B) and Fe(D) turn out to be not much different. Doping parent Fe_3Si with Mn does not change ordering. In the most likely structure of Fe_3Si with B–D type disordering, the low-energy s band splits into two bands. Considered disorder between D and other sublattices turns out not to change substantially neither total nor local magnetic moments.

References

[1] PUGACZOWA-MICHALSKA M., GO A., DOBRZYŃSKI L., LIPIŃSKI S., J. Magn. Magn. Mater., 256 (2003), 46.
[2] GO A., PUGACZOWA–MICHALSKA M., DOBRZYŃSKI L., J. Magn. Magn. Mater., 272–276 (2004), e217.
[3] GO A., PUGACZOWA-MICHALSKA M., DOBRZYŃSKI L., Eur. Phys. J. B, 59 (2007), 1
[4] KUMARAN J.T.T., BANSAL C., Solid State Commun., 69 (1989), 779.
[5] DOBRZYŃSKI L., J. Phys.: Cond. Matter, 7 (1995), 1373.
[6] AL-NAWASHI G.A., MAHMOOD S.H., LEHLOCH A.F.D., SALEH A.S., Physica B, 321 (2002), 167.
[7] ANDERSEN O.K., JEPSEN O., Phys. Rev. Lett., 53 (1984), 2571.
[8] HU C.D., LANGRETH D.C., Phys. Scripta, 32 (1985), 391.
[9] NICULESCU V., RAJ K., BURCH T.J., BUDNICK J.I., Phys. Rev. B, 13 (1976), 3167.
[10] YOON S., BOOTH J.G., Phys. Lett., 48A (1974), 381.
[11] MOSS J., BROWN P.J., J. Phys. F: Met. Phys., 2 (1972), 358.
[12] KÜBLER J., *Theory of Itinerant Electron Magnetism*, Clarendon Press, Oxford, 2000, p. 235.
[13] HINES W.A., MENOTTI A.H., BUDNICK J.I., BURCH T.J., LITRENTA T., NICULESCU V., RAJ K., Phys. Rev. B, 13 (1976), 4060.

Received 2 May 2007
Revised 1 August 2007

Materials Science-Poland, Vol. 25, No. 4, 2007

Electronic properties of LaNiIn doped with hydrogen*

Ł. WASYLKOWICZ[1], A. JEZIERSKI[2**], A. SZYTUŁA[3], B. PENC[3]

[1]Faculty of Technical University, Poznań University of Technology, Nieszawska 17, 60-965 Poznań, Poland

[2]Institute of Molecular Physics, Polish Academy of Sciences, Smoluchowskiego 17, 60-179 Poznań, Poland

[3]M. Smoluchowski Institute of Physics, Jagiellonian University, Reymonta 4, 30-059 Cracow, Poland

Electronic properties of RNiInH (R = La,Ce,Nd) intermetallic hydrides were recently studied both experimentally and theoretically. In the present work, we study the influence of hydrogen on the electronic structure of LaNiIn. The electronic structure is calculated by Augmented Spin Wave (ASW) and Tight Binding Linear Muffin Tin Orbital methods within the spin density approximation. The doped hydrogen atoms modify the band structure near the Fermi level. The density of states at the Fermi level decreases with increasing hydrogen concentration but the compounds have metallic character.

Key words: *hydrides; electronic structure; LaNiIn hydride; LMTO; ASW*

1. Introduction

Metal hybrids alloys are the most promising materials for hydrogen storage because of their hydrogen storage capacity. In the group of RTX intermetallics (R – rare earth metal, T – transition metal and X – p electron element), LaNiIn alloy doped with hydrogen has been studied experimentally and theoretically [1–7].

LaNiIn crystallizes in the ZrNiAl-type structure (space group No. 189) [7]. La atoms are located at 3g position: x, 0, 0.5; 0, x, 0.5; $-x$, x, 0.5 for x = 0.593 and x = 0.6035. In atoms occupy 3f positions: x, 0, 0; 0, x, 0; $-x$, $-x$, 0 for x = 0.242 and x = 0.2437. Ni is located at two positions; 1b: 0, 0, 0.5 and 2c: 1/3, 2/3, 0 and 0, 2/3, 1/3. Hydrogen can be distributed in 4h position (depending on the concentration) 1/3, 2/3, z; 1/3, 2/3, $-z$; 2/3, 1/3, z; 2/3, 1/3, $-z$ for z = 0.659.

Recently, Jezierski at al. [6] studied electronic structure of LaNiIn and $LaNiInH_x$ (x = 1/3, 2/3, 1) using the XPS and *ab initio* LMTO [9] methods. The theoretical re-

---

*Presented at the Conference of the Scientific Network "New Materials for Magnetoelectronics – MAG-EL-MAT 2007", Będlewo near Poznań, 7–10 May 2007.

**Corresponding author, e-mail: andrzej.jezierski@ifmpan.poznan.pl

sults were compared with X-ray photoemission spectra (XPS). In this work, we report the influence of hydrogen on the electronic structure of $LaNiInH_x$ compounds by using the ASW [8] and LMTO [9] methods.

2. Method of calculation

Electronic properties of $LaNiInH_x$ compounds were calculated by *ab initio* augmented spherical wave (ASW) [8] and tight-binding linear muffin-tin orbital (TB LMTO) [9] methods within the framework of the local spin density approximation (LSDA). The exchange correlation potential was assumed in the form proposed by Barth and Hedin [10]. The scalar-relativistic approximation for band electrons and the fully-relativistic approximation of the frozen core electrons were used in both methods. The self-consistent calculations were performed in the atomic spheres approximation (ASA) for 459 (LMTO) and 469 (ASW) k-points in the irreducible Brillouin zone. The *ab initio* calculations of the band structure were performed for the experimental values of the lattice parameters [5]. For the ordered LaNiIn compounds we assumed a = 7.5906 Å and c = 4.05 Å. For the doped hydrogen compound, the calculations were made for a = 7.381 Å and c = 4.6489 Å [5]. The hydrogen atoms can occupy four positions (see Introduction) in ZrNiAl type structure. The electronic structures were calculated for one, two, three and four hydrogen atoms located in 4h position. For the given configuration we obtained the total and partial densities of states. Particularly, we pay attention to the change of the density of states at the Fermi level as well as the contribution of d bands to the density of states near the Fermi level.

3. Results and discussion

The total densities of states calculated by LMTO (solid line) and ASW (broken line) methods for LaNiIn and $LaNiInH_4$ alloys are presented in Fig. 1.

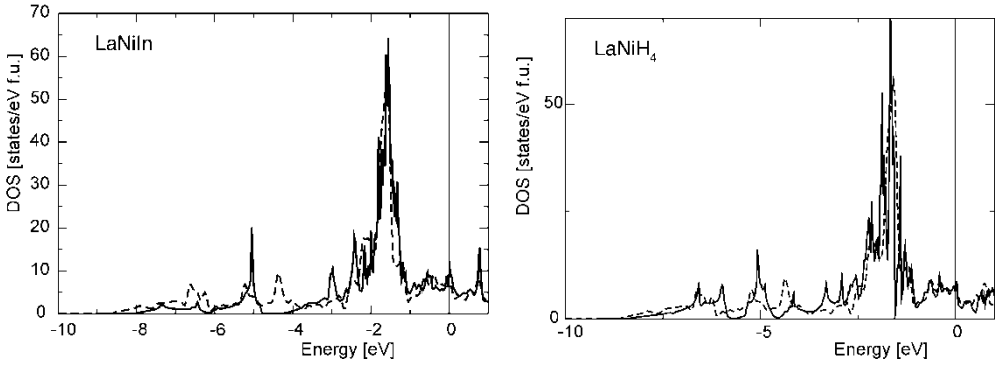

Fig. 1. Total density of states (TDOS) for LaNiIn and $LaNiH_4$ obtained by LMTO (solid line) and ASW (broken line) methods. The Fermi energy is located at E = 0 eV

We observed only a small modification of the shape of the density of states. The density of states at the Fermi level for LaNiIn is 8.14 and 10.48 states/eV f.u. for LMTO and ASW, respectively. In the case of LaNiH4 $N(E_F)$ = 6.85 and 6.76 states/eV f.u. for LMTO and ASW methods, respectively.

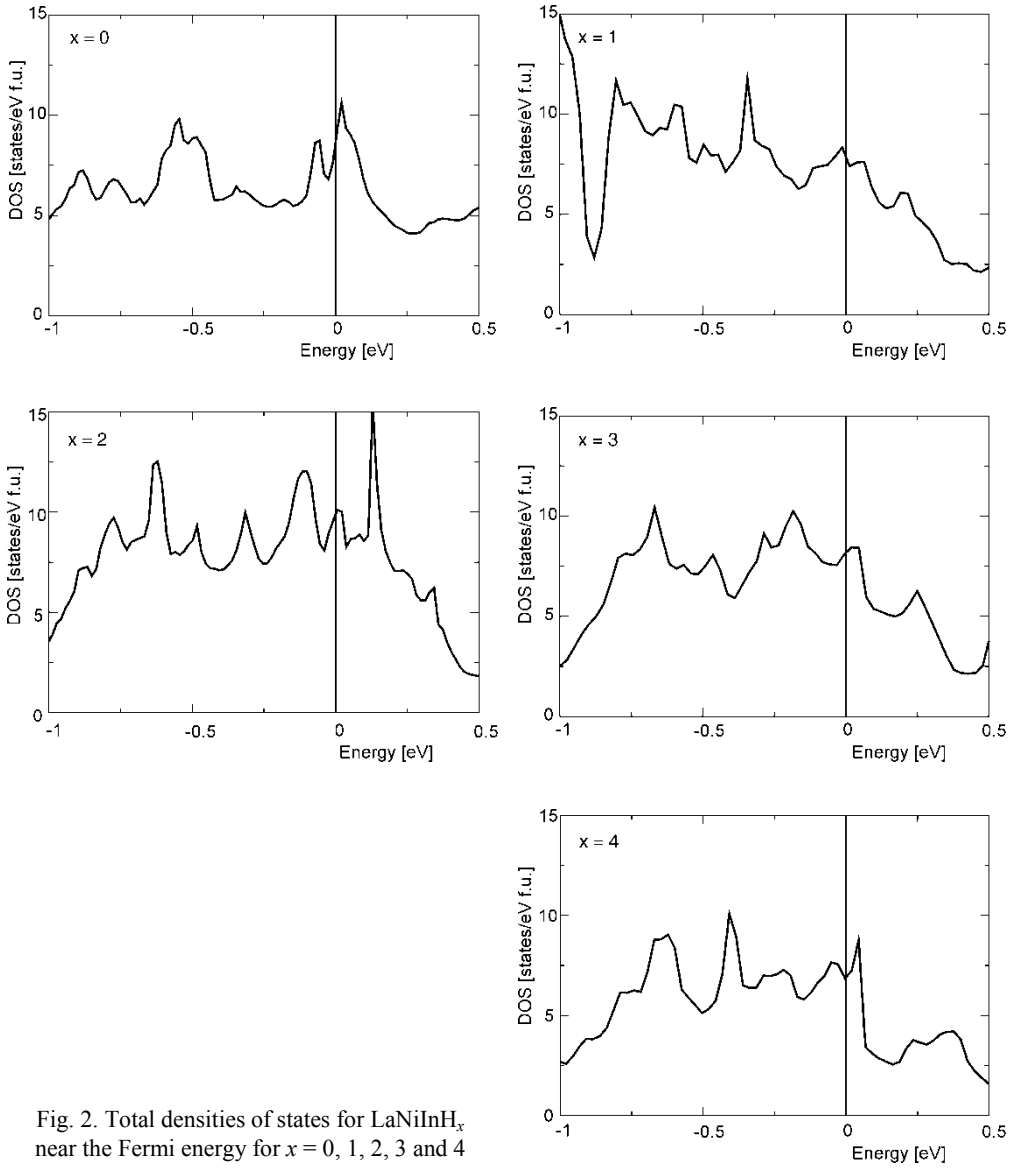

Fig. 2. Total densities of states for $LaNiInH_x$ near the Fermi energy for x = 0, 1, 2, 3 and 4

In Figure 2, we plotted total densities of states near the Fermi level for x = 0, 1, 2, 3 and 4 obtained by the LMTO method. We observe a strong modification of DOS for $-1.0 < E < 0.5$ eV. This change of the density of states is connected to hydrogen atoms

which change the local environment and symmetry of Ni and La atoms. The main contribution to the densities of states near the Fermi energy come from d states of La, Ni and In atoms. The local contributions from La(4d), Ni(3d) and In(3d) to the DOS near the Fermi level are plotted in Fig. 3 for various numbers of hydrogen atoms in the cell.

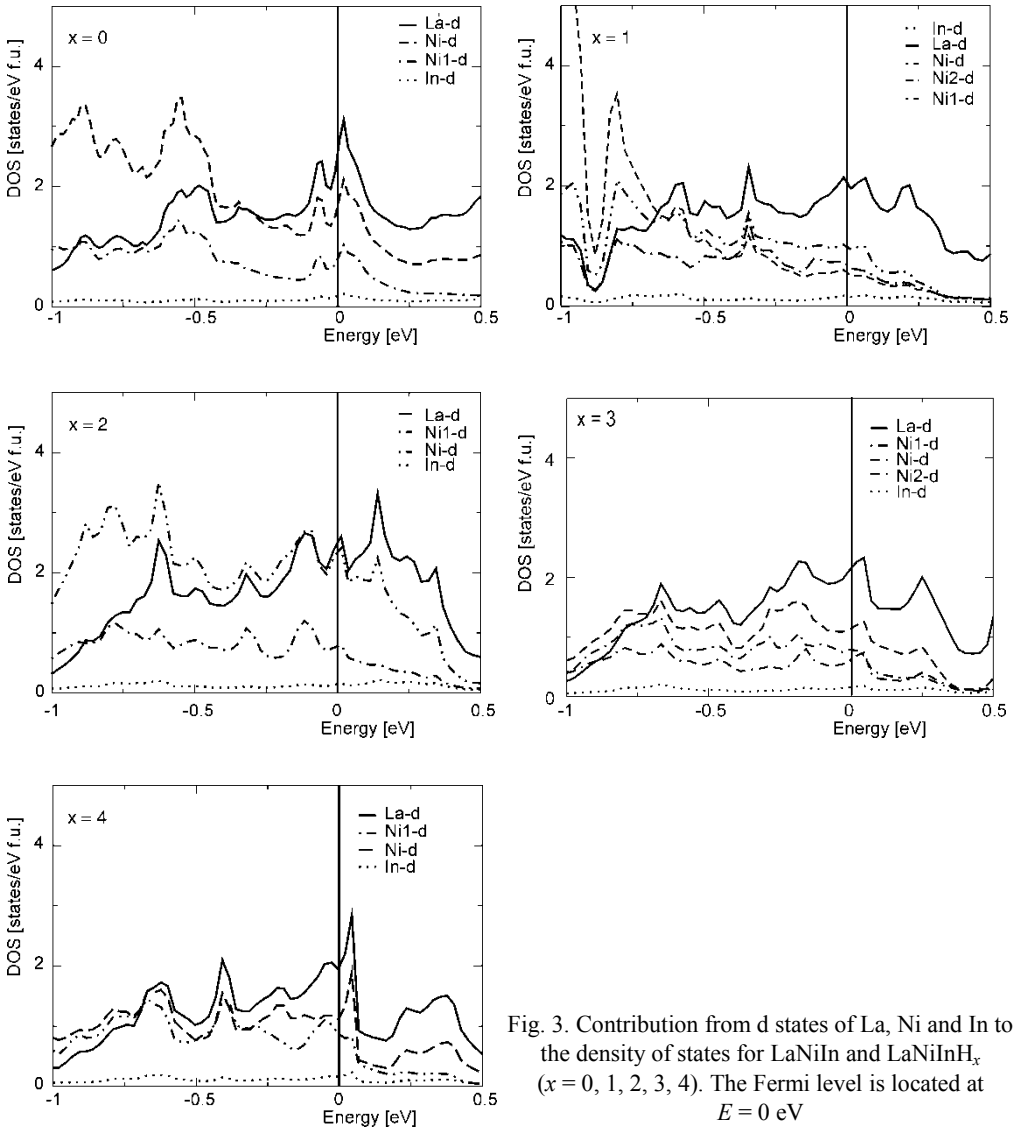

Fig. 3. Contribution from d states of La, Ni and In to the density of states for LaNiIn and $LaNiInH_x$ ($x = 0, 1, 2, 3, 4$). The Fermi level is located at $E = 0$ eV

Hydrogen atoms modify the shape of d states of La and Ni atoms. The substitution of hydrogen in LaNiIn leads to a change of the local symmetry around Ni. This effect gives two or three types of nickel atoms in the unit cell. The ASW and LMTO calculations for pure LaNiIn had shown that the valence band had well localized Ni 3d elec-

trons band near –1.6 eV. The peak located between –5 to –7 eV is due to In 4d electrons. The La 5d bands are located in the energy range from $E = -3$ to 1 eV. The band calculations suggest metallic character of LaNiIn alloys doped with hydrogen.

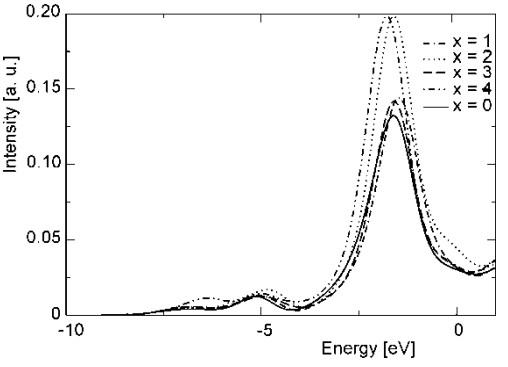

Fig. 4. Theoretical photoemission spectra for $LaNiInH_x$ ($x = 0, 1, 2, 3, 4$). The Fermi energy is located at $E = 0$ eV

In Figure 4, we present the calculated theoretical photoemission spectra of $LaNiInH_x$ ($x = 0, 1, 2, 3, 4$) obtained from the calculated partial density of states convoluted by Gaussian line with a half-width equal to 0.4 eV and scaled using proper photoelectric cross section for partial states [11] for various numbers of hydrogen atoms. We observe a small modification of the main peak with the change of the hydrogen concentration. The peak located near $E = 1.6$ eV was also observed in the XPS measurement [6].

4. Conclusions

The influence of doped hydrogen on the electronic density of states of $LaNiInH_x$ has been investigated. The shapes of the total densities of states obtained by LMTO and ASW methods are similar. In both methods, we observed a modification of the electronic density of states during the increase of the concentration of the hydrogen. The density of states at the Fermi level decreases when the number of hydrogen atoms increases.

Acknowledgement

This work was supported in part (A. J.) by the Polish National Committee for Scientific Research under the contract No. PBZ-KBN-117/T08/07.

References

[1] BYLYK I.I., YARTYS V.A., DENYS R.V., KALYCHAK YA.M., HARRIS I.R., J. Alloys Comp., 284 (1999), 256.
[2] VAJEESTON P., RAVINDRAN P., VIDYA R., KJEKSHUS A., FJELLVAG H., YARTYS V.A., Phys. Rev. B, 67 (2003), 014101.
[3] SATO M., DENYS R.V., RIABOV A.B., YARTYS V.A., J. Alloys Comp., 397 (2005), 99.

[4] DENYS R.V., RIABOV A.B., YARTYS V.A., HAUBACK B.C., BRINKSS H.W., J. Alloys Comp., 356 (2003), 65.
[5] YARTYS V.A., DENYS R.V., HAUBACH B.C., FJELLVAG H., BULYK I.I., RIABOV R.V., KALYCHAK Y.M., J. Alloys Compd., 330 (2002), 132.
[6] JEZIERSKI A., PENC B., SZYTUŁA A., J. Alloys Comp., 404 (2005), 204.
[7] FERRO R., MARAZZA R., RAMBALDI G., Z. Metall., 65 (1974), 37.
[8] EYERT V., *The Augmented Spherical Wave Method, Lecture Notes in Physics*, Vol. 719, Springer, Berlin, 2007.
[9] ANDERSEN O.K., JEPSEN O., Phys. Rev. Lett., 53 (1984), 2571.
[10] VON BARTH U., HEDIN L., J. Phys. C5 (1972), 1629.
[11] YEH J.J., LINDAU I., *Atomic Data. Nuclear Data Tables*, 32 (1985), 1.

Received 7 May 2007
Revised 15 August 2007

Materials Science-Poland, Vol. 25, No. 4, 2007

Current-induced switching of a single-molecule magnet with an arbitrary oriented easy axis*

M. MISIORNY[1], J. BARNAŚ[1, 2**]

[1]Department of Physics, A. Mickiewicz University, Umultowska 85, 61-614 Poznań, Poland

[2]Institute of Molecular Physics, Polish Academy of Sciences,
Smoluchowskiego 17, 60-179 Poznań, Poland

The main objective of this work was to investigate theoretically how tilting of an easy axis of a single-molecule magnet (SMM) from the orientation collinear with magnetic moments of the leads affects the switching process induced by current flowing through the system. We consider a model system that consists of a SMM embedded in the nonmagnetic barrier of a magnetic tunnel junction. The anisotropy axis of the SMM forms an arbitrary angle with magnetic moments of the leads (the latter ones are assumed to be collinear). The reversal of the SMM's spin takes place due to exchange interaction between the molecule and electrons tunnelling through the barrier. The current flowing through the system as well as the average *z*-component of the SMM's spin are calculated in the second-order perturbation description (Fermi golden rule).

Key words: *single-molecular magnet; magnetic switching; spin-polarized current*

1. Introduction

Single-molecule magnets (SMMs) [1] draw attention as potential candidates for devices which can combine conventional electronics with spintronics [2]. Characterized by a relatively large energy barrier the spin reversal of the molecule, an SMM can be used at low temperatures as a molecular memory cell [3]. For these reasons, transport through SMMs is of current interest [3–5]. It has been shown that the molecule spin can be reversed by a spin current (also in the absence of external magnetic field) [6, 7]. The phenomenon of current-induced spin switching is of great importance for future applications. Furthermore, it is now possible to investigate experimentally transport through a single molecule [8–10]. However, using present-day experimental techniques, one can hardly control the orientation of the molecule easy axis [11].

---

*Presented at the Conference of the Scientific Network "New Materials for Magnetoelectronics – MAG-EL-MAT 2007", Będlewo near Poznań, 7–10 May 2007.

**Corresponding autor, e-mail: barnas@amu.edu.pl

The main objective of this paper was to investigate theoretically how tilting of the easy axis of a SMM from the orientation collinear with magnetic moments of the electrodes (leads) affects the switching process and current flowing through the system.

2. Model

The system under consideration consists of a SMM embedded in a nonmagnetic barrier between two ferromagnetic electrodes. Electrons tunnelling through the barrier can interact *via* exchange coupling with the SMM, which may result in magnetic switching of the molecule. Furthermore, we assume that the spin number S of the SMM does not change when current flows through the system, i.e. the charge state of the molecule is fixed. In the case considered here, the anisotropy axis of the molecule (used as the global quantization axis z) can form an arbitrary angle φ with magnetic moments of the leads. To simplify the following description, we neglect the influence of exchange interaction with the leads on the ground state of the molecule. Such an influence, however, can be included *via* an effective exchange field.

The full Hamiltonian of the system reads:

$$H = H_{\mathrm{SMM}} + H_L + H_R + H_T$$

The first term describes the free SMM and takes the form $H_{\mathrm{SMM}} = -DS_z^2$, where S_z is the z component of the spin operator, and D is the uniaxial anisotropy constant. The next two terms of the Hamiltonian H correspond to the two ferromagnetic electrodes, $H_q = \sum_{\mathbf{k}\alpha} \varepsilon^q_{\mathbf{k}\alpha} a^{q+}_{\mathbf{k}\alpha} a^q_{\mathbf{k}\alpha}$ for $q = L$ (left) and $q = R$ (right). The electrodes are represented by a band of non-interacting electrons with the energy dispersion $\varepsilon^q_{\mathbf{k}\alpha}$, where $\mathbf{k}$ denotes the wave vector, α is the electron spin index (+ for spin majority and – for spin minority electrons), and $a^{q+}_{\mathbf{k}\alpha}$ $\left(a^q_{\mathbf{k}\alpha}\right)$ is the relevant creation (anihilation) operator. Finally, the last term of the Hamiltonian H stands for the tunnelling processes and is given by the Appelbaum Hamiltonian [12] rotated by the angle φ around the axis $y' = y$ (see Fig. 1)

$$\begin{aligned} H_T = & \frac{1}{2}\sum_{q,q'}\sum_{\mathbf{k}\mathbf{k}'\alpha\beta} \frac{J_{q,q'}}{\sqrt{N_q N_{q'}}} \boldsymbol{\sigma}_{\alpha\beta}\cdot\mathbf{S} \\ & \times\left\{\cos^2\frac{\varphi}{2}\, a^{q+}_{\mathbf{k}\alpha} a^{q'}_{\mathbf{k}'\beta} + \sin^2\frac{\varphi}{2}\, a^{q+}_{\mathbf{k}\bar{\alpha}} a^{q'}_{\mathbf{k}'\bar{\beta}} - \frac{1}{2}\sin\varphi\left(a^{q+}_{\mathbf{k}\alpha} a^{q'}_{\mathbf{k}'\bar{\beta}} + a^{q+}_{\mathbf{k}\bar{\alpha}} a^{q'}_{\mathbf{k}'\beta}\right)\right\} \\ & + \sum_{\mathbf{k}\mathbf{k}'\alpha}\frac{T_d}{\sqrt{N_q N_{q'}}} a^{L+}_{\mathbf{k}\alpha} a^R_{\mathbf{k}'\alpha} + \mathrm{H.c.} \end{aligned} \qquad (1)$$

where $\boldsymbol{\sigma} = (\sigma^x, \sigma^y, \sigma^z)$ are the Pauli matrices, $\mathbf{S}$ is the SMM's spin operator, and $\bar{\alpha} = -\alpha$. The first term in the above equation describes exchange interaction of the SMM and electrons in the leads, with $J_{q,q'}$ denoting the relevant exchange parameter.

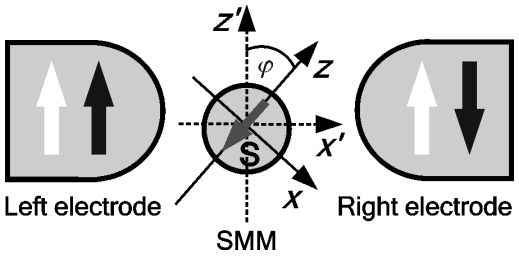

Fig. 1. Schematic picture of the system under consideration for two collinear configurations of the leads' magnetic moments: parallel (white arrows) and antiparallel (black arrows). The axis y (y') is normal to the x–z (x'-z') plane

For the sake of simplicity, we consider only symmetrical situation, where $J_{L,L} = J_{R,R} = J_{L,R} = J_{R,L} \equiv J$. The second term in Eq. (1) represents direct tunnelling between the leads, with T_d denoting the corresponding tunnelling parameter. We also assume that J and T_d are independent of energy and polarization of the leads. Finally, N_q ($q = L, R$) denotes the number of elementary cells in the q-th electrode.

3. Theoretical description

The electric current I flowing through the system is determined with the use of the Fermi golden rule [4, 6]. Up to the leading terms with respect to the coupling constants J and T_d, the current can be expressed by the formula

$$
\begin{aligned}
I = {} & \frac{2\pi}{\hbar} e^2 \left[\left|T_d\right|^2 + \left|J\right|^2 \cos^2\varphi \left\langle S_z^2 \right\rangle \right] \left(D_\uparrow^L D_\uparrow^R + D_\downarrow^L D_\downarrow^R \right) V \\
& + \frac{2\pi}{\hbar} e \left|J\right|^2 \sum_m P_m \sum_{\eta=+,-} A_\eta(m) \left\{ \eta \left[D_\uparrow^L D_\downarrow^R \cos^4\frac{\varphi}{2} + D_\downarrow^L D_\uparrow^R \sin^4\frac{\varphi}{2} \right] \right. \\
& \times \zeta\left(D(\eta 2m+1) + \eta eV \right) - \eta \left[D_\uparrow^L D_\downarrow^R \sin^4\frac{\varphi}{2} + D_\downarrow^L D_\uparrow^R \cos^4\frac{\varphi}{2} \right] \zeta\left(D(\eta 2m+1) - \eta eV \right) \\
& \left. + \frac{\sin^2\varphi}{4} \left(D_\uparrow^L D_\uparrow^R + D_\downarrow^L D_\downarrow^R \right) \left[\zeta\left(D(\eta 2m+1) + \eta eV \right) + \zeta\left(D(\eta 2m+1) - \eta eV \right) \right] \right\}
\end{aligned}
\tag{2}
$$

where e is the electron charge (for simplicity assumed $e > 0$, so the current is positive for electrons tunnelling from the left to right). In the above equation D_σ^q is the density of states (DOS) at the Fermi level in the q-th electrode for spin σ, and $\left\langle S_z^2 \right\rangle = \sum_m m^2 P_m$, where P_m denotes the probability of finding the SMM in the spin state $\left|m\right\rangle$. The voltage V is defined as the difference of the electrochemical potentials of the leads, $eV = \mu_L - \mu_R$. Finally, we introduced: $A_\pm(m) = S(S+1) - m(m \pm 1)$ and $\zeta(\varepsilon) = \varepsilon[1 - \exp(-\varepsilon\beta)]^{-1}$ with $\beta^{-1} = k_B T$.

To compute numerically the current I from Eq. (2), one needs to know the probabilities P_m. To determine them, the SMM's spin is assumed to be saturated in the initial state $|-S\rangle$, and then voltage growing linearly in time is applied [6]. Since the reversal process occurs through all the consecutive intermediate spin states, the probabilities P_m can be found by solving the set of relevant master equations,

$$\begin{cases} c\dfrac{dP_m}{dV} = \displaystyle\sum_{l=-S}^{S}\left\{\gamma_l^- \delta_{l,m+1} + \gamma_l^+ \delta_{l,m-1} - \left(\gamma_l^- + \gamma_l^+\right)\delta_{l,m}\right\} P_l \\ c\dfrac{dP_{\pm S}}{dV} = -\gamma_{\pm S}^{\mp} P_{\pm S} + \gamma_{\pm S\mp 1}^{\pm} P_{\pm S\mp 1} \end{cases} \tag{3}$$

for $-S < m < S$, where $c = V/t$ is the rate at which the voltage is increased. The parameters $\gamma_m^{\pm}$ describe the rates at which the spin z-component (m) is increased/decreased by one. These tunnelling rates have been calculated from the Fermi golden rule and have the form,

$$\begin{aligned} \gamma_m^{\pm} = {} & \frac{2\pi}{\hbar}|J|^2 A_{\pm}(m) \\ & \times\Bigg\{\cos^4\frac{\varphi}{2}\left[D_\uparrow^L D_\downarrow^R \zeta\left(D(\pm 2m+1) \pm eV\right) + D_\downarrow^L D_\uparrow^R \zeta\left(D(\pm 2m+1) \mp eV\right)\right] \\ & + \sin^4\frac{\varphi}{2}\left[D_\uparrow^L D_\downarrow^R \zeta\left(D(\pm 2m+1) \mp eV\right) + D_\downarrow^L D_\uparrow^R \zeta\left(D(\pm 2m+1) \pm eV\right)\right] \\ & + \frac{\sin^2\varphi}{4}\left(D_\uparrow^L D_\uparrow^R + D_\downarrow^L D_\downarrow^R\right)\left[\zeta\left(D(\pm 2m+1) + eV\right) + \zeta\left(D(\pm 2m+1) - eV\right)\right] \\ & + \Bigg[\left(\sin^4\frac{\varphi}{2} + \cos^4\frac{\varphi}{2}\right)\left(D_\uparrow^L D_\downarrow^L + D_\uparrow^R D_\downarrow^R\right) \\ & + \frac{\sin^2\varphi}{4}\left(D_\uparrow^{L2} + D_\downarrow^{L2} + D_\uparrow^{R2} + D_\downarrow^{R2}\right)\Bigg]\zeta\left(D(\pm 2m+1)\right)\Bigg\} \end{aligned} \tag{4}$$

4. Numerical results and discussion

Numerical results have been obtained for the molecule Fe_8 [1, 13] corresponding to the total spin $S = 10$, whose anisotropy constant D is 0.292 K. Apart from this, we assume $J \approx T_d \approx 100$ meV. Calculations have been performed for the temperature $T = 0.01$ K, which is below the molecule blocking temperature $T_B = 0.36$ K, and for $c = 10$ kV/s. It has been also assumed that both leads are made of the same metallic material characterized by the total DOS $D = D_+^q + D_-^q \approx 0.5$ per electronvolt and per

elementary cell, where $D^q_{+(-)}$ denotes the DOS of majority (minority) electrons in the q-th electrode. Furthermore, the q-th electrode is described by the polarization parameter P^q defined as $P^q = (D^q_+ - D^q_-)/(D^q_+ + D^q_-)$. The following discussion is limited to the case, where one electrode (the left one) is fully polarized, $P^L = 1$, whereas the polarization factor of the second electrode can vary from $P^R = 0$ (nonmagnetic) to $P^R = 1$ (half-metallic ferromagnet).

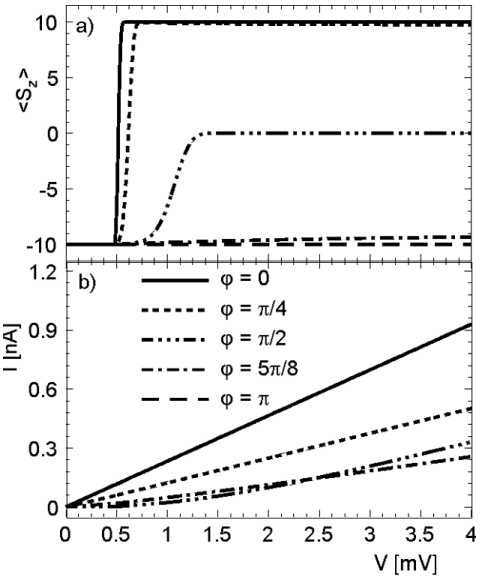

Fig. 2. The average value of the SMM spin $\langle S_z \rangle$ (a) and the current I flowing through the system (b) as functions of the voltage V, calculated for the parallel configuration of the magnetic moments of electrodes with $P^L = 1$ and $P^R = 0.3$

In Figure 2, we show the average value of the z-component of the SMM's spin, $\langle S_z \rangle = \sum_{m=-S}^{S} m P_m$, and the charge current I, calculated for several values of the angle φ and for parallel magnetic configuration of the leads. The case of $\varphi = 0$ ($\varphi = \pi$) corresponds to the situation when the initial SMM's spin is antiparallel (parallel) to the leads' spin moments. One can note that the influence of current on the spin of a molecule gradually disappears as the angle φ approaches π. For $\varphi < \pi/2$, the molecule's spin becomes switched from the state $|-S\rangle$ to the state $|S\rangle$. The switching time, however, becomes longer and longer as the angle φ approaches $\varphi = \pi/2$. At $\varphi = \pi/2$, which corresponds to the situation with the SMM's easy axis perpendicular to the leads' magnetic moments, different molecular spin states $|m\rangle$ become equally probable with increasing voltage, and therefore $\langle S_z \rangle \to 0$. This is a consequence of the fact that when the voltage exceeds the activation energy for the spin-flip process [6], the SMM undergoes transitions to upper and lower spin states with equal rates $\gamma^+_m = \gamma^-_m$ (see Eq. (4)).

When $\varphi > \pi/2$, the spin state of the molecule is only weakly modified by current, and remains strictly unchanged for $\varphi = \pi$. The absence of switching by positive current at large values of φ (for the assumed parameters) is consistent with the conclusion of

Ref. [6] where for collinear configurations and positive current only switching from $|-S\rangle$ to $|S\rangle$ states was allowed, whereas positive current had no influence on the state $|S\rangle$.

The SMM's spin can be reversed due to exchange interaction with tunnelling electrons. The latter flip their spins and hence add to or subtract some amount of angular momentum from the molecule. As the angle φ grows, the spin orientation of tunnelling electrons 'seen' by the molecule and consequently also the transition rates given by Eq. (4) change as well. Figure 2b shows the current flowing in the system as a function of the bias voltage. This current strongly depends on the orientation of the SMM's easy axis. This dependence is a consequence of the fact that the dominant contribution to current is due to the exchange term (first term in Eq. (1)), which is sensitive to the orientation of the SMM's spin. The curves for $\varphi = 0$ and $\varphi = \pi$ overlap (except for a small voltage range where the switching for $\varphi = 0$ takes place – not resolved in Fig. 2b).

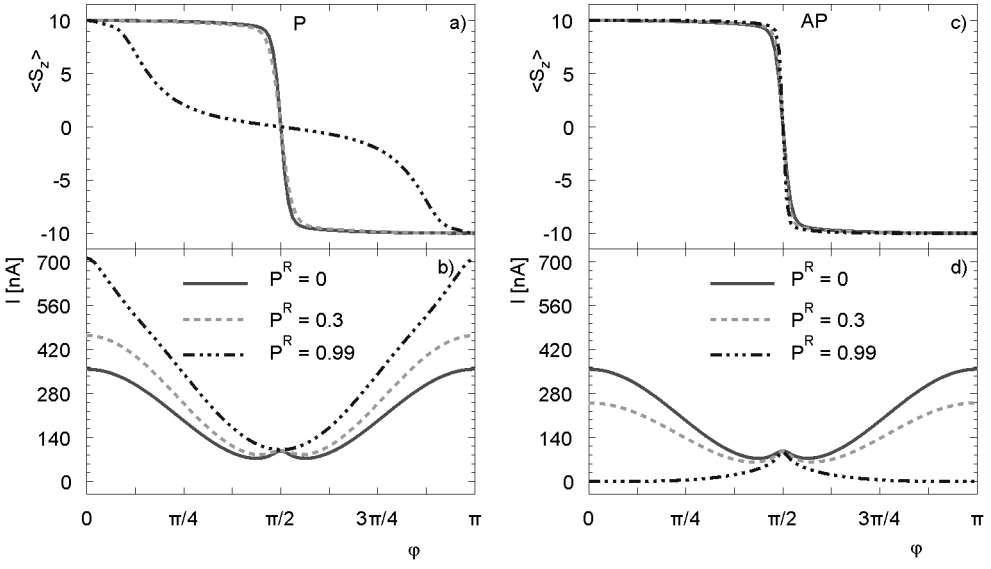

Fig. 3. The average value of the SMM's spin $\langle S_z \rangle$ (a), and the current I flowing through the system (b) as a function of the angle φ in the parallel (P) (a, b) and antiparallel (AP) (c, d) magnetic configurations for $V = 2$ mV and $P^L = 1$

Figure 3 presents the spin z-component $\langle S_z \rangle$ and the current I in both configurations of the leads' magnetic moments, plotted as a function of the angle φ and calculated for $V = 2$ mV. For $\varphi < \pi/2$, the spin switching takes place in both parallel and antiparallel magnetic configurations. Figure 3 also indicates that the current at $\varphi = \pi/2$ is independent of the magnetic configuration as well as on the polarization parameters of the leads.

In conclusion, we have shown that tilting the easy axis of a SMM from the collinear orientation relative to the leads' magnetic moments has a significant influence on

the reversal process of the molecule's spin, as well as on current flowing through the system.

Acknowledgements

This work was supported by funds from the Ministry of Science and Higher Education as a research project in 2006–2009. One of us (M.M.) also acknowledges support from the MAGELMAT network.

References

[1] GATTESCHI D., SESSOLI R., Angew. Chem. Int. Ed., 42 (2003), 268.
[2] JOACHIM C., GIMZEWSKI J.K., AVIRAM A., Nature, 408 (2000), 541.
[3] TIMM C., ELSTE F., Phys. Rev. B, 73 (2006), 235304.
[4] KIM G.-H., KIM T.-S., Phys. Rev. Lett., 92 (2004), 137203.
[5] ELSTE F., TIMM C., Phys. Rev. B, 73 (2006), 235305.
[6] MISIORNY M., BARNAŚ J., Phys. Rev. B, 75 (2007), 134425.
[7] ELSTE F., TIMM C., Phys. Rev. B, 75 (2007), 195341.
[8] HEERSCHE H.B., DE GROOT Z., FOLK J.A., VAN DER ZANT H.S.J., ROMEIKE C., WEGEWIJS M.R., ZOBBI L., BARRECA D., TONDELLO E., CORNIA A., Phys. Rev. Lett., 96 (2006), 206801.
[9] JO M.-H., GROSE J.E., BAHETI K., DESHMUKH M., SOKOL J.J., RUMBERGER E.M., HENDRICKSON D.N., LONG J.R., PARK H., RALPH D.C., Nano Lett., 6 (2006), 2014.
[10] HENDERSON J.J., RAMSEY C.M., DEL BARCO E., MISHRA A., CHRISTOU G., J. Appl. Phys., 101 (2007) 09E102.
[11] TIMM C., Phys. Rev. B, 76 (2007), 14421.
[12] APPELBAUM J., Phys. Rev., 17 (1966), 91
[13] WERNSDORFER W., SESSOLI R., Science, 284 (1999), 133.

Received 30 April 2007

Materials Science-Poland, Vol. 25, No. 4, 2007

Two-level quantum dot in the Aharonov–Bohm ring. Towards understanding "phase lapse"*

P. STEFAŃSKI**

Institute of Molecular Physics of the Polish Academy of Sciences,
Smoluchowskiego 17, 60-179 Poznań, Poland

It is shown theoretically that indirect interaction between two quantum dot levels can generate an anomalous phase shift for a system of the dot placed in one of the arms of the Aharonov–Bohm ring. The interaction between levels arises from the non-conservation of the orbital quantum number during the hopping process of electrons between the levels and leads. Such an unusual "phase lapse" behavior is observed experimentally and still lacks of proper theoretical description.

Key words: *quantum dot; Aharonov–Bohm ring; phase shift; phase lapse*

1. Introduction

The "phase lapse" is a phenomenon which is characterized by a sudden decay of the phase shift [1,2] measured for the quantum dot (QD) in Aharonov–Bohm (A–B) geometry, when the gate voltage shifts the dot energy levels with respect to chemical potential of the leads. Several theoretical attempts have been made (see for example [3, 4]) to describe this unusual feature but none of them seems to be satisfactory. In the present work the evolution of the phase shift is investigated for a model of two-level quantum dot placed in one of the arms of Aharonov–Bohm ring. The levels have different hybridization strengths to the leads; one is well coupled to the leads and conducting, and the second is sharp in energy scale and inactive in transport. The orbital quantum number is not conserved while hopping process of electrons occurs between the dot and the leads. As a consequence, both the levels are coupled to each other via the leads. It causes a considerable deviation from the usual electron wave phase shift behaviour which rises from zero to π when QD level crosses effective Fermi energy. In particular, a lapse of the phase appears. It corresponds well to recent experimental observations of the phase evolution for the QD in Aharonov–

---

*Presented at the Conference of the Scientific Network "New Materials for Magnetoelectronics – MAG-EL-MAT 2007", Będlewo near Poznań, 7–10 May 2007.

**E-mail: piotrs@ifmpan.poznan.pl

Bohm geometry in the limit of small electron number in the dot [2], when the transport through the dot has just been initiated.

2. Hamiltonian of the system

We consider a system composed of a quantum dot placed in one of the arms of Aharonov–Bohm ring (see the inset to Fig. 3 for the schematic picture). The Hamiltonian describing the system has the form:

$$H = \sum_{k,\sigma,\alpha=L,R} \varepsilon_{k\alpha} c^{+}_{k\alpha,\sigma} c_{k\alpha,\sigma} + \sum_{\substack{\gamma=1,2 \\ \sigma}} \varepsilon_{\gamma} d^{+}_{\gamma\sigma} d_{\gamma\sigma} + \sum_{\substack{k,\sigma,\alpha=L,R \\ \gamma=1,2}} \left[t_{\gamma\alpha} c^{+}_{k\alpha,\sigma} d_{\gamma\sigma} + h.c. \right] + \sum_{k,q,\sigma} \left[\tilde{t}_{LR} c^{+}_{qL,\sigma} c_{kR,\sigma} + h.c. \right] \tag{1}$$

The first term describes energy of the left and right lead. The next term represents quantum dot energy with two levels $\gamma = 1, 2$. The third term shows the hopping between the dot and electrodes. The last term describes tunneling through the direct Aharonov–Bohm channel and the track of the phase evolution of electron wave is kept by introduction of the phase dependence of the hopping matrix element between the leads, $\tilde{t}_{LR} = t_{LR} \mathrm{e}^{i\phi}$. The phase acquired by electron wave in the magnetic field perpendicular to the device plane is $\varphi = 2\pi\Phi/\Phi_0$, Φ being enclosed flux by the ring and $\Phi_0 = hc/e$ is a flux quantum.

3. Calculation of the conductance

The current is calculated starting from time evolution of non-equilibrium Green functions under assumption that the $\gamma = 1$ QD level is well coupled to the leads and active in electron transport, whereas $\gamma = 2$ level wave function has only a small, finite overlap with the states in the leads but does not directly participate in transport. It is indirectly coupled to the $\gamma = 1$ level via the leads, which has considerable effect on the phase evolution as will be shown below.

In the current calculation from the left lead we start from the time evolution of the particle number N_L: $J_L = ed\left\langle N_L \right\rangle/dt = (ie/\hbar)\left\langle [N_L, H] \right\rangle$, which gives the following expression:

$$J_L = \frac{ie}{\hbar} \sum_{\sigma,k} \left\{ t_{1L} \left\langle c^{+}_{kL,\sigma} d_{1\sigma} \right\rangle - t^{*}_{1L} \left\langle d^{+}_{1\sigma} c_{kL,\sigma} \right\rangle + \sum_{q} \left[\tilde{t}_{LR} \left\langle c^{+}_{qL,\sigma}\, c_{kR,\sigma} \right\rangle - \tilde{t}_{LR}{}^{*} \left\langle c^{+}_{kR,\sigma} c_{qL,\sigma} \right\rangle \right] \right\} \tag{2}$$

Eq. (2) is then written in terms of non-equilibrium "lesser" Green functions $G^{<}_{1,k\alpha}(t,t') = i\left\langle c^{+}_{k\alpha,\sigma}(t')d_{1\sigma}(t)\right\rangle$ and $G^{<}_{k\alpha',q\alpha}(t,t') = i\left\langle c^{+}_{q\alpha,\sigma}(t')c_{k\alpha',\sigma}(t)\right\rangle$ for $t = t'$. These functions describe electron propagation through QD placed in one of the arms of the Aharonov–Bohm ring and direct propagation through the second A–B arm, respectively.

After taking temporal Fourier transform the current takes the form:

$$J_L = \frac{e}{\hbar}\sum_{\sigma}\left\{\sum_{k}\int\frac{d\omega}{2\pi}2\Re\left[t_{1L}G^{<}_{1,kL}(\omega)\right] + \sum_{k,q}\int\frac{d\omega}{2\pi}2\Re\left[\tilde{t}_{LR}G^{<}_{qL,kR}(\omega)\right]\right\} \tag{3}$$

To obtain explicit expression for the current the "lesser" Green functions have to be known. They are calculated form the equation of motion (EOM) of the equivalent time-ordered Green functions and then Langreth continuation is performed to obtain lesser Green functions [5]. The calculated expression is exact, possible approximations are included only in the QD retarded Green function calculation (see Eq. (5) below).

Similar steps have been performed to obtain the current from the right lead, J_R. Symmetrization of the current and assumption on proportionate coupling to the leads gives the expression for the total current:

$$J = \frac{2e}{h}\sum_{\sigma}\int d\omega\left[f_L(\omega) - f_R(\omega)\right]T_{\sigma}(\omega) \tag{4}$$

where the transmission is expressed as:

$$\begin{aligned} T_{\sigma}(\omega) = T_b &+ \sqrt{\frac{4\Gamma_{1L}\Gamma_{1R}}{\left(\Gamma_{1L}+\Gamma_{1R}\right)^2}T_bR_b}\cos\varphi\frac{\Gamma_{1L}+\Gamma_{1R}}{1+\Gamma_{LR}}\Re G^{r}_{1\sigma}(\omega) \\ &-\frac{1}{2}\left[\frac{4\Gamma_{1L}\Gamma_{1R}}{\left(\Gamma_{1L}+\Gamma_{1R}\right)^2}\left(1-T_b\cos^2\varphi\right)-T_b\right]\frac{\Gamma_{1L}+\Gamma_{1R}}{1+\Gamma_{LR}}\Im G^{r}_{1\sigma}(\omega) \end{aligned} \tag{5}$$

The transmission through direct arm is:

$$T_b = \frac{4\Gamma_{LR}}{\left(1+\Gamma_{LR}\right)^2} \qquad \text{and} \qquad \Gamma_{LR} = \pi^2\left|t_{LR}\right|^2\rho_L\rho_R\,, \qquad \Gamma_{\gamma\alpha} = 2\pi\left|t_{\gamma\alpha}\right|^2\rho_{\alpha}$$

ρ_{α} being the spectral density of the lead α, constant and featureless and the spin index has been suppressed for brevity. The above general equation for the current through A–B ring with the QD has been obtained for the first time in [6].

Conductance through the system in a steady situation for the limit of zero bias voltage is of the form:

$$G = \frac{dJ}{d(eV)}_{eV\to 0} = \frac{2e^2}{h}\sum_{\sigma}\int d\omega\left(-\frac{df(\omega)}{d\omega}\right)T_{\sigma}(\omega) \tag{6}$$

4. Retarded quantum dot Green function

To calculate the conductance through the device, the retarded dot Green function is needed

$$G^r_{1\sigma}(t-t') = -i\theta(t-t')\langle\left[d_{1\sigma}(t), d^+_{1\sigma}(t')\right]_+\rangle$$

We emphasize that it has to be calculated in presence of the $\gamma = 2$ level and in presence of the direct channel. It is derived by the EOM approach and can be written in the form of Dyson equation (in energy domain) for one spin direction: $G^r_1(\omega) = G^{0r}_1(\omega) + \Sigma^r(\omega)G^r_1(\omega)$, where:

$$G^{0r}_1(\omega) = \left[\omega - \tilde{\varepsilon}_{1\sigma} + \frac{\sqrt{\Gamma_{LR}\Gamma_{1L}\Gamma_{1R}}\cos(\phi)}{1+\Gamma_{LR}} + \frac{\frac{i}{2}\left(\Gamma_{1L}+\Gamma_{1R}\right)}{1+\Gamma_{LR}}\right]^{-1} \tag{7a}$$

$$\sum^r(\omega) = \left\{\frac{\left[\frac{1}{2}\sqrt{\Gamma_{LR}}\left(\sqrt{\Gamma_{1L}\Gamma_{2R}}+\sqrt{\Gamma_{2L}\Gamma_{1R}}\right)\cos(\phi)+\frac{i}{2}\left(\Gamma_{12L}+\Gamma_{12R}\right)\right]^2}{\left(1+\Gamma_{LR}\right)^2}\right. + \left.\frac{\left[\frac{1}{2}\sqrt{\Gamma_{LR}}\left(\sqrt{\Gamma_{1L}\Gamma_{2R}}-\sqrt{\Gamma_{2L}\Gamma_{1R}}\right)\sin(\phi)\right]^2}{\left(1+\Gamma_{LR}\right)^2}\right\} G^{0r}_2(\omega) \tag{7b}$$

and $G^{0r}_2(\omega)$ has the form similar to $G^{0r}_1(\omega)$, where index 1 has been replaced by 2, $\Gamma_{\gamma'\alpha} = 2\pi t_{\gamma\alpha}t_{\gamma'\alpha}\rho_\alpha$, the dot levels are shifted uniformly by gate voltage V_g: $\tilde{\varepsilon}_{\gamma\sigma} = \varepsilon_{\gamma\sigma} - V_g$.

5. Calculation of the phase shift

The phase shift of the electron wave propagating through the device is calculated from the generalized Friedel sum rule [7] which describes the relation between phase shift of the electron wave scattered by an impurity and the particle number present at the impurity site. For one spin direction, it has the form of:

$$\delta = \pi n_{\text{imp}} = \pi\int_{-\infty}^{\varepsilon_F} d\omega\rho_{\text{imp}}(\omega) \tag{8}$$

where the integration is taken up to the Fermi level ε_F assumed to be zero, and the spectral density $\rho_{imp}(\omega) = -(1/\pi)\Im G^r_{1\sigma}(\omega)$ of the impurity (in the considered case QD level $\varepsilon_{1\sigma}$) is calculated in the presence of the direct channel and the $\varepsilon_{2\sigma}$ dot level.

6. Numerical results

The evolution of the phase shift for various values of the level splitting defined by Δ is shown in Fig. 1, $\Delta > 0$ means that ε_2 is situated above ε_1 in the energy scale. When the gate voltage increases, both the dot levels are shifted uniformly towards the resultant chemical potential defined in the leads. For a single ε_1 dot level which crosses chemical potential, the phase shift changes from 0 to π as expected for a resonant level model (see inset of Fig. 1).

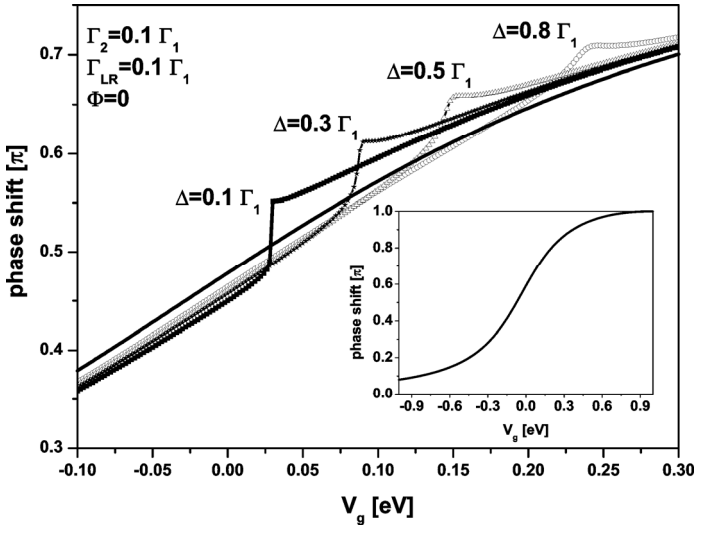

Fig. 1. Evolution of the phase shift of the electron wave traversing the device with respect to gate voltage for various spacings between QD levels ε_1 and $\varepsilon_2 = \varepsilon_1 + \Delta$; ε_2 is above ε_1 in energy scale. The values of Δ are indicated in the figure. The bold solid line (and the inset) shows a phase shift for a single ε_1 active dot level. The calculation has been made for the Aharonov–Bohm phase $\Phi = 0$

The situation changes when the influence of the ε_2 level is also considered. When ε_2 approaches the Fermi level, an increase of the phase shift appears which is followed by a dip. The increase of the phase is due to a temporal increase of the particle number of ε_1 level when ε_2 (interacting with ε_1 via electrodes) crosses chemical potential and is being filled by electrons. The anomaly then vanishes when ε_2 is further shifted below the Fermi level, becoming fully occupied, and its influence on ε_1 level starts to be screened and negligible. The anomaly gets smoother shape when the splitting between the levels increases.

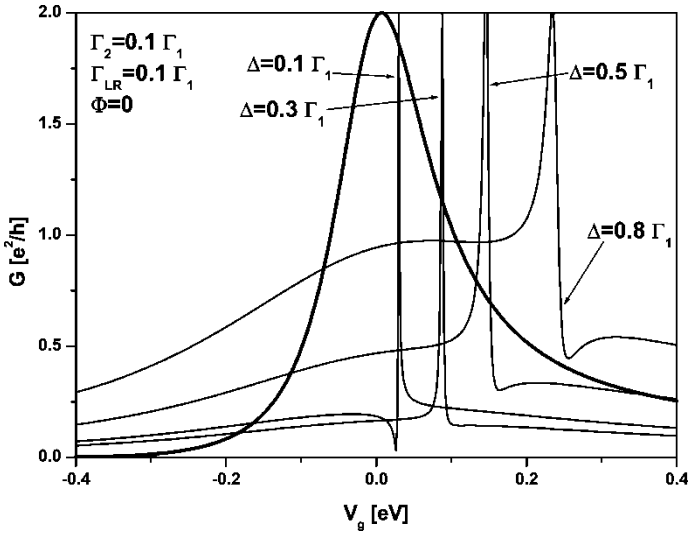

Fig. 2. Conductance through the device calculated for the same parameters as in Fig. 1. The bold solid line shows the conductance for a single QD level ε_1 only

The results of conductance calculations for the same parameters as in Fig. 1 are depicted in Fig. 2. Although ε_2 does not participate directly in electron transport through the device, it has considerable influence on the conductance shape. The bold continuous curve shows the conductance for ε_1 only level. The asymmetry of the conductance peak

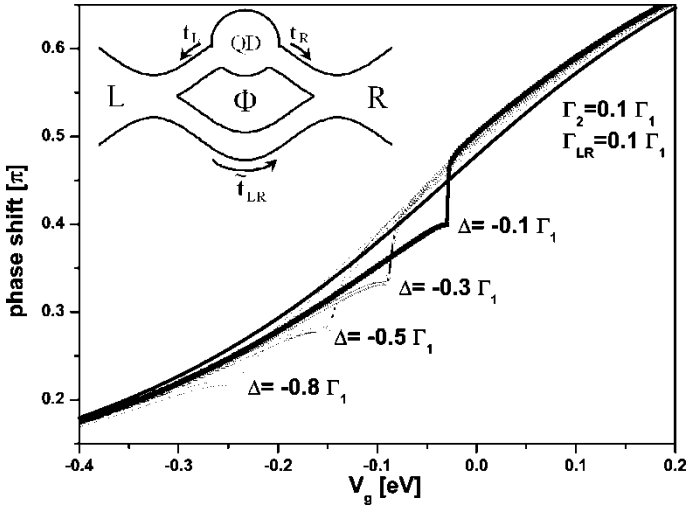

Fig. 3. Evolution of the phase shift with respect to gate voltage of the electron wave traversing the device for various spacings between QD levels ε_1 and $\varepsilon_2 = \varepsilon_1 + \Delta$; ε_2 is below ε_1 in energy scale. The values of Δ are indicated in the figure. The inset shows the scheme of the device under consideration

arises from the Fano effect [8] which develops itself due to the presence in transport of the direct channel apart from resonant dot level. Inclusion of the ε_2 level, which is coupled indirectly to conducting ε_1, causes the appearance of sharp Fano resonances, whose shapes depend on the QD level splitting. A similar feature (not shown) appears for $\Delta < 0$, with Fano resonance shapes being mirror reflected. It shows that the position of ε_2 with respect to the Fermi level determines the shape of the Fano conductance peaks through ε_1 and Fano parameter $q \propto -\Gamma_2/\varepsilon_2$. A similar situation has been encountered in the case of a large dot with strongly variable hybridization of the levels to the leads [9].

Results in Figure 3 are calculated for the case when the ε_2 level lies below ε_1 in the energy scale ($\Delta < 0$). When the gate voltage decreases, ε_1 crosses the Fermi energy as the first, is followed by ε_2 crossing. It results in a temporal decrease of particle number of ε_1; a part of charge from ε_1 can be absorbed into ε_2 which becomes unoccupied when approaching the Fermi level. It results in the appearance of the minimum of the phase shift, also observed experimentally [2]. The inset of Fig. 3 shows the scheme of the device under consideration. The calculated anomalies are very weakly sensitive to the external Aharonov–Bohm phase (not shown).

In conclusion, we have shown that indirect coupling between the QD energy levels and large difference of their coupling strength to the leads causes an anomaly of the phase shift, as observed experimentally for the Aharonov–Bohm geometry. The shape of the anomaly depends on the QD level arrangement in energy scale.

Acknowledgements

The work was supported in part by the Ministry of Science and Higher Education within the research project for years 2004–2007, as part of the European Science Foundation EUROCORES Programme FoNE by funds from the Ministry of Science and Higher Education and EC 6FP (contract N. ERAS-CT -2003-980409), and the EC project RTNNANO (contract N. MRTN-CT-2003-504574).

References

[1] SCHUSTER R., BUKS E., HEILBLUM M., MAHALU D., UMANSKY V., STRINKMAN H., Nature, 385 (2000), 779.
[2] AVINUN-KALISH M., HEILBLUM M., ZARCHIN O., MAHALU D., UMANSKY V., Nature, 436 (2005), 529.
[3] SILVESTROV P.G., IMRY Y., Phys. Rev. Lett., 85 (2000), 2565.
[4] SILVA A., OREG Y., GEFEN Y., Phys. Rev. B, 66 (2002), 195316
[5] LANGRETH D.C., [in:] *Linear and Nonlinear Transport in Solids*, Plenum Press, New York, 1976.
[6] HOFSTETTER W., KÖNIG J., SCHOELLER H., Phys. Rev. Lett., 87 (2001), 156803.
[7] HEWSON A.C., *The Kondo Problem to Heavy Fermions*, Cambridge University Press, 1993.
[8] FANO U., Phys. Rev., 124 (1961), 1866.
[9] STEFAŃSKI P., TAGLIACOZZO A., BUŁKA B.R., Phys. Rev. Lett., 93 (2004), 186805.

Received 5 May 2007
Revised 10 July 2007

Materials Science-Poland, Vol. 25, No. 4, 2007

Electronic and electrochemical properties of Mg_2Ni alloy doped by Pd atoms*

A. SZAJEK[1**], I. OKOŃSKA[2], M. JURCZYK[2]

[1]Institute of Molecular Physics, Polish Academy of Sciences,
Smoluchowskiego 17, 60-179, Poznań, Poland

[2] Institute of Materials Science and Engineering, Poznań University of Technology,
pl. Skłodowskiej Curie 5, 60-965 Poznań, Poland

The structure and electrochemical properties of nanocrystalline Mg_2Ni and Mg_2Ni/Pd nanocomposite have been studied. The materials were prepared by mechanical alloying. In nanocrystalline Mg_2Ni powder, discharge capacities up to 100 $mA \cdot h \cdot g^{-1}$ were measured. It was found that mechanically coated Mg-based alloys with palladium have effectively reduced the degradation rate of the studied electrode materials. Finally, the properties of nanocrystalline alloys and their nanocomposites were compared to those of microcrystalline samples. The electronic structure was studied by *ab initio* calculations, which showed that the 3b positions in the unit cell are preferred by the Pd impurities.

Key words: *Mg-based alloy; Pd coating; nanocrystalline alloy; metal hydride; electronic structure*

1. Introduction

Magnesium-based alloys have been extensively studied during last years but the microcrystalline Mg_2Ni alloy can reversibly absorb and desorb hydrogen only at high temperatures [1, 2]. Substantial improvements in the hydriding-dehydriding properties of Mg-type metal hydrides could possibly be achieved by formation of nanocrystalline structures [3, 4]. Additionally, it was found that the electrochemical activity of nanocrystalline hydrogen storage alloys can be improved in many ways, by alloying with other elements, by ball-milling the alloy powders with a small amount of nickel or graphite powders [4–7]. In order to optimize the choice of the intermetallic compounds for a battery application, a better understanding of the role of each alloy con-

---

*Presented at the Conference of the Scientific Network "New Materials for Magnetoelectronics – MAG-EL-MAT 2007", Będlewo near Poznań, 7–10 May 2007.

**Corresponding author, email: szajek@ifmpan.poznan.pl

stituent on the electronic properties of the material is crucial. The nanocrystalline metal hydrides offer a breakthrough in prospects for practical applications. Their excellent properties (significantly exceeding those of traditional hydrides) result from combined engineering of many factors: alloy composition, surface properties, microstructure, grain size and others.

We have synthesized nanocrystalline Mg_2Ni alloy and Mg_2Ni/Pd nanocomposite. The influence of microstructure on the structural, electrochemical and electronic properties of synthesized materials was studied.

2. Experimental and computational details

Nanocrystalline Mg-type alloys were prepared using mechanical alloying followed by annealing. The powders were examined by XRD analysis, using CoK_α radiation. Mechanically alloyed (MA) and annealed Mg_2Ni powder was mixed with 10 wt. % of palladium powder (74 μm, purity 99.9 %) and milled for 1 h in a SPEX Mixer Mill. The weight ratio of hard steel balls to mixed powder was 30:1. Independently, the microcrystalline Mg_2Ni alloy was synthesized by diffusion method.

Table 1. Structure, lattice parameters and discharge capacities for nanocrystalline Mg_2Ni-type materials[a]

Material	Structure and lattice constants [Å]	Discharge capacity [mA·h/g]	
		1st cycle	3rd cycle
Nanocrystalline Mg_2Ni	hexagonal, a = 5.216, c = 13.246	100	5
Nanocomposite Mg_2Ni/Pd	hexagonal/cubic, a = 5.216, c = 13.246/a = 3.890	308	162
Microcrystalline Mg_2Ni	hexagonal, a = 5.223, c = 13.30	–	–

[a] Data for parent microcrystalline Mg_2Ni alloy were also included for comparison.

In order to study electronic structure of the Mg_2Ni and $Mg_2Ni_{0.9}Pd_{0.1}$ compounds the full-potential local-orbital (FPLO) method has been used [8, 9]. The scalar-relativistic mode was used in the calculations including coherent potential approximation (CPA) [10] to take into account chemical disorder introduced by Pd impurities. The calculations were carried out for the hexagonal Mg_2Ni-type structure with $P6_222$ space group and experimental values of the lattice constants (Table 1). For the calculations we assumed the following configurations of atoms: core + semi core (2s2p) + valence (3s3p3d) electrons for Mg atoms, core + semi core (3s3p) + valence (4s4p3d) electrons for Ni atoms, and core + semi core (4s4p) + valence (5s5p4d) electrons for Pd atoms. The calculations were performed for the reciprocal space mesh containing 252 (for doped systems) and 2310 (for Mg_2Ni) points within the irreducible wedge (1/12) of the Brillouin zone using the tetrahedron method [11] for integrations.

The exchange-correlation potential was assumed in the form proposed by Perdew and Wang [12]. The self consistent criterion was equal to 10^{-8} Ry for the total energy.

3. Results and discussion

The effect of MA processing was studied by X-ray diffraction and by electrochemical measurements. In the present work, nanocrystalline and microcrystalline Mg_2Ni alloy and Mg_2Ni/Pd nanocomposite have been prepared by MA method followed by annealing, by a diffusion method and by ball milling, respectively (Table 1).

3.1. Mg_2Ni-type alloys

Figure 1 shows a series of XRD spectra of mechanically alloyed 2Mg–Ni powder mixture (0.453 wt. % Mg + 0.547 wt. % Ni) subjected to milling in increasing time.

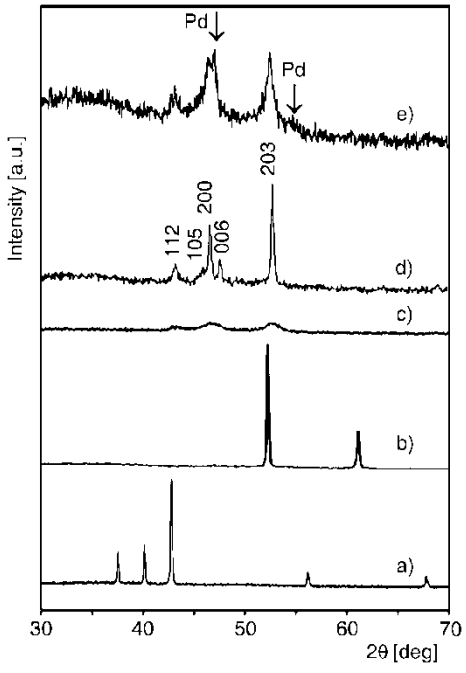

Fig. 1. X-ray diffraction patterns ($CoK_{\alpha 1}$) of pure powders of magnesium (a) and nickel (b) and mixture of 2Mg and Ni powders after MA for 45 h (c) followed by annealing at 723 K for 1 h (d); curve (e) represents XRD spectrum of Mg_2Ni/Pd composite prepared by MA for 1 h of nanocrystalline Mg_2Ni (see Fig. 1d) mixed with 10 wt. % Pd powder

The originally sharp diffraction lines of Mg and Ni (Fig. 1a) gradually become broader and their intensities decrease with milling time. The nanostructured Mg_2Ni with broad diffraction peaks are already found after 5 h of MA process. The powder mixture milled for more than 30 h has transformed directly to a hexagonal-type phase (Fig. 1b). Finally, the obtained powder was heat treated in high purity argon atmosphere at 450 ºC for 0.5 h to obtain the desired microstructure (Fig. 1c). Table 1 reports

the cell parameters of all the studied materials. The average size of amorphous 2Mg-Ni powders (AFM studies) was of the order of 30 nm.

At room temperature, original nanocrystalline alloy, Mg_2Ni, absorbs hydrogen but almost does not desorb it. At temperatures above 250 ºC, the kinetics of the absorption–desorption process improves considerably and for nanocrystalline Mg_2Ni alloy the reaction with hydrogen is reversible. The hydrogen content in this material at 300 ºC is 3.25 wt. %. Upon hydrogenation, Mg_2Ni transforms into the hydride Mg_2Ni–H phase [13].

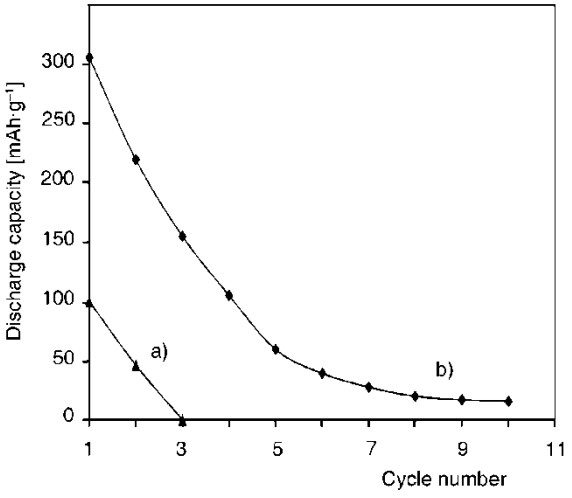

Fig. 2. Discharge capacity as a function of the cycle number for MA and annealed Mg_2Ni (a) and Mg_2Ni/Pd electrodes (b) (solution, 6 M KOH, 20 ºC)

The Mg_2Ni electrode, mechanically alloyed and annealed, displayed the maximum discharge capacity (100 $mA \cdot h \cdot g^{-1}$) at the first cycle but degraded strongly with cycling (Fig. 2). The poor cyclic behaviour of Mg_2Ni electrodes is attributed to the formation of $Mg(OH)_2$ on the electrodes which has been considered to arise from the charge -discharge cycles.

3.2. Effect of ball-milling with palladium

In order to improve the electrochemical properties of the studied nanocrystalline electrode materials, the ball-milling technique was applied to the Mg-based alloys using the palladium as surface modifiers (Fig. 1). Figure 2 and Table 1 show the discharge capacities as a function of the cycle number for studied nanocomposite material. The discharge capacity of nanocrystalline Mg_2Ni coated with palladium powder was increased. The elemental palladium was distributed on the surface of ball milled alloy particles homogenously and role of these particles is to catalyse the dissociation of molecular hydrogen on the surface of studied alloy. Mechanical coating with palla-

dium effectively reduced the degradation rate of the studied electrode materials. Compared to that of the uncoated powders, the degradation of the coated ones was suppressed. Recently, Iwakura et al. [14] have demonstrated that the modification of graphite on the MgNi alloy in the MgNi–graphite composite is mainly a surface one. Graphite inhibits the formation of new oxide layer on the surface of the material once the native oxide layer is broken during the ball-milling process.

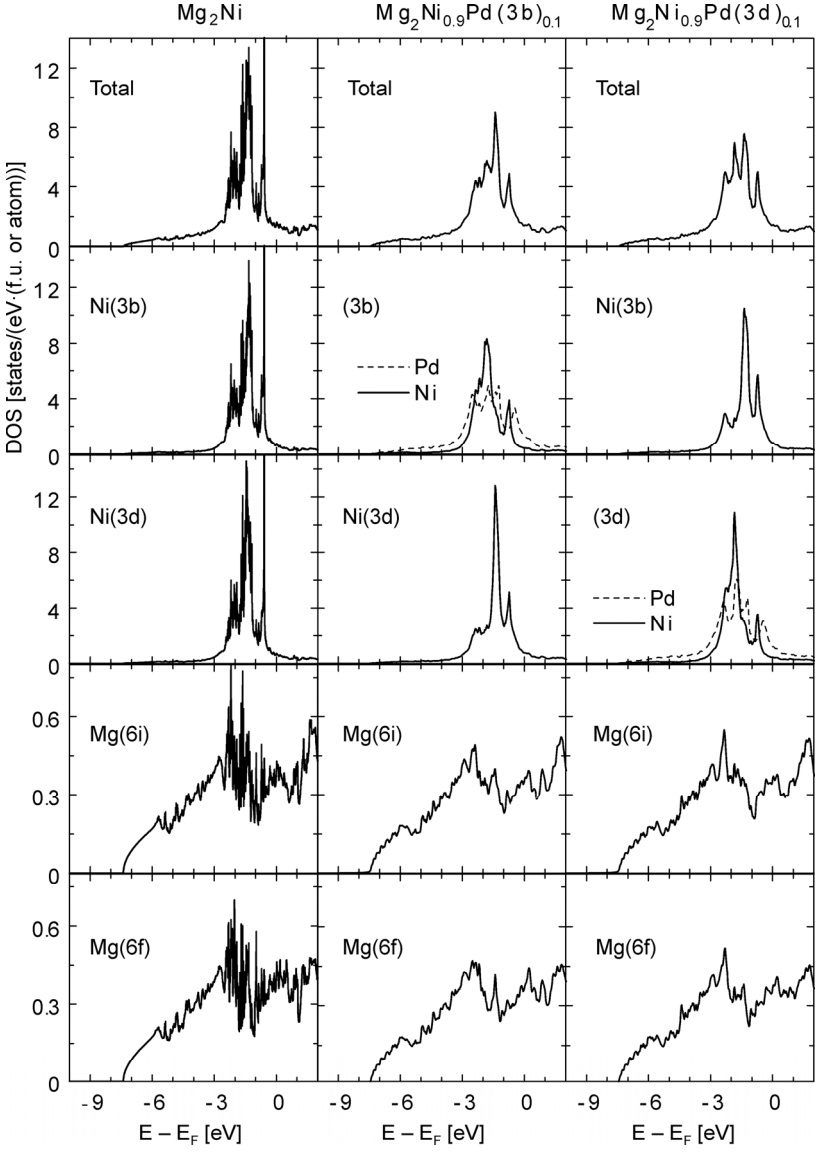

Fig. 3. Densities of states, total (per formula unit) and site projected (per atom) for Mg_2Ni and doped systems by Pd impurities located in 3b or 3d sites

The results of band structure calculations are presented in Fig. 3. We assumed that Pd impurities may replace only Ni atoms in 3b and 3d sites, the Mg sites do not accommodate Pd impurities. Figure 3 presents the DOS plots for the Mg_2Ni alloy and the doped systems $Mg_2Ni_{0.9}Pd_{0.1}$. The results for Mg_2Ni alloy are similar to those obtained earlier [15] using the LMTO method. Here, these results are treated as reference to monitor changes caused by the Pd impurities. We observe that the DOS plots for the doped systems are broadened, especially in sites occupied simultaneously by Pd and Ni atoms. The valence bands are dominated by Ni and Pd atoms because of large number of Ni(3d) and Pd(4d) electrons. The contribution provided by the Mg atoms is very small. The total energy calculations showed that 3b sites are preferred by the Pd impurities.

4. Conclusions

It was found that milling of 10 wt. % of palladium is sufficient to improve the discharge capacity of studied Mg-based nanocomposites. The experimental XPS valence bands measured for MA nanocrystalline alloys showed a significant broadening compared to those obtained for the microcrystalline samples with the same chemical composition. This is probably due to a strong deformation of the nanocrystals in the mechanically alloyed samples. The substitution of Mg in Mg_2Ni by transition metals leads to significant modifications of the shape and width of the valence band of the nanocrystalline as well as microcrystalline samples. Especially, the valence band shape of the MA nanocrystalline alloys is considerably modified compared to that measured for the microcrystalline samples. The strong modifications of the electronic structure in the MA nanocrystalline alloys could significantly influence their hydrogenation properties. The mechanical alloying is a suitable procedure for obtaining nanocrystalline Mg_2Ni-based alloy electrodes.

The *ab initio* band structure calculations showed that the valence bands are dominated by the Ni(3d) and Pd(4d) electrons, and the Pd impurities prefer 3b sites in the unit cell.

Acknowledgements

This work was supported by the Polish National Committee for Scientific Research under the contract No. PBZ-KBN-117/T08/07.

References

[1] ZALUSKI L., ZALUSKA A., STRÖM-OLSEN J.O., J. Alloys Compd., 217 (1995), 245.
[2] GASIOROWSKI A., IWASIECZKO W., SKORYNA D., DRULIS H., JURCZYK M., J. Alloys Compd., 364 (2004), 283.
[3] SCHLAPBACH L., ZÜTTEL A., Nature (London), 414 (2001), 353.
[4] JURCZYK M., Bull. Pol. Ac. Sci.: Tech., 52 (2004), 67.

[5] BOUARICHA S., DODELET J.P., GUAY D., HUOT J., SCHULTZ R., J. Alloys Compd., 325 (2001), 245.
[6] JURCZYK M., J. Mater. Sci., 39 (2004), 5271.
[7] SZAJEK A., JURCZYK M., SMARDZ L., OKOŃSKA I., JANKOWSKA E., J. Alloys Compd., 436 (2007), 345.
[8] KOEPERNIK K., ESCHRIG H., Phys. Rev. B, 59 (1999), 1743.
[9] OPAHLE I., KOEPERNIK K., ESCHRIG H., Phys. Rev. B, 60 (1999), 14035.
[10] KOEPERNIK K., VELICKY B., HAYN R., ESCHRIG H., Phys. Rev. B, 55 (1997), 5717.
[11] BLÖCHL P., JEPSEN O., ANDERSEN O.K., Phys. Rev. B, 49 (1994). 16223.
[12] PERDEW J.P., WANG Y., Phys. Rev. B, 45 (1992), 13244.
[13] GUPTA M., BERLIN E., SCHALPBACH L., J. Less-Common Met., 103 (1984), 389.
[14] IWAKURA C., INOUE H., ZHANG S.G., NOHARA S., J. Alloys Compd., 293–295 (1999), 653.
[15] SZAJEK A., JURCZYK M., OKOŃSKA I., SMARDZ K., JANKOWSKA E., SMARDZ L., J. Alloys Compd., 436 (2007), 345.

Received 10 May 2006

Materials Science-Poland, Vol. 25, No. 4, 2007

New superconducting phases in $Mo_2Re_3B_x$–$Mo_3Re_2B_x$ eutectic*

B. ANDRZEJEWSKI[1**], E. GUILMEAU[2], A. KOWALCZYK[1], A. SZLAFEREK[1]

[1]Institute of Molecular Physics, Polish Academy of Sciences,
Smoluchowskiego 17, 60-179 Poznań, Poland

[2]Laboratoire CRISMAT, UMR 6508 CNRS-ENSICAEN, 6, Bd. du Maréchal Juin
14050 Caen Cedex, France

We report on the discovery and on some basic properties of the eutectic alloy composed of two new superconducting phases; $Mo_2Re_3B_x$ with T_c = 8.7 K and of $Mo_3Re_2B_x$ with T_c = 6.6 K (where $x \approx 1$). The two phases in the eutectic form complex globular structure and areas of locally ordered lamellar patterns. The lamellae are separated by thin interface of excess boron and behave like a regular network of Josephson junctions. Distinct two-step superconducting transition indicates that this eutectic belongs to inhomogeneous systems with no evidence for the proximity effect. The parameters of the dominating $Mo_3Re_2B_x$ phase are as follows: the lower and the upper critical fields are equal to $\mu_0 H_{c1}$ = 13 mT and to $\mu_0 H_{c2}$ = 6.5 T, respectively. This corresponds to the penetration depth λ = 2040 Å, to the coherence length ξ = 70 Å and to Ginzburg –Landau parameter κ = 29. Linear temperature dependence of $H_{c2}(T)$ may be due to unconventional mechanism of superconductivity in dominating $Mo_3Re_2B_x$ phase.

Key words: *intermetallic compounds; eutectics; superconductor; critical field*

1. Introduction

Boride compounds are promising superconductors because they exhibit high frequency vibration of lighter elements and strong electron-phonon interaction which may lead to enhanced critical temperatures. The best candidates for superconductors should be AB_2-type diborides, but none of the systems with light alkali metal A = Li, Be or Al exhibit superconductivity. Except MgB_2 with a record critical temperature equal to T_c = 39 K [1], there was reported only low temperature superconductivity in

---

*Presented at the Conference of the Scientific Network "New Materials for Magnetoelectronics – MAG-EL-MAT 2007", Będlewo near Poznań, 7–10 May 2007.

**Corresponding author, e-mail: and@ifmpan.poznan.pl

heavy metal diborides like $BeB_{2.75}$ with T_c = 0.72 K [2], NbB_2 (T_c = 3.87 K) [3], TaB_2 (T_c = 9.5 K) [4] and in ZrB_2 below 5.5 K [5]. Superconducting systems with rhenium are also known, for example ReB (T_c = 2.8 K) [6], Re_3B (T_c = 4.7 K), ReB_2 (T_c = 4.5–6.3 K) [7] and Re_7B_3 with T_c = 3.3 K [8].

Superconductivity appears also in ternary MReX type compounds where M = Mo, W and X = B, C [9, 10]. Examples are $W_7Re_{13}B$ and $W_7Re_{13}C$. Some superconducting materials can be obtained in a form of eutectics in which superconducting phase is embedded in a matrix phase. The matrix phase can be normal metal, another superconductor, semiconductor or dielectric and it strongly influences basic superconducting properties of the eutectic [11]. The behaviour of eutectic also depends on geometry and structure of the superconducting and normal phases. In general, eutectics exhibit two extreme behaviours: properties of eutectic can be more or less a simple sum of properties of the two phases [12] or it can behave as a completely homogeneous system due to the proximity effect [13]. Fine superconducting structures (for example lamellae) in an eutectic separated by normal or insulating matrix sometimes can form network of the Josephson junctions [14]. In the present paper, we report on superconductivity in $Mo_2Re_3B_x$–$Mo_3Re_2B_x$ eutectic system composed of new, superconducting phases.

2. Experimental

$Mo_2Re_3B_x$–$Mo_3Re_2B_x$ eutectic has been synthesized by the method of induction melting of the constituent elements under argon atmosphere in a water-cooled boat. Fine powders of Mo, Re and B with the total mass about 1 g were used for the alloying. To ensure homogeneity, the ingot was inverted and remelted several times. In spite of this procedure, we found nonstoichiometric phases and excess of rhenium near the surface of the ingot. Thus, the investigated sample was cut from the interior of the ingot.

The microstructure and composition of the sample was investigated using Zeiss Ultra 55 scanning electron microscope (SEM) equipped with energy dispersion spectroscopy (EDS) probe. Magnetometric measurements were performed by means of Quantum Design MPMS SQUID magnetometer and also by Oxford Instruments Ltd. MagLab 2000 System. The magnetic measurements were corrected for demagnetizing effect. The demagnetizing coefficient N of the investigated sample was assumed to be 0.22. Quantum Design PPMS 7T bridge and a standard four point contact method were used for the electric transport measurements. The current strength was equal to 1 mA.

3. Results and discussion

An eutectic system arises during solidification of an initial melt, when two phases in the melt do not form a solution for any relative concentration. An example of the polished surface of our eutectic sample is presented in Fig. 1. There are visible large globules or

grains of the grey phase with dimensions of a few tenth of μm separated by regions composed of lamellae of the two phases – grey and black one. The details of lamellar structure, which is typical of some eutectic systems, are presented in the inset to Fig. 1.

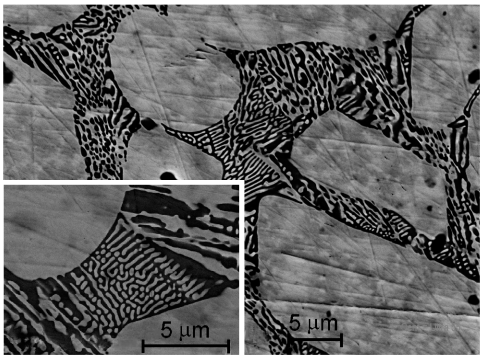

Fig. 1. The SEM micrography of $Mo_2Re_3B_x$–$Mo_3Re_2B_x$ sample. Inset: the example of regular lamellar structure between globules of $Mo_3Re_2B_x$ phase

The eutectic exhibits some similarity to granular superconductors composed of grains separated by normal matrix because at interfaces between the two phases there exists a normal layer of metallic boron. This conclusion is confirmed by the eutectic resistivity dependence in a wide temperature range shown in Fig. 2. The resistivity of this eutectic is rather high as for metals and it decreases gradually with temperature. The residual resistivity ratio (RRR), which defines resistivity changes versus temperature; RRR = R(10 K)/R(300K) is also high and equal to 0.7. The semiconducting layer of boron deposited at interfaces increases significantly resistivity of the system and makes it almost independent of temperature. An identical behaviour was found in similar ternary borides $W_7Re_{13}B$ and $Mo_7Re_{13}B$ and explained in the same way [9, 10].

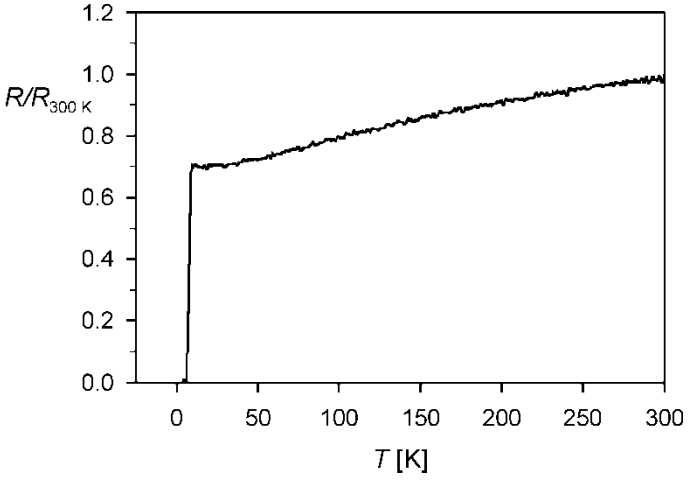

Fig. 2. The temperature dependence of normalized resistivity $R(T)/R(T = 300\ \mathrm{K})$ of $Mo_2Re_3B_x$–$Mo_3Re_2B_x$ eutectic

In the lamellar regions, a regular Josephson junction network exists, which is confirmed by very strong absorption of microwave energy observed in this eutectic [15]. Large grains of grey phase dominate in the alloy, because the initial melt was probably shifted out of the optimal eutectic composition. The chemical compositions of the two phases were determined by means of EDS, based on the energy spectrum and the relative intensities of X-ray radiation. The grey phase was identified as $Mo_3Re_2B_x$ compound and the black phase as $Mo_2Re_3B_x$. The accurate determination of boron content was difficult because of low energy of the boron line and small dimensions of the black lamellae which were almost at the limit of the spatial resolution of the electron beam. The detailed discussion devoted to identification of phases in this eutectic was presented in ref. [15]. There is no trace of $Mo_7Re_{13}B$ phase reported earlier by Kawashima [10] in the EDS spectra, probably due to different thermal conditions during the alloying process.

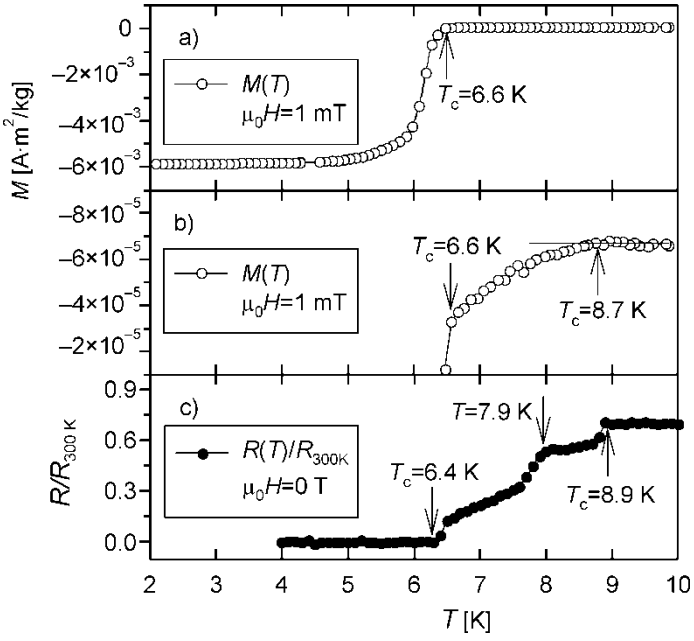

Fig. 3. Superconducting transition in the eutectic system; the magnetisation $M(T)$ vs. temperature (a), the details of superconducting transition (b) and the resistive superconducting transition (c)

The details of superconducting transition in magnetic and electric properties are shown in Fig. 3. The diamagnetic moment appears below 6.6 K (Fig. 3a), however a subtle drop of the magnetic signal occurs also at higher temperature equal to 8.7 K (Fig. 3b). The main superconducting transition is quite sharp with the transition width at 50% of diamagnetic moment equal to 0.4 K. The double-step nature of superconducting transition is more clearly seen in the resistivity dependence on temperature (Fig. 3c). The first step in resistivity occurs at 8.9 K which corresponds well to the

subtle transition at 8.7 K in magnetic properties. The sample looses resistivity at 6.4 K, slightly below the temperature of the main superconducting transition. There is also another feature in the electrical resistivity at 7.9 K.

The complex nature of superconducting transition is caused by the presence of two superconducting phases and by the structure of this eutectic. The transition at higher temperature is related to the black lamellae of $Mo_2Re_3B_x$ phase characterised by a small volume but large extent. In the magnetic properties, this phase is almost unnoticeable because of its negligible volume but it shunts electrically large part of the sample due to its elongated shape. The superconducting transition in the dominating grey $Mo_3Re_2B_x$ globules leads to a sudden appearance of a diamagnetic signal at 6.6 K and also shunts totally the sample below 6.4 K. The drop in electrical resistivity observed at 7.9 K is an effect of electrical percolation in the system of $Mo_2Re_3B_x$ lamellae.

Two distinct different superconducting transitions indicate that the whole eutectic behaves like an inhomogeneous system with properties which are more or less a simple sum of the properties of the two phases. Also the proximity effect is rather absent in this case. This allows one to investigate and to separate some physical properties belonging to each phase present in the eutectic [12]. However, the amount of $Mo_2Re_3B_x$ phase is too low to determine any parameter except the critical temperature. Therefore, in this report we determine basic parameters like critical fields, coherence and penetration depth for the dominating $Mo_3Re_2B_x$ phase only. The dependence of the upper critical field on temperature, $H_{c2}(T)$, of $Mo_3Re_2B_x$, equivalent to the $T_c(H)$ dependence is shown in Fig. 4.

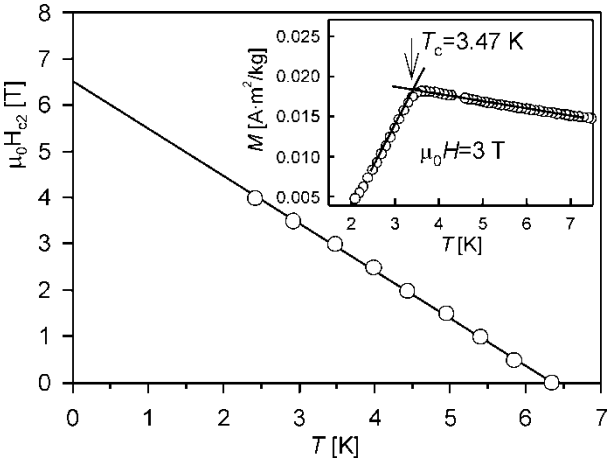

Fig. 4. Upper critical field $H_{c2}(T)$ for $Mo_2Re_3B_x$–$Mo_3Re_2B_x$ eutectic. The inset presents the way of determination of the critical temperature $T_c(H)$ for a selected magnetic field (3 T in this case)

The critical temperatures corresponding to selected magnetic fields $T_c(H)$ are determined from the intersection of two straight lines fitting the relevant linear regimes

of $M(T)$ curves above and below the superconducting transition, respectively (see inset to Fig. 4). Surprisingly, the best fit to the field $H_{c2}(T)$ experimental data is obtained using the linear relation; $H_{c2}(T) = H_{c2}(0)(1 - t)$ where t is the reduced temperature $t = T/T_c$. The usual parabolic dependence [16, 17]; $H_{c2}(T) = H_{c2}(0)(1 - t^2)$ is invalid in this case. This may indicate an unconventional mechanism of superconductivity in $Mo_3Re_2B_x$. A similar linear dependence of $H_{c2}(T)$ is observed in MgB_2 [18, 19], $BeB_{2.75}$ [2] and in ZrB_{12} [5]. From the best linear fit one obtains the value of the upper critical field $\mu_0 H_{c2}(0) =$ 6.5 T and the slope dH_{c2}/dT equal to –1.02 T/K. The upper critical field estimated from the Werthamer–Helfand–Hohenberg formula [20]; $H_{c2}(0) \approx -0.69 T_c (dH_{c2}/dT)$ for this value of slope and for $T_c = 6.4$ K is much lower than the experimental result and equal to $\mu_0 H_{c2}(0) = 4.5$ T. However, both values are well below the paramagnetic limit $\mu_0 H_p = 1.84 T_c$ which is equal to 11.8 T. This suggests that other mechanisms than pair breaking due to Zeeman coupling limit the value of the upper critical field in Mo_3Re_2B. Another basic parameter, namely the coherence length ξ can be calculated from the relationship: $\mu_0 H_{c2} = \Phi_0/2\pi\xi^2$ where $\Phi_0 = 2\times10^{-15}$ Wb is flux quantum. For $\mu_0 H_{c2} = 6.5$ T it is equal to 70 Å.

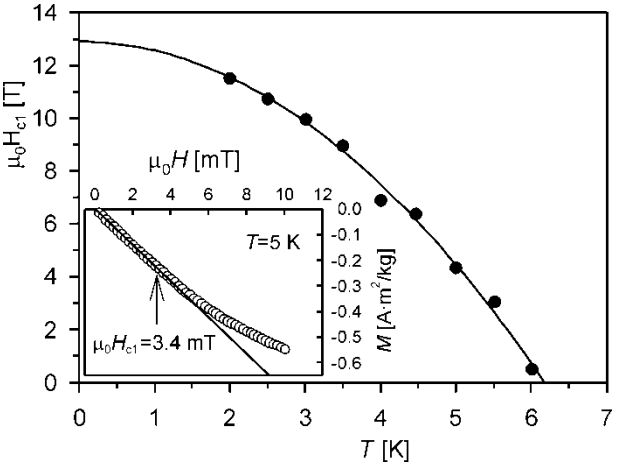

Fig. 5. The lower critical field $H_{c1}(T)$ corrected for the demagnetising effect. The inset shows the magnetisation versus applied magnetic field $M(H)$ for 5 K and the criterion for determination of $H_{c1}(T)$. The data in the inset are as measured (not corrected)

The values of lower critical field of Mo_3Re_2B for selected temperatures may be determined using as a criterion the deviation from linearity of the initial part of magnetization $M(H)$, which is presented in the inset to Fig. 5. The dependence of lower critical field on temperature $H_{c1}(T)$ corrected for the demagnetizing effect is shown in Fig. 5. It is evident that the lower critical field exhibits usual negative curvature and can be well fitted with the parabolic function $H_{c1}(T) = H_{c1}(0)(1 - t^2)$. The parameter of the best fit $\mu_0 H_{c1}(0)$ is equal to 13 mT. Based on the equation $\mu_0 H_{c1}(0) = (\Phi_0/4\pi\lambda^2)\ln(\lambda/\xi)$, the value of $H_{c1}(0)$ corre-

sponds to the penetration depth equal to $\lambda = 2040$ Å. Knowing the coherence length ξ and the penetration depth λ, we can calculate the Ginzburg–Landau parameter $\kappa = \lambda/\xi$. It amounts to 29, being rather high as for intermetallic superconductors.

4. Conclusions

We have synthesized and investigated basic properties of an eutectic alloy composed of two new superconducting compounds, namely of $Mo_2Re_3B_x$ and $Mo_3Re_2B_x$ phases. The SEM examination of the surface of the eutectic revealed complex globular structure and areas with locally ordered lamellae. The two phases are separated by thin layer of metallic boron, which leads to enhanced resistivity of the eutectic. Ordered lamellae of $Mo_2Re_3B_x$ and $Mo_3Re_2B_x$ phases form a regular network of the Josephson junctions.

This eutectic belongs to inhomogeneous systems with no proximity effect, which allows one to investigate the properties of each phase separately. Accordingly, the superconducting transitions at 6.6 K and 8.7 K can be associated with $Mo_3Re_2B_x$ and $Mo_2Re_3B_x$, respectively. The critical fields of the dominating $Mo_3Re_2B_x$ phase are $\mu_0 H_{c1}$ = 13 mT and $\mu_0 H_{c2}$ = 6.5 T. This corresponds to the penetration depth $\lambda = 2040$Å, to the coherence length $\xi = 70$ Å and to the Ginzburg–Landau parameter $\kappa = 29$. The amount of $Mo_2Re_3B_x$ phase is too low to determine any parameter except the critical temperature. Linear temperature dependence of $H_{c2}(T)$ observed in $Mo_3Re_2B_x$ phase may be due to an unconventional mechanism of superconductivity.

Acknowledgements

This work was financed within the funds of the Ministry of Education and Science, Poland under the contract No. N515 028 31/1103.

References

[1] NAGAMATSU J., NAKAGAWA N., MURANAKA T., ZENITANI Y., AKIMITSU J., Nature, 410 (2001), 63.
[2] YOUNG D.P., GOODRICH R.G., ADAMS P.W., CHAN J.Y., FRONCZEK F.R., DRYMIOTIS F., HENRY L.L., Phys. Rev. B., 65 (2002), 180518.
[3] COOPER A.S., CORENZWIT E., LONGINOTTI L.D., MATTHIAS B.T., ZACHARIASEN W.H., Proc. Nat. Acad. Sci., 67 (1970), 313.
[4] KACZOROWSKI D., ZALESKI A.J., ŻOGAŁ O.J., KLAMUT J., ArXiv: cond-mat/0103571.
[5] GASPAROV V.A., SIDOROV N.S., ZVERKOVA I.I., Phys. Rev. B., 73 (2006), 094510.
[6] SAVITSKII E.M., BARON V.V., EFIMOV Y.V., BYCHKOVA M.I., MYZENKOVA L.F., *Superconducting Materials*, Plenum Press, New York, 1973.
[7] STRUKOVA G.K., DEGTYAREVA V.F., SHOVKUN D.V., ZVEREV V.N., KIIKO V.M., IONOV A.M., CHAIKA A.N., ArXiv: cond-mat/0105293.
[8] KAWANO A., MIZUTA Y., TAKAGIWA H., MURANAKA T., AKIMITSU J., J. Phys. Soc. Jpn., 72 (2003), 1724.
[9] KAWASHIMA K., KAWANO A., MURANAKA T., AKIMITSU J., J. Phys. Soc. Jpn., 74 (2005), 700.
[10] KAWASHIMA K., KAWANO A., MURANAKA T., AKIMITSU J., Phys., B 378–380 (2006), 1118.

[11] LIVINGSTON J.D., J. Appl. Phys., 38 (1967), 2408.
[12] CURRIE P.D., FINLAYSON T.R., RACHINGER W.A., Scripta Met., 11 (1977), 59.
[13] LUTES O.S., CLAYTON D.A., Phys. Rev., 145 (1966), 218.
[14] ISAKOV G.I., Inorg. Mater., 39 (2003), 1117.
[15] ANDRZEJEWSKI B., GUILMEAU E., KOWALCZYK A., JURGA W., Acta. Phys. Polon. A, in press
[16] GORTER C.J., CASIMIR H.B.G., Phys Z., 35 (1934), 963.
[17] GORTER C.J., CASIMIR H.B.G., Z. Techn. Phys., 15 (1934), 539.
[18] LYARD L., SAMUELY P., SZABO P., KLEIN T., MARCENAT C., PAULIUS L., KIM K.H.P., JUNG C.U., LEE H.-S., KANG B., CHOI S., LEE S.-I., MARCUS J., BLANCHARD S., JANSEN A.G.M., WELP U., KARAPETROV G., KWOK W.K., Phys. Rev. B, 66 (2002), 180502R.
[19] SOLOGUBENKO A.V., JUN J., KAZAKOV S.M., KARPINSKI J., OTT H.R., Phys. Rev. B., 65 (2002), 180505R.
[20] WERTHAMER N.R., HELFAND E., HOHENBERG P.C., Phys. Rev., 147 (1966), 295.

Received 8 May 2007
Revised 10 July 2007

Materials Science-Poland, Vol. 25, No. 4, 2007

Ferromagnetic and spin-glass properties of single-crystalline U_2NiSi_3*

M. SZLAWSKA**, A. PIKUL, D. KACZOROWSKI

Institute of Low Temperature and Structure Research,
Polish Academy of Sciences, P No. 1410, 50–950 Wrocław 2, Poland

A single crystal of U_2NiSi_3 was investigated by means of magnetization, electrical resistivity and heat capacity measurements. Whereas the DC magnetic data clearly manifest strongly anisotropic ferromagnetism, the AC magnetic susceptibility data are consistent with spin-glass behaviour, reported previously for polycrystalline samples. Moreover, no distinct anomalies around T_C occur in the specific heat and electrical resistivity characteristics. Altogether the results obtained for single-crystalline U_2NiSi_3 indicate rather an unusual state of coexistence of ferromagnetism and spin-glass freezing.

Key words: *uranium; ternary silicide; spin glass; ferromagnetism*

1. Introduction

Most of the ternary intermetallic phases U_2TSi_3 (T = 3d-, 4d- or 5d-electron transition metal) crystallize in a hexagonal structure of the AlB_2 type or its disordered derivatives [1, 2]. Recently, they have attracted much attention because of their unusual magnetic properties related to atomic disorder or topological frustration in the uranium sublattice [3, 4]. Polycrystalline samples of U_2NiSi_3 were previously studied and characterized as a cluster-glass system with the spin-freezing temperature T_f = 22 K [3, 5]. On the contrary, a neutron diffraction experiment performed on a single crystal has revealed a long-range ferromagnetic ordering below T_C = 30 K with sizeable uranium magnetic moments of $0.6\mu_B$ oriented perpendicular to the hexagonal *c* axis [6]. This indispensable discrepancy motivated us to undertake a reinvestigation of the bulk properties of U_2NiSi_3 on single-crystalline specimens.

---

*Presented at the Conference of the Scientific Network "New Materials for Magnetoelectronics – MAG-EL-MAT 2007", Będlewo near Poznań, 7–10 May 2007.

**Corresponding author, e-mail: M.Szlawska@int.pan.wroc.pl

2. Experimental

Single crystal of U_2NiSi_3 was grown by the Czochralski pulling method in a tetra -arc furnace under argon atmosphere. Using a KUMA diffraction four circle diffractometer equipped with a CCD camera, its crystal structure was proved to be hexagonal AlB_2-type. DC magnetic measurements were performed in the temperature range 1.72–400 K and in magnetic fields up to 5 T using a Quantum Design SQUID magnetometer. The AC magnetic susceptibilities were measured between 10 and 40 K within the frequency range 10–10 000 Hz using an Oxford Instruments AC-susceptometer. The electrical resistivities were measured from 5 to 300 K by a conventional four -point DC technique. Heat capacities were studied within the temperature interval 2–100 K employing a quantum design PPMS platform.

3. Results and discussion

Figure 1 shows low-temperature dependences of the magnetization measured in zero-field-cooled (ZFC) and field-cooled (FC) regimes in a magnetic field applied parallel ($\sigma_\parallel$) and perpendicular ($\sigma_\perp$) to the *c* axis. The isothermal magnetization measured at 2 K with the field applied along the two characteristic directions is presented in Fig. 2. The overall shapes of these curves as well as the magnitude of $\sigma_\perp$ obtained in the FC mode unambiguously indicate strongly anisotropic ferromagnetism with a pronounced domain effect. The magnetic moments are confined to the basal hexagonal plane. The Curie temperature, defined as the inflection point on the $\sigma_\perp(T)$ variation, amounts to 26 K.

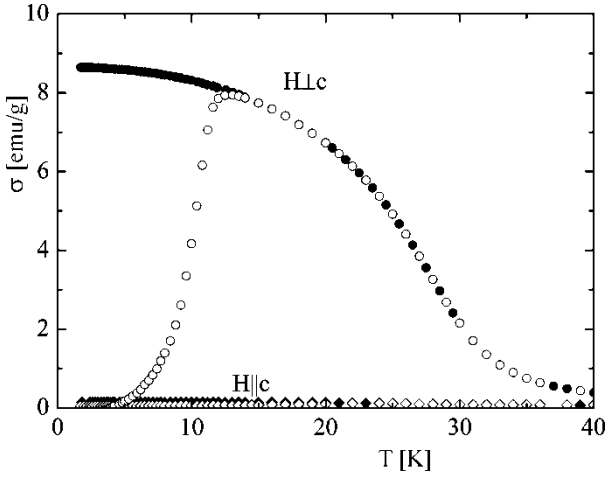

Fig. 1. Temperature dependences of the magnetization in U_2NiSi_3 measured in the ZFC (open symbols) and FC (full symbols) regimes with magnetic field (H = 1 kOe) applied parallel and perpendicular to the *c*-axis

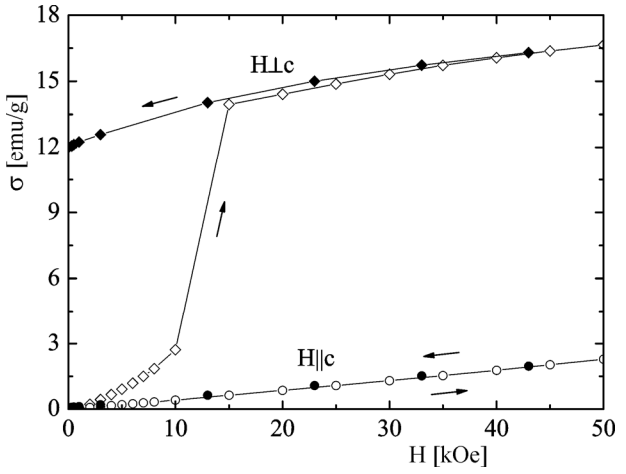

Fig. 2. Magnetization isotherms for U_2NiSi_3 taken at 1.7 K with increasing and decreasing magnetic field (H = 1 kOe) applied parallel and perpendicular to the c-axis

As shown in Fig. 3, a strong magnetocrystalline anisotropy is observed also in the paramagnetic state. The magnetic susceptibility measured along the c axis ($\chi_{\parallel}$) is much smaller than the component taken within the ab plane ($\chi_{\perp}$). Above ca. 100 K, the $\chi_{\parallel}(T)$ and $\chi_{\perp}(T)$ variations can be described by the modified Curie–Weiss law with the following parameters: $\chi_{0\parallel} = 6\times10^{-4}$ emu/mol, $\mu_{\mathrm{eff}\parallel} = 2.47\mu_B$, $\theta_{\mathrm{p}\parallel} = -14$ K and $\chi_{0\perp} = 8\times10^{-4}$ emu/mol, $\mu_{\mathrm{eff}\perp} = 2.64\mu_B$ and $\theta_{\mathrm{p}\perp} = 31$ K.

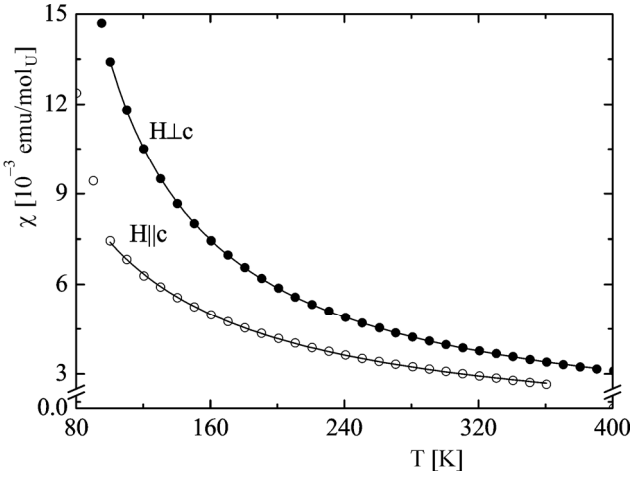

Fig. 3. Temperature dependences of the magnetic susceptibility of U_2NiSi_3 measured with magnetic field (H = 10 kOe) applied parallel and perpendicular to the c-axis. The solid lines represent fits to the experimental data of the modified Curie–Weiss law with the parameters given in the text

The ferromagnetic ordering in single-crystalline U_2NiSi_3, being evident in the magnetic characteristics, manifests only faintly in the heat capacity and electrical transport data.

The electrical resistivity, measured with the current flowing along ($\rho_{\parallel}$) and perpendicular ($\rho_{\perp}$) to the *c* axis, shows only tiny anomalies at T_C (see Fig. 4). Above ca. 60 K, the two resistivity components change with the temperature in a metallic manner, yet at lower temperatures some anomalous features are seen. Both curves exhibit shallow minima near 50 K, and in the ordered state the resistivities slightly increase with decreasing temperature. Worth noting is also that the overall changes in the values of $\rho_{\parallel}$ and $\rho_{\perp}$ over the entire temperature range are very small. The observed behaviour is likely to results from the presence of sizeable atomic disorder (i.e., Ni and Si atoms occupying same crystallographic site) in the unit cell of the compound studied.

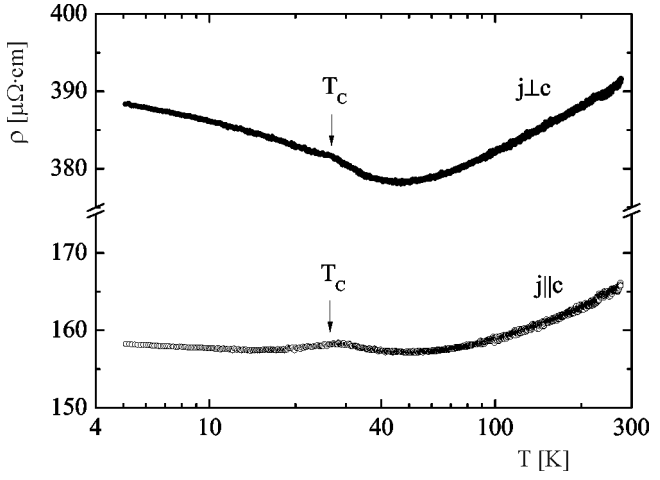

Fig. 4. Temperature dependences of the electrical resistivity of U_2NiSi_3 measured with the current flowing along and perpendicular to the *c*-axis. The arrows indicate the Curie temperature

The temperature dependence of the specific heat of U_2NiSi_3 is displayed in Fig. 5. The magnetic phase transition at T_C manifests itself only as a small kink on the $C(T)$ curve. As shown in the inset to Fig. 5, the plot C/T vs. T^2 yields for $T \to 0$ rather large linear contribution to the specific heat of about 140 mJ/($mol_U \cdot K^2$). This enhancement of the low-temperature heat capacity can be considered as another indication of the structural disorder in the sublattice of nonmagnetic atoms.

The results of the AC magnetic susceptibility studies are summarized in Fig. 6. Both components to the AC susceptibility, real and imaginary, form pronounced peaks close to T_C. Their positions depend on the frequency of alternating field, namely they systematically shift towards higher temperatures with increasing frequency. Simultaneously, the magnitude of the real component at the maximum decreases and that of the imaginary component rapidly increases. Such a behaviour is characteristic of spin glasses. The frequency dependence of the freezing temperature, defined as a maximum on the $\chi'(T)$ curve, is shown in the inset to Fig. 6. This variation can be well described using the empirical Vogel–Fulcher law [7]

$$\omega = \omega_0 \exp\left(-E_a/k_B\left(T_f - T_0\right)\right)$$

where ω_0 is the characteristic frequency, E_a denotes the activation energy and T_0 is the Vogel–Fulcher temperature.

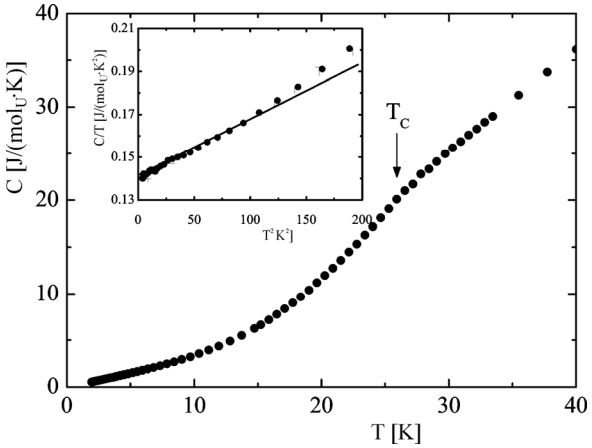

Fig. 5. Temperature variation of the specific heat of U_2NiSi_3; the arrow indicates the Curie temperature, as derived from the magnetic measurements. The inset displays the low-temperature data in the representation C/T versus T^2. The solid line emphasizes a straight-line behaviour for $T \to 0$

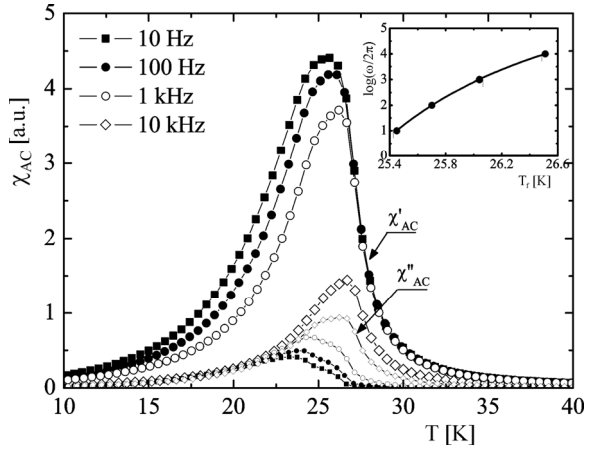

Fig. 6. Temperature dependence of real (χ'_{AC}) and imaginary (χ''_{AC}) components of the AC magnetic susceptibility of U_2NiSi_3 between 10 and 40 K (H = 10 Oe) at the frequencies 10 Hz $\leq \omega/2\pi \leq$ 10 kHz. The inset shows the frequency dependence of the freezing temperature T_f. The solid line represents the fit to the experimental data of the Vogel–Fulcher law with the parameters given in the text

The least squares fit of the experimental T_f versus $\omega/2\pi$ data for U_2NiSi_3 yields the following parameters: $\omega_0/2\pi = 10^9$ Hz, E_a/k_B = 31.9 K and T_0 = 23.7 K. The characteristic frequency is of the order of magnitude typical of metallic spin-glass systems.

Moreover, the characteristic temperature T_0 is somewhat lower than the Curie temperature $T_C = 26$ K, as predicted for spin glasses [7].

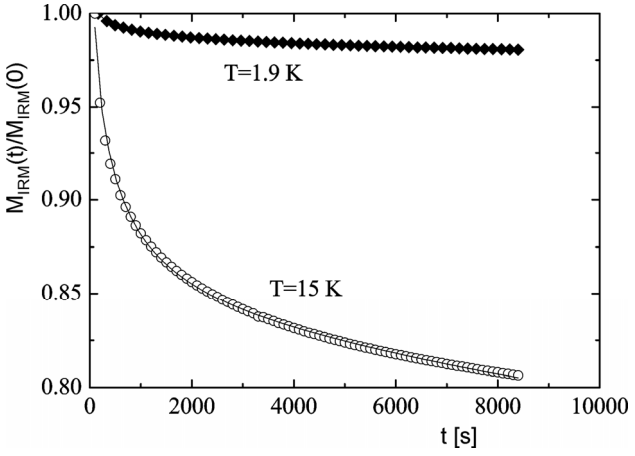

Fig. 7. Time dependence of the isothermal remanent magnetization in U_2NiSi_3 measured at 1.9 and 15 K upon applying magnetic field of 20 kOe perpendicular to the *c* axis for 5 min and switching it off. The solid lines are the fits to the experimental data of the formula $M_{IRM}(t) = M_0 + \alpha \ln t + \beta \exp(-t/\tau)$ with the parameters given in the text

Figure 7 shows the time dependence of reduced isothermal remanent magnetization (IRM) in U_2NiSi_3 recorded at 1.9 and 15 K. The sample was first zero-field cooled from a temperature much higher than T_f, then a magnetic field of 20 kOe was applied perpendicular to the *c* axis for 5 min and switched off at $t = 0$. As is apparent from Fig. 7, the IRM decay at both temperatures can be accurately described by the equation:

$$M_{IRM}(t) = M_0 + \alpha \ln t + \beta \exp(-t/\tau)$$

appropriate for non-magnetic atom disorder (NMAD) spin-glasses [4]. The least-squares fitting parameters: $M_0 = 11.9$ emu/g, $\alpha = -0.006$ emu/g, $\beta = -0.004$ emu/g, $\tau = 2872$ s for 1.9 K and $M_0 = 4.19$ emu/g, $\alpha = -0.02$ emu/g, $\beta = -0.01$ emu/g, $\tau = 3454$ s for 15 K are similar to the values reported for other NMAD systems [4, 8, 9]. An important feature of this class of spin glasses is the presence of the exponential term in the expression for $M_{IRM}(t)$, while for other spin glasses just the logarithmic term weighted by the magnetic viscosity parameter α is sufficient to properly describe their IRM behaviour [7–9].

4. Summary

The results of AC magnetization, magnetic relaxation, specific heat and electrical resistivity measurements of single-crystalline U_2NiSi_3 can be considered as strong

evidence for the formation of a spin-glass state in agreement with our initial hypothesis [3] and more recent results [5]. However, the freezing temperature T_f = 25–27 K (dependent on the frequency), determined in the present studies, somewhat differs from the value of 22 K given in the previous reports. On the other hand, the DC magnetic data obtained for the U_2NiSi_3 single crystal evidently indicate strongly anisotropic ferromagnetism which seems to support the conclusion derived from the neutron diffraction data [6]. Again, the Curie temperature T_C = 26 K is notably different from that reported before (T_C = 30 K [6]). Most likely these discrepancies arise due to small differences in the level of atomic disorder and/or possible deviations from the ideal stoichiometry in the previously studied polycrystalline samples and the single crystal investigated in the present work.

In conclusion, new results obtained for a single crystal of U_2NiSi_3 reveal the coexistence of long-range ferromagnetic ordering and spin-glass state with the Curie temperature equal to the freezing temperature. A similar behaviour was previously observed in isostructural compounds U_2RhSi_3 and U_2IrSi_3 which were classified as ferromagnetic cluster glass systems [5, 8]. A deeper insight into the intriguing physical behaviour of this series of uranium ternaries can be expected from neutron diffraction investigations. For this reason both elastic (to provide direct evidence for long-range ferromagnetic order) and inelastic (to study spin dynamics) neutron experiments on U_2NiSi_3 single crystals (they are large enough) are planned in the nearest future.

Acknowledgement

The authors are grateful to Dr. J. Stępień-Damm for orienting the U_2NiSi_3 single crystal on a four-circle diffractometer and to Dr. A. Zaleski for measuring the AC magnetic susceptibility. This work was supported by the Ministry of Science and Higher Education within research project No. N202 116 32/3270.

References

[1] PÖTTGEN R., KACZOROWSKI D., J. Alloys Compd., 201 (1993), 157.
[2] CHEVALIER B., PÖTTGEN R., DARRIET B., GRAVEREAU P., ETOURNEAU J., J. Alloys Comp. 233 (1996), 150.
[3] KACZOROWSKI D., NOEL H., J. Phys.: Condens. Matter, 5 (1993), 9185.
[4] LI D.X., SHIOKAWA Y., HOMMA Y., UESAWA A., DÖNNI A., SUZUKI T., HAGA Y., YAMAMOTO E., HONMA T., ONUKI Y., Phys. Rev. B, 57 (1998), 7434.
[5] LI D.X., DÖNNI A., KIMURA Y., SHIOKAWA Y., HOMMA Y., HAGA Y., YAMAMOTO E., HONMA T., ONUKI Y., J. Phys.: Cond. Matter, 11 (1999), 8263.
[6] SCHRÖDER A., COLLINS M.F., STAGER C.V., GARRETT J.D., GREEDAN J.E., TUN Z., J. Magn. Magn. Matt., 140–144 (1995), 1407.
[7] MYDOSH J.A., *Spin Glass. An Experimental Introduction*, Taylor and Francis, London, 1993.
[8] LI D.X., KIMURA A., HOMMA Y., SHIOKAWA Y., UESAWA A., SUZUKI T., Solid State Comm. 108 (1998), 863.
[9] LI D.X., NIMORI S., SHIOKAWA Y., HAGA Y., YAMAMOTO E., ONUKI Y., Phys. Rev. B 68 (2003), 172405.

Received 6 May 2007
Revised 13 June 2007

Materials Science-Poland, Vol. 25, No. 4, 2007

Magnetic and magnetoresistive properties of CoFe/Au/Co/Au multilayered structures*

B. SZYMAŃSKI**, M. URBANIAK, F. STOBIECKI

Institute of Molecular Physics, Polish Academy of Sciences,
ul. Smoluchowskiego 17, 60-179 Poznań, Poland

Sputter deposited $(Co_{90}Fe_{10}\ t_{CoFe}/Au\ 2.7nm/Co\ 0.6nm/Au\ 2.7nm)_{10}$ multilayers with t_{CoFe} in the 0.4–3.0 nm range were investigated. Magnetic reversal $M(H)$ and magnetoresitance $R(H)$ curves were measured. For $t_{CoFe} \geq 1.2$ nm, the $R(H)$ characteristics are similar to that of the prototype system (NiFe/Au/Co/Au), i.e. the system characterized by alternating in plane (NiFe) and out-of-plane (Co) magnetic anisotropy. However, for smaller t_{CoFe}, the effective anisotropy of CoFe layers switches from the in-plane anisotropy to the perpendicular one. This transition is a reason of a strong decrease of the GMR amplitude for $t_{CoFe} < 1.2$ nm. The relatively large values of GMR amplitude (≈ 7%) and saturation field (900 kA/m) were obtained for sample with $t_{CoFe} = 3$ nm, measured in perpendicular field configuration. The result indicates a distinct improvement of parameters important for application of studied films as magnetoresistive sensors characterized by the linear $R(H)$ dependence in a broad range of magnetic field.

Key words: *magnetic multilayers; perpendicular magnetic anisotropy; GMR sensor*

1. Introduction

In our previous papers [1–3], we have demonstrated that $(NiFe/Au/Co/Au)_N$ multilayers (MLs) characterized by in-plane and out-of-plane anisotropy for Ni–Fe and Co layers, respectively, can by applied as magnetoresistive sensors for quantitative measurements of magnetic field up to 500 kA/m. To extend further the range of magnetic field corresponding to the linear $R(H)$ dependence we have replaced $Ni_{80}Fe_{20}$ layers by $Co_{90}Fe_{10}$, i.e., by layers with a higher saturation magnetization. The thickness of Au layer t_{Au}=2.7 nm was chosen to ensure a negligible coupling between ferromagnetic layers. Because properties of the Co layer sandwiched between gold layers are well known [1] it allows us to determine magnetic properties of the $Co_{90}Fe_{10}$ layer, the function of t_{CoFe} from the analysis of $M(H)$ and $R(H)$ curves. We have chosen the layer with $t_{Co} = 0.6$ nm because it is continuous and shows a strong perpendicular anisotropy.

---

*Presented at the Conference of the Scientific Network "New Materials for Magnetoelectronics – MAG-EL-MAT 2007", Będlewo near Poznań, 7–10 May 2007.

**Corresponding author, e-mail: szyman@ifmpan.poznan.pl

2. Experimental

A set of $(Co_{90}Fe_{10}\ t_{CoFe}/Au\ 2.7\ nm/Co\ 0.6\ nm/Au\ 2.7\ nm)_{10}$ MLs with t_{CoFe} in the range from 0.4 to 3.0 nm was prepared using UHV magnetron sputtering [1]. The samples were deposited at room temperature onto naturally oxidized Si(100) wafers. A good periodic structure of MLs was confirmed by low- and high-angle X-ray diffraction. Magnetoresistance $R(H)$ and magnetization reversal $M(H)$ were studied at room temperature for a magnetic field applied perpendicular to the sample plane. $M(H)$ loops were recorded with vibrating sample magnetometer. $R(H)$ curves were recorded with current in plane configuration (CIP). The GMR(H) dependence was determined as $[R(H) - R(1600\ kA/m)]/R(1600\ kA/m)$ where $R(1600\ kA/m)$ is electrical resistance at $H = 1600$ kA/m. The maximum value of GMR(H) defines the GMR amplitude.

3. Results and discussion

The exemplary $M(H)$ and $R(H)$ curves of $(Co_{90}Fe_{10}\ t_{CoFe}/Au\ 2.7\ nm/Co\ 0.6\ nm/Au\ 2.7\ nm)_{10}$ MLs ($0.4 \le t_{CoFe} \le 3.0$ nm) are shown in Fig. 1. For $t_{CoFe} \ge 1.2$ nm (Figs. 1a–c), the magnetization reversals of CoFe and Co layers are distinct and we can determine fields corresponding to the nucleation (H_N^{Co}) and annihilation (H_A^{Co}) of stripe domains

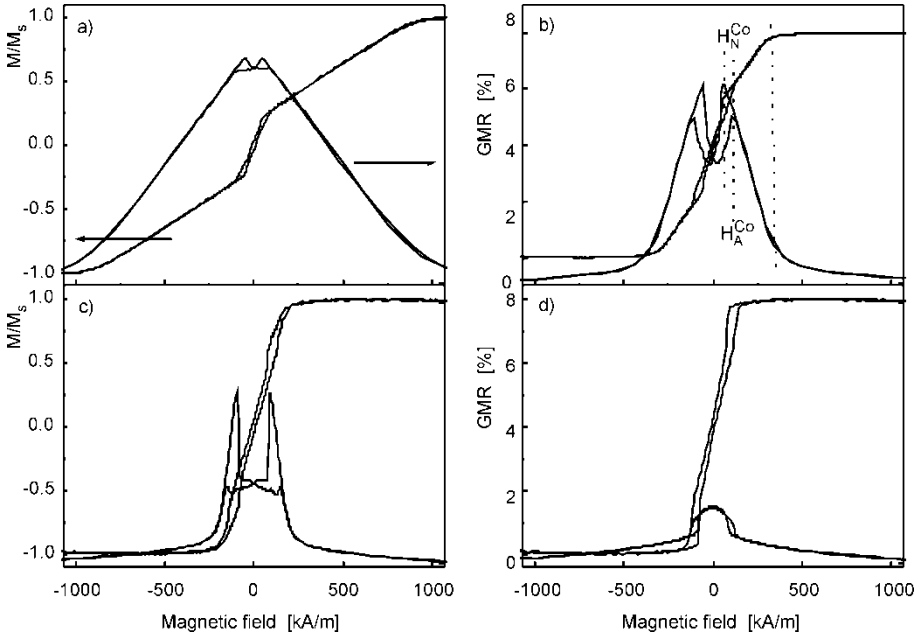

Fig. 1. Exemplary hysteresis loops and magnetoresistance curves of $(Co_{90}Fe_{10}\ t_{CoFe}/Au\ 2.7\ nm/Co\ 0.6\ nm/Au\ 2.7\ nm)_{10}$ MLs with various t_{CoFe}: a) 3.0 nm, b) 1.5 nm, c) 1.2 nm, d) 1 nm

in Co layers as well as saturation field of CoFe layers (H_S^{CoFe}). This behaviour is similar to that observed for ($Ni_{80}Fe_{20}$/Au/CoAu) multilayers [3] and therefore $M(H)$ and $R(H)$ dependences can be described in a similar way. Due to thick spacer layer (t_{Au} = 2.7 nm), the interlayer coupling between ferromagnetic layers is weak (except dipolar coupling caused by the domain structure) and their magnetization reversals can be treated as nearly independent of each other. However, as we have mentioned in [3], this is true for H_N^{Co}, $H_A^{Co} \leq |H| \leq H_S^{CoFe}$ (non-hysteretic range) where the coherent rotation of magnetization in CoFe layers takes place and the magnetization of Co layers is aligned along the field direction. In this field range, $R(H)$ dependences are linear and reversible. On the contrary, for $|H| \leq H_N^{Co}$, H_A^{Co} a strong ferromagnetic coupling originating from the stripe domain structure of Co layers strongly influences the magnetic configuration of the system. As a consequence, the resistance is reduced. In particular, at $H = 0$ the angle Θ between the magnetization directions of CoFe and Co is lower than 90º (for MLs with zero coupling, the mutually perpendicular orientation of magnetization in Co and CoFe layers is expected at remanence).

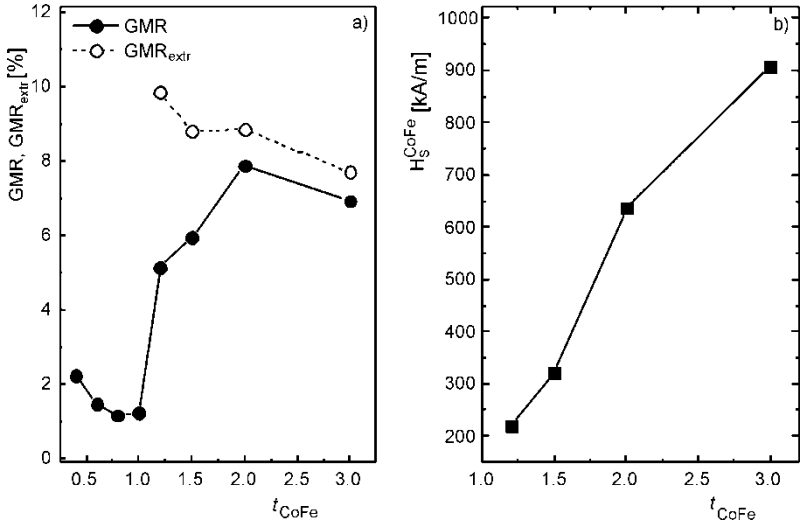

Fig. 2. The GMR amplitude and the extrapolated GMR_{extr} values (a) as well as the saturation field H_S^{CoFe} of the MLs as a function of t_{CoFe} (b). The extrapolated GMR values were determined by extrapolation of the linear part of GMR curves to zero field

The main difference between previously investigated ($Ni_{80}Fe_{20}$/Au/Co/Au) and ($Co_{90}Fe_{10}$/Au/Co/Au) multilayers concerns changes of the saturation field and the GMR amplitude with the thickness of NiFe and CoFe, respectively. For (NiFe/Au /Co/Au) MLs both dependences, i.e., GMR(t_{NiFe}) and $H_S(t_{NiFe})$ are presented in Fig. 3 in [2], for (CoFe/Au/Co/Au) MLs they are shown in Fig. 2. In GMR(t_{CoFe}) dependence an abrupt increase of GMR value is observed at $1 \leq t_{CoFe} \leq 1.2$ nm (compare also Figs. 1c and d). This effect is related to the transition of effective magnetic anisotropy

of CoFe layers from the perpendicular (for $t_{CoFe} \leq 1$ nm) to in-plane (for $t_{CoFe} \geq 1.2$ nm). The anisotropy changes with the thickness of CoFe layers are caused by the competition between volume and surface anisotropy [4]. Due to high concentration of Co in CoFe layers, the thickness at which the reorientation of magnetization takes place is reduced only by 0.2 nm as compared to Co layers, sandwiched between Au. The field range at which the linearity requirement of $R(H)$ is fulfilled, is crucial for application of investigated films as magnetoresistive sensors. This range is determined mainly by the saturation field of CoFe layers (H_S^{CoFe}) which is the measure of the anisotropy. The H_S^{CoFe} (t_{CoFe}) dependence for $t_{CoFe} \geq 1.2$ nm is demonstrated in Fig. 2b and indicates that for (CoFe/Au/Co/Au) MLs, H_S^{CoFe} can be tuned in a broad range. In particular, for the MLs with $2 \leq t_{CoFe} \leq 3$ nm the larger range of linear $R(H)$ dependence and the larger GMR amplitude as for (NiFe/Au/Co/Au) MLs can be simultaneously realized.

Finally, we will discuss specific changes of the magnetoresistance effect of our (CoFe/Au/Co/Au) MLs with the thickness of CoFe layers in the range corresponding to the magnetic reorientation transition. The (CoFe 1.2 nm/Au 2.7 nm/Co 0.6 nm/Au 2.7 nm)$_{10}$ sample is characterized by in-plane and perpendicular anisotropy of CoFe and Co layers, respectively. Due to a very weak anisotropy (low value of saturation field), the reaction of the 1.2 nm thick CoFe layer on stray fields caused by domains of Co layers is very strong (Fig. 1c). Therefore, for this sample the resistance is strongly reduced at $H = H_N$ and the difference between the measured GMR amplitude and the extrapolated GMR value (corresponding to $\Theta = \pi/2$) is particularly large (Fig. 2a). Moreover, the range of reversible changes in $R(H)$ is also strongly reduced as compared to MLs with larger t_{CoFe}. For (CoFe/Au/Co/Au) MLs with $t_{CoFe} \leq 1$ nm (Fig. 1d), the effective anisotropy of CoFe layers is perpendicular. Thus, the MLs are composed of two types of ferromagnetic layers each having perpendicular anisotropy. Their $R(H)$ dependences are distinctly different from those analyzed previously. The $R(H)$ and $M(H)$ dependences for ML with $t_{CoFe} = 1$ nm are presented in Fig. 1d. The character of $R(H)$ dependence for other MLs with $t_{CoFe} < 1$ nm is similar. For these samples, the linear and reversible range of the $R(H)$, characteristic of MLs with alternating in-plane and perpendicular anisotropy (Fig. 1a–c), is not present (small changes of resistance for $|H| \geq H_N$ (H_A) are related to the electron scattering on superparamagnetic precipitations [5]). The resistance increase at H_N and decrease at H_A (Fig. 1d) can be explained as follows. At $H = H_N$, the stripe domain structure is formed simultaneously in Co and CoFe layers. Due to a strong dipolar coupling ferromagnetic in nature, the shapes and dimensions of the domains and orientations of their magnetic moments are the same in all ferromagnetic layers. However, for such a magnetic configuration, a part of electrons traversing the structure in the vicinity of the domain walls interacts with ferromagnetic domains characterized by antiparallel configuration of magnetizations. The probability of this process, as compared to scattering in ferromagnetic regions with the parallel magnetic moment configuration, is negligible in MLs with large domains.

However, this effect can be essential in MLs with narrow stripe or labyrinth domains. For investigated layered films with perpendicular anisotropy of all ferromagnetic layers and stripe domain structure, the GMR effect measured in CIP geometry is about 1% (Fig. 2a). This value is about twenty times smaller than that expected for transition from antiparallel to parallel magnetic configuration. The latter should be twice larger than the extrapolated GMR amplitude corresponding to the transition between mutually parallel and perpendicular magnetic configurations (Fig. 2a).

4. Conclusions

Magnetic and magnetoresisitve properties of sputtered $(Co_{90}Fe_{10}\ t_{CoFe}$/Au 2.7 nm/Co 0.6 nm/Au 2.7 nm$)_{10}$ MLs with t_{CoFe} in the range from 0.4 nm to 3.0 nm were investigated. We have found that for the $2 \le t_{CoFe} \le 3$ nm the $R(H)$ dependences are linear and non-hysteretic and show GMR amplitudes of 6–8%. Thus, the replacement of NiFe layer by CoFe layer results in a considerable improvement of parameters important for the application of investigated MLs as magnetic field sensors for quantitative measurements of magnetic field in a broad range. We have also demonstrated that $R(H)$ measurements are a very sensitive tool for determination of magnetic reorientation transition in ultrathin ferromagnetic films.

Acknowledgements

Supported by the State Committee for Scientific Research with Grant No. 3 T08A 03127 and from the science resources as a joint research program within the scientific network "New materials and sensors for optoelectronics, informatics, energetic and medicine".

References

[1] STOBIECKI F., SZYMAŃSKI B., LUCIŃSKI T., DUBOWIK J., URBANIAK M., RÖLL K., J. Magn. Magn. Mater., 282 (2004), 32.
[2] SZYMAŃSKI B., STOBIECKI F., URBANIAK M., J. Alloy Compd., 423 (2006), 236.
[3] URBANIAK M., STOBIECKI F., SZYMAŃSKI B., EHRESMANN A., MAZIEWSKI A., TEKIELAK M., J. Appl. Phys., 101 (2007), 013905.
[4] CHAPPERT C., LE DANG K., BEAUVILLAIN P., HURDEQUINT H., RENARD D., Phys. Rev. B, 34 (1986), 3192.
[5] LUCIŃSKI T., J. Magn. Magn. Mater., 219 (2000), 303.

Received 4 May 2007
Revised 2 July 2007

Materials Science-Poland, Vol. 25, No. 4, 2007

Structure and magnetism of Co_2CrAl Heusler alloy films*

J. DUBOWIK[1**], I. GOŚCIAŃSKA[2], Y. V. KUDRYAVTSEV[3], V. A. OKSENENKO[3]

[1]Institute of Molecular Physics, Polish Academy of Sciences, 60-179 Poznań, Poland

[2]Department of Physics, A. Mickiewicz University, 61-614 Poznań, Poland

[3]Institute of Metal Physics, National Academy of Sciences of Ukraine, Kiev142, Ukraine

We report on magnetic properties of Co_2CrAl thin films. Low-field magnetization measurements show that the films with the best $B2/L21$ structure exhibit ferromagnetic order below the Curie temperature $T_C \approx 330–340$ K and below 200 K they exhibit magnetic characteristics suggesting the presence of antiferromagnetic ordering. Our ferromagnetic resonance measurements confirm a complex magnetic phase diagram of Co_2CrAl due to a disorder between Co and Cr sites in nominally $L2_1$ or $B2$ structures.

Key words: *magnetic properties; Co_2CrAl thin film; Heusler alloy*

1. Introduction

Heusler alloys (HA) have attracted scientific and technological interest for their potential use as materials for spintronic devices since some of them are half-metallic ferromagnets, i.e., they exhibit a complete spin polarization at the Fermi level. For example, Ishida et al. [1] have shown that Co_2CrAl HA has a complete spin polarization at the Fermi level. Later on, Galanakis [2] predicted that Co_2CrAl may preserve nearly half-metallic behaviour even at the surface, which in most HA can be regarded as a two-dimensional defect. In HA, the defects (atomic disorder, for example) are known to substantially deteriorate half-metallicity. In Co_2CrAl, it has been found [3] that Co/Cr type of atomic disorder destroys spin polarization while Cr/Al disorder does not significantly influence its half-metallicity.

Co_2CrAl HA can be regarded as the end-point of a series of $Co_2Cr_{1-x}Fe_xAl$ (further referred to as CCFA) which have recently received much attention for their remarkable

---

*Presented at the Conference of the Scientific Network "New Materials for Magnetoelectronics – MAG-EL-MAT 2007", Będlewo near Poznań, 7–10 May 2007.

**Corresponding author, e-mail: dubowik@ifmpan.poznan.pl

magnetoresistive properties found in pressed powder compacts [4]. Thin CCFA films have been extensively investigated in the context of potential applications in spintronic devices, too. Inomata et al. [6] have shown that a magnetic tunnelling junction based on the Heusler alloy $Co_2Cr_{0.6}Fe_{0.4}Al$ with a disordered $B2$ structure has a relatively large tunnel magnetoresistance of 16% at RT and ~26.5% at 5 K. Hirohata et al. [8] reported on deposition of Co_2CrAl films on GaAs substrates by using MBE in a UHV environment. They have shown that the Co_2CrAl films have a mixed $L2_1/B2$ (or even $A2$) structure.

Even though the CCFA HA hold a promise for the realization of half-metallicity at RT, their magnetic properties have been found to largely differ from the theoretically predicted [2] for the $L2_1$ structure (~ $3\mu_B$ per formula unit ≈ 600 G), where the magnetic moments of Co and Cr are 0.76 and $1.54\mu_B$, respectively. For example, the magnetic moment per formula unit at 5 K has been estimated to ~ $0.9\mu_B$ for Co_2CrAl thin films with $B2$ structure [6]. It is significantly lower than ~ $1.7\mu_B$ reported for a polycrystalline bulk alloy [9] with $A2$ structure and about 3 times lower than the theoretical value. Generally, the same as in other HA, it has been found that the magnetic properties (the Curie temperature and the saturation magnetization) of Co_2CrAl are strongly depressed due to disorder and inhomogeneities at the micrometric level and depends on the method of synthesis [4]. In this paper, we study magnetic properties of polycrystalline Co_2CrAl thin films with various structural ordering. We show that, depending on the ordering, low temperature magnetic properties and the Curie temperature of Co_2CrAl thin films may vary substantially.

2. Experimental details

Bulk Co_2CrAl HA was prepared by melting Co, Cr and Al pieces of 99.99% purity together in an arc furnace with a water-cooled Cu hearth under Ar atmosphere at the pressure of 1.3 atm. To promote the volume homogeneity, the ingot was remelted 5 times and then annealed at 1273 K during 10 h under vacuum. The X-ray fluorescence analysis revealed the alloy composition of $Co_{0.517}Cr_{0.245}Al_{0.238}$ (hereafter referred to as Co_2CrAl). Co_2CrAl alloy films about 100 nm thick with various degrees of the structural order were prepared by flash evaporation onto glass and NaCl substrates simultaneously under vacuum better than 2×10^{-5} Pa. To obtain the Co_2CrAl films with the maximum possible disorder, we deposited them onto substrates cooled by liquid nitrogen ($T_s \approx 150$ K). Such as-deposited Co_2CrAl films were then subsequently annealed at 538, 608 and 760 K for 1 h under high vacuum. Additionally, some Co_2CrAl films were also deposited onto substrates at 723 K. The Co_2CrAl alloy films with various structural order are referred as the films in states 1 ($T_s \approx 150$ K), 2 ($T_{ann} = 538$ K), 3 ($T_{ann} = 608$ K), 4 ($T_{ann} = 760$ K) and 5 ($T_s = 723$ K), respectively (see Table 1). The structural characterization of the samples was carried out by selective-area microdiffraction of transmission electron microscopy (TEM) for the films deposited and separated from the NaCl substrates. The structural properties of Co_2CrAl films are summarized in Table 1.

Table 1. Structure, microstructure and magnetic properties of the Co_2CrAl films in various structural states depending on the annealing temperature (T_{ann}) or the substrate temperature (T_s). T_C is the Curie temperature, M_S – saturation magnetization at RT. NM – nonferromagnetic

Film state	T_s [K]	T_{ann} [K]	Lattice parameter [nm]	Structure	Mean grain size [nm]	T_C [K]	M_S [emu/cm^3]
1	150	293	0.578	amorphous	< 2	NM	NM
2	150	538	0.572	*A*2	~ 10	270	NM
3	150	608	0.572	*B*2	~ 1000	290	90
4	150	760	0.570	*B*2/$L2_1$	~ 1000	340	200
5	728		0.570	*B*2	~ 20- 30	330	220

Magnetic properties were investigated in the temperature range 5–350 K using SQUID magnetometer at low external magnetic field of 100 Oe. The temperature dependences of the out-of-plane ferromagnetic resonance (FMR) at 9.3 GHz were investigated in 80–350 K temperature range. The hysteresis loops were measured with a vibrating sample magnetometer at RT and 175 K.

3. Results and discussion

A standard method applied to order structurally HA films is their annealing at elevated temperatures [7] or deposition onto heated substrates [8]. Figure 1 shows TEM diffractograms and dark field TEM images of the Co_2Cr Al films deposited onto substrates cooled at 150 K (Fig. 1a – state 1) and subsequently annealed at 538 K (Fig. 1b – state 2), 608 K (Fig. 1c – state 3) and 760 K (Fig. 1d – state 4), respectively.

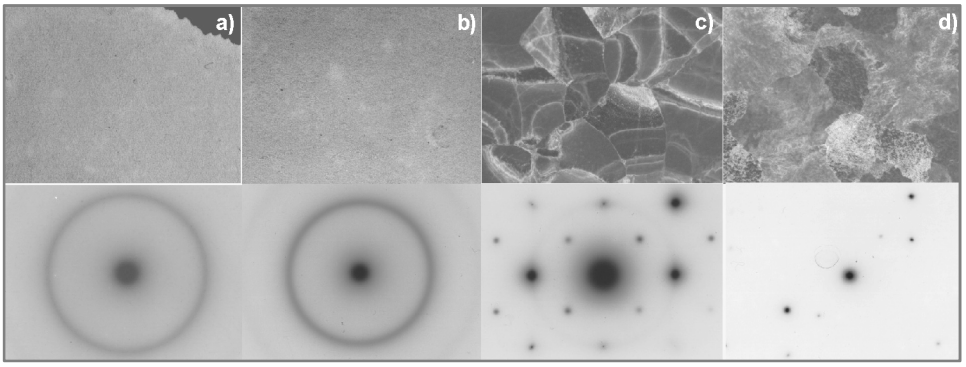

Fig. 1. Room temperature TEM micrographs and diffraction patterns for the Co_2CrAl films deposited onto NaCl substrates at 150 K (a), annealed at 538 K (b), 608 K (c) and 760 K (d)

The films in state 1 are nanocrystalline or amorphous. Annealing at 538 K results in their crystallization with *A*2 type of ordering and a very small grain size of 10 nm. Annealing at higher temperatures (Figs. 1c, d) leads not only to a further increase of

structural order to $B2$ (T_{ann} = 608 K) or a mixed $B2/L2_1$ (T_{ann} = 760 K) structure but also to a significant grain size growth up to 1000 nm.

Such a large growth in structural order brings about a growth in ferromagnetic ordering. As can be seen in Table 1, both the Curie temperature T_C and the saturation magnetization M_S increase with the growth in structural ordering. But even the best-ordered Co_2CrAl films (state 4) have magnetization much lower than theoretically predicted M_S = 600 G [2].

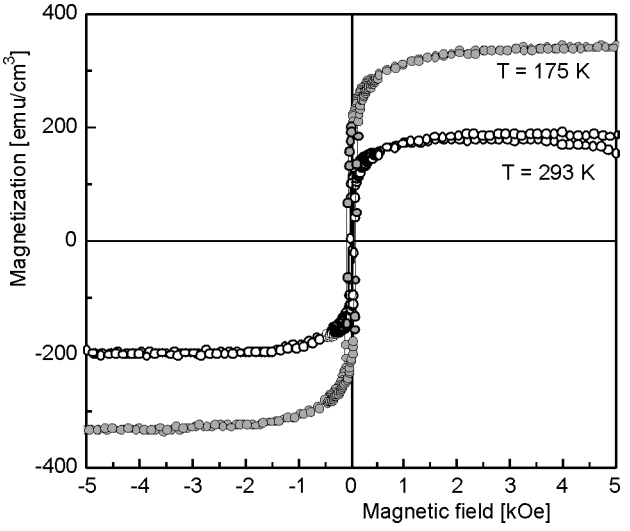

Fig. 2. Magnetization measured at 175 K and 293 K as a function of magnetic field for $B2/L2_1$ ordered Co_2CrAl film annealed at 760 K (state 4)

Figure 2 shows the hysteresis loops of the Co_2CrAl film in state 4 recorded at 175 and 293 K, respectively. The saturation magnetization at 175 K is only 350 G what gives 1.7μ_B per formula unit. Similar results have been reported by Inomata et al. [6]. In state 4 the Co_2CrAl film is a soft magnet: its coercivity H_C is 80 Oe at 175 K, decreasing to 30 Oe at 293 K. Nevertheless, despite low coercivity, the magnetization at 175 K saturates at relatively high fields of the order of 2–3 kOe, suggesting the existence of local antiferromagnetic (AF) interactions at low temperatures even in the best-ordered films. This may be attributed to Cr atoms partially occupying Co sites, as was theoretically suggested by Miura et al. [3], who have shown that Cr atoms occupying Co sites are antiferromagnetically coupled with Co atoms. To check such a scenario, we measured the temperature dependence of the magnetic moment in a low external magnetic field of 100 Oe in a zero-field-cooled state (ZFC) by cooling it from 350 K to 5 K in the absence of magnetic field. Subsequently, magnetic field was applied and the measurements were taken on increasing temperature up to 350 K. Then, without removing the external field, the measurement was made on decreasing temperature, i.e., in a field-cooled (FC) state. Figure 3 shows the results of ZFC and FC

measurements for the Co_2CrAl film in state 4. It is seen that ZFC curve does not retrace the FC curve in a similar way as in the magnetic materials with competing F/AF interactions (e.g., spin glasses). In our best-ordered Co_2CrAl films, such a behaviour would be rather explained as resulting from coexistence of AF exchange within ferromagnetic matrix. The nature of the onset of AF ordering in Co_2CrAl films at low temperatures is not clear at present: it can either arise from a structural martensitic transformation (as in some HA, for example Ni–Mn–Sn HA [10]) or it is just related to a local AF exchange leading to non-collinear spin structures which can pin the ferromagnetic domains in different configuration depending on whether the sample is cooled in an external field or not. The Curie temperature T_C estimated from the low-field magnetization measurements is 340 K.

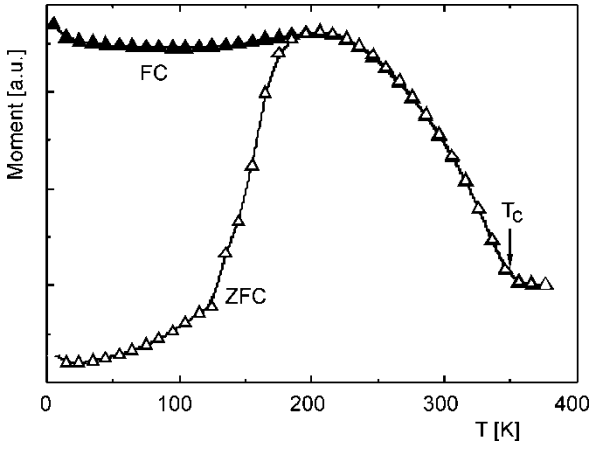

Fig. 3. FC (solid symbols) and ZFC (open symbols) $M(T)$ dependences for the $B2/L2_1$ ordered Co_2CrAl film annealed at 760 K (state 4)

The anomalous ZFC characteristics for the best ordered Co_2CrAl film with $B2/L2_1$ structure is confirmed by the FMR results. Figure 4a shows the temperature dependence of the effective magnetization $4\pi M_{\text{eff}}$ for the film in the state 4 and 3, for comparison. $4\pi M_{\text{eff}} = H_r^{\text{perp}} - \omega/\gamma$ was calculated from the resonance field H_r^{perp} measured in the perpendicular configuration assuming g-factor equal 2.1, i.e., the same as for other HA [11]. It is seen that $4\pi M_{\text{eff}}$ of the Co_2CrAl film in state 4 experiences a similar anomalous behaviour as ZFC magnetization, i.e., it decreases substantially below 200 K. If the temperature behaviour of $4\pi M_{\text{eff}}$ were regular (as is shown in Fig. 4a by a dashed curve), the extrapolated to 0 K $4\pi M_{\text{eff}}$ value would attain ~5200 G ($M_{\text{eff}} \approx 400$ G) in a rough agreement with our static magnetization data (Fig. 2). On the other hand, $4\pi M_{\text{eff}}$ vs. T for the film in state 3 is quite regular with the value extrapolated to 0 K of the order of 4000 G ($M_{\text{eff}} \approx 320$ G). The estimated T_C for the film in state 3 is of ~290 K in agreement with the low-field magnetization data. However, for the film in state 4 the FMR signal is observed at temperatures higher than T_C = 340 K. It

would indicate the existence of the local ferromagnetic correlations well above T_C in the Co_2CrAl films with the highest structural ordering. We argue that the Co/Cr antisite disorder seems to be responsible for these high-temperature ferromagnetic correlations. According to the theoretical calculations [12], the Cr magnetic moment strongly depends not only on the kind of surrounding atoms but also on the arrangement of these atoms around the Cr atom. Hence, both anomalous behaviour of $4\pi M_{eff}$ at low temperatures due to mixed ferro-/antiferromagnetic exchange and the high-temperature correlations above T_C may be regarded as the experimental evidences of a local structural disorder of Co and Cr atoms.

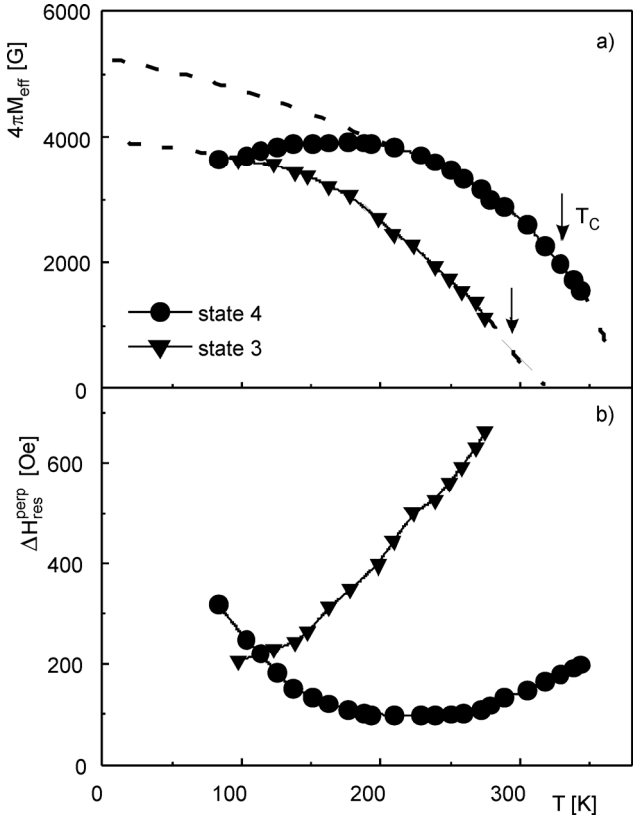

Fig. 4. Temperature dependences of the effective magnetization $4\pi M_{eff}$ of the Co_2CrAl films annealed at 608 K (state 3) and 760 K (state 4) (a); FMR resonance linewidth ΔH for the same films (b)

FMR linewidth ΔH is a sensitive measure of the presence of magnetic inhomogeneities in magnetic thin films [13]. Inhomogenetities of the internal effective magnetic field lead to an inhomogeneous broadening of the FMR linewidth. Therefore, the presence of the low temperature transformation to a mixed ferro-/antiferromagnetic state should perturb the temperature behaviour of ΔH in Co_2CrAl films at low temperatures.

Fig. 4 (b) shows the temperature dependencies of ΔH measured for the films in state 3 and 4, respectively. It is seen that ΔH for the film in state 3 is relatively large and increases monotonically on approaching T_C due to the presence of critical correlations near the phase transformation and significant magnetic inhomogeneities [13]. For the film in state 4 the linewidth is very narrow (~90 Oe) and nearly independent of temperature in a range of $175<T<275$ K indicating a very good film quality. However, at low temperatures below ~175 K, it strongly increases. We attribute such an increase to the presence of a mixed ferro-/antiferromagnetic mixed state.

4. Summary

The structure, microstructure and magnetic properties of Co_2CrAl thin films were investigated. The best-ordered Co_2CrAl films annealed at $T_{ann}>700$ K reveal a mixed $B2/L2_1$ structure and the saturation magnetization (extrapolated to 0 K) of 400 G (~$2\mu_B$ per formula unit). The presence of anomalous behaviour in low-field magnetization and FMR response below 175 K can be accounted to the disorder between Co and Cr sites, which makes a considerable reduction of the total magnetic moment per formula unit and the presence of a mixed ferro-/antiferromagnetic exchange coupling.

References

[1] ISHIDA S., FUJII S., KASHAWAGI S., ASANO S., J. Phys. Soc. Jpn., 64 (1995), 2152.
[2] GALANAKIS I., J. Phys.: Condens. Matter, 14 (2002), 6329.
[3] MIURA Y., NAGAO K., SHIRAI M., Phys. Rev. B, 69 (2004), 14413.
[4] DE TERESA J.M., SERRATE D., CORDOBA R., YUSUF S.M., to be published in J. Alloys Compd. (2006), doi :10.1016/j.allcom.2006.10.104.
[5] FELSER C., HETKAMP B., KRONAST F., SCHMITZ D., CRAMM S., ELMERS H-J., FECHER G.H., WURMEL S., BLOCK T., VALDAITSEV D., NEPIJKO S.A., GLOSKOVSKII A., JAKOB G., SHÖNHESSE G., EBERHARDT W., J. Phys.: Condens. Matter, 15 (2003), 7019.
[6] INOMATA K., TEZUKA N., OKAMURA S., KUREBAYASHI H., HIROKATA A., J. Appl. Phys., 95 (2004), 7234.
[7] KUDRYAVTSEV Y.V., OKSENENKO V.O., LEE N.N., LEE Y.P., RHEE J.Y., DUBOWIK J., J. Appl. Phys., 97 (2005), 113903.
[8] HIROHATA A., OKAMURA H.S., KIKUCHI M., MASAKI T., NOZAKI T., TEZUKA N., INOMATA K., J. Appl. Phys., 97 (2005), 10C308.
[9] ZHANG M., WOLF A.L., ZHANG L., TEQUS O., BRÜCKE E., WU G., DE BOER F.R., J. Appl. Phys., 97 (2005), 10C301.
[10] KRENKE T., ACET M., WASSERMANN E.F., MOYA X., MAÑOSA L., PLANES A., Phys. Rev. B, 72 (2005), 014412.
[11] PECHAN M.J., YU C., CARR D., PALMSTRÖM C.J., J. Magn. Magn. Mater., 286 (2005), 340.
[12] ANTONOV V.N., DÜRR H.A., KUCHERENKO YU., BEKENOV L.V., YARESKO A.N., Phys. Rev. B, 72 (2005), 054441.
[13] FARLE M., Rep. Prog. Phys., 61 (1998), 755.

Received 3 May 2007
Revised 4 July 2007

Materials Science-Poland, Vol. 25, No. 4, 2007

Magnetic properties of $(Co/Au)_N$ multilayers with various numbers of repetition N*

P. MAZALSKI[1], I. SVEKLO[1], M. TEKIELAK[1**], A. KOLENDO[1], A. MAZIEWSKI[1], P. KUŚWIK[2], B. SZYMAŃSKI[2], F. STOBIECKI[2]

[1]Institute of Experimental Physics, University of Białystok, Lipowa 41, 15-424 Białystok, Poland

[2]Institute of Molecular Physics, Polish Academy of Sciences, Smoluchowskiego 17, 60-179 Poznań, Poland

Magnetization reversal processes and magnetic domain structures have been studied in multilayered systems consisting of magnetostatically coupled cobalt layers separated by non-magnetic/soft-magnetic ones. Observations of the domain structures have been performed at room temperature using Kerr microscopy and magnetic force microscopy technique. The studies have been focused on the key characteristics of magnetic hysteresis loops as well as the domain structures and domain periods in such systems.

Key words: multilayers; ultrathin film; cobalt; domain structure; hysteresis loop

1. Introduction

Magnetic multilayers have been the subject of intensive research. Interest in such systems has grown rapidly, being motivated by the search of new magnetic materials, their novel magnetic properties and applications. Properties of magnetic multilayers can be easily manipulated by varying the thickness of both the magnetic and non-magnetic layers as well as by varying the number of layers [1–3]. It is known that in magnetic multilayers with perpendicular anisotropy, the saturation field of stripe domains exhibits a non-trivial dependence on the thickness of non-magnetic spacing [4]. Influence of ultrathin film thickness on the size of domain structure has been recently described [5].

In the paper, the influence of Co and Au layer thicknesses as well as the number of repetitions N on the magnetic properties of Co/Au multilayers has been presented.

---

*Presented at the Conference of the Scientific Network "New Materials for Magnetoelectronics – MAG-EL-MAT 2007", Będlewo near Poznań, 7–10 May 2007.

**Corresponding author, e-mail: tekmar@uwb.edu.pl

2. Samples and experiment

A few series of $[Co/Au]_N$ and $[Py/Au/Co/Au]_N$ (Py = $Ni_{80}Fe_{20}$) magnetic multilayers were deposited by dc magnetron sputtering in UHV conditions on an oxidized silicon substrate with the following structure:

- buffers – either Au (5 nm) or $[Py\ (2\ nm)/Au\ (2\ nm)]_{10}$,
- multilayers – either $[Co\ (d_{Co})/Au\ (d_{Au})]_N$ or $[Py\ (2\ nm)/Au\ (d_{Au})/Co\ (d_{Co})/Au\ (d_{Au})]_N$,

with d_{Co} = 0.6–1.5 nm, d_{Au} = 1.5 nm, 3 nm, and N = 1–15.

Sample composition was controlled by the XRF technique. Such specific types of structures were produced in order to examine the influence of magnetic (Co), non-magnetic (Au) and soft magnetic (Py) layers on the magnetic properties of nanostructures and their domain structures. All magnetic measurements in multilayer samples were done ex-situ at room temperature using the following techniques: magneto-optical Kerr effect (MOKE) for magnetic domain structure visualization, magneto-optical millimagnetometry for recording hysteresis curves as a function of magnetic field applied perpendicularly to the sample plane and atomic and magnetic force microscopy (AFM/MFM) for both surface structure and magnetic domain structure imaging beyond the optical resolution. The study of magnetization reversal was performed using a MOKE-based magnetometer with the laser wavelength of 640 nm and a spot diameter of 0.5 mm. The polar magnetization component was measured as a function of the sweeping magnetic field. The LabView program controlled the measurements of the hysteresis loop and in real-time calculated saturation, remanence and the coercive field.

Magnetic domain structure was visualized using the polar Kerr effect. A Carl Zeiss Jenapol optical polarizing microscope with xenon lamp illumination was equipped with a high sensitivity camera with a cooled CCD element and a computer controlled frame grabber. The video signal was electronically processed, subsequently digitized, and then improved by standard image processing techniques (including subtracting the reference image). A computer controlled set-up enabled the adjustment of image acquisition time as well as the generation of pulses of magnetic field oriented perpendicularly to the film plane and characterized by the duration of amplitude and time. The images presented in the paper were acquired in a zero magnetic field. The following procedure was used for magnetic domain generation and visualization: the sample was saturated in magnetic field, then the field was reduced to zero and the reference image I_R recorded. A magnetic field pulse in the opposite direction with the amplitude smaller than saturation was applied and the domain structure image I recorded. The final resulting image was calculated as the difference between the domain structure image I and the reference image I_R.

The MFM technique was used for imaging the magnetic structures beyond the optical resolution [6, 7]. In our case, an NT-MDT NTEGRA system equipped with low magnetic moment MFM tips (MESP-LM, Veeco) was used. A tapping/lift mode enables obtaining of both the topography and the map of magnetic interaction between the sample and a tip.

3. Results and discussion

The influence of the repetition number N on both geometry of the domain structure and magnetization processes is illustrated in Fig. 1, obtained for 0.6 nm thick Co in the [Py (2 nm)/Au (2 nm)]$_{10}$/[Co (0.6 nm)/Au (1.5 nm)]$_N$ series. For small N, large irregular domain structures were observed. The geometry of the domains is determined by defects. Magnetization reversal process, starting from a "black" state by the appearance of limited number of irregular "white" domains, is illustrated in Fig. 1a, b.

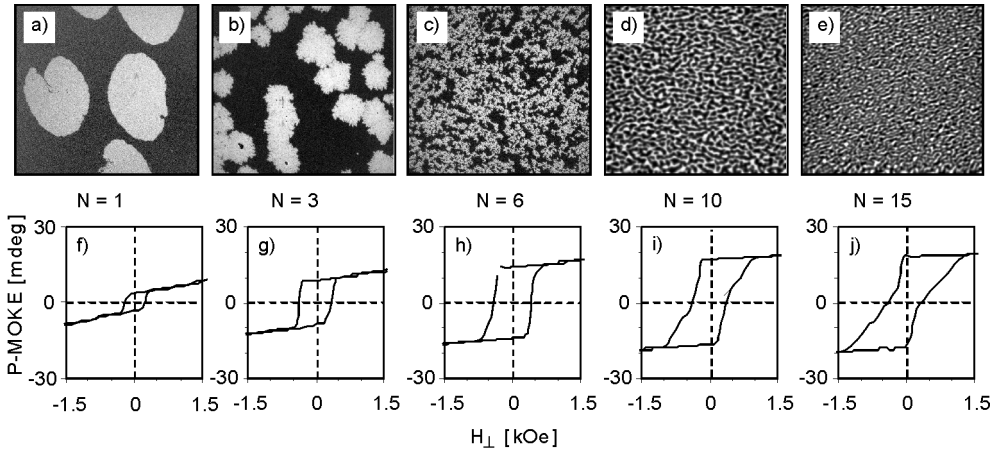

Fig. 1. Domain patterns and corresponding magnetooptic hysteresis loops for [Py (2 nm)/Au (2 nm)]$_{10}$/(Co (0.6 nm)/Au (1.5 nm)]$_N$ samples with various repetition numbers N. Image sizes are: a), b), c) 400×400 μm^2, d), e) 20×20 μm^2. Images a–c) and d), e) were recorded by magnetooptic and MFM techniques, respectively

With the increase of the repetition number N, stronger magnetostatic forces induce the ordering of domains and transition into stripe-like structures with submicrometer sizes is observed. Submicrometer domain structure periods were observed for all samples with large N. The repetition number induced the evolution of magnetization curves as illustrated in Fig. 1f–j. A rectangular hysteresis loop with negative nucleation field H_N in respect to the saturation field H_S was recorded for $N = 1$ (Fig. 1f). Similar loops were discussed in [8]. Upon increasing N, magnetostatic forces stimulate the increase of the saturation field H_S and the increase of the nucleation field H_N which could cross zero and become positive (parallel to H_S).

The influence of cobalt thickness on the magnetic properties of [Py (2 nm)/Au (2 nm)]$_{10}$/[Co (d_{Co})/Au (1.5 nm)]$_{15}$ samples is presented in Fig. 2. A relevant characteristic of such systems ($N = 15$) is the magnetic stripe domain structure. When cobalt thickness increases both the saturation and the nucleation fields increase and the mean size of the domain structures decreases. The effect is connected with the decrease of the domain wall energy in relation to the d_{Co}-induced magnetic anisotropy [5].

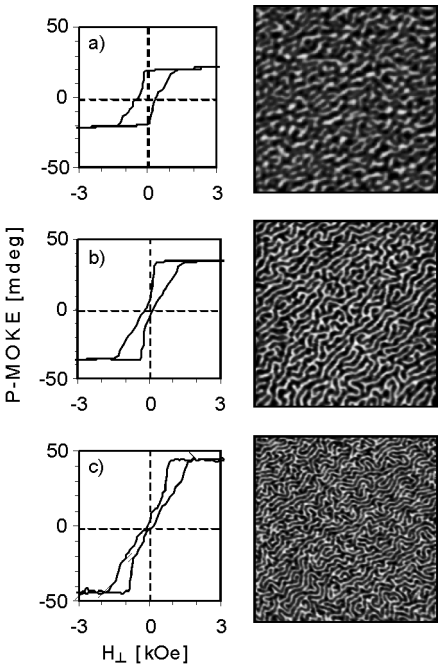

Fig. 2. MOKE hysteresis loops and MFM magnetic domain structure images recorded in samples $[Py\ (2\ nm)/Au\ (2\ nm)]_{10}/[Co(d_{Co})/Au\ (1.5\ nm)]_{15}$: a) $d_{Co} = 0.6$ nm, b) $d_{Co} = 1.0$ nm, c) $d_{Co} = 1.5$ nm. Image sizes are $10\times10\ \mu m^2$

Figure 3 shows magnetic hysteresis loops and domain structure images depending on the non-magnetic Au layer thickness d_{Au} for the fixed magnetic layer thickness $d_{Co} = 1.5$ nm. The magnetic domain structure period increases versus non-magnetic layer thickness. This is connected with the decrease of magnetostatic forces (a decrease in magnetostatic coupling) connected with d_{Au} increase. Multilayers with $d_{Co} = 0.6$ nm and $d_{Co} = 1.0$ nm exhibit a similar evolution with the increase of the gold layer thickness.

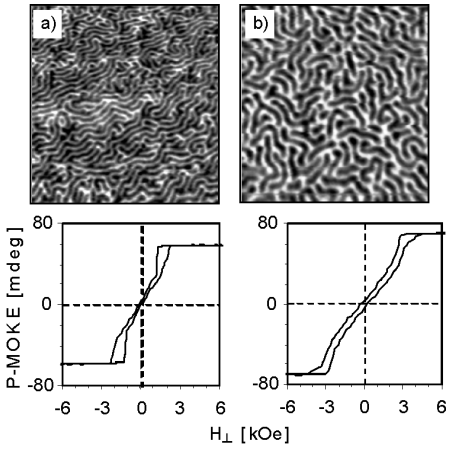

Fig. 3. Domain structure images and MOKE hysteresis loops in samples $Au\ (5\ nm)/([Co\ (1.5\ nm)/Au(d_{Au})]_{15}$ for various Au layer thicknesses: a) $d_{Au} = 1.5$ nm, b) $d_{Au} = 3.0$ nm. Image sizes are $5\times5\ \mu m^2$

One can find a significant influence of the permalloy layer on domain patterns and magnetization processes (Figs. 1, 4). Introduction of Py layers leads to screening of the magnetic field from adjacent Co layers and to the increase of the spacer thick-

ness. Because the magnetostatic coupling between Co layers is weaker, magnetization reversal occurs more independently in a particular layer. This effect is visible in Fig. 4a and b, as domains with multiple shades of gray or in multi-jumps in hysteresis loops. A similar magnetization reversal was observed in [9] for Co/Pt multilayer.

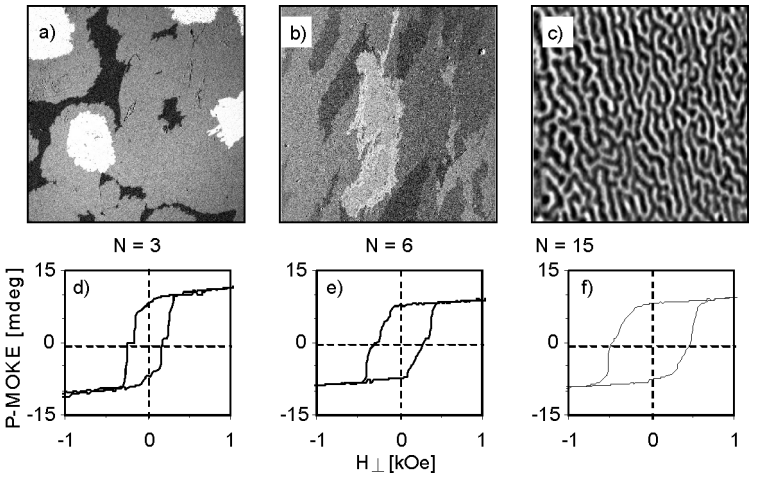

Fig. 4. Domain patterns and corresponding magnetooptic hysteresis loops recorded for $[Py\ (2\ nm)/Au\ (1.5\ nm)/Co\ (0.6\ nm)/Au\ (1.5\ nm)]_N$ for various repetitions numbers: a), d) $N = 3$, b), e) $N = 6$, c), f) $N = 15$. Images sizes are: a), b) $400\times400\ \mu m^2$, c) $15\times15\ \mu m^2$

MFM measurements in an external magnetic field applied perpendicular to the sample plane (Fig. 5) demonstrate that the magnetization process goes through domain wall motion. Bubble domain structure was observed while approaching saturation field (Fig. 5c).

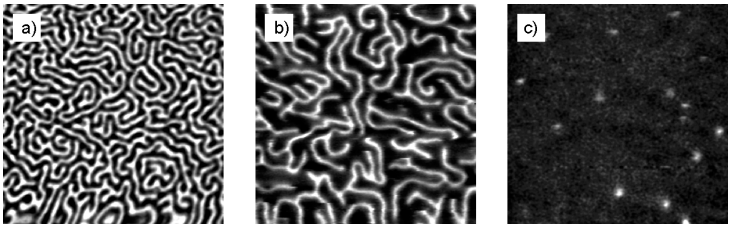

Fig. 5. Evolution of magnetic domain structure in external magnetic field applied perpendicular to the sample plane for $Au\ (5\ nm)/[Co\ (1\ nm)/Au\ (1.5\ nm)]_{15}$: a) $H = 0$ Oe, b) $H = 1.5$ kOe, c) $H = 2.1$ kOe recorded with MFM. Scan size is $5\times5\ \mu m^2$

4. Conclusion

We have studied the magnetic properties and magnetic domain structures of $[Co/Au]_N$ and $[Py/Au/Co/Au]_N$ multilayers grown with various numbers of repetition

N on different thicknesses of magnetic (Co), non-magnetic (Au) and soft–magnetic (Py) layers. All the analyzed multilayers display a decreased period of magnetic domain structure as the cobalt layer thickness grows, a decreased magnetic domain structure period with the increase number of repetition *N* and an increased domain structure period versus non-magnetic layer thickness.

Acknowledgements

This work was supported by the Marie Curie Fellowships for "Transfer of Knowledge" ("NANO -MAG-LAB" N 2004-003177).

References

[1] BARNES J.R., O'SHEA S.J., WELLAND M.E., KIM J.Y., EVETTS J.E., SOMEKH R.E., J. Appl. Phys., 76 (1994), 2974.
[2] DONZELLI O., PALMERI D., MUSA L., CASOLI F., ALBERTINI F., PARETI L., TURILLI G., J. Appl. Phys., 93, (2003), 9908.
[3] BELLIARD L., MILTAT J., KOTTLER V., MATHET V., CHAPPERT C., VALET T., J. Appl. Phys., 81 (1997), 8.
[4] DRAAISMA H.J.G., DE JONGE W.J.M., J. Appl. Phys., 62 (1987), 3318.
[5] KISIELEWSKI M., MAZIEWSKI A., POLYAKOVA T., ZABLOTSKII V., Phys. Rev. B 69 (2004), 184419 and references therein.
[6] ZHU X., GRÜTTER P., MRS Bull., 29 (2004), No. 7.
[7] HOPSTER H., OEPEN H.P., *Magnetic Microscopy of Nanostructures*, Springer, Berlin, 2005.
[8] FERRE J., GROLIER V., MEYER P., MAZIEWSKI A., STEFANOWICZ E., TARASENKO S.V., TARASENKO V.V., KISIELEWSKI M., RENARD D., Phys. Rev. B, 55 (1997), 15092.
[9] ROBINSON M., AU Y., KNEPPER J.W., YANG F.Y., SOORYAKUMAR R., Phys Rev. B, 73 (2006), 224422.

Received 10 May 2007
Revised 6 August 2007